AD-A279 028

||||||||||||||||||||||||||

②

AFOSR CONTRACTORS MEETING

IN PROPULSION

JUNE 14-18, 1993

ATLANTIC CITY, NJ

DTIC
ELECTE
S MAY 0 6 1994
B D

94-13629

||||||||||||||||||||||||

DTIC .... D I

94 5 05 017

REPORT DOCUMENTATION PAGE

Public reporting burden for this collection of information is estimated to average 1 hour per response, including the time for reviewing instructions, searching existing data sources, gathering and maintaining the data needed, and completing and reviewing the collection of information. Send comments regarding this burden estimate or any other aspect of this collection of information, including suggestions for reducing this burden, to Washington Headquarters Services, Directorate for Information Operations and Reports, 1215 Jefferson Davis Highway, Suite 1204, Arlington, VA 22202-4302, and to the Office of Management and Budget, Paperwork Reduction Project (0704-0188), Washington, DC 20503.

1. AGENCY USE ONLY (Leave blank)	2. REPORT DATE 20 April 1994	3. REPORT TYPE AND DATES COVERED Technical

4. TITLE AND SUBTITLE

(U) AFOSR Contractors Meeting in Propulsion

5. FUNDING NUMBERS

PE - 61102F
PR - 2308

6. AUTHOR(S)

M A Birkan and J M Tishkoff

7. PERFORMING ORGANIZATION NAME(S) AND ADDRESS(ES)

Air Force Office of Scientific Research
Building 410
Bolling AFB DC 20332-6448

8. PERFORMING ORGANIZATION REPORT NUMBER

AFOSR-TR· 94 0275.

9. SPONSORING/MONITORING AGENCY NAME(S) AND ADDRESS(ES)

AFOSR/NA
110 Duncan Avenue, Suite B115
Bolling AFB DC 20332-0001

10. SPONSORING/MONITORING AGENCY REPORT NUMBER

11. SUPPLEMENTARY NOTES

12a. DISTRIBUTION/AVAILABILITY STATEMENT

Approved for public release; distribution is unlimited

12b. DISTRIBUTION CODE

13. ABSTRACT (Maximum 200 words)

Abstracts are given for research in airbreathing combustion, rocket propulsion, and diagnostics in reacting media supported by the Air Force Office of Scientific Research.

14. SUBJECT TERMS

Instability, Flames, Propulsion, Gas Turbines, Combustion, Shear Layer, Supersonic, Soot, Sprays, Lasers, Fluorescence, Spectroscopy, Rocket, Plasma, Scramjets

15. NUMBER OF PAGES

337

16. PRICE CODE

17. SECURITY CLASSIFICATION OF REPORT	18. SECURITY CLASSIFICATION OF THIS PAGE	19. SECURITY CLASSIFICATION OF ABSTRACT	20. LIMITATION OF ABSTRACT
Unclassified	Unclassified	Unclassified	UL

NSN 7540-01-280-5500

Standard Form 298 (890104 Draft)
Prescribed by ANSI Std. 239-18
298-01

AFOSR CONTRACTORS MEETING IN PROPULSION

Bally's Park Place Casino Hotel and Tower, Atlantic City NJ
14-18 June 1993

MONDAY 14 JUNE 1993

01:15 - 01:30   Welcome and Administrative Announcements

SUPERSONIC COMBUSTION
Chairman: E S Oran, Naval Research Laboratory

01:30 - 02:15   Turbulent Reacting Flows and Supersonic Combustion
C T Bowman, M G Mungal, R K Hanson, and W C Reynolds,
Stanford University

02:15 - 03:00   Chemical Reactions in Turbulent Mixing Flows
P E Dimotakis, California Institute of Technology

03:00 - 03:30   **BREAK**

03:30 - 04:00   Ramjet Research
A S Nejad, WL/POPT

04:00 - 04:30   Theories of Turbulent Combustion in High Speed Flows
F A Williams and P A Libby, University of California, San Diego

04:30 - 05:00   Controlling Combustion and Maximizing Heat Release in a
Reacting Compressible Free Shear Layer
L Keefe, Nielsen Engineering and Research, Inc.

05:00 - 07:30   **BREAK**

07:30 - 09:30   **WORKSHOPS**

Supersonic Combustion and Compressible Turbulence
K Kailasanath, Naval Research Laboratory

Soot
R J Santoro, Pennsylvania State University

TUESDAY, 15 JUNE 1993

TURBULENT COMBUSTION MODELING AND EXPERIMENTS
Chairman: T A Jackson, WL/POSF

08:30 - 09:00   Investigation of the Laminar Flamelet Model of Turbulent Diffusion
Flames
G Kosaly and J J Riley, University of Washington

09:00 - 09:30   Development and Assessment of Turbulence-Chemistry Models in
Highly Strained Non-Premixed Flames
S M Correa, General Electric Corporate Research and
Development

09:30 - 10:00   Mapping Closures for Turbulent Combustion
S B Pope, Cornell University

10:00 - 10:30   **BREAK**

10:30 - 11:00   Reaction Zone Models for Vortex Simulation of Turbulent
Combustion
A F Ghoniem, Massachusetts Institute of Technology

11:00 - 11:30   Two- and Three-Dimensional Measurements in Flames
M B Long, Yale University

11:30 - 12:00   High Resolution Measurements of Mixing and Reaction Processes
in Turbulent Flames
W J A Dahm, University of Michigan

12:00 - 01:30   **LUNCH**
FLAMES AND MIXING
Chairman: A S Nejad, WL/POPT

01:30 - 02:00   Combustion Research
W M Roquemore, WL/POSF

02:00 - 02:30   Studies on High-Pressure and Unsteady Flame Phenomena
C K Law, Princeton University

02:30 - 03:00   A Study of Mixing and Combustion in the Presence of a Strong
Streamwise Vorticity
M Samimy and L Kennedy, Ohio State University

03:00 - 03:30   **BREAK**

RAM ACCELERATORS AND OBLIQUE DETONATION WAVES

03:30 - 04:00 Fundamental Research to Advance Ram Accelerator Technology
Capt R Drabczuk, WL/MNSH

04:00 - 04:30 Numerical Studies of the Ram Accelerator
E S Oran, J P Boris, K Kailasanath,and C-P Li, Naval Research
Laboratory

04:30 - 05:00 Initiation and Modification of Reaction by Energy Additions: Kinetic
and Transport Phenomena
F E Fendell and M-S Chou, TRW Space and Technology Group

05:00 - 07:30 **BREAK**

07:30 - 09:30 **WORKSHOPS**

Status and Future Directions for Modeling Turbulent
Combustion
A F Ghoniem, Massachusetts Institute of Technology

Supercritical Fuel Behavior
L D Chen, University of Iowa

WEDNESDAY, 16 June 1993

08:30 - 10:00 Business Meeting for AFOSR Grantees and Contractors Supported
In Dr Tishkoff's Research Subareas

10:00 - 10:30 **BREAK**

10:30 - 12:30 **WORKSHOP AND GENERAL DISCUSSION**

Transitioning Research To Propulsion Technology
W M Roquemore, WL/POSF

12:30 - 14:30 **LUNCH**

14:30 - 17:00 **INVITED SPEAKERS**
(Agenda will be provided at the meeting)

THURSDAY, 17 JUNE 1993

SOLID-PROPELLANT ROCKET DYNAMICS
Chairman: T Edwards, Wright Laboratory

08:30 - 09:20	Nonsteady Combustion Mechanisms of Advanced Solid Propellants M Branch, University of Colorado; M Beckstead, Brigham Young University; M Smooke, Yale University; V Yang, Penn State University
09:20 - 09:40	Thermal Decomposition Mechanisms of New Polycyclic Nitramines T B Brill, University of Delaware
09:40 - 10:00	Combustion Kinetics of HEDMs and Metallic Fuels A Fontijn, RPI
10:00 - 10:20	**DISCUSSION ON PROPELLANT COMBUSTION DYNAMICS PROGRAM**
10:20 - 10:40	**BREAK**
10:40 - 11:00	Nonlinear Acoustic Processes in Solid Rocket Engines D R Kassoy, University of Colorado
11:00 - 11:20	DNS of Acoustic-Mean Flow Interactions in Solid Rockets S Mahalingam, University of Colorado
11:20 - 11:40	Flame Driving and Flow Turning Losses in Solid Rockets B T Zinn, Georgia Tech
11:40 - 12:00	Combustion and Plumes D Weaver, Phillips Laboratory
12:00 - 12:30	**DISCUSSION ON CHAMBER DYNAMICS PROGRAM**
12:30 - 14:00	**LUNCH**

PLASMA PROPULSION
Chairman: R H Frisbee, Jet Propulsion Laboratory

ARCJET PROPULSION

14:00 - 14:20	Laser Fluorescence Diagnostics for Arcjet Thrusters D Keefer, UTSI
14:20 - 14:40	Fundamental Studies of the Electrode Regions in Arcjet Thrusters M Cappelli, Stanford University
14:40 - 15:00	Plasma Diagnostics R Spores, Phillips Laboratory
15:00 - 15:30	**BREAK**
15:30 - 15:50	Performance Characteristics of Plasma Thrusters M Manuel-Martinez, MIT
15:50 - 16:10	Laser Sustained Plasmas at Non-LTE Conditions H Krier, University of Illinois at Urbana-Champaign
16:10 - 16:30	**DISCUSSION ON THE ARCJET PROGRAM**
16:30 - 16:50	**BREAK**

CLUSTER ION PROPULSION

16:50 - 17:10	A High Thrust Density, C60 Cluster, Ion Propulsion V J Hruby, Busek Co, Inc.
17:10 - 17:30	Electrostatic Ion Propulsion using C60 Molecules D Goodwin, Caltech
17:30 - 17:50	**DISCUSSION ON THE CLUSTER ION PROPULSION**

FRIDAY, 18 JUNE 1993

LIQUID-PROPELLANT ROCKETS
Chair: D Weaver, Phillips Laboratory

08:30 - 08:50	Fundamentals of Acoustic Instabilities in Liquid-Propellant Rockets F A Williams, University of California
08:50 - 09:10	Modeling Liquid Jet Atomization Processes S D Heister, Purdue University
09:10 - 09:30	Nonlinear Response of Intrinsic Acoustic Oscillations in Combustion-Driven Devices S B Margolis, Sandia National Laboratories
09:30 - 09:50	Acoustic Waves in Complicated Geometries and their Interactions with Liquid-Propellant Droplet Combustion V Yang, Penn State
09:50 - 10:10	**DISCUSSION ON ATOMIZATION/COMBUSTION MODELING**
10:10 - 10:30	**BREAK**
10:30 - 10:50	Supercritical Droplet Behavior D G Talley, Phillips Laboratory
10:50 - 11:10	Combustion Instability Phenomena of Importance to Liquid Propellant Rocket Engines R J Santoro, Penn State
11:10 - 11:30	Liquid Rocket Motor Combustion Stability Using Coaxial Injectors M M Micci, Penn State
11:30 - 11:50	**DISCUSSION ON EXPERIMENTAL STUDIES of INJECTION PROCESSES**
11:50	**ADJOURN**

A STUDY OF MIXING AND COMBUSTION IN SUPERSONIC FLOW

AFOSR Contract No. 90-0151

Principal Investigators: C. T. Bowman, R. K. Hanson, M. G. Mungal and W. C. Reynolds

Department of Mechanical Engineering
Stanford University
Stanford, CA 94305-3032

SUMMARY/OVERVIEW:

An experimental and computational investigation of supersonic combustion flows is being conducted to gain a more fundamental understanding of mixing and chemical reaction in supersonic flows. The research effort comprises three interrelated elements: (1) an experimental study of mixing and combustion in a supersonic plane mixing layer; (2) development of laser-induced fluorescence techniques for time-resolved, two-dimensional imaging of species concentration, temperature and velocity; and (3) numerical simulations and analyses of compressible reacting flows.

TECHNICAL DISCUSSION:

Experiments in Reacting Supersonic Flows

This aspect of our research focuses on the experimental study of the combined effects of compressibility and heat release on the structure of a reacting mixing layer. The experiments are performed in a large-scale blowdown facility that produces a plane mixing layer between a supersonic, high-temperature oxidizer stream and a subsonic, ambient temperature fuel stream. The high-temperature stream is produced by burning oxygen-enriched air and hydrogen in a vitiation heater and expanding the combustion products through a supersonic nozzle. The fuel stream is produced by mixing hydrogen with an inert gas and expanding the mixture to a subsonic Mach number. Several techniques are used to visualize the mixing layer: instantaneous schlieren images provide mixing layer growth rates; time-averaged ultraviolet emission images are used to establish the mean location of the reaction zone; and, simultaneous planar laser-induced fluorescence (PLIF) images of OH and acetone are used to determine the instantaneous structure of the reacting mixing layer.

A range of experimental conditions that provide variation in convective Mach number and heat release are under investigation. A representative selection of flow images is shown in Fig. 1 for a low-heat release, compressible condition. Figure 1a shows a composite schlieren image of the flow. A composite time-averaged UV emission image is shown in Fig. 1b. Comparison of Figs. 1a and 1b shows that the mean reaction zone is located on the high-speed, high-temperature side of the mixing layer and that the mean flame standoff distance from the splitter tip is approximately 5 cm. Figure 1c shows a typical simultaneous OH/acetone PLIF image. The acetone image indicates the regions of unburned fuel, while the OH image indicates regions of burning (for further details, see Ref. 1). Detailed examination of a number of images reveals the following structural features: a distinct boundary exists between regions of OH signal and regions of acetone signal; in regions where acetone signal is observed, there appears to be two levels of fluorescence, separated by a distinct boundary. These images suggest a mixing layer structure comprising primarily two zones: a hot combustion zone adjacent to the high-temperature, oxidizing stream and a cooler, non-reacting zone adjacent to the ambient temperature fuel stream. The structural features in the images are reminiscent of those seen in nonreacting mixing layers at similar levels of compressibility.
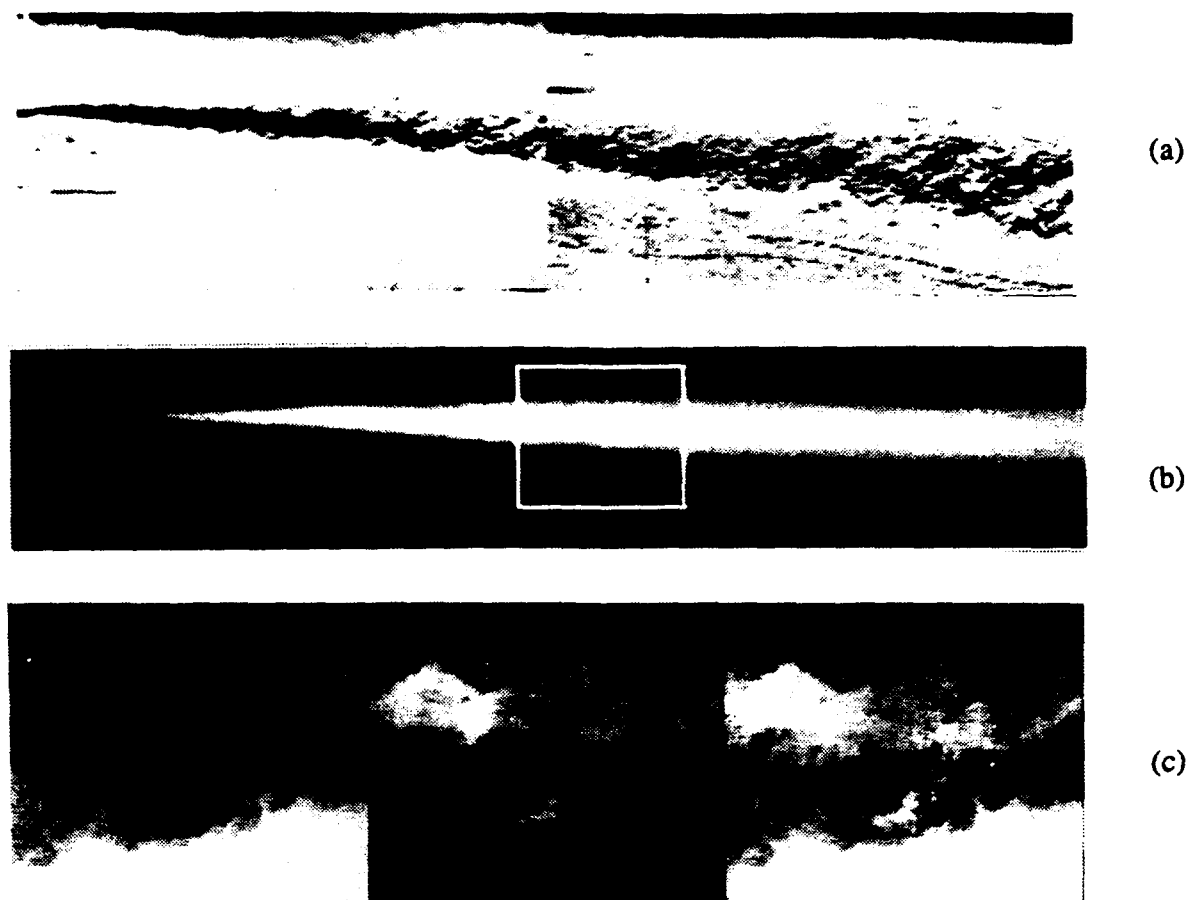
(a)

(b)

(c)

Fig. 1 Images of a $M_{c1} = 0.8$ reacting flow (From Ref. 1). High-speed stream conditions ($T_{o1} = 1600K$, $M_1 = 1.4$, $X_{O2} = 0.23$); low-speed stream conditions ($T_{o2} = 270K$, $M_2 = 0.3$, $X_{H2} = 0.10$): (a) schlieren image; (b) time-averaged UV emission image; the rectangular box shows the location of the PLIF images; (c) simultaneous OH/acetone PLIF images: left, acetone image; center, OH image; right, superposed OH/acetone image.

In addition to the reacting flow experiments, some preliminary experiments have been performed in nonreacting flows with the goal of increasing the amount of mixing in compressible mixing layers. The approach is the use of mild unstable streamwise curvature to enhance the Taylor-Goertler instability of the flow. A 15 percent increase in spreading was achieved, with increased three-dimensionality present in the layer. These early experiments also suggest that the combined use of select disturbances and curvature promises greater enhancement; these approaches will be investigated in the near future.

Development of Supersonic Flow Diagnostics

This aspect of our research is aimed at establishing planar laser-induced fluorescence (PLIF) techniques for imaging in supersonic flowfields. Successful methods will be applied in the supersonic combustion facility. During the past year, good progress has been made in establishing methods for quantitative imaging of three gasdynamic parameters: rotational temperature, vibrational temperature, and velocity.

Our recent work includes two key experimental advances: (1) the use of two tunable dye laser sources and two intensified CCD cameras, which enable acquisition of two closely-spaced (250 nsec) PLIF images for the same measurement plane; and (2) the use of on-line monitoring of

- 8 -

laser energy, sheet intensity distribution and laser spectral distribution for each laser pulse. The ability to acquire essentially instantaneous images at two wavelengths is important, since it provides access to rotational and vibrational temperature through Boltzmann ratios, and on-line measurement of laser parameters is essential in improving the quantitativeness of PLIF data.

An example of this work is shown in Fig. 2. Here, two PLIF images of rotational temperature in a $NO/H_2O/Ar$ mixture that was shock-heated and then expanded through a supersonic nozzle are shown. The images acquired with the two-laser, two-camera strategy, are shown. The temperature is inferred from the ratio of PLIF signals acquired via excitation of rotational levels in the $v = 0$ level of NO (Fig. 2a), and also via excitation of rotational levels in two separate vibrational levels (Fig. 2b). A comparison with calculated rotational temperatures obtained using method of characteristics (MOC) is shown in Fig. 2c. A more detailed description of this work is given in Ref. 2.
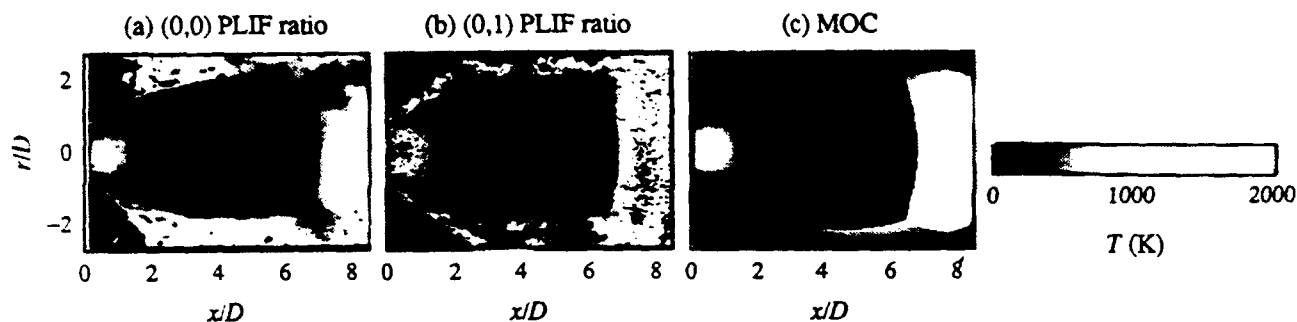

Fig. 2 Rotational temperature images obtained from: (a) the ratio of (0,0) $Q_2+R_{12}(6)$ to (0,0) $Q_1+P_{21}(5)$ frame-averaged images; and (b) the ratio of (0,1) $P_2+Q_{12}(6)$ to (0,1) $Q_1+P_{21}(5)$ frame-averaged images; (c) MOC calculation (from Ref. 2).

We also have obtained results for the instantaneous vibrational temperature and for velocity. For velocity measurements, only one laser, set to a specific wavelength and passed through the flow in two directions (with one beam delayed by 300 nsec), is used. The two PLIF images can be converted to two components of velocity in the case of axisymmetric flows. Two lasers and four cameras could be used to obtain instantaneous, two-component velocity images in a nonaxisymmetric flow.

Analysis and Simulation of Supersonic Reacting Mixing Layers

In this phase of our program, we are using a combination of linear stability analysis and direct numerical simulations to investigate the structure of the large-scale eddies and reaction zone in a model representation of the reacting mixing layer between two streams moving supersonically with respect to one another. The mean field of the model flow develops in time, and it is assumed that this corresponds approximately to the development that would be seen by an observer moving with the eddies in a spatially-developing flow. The analyses and simulations consider the three-dimensional, time-dependent character of the flow using simple one-step, finite-rate chemistry.

Results to date show that the key to the flow structure is the profile of *mean vorticity times mean density*. Stability analysis shows that eddies form in regions where this profile has a maximum and move approximately at the mean speed at this location. In a cold or subsonic mixing layer, there is but one such peak in the middle of the layer, where the mean velocity gradient is largest, and, hence, the flow structure is a single set of eddies. At low convective Mach numbers, these eddies are highly two-dimensional, but as the convective Mach number is increased beyond 0.6, the structures become more oblique (hairpins).

With high heat release or at high convective Mach number, the mean density can be very low in the vicinity of the flame, with the result that the critical profile has two peaks, one on each side of the flame, which resides near the point of maximum mean velocity gradient. Hence, in this situation, there are two sets of eddies, one in each stream. The mixing layer then consists of co-layers, each of which moves independently (see Fig. 3). Each co-layer mixes fluid from its free-stream with product from the flame zone, but there is no direct mixing of fluid from the two streams and, hence, no direct mixing of fuel and oxidizer. Heat release also reduces the tendency towards three-dimensionality, so that, even at convective Mach numbers above 0.6, the dominant structure in each co-layer is a nearly two-dimensional transverse vortex. There is very little interaction between the co-layers.
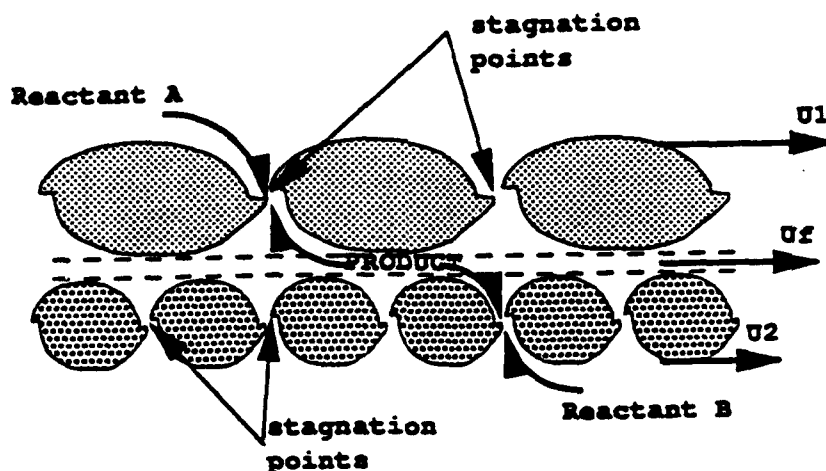

Fig. 3. Schematic representation of the compressible plane reacting mixing layer (from Ref. 3).

The simulations show that the onset of small-scale streamwise vortices (the small-scale transition) occurs in each co-layer *in the absence of large-scale transverse vortex pairing* (unlike uniform-density mixing layers), and that after this transition the co-layers remain essentially independent. The flow structure is then preferentially spanwise large-scale structures with superimposed small-scale energetic streamwise vortices that act to enhance the mixing and, hence, the reaction rate. This suggests that artificial introduction of streamwise vortices may provide a means for enhancing reaction in supersonic mixing layers.

References

1. Miller, M. F., Island, T. C., Yip, B., Bowman, C. T., Mungal, M. G. and Hanson, R. K., "An Experimental Study of the Structure of a Compressible, Reacting Mixing Layer," AIAA-93-0354, 31st AIAA Aerospace Sciences Meeting, Reno, NV, Jan. 1993.

2. Palmer, J. L. and Hanson, R. K., "Planar Laser-Induced Florescence Imaging in Free Jet Flows with Vibrational Nonequilibrium," AIAA-93-0046, 31st AIAA Aerospace Sciences Meeting, Reno, NV, Jan. 1993.

3. Planche, O.H., and Reynolds, W.C., "A Numerical Investigation of the Compressible Reacting Mixing Layer," Report TF-56, Thermosciences Division, Department of Mechanical Engineering, Stanford University, 1992.

CHEMICAL REACTIONS in TURBULENT MIXING FLOWS

P. E. Dimotakis* and A. Leonard**

Graduate Aeronautical Laboratories
California Institute of Technology, Pasadena, CA 91125

Summary/Overview

The purpose of this research is to conduct fundamental investigations of turbulent mixing, chemical reaction, and combustion processes; in turbulent, subsonic, and supersonic free shear flows. The program is comprised of an experimental effort, an analytical and modeling effort, a computational effort, and a diagnostics development and data-acquisition effort, as directed by the specific needs of our experiments. To elucidate molecular transport effects, experiments and theory concern themselves with both liquids and gases. The computational studies are, at present, focused on fundamental issues pertaining to the numerical simulation of compressible flows with strong fronts.

Technical discussion

Recent turbulent mixing data on shear layers and jets suggest that the mixing transition, documented to take place at $Re \approx 10^4$ in shear layers, also occurs in turbulent jets. Analogous transitions, at roughly the same Reynolds number, also seem to occur in a variety of other flows, suggesting that such a transition is a universal property of turbulence.[1] On the basis of scaling arguments, it was argued that the transition Reynolds number of $Re \approx 10^4$ represents a minimum Reynolds number for fully-developed turbulence. At higher Reynolds numbers, the dependence of mixing phenomena on Reynolds number is found to be much weaker, but not universal.

Previous results in compressible shear layers are difficult to interpret as a consequence of possible Reynolds number effects. Although compressibility effects on mixing have been addressed in work to date, the issue of Reynolds number effects in compressible flows has only been raised.[2,3] We have recently conducted a series of four "flip" experiment pairs,[4,5] at moderate compressibility, to address Reynolds number effects. The experiments utilized mixtures of helium and argon, to vary Reynolds number, and consisted of two flows with identical compressibility, and velocity, density, and specific heat ratios. The resulting chemical product thicknesses for low ϕ are plotted in Fig. 1, along with previous subsonic data, and the two compressible points from Hall *et al.*[2]

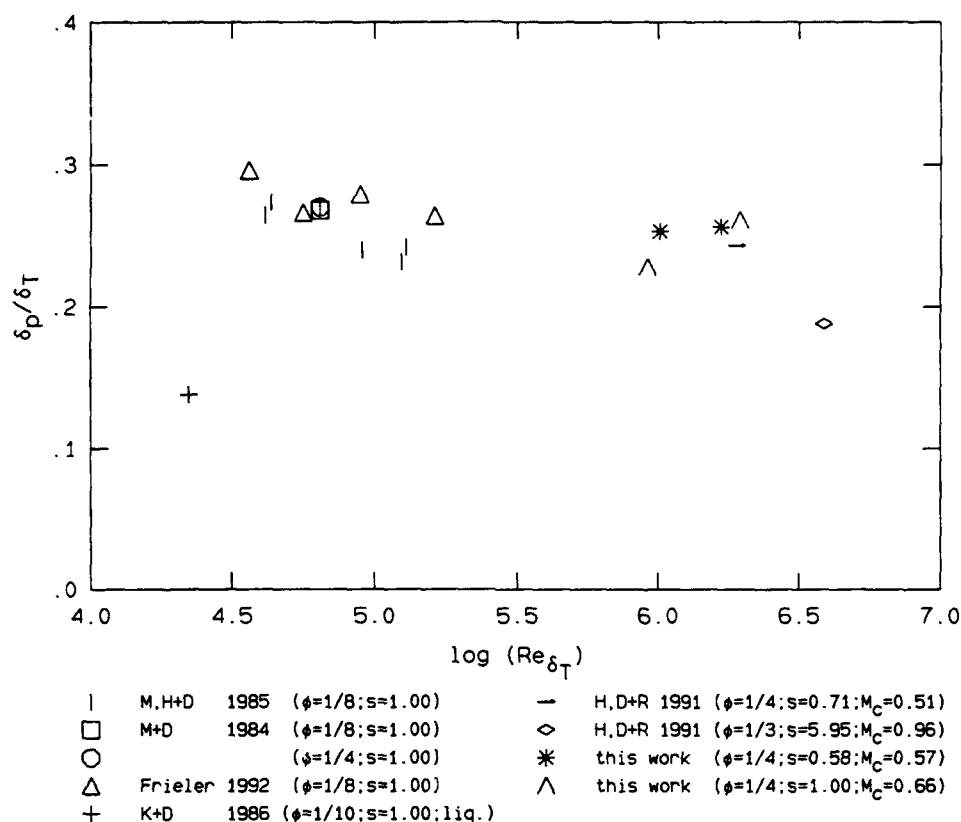* Professor, Aeronautics & Applied Physics.

** Professor, Aeronautics.

Plot axes: vertical axis δ_p/δ_T from .0 to .4; horizontal axis $\log (Re_{\delta_T})$ from 4.0 to 7.0

Legend:

I	M,H+D	1985	$(\phi=1/8;s=1.00)$
□	M+D	1984	$(\phi=1/8;s=1.00)$
O			$(\phi=1/4;s=1.00)$
△	Frieler	1992	$(\phi=1/8;s=1.00)$
+	K+D	1986	$(\phi=1/10;s=1.00;liq.)$

—	H,D+R	1991	$(\phi=1/4;s=0.71;M_c=0.51)$
◇	H,D+R	1991	$(\phi=1/3;s=5.95;M_c=0.96)$
*	this work		$(\phi=1/4;s=0.58;M_c=0.57)$
∧	this work		$(\phi=1/4;s=1.00;M_c=0.66)$

FIG. 1 Normalized chemical product thickness for low stoichiometric mixture ratios, ϕ. The symbol s, in the legend, denotes the shear layer freestream density ratio, ρ_2/ρ_1, for each experiment.

The data do not indicate a strong dependence of the mixing on Reynolds number, in the range they cover. This confirms the observation that the difference between the high and medium compressibility cases in Hall *et al.*is primarily due to compressibility and not the difference in Reynolds number.[2] The new results are also consistent with the previously documented decrease of chemical product formation in incompressible shear layers, with increasing Reynolds number.[6-8] The overall reduction in mixing seems mostly attributable to Reynolds number effects, *i.e.*, compressibility effects do not appear dominant at medium compressibility.[1]

Our work in non-premixed turbulent jet flames was extended to the study of the effects of heat release.[†] These were investigated for a range of adiabatic flame temperatures where the flow is no longer in purely jet-momentum-dominated flow regime. Line-integrated temperature measurements[9,10] were performed along the axial direction in the flame and post-flame regions. The measurements revealed a

---

† This part of the work was co-sponsored by the Gas Research Institute.

substantial temperature overshoot in the flame region, close to the flame tip, and a net cooling in the post-flame region. These new, previously unmodeled, results are significant in the context of radiative heat transfer, as well as NO_x production, which are very sensitive to the temperature field in the combustion region.

In our investigation of liquid-phase turbulent mixing flows, during this last year, we focused on the behavior of conserved isoscalar surfaces in the far field of turbulent jets. Using a low-noise, high-resolution ($1,024 \times 1,024$ pixel), cryogenically cooled, CCD camera, we have obtained spatial images of the scalar field across the full transverse extent of the jet. Preliminary experiments were performed at a Reynolds number of 1.8×10^4, corresponding to flow conditions in fully-developed turbulent flow,[1] with the intent of studying the evolution of the geometric properties of the three-dimensional, isoscalar surfaces as a function of Reynolds number. In other work in liquid-phase, turbulent jet mixing, recent data on the behavior of the scalar fluctuations, in the far field of turbulent jets,[11] were processed to yield spectral information as a function of Reynolds number. The new spectra do not exhibit the expected, Reynolds-number independent, power-law behavior and do not support the classical k^{-1} theories below the Kolmogorov scale.[12]

Progress in our computational work to date has been documented in two, recent, publications.[13,14] In this effort, a new approach for computing multidimensional flows of an inviscid gas has been developed. It may be considered an extension of the method of characteristics to multidimensional, unsteady gas dynamics. In work in prorgess, the new method is being tested and compared with other conventional schemes. Specifically, we have developed our own version of the Godunov scheme known as MUSCL and compared with results published in the literature (e.g., Ref. 15). In addition, we are currently computing a variety of flows aimed at understanding the physics of the interaction of shock waves with a shear layer, or contact discontinuity. This effort is helped by the adaptive gridding capability that we have developed. A hierarchy of overlapping grids can be used to compute different parts of the flow with different resolution. This is particularly important when computing regions of wave interaction where a higher resolution is often needed.

In our work on diagnostics development and instrumentation, we have made significant advances in Image Correlation Velocimetry (work cosponsored by ONR Grant N00014-91-J-1968),[16] as well as high-speed, single- and dual-image data acquisition. These will be discussed at the Contractors' meeting.

References

[1] Dimotakis, P. E., "Some issues on turbulent mixing and turbulence," GALCIT Report FM93-1 (1993).

[2] Hall, J. L., Dimotakis, P. E., and Rosemann, H., "Some measurements of molecular mixing in compressible turbulent mixing layers," *AIAA 22nd Fluid Dynamics, Plasma Dynamics and Lasers Conference*, Paper 91-1719 (1991).

[3] Dimotakis, P. E., "Turbulent Free Shear Layer Mixing and Combustion," *High Speed Flight Propulsion Systems*, in *Progress in Astronautics and Aeronautics* **137**, Ch. 5, 265–340 (1991).

[4] Koochesfahani, M. M., Dimotakis, P. E., and Broadwell, J. E., "A 'Flip' Experiment in a Chemically Reacting Turbulent Mixing Layer," *AIAA J.* **23**, 1191–1194 (1985).

[5] Koochesfahani, M. M., and Dimotakis, P. E., "Mixing and chemical reactions in a turbulent liquid mixing layer," *J. Fluid Mech.* **170**, 83–112 (1986).

[6] Mungal, M. G., and Dimotakis, P. E., "Mixing and combustion with low heat release in a turbulent mixing layer," *J. Fluid Mech.* **148**, 349–382 (1984).

[7] Mungal, M. G, Hermanson, J. C., and Dimotakis, P. E., "Reynolds Number Effects on Mixing and Combustion in a Reacting Shear Layer," *AIAA J.* **23**, 1418–1423 (1985).

[8] Frieler, C. E., *Mixing and Reaction in the Subsonic 2-D Turbulent Free Shear Layer*, Ph.D. thesis, California Institute of Technology (1992).

[9] Gilbrech, R. J., *An Experimental Investigation of Chemically-Reacting, Gas-Phase Turbulent Jets*, Ph.D. thesis, California Institute of Technology (1991).

[10] Gilbrech, R. J., and Dimotakis, P. E., "Product Formation in Chemically-Reacting Turbulent Jets," *AIAA 30th Aerospace Sciences Meeting*, Paper 92–0581 (1992).

[11] Miller, P. L., *Mixing in High Schmidt Number Turbulent Jets*, Ph.D. thesis, California Institute of Technology (1991).

[12] Miller, P. L., and Dimotakis, P. E., "Measurements of scalar power spectra in high Schmidt number turbulent jets," GALCIT Report FM92-3 (1992).

[13] Lappas, T., *An Adaptive Lagrangian Method for Computing 1-D Reacting Flows and the Theory of Riemann Invariant manifolds for the Compressible Euler Equations*, Ph.D. thesis, California Institute of Technology (1993).

[14] Lappas, T., Leonard, A., and Dimotakis, P. E., "An Adaptive Lagrangian Method for Computing 1-D Reacting and Non-Reacting Flows," *J. Comp. Phys.* **104**, 361–376 (1993).

[15] Woodward, P. R., and Colella, P., "The Numerical Simulation of Two-Dimensional Fluid Flow with Strong Shocks," *J. Comp. Phys.* **54**, 115–173 (1984).

[16] Tokumaru, P. T., and Dimotakis, P. E., "Image correlation velocimetry," GALCIT Report FM92-1 (1992).

Supersonic Combustion Research Laboratory: Part I Design and Fabrication

AFOSR TASK 2308BW

Nejad, A. S.
Aero Propulsion and Power Directorate
Wright-Patterson AFB, Ohio 45433-7655

Summary and Overview

The experimental Research Branch of the Advanced Propulsion Division at Wright Laboratory began taking steps toward the development and installation of a supersonic combustion research facility during FY93. With the push towards hypersonic flight regimes, a large-scale in-house research facility devoted to the study of supersonic fuel-air mixing and combustion provides a clear vehicle for enhancing the basic knowledge and data base through the use of conventional and state-of-the-art non-intrusive diagnostic techniques. These techniques are employed to gain a better understanding of the behavior of the turbulent flows within realistic combustor geometries with and without heat release.

Extensive modifications were required to prepare the existing test cell in building 18C, Room 19 for accepting a supersonic test apparatus. These modifications included the addition of a climatically controlled filtered explosion-proof enclosure to house the supersonic combustion tunnel and the associated laser diagnostic instrumentations, an office space, utility fluids (including water, nitrogen, and shop air) and high voltage explosion proof electrical outlets for the laser systems. Also required for operation of the large-scale supersonic test facility was an air supply system that utilized the air handling capabilities of the Tech Air Facility within the Aero Propulsion and Power Directorate's laboratory complex. The final components required were the actual supersonic combustion tunnel and computer control system used to monitor the supply system valves and flow parameters. An in-house effort to design, fabricate, and install the test hardware began in January 1992 and finished in March 1993. Also during this time, the air supply system installation was completed and the control system logic was developed and installed. Check-out tests of the facility were accomplished in early December 1992 and proved the system successful from the standpoint of system compatibility with Air Tech capabilities and control system.

Combustion Facility Design

Specific operational goal were set at the initiation of the design effort. These goals dealt not only with the air flow characteristics of the facility, but the system maintenance features as well. The underlying objective of the effort was to develop an in-house supersonic research facility capable of allowing studies of the enhancement and control of fuel-air mixing in supersonic combustors with conventional and state-of-the-art non-intrusive diagnostic techniques such as Schlieren

photography, LDV (Laser Doppler Velocimetry), PLIF (Planar Laser Induced Fluorescence), PIV (Particle Image Velocimetry), Mie scattering, and CARS (Coherent Anti-Stokes Raman Scattering). Other design objectives are listed below.

- Variable Mach number capability (1.5 to 3.0)

- Continuous flow operation

- Maximum stagnation conditions of 400 psia and 1660 °R at peak flow rate of 34 lbm/sec

- Nominal 5 inch by 6 inch test section with allowance for nozzle boundary layer growth

- Nominal test section conditions of 7.35 psia and 525 °R

- Optical access to the test section from three side walls and one providing an end-view looking upstream into the combustor

- Spray cooled diffuser to allow combustion and exhaust in to the air facility coolers

- Modularity for ease of maintenance and future facility expansion

- Thermal expansion compensation to negate test section growth movement

The result of the design effort is shown schematically in Figure 1 and the actual supersonic combustion tunnel installed in Room 19 is shown in Figure 2. The nominal operating conditions are given in Table 1.

Much work remains for this facility before mixing experiments commence. In addition to check out tests, a complete facility calibration is necessary to document the flow qualities of the new tunnel. Of specific interest are tunnel boundary layer surveys, test section Mach number distribution, nozzle pressure distribution, and flow visualization with in the test section all for a variety of design and off-design operating conditions. These tests will serve as baseline documentation for all future experiments which will be undertake in the new facility.

Table 1: Nominal Operating Conditions

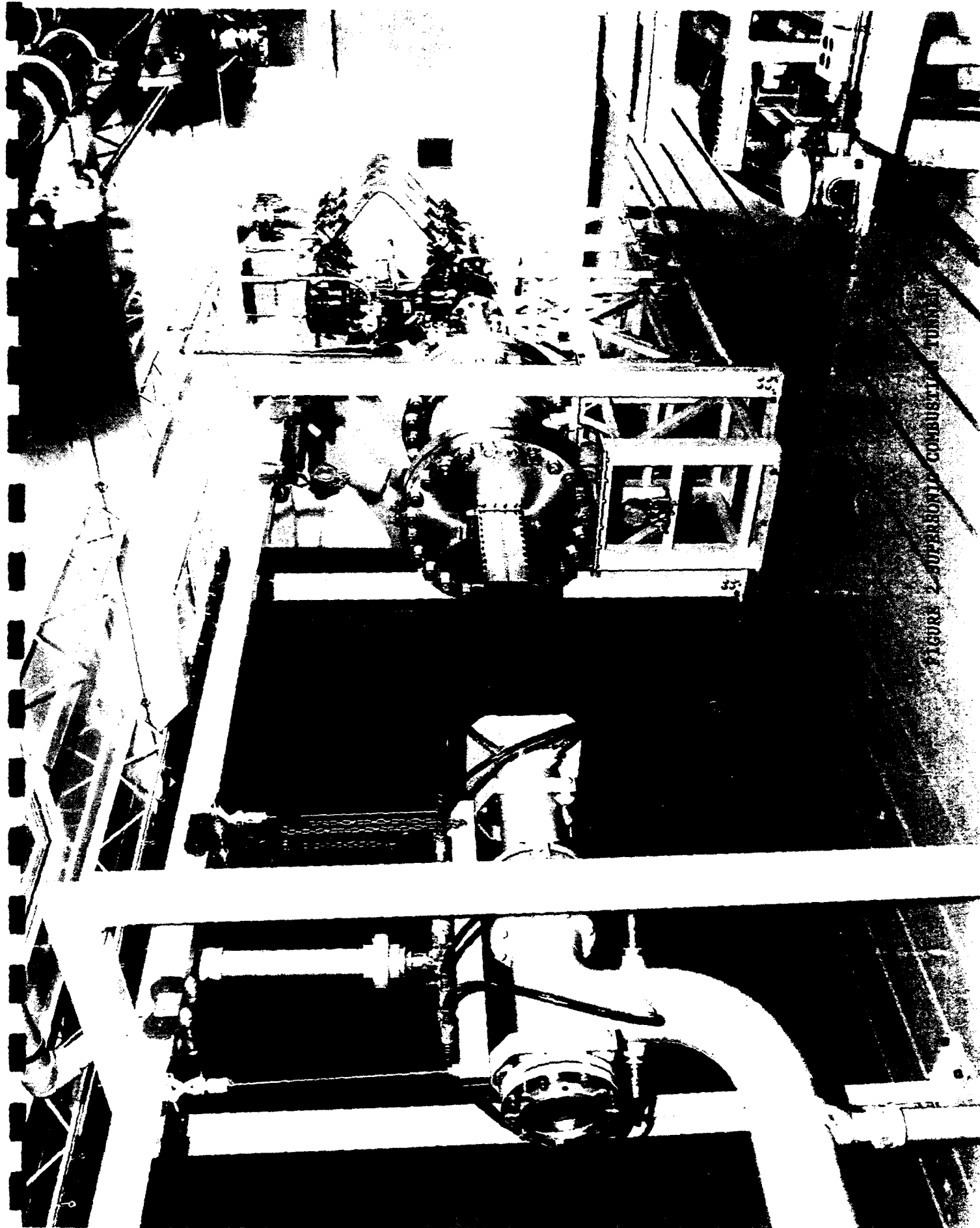| Mach No	P, psia	T, °R	P_o, psia	T_o, °R	m, lbm/sec
1.5	7.35	525	26.98	761	13.70
2.0	7.35	525	57.50	945	18.26
2.5	7.35	525	125.6	1181	22.82
3.0	7.35	525	270	1470	27.40

FIGURE 2. SUPERFRONT COMBUSTION TURBINE

THEORIES OF TURBULENT COMBUSTION IN HIGH SPEED FLOWS
(AFOSR Grant No. F49620-92-J-0184)

Principal Investigators: F. A. Williams and P. A. Libby

Department of Applied Mechanics and Engineering Sciences
University of California San Diego, La Jolla, CA 92093-0310

Summary/Overview

The objective of this research is to improve understanding of the chemical kinetics and fluid dynamics of turbulent combustion in high-speed flows. At present, ignition properties and flow structures of counterflowing streams of hydrogen and air are being addressed by numerical and asymptotic approaches. The results may help to enhance capabilities of reasonable computations of high-speed reacting flows.

Technical Discussion

This grant is a continuation of a previous AFOSR grant having the same general objectives. The final reference citations for publication of research supported by the previous AFOSR grant, not available for the previous year's summary, is listed as initial references [1,2]. With attention focused on flamelets in hydrogen-air system, three separate studies presently underway are reported here; two of these studies involve laminar counterflow diffusion flames and the other is directed towards understanding turbulent flamelets in strained fields.

The motivation for focusing on the flamelets stems from the initial evaluation, under the previous grant, indicating that in the application to aerospace propulsion, the hydrogen-air system lies in the reaction-sheet regime. Those initial estimates were made prior to development of the extensive database on hydrogen-air diffusion flames, from the previous grant. Because of this, it seemed reasonable at the outset to reevaluate the combustion regimes, on the basis of the new information that has now been accumulated. The results of this reevaluation are shown in Figure 1. which reaffirms that reaction-sheet regimes are most relevant. In comparison with the original estimate, there has been a narrowing of the most probable range and a downward displacement of towards the distributed-reaction regime as a consequence of the improved chemical-kinetic and combustion information.

Ignition in Hydrogen-Air Mixtures

Previous work addressed steady burning and extinction in hydrogen-air systems but did not consider the ignition branch of the diffusion-flame S curve. Autoignition of hydrogen with hot air is of fundamental interest in high-speed propulsion; for instance, in a supersonic combustor the fuel jet is expected to be injected into and ignited by a stream of hot air heated by shocks. Typical studies of ignition focus on the chemistry with little or no attention being paid to the fluid dynamics. Complex interactions which are likely to play an important role in the ignition processes in real flows are thus ignored. To help to understand these interactions, current attention is focused on the ignition of a cold jet of hydrogen impinging against an opposed jet of heated air.

The problem is reduced to a two-point boundary-value problem for ordinary differential equations. The numerical solution to the discretized equations, normally obtained employing Newton's method or a variant thereof, encounters difficulties in the neighborhood of turning points where the derivative of the solution with respect to a parameter of the problem becomes infinite (for example, at the extinction condition). To circumvent these difficulties, a modification of the basic algorithm is introduced in the present work, employing a path-

tracing continuation method of Smooke, in which points on the arc of solutions are computed. This method has now succeeded in generating the ignition branch.

Computations began with the 21-step mechanism which was used for extinction studies reported earlier [2,3]. Numerical integrations were also performed with a different chemical scheme proposed by Smooke and his coworkers. For dilute hydrogen flames at one atmosphere pressure, a large discrepancy in the extinction and ignition strain rates was observed with increasing feed temperature of the air stream. Furthermore, thermal diffusion was seen to play a surprisingly important role in diluted flames (see Figure 2). In view of these unexpected preliminary results, a critical assessment of the reaction rates was deemed warranted. After an extensive survey of the literature and discussions with other researchers, especially Yetter, the 21-step chemical-kinetic scheme with associated rate parameters shown in Table 1 was selected are representing the best information currently available.

To test the updated chemistry, flame speeds for hydrogen-air, wet CO and methane-air mixtures were calculated. Figure 3 shows the dependence of the hydrogen-air flame speeds on the initial hydrogen concentration. Also shown in Figure 3 are the experimental results obtained by various researchers and the numerical results from Smooke and co-workers. The agreement between theory and experiment is seen to remain excellent over a wide range of initial conditions. A flame speed of 38.6 cm/s for stoichiometric methane-air flames was obtained, in good agreement with the experimental value of 38–40 cm/s. Of particular interest in the new chemical scheme is the rate of the chain-branching reaction $H + O_2 \rightarrow OH + O$, which is based on the recent Stanford shock-tube experiments. The new rate provides a slightly larger radical pool, and unlike the rate recommended by Baulch et al. in their recent 1992 review, exhibits the correct direction of the temperature dependence for the reverse reaction $OH + O \rightarrow H + O_2$ in the temperature range of 500–3000 K.

Calculations to characterize the ignition of hydrogen-air mixtures over a wide range of conditions of interest in high-speed propulsion devices are now being performed with the updated chemical scheme.

Structures of Counterflow Diffusion Flames with Small Stoichiometric Mixture Fractions

Asymptotic methods were used to evaluate a characteristic diffusion time for counterflow diffusion flames, a quantity of utmost importance in analyses of flame structure and extinction. Attention was restricted to the important limit of small values of the stoichiometric mixture fraction, which resulted in large values of the stream function at the reaction sheet, f_s, a quantity which was then employed as a large expansion parameter. As shown in Figure 4, three distinct layers were identified inside the viscous layer: (1) a convective-diffusive layer on the oxidizer side of the reaction sheet, (2) a rotational inviscid layer on the fuel side of the reaction sheet, and (3) a fuel-product mixing layer in the vicinity of the stagnation plane; all three of these layers were analyzed and matched. The matching produced analytic expressions for the stream function and mixture fraction at the reaction sheet and corrected formulas for the characteristic diffusion time previously derived on the basis of constant-density or nonreactive-mixing assumptions. Comparison between analytical and numerical results demonstrate that the analytical results obtained from the present analysis provide accurate expressions for the characteristic diffusion times and stoichiometric scalar dissipation rates [4]. The results provide improved predictions of the diffusion-flame structure and extinction.

Nonpremixed Flames in Stagnating Turbulence

It is becoming widely recognized that the study of flames in stagnating turbulence provides a powerful vehicle for examining fundamental issues in turbulent combustion. For the present discussion the flow of interest consists of two coaxial, axisymmetric and closely spaced jets within which a turbulence-generating grid is installed. By changing the mean velocity from each jet, the entire range of chemical behavior from equilibrium to extinction can be covered in one experimental setup. The initial experimental investigations of these flames were confined to premixed systems, i. e. to a turbulent reactant stream either impinging on a wall or opposing another reactant stream, but recently preliminary results of an experiment involving a flame in a turbulent methane stream opposing a turbulent airstream have been reported. Since the only theory of flames in stagnating turbulence is concerned with premixed systems, an analysis of the nonpremixed case has been started under the present program.

The initial results are based on the thin-flame approximation and on chemical equilibrium, with matching to outer zones imposed on each side of the flame. This approximation involves two nonreactive streams impinging on the opposite sides of a turbulent flame whose thickness is small compared with the jet spacing. The resultant calculated temperature distribution exhibits a peak value and general shape in excellent agreement with experiments, but the predicted thickness in physical space is an order of magnitude too small. In brief, the thin-flame approximation is not applicable to the experimental conditions. The combination of heat release and of turbulent length scale preclude quantitative comparison of theory with these experiments. Accordingly, an alternative analysis has been developed, describing in one set of equation the entire flow from one jet exit plane to the other. The numerical treatment of this new set of equation is underway. Initial application will be to the methane-air system, to permit comparison with available experimental data; if the agreement is satisfactory, with or without refinements to the theory, the analysis will then be applied to the hydrogen-air system. Additional studies along these lines involve the effects of finite chemical rates, so that extinction and ignition can be analyzed. These studies will clearly relate to the flamelet analyses described earlier.

References

[1] G. Balakrishnan, C. Treviño, and F. Mauss. Asymptotic structure of hydrogen-air diffusion flames. *Combustion and Flame*, 91(3-4):246–256, December 1992.

[2] E. Gutheil, G. Balakrishnan, and F. A. Williams. Structure and extinction of hydrogen-air diffusion flames. In N. Peters and B. Rogg, editors, *Reduced Kinetic Mechanisms for Application in Combustion Systems.* Springer Verlag, Berlin, 1993.

[3] G. Balakrishnan. *Studies of Hydrogen-Air Diffusion Flames and of Compressibility Effects, Related to High Speed Propulsion.* PhD thesis, University of California San Diego, September 1992.

[4] J. S. Kim and F. A. Williams. Structures of flow and mixture fraction fields for counterflow diffusion flames with small stoichiometric mixture fractions. *SIAM Journal on Applied Mathematics*, 53(6), to appear, December 1993.
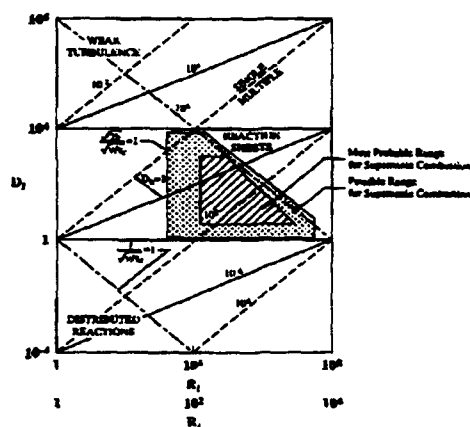
Figure 1: The regimes of hydrogen-air supersonic combustion for aerospace-plane applications, in a plane of large-eddy Reynolds number R_ℓ and Damköhler number D_ℓ.
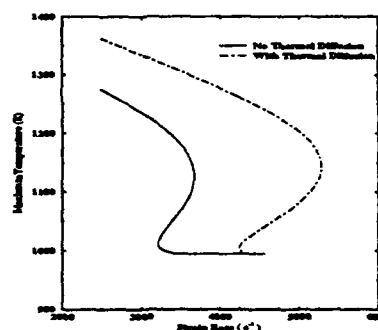

Figure 2: The dependence of the maximum temperature on the strain rate for a diluted hydrogen air flame. Mole fraction of hydrogen in fuel feed = 0.16. Temperature of the fuel and oxidizer streams are 298 K and 995 K respectively
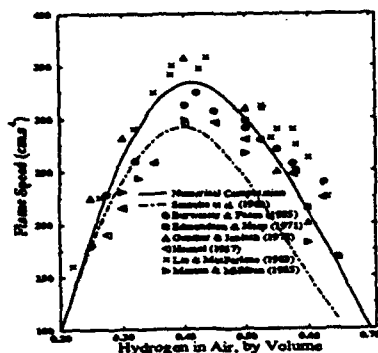
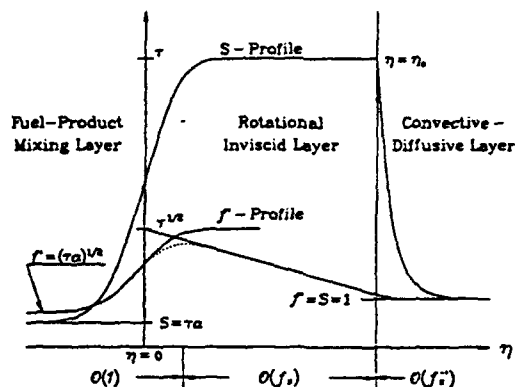**Figure 3:** Effect of hydrogen concentration on burning velocity.

Figure 4: Schematic illustration of the distinct layers in the structure of a counterflow diffusion flame for small values of the expansion parameter f_s^{-1}

Table 1: *Specific Reaction-Rate Constants for the Hydrogen-Oxygen Reaction System Adopted in the Present Study.*

No.	Reactions	A[a]	n[a]	E[a]
1	$H + O_2 \rightleftharpoons OH + O$	3.52×10^{16}	-0.7	17070
2	$H_2 + O \rightleftharpoons OH + H$	5.06×10^4	2.67	6290
3	$OH + OH \rightleftharpoons H_2O + O$	$k = 5.46 \times 10^{11} \exp(0.00149T)$		
4	$H_2 + OH \rightleftharpoons H_2O + H$	1.17×10^9	1.3	3626
5[b]	$H + O_2 + M \rightarrow HO_2 + M$	6.76×10^{19}	-1.42	0
6	$H + HO_2 \rightarrow OH + OH$	1.70×10^{14}	0.0	874
7	$H + HO_2 \rightarrow H_2 + O_2$	4.28×10^{13}	0.0	1411
8	$OH + HO_2 \rightarrow H_2O + O_2$	2.89×10^{13}	0.0	497
9[c]	$H + H + M \rightarrow H_2 + M$	1.80×10^{18}	-1.0	0
10[b]	$H + OH + M \rightarrow H_2O + M$	2.20×10^{22}	-2.0	0
11	$HO_2 + HO_2 \rightarrow H_2O_2 + O_2$	3.02×10^{12}	0.0	1390
12[d]	$H_2O_2 + M \rightleftharpoons OH + OH + M$	1.20×10^{17}	0.0	45500
13	$H_2O_2 + OH \rightleftharpoons H_2O + HO_2$	7.08×10^{12}	0.0	1430
14	$O + HO_2 \rightleftharpoons OH + O_2$	2.00×10^{13}	0.0	0
15	$H + HO_2 \rightleftharpoons O + H_2O$	3.10×10^{13}	0.0	1720
16[b]	$H + O + M \rightleftharpoons OH + M$	6.20×10^{16}	-0.6	0
17[b]	$O + O + M \rightleftharpoons O_2 + M$	6.17×10^{15}	-0.5	0
18	$H_2O_2 + H \rightleftharpoons H_2O + OH$	1.00×10^{13}	0.0	3590
19	$H_2O_2 + H \rightleftharpoons HO_2 + H_2$	4.79×10^{13}	0.0	7950
20	$O + OH + M \rightleftharpoons HO_2 + M$	1.00×10^{16}	0.0	0
21	$H_2 + O_2 \rightleftharpoons OH + OH$	1.70×10^{13}	0.0	47780

[a] Units: mol/cm^3, s^{-1}, K, cal/mol; rates for reverse steps obtained from JANAF thermochemical equilibrium data.

[b] Chaperon Efficiencies: H_2: 2.5, H_2O: 12.0, O_2: 1.0 and N_2: 1.0

[c] Chaperon Efficiencies: H_2: 1, H_2O: 6.5, O_2: 0.4 and N_2: 0.4

[d] Chaperon Efficiencies: H_2: 2.5, H_2O: 15.0, O_2: 1.0 and N_2: 1.0

CONTROLLING COMBUSTION AND MAXIMIZING HEAT RELEASE IN A REACTING COMPRESSIBLE FREE SHEAR LAYER

Principal Investigators: Laurence Keefe

Nielsen Engineering & Research, Inc.
510 Clyde Avenue
Mountain View, CA 94043-2287

SUMMARY

The objective of the work is to study the interaction between heat release and mixing in compressible shear layers by analysis and computation, with an eye to finding flow configurations that maximize the heat release per unit distance in the streamwise direction. Analytic solutions of some steady heat release problems indicate that heat release can enhance entrainment velocities, but the magnitude of these velocities is often quite small relative to existing turbulent fluctuations. This tends to explain the lack of clear cut changes in numerical simulations of shear layers with steady heating. Time dependent simulations with simple chemistry are currently being employed in an effort to reproduce the experimental results of Keller and Daily, who find entrainment increasing with heat release in an air-propane system. A variational approach to maximizing heat release has so far foundered on the analytical complexity of the Euler equations connecting the flow to even the simplest models of heat release.

THEORETICAL EXAMPLE

Prompted by the inconclusive results of steady heat release simulations in a spatially growing shear layer, an analytic heat release example was solved to better understand the functional dependence of the entrainment velocity upon heat release parameters. The analysis begins with the expression for V, the velocity normal to the layer, gotten from a y-differentiation of the expression for the potential ϕ that solves the governing Poisson equation.

$$V(x,y) = \phi_y(x,y) = \frac{(\gamma-1)}{2\pi a_\infty^2 \beta^2} \int_\xi \int_\eta \frac{(y-\eta)h_{f_\xi}}{[(x-\xi)^2 + (y-\eta)^2]} \, d\eta \, d\xi \qquad (1)$$

Note the asymmetry of the kernel in Eq. (1); unless h_{f_ξ} has some asymmetry in η with respect to the y-value of the field point, the η integral evaluates to zero. Thus, for a given heat release distribution h_{f_ξ}, it is only its component odd with respect to y that is important to the entrainment velocity V at y.

For simplicity, a separable form for $h_f(\xi,\eta)$ is assumed, $h_f(\xi,\eta)= Hf(\xi)g(\eta)$. Now $g(\eta)$ can be decomposed about any y into a sum of odd and even functions $g_o(y-\eta) + g_e(y-\eta)$, and only g_o contributes to the integral. To understand the subsequent behavior of V we choose a generic form for $g_o(y-\eta)$ that has properties appropriate for the odd component of a single maximum (in η) heat release profile. It is

$$g_o(y-\eta) = \frac{-2\alpha}{\pi} \frac{b^3 (y-\eta)}{\left[1 + b^2 (y-\eta)^2\right]^2} \qquad (2)$$

The constant α controls the sign of the contribution of the heat release above and below y and is typically positive for y positive, and negative for y negative. Substituting Eq. (2) into Eq. (1) and employing contour integration we obtain

$$V(x,y) = \frac{\alpha b^2 (\gamma-1)H}{2\pi a_\infty^2 \beta^2} \int_{\xi=-\infty}^{\infty} \frac{f_\xi}{\left[b(x-\xi)+1\right]^2} d\xi \qquad (3)$$

Thus, for increasing heat release downstream, $f_\xi > 0$, entrainment is decreased, but for $f_\xi < 0$, decreasing heat release downstream, entrainment is <u>increased</u> by heat release. The case of constant total heat release per unit streamwise distance, but with the heat release region spreading laterally with the shear layer corresponds to this latter case $f_\xi < 0$ and is shown schematically in Figure 1.

The problem with the numerical simulations now becomes clearer. The magnitude of V expected in the simulations can be estimated from the analysis using values of the constants used in the simulations. Thus $H = Da_\infty^2/(\gamma-1) = .002a_\infty^2/\gamma-1$, $b^2=2.$, $\beta^2 = .84$ and $h_{f\xi} \sim [-1.,-.03]$. These values result in a 30% centerline temperature rise in the simulations. Then

$$V \sim - \frac{b^2 (\gamma-1)}{2 \pi a_\infty^2 \beta^2} \frac{Da_\infty^2}{(\gamma-1)} h_{f_\xi}$$

$$\sim -.00076\, h_{f_\xi} \qquad (4)$$

The heat release distribution induces entrainment velocities one to two orders of magnitude smaller than the typical turbulent values of V' in the shear layer. Such effects, though real, could easily be indistinguishable.

NUMERICAL SIMULATIONS

Work has just begun on simulations of spatially developing shear layers with simple(A + B → C), finite rate chemistry, in an attempt to duplicate the experimental results of Keller

and Daily.[1] Contrary to most experiments, they find an increase in mixing rate with heat release in a propane-air system.

VARIATIONAL APPROACH TO HEAT RELEASE MAXIMIZATION

The desire is to maximize the volumetric heat release J.

$$J = \int_{x=x_o}^{x_o+L} \int_{y=-\infty}^{\infty} h_f(\phi, \phi_x, \phi_y, \phi_{xx}, \phi_{xy}\ldots?)\,dy\,dx \qquad (5)$$

subject to the constraint that the velocity field satisfy $\phi_{xx} + \phi_{yy} = (\gamma-1)h_{fx}/a_-^2$. The key here is to find plausible models to link the specific heat release h_f to the local velocity field (ϕ, ϕ_x, $\phi_y\ldots$). Till now the research has centered on functionals dependent upon streamline length and/or some positive definite function of the streamline curvature. These two quantities provide a characterization of the length and wrinkledness of interfaces between reactants, and the expectation is that the longer and more convoluted this interface, the greater the total product formation and heat release. The variational problem involves finding a flow configuration that balances streamline convolution against the diffusive or averaging character of the potential flow constraint. As an example, consider the heat release functional that depends on the streamline curvature (in terms of the potential ϕ)

$$K = \frac{\phi_{xy}/\phi_x \left[1 - (\phi_y/\phi_x)^2 \right]}{\left[1 + (\phi_y/\phi_x)^2 \right]^{3/2}} \qquad (6)$$

The curvature may be negative, and thus the heat release can be connected to it only through some positive valued function of K. It has been assumed $h_f - K^2 = F$. The Euler equation for this functional is

$$-\frac{\partial}{\partial x} F_{\phi_x} - \frac{\partial}{\partial y} F_{\phi_y} + \frac{\partial^2}{\partial x \partial y} F_{\phi_{xy}} = 0 \qquad (7)$$

Expanding the x- and y- partial derivatives gives

$$-\phi_{xx}F_{\phi_x\phi_x} - 2\phi_{xy}F_{\phi_x\phi_y} - \phi_{yy}F_{\phi_y\phi_y} + \phi_{xx}\phi_{xy}F_{\phi_x\phi_x\phi_{xy}} +$$

$$\left[\phi_{xx}\phi_{yy} + \phi_{xy}^2 \right] F_{\phi_x\phi_y\phi_{xy}} + \phi_{xy}\phi_{yy}F_{\phi_y\phi_y\phi_{xy}} + \phi_{xxyy}F_{\phi_{xy}\phi_{xy}}$$

$$+ \left[\phi_{xy}\phi_{xxy} + \phi_{xx}\phi_{xyy} \right] F_{\phi_x\phi_{xy}\phi_{xy}} + \phi_{xxy}\phi_{xyy}F_{\phi_{xy}\phi_{xy}\phi_{xy}} +$$

$$\left[\phi_{xy}\phi_{xyy} + \phi_{yy}\phi_{xxy} \right] F_{\phi_y\phi_{xy}\phi_{xy}} = 0. \qquad (8)$$

Realizing that all of the partial derivatives of F with respect to ϕ_x, ϕ_y and ϕ_{xy} are rational functions of these arguments, it is quickly clear that the resulting equation for ϕ is high order and strongly nonlinear(6th order polynomials in ϕ_x, etc.). No obvious simplifications have been found to make the equation analytically tractable, and the strong nonlinearity urges caution in numerical treatment. At present there is a search for other heat release functionals that produce more tractable equations.

REFERENCES

1. Keller, J.O. and Daily J.W.: The Effects of a Highly Exothermic Chemical Reaction on a Two-dimensional Mixing Layer. AIAA Journal 23, 1985, p1937.
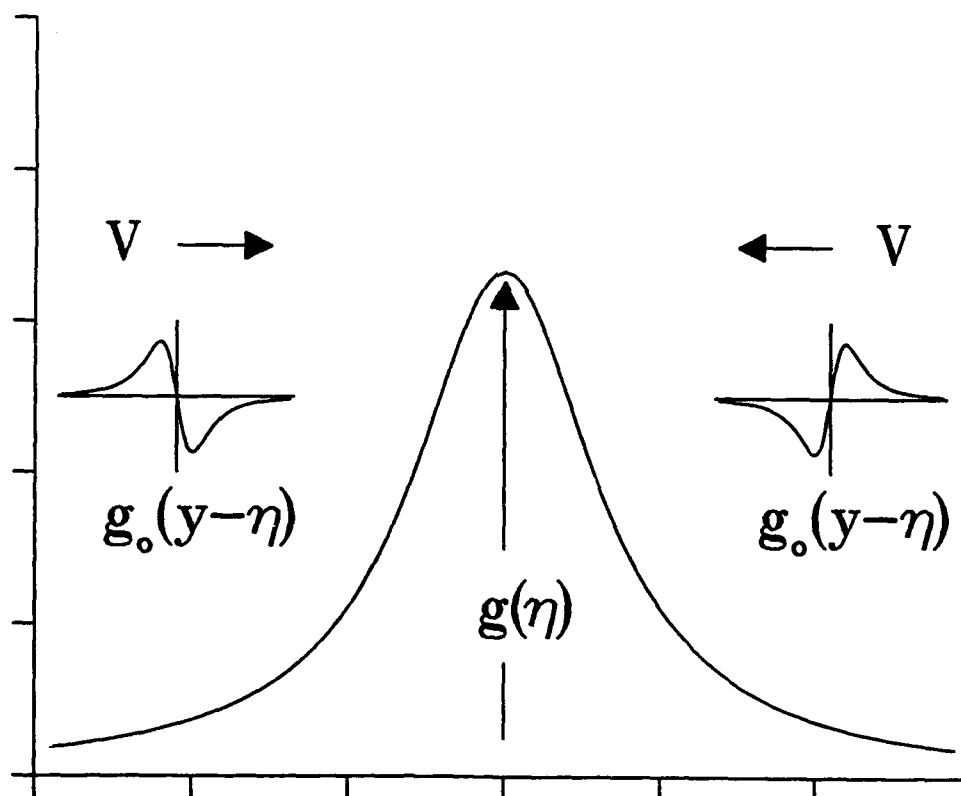
Figure 1. Entrainment velocities due to heat release, $f_\xi < 0$.

INVESTIGATION OF THE LAMINAR FLAMELET
MODEL OF TURBULENT DIFFUSION FLAMES

George Kosály and James J. Riley

Department of Mechanical Engineering
University of Washington FU-10
Seattle, Washington 98195

SUMMARY/OVERVIEW

The original objective of this research program was the investigation of the validity of the stationary laminar flamelet model (SLFM). The research was broadened to include the investigation a new closure model (Conditional Moment Closure, CMC). The investigations have been performed via direct numerical simulations (DNS) and theoretical analysis. Closure modeling is aimed at decoupling the chemistry model from the turbulence model thereby making possible the inclusion of realistic chemistry schemes in turbulent combustion predictions.

TECHNICAL DISCUSSION

The simulated velocity field was decaying, incompressible and isotropic, Re_λ changing between 35 and 20. The computational domain sizes were 64^3, 128^3. Using the larger domain with the above Re_λ values resulted in high spatial resolution which was required to investigate individual reaction zones. The scalar fields were either initialized homogeneously in space, or in slabs. The latter arrangement models a mixing-layer with chemical reaction. Fuel and oxidant were initialized as $Y_F(\underline{x},0) = Z(\underline{x},0)$, $Y_O(\underline{x},0) = 1-Z(\underline{x},0)$, where Z is the mixture fraction (Le = 1). The chemistry schemes used were $F + r O \rightarrow (r+1) P$ (T = const) and a ten-reaction scheme with heat release corresponding to H_2–O_2 combustion. In the latter case partial-equilibrium of the two-body shuffle reactions has been assumed. In the simple reaction cases $\dot{w}_F = -A Y_F Y_O$. We have considered six different simple reaction cases corresponding to $Z_{st} = 0.25, 0.5$, and $Da_o = A\ell_o/u_o = 0.5, 2, 8$. Figure 1 shows the boundaries of the cloud of the simulated values of Y_F vs Z for $Z_{st} = 0.25$, $Da_o = 8$. The cloud is bordered by the frozen (FR) and equilibrium chemistry (EC) lines. Also shown is the RD (reaction dominated) limit that follows from the equation $dY_F/dt = \dot{w}_F$ with $Y_F(0) = Z$.

Conditional Moment Closure (CMC). The model equation in the simple chemistry case is:[1]

$$\partial Q_F(\eta,t)/\partial t = 1/2 \; \langle\chi|\eta\rangle_t \, \partial^2 Q_F(\eta,t)/\partial\eta^2 - A Q_F(\eta,t)Q_O(\eta,t) . \tag{1}$$

$$Q_F(\eta,0) = \eta, \; Q_O(\eta,0) = 1-\eta \, , \; Q_F(\eta,t) = \begin{cases} 0, & \eta = 0 \\ 1, & \eta = 1 \end{cases} , \quad Q_O(\eta,t) = \begin{cases} 1, & \eta = 0 \\ 0, & \eta = 1 . \end{cases} \tag{2}$$

Here $Q_F(\eta,t) \equiv \langle Y_F(\underline{x},t)\,|\,Z(\underline{x},t) = \eta\rangle$, $\langle\chi/\eta\rangle = \langle\chi(\underline{x},t)\,|\,Z(\underline{x},t) = \eta\rangle$. The main physical idea behind this modeling is that, while the averaged mass fractions and reaction rates are strongly dependent on the transversal coordinate, conditioning on Z "absorbs" much of this dependency. Similarly, while the mass fractions fluctuate wildly around their averages, the fluctuations around the conditional average are small. Equation (1) requires $\langle\chi|\eta\rangle$ as input ($\chi = 2D\nabla Z \cdot \nabla Z$).

Figure 2a refers to the spatially homogeneous scalar initialization[2,3] and shows $\langle\dot{w}_F\rangle/A = \langle Y_F Y_O\rangle$ vs time for three chemistry rates. The lines exhibit the data. The dots refer to the prediction assuming $\langle\chi|\eta\rangle_t = \langle\chi\rangle_t$, the crosses show predictions assuming local counterflow like mixing (LCFLM)[4,5]; that is, $\langle\chi|\eta\rangle_t = \langle\chi|0.5\rangle_t F_\ell(\eta)$, where $F_\ell(\eta) = \exp\{-2[erf^{-1}(1-2\eta)]^2\}$. The figure shows that CMC is valid at all chemistry rates but its validity is dependent on the modeling of $\langle\chi|\eta\rangle$. Figure 2b shows $\langle w_F\rangle$ vs y at a given time (spatial mixing layer) for $Da_o = 5$. The CMC-prediction was evaluated assuming LCFLM to model $\langle\chi|\eta\rangle$. Figures 3a,b show the major species vs mixture fraction in the ten reaction scheme of H_2/O_2 combustion. Figure 3a shows DNS data, Fig. 3b exhibits laboratory results.[6] The non-dimensional reaction rate and time were chosen such that the simulated data were close to the laboratory results. Comparison of the simulated data of the major species and the radicals (not shown here) to the CMC predictions[7] demonstrate further that the quality of the CMC-prediction depends on the modeling of

$<\chi|\eta>$. Taking the $<\chi|\eta>$ data from the simulations results in excellent prediction of both the major species and radicals. Our conclusions regarding CMC-modeling are: 1) CMC works well both for fast and slow chemistry rates and is therefore an excellent candidate for application in turbulent combustion where very different chemistry rates can be relevant simultaneously. 2) In its simplest form given in eqs. (1),(2), CMC is only valid as long as $<\chi|\eta>$ is independent of the transversal coordinate. 3) CMC validity depends crucially on the modeling of $<\chi|\eta>$. Since most of our simulations referred to cases when the pdf of Z is not yet fully centered at $Z = <Z>$ we found LCFLM-modeling most satisfactory. For more developed mixing new modeling is required.

Stationary Laminar Flamelet Model (SLFM). The model equation in the simple chemistry case can be written as[4]:

$$1/2\chi d^2Y_F/dZ^2 = AY_FY_0 \qquad (3) \qquad\qquad Y_F = \begin{cases} 0, & Z = 0 \\ 1, & Z = 1 \end{cases}. \qquad (4)$$

Equations (3),(4) provide local predictions, valid for individual reaction zones. Peters[4] introduces the LCFLM assumption to evaluate the local scalar dissipation as $\chi = \chi_0 F\ell(Z)$, here χ_0 is the local value of χ @ $Z = 0.5$. Different values of χ_0 correspond to different flamelets. More customary is to categorize the flamelets according to χ_{st} (χ@$Z = Z_{st}$). Reference 4 defines a local Damköhler-number (Daℓ) and argues that the SLFM prediction is valid if Da$\ell \gg 1$. (Isothermal case.) In the simple chemistry case Da$\ell = A/\chi_{st}$, whence the following expectations follow: (1) For the same turbulence SLFM validity improves with increasing values of the chemistry rate (A) and decreasing values of Z_{st}. (2) For identical values of A and Z_{st}, SLFM is better for reaction zones where χ_{st} is smaller. Figures 4a,b,c refer to the spatially homogeneous, simple chemistry case. The figures show $<Y_F|Z = Z_{st},\chi=\chi_{st}>$ vs χ_{st}/A. The full line is the SLFM prediction, 0, +, and Δ indicate the simulated data for different times. Comparison of Figs. 4a and 4b show that the model indeed improves with increasing chemistry rate. Comparison of Figs. 4b and 4c demonstrates the improvement with the decrease of Z_{st}. Figures 4a,b,c demonstrate that — contrary to expectation — reaction zones associated with lower values of χ_{st} deviate more from the SLFM prediction. On the bottom of the figure the pdf of χ conditioned on $Z = Z_{st}$ is shown for different times. The deviations of the volume averages from their predictions (not shown here) come mostly from regions where χ is relatively small. To explain the unexpected result recall that SLFM is a one-dimensional reaction model, therefore a one-dimensional mixing environment is conducive to its validity. Simulated and laboratory data both demonstrate that regions of quasi-one dimensional molecular mixing are associated with high values of χ. SLFM is, furthermore, a quasi-stationary reaction model. We have investigated the issue of quasi-stationarity by considering a fully-one dimensional case (Sc $\gg 1$, initial region of mixing as defined in Ref. 5) and have estimated the contribution of the neglected time derivative on the LHS of eq. (3). The theoretical results show that the assumption of $A/\chi_{st} \gg 1$ may not be sufficient to guarantee the negligibility of the time derivative even in the isothermal case. Our conclusions regarding SLFM are: 1) SLFM improves for large chemistry rates and low values of Z_{st}. 2) SLFM provides substantial improvement over EC-modeling. 3) The original derivation of this model does not account for the influence of the dimensionality of the mixing and may not address in full detail the condition for quasistationarity.

Our work toward improved closure modeling is part of a continuing effort to understand and model mixing and reaction in turbulence. Reference 9 provides new interpretation of measured spectra of reacting species in turbulence.

REFERENCES

1. Bilger, R.W., *Phys. Fluids A*, 5, 441, 1993.
2. Mell, W.E., Nilsen, V., Kosály, and Riley, J.J., Short Communication, *Comb. Sci. Tech.*, 91, 179, 1993.
3. Mell, W.E., Kosály, and Riley, J.J., "An Investigation of Closure Models for Non-premixed Turbulent Reacting Flows," *AIAA*, 93-0104, Jan 11-14, Reno, Nevada.
4. Peters, N., *Progr. Energy. Comb. Sci.*, 10, 319, 1984.
5. Kosály, G., and Mell, W.E., "The Mapping Closure Approach to Scalar Mixing," *Phys. Fluids A*, (presently under revision, 1993).
6. Barlow, R.S., Dibble, R.W., Chen, F.-Y., and Lucht, R.P., *Combustion and Flame*, 82, 235, 1990.
7. Montgomery, C.F., Kosály, G., and Riley, J.J. "Direct Numerical Simulation of Turbulent H_2-O_2 Combustion Using Reduced Chemistry," *AIAA 93-0248*, Jan 11-14, Reno, Nevada.
8. Mell, W.E., Nilsen, V., Kosály, G., and Riley, J.J., "Investigation of Closure Models for Non-premixed, Reacting Turbulent Flows," (manuscript to be submitted to *Phys. Fluids A*).
9. Kosály, G., *Journal of Fluid Mechanics*, 246, 489, 1993.

GK/2
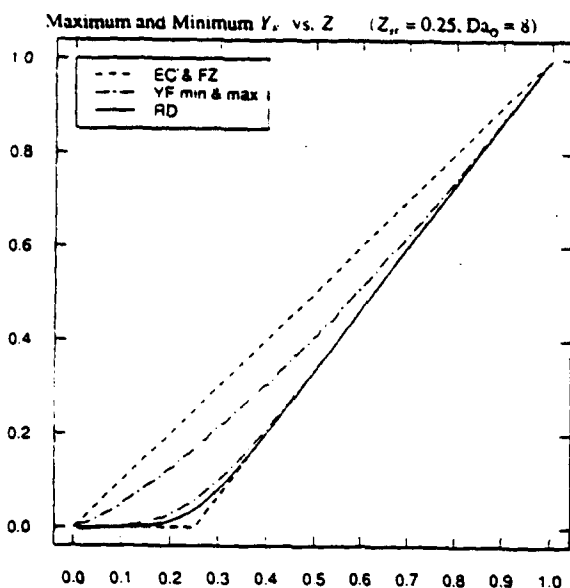
Figure 1: Maximum and minium Y_F and the frozen (FZ), equilibrim (EC), reaction dominated (RD) chemistry limits vs. Z at a given time (t = 1).
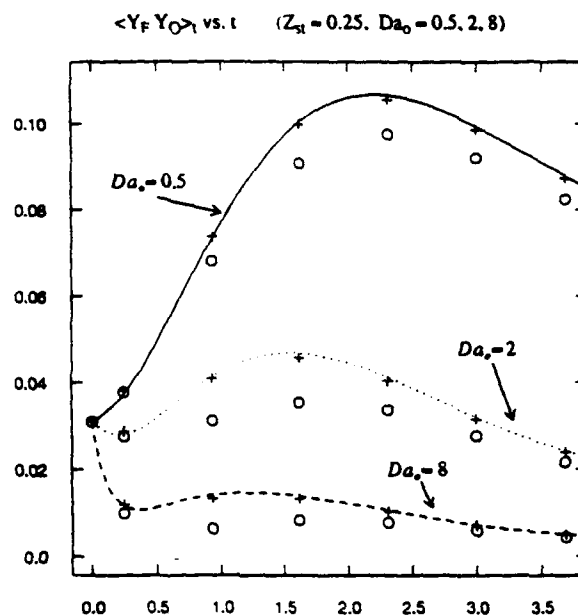

Figure 2a: $<Y_F Y_o>$, vs. t. Lines are DNS data, symbols are CMC results. CMC with counter flow mixing model are plusses. CMC with $<\chi|\eta>, = <\chi>,$ are circles.
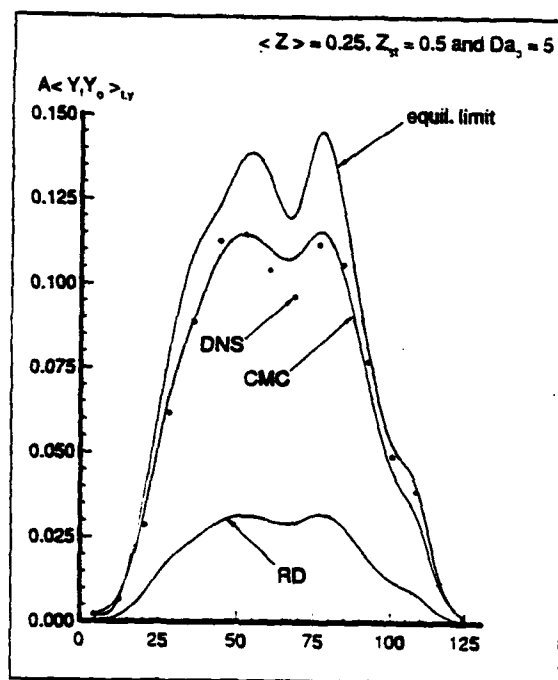

Figure 2b: Average reaction rate versus transversal coordinate for scalar mixing layer. The CMC prediction shown was calculated using $<\chi/\eta> = <\chi/0.5>F_i(\eta)$.
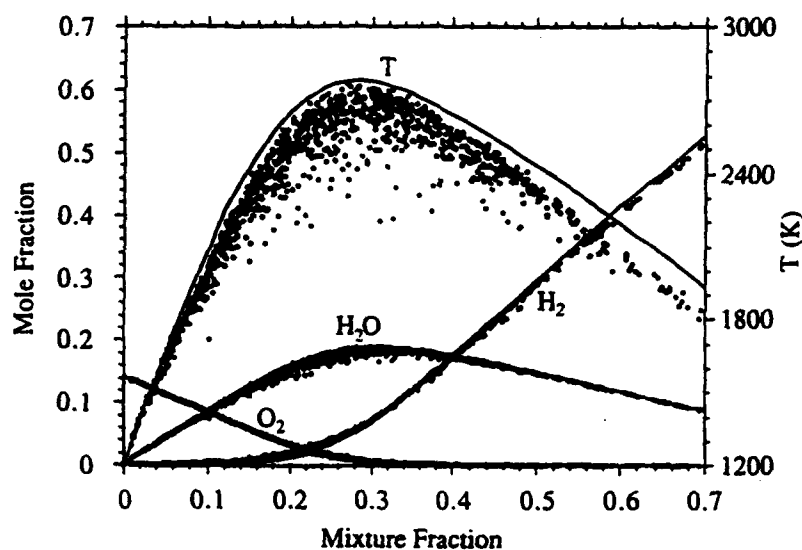
Figure 3a. Major species mole fractions and temperature from simulations. Nondimensional reaction rate parameter, $A = 0.5$, time (nondimensionalized by initial large-eddy turnover time) $t = 3.22$. The time and A value were chosen for similarity to experimental results. Solid curves indicate chemical equilibrium.
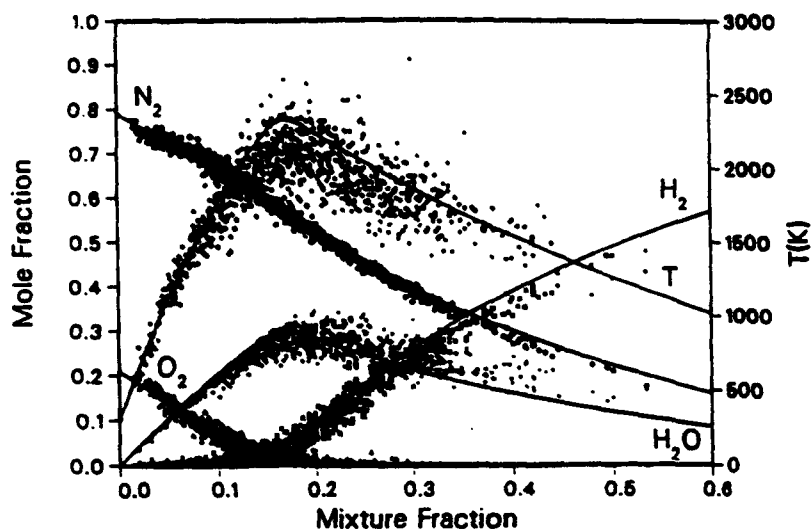
Figure 3b. Major species mole fractions and temperature measured by Raman scattering in an H_2-Argon/air jet diffusion flame from Barlow et al. Nozzle $Re = 17000$, $x/d = 30$, $y/d = 2$. Solid curves indicate chemical equilibrium.

Figure 4a: $<Y_r|Z=Z_n, \chi=\chi_n>$, vs. χ_n/A at three different times. Solid line is the SLFM solution. Symbol/Lines are the DNS data for $t = 1$ (circles), $t = 2.3$ (plusses), $t = 3.68$ (triangles). Curve at bottom of figure are the scaled pdfs. $p(\chi|Z=Z_n)$, at the different times.
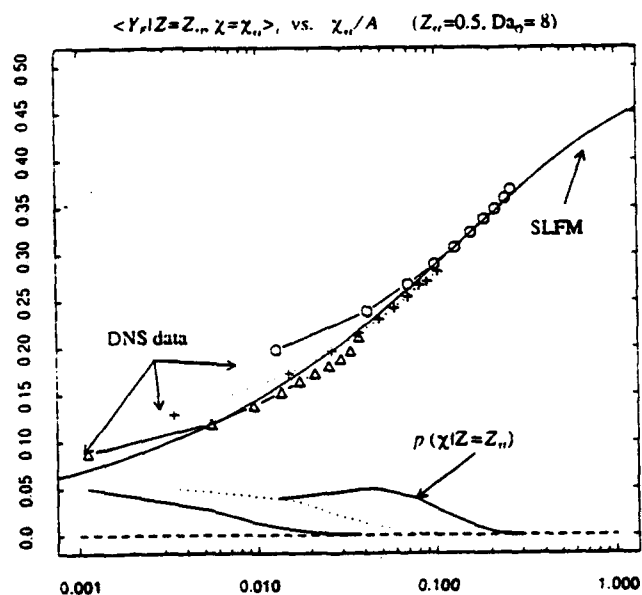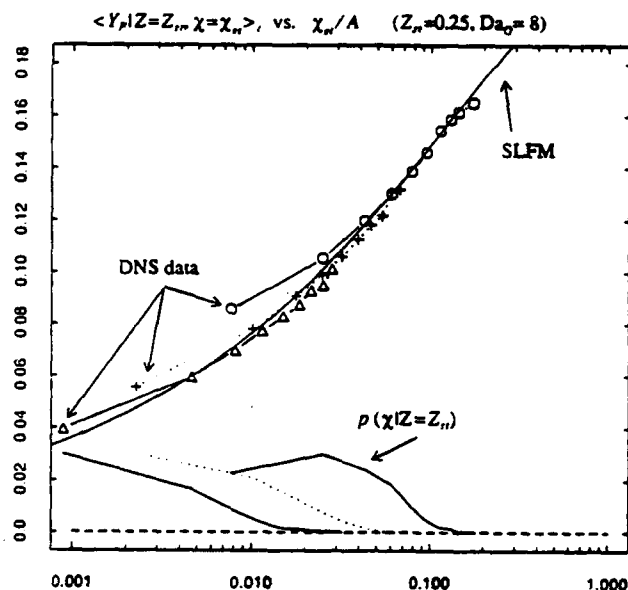

Figure 4b: $<Y_r|Z=Z_n, \chi=\chi_n>$, vs. χ_n/A at three different times. Solid line is the SLFM solution. Symbol/Lines are the DNS data for $t = 1$ (circles), $t = 2.3$ (plusses), $t = 3.68$ (triangles). Curve at bottom of figure are the scaled pdfs. $p(\chi|Z=Z_n)$, at the different times.

Figure 4c: $<Y_r|Z=Z_n, \chi=\chi_n>$, vs. χ_n/A at three different times. Solid line is the SLFM solution. Symbol/Lines are the DNS data for $t = 1$ (circles), $t = 2.3$ (plusses), $t = 3.68$ (triangles). Curve at bottom of figure are the scaled pdfs. $p(\chi|Z=Z_n)$, at the different times.

TURBULENCE-CHEMISTRY MODELS IN HIGHLY STRAINED NON-PREMIXED FLAMES

AFOSR Contract F49620-91-C-0072

Sanjay M. Correa
General Electric Research Center
Schenectady, New York, 12301

SUMMARY: OBJECTIVES AND PRIOR RESULTS

The objective of this research program is to develop and assess models for turbulence-chemistry interactions in highly strained flames. The framework provided by particle-tracking pdf models is emphasized. The data are typically obtained by laser Raman or LIF. Recirculating flow is emphasized, marking a break from the simpler "parabolic" jet flames. The models can then be combined with CFD codes to predict flame stability, flow/temperature fields and trace emissions from air-breathing combustors. Previously, a method for combining conventional pressure-corrected "elliptic" CFD codes with the joint velocity-composition pdf model was described and the predictions were favorably compared with Raman data (mixture fraction, major species, and temperature) in a 27.5% CO/ 32.3% H_2/ 40.2% N_2 — air flame stabilized in the recirculation zone behind a bluff body [1]. Chemistry was accounted for by a two-variable (mixture fraction and reaction progress variable for the radical pool) partial equilibrium scheme. Also, raw Raman data were procured for a 100% methane-air flame in the same apparatus (Fig. 1). Progress in the past year follows.
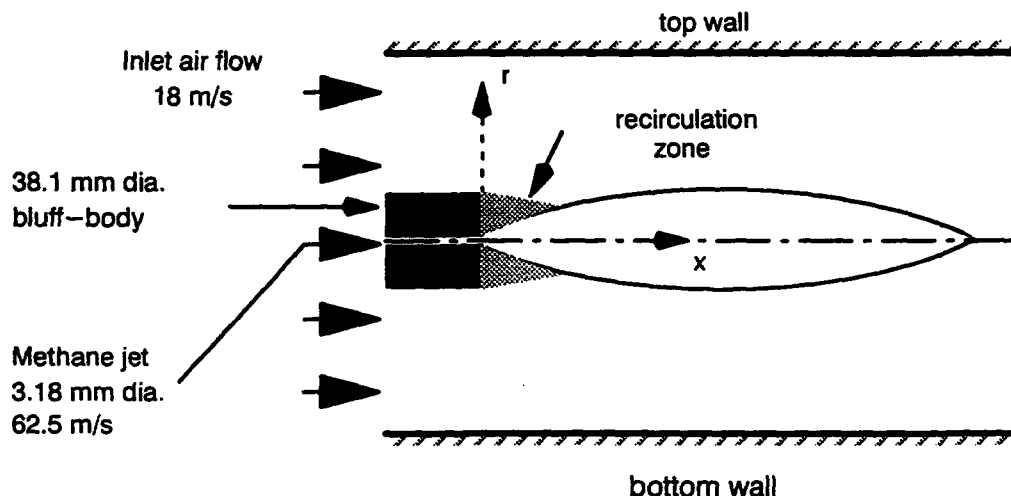

Figure 1. Bluff-body stabilized methane "diffusion" flame in 15 cm x 15 cm tunnel.

PROGRESS IN THE PAST YEAR

The methane-air Raman data obtained in the apparatus of Fig. 1 have been reduced, the 4-step 5-variable "reduced" methane-air kinetic scheme has been implemented by means of table look-up in the CFD/pdf code referred to above, and preliminary computations of the methane-air flame have begun. In the course of these developments, it became apparent that (i) reactive scalar turbulence should be examined in detail, (ii) the reduced chemistry scheme should be compared with the full scheme in something other than the traditional contexts of laminar flames or stirred reactors, and (iii) new "particle" algorithms were required. To these ends, the "Partially Stirred Reactor" or PaSR model was developed.

The PaSR model [2, 3] may be derived from the joint pdf equation [4] and solved by similar techniques. Physically, reactants flow into a box whose contents − reactants, products and intermediates − are mixed by turbulence of a prescribed frequency. A steady state of "unmixedness" is maintained by the compositional difference between the inlet stream and the contents of the reactor. The pdf $P(Y_k)$ of mass fractions Y_k of chemical species in the reactor is represented by the N_p− particle ensemble

$$Y_k^{(1)}, Y_k^{(2)}, ...Y_k^{(n)}, ...Y_k^{(N_p)}; \qquad k = 1, ...N_s$$

where $N_s \equiv$ number of species and $N_p \equiv$ number of particles. Scalar mixing is accounted for by the "Inter-action−by−Exchange−with−the−Mean" [IEM] sub−model. The particle equations are

$$\frac{dY_k^{(n)}}{dt} = -C_\phi \omega (Y_k^{(n)} - \overline{Y}_k) + w_k^{(n)} \frac{M_k}{\varrho^{(n)}}; \qquad k = 1, ...N_s \qquad (1)$$

where ω is the mixing frequency in the IEM model, $w_k^{(n)}$ is the molar production rate of species "k" per unit volume for the nth particle, M_k is the molecular weight of species "k" and $\varrho^{(n)}$ is the density of the nth particle. Equation 1 is solved as shown, without fractional steps, and so mixing and chemistry are accounted for simultaneously. The corresponding equation for particle temperature is

$$\overline{C}_p \frac{dT^{(n)}}{dt} = \frac{dH^{(n)}}{dt} - \sum_{n=1}^{N_s} h_k \frac{dY_k^{(n)}}{dt} \qquad (2)$$

where $H^{(n)}$ is the total enthalpy of particle "n". Hence, the PaSR is described by a coupled system of (N_s+1) x N_p first−order o.d.e.'s in time ($\approx$ 20,000 here).

The mass flow rate m into the PaSR is discretized into N_{in} particles per global time step. Particles, which are selected randomly from the ensemble, flow out at the same mass flow rate. Particles in the ensemble evolve according to Eqs. 1 and 2. The integration is continued until a stochastic steady state is achieved. Scatterplots, pdf's, and correlations of interest can be obtained from the steady state ensemble. The global residence time can be computed as $\tau \equiv \overline{\varrho}V/m$, where $\overline{\varrho}$ is the mean density (obtained by appropriately summing over individual particle masses and volumes) and V is the reactor volume; τ also converges.

The PaSR code was first written for serial computers [2] and then "parallelized" by a manager−worker technique [3]. Figure 2 shows that the speedup is linear in the number of processors of a parallel machine until the number of particles per processor decreases below 10, when load−leveling between processors cannot be maintained. This number will change when full chemistry/time−accurate integration is replaced by reduced chemistry/table look−up. The overall increase in speed over serial computers permits computation of the methane−air system. Figure 3 shows typical results for a 30 atm, 1200K (inlet) premixed methane−air system. Figure 3 (a) shows the convergence of ensemble−mean temperature to a stochastic steady−state; the degree of turbulence in the corresponding time−histories of species is greatest for CO (among major species). Figure 3 (b) shows that the PaSR solutions properly meet the limits imposed by PSR and PFR models: note that with this choice of inlet conditions, reactor volume and mass flow (such that the residence time τ turns out to be approx. 2 ms) the flame blows out in the low frequency limit. Figure 3 (c) shows that the "skeletal" mechanism (used as the basis for the 4−step reduced scheme) cannot reproduce the full scheme's results at low frequency, where ignition chemistry becomes important. Figure 3 (d) shows that the ignition−extinction bifurcation can be accounted for. These and other results are described in detail for CO/H_2−air systems in Ref. 2 and for CH_4−air systems in Refs. 3 and 5.

Aside from intrinsic value as a tool for finite−rate mixing and chemistry, and as a testbed for reduced kinetics, the PaSR may be viewed as being a single control volume in the CFD mesh. Hence the lessons learned in parallelization (dynamic rather than static allocation, allocation by particles, etc.) and in problems with the reduced chemistry (ignition) are directly applicable to the CFD/pdf computation introduced above.

REFERENCES

1. Correa, S.M. and Pope, S.B.,"Comparison of a Hybrid Monte−Carlo PDF/Finite−Volume Mean Flow Model with Bluff−Body Raman Data," *Twenty−Fourth (International) Symposium on Combustion,* The Combustion Institute, Pittsburgh, PA, pp. 279−285, 1992.

2. Correa, S.M.,"Turbulence−Chemistry Interactions in the Intermediate Regime of Premixed Combustion," in press, *Comb. and Flame.*

3. Correa, S.M. and Braaten, M.E.,"Parallel Simulations of Partially−Stirred Methane Combustion," submitted to *Comb. and Flame.*

4. Pope, S.B.,"Computations of Turbulent Combustion: Progress and Challenges," *Twenty−Third (International) Symposium on Combustion,* The Combustion Institute, Pittsburgh, PA, pp. 591−612, 1990.

5. Correa, S.M.,"Models for High−Intensity Turbulent Combustion," 2nd US National Congress on Computational Mechanics, Washington, DC, August 16−18, 1993; submitted to *J. Comp. Sys. Engg.*
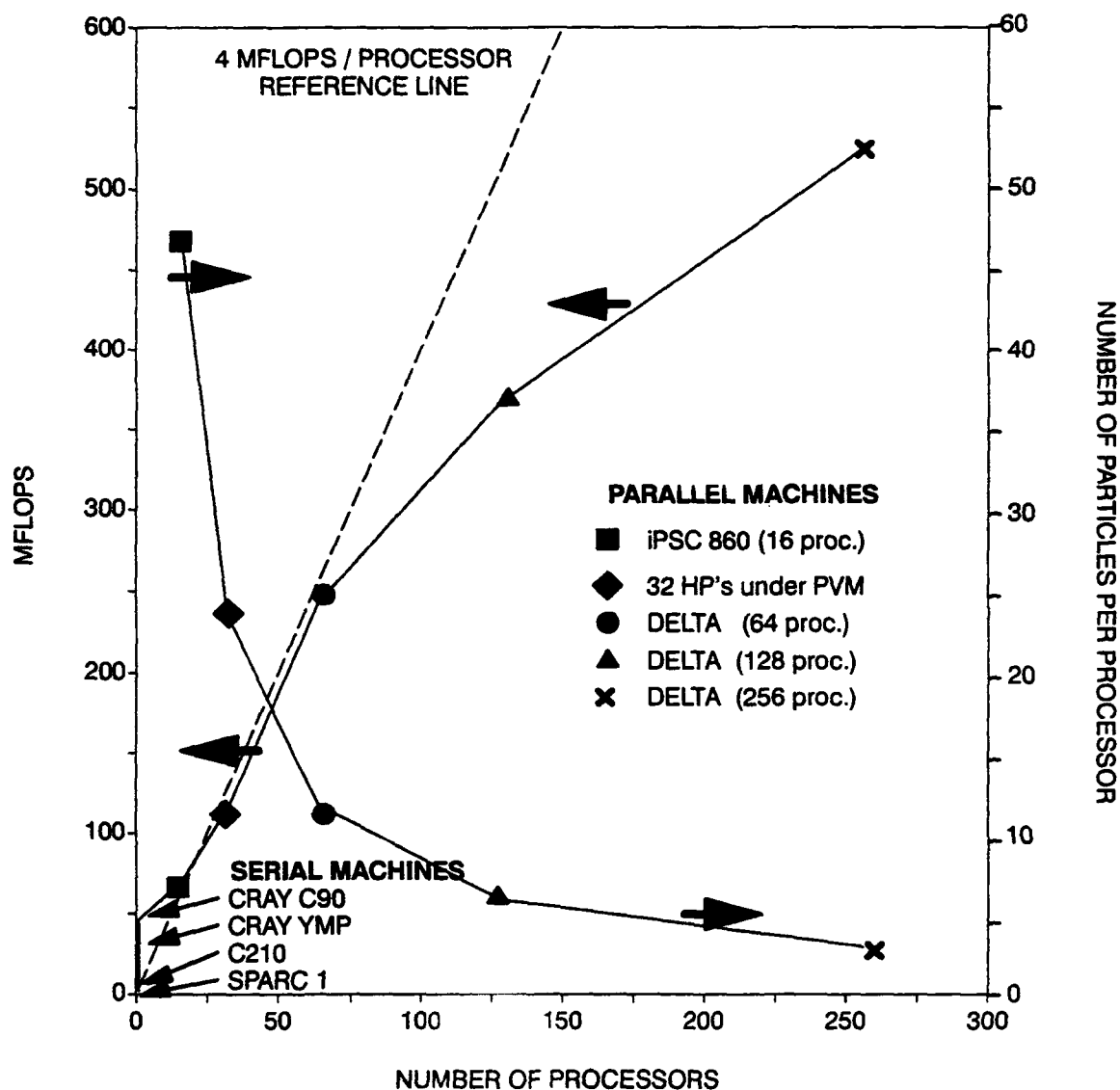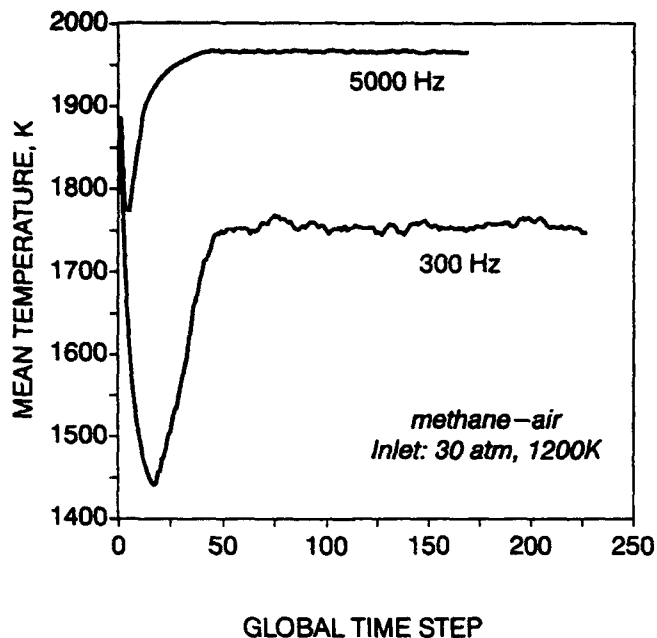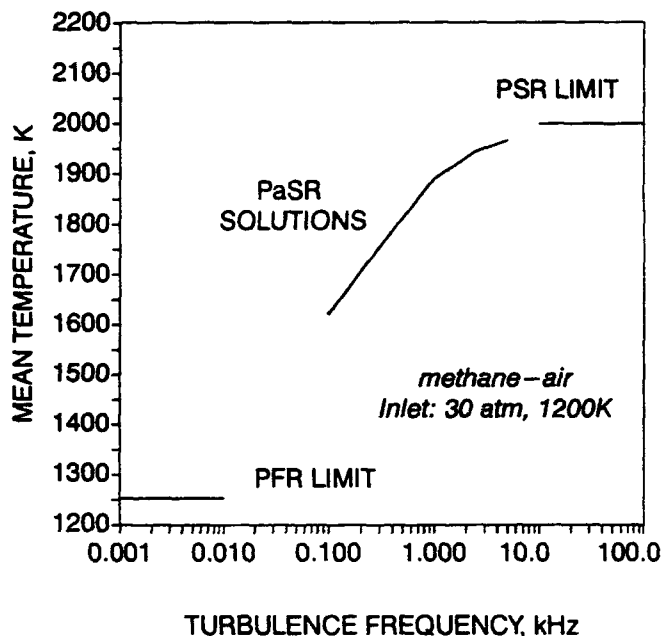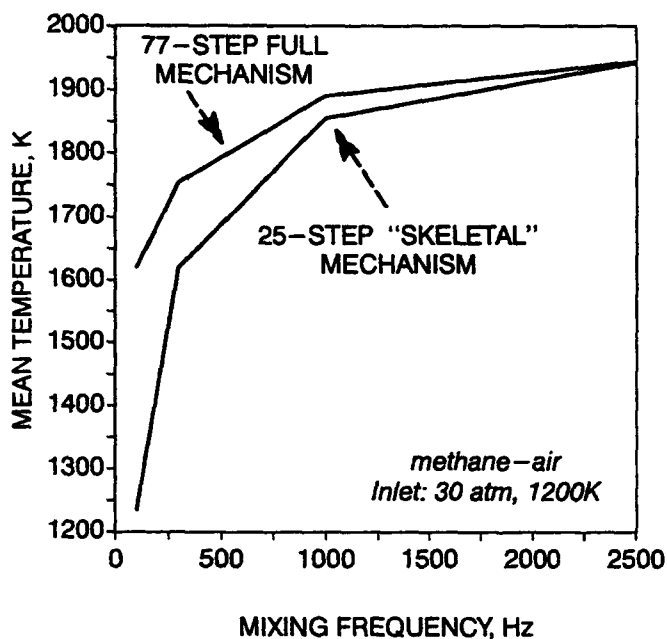
Figure 2. Parallelization of the particle chemistry/IEM mixing "PaSR" model. Standard calculation of CO/H2 chemistry with 750 particles and 360 global time steps.
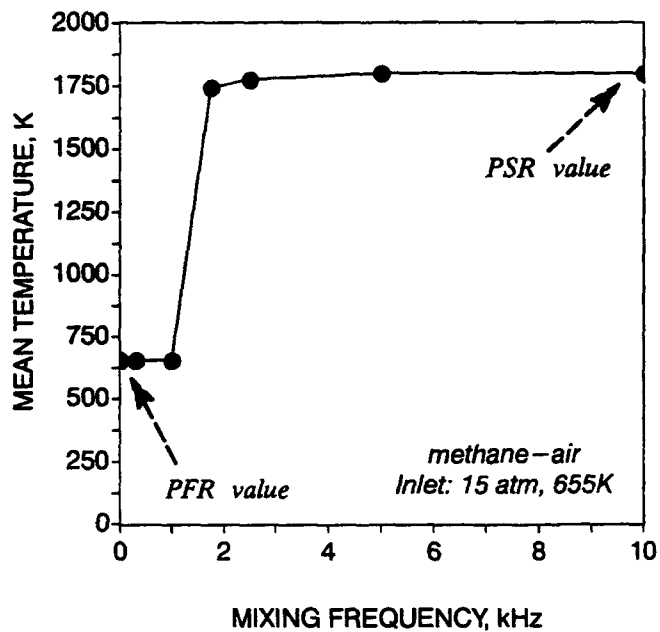
(a) Convergence of PaSR to stochastic steady state.

(b) Mean PaSR temperature and bounding values.

(c) Comparison of skeletal and full (lean) schemes.

(d) An example of ignition–extinction in the PaSR.

Figure 3. Selected results from the homogeneous–flow scalar–pdf "PaSR" model.

MAPPING CLOSURES FOR TURBULENT COMBUSTION
AFOSR 91-0184
Principal Investigator: S.B. Pope

Cornell University
Ithaca, NY 14853

SUMMARY

The overall objective of the research program is to develop and test an improved model for the process of molecular diffusion in turbulent reactive flows. In application to turbulent combustion, a major shortcoming of existing models is that they are non-local in composition. A model has been developed, based on the construction of a Euclidean minimum spanning tree (EMST). This model is inspired by the mapping closure, and reduces to it in the case of a single composition. In general, the model is asymptotically local, and hence overcomes a major flaw in previous models.

Additionally, studies have been made of stochastic Lagrangian models for turbulent reactive flows; and an exact expression has been obtained for the probability density function of temperature (or other random quantities) in statistically stationary turbulence.

INTRODUCTION

The treatment of molecular diffusion remains one of the major difficulties to be overcome in models of turbulent combustion. One view of the overall problem is obtained by considering how, at a given point within a turbulent combustion device, the fluid composition changes with time. There are three processes that cause this change: convection, reaction, and molecular diffusion. In pdf methods the first two of these processes are treated exactly, while the third—molecular diffusion—has to be modelled. Many other theoretical and experimental studies lead to the same conclusion: the major current issue in turbulent combustion is to understand and model the effects of molecular diffusion.

A most promising recent advance is the development of *mapping closures* (Chen et al. 1989, Kraichnan 1990, Pope 1991, Gao 1991). This is a new formalism that yields "constant-free" pdf closures. In its initial application to the marginal pdf of a scalar (Pope 1991) the accuracy of the mapping closure has been remarkable.

For simple test cases, analytic solutions to the mapping-closure equations can be obtained. But for application to inhomogeneous flows of practical importance, the closure needs to be implemented as a particle method. For a single scalar, a particle-implementation has been developed by Pope (1991). The principal achievement of the current research is an extension of these ideas to the case of multiple scalars: this is described in the next Section.

The process of molecular mixing is not, of course, independent of the velocity field that is convecting and distorting the composition fields. In pdf methods, there are separate stochastic models for the evolution of velocity and composition following fluid particles. Two papers concerning these models and their interconnection have been written (Pope 1993, 1994).

Finally, a new *exact* result has been obtained for the pdf of *any* stationary random process, such as the temperature at a point in a turbulent combustion device. This is described in the third Section.

EMST MIXING MODEL

The term "mixing model" refers to a turbulence sub-model that describes the evolution of the pdf of composition. In the Lagrangian-pdf framework, the mixing model specifies how the composition $\phi(t)$ evolves following a fluid particle. In one popular model (IEM) $\phi(t)$ relaxes to the local mean value $\langle\phi\rangle$ at a specified rate. In another class of models (particle-interaction models), the composition of the n-th particle in an ensemble $\phi^{(n)}(t)$ changes by an exchange with another randomly selected particle (m, say, with composition $\phi^{(m)}(t)$).

Such mixing models have been extensively examined for inert flows (e.g. Pope 1982) and several shortcomings have been identified and are now well-appreciated. More recently a different shortcoming—peculiar to reacting flows—has been identified. Specifically, the physics of the problem shows that mixing is *local in composition space* whereas the models cited above are non-local.

The EMST mixing model, now described, is an asymptotically local model, inspired by the mapping closure. We consider first a single scalar $\phi(\mathbf{x}, t)$ in homogeneous turbulence. In a particle method, the pdf of ϕ is represented by an ensemble of N particles, the n-th having the scalar value $\phi^{(n)}(t)$. For this problem, the mapping closure yields a fascinating particle method (Pope 1991). Let the particles be ordered so that

$$\phi^{(1)}(t) \leq \phi^{(2)}(t) \leq \ldots \leq \phi^{(N)}(t). \tag{1}$$

Then (according to the mapping closure) the particles evolve by a coupled set of ode's

$$\frac{d}{dt}\phi^{(n)}(t) = B_{n+\frac{1}{2}}[\phi^{(n+1)} - \phi^{(n)}] + B_{n-\frac{1}{2}}[\phi^{(n-1)} - \phi^{(n)}], \tag{2}$$

where (for large N) the positive coefficients are

$$B_{n+\frac{1}{2}} = N^2 A\left(\frac{n+\frac{1}{2}}{N}\right), \tag{3}$$

and A is a known function. (The coefficients $B_{\frac{1}{2}}$ and $B_{N+\frac{1}{2}}$ are zero, so $\phi^{(0)}$ and $\phi^{(N+1)}$ can remain undefined.) A simple interpretation of Eq. (2) is that $\phi^{(n)}(t)$ is drawn to its two neighbors at a rate proportional to its separation from them. Note that as N tends to infinity, the difference between $\phi^{(n)}$ and $\phi^{(n\pm1)}$ tends to zero. Hence the method is (asymptotically) local.

Consider now the general case in which there are σ compositions: in a typical combustion problem (employing simplified kinetics) σ may be 5. Then the composition of the n-th particle is denoted by

$$\phi^{(n)}(t) = \{\phi_1^{(n)}(t), \ \phi_2^{(n)}(t), \ldots, \ \phi_\sigma^{(n)}(t)\}, \tag{4}$$

and it can be regarded as a point in the σ-dimensional composition space. Thus the ensemble of N particles correspond to N points in σ-space.

The concept of ordering—as used in Eq. (1)—is peculiar to one-space. There is no direct equivalent in multi-dimensional spaces, and so a direct extension of the model defined by Eq. (2) is not possible.

However, we have developed a model, inspired by Eq. (2), which is asymptotically local, and which reduces to Eq. (2) in the one-composition case. It is based on Euclidean minimum spanning trees (EMST). An example of an EMST (for $\sigma = 2$, $N = 400$) is shown in Fig. 1.

By definition, the EMST is the set of edges joining the points, such that all points are connected, with the $N-1$ edges chosen (out of the N^2 possibilities) so that their total length is minimal. By this construction, one or more neighbors are identified for each particle, and hence evolution equations analogous to Eq. (2) can be constructed.

This model has been implemented and tested in up to 10 dimensions. A great deal of effort has been concentrated on the specification of the coefficients (analogous to $B_{n\pm\frac{1}{2}}$ in Eq. 2). A Gaussian test case has been developed which sheds light on the specification. Results for this, and other cases, will be given at the meeting.

EXACT EXPRESSION FOR STATIONARY PDF

Central to this project, and indeed to many issues in turbulence, is the shape adopted by the pdf's of different flow properties. In turbulent combustion the importance of pdf's has been recognized for over twenty years. In the theoretical turbulence community there is now much interest in the topic, since pdf's are a natural diagnostic for intermittency.

Together with Emily Ching, we have obtained a surprisingly simple exact expression for the pdf of amplitude of *any* stationary random process (Pope & Ching, 1993). Consider, for example, the temperature $T(t)$ measured as a function of time at a particular point in a turbulent reacting flow. Let $X(t)$ be the standardization of $T(t)$, i.e.

$$X(t) \equiv (T(t) - \langle T \rangle)/\sigma_T, \qquad (5)$$

where $\langle T \rangle$ and σ_T are the mean and standard deviation of $T(t)$. The result we have obtained for $P(x)$, the pdf of X, is

$$P(x) = \frac{C_1}{\langle \ddot{X}^2 | x \rangle} \exp \left\{ \int_0^x \frac{\langle \ddot{X} | x' \rangle}{\langle \ddot{X}^2 | x' \rangle} dx' \right\}, \qquad (6)$$

where C_1 is a normalization constant, and $\langle \ddot{X} | x \rangle$ denotes the expectation of the second time derivative of $X(t)$ conditional on $X(t) = x$.

In experiments, simulations and modelling, this formula provides a valuable connection between the pdf and the time derivatives of the signal. As discused by Pope & Ching (1993) it sheds light on the tail-shape of pdf's, and it explains the success of a previous empirical expression due to Ching.

REFERENCES

Chen, H., Chen S., and Kraichnan, R.H. (1989) Phys. Rev. Lett., 63, 2657.

Gao, F. (1991) Phys. Fluids A, 3, 511.

Kraichnan, R.H. (1990) Phys. Rev. Lett., 65, 575.

Pope, S.B. (1982) Combust. Sci. Technol. 28, 131.

Pope, S.B. (1991) Theoretical and Computational Fluid Dynamics, 2, 255.

Pope, S.B. (1993) Phys. Fluids A (to be published).

Pope, S.B. (1994) Annu. Rev. Fluid Mech. 26 (to be published).

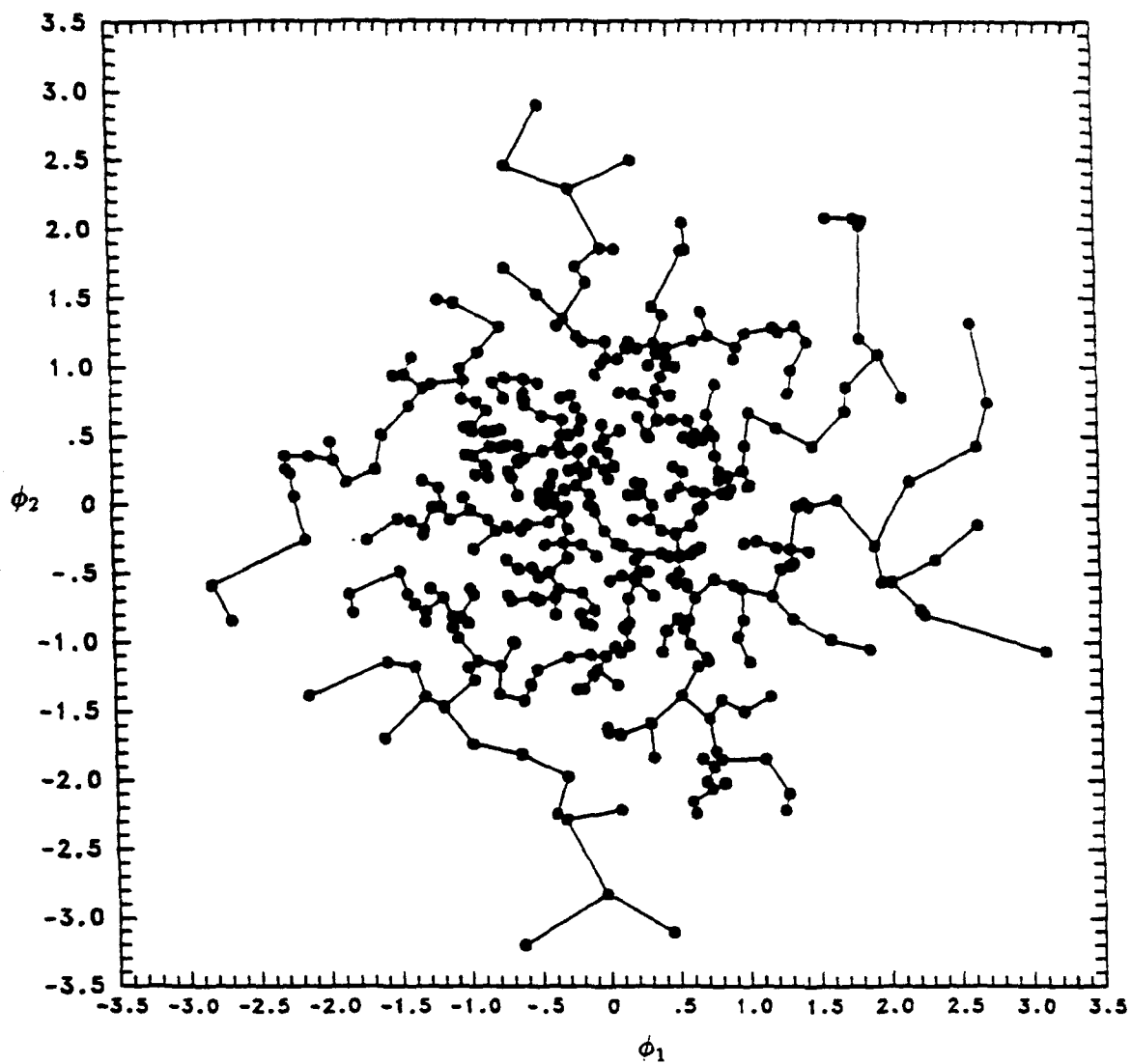Fig. 1: Euclidean Minimum Spanning Tree Connecting
400 points with compositions ($\dot{\phi}_1$, $\dot{\phi}_2$).

REACTION ZONE MODELS
FOR VORTEX SIMULATION OF TURBULENT COMBUSTION

(AFOSR Grant No. 92-J-0445)

Principal Investigator: Ahmed F. Ghoniem

Department of Mechanical Engineering
Massachusetts Institute of Technology
Cambridge, MA 02139

SUMMARY/OVERVIEW

The objectives of this project are to: (1) develop numerically efficient and physically accurate reaction zone models which can be incorporated in numerical turbulent flow simulation; (2) develop rigorous models for flow-combustion two-way coupling which are compatible with the reaction zone models and the vortex simulation of the turbulent flow; and (3) apply these algorithms to simulate turbulent reacting shear flow and investigate the effect of the flow and thermochemical parameters on the mixing, burning rate, and formation of minor species. The approach used in developing these models is based on exploiting the wide disparity of scales in turbulent combustion: chemical, diffusion and convection scales, which lends itself to asymptotic expansion methods and makes it possible to systematically reduce the governing equation in different zones of the physical domain into simpler forms. This systematic decomposition of the physical domain and the reduction of the governing equations provide the boundary conditions, which in essence represent the coupling modes between these domains, for the problem within each subdomain. Lagrangian vortex methods are used to solve the fluid dynamics problem, the transport element method is applied to determine the mixing field in the form of the distribution of conserved scalars, and a two-point boundary valve problem solver is incorporated to compute the burning rate and reaction zone structure within the reaction zone.

TECHNICAL DISCUSSION

Numerical simulation of turbulent shear flow has progressed significantly over the past decade. It is now possible to perform a simulation which can capture the formation of the large vorticity scales and their interaction dynamics in free and forced shear layers [1,2]. Using Lagrangian vortex methods; in which one concentrates the computational elements in the zones of a non-zero vorticity, applies the velocity field to transport the elements and uses the evolving strain field to reduce the scales of elements exposed to strong positive strain, long time accurate simulation of the dynamic field is possible without imposing an unreasonable burden on the computational resources. In the context of these methods, mixing is computed using a compatible scheme in which scalar gradients, and not their concentrations, are transported along with the vortex elements while the gradient magnitudes are adjusted according to the local strain field and rotation. Similar to the vortex method, the transport element method possesses natural adaptivity to rapidly changing flows, as observed during transition, post transition and the cascade towards small scale, which allows one to continue the simulation far into the strongly nonlinear stages.

Having computed the mixing field established between two streams, one can then proceed to evaluate the rate of burning given, e.g., a one-step chemical kinetics scheme. In a dilute mixture with temperature-independent, constant-rate kinetics, this step is simple to incorporate and the results can be used to examine the role of the large-scale dynamics in the mixing that precedes the formation of products. These calculations, however, could not capture some important non equilibrium processes such ignition, extinction, premixing and induction delay which are known to play important roles in high mixing rate combustion. In temperature-dependent kinetics, the problem is much more difficult especially for realistic values of the activation energy since the chemically active zone becomes much thinner than the mixing zone,

the ratio between their magnitudes being approximately the Zeldovich number, which itself is much smaller than the typical convective scales of the flow, which scales as the Damkohler number.

Given that the numerical schemes must accurately capture these different zones, it is possible to run a direct simulation of a reacting shear flow only at relatively low values of the Damkohler and Zeldovich numbers. Such simulations have been used to study the effect of combustion on the flowfield showing how the generation of vorticity via the baroclinic torque and the acceleration induced by the volumetric expansion combined lead to reduction in the growth rate and overall burning rate within the shear layer. The simulations were also used to show how forcing could be used for mixing enhancement and to counter the effect of heat release. The simulation however become exceedingly expensive as the activation energy and the adiabatic flame temperature increased. (We note in passing that high Damkohler number simulations only pose minor difficulties since the computations of the flow are confined essentially within the mixing zone.) To overcome these restrictions, we have launched a new activity to develop reaction zone models which can be used in connection with vortex simulation to model turbulent combustion [3,4].

The approach we have followed is based on two observations:
(1) As the Damkohler number increases, the reacting field behaves as if the kinetics were infinitely fast, i.e., the overall flame (convective-diffusive-reactive zone) becomes a thin front convoluted within the eddy structure. This is shown by comparing figure 1, which depicts results, in terms of a conserved scalar, of two simulations: (a) constant-density computation, and (b) flame-sheet, infinite rate kinetics approximation with variable density, and figure 2, which exhibits results of a finite-rate kinetics computation in terms of (a) the conserved scalar field, and (b) the reaction rate field. The first case is obtained by solving the equations governing a conserved scalar (Schvab-Zeldovich variable) and determining the flame location according to stoichiometry. As the figures show, high Damkohler number reacting shear flows exhibit a thin reaction zone, similar to that assumed to exist in the flame sheet limit. This result agrees with the theoretical prediction that as the Damkohler number increases, the convection-diffusion thickness of the flame should scale as $\sqrt{\tau_s D}$ where D is the diffusion coefficient and τ_s is the flow time scale.
(2) As the Zeldovich number increases, the reaction zone within the overall "flame" becomes even smaller with $\delta/\Delta \sim O(1/Z_e)$ where δ and Δ are the reaction zone thickness and flame zone thickness, respectively, while $Z_e = T_a(T_b-T_u)/RT_b^2$ where T_b and T_u and T_a are the adiabatic flame temperature, reactants temperatures, activation temperature, respectively. In a direct simulation, even if the resolution is made sufficiently high so as to capture the mixing zone, the reaction zone becomes embedded within a very thin front. This is illustrated in figure 2 which shown the reaction rate for the case shown in figure 1c where at the late stages, the reaction zone in the dark shading on the outer edges of the braids and the eddies.

To take advantage of these observations in facilitating combustion modeling in turbulent flow simulations, we are developing an overall framework for the modeling of combustion in turbulent simulations. The first step was to construct an unsteady strained flame solver which can be used to simulate combustion at high Damkohler number, large activation energy [5,6]. The model is based on the solution of a two-point boundary value problem in a transform plane whose coordinate is the strained normal to the original flame front. In the conventional terminology, this is an unsteady flame sheet model. Since a normal must be uniquely defined, an implicit assumption here limits the local radius of curvature to values lager than the convection-diffusion thickness of the flame front. Applying a series of coordinate transformation to the one-dimensional problem, which is based on an apriori knowledge of the basis functions of the solution and that leads to implicit and automatic mesh adaptivity, allows one to obtain the

solution more efficiently. Besides the this flame assumption, there are no other modeling approximations. The model is applicable to premixed, partially premixed and nonpremixed combustion, in the case of simple or complex transport and simple or complex kinetics.

The model has been tested extensively by comparing its results with those obtained using conventional approaches under conditions of slow and fast, steady and oscillating strains. The important effects of multi-step chemistry, detailed transport, heat loss and unsteady strain are all incorporated. All test results indicate that this approach is more efficient, and as accurate as the conventional approach. A sample of the results are show in figure 3 where the detailed flame structure are shown with (a) no strain and (b) high, near extinction strain. We are currently investigating how to properly couple this model with the flow simulation code. We are also investigating approaches to model locally homogeneous reaction zones, where the thin flame approximation fails, using the same mixture fraction approach but integration, instead of the time-dependent reaction-diffusion equations, a set of plug flow reactor equations the proper exchange applied on the boundary conditions.

REFERENCES

1 Ghoniem in Numerical Approaches in Combustion, **135**, Chapter 10, pp. 305-348, 1991.
2 Knio, O.M.and Ghoniem, A.F., *J. Fluid Mech.*, (1992) **243**, pp. 353-392.
3 Ghoniem et al., *24th Symposium (International)* (1992) pp..223-230.
4 Soteriou and Ghoniem, "Reaction Zone Models for the Numerical Simulation of turbulent Combustion," for presentation at the Second U.S. National Congress on Computational Mechanics, Aug. 16, 1993, Washington, D.C.
5 Soteriou and Ghoniem, "Mixing Suppression, and its reversal by forcing, due to heat release in a reacting shear layer," for presentation at *ICDER,* Aug. 3, Portugal.
6 Petrov and Ghoniem, "A computational model for unsteady strained laminar premixed flames," for presentation at *ASME Winter Annual Meeting*, 1993.
7 Petrov and Ghoniem, "Effect of detailed transport and kinetics of the response of premixed flames to external flows," to be submitted to *Combust. Sci and Tech.*
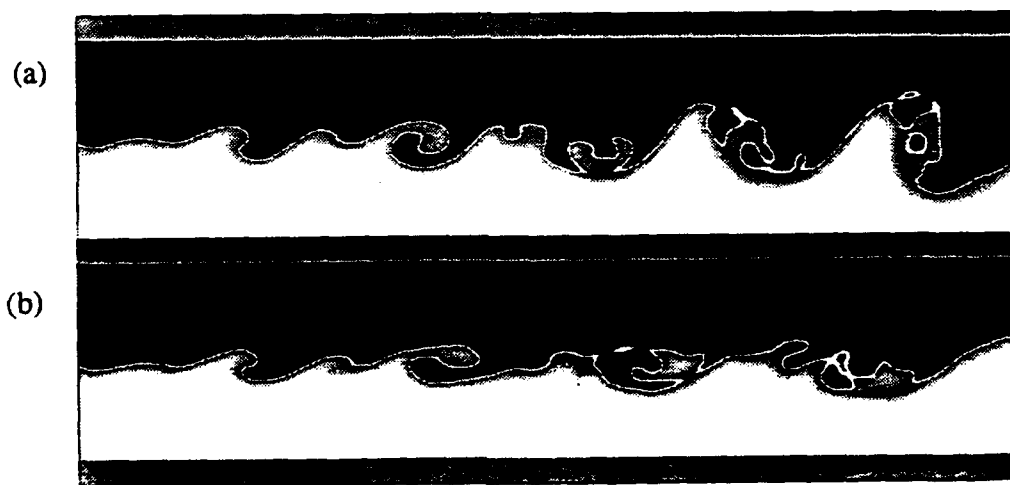
Figure 1. The conserved scalar field in (a) a constant density, and (b) a variable density reacting shear layer obtained using the infinite chemistry approximation. The velocity ratio is two and the reduced enthalpy of reaction is six.
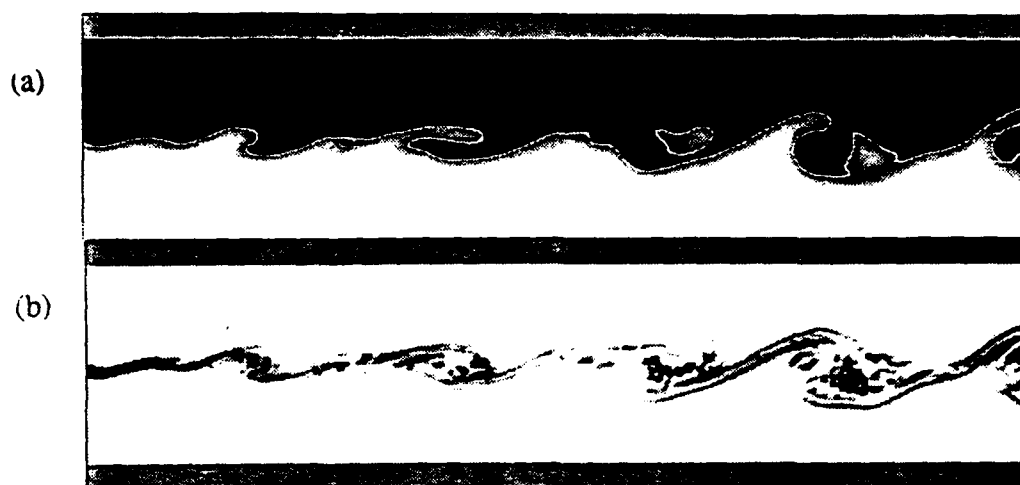
(a)

(b)

Figure 2. (a) The conserved scalar field, and (b) the reaction rate field of a reacting shear layer at the same condition as in figure 1 but with Damkohler number of 1026, normalized activation temperature of 10 and Karlovitz number of 0.49.
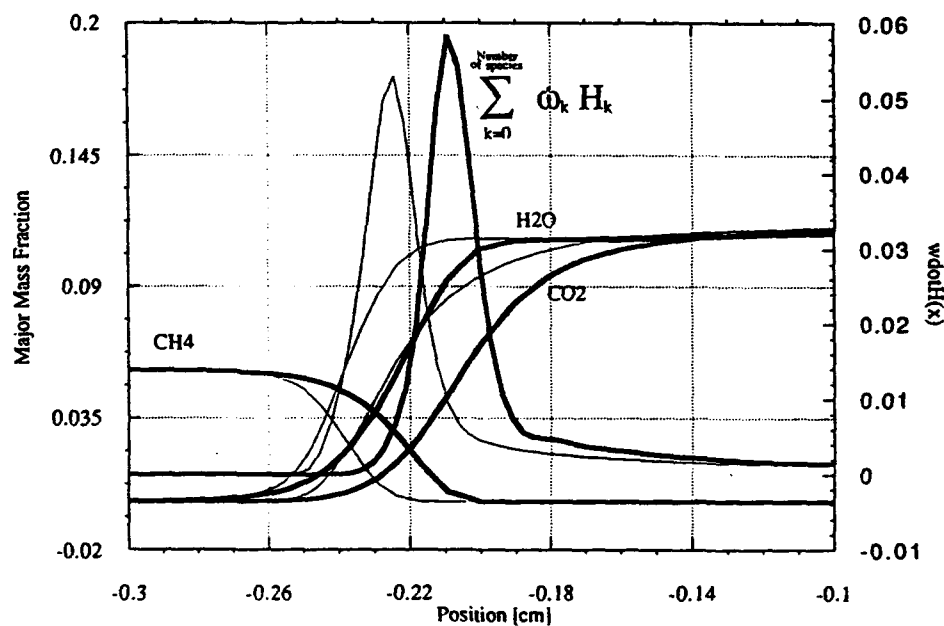

Figure 3. The distribution of major species in a methane-air premixed flame with zero strain, dark lines, and near extinction for Karlovitz number of 0.1 at t = 0.00009 sec.

TWO- AND THREE-DIMENSIONAL MEASUREMENTS IN FLAMES

Co-Principal Investigator: Marshall B. Long

Yale University
Department of Mechanical Engineering and Center for Laser Diagnostics
New Haven, Connecticut 06520-2157

SUMMARY/OVERVIEW

Laser-based imaging techniques are being developed and applied to the study of turbulent reacting flows. These techniques incorporate a variety of light scattering mechanisms to allow the measurement of the spatial characteristics of temperature, species concentrations, and velocity. The data provided by these measurements can afford a better understanding of the interaction of turbulence and chemistry in turbulent flames. Specific issues being addressed include effects of differential diffusion,[1] simultaneous velocity and scalar imaging,[2] and simultaneous multi-species imaging.[3,4] Currently, we are developing a new technique for imaging the mixture fraction in turbulent nonpremixed flames and are investigating the capabilities and limitations the technique.[5]

TECHNICAL DISCUSSION

The mixture fraction is of critical importance for many models of turbulent nonpremixed combustion. Under the idealized conditions of high Damkohler number, chemical equilibrium, and equal diffusivities, knowledge of this conserved scalar allows the derivation of essentially all quantities of interest in the flame. In a cold flow, the mixture fraction can be determined by the measurement of a single scalar quantity. In flames, however, the measurement of many species is required. The mixture fraction has been determined at a single point in turbulent flames from simultaneous measurements of the major species using spontaneous Raman scattering. Because of the weakness of the Raman process, prospects for extending this approach to two dimensions are remote. Multi-dimensional measurements of the mixture fraction would be highly desirable because of the possibility of obtaining gradients and the scalar dissipation (proportional to the square of the mixture fraction gradient).

A means of determining the mixture fraction without measuring all of the major species has recently been proposed. In this approach, measurements of the Rayleigh scattering and of the fuel concentration are combined in an iterative process to determine the mixture fraction. The flame selected for this study was a turbulent nonpremixed acetaldehyde flame. Acetaldehyde (CH_3CHO) was chosen for its relatively high fluorescence yield and small variation of fluorescence intensity with temperature, which allows the fuel concentration to be found directly from the acetaldehyde fluorescence. Another attractive characteristic relates to the flame chemistry of acetaldehyde, which is quite close to that of methane.

The experimental configuration used for Rayleigh scattering/acetaldehyde fluorescence imaging is shown schematically in Fig. 1. The flow was illuminated by two

overlapping laser sheets. The first, formed from the second harmonic of a Nd:YAG pumped dye laser (320 nm, 10 mJ per 10 ns pulse; 10 mm sheet height), excited fluorescence from the acetaldehyde fuel. The second illumination sheet, from a flashlamp-pumped dye laser (532 nm, 2 J per 2 μs pulse, 2 cm sheet height), excited Rayleigh scattering. The fuel fluorescence was imaged onto a gated image intensifier that was optically coupled to a cooled CCD detector. The Rayleigh scattering was imaged onto a separate gated intensifier optically coupled to the second CCD detector. The two lasers and image intensifiers were fired sequentially with a pulse separation of ~3 μsec. This temporal separation ensured that there was no interference between the detected signals from the two laser sheets, but was short compared to the smallest flow time scales.

A matched pair of Rayleigh and fluorescence images from a turbulent acetaldehyde-air flame is shown in Fig. 2 (a) and (b). The fuel was a mixture of acetaldehyde diluted 1/1 by air (on a mass basis) to eliminate soot. It emanated from piloted burner (d = 3.9 mm) with a velocity corresponding to Re = 18,000. The flame was enshrouded in a low velocity filtered air coflow in order to keep the measurement area clear of particles, which would interfere with the Rayleigh images.

A conserved scalar, β, based on the fuel mass fraction (Y_f) and the enthalpy (H = $c_p T/Q$) served as the basis for determining the mixture fraction, ξ:

$$\beta = Y_f + c_p T/Q$$

$$\xi \equiv \frac{\beta - \beta_2}{\beta_1 - \beta_2} = \frac{Y_f + c_p/ Q(T - T_2)}{Y_{f,1} + c_p/ Q(T_1 - T_2)}$$

where the subscripts denote the fuel (1) and oxidizer (2) streams. Y_f is obtained from the fluorescence images and T is related to the Rayleigh images. The mixture fraction can be expressed in terms of the fluorescence signal, F, and the Rayleigh signal, Ra, as follows:

$$\xi = \frac{C_1 \, a_T \, F}{W \, Ra \, F_{cal}} + C_2 \, (a_T / Ra - T_{ambient}).$$

C_1, C_2, and F_{cal} are calibration constants, a_T is proportional to the local Rayleigh cross section, and W is the local mixture mole weight. Since a_T and W are both functions of ξ, an iterative process was used on a pixel by pixel basis to derive the temperature and mixture fraction. The procedure converges quickly, usually within less than four iterations.

The calculated mixture fraction and temperature are shown in Fig. 2 (c) and (d). Evident in the temperature mappings are the high temperature zones on the outer edge of the flame. As expected, the mixture fraction peaks in the unburned regions near the center of the jet. The results of this preliminary study show significant promise in terms of obtaining useful measurements of the mixture fraction. The strength of the signals from the Rayleigh scattering and the fuel fluorescence allows computations of the mixture fraction high in spatial resolution and low in noise, thus making determination of the scalar dissipation feasible.

REFERENCES

1) M. B. Long, S. H. Stårner, and R. W. Bilger, "Differential Diffusion in Jets Using Joint PLIF and Mie Imaging," Combust. Sci. Tech., in press.

2) K.M. Lyons, J. Frank, and M.B. Long, "Simultaneous Velocity and Concentration Imaging in a Gas Phase Jet," to be submitted.

3) S.H. Stårner, R.W. Bilger, R.W. Dibble, R.S. Barlow, D.C. Fourguette and M.B. Long, "Joint Planar CH and OH LIF Imaging in Piloted Turbulent Jet Diffusion Flames Near Extinction," accepted for publication in *Proceedings of the Twenty-Fourth Symposium (International) on Combustion*, Sydney Australia, July 5-10, 1992.

4) M.B. Long, "Multi-Dimensional Imaging in Combusting Flows by Lorenz-Mie, Rayleigh, and Raman Scattering," to appear in *Diagnostics for Flows with Combustion*, A.K.M.P. Taylor, ed. (Academic Press, 1993).

5) S.H. Stårner, R.W. Bilger, K.M. Lyons, D.F. Marran, and M.B. Long, "Planar Mixture Fraction Measurements in Turbulent Flames by a Joint Rayleigh and Fuel LIF Method," submitted to *Proceedings of the 14th International Colloquium on the Dynamics of Explosions and Reactive Systems*
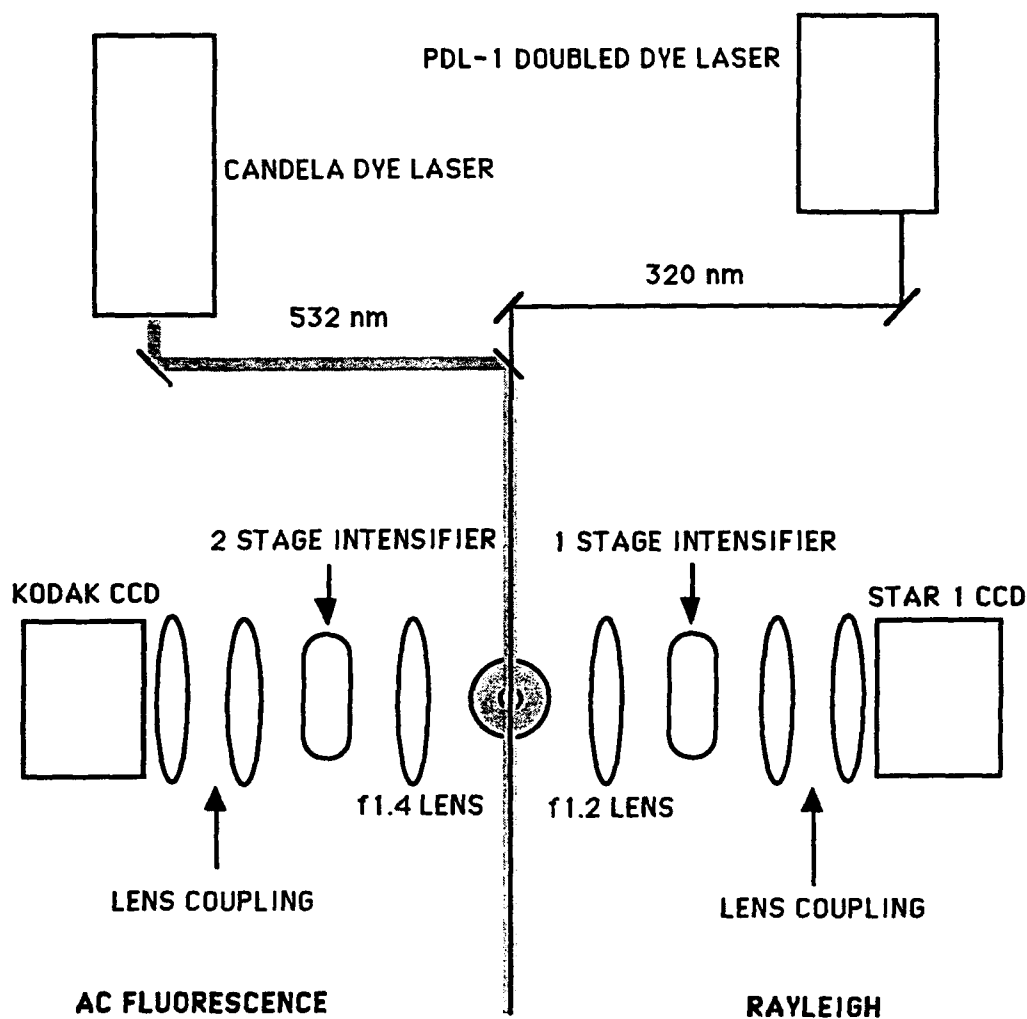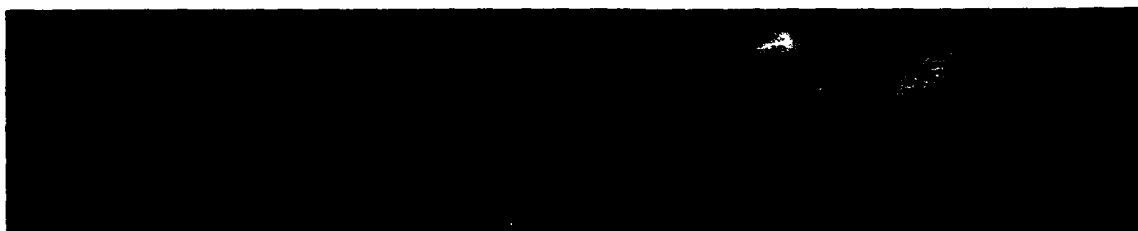
Fig. 1. A schematic diagram of the mixture fraction imaging experiment. Two overlapping laser sheets illuminate the turbulent nonpremixed flame. One CCD camera images Rayleigh scattering from the flame while the other detects the fluorescence from the acetaldehyde/air fuel.

Rayleigh

(a)

Fluorescence

(b)

Mixture Fraction (0 - .8)

(c)

Temperature (300 - 1900)

(d)

Fig. 2. Images of the Rayleigh scattering and fluorescence from a piloted, turbulent diffusion flame of acetaldehyde (Re = 18,000) and the computed temperature and conserved scalar fields. The measurements have been made 25 d downstream (d = 3.9 mm) and cover 4.5 mm in the axial direction by 23 mm in the radial direction. The Rayleigh image (a) shows the distribution of light scattered elastically from the flame and the ambient air, while the fluorescence image (b) is indicative of the distribution of unburned fuel. Using the data from (a) and (b) and suitable calibrations, both the mixture fraction distribution (c) and the temperature distribution (d) were computed in an iterative manner. In each image, the scalar value is represented by a linear gray scale with lighter shades corresponding to larger values.

HIGH RESOLUTION MEASUREMENTS OF MIXING AND REACTION PROCESSES IN TURBULENT FLOWS

Werner J.A. Dahm

Gas Dynamics Laboratories
Department of Aerospace Engineering
The University of Michigan
Ann Arbor, MI 48109-2140

Summary/Overview

This research program is an experimental and theoretical investigation into the fine scale structure of mixing and combustion processes in turbulent flows. It has the following three specific objectives: *(i)* to develop and implement new, high-resolution, four-dimensional, quantitative imaging methods for direct experimental measurements of the small scale structure of mixing and chemical reaction processes in turbulent flows, *(ii)* to use these new imaging methods to investigate the detailed physical structure and dynamics of molecular mixing and chemical reactions in turbulent flows, and *(iii)* to incorporate results from these experimental studies into improved models of reacting turbulent flows. Results are providing remarkable new insights into the nature of the small scales of mixing and combustion processes in turbulent flows. These are contributing to predictive submodels allowing computations of the fine structure of reacting flows for improved high-speed air-breathing propulsion systems.

Technical Discussion

Work during the past year has focussed on two major technical areas. The first involves detailed numerical analyses of our four-dimensional (x-y-z-t) spatio-temporal imaging measurements of the small scale structure of $Sc \approx 1$ conserved scalar mixing in turbulent flows. A sample of an individual three-dimensional (x-y-z) spatial data volume from one of these measurements is shown in Fig. 1. Each such data volume consists of over 16 million individual data points, and each experiment produces in excess of 150 such data volumes spanning a total of more than 3 billion point measurements. The imaging technique for obtaining these novel data has been outlined in our previous abstracts, as well as in Refs. [1] - [4]. The data are fully-resolved down to the finest lengthscales arising in the scalar gradient field in all three space dimensions, and can therefore be directly differentiated using linear central differences to determine the scalar gradient vector field $\nabla\zeta(x,t)$ and the associated scalar energy dissipation rate field $\nabla\zeta\cdot\nabla\zeta(x,t)$. Analysis of the resulting joint scalar and scalar dissipation volumes proceeds in much the same way as is done in postprocessing of DNS data. A key finding has been that essentially *all* the molecular mixing occurs in thin strained laminar diffusion layers of the type seen in Fig. 1(b). Our numerical analyses of the detailed internal structure of the molecular mixing within these layers has confirmed that strain-limited solutions of the conserved scalar transport equation provide a remarkably accurate model of the scalar energy dissipation profiles within these layers. Analyses during the past year have addressed the topology which the scalar dissipation layers assume as a result of their repeated stretching and folding by the turbulent strain rate and vorticity fields. The aim has been to obtain quantitative measures of the scaling which this topology satisfies, and to relate these to the dynamics of the "turbulent cascade" represented by this stretching and folding process. From the three-dimensional spatial character of the turbulent dissipation rate field in any given data volume (see Fig. 1b), we construct the surface of local layer-normal dissipation maxima and compute the distribution of dissipation layer separations λ/λ_ν, as shown in Fig. 2. The roughly lognormal form appears consistent with the scale similarity arguments, but for large and small layer separations we obtain asymptotic power law forms. The λ^{-1} scaling for small separations appears consistent with a parallel

sheet arrangement at those scales, while the λ^{-3} scaling for large separations may arise from the continual creation of larger separations by the entrainment characteristic of open systems. Our continuing work in this area aims to develop a dynamical model of the scalar dissipation field based on the strain and vorticity field dynamics.

The second major area of work during the past year has sought to extend our earlier results in Ref. [5] for the equilibrium spatial structure of species concentration fields $Y_i(x,t)$ and reaction rate fields $w_i(x,t)$ to nonequilibrium chemistry in Ref. [6]. The objective is to understand the changes in the structure of these fields as the flow is driven to increasing deeper levels of chemical nonequilibrium typical of high-speed propulsion systems. This is based on our fully-resolved, two-dimensional, Rayleigh imaging measurements of the $Sc \approx 1$ conserved scalar field in gaseous turbulent flows. Our earlier work has shown that, even at unity Schmidt number, essentially all of the molecular mixing occurs in similar layer-like structures as seen in Fig. 1. Here the aim is to determine the implications of this structure for nonequilibrium chemistry. Self-similar far-field scalings allow the scalar and dissipation rate data to be mapped to any downstream location in a turbulent jet flow. The data are then coupled with a strained laminar flamelet library for hydrogen-air chemistry to produce the instantaneous species concentration and reaction rate fields for several increasing levels of chemical nonequilibrium. The Reynolds number is held constant while the Damköhler number is systematically varied by changing the effective nozzle diameter. Comparisons at different downstream locations in the jet allow effects due to the decreasing scalar values to be separated from effects due to the varying degree of chemical nonequilibrium. The combined results are yielding a clearer physical picture of the structure of the molecular mixing and chemical reaction processes in turbulent reacting flows. Figure 3 shows results for the OH mass fraction fields $Y_{OH}(x,t)$ for two different cases for which conditions in the flame range locally from moderate to deep nonequilibrium conditions. The layer-like OH zones seen near equilibrium broaden with increasing local Damköhler number and with increasing downstream location in the flame, as is also seen in direct measurements. It is remarkable, however, that despite the wide variations in the OH concentration field structure seen in Fig. 3, all of these fields ultimately resulted from the same simple layer-like structure in the scalar dissipation rate field of a single data plane. This appears to have considerable potential for understanding the wide variations apparent in the OH concentration fields into a single underlying canonical structure. Evidently, the simple layer-like structure suffices to reconcile both the layer-like and broad OH zones appearing in various measurements under differing conditions of nonequilibrium and locations in the flame.

References

1. Dahm, W.J.A., Southerland, K.B. & Buch, K.A. (1991) "Direct, high-resolution, four-dimensional measurements of the fine scale structure of Sc - 1 molecular mixing in turbulent flows," Physics of Fluids A 3, 1115-1127.

2. Dahm, W.J.A., Southerland, K.B. & Buch, K.A. (1991) "Four-dimensional laser induced fluorescence measurements of conserved scalar mixing in turbulent flows," in Applications of Laser Techniques to Fluid Mechanics, R. Adrian, Ed. Springer Verlag, Berlin.

3. Dahm, W.J.A. and Buch, K.A. (1991) "Fine structure characteristics of large Schmidt number molecular mixing in turbulent flows," to appear in Chemical Reactions and Physical Processes in Turbulent Liquids, J. Hunt, Ed., Cambridge University Press.

4. Dahm, W.J.A. "Experimental studies of the fine scale structure of mixing in turbulent flows," Proceedings of the 13th Symposium on Turbulence, University of Missouri-Rolla, Rolla, MO.

5. Buch, K.A., Dahm, W.J.A., Dibble, R.W. and Barlow, R.S. (1992) "Structure of equilibrium reaction rate fields in turbulent jet diffusion flames," Proc. 24th Int'l. Symp. on Combustion, 295-301, The Combustion Institute, Pittsburgh.

6. Dahm, W.J.A and Bish, E.S. (1992) "High-resolution measurements of molecular transport and reaction processes in turbulent combustion," to appear in Turbulence and Molecular Processes in Combustion, Elsevier.
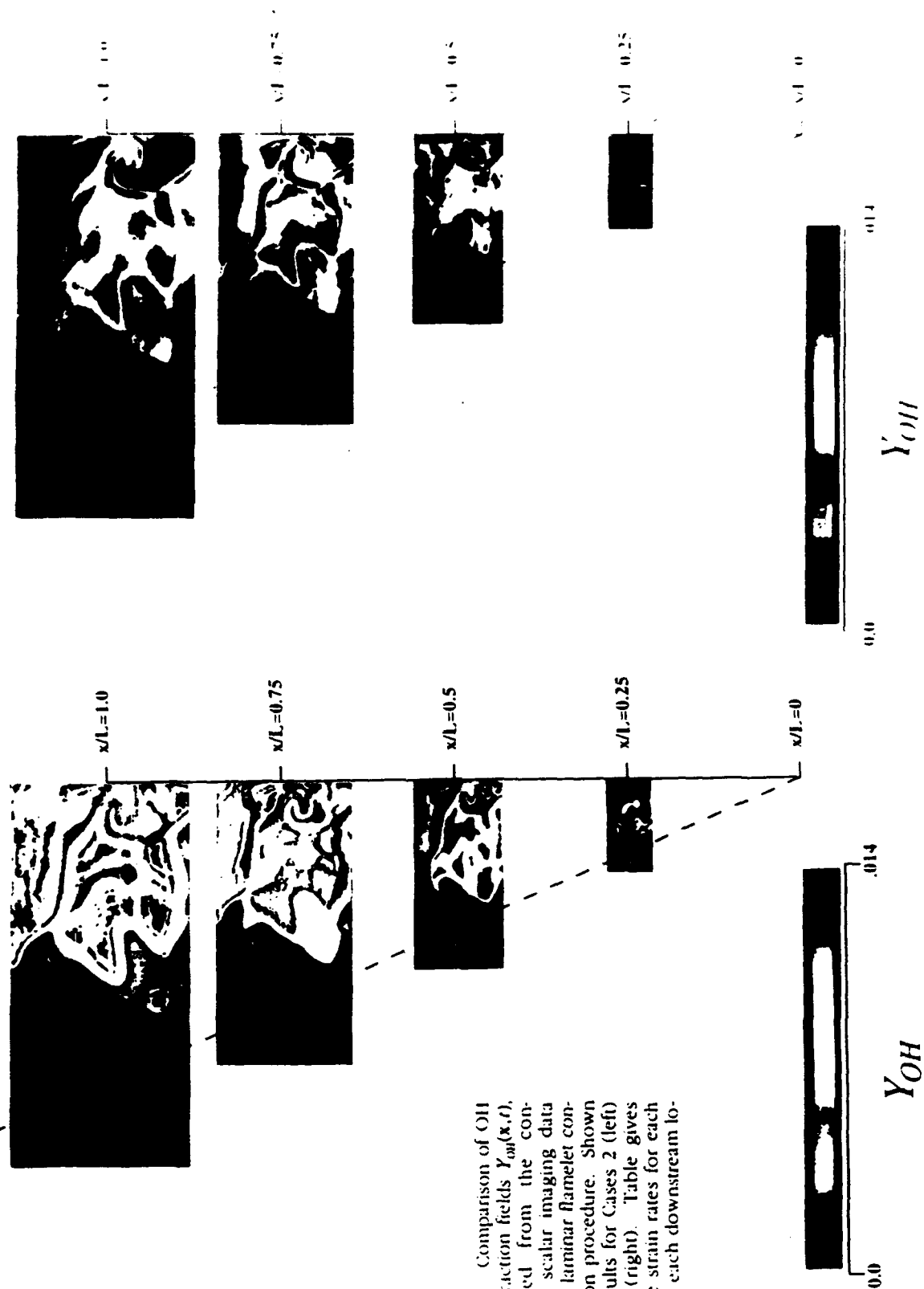
Fig. 1a. $\zeta(\mathbf{x},t)$.

Fig. 1b. $log_e \nabla \zeta \cdot \nabla \zeta(\mathbf{x},t)$.
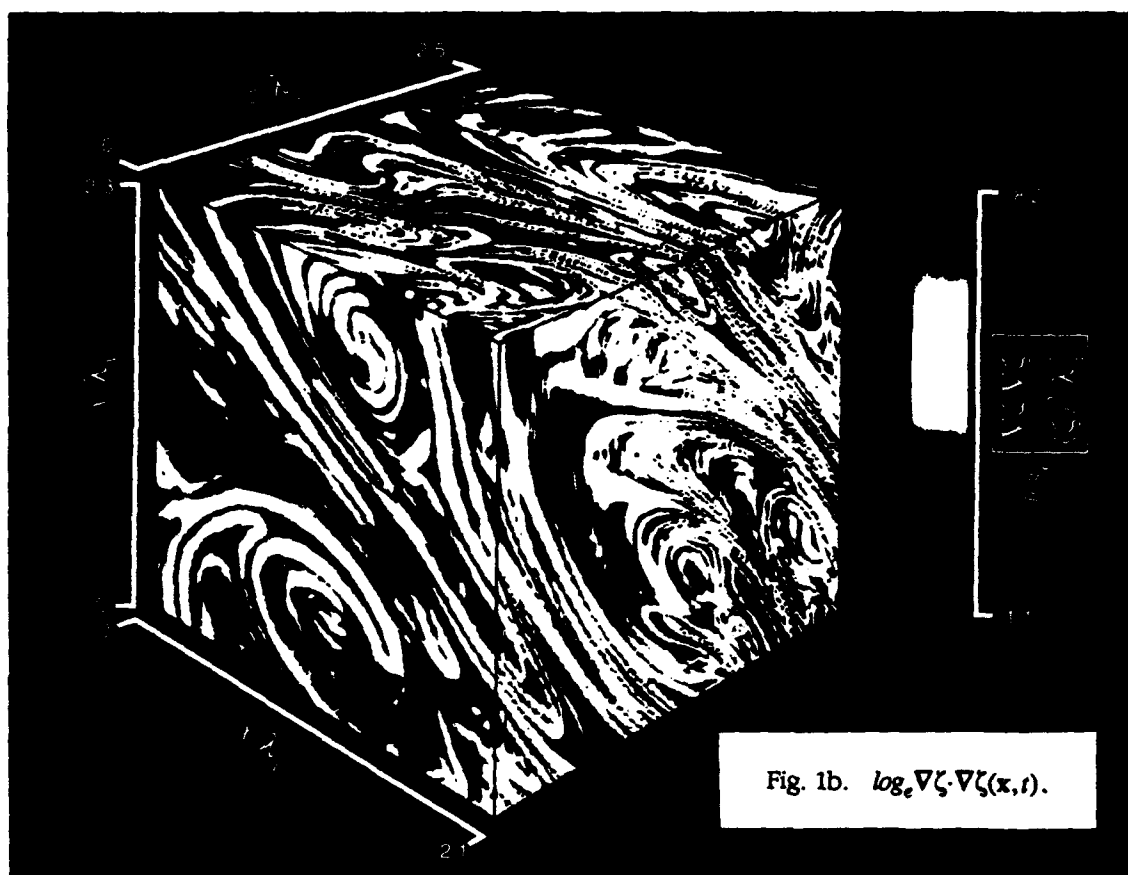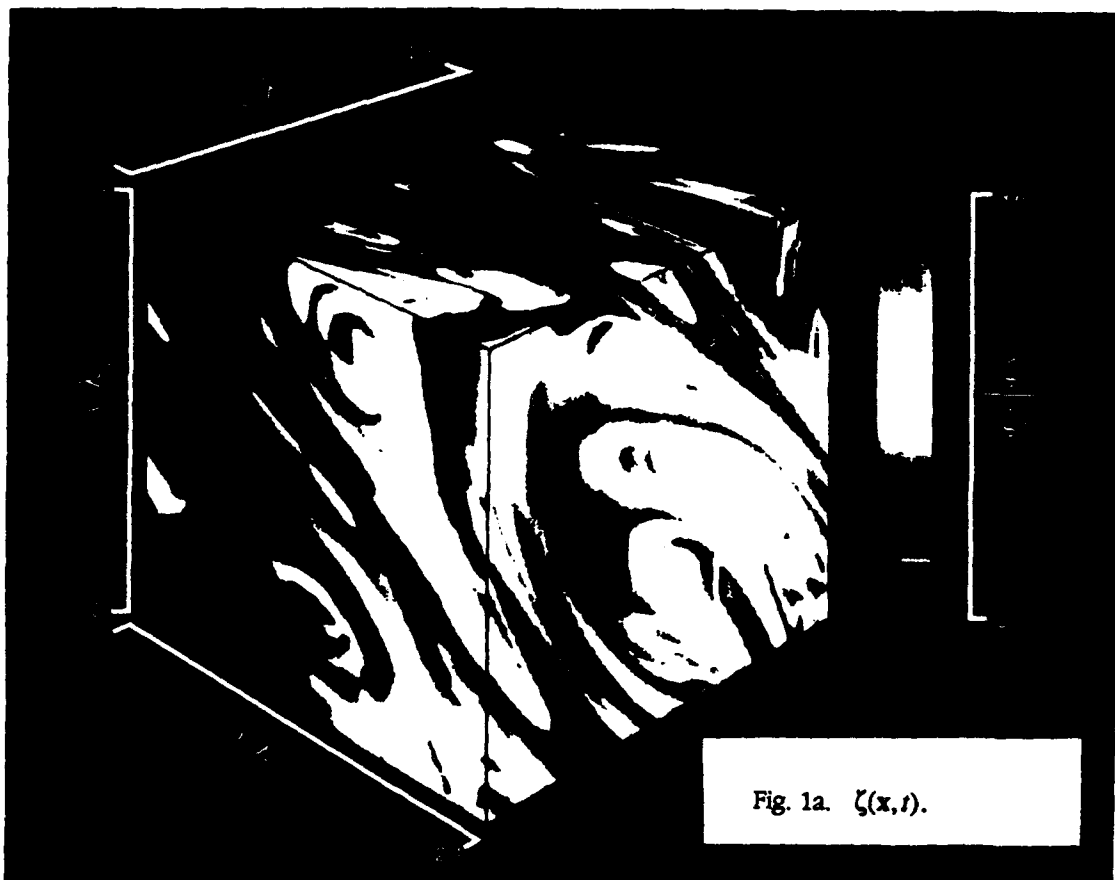
Fig. 3. Comparison of OH mass fraction fields $Y_{OH}(x,t)$, obtained from the conserved scalar imaging data via the laminar flamelet construction procedure. Shown are results for Cases 2 (left) and 3 (right). Table gives relative strain rates for each case at each downstream location.

COMBUSTION RESEARCH

Work Unit 2308S705

Principal Investigator: W. M. Roquemore

Aero Propulsion and Power Directorate

Wright-Patterson AFB OH 45433-7103

SUMMARY/OVERVIEW:

This presentation is in two parts. The first part involves numerical studies of transitional jet diffusion flames. The second part of the presentation involves studies of a vortex flame interaction that is similar to that observed in turbulent jet flames. Transitional jet diffusion flames are studied using a time-dependent, axisymmetric, third-order accurate, computational fluid dynamics based model. Previous experimental studies of transitional jet flames have shown that they have a double vortex structure with large scale buoyancy driven vortices outside the flame surface and smaller Kelvin-Helmholtz type vortices in the shear layer of the fuel jet inside the flame surface. The model correctly predicts the shapes and the time and spatial evolution of these complex structures. Computational experiments are also performed to examine the long standing question: Why do the vortices inside transitional jet flame have very long coherence lengths as compared to those of cold jets? It is found that buoyancy is a major factor.

Vortex-flame interactions are important to the fundamental understanding of turbulent jet diffusion flames. However, they are difficult to study because the interactions occur randomly in time and space and involve vortices with different sizes, shapes, and velocities. The second part of this talk will present the initial results of an isolated vortex-flame interaction event that is periodically reproduced. The interaction has features that are similar to those observed in turbulent jet diffusion flames. A direct numerical simulation with temperature and concentration dependent transport coefficients, one-step fast chemistry, and unity Lewis number is used to investigate the dynamic characteristics of the vortex-flame interaction.

TECHNICAL DISCUSSION:

In 1980, Yule et al. (Vol. 19, No. 6, AIAA Journal) observed large scale vortex structures outside and inside the visible flame surface in a transitional jet diffusion flame. Since this observation, numerous groups have observed and attempted to explain the dual vortex structure in jet flames. An unusual characteristic of the inner structures is their long coherence length, which can extend more than 20 jet diameters downstream as compared to about four diameters for cold jets. The long coherence length of the inner structures is important in the way jet diffusion flames transition to turbulent flames. Although numerous speculations exist in the literature, the cause of the long coherence length has remained a mystery. Our studies show that buoyancy is an important factor in the coherence of the inner structures. Direct numerical simulations of the time-dependent Navier Stokes equations are used to capture both the inner and outer structures of jet diffusion flames. Confidence in the computations is established by good agreement between experiments and numerical results. Computational experiments provide the insight into the origin of the inner structures and are used to illustrate how buoyancy contributes to their long coherence length. The buoyant acceleration of the hot gases of the flame entrains fluid that would normally be entrained by the inner vortices of the jet shear layer and cause their rapid dissipation. The buoyant acceleration also reduces the velocity gradient in the jet shear layer and this reduces the driving process that causes fluid to be entrained by the vortices.

The convective and rotational motion of the large outside vortices also results in very different type of growth and merging processes in the small scale structures in transitional jet flames. It is observed experimentally and demonstrated by direct numerical simulations that the inner vortices, which happen to be at the location where the flame pinches in as a result of the motion of the outer vortices, are longer than their neighbors. This can be understood by visualizing the dynamics of the radial flame oscillations induced by the outer vortices. As the flame is squeezed in towards the centerline, the fluid inside the flame accelerates in much the same way as it would if it was flowing in a flexible tube in which the walls were flexing in and out. The dynamics of the flame oscillation are such that all of the inner vortices that pass the locations where the flame is moving inward, undergo a local axial stretching or elongation due to the acceleration of the inner fluid. The elongation process can also result in a head-to-tail type of merging of the inner vortices. This is very different from the merging observed in conventional shear layers where the vortices roll around each other and grow radially. The elongation and axial merging process have a significant impact on the spectrum of transitional jet flames. Direct numerical simulation experiments provide physical insights into the interpretation of the experimentally observed spectra of these flames.

Lean blowout, altitude relight, emissions, and combustion efficiency are of practical importance in the design of gas turbine combustors. They all involve turbulent combustion processes that need to be better understood if accurate combustor design models are to be developed. Turbulent jet diffusion flames are used to gain insight into turbulent combustion processes and to develop numerical models for use in combustor design. Although considerable progress has been made in understanding turbulent jet diffusion flames, there still remain many important questions about the turbulent combustion processes and the simplifying assumptions required to effectively model them. The conceptual view of turbulent reaction zones and the interplay between turbulence and chemistry are germane to modeling approaches. In our study the statistical fabric of a turbulent reaction zone is viewed as ensembles of vortex-flame interactions. The statistics of the problem are eliminated by isolating and studying a single vortex-flame interaction.

It is important to understand the individual vortex-flame interactions for several reasons. First, they can increase or decrease the turbulent reaction rate. Vortex-flame interactions can increase the surface area of the flame which leads to an overall increase in the global reaction rate and a reduction in the length of the flame. However, if the vortex-flame interactions are sufficiently strong, they can reduce the reaction rate. For example, a vortex with a high radial velocity can pass through the flame creating a localized hole in which no chemical reactions take place. The holes can cause the flame to split or lift when they form near the jet exit. When the holes represent a large fraction of the flame surface, the global reaction rate is expected to decrease. This can lead to a reduction in combustion efficiency and flame blow-out. Second, vortex-flame interactions may be building blocks for statistical theories of turbulent flames. It is conceivable that an ensemble of only a relatively few basic types of vortex-flame interactions needs to be considered to accurately represent the statistical result.

This talk presents the initial results of a vortex-flame interaction that, when viewed in two-dimensions, appears similar to those observed in turbulent jet diffusion flames. A counter-rotating pair of ring vortices is formed by driving the flow. Acoustic forcing of the fuel produces a vortex-flame interaction that results in an outward bulge of the flame surface that becomes extended to the point that a flame is no longer visible by eye or OH imaging. When this happens, a hole is said to exist. In reality the hole is a ring that extends around the flame but, in a two-dimensional plane, it appears as a hole and will be referred to as such in this talk. Planer visualization and line-temperature measurement techniques are phase-locked to the driving pulse so that the interaction can be strobed at different time steps. A direct numerical simulation with concentration dependent transport coefficients, one-step fast chemistry, and unity Lewis number is used to investigate the dynamic characteristics of the flame-vortex interaction.

ADVANCED SUPERCRITICAL FUELS

AFOSR Task # 93WL

Principal Investigators: Tim Edwards, Jim Gord, Mel Roquemore

USAF Wright Laboratory
WL/POSF Bldg 490
1790 Loop Rd N
Wright Patterson AFB, OH 45433-7103

SUMMARY/OVERVIEW:

Increases in aircraft and engine performance are increasing the heat load being transferred into an aircraft's primary coolant--the fuel. This research is aimed at understanding the limitations of operation of fuel heated to 900 F (480 C). Important areas are known to be thermal stability, heat transfer/flow instabilities, and physical properties. In the initial stages of this research, thermal stability results are reported.

TECHNICAL DISCUSSION

Development of thermally stable jet fuels has been recognized as a critical research area because an aircraft's fuel is the only practical means of absorbing dramatically increasing on-board heat loads. Current practice for Air Force engines is to limit the fuel to 163 C (325 F) bulk temperature and 205 C (400 F) wetted wall temperature. The Air Force would like to develop fuels in the near term with thermal stability limits at least 55 C (100 F) higher than this [1]. In the long term, the heat management requirements of future Air Force aircraft are expected to be sufficiently demanding that the aircraft fuel system will need to operate at much higher temperatures. The goal for this fuel is to increase the thermal stability to 483 C (900 F, hence the name "JP-900" [2]).   This high temperature is above the fuel thermodynamic critical temperature, which typically ranges from 370-415 C (700-780 F) for current jet fuels [3]. Typical fuel system pressures are approximately 34-68 atm (500-1000 psia), well above the fuel critical pressure (19-24 atm). The physical and chemical properties of supercritical fuels are expected to be dramatically different from gases and liquids. There is little information available on the properties of fuels when operated at supercritical conditions [2].

One area of concern for fuels operating at high temperatures is their thermal decomposition and the formation of insoluble products that deposit onto metal surfaces (fouling). This area has been studied in heated metal tubes (simulating aircraft nozzles and heat exchangers) by various investigators [4,5,6]. The residence time of a given fuel molecule inside the heated tube is typically on the order of seconds, while the test time (or the amount of time the metal surface is exposed to heat and fuel flow) is on the order of hours. Several researchers have seen a peak in surface deposition near 370 C (700 F) when the deposition is plotted against wetted wall or film temperature. This is illustrated in Figure 1 with data taken at Wright Laboratory in a "typical" jet fuel. In this test, fuel flows through a stainless steel tube inside of a furnace, simulating a heat exchanger tube. The fuel is heated to ~900 F (480 C). Thermal stability is assessed by deposition on the tube and on a 2 μm stainless steel filter downstream. Deposition is measured by the carbon burnoff technique. The decrease in deposition between approximately 375 and 480 C (700-900 F) has been attributed either to temperature-dependent auto-oxidation chemistry [1,2,4] or to enhanced solubility of the deposit in the supercritical fuel [5]. The peak disappears if the dissolved oxygen in the fuel, typically about 70 ppm in air-saturated fuel, is removed [4,6]. One of the goals of this work is to investigate the source of this

deposition peak and determine ways to reduce, avoid, or eliminate it without resorting to removing the dissolved oxygen from the fuel.

One way of minimizing the deposition is to increase the thermal stability of the fuel by further processing to remove heteroatoms, olefins, and other compounds which lower the thermal stability of the fuel. The deposition results for a pure hydrocarbon and a highly processed jet fuel are shown in Figure 2. Note that the deposition has been reduced by a factor of about 50 over that shown in Figure 1 for a typical jet fuel. Figure 2 also demonstrates results seen throughout this research--deposition peaks for hydrocarbons of widely varying critical temperatures always occur at very similar wall/fuel temperatures for fixed flow conditions. Changing flow conditions can shift this deposition peak by at least 200 C [5,6]. This was verified for hydrocarbons ranging from n-octane (T_c=296 C) to n-hexadecane (T_c=447 C). This demonstrates that the deposition peak is not related to the critical properties of the fuel, but rather is a chemical kinetic effect. Other work at WL has indicated that surface deposition is closely related to oxygen consumption; that is, the decrease in deposition at wall temperatures above 450-500 C occurs . because all of the dissolved oxygen has been consumed [9,10].

The tendency of various classes of hydrocarbons to form insoluble deposits has been studied. As shown in Table 1, n-paraffins and naphthenes such as decalin are very thermally stable. Interestingly, methylcyclohexane has a relatively low thermal stability. This has been confirmed on the Jet Fuel Thermal Oxidation Tester (JFTOT), where MCH behaves similarly to typical jet fuels. The surface deposition from fuel heated to 900 F (480 C) correlates fairly well with the JFTOT breakpoint. The JFTOT is the standard thermal stability test for jet fuel. The filter deposition correlates much more poorly with the JFTOT breakpoint, most notably for JP-7 as shown in Table 1 and Figure 3. The reason for this unusual behavior are being investigated.

1.   T. Edwards, T., S. D. Anderson, J. A. Pearce, and W. E. Harrison III, "High Temperature, Thermally Stable JP Fuels - An Overview," AIAA Paper 92-0683, presented at AIAA Aerospace Sciences Meeting, Jan. 1992.
2.   Edwards, T., "USAF Supercritical Hydrocarbon Fuels Interests," AIAA Paper 93-0807, to be presented at AIAA Aerospace Sciences Meeting, Reno, NV, Jan. 1993.
3.   Martel, C. R., "Air Force Aviation Fuel Thermal Oxidation Stability R&D, " in NASA TM 79231 "Jet Fuel Thermal Stability", W. F. Taylor, ed., Nov. 1978.
4.   Hazlett, R.N., J.M. Hall, and M. Matson, Ind. Eng. Chem. Prod. Res. Dev., Volume 16(2): p. 171-177, 1977; Bradley, R., R. Bankhead, and W. Bucher, Air Force Aero Propulsion Laboratory Report AFAPL-TR-73-95, April 1974; Marteney, P.J. and L.J. Spadaccini, Journal of Engineering for Gas Turbines and Power (ASME Transactions), Volume 108, pp. 648-653, 1986; Taylor, W.F., Ind. Eng. Chem. Prod. Res. Dev., Volume 13(2), pp. 133-138, 1974, and Ind. Eng. Chem. Prod. Res. Dev., Volume 19, pp. 65-70, 1980; Chin, J. S., and Lefebvre, A. H., Journal of Propulsion and Power, Vol 8, No. 6, pp. 1152-1156, 1992.
5.   Edwards, T., Zabarnick, S., "Supercritical Fuel Deposition Mechanisms," AIChE Paper 58d, Miami Beach, FL, Nov. 92.
6.   Edwards, T., Liberio, P., "The Thermal-Oxidative Stability of Fuels at 900 F (480 C)," paper being prepared for 3/94 ACS meeting in San Diego, CA.
7.   Faith, L. E., Ackerman, G. H., and Henderson, H. T., "Heat Sink Capabilities of Jet A Fuel: Heat Transfer and Coking Studies," NASA CR-72951, July 1971.
8.   Hines, W. S., and Wolf, H., "Pressure Oscillations Associated With Heat Transfer to Hydrocarbon Fluids at Supercritical Pressures and Temperatures," ARS Journal, March 1962, 361-366.
9.   Heneghan, S. P., Martel, C. R., Williams, T. F., and Ballal, D. R., "Effects of Oxygen and Additives on the Thermal Stability of Jet Fuels," paper to be presented at the 38th ASME International Gas Turbine and Aeroengine Congress, May 24-27, 1993, Cincinnati, Ohio.
10.   Jones, E. G., Balster, W. J., and Post, M. E., "Degradation of a Jet A Fuel in a Single-Pass Heat Exchanger, " paper to be presented at the 38th ASME International Gas Turbine and Aeroengine Congress, May 24-27, 1993, Cincinnati, Ohio.
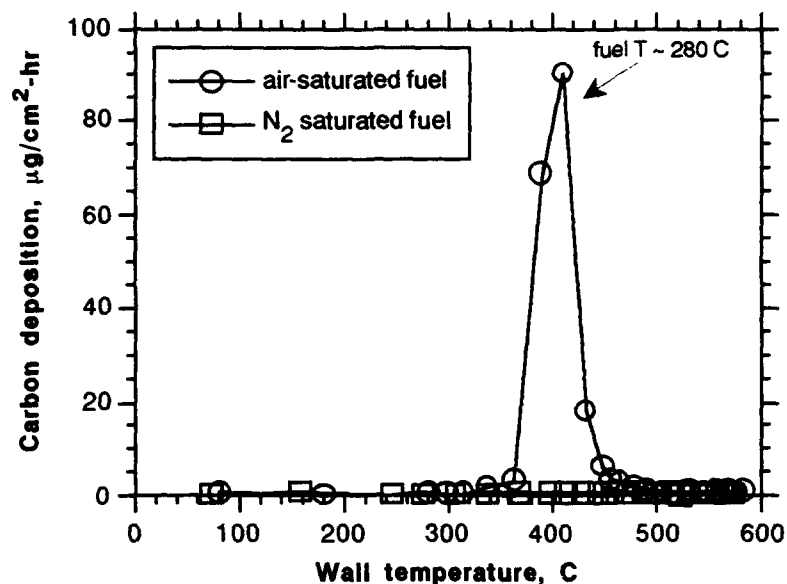
Figure 1. Effect of fuel de-oxygenation in single-tube heat exchanger test. Jet A-1 fuel, 69 atm (1000 psi), 12 ml/min, fuel outlet temperature ~480 C (900 F), 15 hr tests. The downstream filter contained 1410 μg (air-saturated fuel) and 190 μg (N$_2$ saturated fuel).
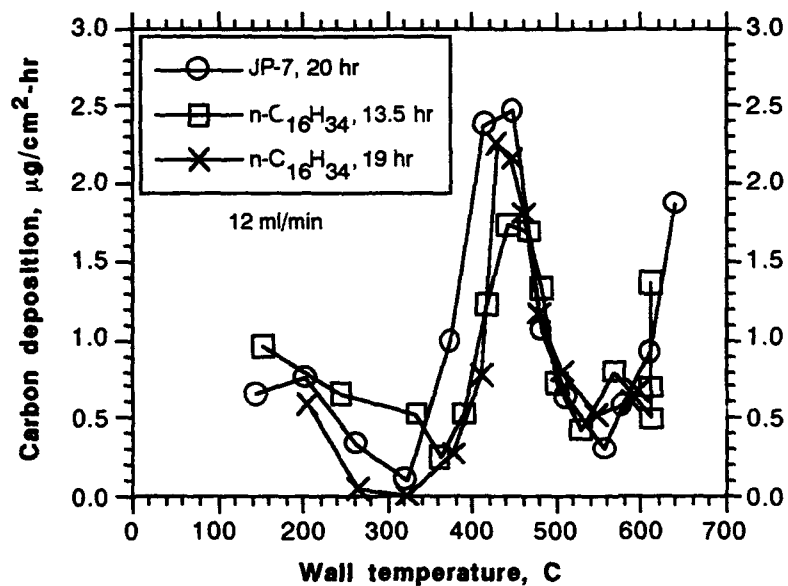

Figure 2. Deposition results for n-hexadecane and JP-7. Air sparged fuels, 69 atm, 12 ml/min. Fuel heated more rapidly to higher temperatures than Figure 1, hence appearance of pyrolytic deposition at wall temperature >600 C.
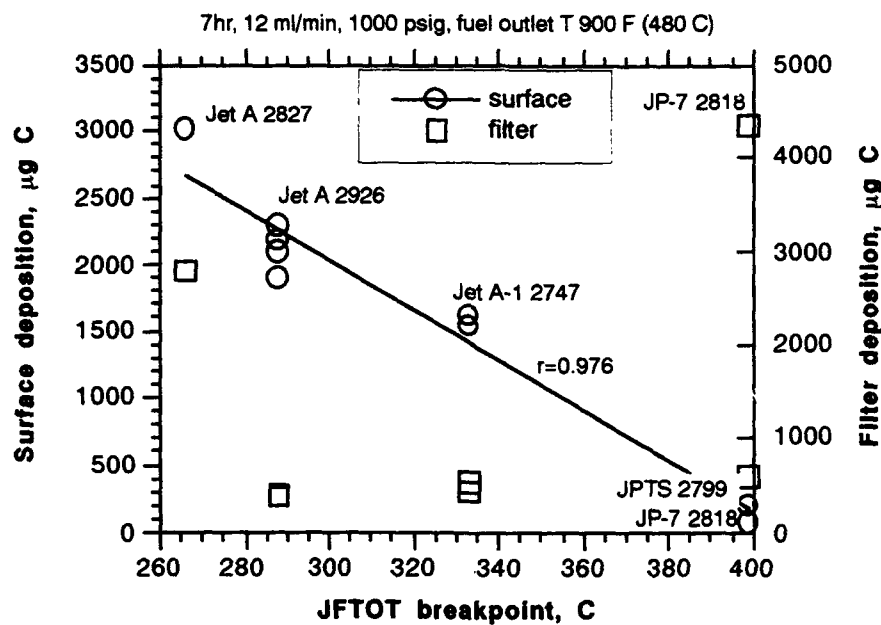
Figure 3. Relationship between JFTOT breakpoint (tube) and surface/filter deposition. 7 hr tests, 1000 psig, 12 ml/min. JP-7 breakpoint estimated to be 400 C.

Table 4. Deposition results for tests. Conditions: 12 ml/min, 1000 psig, air-sparged fuel. JP-10 is exo-tetrahydrodi(cyclopentadiene).

Test #	Fuel	Test time, hrs	Surface carbon deposition, μg	Filter carbon, μg
12/92-2	JP-10 1128	22	376	4300
12/92-4	MCH	15.5	4390	1070
11/92-2	MCH	22	4618	n/a
PL10/25	decalin	20	177	n/a
12/92-6	JP-7 2818	19	141	14880
3/93-1	JP-7 2818	22	157	13690

STUDIES ON HIGH PRESSURE AND UNSTEADY FLAME PHENOMENA

(AFOSR Grant No. F49620-92-J-0227)

Principal Investigator: Chung K. Law

Princeton University
Princeton, NJ 08544

SUMMARY/OVERVIEW

The objective of the present program is to study the structure and response of steady and unsteady laminar premixed and nonpremixed flames in reduced and elevated pressure environments through (a) non-intrusive experimentation, (b) computational simulation using detailed flame and kinetic codes, and (c) asymptotic analysis with reduced kinetic mechanisms. During the reporting period progress has been made in the following projects: (1) a theoretical and experimental study of unsteady diffusion flames; (2) a computational and experimental study of methane/air flames at elevated pressures; (3) an asymptotic analysis of the structure of methane/air premixed flames with reduced chemistry; (4) an asymptotic analysis of the extinction of laminar premixed flames with volumetric heat loss and chain mechanisms; and (5) asymptotic analyses of ignition in the supersonic laminar flat-plate boundary layer and mixing layer.

TECHNICAL DISCUSSIONS

1. Studies on Unsteady Diffusion Flames

A crucial influence on the flame behavior which so far has not been adequately addressed is the effect of unsteadiness of the environment on the flame behavior. This issue is of particular relevance to the modeling of turbulent flames through the concept of laminar flamelets. These flamelets are subjected to fluctuating flows with various intensities of straining, and it is reasonable to expect that the flame would respond differently in an oscillating strained flow field than in a steady strained flow field.

During the reporting period we have first analyzed the structure and response of a one-dimensional chambered flame in an oscillating flow field with small amplitudes of fluctuation, using large activation energy asymptotics. In particular, we have been concerned with the situation in which the characteristic time for flow unsteadiness is comparable with that of convection and diffusion, yet much larger than that of chemical reaction. In such cases, flames can be described as quasi-steady reactive layers embedded in, and interacting with, time-varying non-reactive transport zones. Figure 1 illustrates the typical behavior of flame location and temperature in response to an oscillating flow field. The deviation from the mean flame location and temperature are seen to decrease as the frequency of flow oscillation increases. Thus, as the frequency increases, flow unsteadiness becomes extremely rapid that flame cannot readily respond in a quasi-steady manner, i.e. the flame is hardly affected by the unsteady flow in the high frequency limit. By further analyzing the reaction zone structure, we have assessed the effect of the unsteady flow field on the extinction characteristics of the flame. Figure 2 shows the range of the extinction Damköhler number fluctuation as a function of frequency. Here the two solid curves indicate the maximum and the minimum values of fluctuation through one period. Since the system Damköhler number is a property of a given mixture composition, extinction is expected to occur when the system Damköhler number is smaller than the fluctuating value. The intersection of $Da_{Ex,MAX}(\omega)$ and Da_{SYSTEM} curves gives the cut-off frequency of unsteady flow field, beyond which the unsteady effect can be neglected in the extinction behavior. It may be possible to properly correlate this cut-

off frequency with the characteristic length scale of turbulent eddies to provide a better idea of turbulent combustion regimes. Effects of Lewis number on the flame response as functions of frequency is found to be quantitative, although they could be quite important in the instantaneous behavior.

To investigate the more realistic situation of stretched flames, an asymptotic analysis of a counterflow diffusion flame in an oscillating flow field is in progress. Experimental studies are also being performed using acoustic generators to impose an unsteady flow field.

2. Studies on High-Pressure Diffusion Flames

We have previously performed extensive measurements of the laminar flame speeds of a variety of hydrocarbon fuels with air for pressures up to three atmosphere. Through these studies we have come to recognize the significance of the system pressure in influencing chemical kinetics in general and the flame burning rate in particular. For example, in combustion modeling with the simplified kinetics of one-step overall reaction, the pressure exponent n is usually assumed to be a constant which is also frequently taken to be two for a second order reaction. Our results, however, have shown that not only n is not a constant, but it invariably is less than two. Specifically, it is close to one for the stoichiometric burning of methane in atmospheric air. Furthermore, it decreases with increasing pressure and inert dilution. In a highly-diluted situation it can even assume negative values, indicating that the flame burning intensity decreases with increasing pressure. Such behavior can be explained on the basis of the relative efficiencies of the two-body high-activation-energy, temperature-sensitive branching reactions versus the three-body, low-activation-energy, temperature-insensitive termination reactions.

Recognizing the importance of pressure on the flame behavior, and that practical aero-engines do operate under pressures much higher than those studied, we have constructed a high-pressure burner with an operational limit of 15 atmospheres. We have subsequently conducted experimentations on the extinction of counterflowing methane/air diffusion flames up to 8 atmosphere. In Fig.3 the measured density-weighted extinction strain rate is plotted versus the system pressure, for the pressure range of 0.13 to 7 atmospheres. The counterflow flame has also been computationally simulated with detailed transport properties and chemistry, and the extinction states determined. Figure 3 shows that the density-weighted strain rate increases with pressure, and that the experimental and computed values agree well with each other. The kinetic structure of the flame is currently being studied.

3. Asymptotic Structure of Premixed Methane/Air Flames

In many of the previous flame studies using reduced mechanisms, the activation energies of the individual elementary reactions are not considered to be large enough to employ large activation energy asymptotics. Instead, the reaction rates are assumed to have a power law dependence on temperature, and the ratio of the individual reaction rates are used as small parameters in the so-called rate-ratio asymptotics. Since the power law dependence on temperature does not exhibit the same kind of sensitivity to temperature variations as the Arrhenius approximation, the response of the flame to various external perturbations is not very significant. Consequently, analyses of this kind have yielded results which are not completely satisfactory. For example, for premixed methane/air flames, it was found that the Damköhler number from the leading order flame structure analysis does not depend on the burning rate, and therefore needs to be determined in a somewhat *ad hoc* manner. Furthermore, the key termination reaction was found to be the propagation step rather than the three-body recombination reaction.

In the present study we have analyzed the structure of premixed methane/air flames, using the four-step reduced mechanism of Peters and Williams, but retaining the Arrhenius form for the individual reactions except for the three-body recombination reaction which has zero activation energy. Thus activation energy asymptotics can still be applied and a complete description of the flame structure is provided. The role of each of the overall reaction steps is determined, and the key termination reaction is found to be the three-body recombination reaction. The results include the evaluation of the burning rate in terms of pressure, equivalence ratio, and a parameter that represents the ratio of the competing rates of the branching and termination reactions. In particular, we find that when this rate-ratio is reduced to a critical value, the burning rate decreases to zero and

the flame "extinguishes". For the opposite limit that the rate-ratio is large, we find that the burning rate asymptotes to a constant value, and the problem is governed by that of the premixed flame regime of Liñán. Consequently, we are able to adopt his correlation curve as an approximate expression for the burning rate in this limit.

This work is reported in Publication No. 1.

4. Nonadiabatic Laminar Flame Propagation with Chain Mechanisms

A classical model problem for the study of premixed flame extinction is that of Spalding, who analyzed the one-dimensional freely-propagating flame with temperature sensitive one-step overall reaction and radiative heat loss. Subsequent activation energy asymptotics shows that at the extinction turning point the scaled heat loss rate is e^{-1} while the flame burning rate normalized by its adiabatic value is $e^{-1/2}$. Recently, numerical computations of the flame with detailed transport and chemistry have shown that the flame again extinguishes at about 60% ($\sim e^{-1}$) of the adiabatic value, indicating the possibility that this value may be a near constant, regardless of the reaction and loss mechanisms.

In the present study we have provided a fairly general proof of the above possibility based on activation energy asymptotics. Recognizing that previous analytical studies with one-step overall reaction cannot capture the inherently-important chain branching and termination nature of realistic reaction schemes, we have employed the Zeldovich-Liñán two-step mechanism, which consists of a branching reaction and a competing recombination reaction. This is believed to be the simplest representation of the chain nature of realistic reaction mechanisms. The analysis shows that extinction again occurs at e^{-1} of the laminar burning rate.

This work is reported in Publication No. 2.

5. Ignition in the Supersonic Laminar Boundary Layer

The development of the scramjet engine for supersonic propulsion and the scramaccelerator for hypervelocity projectile launching has renewed interest in supersonic combustion. In contrast to subsonic situations, high-speed flows generate a considerable amount of heat through viscous dissipation, which can play an essential role in such practical issues as ignition delay and flame stabilization in supersonic propulsion, and premature ignition in scramaccelerators. The fundamental combustion phenomenon here is ignition within chemically-reactive supersonic boundary layer flows. In the present study we have performed a comprehensive numerical and asymptotic study of the weakly-reactive laminar supersonic flat-plate boundary layer and mixing layer flows with O(1) viscous heating and simplified, one-step overall reaction, up to the state of ignition. We have identified the structure of the boundary layer flow under all possible heating and ignition situations, and consequently determined explicit expressions for the associated ignition distance in terms of all relevant parameters. Specifically, for the flat-plate problem we have shown that there are three distinctively different ignition situations, namely when the wall is: (a) adiabatic such that viscous heating is the only ignition source, (b) isothermal and subadiabatic in the inert limit, and (c) isothermal and superadiabatic in the inert limit. It is clear that external heating from the wall is the dominant source for ignition in the second case and is therefore relevant for relatively low Mach number flows, while in the first and third cases viscous heating is the dominant source for ignition and therefore they are relevant for high Mach number flows. Similar considerations can be extended to the laminar mixing layer.

Figure 4 shows a suitably nondimensionalized streamwise distance for ignition as a function of the flow Mach number. It is seen that while the ignition distance increases with the flow Mach number for low speed flows up to about sonic flow, it decreases rapidly for higher Mach number flows. Furthermore, such a decrease is very rapid, occurring in an exponential manner. This is reasonable in that the ignition should depend on the temperature of the ignition kernel in an Arrhenius manner, while the static temperature varies quadratically with the Mach number.

The analyses on the flat-plate and mixing layer flows are reported in Publication No. 3 and 4 respectively.

MAJOR PUBLICATIONS (April, 1992 – March, 1993)

1. "The structure of premixed methane-air flames with large activation energy," by J.K. Bechtold and C.K. Law, *Combustion and Flame*, submitted.

2. "Laminar flame propagation with volumetric heat loss and chain branching-termination reactions," by B.H. Chao and C.K. Law, *International Journal of Heat and Mass Transfer*, in press.

3. "Analysis of thermal ignition in supersonic flat-plate boundary layers," by H.G. Im, J.K. Bechtold and C.K. Law, *Journal of Fluid Mechanics*, Vol. 249, pp. 99-120 (1993).

4. "Analysis of thermal ignition in the supersonic mixing layer," by H.G. Im, B.H. Chao, J.K. Bechtold and C.K. Law, *AIAA Journal*, in press.
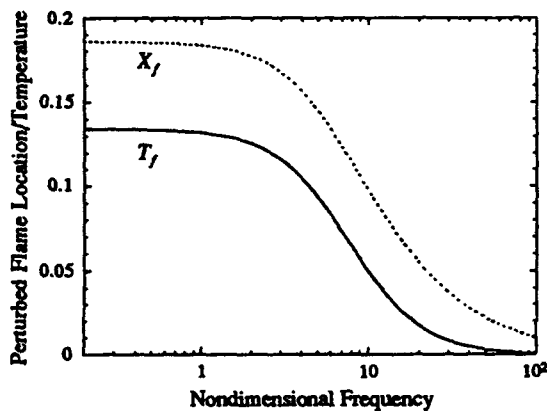
Figure 1
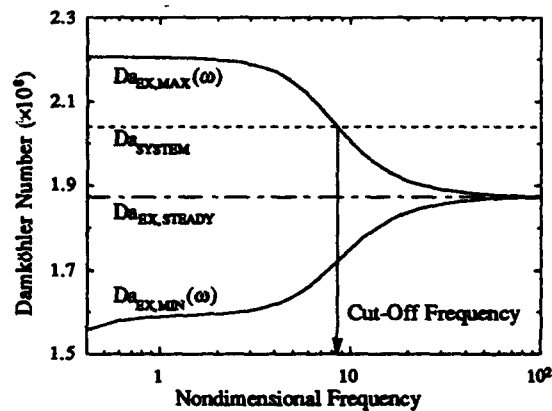
Figure 2
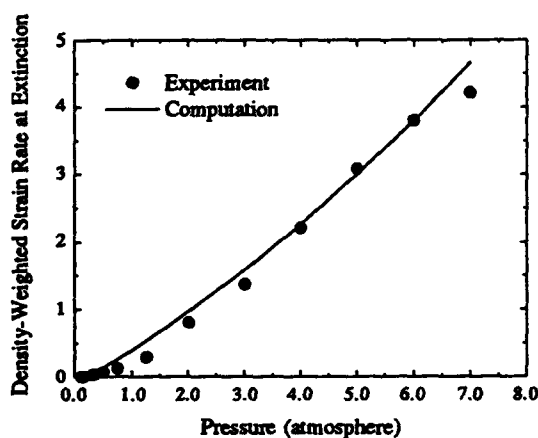
Figure 3
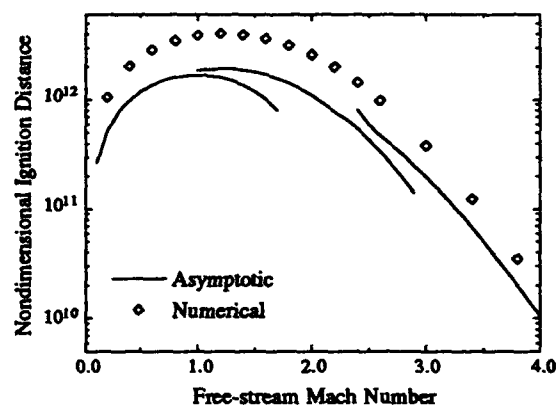
Figure 4

A STUDY OF MIXING AND COMBUSTION IN THE PRESENCE OF A STRONG STREAMWISE VORTICITY

M. Samimy and L. A. Kennedy

Department of Mechanical Engineering
The Ohio State University
Columbus, Ohio 43210

SUMMARY/OVERVIEW

The purpose of this research is to investigate the effect of passively generated streamwise vortices on the mixing process in an axisymmetric model combustor. Noncombusting experiments will initially be performed at the Ohio State University but eventually combusting experiments will be conducted at Wright Laboratory, Wright-Patterson Air Force Base. Streamwise vortices of different strength will be generated and various diagnostics from planar filtered Rayleigh/Mie scattering to laser velocimetry techniques will be used to explore the nature of these vortices and their effect on the mixing process.

TECHNICAL DISCUSSION

Mixing is an important phenomena in all combustion systems from coal fired boilers, to furnaces, to gas turbine engines. How quickly and how well a fuel and oxidant can be mixed will have a major influence on the combustion efficiency, heat release rate, pollutant formation, combustor size, and many other pertinent parameters. It is widely accepted that the vorticity dynamics greatly impact the mixing process. The streamwise vortices passively generated in flows, in addition to spanwise vortices or vortex rings, have been found to mix fluid streams quickly and efficiently. One of the devices that is used to produce streamwise vortices is called a lobed mixer. Many studies have shown that a lobed mixer used as a mixer nozzle in a gas turbine engine efficiently mixes the hot and cold fluid streams and can lower specific fuel consumption.

Work performed up to now involved designing, fabricating and setting up a facility to be used for the experiments. A schematic of the test section is given in Fig. 1. The flow geometry consists of a central tube, at the end of which is attached the lobed mixer nozzle, surrounded by an annular air flow. The central (primary) air flow will also serve as the fuel flow for the combustion studies. The air supply is generated at 16.4MPa (2400psi) by two four-stage compressors and is stored in two tanks of volume 42.5m^3 (1500ft^3). The system is designed so that test section velocities up to 120m/sec (395ft/sec) can be generated and varied independently in order to perform tests at various velocity ratios. A 100kW heater

has also been made available so flows with varying density/temperature can be studied.

The major planned tasks of the study are:

1. Perform flow visualization experiments for the axisymmetric lobed mixer geometry. The methods planned are a passive scalar type such as smoke visualization, and two product formation types such as titanium tetrachloride seeding, and water particle formation by heating and humidifying the central air stream, and visualizing the scattered light from the resulting water droplets formed when the primary air mixes with the cooler secondary air. Mie scattering is used in all three methods, however, we hope to be able to monitor the interface between the two flow streams more closely with the last two techniques than with the passive scalar method. Several geometries will be studied for the purpose of identifying the large scale, coherent structures in the flow, and the factors influencing their formation and downstrear development.

2. Perform detailed quantitative measurements of the flow fields for a selected number of geometries--based on the flow visualizations. These measurements may include the techniques of laser Doppler velocimetry, filtered Rayleigh scattering, and coherent anti-Stokes Raman spectroscopy.

3. Study the mechanisms of vorticity dynamics and its effect on mixing efficiency, and ultimately combustion efficiency.

4. Study the effect of different lobed mixer geometries on mixing. Lobed mixers tend to act as stirrers in a flow field until the vortices break down and molecular mixing takes place. Exploring how this breakdown is affected by lobe geometry (and flow conditions) will be emphasized in this work. Different geometries could include changing the number of lobes, lengthening the lobe, varying the width of each lobe, changing the wall thickness of the lobe, and may even include using vortex generator tabs.

Figures 2 and 3 show the stagnation/settling chamber and a typical lobed mixer to be used for the initial tests. Also shown in Fig. 3 is a circular nozzle to be tested for comparison purposes. Recently we have decided to modify the existing contraction section and the central fuel tube so that the same system can be easily used at both the Ohio State University and Wright-Patterson AFB.
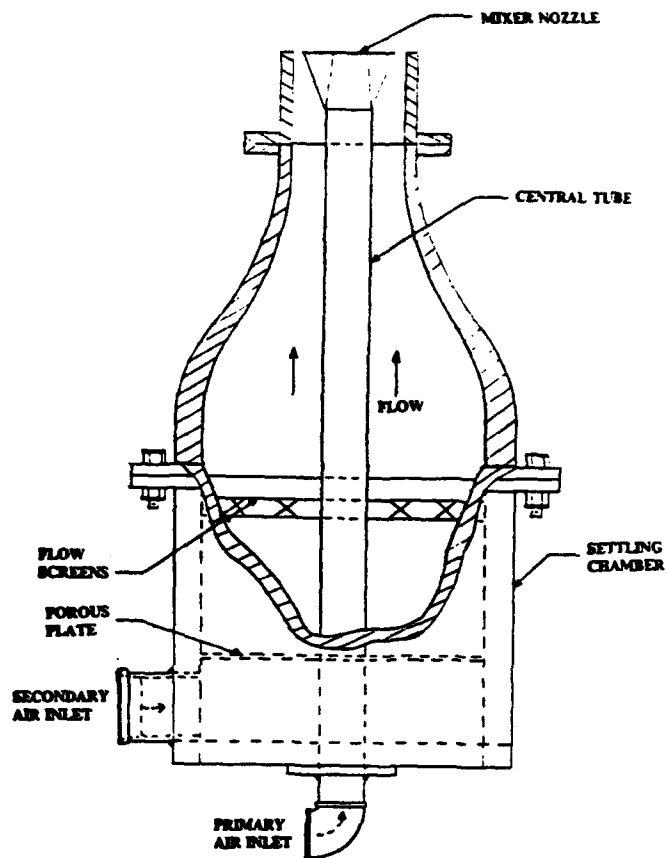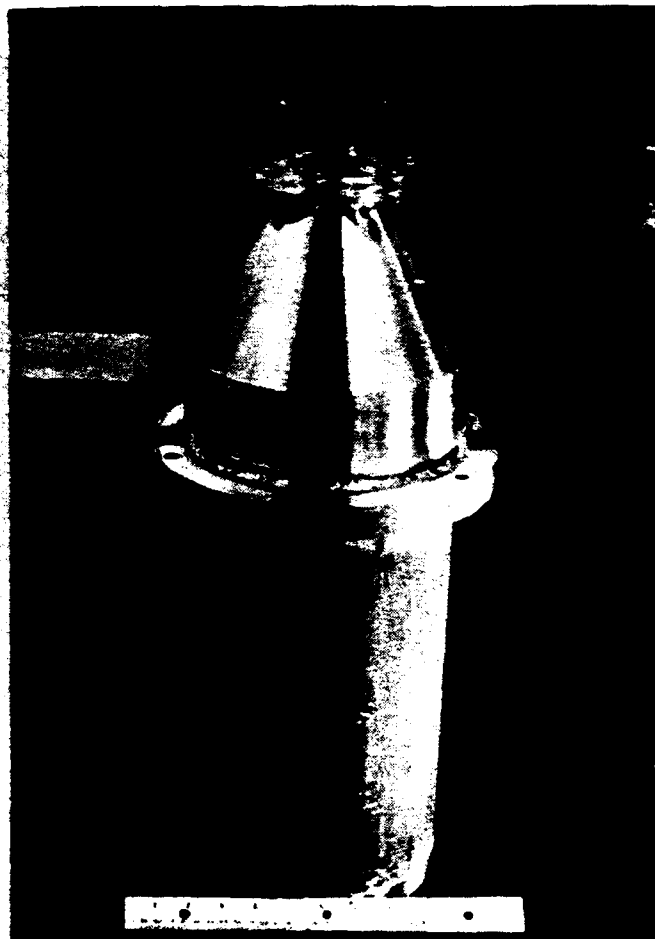
Figure 1 Schematic of flow facility.

MIXER NOZZLE

CENTRAL TUBE

FLOW

FLOW SCREENS

SETTLING CHAMBER

POROUS PLATE

SECONDARY AIR INLET

PRIMARY AIR INLET

Figure 2 Settling chamber, contraction
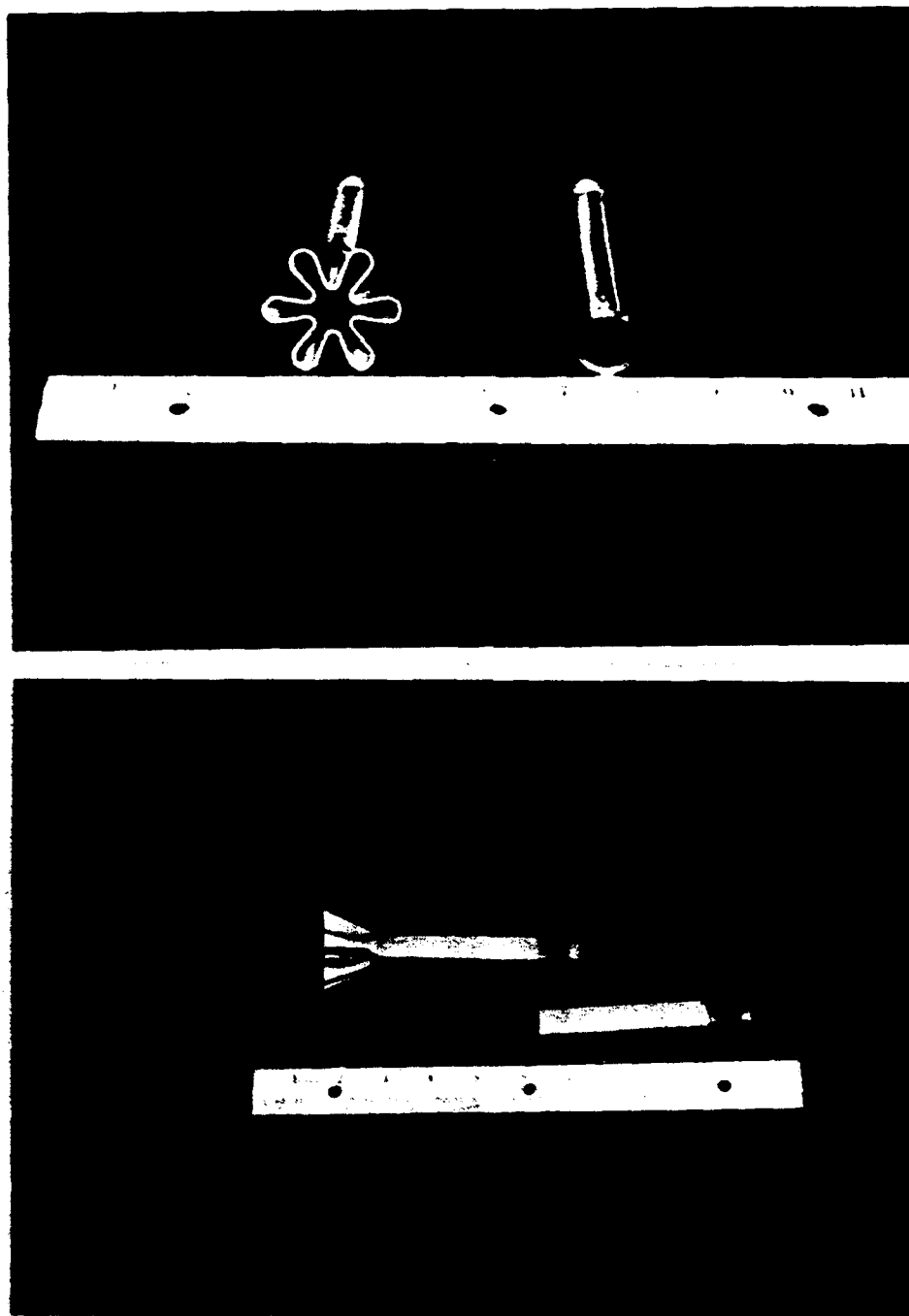section and nozzle test section.

Figure 3 Top and side views of a typical lobed mixer nozzle and baseline circular nozzle.

FUNDAMENTAL RESEARCH TO ADVANCE RAM ACCELERATOR TECHNOLOGY

AFOSR Contract No.92WL038

Capt. Randall Drabczuk
WL/MNSH
Eglin AFB, Florida 32542-6810

Glenn E. Rolader
Science Application International Corporation
Shalimar, Florida 32579

Raj Sinha
Science Application International Corporation
Ft. Washington, PA 19034-3211

Eugene Clothiaux
Department of Physics
Auburn University
Auburn, Alabama 36849

SUMMARY/OVERVIEW:

The fundamental processes that occur in a ram accelerator, such as shock-boundary layer interaction, boundary layer combustion, transient compressible turbulence, the relationship between projectile integrity and combustion ignition, high-pressure kinetics, and the transition from deflagration to detonation in the ram accelerator environment, are not completely understood. As a result, the Armament Directorate of Wright Laboratories, located at Eglin Air Force Base, in conjunction with the Air Force Office of Scientific Research (AFOSR), has initiated a research program to advance ram accelerator technology. This research effort has three principal areas of focus: (1) design and development of a ram accelerator research facility at Eglin AFB, (2) development and utilization of optical diagnostic techniques for the high-pressure combustion environment that exists in the ram accelerator, and (3) development of advanced computational fluid dynamic (CFD) models.

TECHNICAL DISCUSSION:

1. Ram Accelerator Research Facility

The design of the in-house ram accelerator facility is complete, and construction is underway. Preliminary tests should be finished by October 1993. The system is comprised of an injector, vent section, ram acceleration section, deceleration tube, catch tank, a gas handling system, two vacuum systems, a programmable logic controller, and a data acquisition system. The injector is a conventional 155 mm Howitzer sleeved down to 93 mm capable of accelerating 7 lb projectiles to 1.5 km/s. A 10' vent section connects the injector to the ram accelerator proper. The 93 mm diameter ram accelerator section, presently 20' in length, has four diametrically opposing instrumentation ports every 10" axially. The ram accelerator is connected to a deceleration tube presently 50' in length that leads to a high-energy catch tank. The gas handling system, capable of loading up to five different gases into up to five separate ram acceleration sections, has been designed to operate within 2% mass accurate. Each gas passes through a separate metering valve to ensure that the flow rates are within the range of mass flow meters, which are utilized to measure the mass flow rate into the barrel. Two

independent vacuum systems are utilized: one to evacuate the injector flight tube and one to remove air from the ram accelerator sections prior to loading. Several hydrogen and methane detectors are strategically located in the facility to detect leaks. Each ram acceleration section has a sample bottle for post shot composition analysis and an attached pipe leading out of the building to vent during an abort. The total system is monitored/controlled by a Programmable Logic Controller (PLC) in the research bay. A second PLC, located in the control room, monitors the other PLC and generates panel displays of the mass and partial pressure of each gas loaded into each segment. The data acquisition system is comprised of a 486 microcomputer with a GPIB card, four Nicole scopes, and a 40 channel Lecroy data digitizer.

2.   Diagnostics Research:

The primary diagnostics previously employed in ram accelerators have been magnetic pick-up coils to sense magnets embedded in the projectile and pusher plate, pressure transducers, and luminosity probes [1-3]. Similar probes will be utilized in the initial tests, but part of this research effort is to develop advanced high-pressure optical diagnostic techniques. Specifically, the utility of Schlieren photography, x-ray shadowgraphy, and Raleigh scattering will be studied. Two diagnostic development test fixtures have been designed and are under construction: a high-pressure shock tube and a gas containment vessel into which projectiles will be fired supersonically. Both devices have a 75 mm square cross-section to minimize optical distortion. The shock tube has a projectile shaped ramp mounted at the location of the optical ports, and the optical techniques will be utilized to study the shock front as it moves over the ramp. A gas gun will fire spherically blunted 15 mm diameter cylinders at supersonic velocities into a combustible mixture within the gas containment vessel. Optical techniques will be applied to study the shock-induced combustion. This part of the research initially will be similar to experiments performed by Lehr [4]; however, the pressure will be increased significantly to ascertain both the validity of the diagnostic techniques at high pressures and the effect of pressure on shock induced combustion/detonation. The Schlieren photography will be employed in two ways: first utilizing a Q-switched ruby laser illumination of the entire shock tube width and film, and secondly, a continuous high intensity lamp for illumination and an image converter camera will be utilized. As the gas pressure increases the utility of Schlieren photography decreases; consequently, x-ray shadowgraphy, which depends on the change in the illumination due to absorption along the line of sight by the gas constituents, is being developed. X-ray shadowgraphy has been utilized to observe density gradients in the flow as the pressure increases up to values in the kbar regime [5].

3.   Computational Fluid Dynamic Research:

The major emphasis of the computational fluid dynamic research is on advanced numerics (e.g., dynamic adaptive grids), turbulence modeling in a transient environment (e.g., LES simulations), 3D effects (e.g., vortex shedding from fins), and combustion phenomena in the high Re, high-pressure ram accelerator environment. This research includes the development of computational models for the complete ram accelerator geometry and several simple-geometry, unit problems to isolate specific phenomena that occur in the ram accelerator.

A transient, two-dimensional, axisymmetric, finite-volume model for the ram accelerator geometric has been developed. The model is fully implicit with strongly coupled combustion chemistry and utilizes upwind numerics (Roe/TVD). This model was utilized to study the effect of pressure on shock velocity by performing non-reacting gas calculations with both an ideal equation of state and a viral equation-of-state. It was found that in the ram accelerator pressure regime, compressibility effects significantly increase the shock velocity [6].

A large part of the initial numerical research has been on the required grid adaptation to resolve shocks, combustion fronts, and the wake region. Non-reacting gas ram acceleration calculations were performed with a uniformly spaced grid and a grid adapted to the pressure

gradient [7]. This work clearly demonstrated that to crisply resolve shock waves in the ram accelerator environment, adaptive gridding is desirable.

The grid adaptation research was extended to study shock-induced combustion, an area of particular relevance to the ram accelerator. Shock-induced combustion has been the focus of much investigation in the CFD research community but success has been limited. It has been hypothesized that very high spatial resolution of the induction zone between the shock front and energy release (flame) front is a prerequisite for such a simulation. The principal reason for such a stringent requirement results from the fact that the induction zone is characterized by exponential growth rates in the concentrations of chain breaching radicals (OH, HO_2, H, etc. in the case of hydrogen/oxygen premixed combustion). The usage of a spatially uniform fine grid is an unsatisfactory remedy since the appropriate level of shock and flame front resolution is only possible at an enormous computational expense. Furthermore, utilizing too coarse of a grid results in a simulation that is not grid resolved and leads to inaccurate predictions. Adapted grids where the grid provides local refinement in proportion to that required to resolve embedded discontinuities is an attractive alternative.

The benchmark experiments of Lehr and his co-workers at ISL [4] consisted of a spherically blunted 15 mm diameter cylinder fired into a stoichiometric H_2/Air and H_2/O_2 mixtures at various Mach numbers. Lehr showed that the reaction wave pulsates at a constant frequency if the model velocity is less than the detonation velocity of the mixture and that the pulsation frequency increases with velocity. At velocities above the gas detonation velocity, there is no apparent pulsation. A CFD simulation was performed for one of Lehr's experiments: a model fired into a H_2/Air mixture at 30 torr and 292 °K at a Mach number of 6.46. Under these conditions, the combustion front is steady (the model velocity is above the mixture detonation velocity), and both the shock and flame front are clearly identifiable. Figure 1 shows the density contours obtained with an evenly spaced grid along with the location of shock and flame fronts. The qualitative features of the desired flow field were well reproduced. However, as shown in the figure, there is significant disparity between the observed and calculated shock and flame fronts. In particular the numerical simulation over predicted the stand-off distance of both fronts suggesting an excess of numerical damping (or inadequate resolution). The simulation was subsequently repeated in conjunction with an adaptive gridding technique where the grid was periodically updated during the course of the convergence process to better resolve embedded flow structures and align itself with the dominant flow features. This adaptive grid solution along with the experimental data is shown in Figure 2, and the numerical solution was found to compare favorably with the measurements. Furthermore, the desired higher quality solution was obtained without any undue computational expense since the number of grid points was not increased.

REFERENCES:

1.   A. Hertzberg, A.P. Bruckner, and D.W. Bogdanoff, "Ram Accelerator: A New Method for Accelerating Projectiles to Ultrahigh Velocities," AIAA Journal, Vol. 26, pp. 195-203, (1988).

2.   D.L. Kruczynski, "Requirements, Design, Construction, and Testing of a 120-mm Inbore Ram Accelerator," 28th JANNAF Combustion Meeting, CPIA publication 573, Vol. 1, (1991).

3.   M. Giraud, J.F. Legendre, G. Simon, and L. Catoire, "Ram Accelerator in 90 mm Caliber. First Results Concerning the Scale Effect in the Thermally Chocked Propulsion Mode," 13th International Symposium on Ballistics, Stockholm, Sweden, (1-3 June 1992).

4.   H.F. Lehr, "Experiments in Shock-Induced Combustion," Astronautica Acta, Vol. 15 (4 and 5), pp. 589-597, (1977).

5.   Private communication between Dr. K.N. Koshelev of the Institute of Spectroscopy, Russian Academy of Sciences, (Troitsk) Moscow, and Dr. Eugene Clothiaux of Auburn University, (1992).

6.   N. Sinha, B.Y. York, S.M. Dash, R. Drabczuk, and G.E. Rolader, "Transient Simulation of Ram Accelerator Flowfields," 29th JANNAF Combustion Subcommittee Meeting, Hampton, Virginia, (October 1992).

7.   N. Sinha, B.Y. York, S.M. Dash, R. Drabczuk, and G.E. Rolader, "Progress Towards the Development of Transient Ram Acceleration Simulation as Part of the U.S. Air Force Armament Directorate Research Program," AIAA/SAE/ASME/ASEE 28th Joint Propulsion Conference and Exhibit, AIAA 92-3248, Nashville, TN , (July 1992).
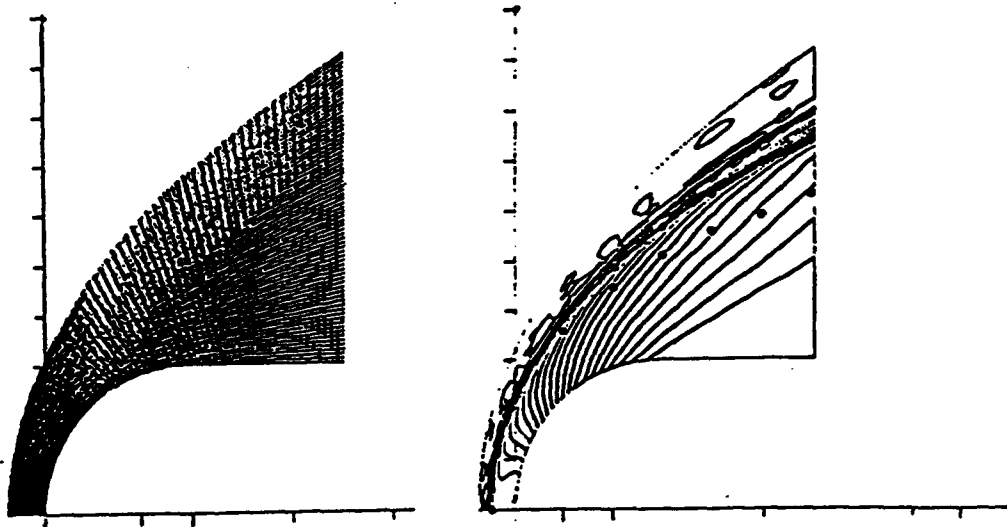
Figure 1.   Grid and Pressure Contours with a Uniformly Spaced Grid (●●● Indicates the Experimentally Observed Shock and Flame Front).
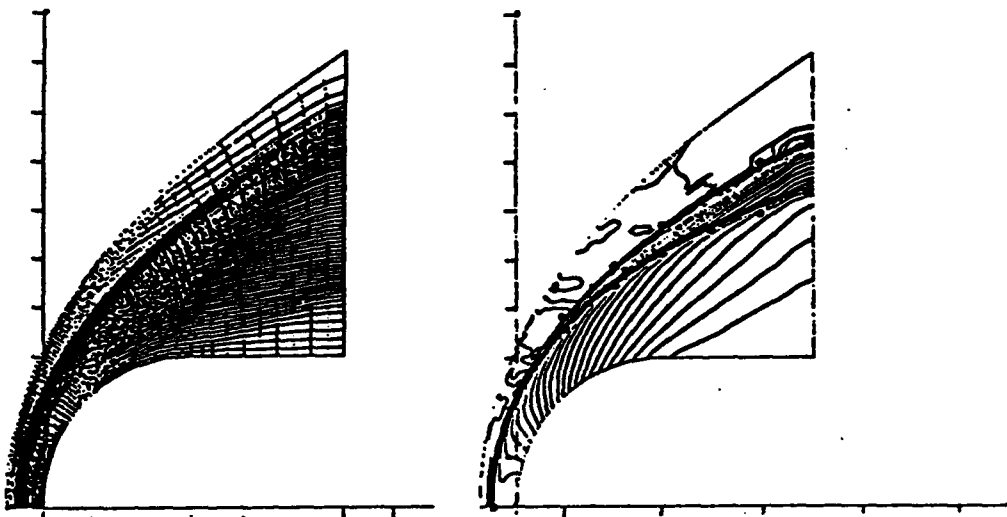
Figure 2.   Grid and Pressure Contours with an Adaptive Grid (●●● Indicates the Experimentally Observed Shock and Flame Front).

NUMERICAL STUDIES FOR THE RAM ACCELERATOR
AFOSR-MIPR-93-0024

Chiping Li, K. Kailasanath, Elaine S. Oran, and Jay P. Boris

Laboratory for Computational Physics, Code 6400
Naval Research Laboratory, Washington, DC 20375

SUMMARY/OVERVIEW

Time-dependent, multidimensional Euler and Navier-Stokes reactive-flow simulations have been performed to study basic issues in the development of the ram accelerator. In the past year, our studies have focused on the unsteady features of the reactive flow field around accelerating ram-accelerator projectiles. In these studies, we investigated several important contributing factors to the unsteadiness of the flow field. The simulations show that: (1) the projectile acceleration is one of the controlling factors of the detonation structure on the projectile in the detonation mode and significantly affects the shock structure on the projectile in the thermally-choked mode; (2) large-scale flow structures generated in the recirculation region behind the projectile create strong pressure oscillations in the flow field and on the projectile body in the thermally choked mode; and (3) the strength of the energy release in combustion also affects the development of the shock structure and the pressure distribution on the projectile in the thermally choked mode. In the last year, we also continued our study on the effect of the boundary layer. The simulations show detailed shock and expansion structures generated by the boundary layer near the leading edge. The expansion waves behind the leading shock decrease the temperature and pressure in the main flow and actually reduce the strength of the boundary-layer effect on the detonation structure.

TECHNICAL DISCUSSION

In the ram accelerator, a projectile which resembles the central body of a ramjet is accelerated by the high pressure generated by detonation and other types of shock induced combustion in premixed fuel-oxidizer mixtures. The reactive flow field around the accelerating projectile is highly transient and, therefore, the thrust on the projectile is also unsteady. In different velocity regimes, major contributing factors to the unsteadiness may be quite different. When the projectile velocity is higher than the C-J velocity, high pressures may be produced by detonation waves on the projectile body (detonation mode, figure 1). In the detonation mode, the projectile acceleration is the major cause for the flow unsteadiness. When the projectile velocity is lower than the C-J velocity of the mixture, high pressures can be generated by thermally choking the flow downstream from the projectile (thermally choked mode, figure 2). In this mode, in addition to the projectile acceleration, the large-scale flow structure generated in the recirculation region immediately behind the projectile and the shock motion related to the strength of the energy release in the shock-induced combustion also create unsteady features in the flow field. Our approach here is to use the time-dependent, multidimensional numerical simulation as a tool to study these transient features and their effects on the performance of the ram accelerator.

Developments in Numerical Methodology

In order to accurately and efficiently represent complex shapes of the projectiles in ram accelerators on orthogonal meshes, virtual cells are embedded (VCE) in the projectile surface. This technique allows one to calculate flow fields around complicated geometric shapes without incurring the computational penalty associated with either unstructured grids, that are difficult to be vectorized or parallelized or body-fitted meshes, that require small time-steps or long iteration times. Also, different virtual cells based on geometric changes can be easily embedded in the original, orthogonal mesh. Therefore, this technique is particularly suitable for studying the impact of the projectile shape on the performance of the ram accelerator.

Since the rapid acceleration of the projectile significantly affects the flow field in the ram accelerator, it is necessary to conduct time-dependent simulations of the reactive flow around the projectile to study the performance of such systems in different velocity regimes. The acceleration of the projectile is coupled to the flow calculations by using noninertial source (NIS) terms. The computational results

show that this approach yields smooth changes in the flow field for projectiles of very high acceleration (up to approximately 10^7g).

Unsteadiness in the Thermally Choked Mode

The ram accelerator operates in the thermally choked mode when the velocity of the projectile is lower than the C-J velocity of the operating mixture. As an example, figure 3 shows the simulated flow field for the $H_2:O_2:N_2/2:1:3.76$ mixture when the projectile velocity is 1250 m/s. In the simulations using different mixture ratios ($H_2:O_2:N_2/2:1:7$ to $H_2:O_2:N_2/2:1:0$), development of the flow field and combustion process is similar to the case shown in figure 3. On the contracting part of the projectile body, a near-normal shock is maintained by the high pressure generated by the combustion which chokes the flow downstream from the projectile. The simulations show that the same projectile can be continuously accelerated from 1200 m/s to 2000 m/s using different mixtures to generate thermally choked combustion repeatedly.

The flow field in a thermally choked ram accelerator is highly transient. The location and strength of normal shock on the projectile body are unsteady and strongly affected by the energy release in the combustion and the projectile acceleration. The simulations show that the conditions under that a normal shock can be kept on the contracting part of the projectile body are difficult to maintain. In the simulation for the mixture of $H_2:O_2:N_2/2:1:3.76$, the duration in which the shock can be maintained is of the order of 100 μs and the projectile-velocity increase in this period is approximately 400 m/s in a distance of about 2-3 m. The simulations for other flow and mixture conditions show that this duration is very sensitive to the energy content of the mixture as well as to the ignition process. Another important cause of the flow unsteadiness is the strong acceleration of the projectile: the projectile velocity changes significantly in the time span (order of 10^{-4} s) for the fluid to pass over the projectile. As the projectile is accelerated, the angle of the oblique shock initiated at the tip gradually decreases and the normal shock located on the contracting part of the body moves downstream. The choking condition due to combustion behind the projectile is also being relieved and, as a consequence, the pressure on the rear part of the projectile decreases, resulting in reduction in the total thrust. Furthermore, large-scale flow structures generated in the recirculation zone also cause flow unsteadiness. These large-scale structures also interact with the combustion process and generate strong oscillations in the flow field. The amplitude of the fluctuation in the thrust exceeds the average thrust value by about a factor of two.

Unsteadiness in the Detonation Mode

Detonation is the most efficient form of shock-induced combustion and can generate very high pressures. In order to maximize thrust and minimize losses, a detonation has to be generated and stabilized at an appropriate location on the projectile body so that it produces an optimal pressure distribution. During the acceleration, the leading and reflected shocks are gradually strengthened and the temperature behind the shocks is rising accordingly. Therefore, the oblique detonation stabilized on the projectile body jumps upstream from one reflected shock to another. However, the basic structure of the detonation remains largely the same during the acceleration. Figure 4, a simulation conducted for the $H_2:O_2:N_2/2:1:3.76$ mixture shows that the detonation is located at the widest part of the projectile and the high-pressure region covers the front half of the contracting part of the projectile. This pressure distribution yields a significant positive thrust which results in acceleration ranging from 2×10^5g to 3×10^5g. The detonation structure on the projectile body is very stable under a wide range of flow and mixture conditions. In the simulation, the projectile is being continuously accelerated from Mach 8 (3200 m/s) to Mach 10 (4000 m/s) in a distance of 12 meters. Also, fluctuation in the total thrust in the detonation mode is much smaller than that in the thermally choked mode and the effect of the large-scale flow structure is much weaker.

Shock-Boundary-Layer Structure in Supersonic Flows

Our previous studies have shown that the boundary layer increases the leading-shock strength and shortens the induction distance. One of the important effects of the boundary layer is the temperature increase due to the strengthened leading shock. Therefore, highly resolved numerical simulations are conducted to investigate the initial development of boundary layers near the leading edge of a flat plate in supersonic flows of different Mach numbers. The simulations show complex flow structures

including: (1) a bow shock generated by the boundary layer, which is detached from the leading edge; (2) a stagnation region at the leading edge where the flow comes to stop; and (3) an expansion area above and behind the stagnation region, through which the flow adjusts to the free-stream condition. These expansion waves decrease the temperature and pressure in the main flow and actually reduce the strength of the boundary-layer effect on the detonation structure. Also, the large pressure and density gradients in the expansion region may destabilize the flow, leading to generation of large scale structures and transition to the turbulence and these effects will be further studied.

PUBLICATIONS AND PRESENTATIONS

Structure of Reaction Waves behind Oblique Shocks, C. Li, K. Kailasanath, and E.S. Oran, in press, *Progress in Aeronautics and Astronautics*, Washington, DC, 1992.

Numerical Simulations of Reactive Flows in Ram Accelerator, C. Li, A.M. Landsberg, K. Kailasanath, E.S. Oran, and J.P. Boris, *CPIA* Publication 593, pp.279-288, Columbia, MD, 1992.

Effects of Boundary Layers on Oblique-Detonation Structures, C. Li, K. Kailasanath, and E.S. Oran, *AIAA* Paper 93-0450, American Institute of Aeronautics and Astronautics, Washington, DC, 1992.

Detonation Structures behind Oblique Shocks, C. Li, K. Kailasanath, and E.S. Oran, submitted to *Physics of Fluids*, March, 1992.

Structure of Supersonic Boundary Layers, C. Li, K. Kailasanath, and E.S. Oran, *the 45th Annual Meeting of the Division of Fluid Dynamics of the American Physical Society*, Tallahasse, FL, 1992

Analysis of Transient Flows in Thermally Choked Ram Accelerators, C. Li, K. Kailasanath, E.S. Oran, A.M. Landsberg, and J.P. Boris, *AIAA* Paper 93-1916, American Institute of Aeronautics and Astronautics, Washington, DC, 1993.

Numerical Simulations of Transient Reactive Flows in Ram Accelerators, C. Li, K. Kailasanath, E.S. Oran, A.M. Landsberg, and J.P. Boris, *AIAA* Paper 93-2187, American Institute of Aeronautics and Astronautics, Washington, DC, 1993.

Transient Behavior of Oblique Detonations on Accelerating Ram-Accelerator Projectiles, C. Li, K. Kailasanath, and E.S. Oran, *the Joint Technical Meeting of the Eastern and Central States Sections of the Combustion Institute*, New Orleans, LA, 1993

Naval Ship Superstructure Design: Complex Three-Dimensional Flows Using an Efficient Parallel Method, A.M. Landsberg, J.P. Boris, W. Sandberg, and T.R. Young, *the High Performance Computing Symposium*, Arlington, VA, 1993
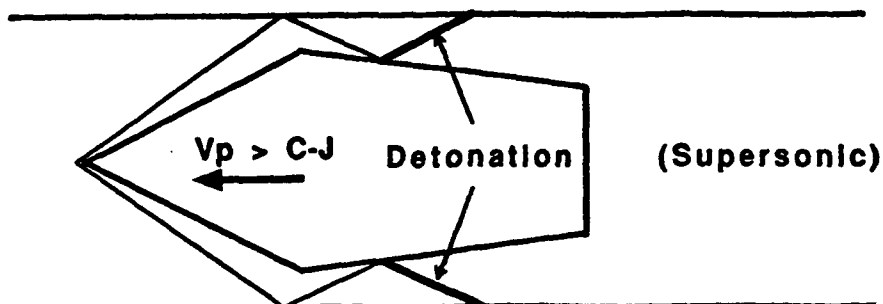
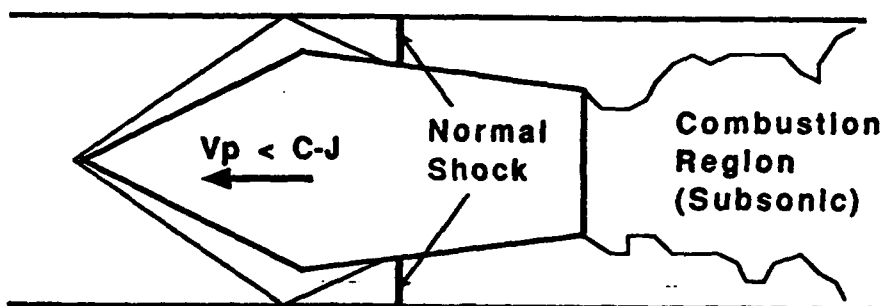Figure 1 Schematic of a ram accelerator in the detonation mode.

Figure 2 Schematic of a ram accelerator in the thermally-choked mode.

Figure 3 Flow properties from a simulated flow field in a ram accelerator in the thermally-choked mode. The projectile is traveling at about 1250 m/s in the mixture of $H_2:O_2:N_2/2:1:3.76$. A normal shock is located on the contracting part of the projectile body and is supported by the $\qquad$ tion behind the projectile. The projectile is accele $\qquad$ g at about 3.0×10^4g at this moment.

Figure 4 Flow properties from a simulated flow field in a ram accelerator in the detonation mode. The projectile is traveling at about 3400 m/s in the mixture of $H_2:O_2:N_2/2:1:3.76$. A oblique detonation is located on the widest part of the projectile body. The projectile is accelerating at about 2.5×10^4g at this moment.

IGNITION AND MODIFICATION OF REACTION BY ENERGY ADDITION: KINETIC AND TRANSPORT PHENOMENA

Principal Investigator(s): Francis Fendell and Mau-Song Chou

Center for Propulsion Technology and Fluid Mechanics
TRW Space & Electronics Group, One Space Park, Redondo Beach, California

SUMMARY/OVERVIEW

High-speed air-breathing combustion systems necessitate the release of chemical energy during the relatively brief residence time of reactants within combustors of practical length: mixing, ignition, and chemical reaction must be achieved in a relatively short time. Towards this challenge, we have developed the concept of a supersonic combustor based on a nonintrusively stabilized oblique (conically configured) detonation wave. The conical wave is the result of the interaction of a train of spherical detonation waves, each initiated (in a very-fast-flowing gaseous fuel/air mixture) by energy deposition from a rapidly repeated pulsed laser. We address the proof-of-principle technology for such a supersonic combustor, in which relatively small entropy rise is incurred, by fundamental experiments and analyses.

Specifically, for fuel/air mixtures of practical interest, we seek to fulfill the need for data on the minimum deposition energy, minimum pulse duration, and minimum deposition volume required for the direct (nonintrusive) initiation of a Chapman-Jouguet (CJ) detonation; i.e., we seek data on direct initiation without either overdriv ... 'blast-wave decay) or underdriving (deflagration-to-detonation transition). We also ex .... the consequences for engine performance of inhomogeneity and off-stoichiomet.   the cold mixture.

TECHNICAL DISCUSSION

We seek to span a stream of supersonically flowing fuel/air mixture with flame, within a modest distance downwind of the transverse plane containing the ignition source, located at a fixed, on-axis site in an axisymmetric combustor. The members of a train of spherical detonation waves, each directly initiated [in a mixture flowing faster than the Chapman-Jouguet (CJ)-wave speed] by one pulse from a rapidly repeated pulsed laser, interact to form a nonintrusively stabilized conical (oblique) CJ detonation wave (Fig. 1).[1] The "corrugations" in the conical wave are smoothed as the temporal interval between the periodic pulses is reduced (Fig. 2). A cellular structure is observed for all real CJ detonations, so the conical wave has finite thickness, but, as long as the thickness is much smaller than other dimensions in the flow field, the finite structure is not of engineering consequence and does not compromise any of this discussion.

If axial position $x = 0$ [or $x' = (x - L) = - L$] is the site of energy deposition (Fig. 1) in a circular-pipe-type inlet of radius r_{pipe}, then the conical-detonation-wave/container interaction occurs at downwind distance $x = L = r_{pipe}/\tan \beta$, with $\sin \beta = u_{CJ}/u_o$, where, by design, the known CJ-detonation-wave speed for the mixture $u_{CJ} < u_o$, the (supersonic) speed of the oncoming mixture. For $x > L$, the flow is no longer selfsimilar; a (say, method-of characteristics) solution of the steady isentropic supersonic flow in trial axisymmetric containers of cross-section

A(x), with $A_x(x) > 0$, suggests a nozzle configuration for which, within a relatively short streamwise distance, the detonated mixture is uniformized for exhaust at ambient pressure.[2] The thrust so generated is achieved probably with smaller entropy rise than that incurred for any alternative supersonic combustor predicated on the burning of a well-mixed throughput.

We have derived[3] that a conservative value for the energy E (and time scale) required for direct initiation without overdriving is given by

$$E = E_{CJ}[1+(t/t_m)]^3, \quad t_m = \lambda/u_{CJ}, \quad E_{CJ} = \rho_o V_o q, \tag{1}$$

where ρ_o is the initial mixture density, $V_o = (4/3) \pi \lambda^3$, q is the chemical exothermicity per mass of mixture, λ is the (empirically established) cell size, and t is the time interval of energy deposition. This result is predicated on the sufficiency (for sustained CJ-wave propagation to ensue) of depositing, in a cell-sized volume, the energy chemically derivable from the (presumably) detonable mixture in that volume. If the temporal interval for the energy deposition becomes comparable to, or exeeds, the wave-dispersion time scale t_m, which is much briefer than a characteristic diffusive-transport time, then the required energy E increases very significantly. The advantage afforded by multi-nanosecond-duration laser pulses in reducing the energy requirement E is quantified. In fact, deposition of energy over a volume with dimension of cell size may not be necessary, so a value of E smaller than that of Eq.(1) may suffice.

We have considered the entropy rise associated with the reflected shocks formed in already-detonated mixture when neighboring detonations in a pulsed-laser-initiated train interact. According to our analysis[3], this particular source of entropy rise is minimized if the time interval between the very brief laser pulses is minimized. However, one ought not pulse so frequently that the (wasteful) deposition of two pulses into the same element of mixture occurs. This result on pulsing interval is derived conveniently from a model in which the spherical detonations are idealized as spherical fronts without structure, because the entropy rise associated with the spherical-detonation fronts is not at issue. Also, attention in our analysis is limited to the early-time reflections, with which the strongest shocks are associated; weaker subsequent reflections are not examined.

As a first step toward characterizing the tolerable spatial scale of unmixedness in the cold mixture, we have examined what radius of spherical "blob" of initially unmixed fuel and air (taken to be present in the cold blob in same stoichiometric proportion as characterizes the well-mixed portion of the throughput) could be burned prior to discharge from the combustor nozzle.[5] The preponderance of the throughput is taken to be well-mixed fluid, converted to product in the detonation wave. We have treated a finite-radius sphere, initially with one hemisphere of fuel and the other of air. These reactants interdiffuse upwind of the transit of the detonation wave, and the mixed portion is taken to be converted virtually instantaneously to product species during wave transit; the residual reactants are burned in a diffusion flame as the sphere is convected downwind by the high-speed flow. The radius of the sphere and the transport coefficients are altered, albeit not greatly, during wave transit. The diffusion flame lies on the equator, and, while most of the reactants are burned rapidly, complete burnup requires infinite time, if the values of the (stoichiometrically adjusted) mass fractions in each hemisphere are equal; otherwise, burnout occurs in finite time, with the last vestige of flame sited at the pole of the hemisphere with the stoichiometrically deficient reactant. While the temperature of the expanding product gas enveloping the blob probably remains sufficiently high so that vigorous diffusive burning is sustained, the effective burnout time increases with the square of the blob radius, and may exceed the length of a viable nozzle for too large a blob.

In support of this technology, laser-initiated-detonation experiments were conducted both an open system at one atmosphere, and also in a closed tube at various pressures. In the open system, a flat-flame burner was used to achieve uniform flow. In the closed system, a cylindrical

tube of 1.6-cm diameter and 1-m length had a quartz window at one end to permit laser-beam access. A Lambda Physik argon-fluoride excimer laser provided a source of 193-nm-wavelength radiation. Pressure transducers (Kistler, Model 211B2) recorded pressure rise; a photomultiplier with a monochromator recorded OH emission at 308 nm; and an image converter (IMACON) camera monitored the temporal and spatial evolution of the detonation wave.

Detonations were directly initiated in mixtures of C_2H_2/O_2, $C_2H_2/O_2/N_2$, $H_2/O_2/C_2H_2$, and $CH_4/O_2/C_2H_2$. The minimum laser energy required for initiation is 12 ± 2 mJ for a $(1.5\ C_2H_2 + O_2)$ mixture at one atmosphere, in both the open system (Fig. 3) and also the closed system (Fig. 4). The energy absorbed in the vicinity of the laser focal volume (about $10^3\ \mu m^3$) is about 8 mJ, owing to the absorption by the gaseous medium before the radiation reaches the focal point. The energy required for initiation increases substantially as the C_2H_2 mole fraction deviates from about 0.4, for which the C_2H_2/O_2 ratio is about 2/3. The energy required also increases markedly by the addition of N_2 to C_2H_2/O_2, and is about 400 mJ for an N_2/O_2 ratio of about 1.1 (Fig. 4). We have also demonstrated initiation of detonation in $H_2/O_2/C_2H_2$ and $CH_4/O_2/C_2H_2$, mixtures in which C_2H_2 serves as a sensitizer and possibly also a promoter (Fig. 5). Results from the closed tube showed that the laser energy required is approximately inversely proportional to the pressure.

The detonation-wave speed in atmospheric C_2H_2/O_2 mixtures was measured to be about 2.3-2.9 km/s, in good agreement with CJ speed. The corresponding peak pressure is about 34 atmospheres, and about 103 atmospheres with enhancement from wave reflection. In a test with an inert C_2H_2/N_2 mixture, the deposit of the excimer-laser energy (about 300 mJ) resulted in a pressure rise of about only 0.1 atmospheres. This suggests that our initiation differs from the conventional initiation of detonation, which involves the prior creation of a blast wave, e.g., by electric spark, exploding wire, or chemical explosive. We measured a required laser energy which is substantially smaller than that of conventional initiation methods. Conceivably, our initiation may be promoted by photochemical reaction, specifically, via reactions involving the reactive photofragments C_2H and H, generated by the photolysis of C_2H_2.

REFERENCES

[1]Carrier, G., Fendell, F., McGregor, D., Cook, S., and Vazirani, M., "Laser-Initiated Conical Detonation Wave for Supersonic Combustion," Journal of Propulsion and Power, Vol. 8, March-April 1992, pp. 472-480.

[2]Fendell, F., Mitchell, J., McGregor, R., and Sheffield, M., "Laser-Initiated Conical Detonation Wave for Supersonic Combustion. II," Journal of Propulsion and Power, Vol. 9, March-April 1993, pp. 182-190.

[3]Carrier, G., Chou, M.-S., and Fendell, F., "Laser-Initiated Conical Detonation Wave for Supersonic Combustion. III," Paper 92-03247, presented at the AIAA 28th Joint Propulsion Conference, Nashville, TN, July 1992.

[4]Chou, M.-S., Fendell, F. E., and Behrens, H. W., "Theoretical and Experimental Studies of Laser-Initiated Detonation Waves for Supersonic Combustion," presented at the SPIE International Symposium on Laser Applications in Combustion and Laser Diagnostics, Los Angeles, CA, January 1993.

[5]Carrier, G. F., Fendell, F. E., and Chou, M.-S., "Laser-Initiated Conical Detonation Wave for Supersonic Combustion--a Review," presented at the 2nd ICASE/NASA Langley Research Center Workshop on Combustion, Newport News, VA, October 1992 (to be published by Springer Verlag).
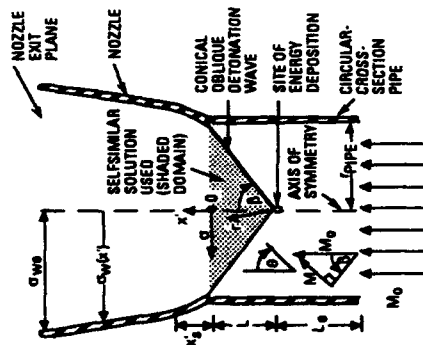
Fig. 1. Schematic (not to scale) of a supersonic combustor, where $\sin \beta = M/M_o$, $M_o = u_o/a_o$, $M = u_{CJ}/a_o$, a_o being the sound speed of the cold mixture and $L = r_{pipe}/\tan \beta$. The pipe container is flared at the position of intersection with the nearly conical detonation wave, to avoid reflected shocks.
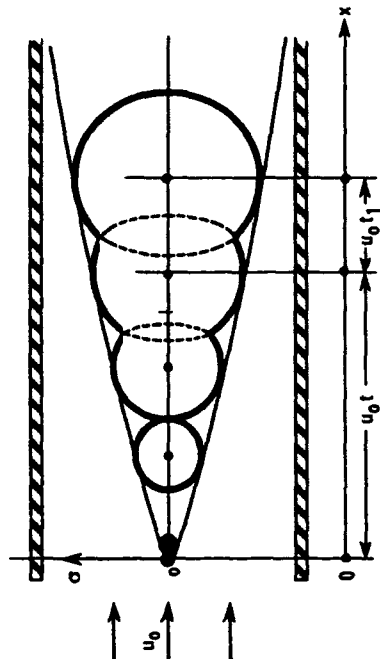

Fig. 2. A cone conceptually envelope a train of spherical detonations, each directly initiated by a pulse of energy, deposited at the origin ($\sigma = 0$, $x = 0$) with period t_1. The flow speed u_o exceeds the Chapman-Jouguet (CJ)-wave speed u_{CJ}. Dashed curves denote entropy-increasing reflected shocks from the interaction of neighboring detonations.
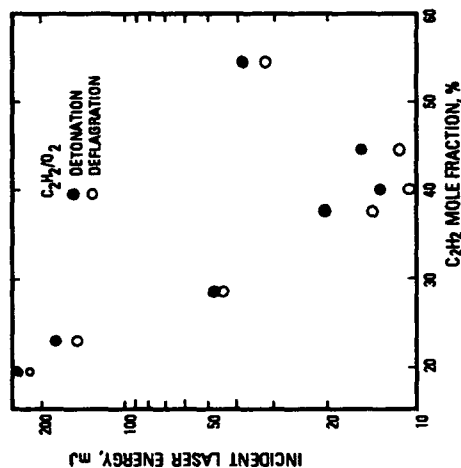
Fig. 3. The minimum energy sufficient for detonation, and the maximum energy compatible with deflagration, in C_2H_2/O_2. The smallest sufficient value, for C_2H_2 mole fraction ≈ 0.4, suggests that initiation entails the product CO, not CO_2.
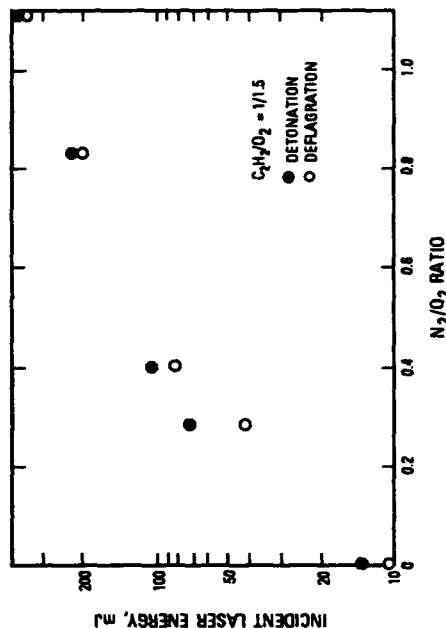
Fig. 4. Same as Fig. 3, for $C_2H_2/O_2/N_2$.
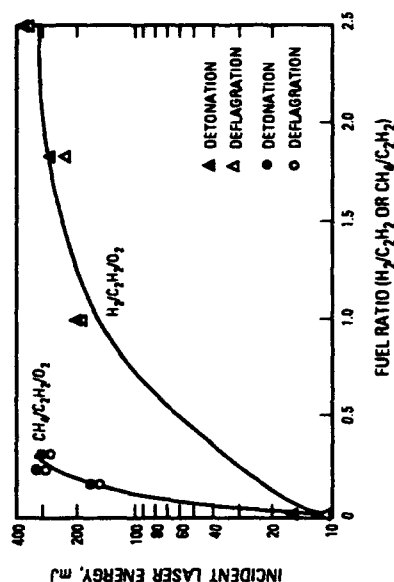
Fig. 5. Same as Fig. 3, for H_2/C_2H_2 and CH_4/C_2H_2 ratios, in $H_2/C_2H_2/O_2$ and $CH_4/C_2H_2/O_2$, respectively. The fuel/O_2 ratio is stoichiometric for production of CO and H_2O.

RTM 50.00/75.01

- 76 -

STRUCTURE AND CHEMICAL KINETICS OF FLAMES SUPPORTED BY NITROGEN OXIDES

AFOSR Grant Contract No. 90-0121

M.C. Branch, J.J. Cor and G. Fiechtner
Center for Combustion Research
Mechanical Engineering Department
University of Colorado
Boulder, Colorado 80309-0427

SUMMARY/OVERVIEW:

Flames supported by nitrogen oxides arise during the gas phase combustion near the surface of many energetic materials containing carbon, hydrogen, nitrogen and oxygen. We have undertaken experimental and modeling studies in order to develop reaction mechanisms appropriate for such systems. The understanding of the reaction chemistry of the propellant system is important in modeling overall propellant performance as a substitute for costly empirical testing of the many possible propellant formulations. Comparison between modeling and experiments for burner stabilized flames shows that the reaction mechanism developed accurately predicts the major species concentrations in a variety of fuel/NO_x flames. In addition, reasonable agreement has been found between modeling and experimental results for burning velocity of flames of the same mixtures.

TECHNICAL DISCUSSION:

We have completed detailed comparisons of calculations and measurements of the structure and burning velocity of fuel/NO_x mixtures using a 272 step reaction mechanism. The comparison between the calculated flame structure and the experimental flame structure for stable species was found to be very good for fuel/N_2O flames and good for fuel/NO_2 flames (see Fig. 1-3). The concentration profiles for radical species were found to be generally well represented qualitatively but not well represented quantitatively. It was concluded that, despite some remaining difficulties with the reaction mechanism, it appeared to be reliable in describing the overall combustion behavior of a wide range of fuel and oxidizer mixtures.

The most important reactions of the oxidizer (N_2O or NO_2) are with H atoms and, to a lesser extent, with CO. Reaction of either oxidizer with H is a chain propagating reaction, in contrast with the chain branching reaction of H with O_2 which is of equal importance in fuel oxidation by O_2. In addition, the reaction of NO_2 with H is slower than N_2O with H. Finally, the reaction of N_2O with CO can be significant both in consumption of CO and formation of CO_2. This situation is again in contrast with the oxidation chemistry of systems by O_2 in which the conversion of CO to CO_2 is almost entirely be reaction of CO with OH. The difference between the use of N_2O or NO_2 as oxidizer is that the former produces primarily N_2 while the latter produces NO. The subsequent slow reduction of NO to N_2, even when it is thermodynamically favored, accounts for the most striking difference between the two oxidizers. The most important effects of the oxidizer, therefore, are that the nitrogen oxides are less effective chain carriers and lead to slower reaction rates compared to O_2.

The 272 step reaction mechanism was also used to model the burning of free-standing flames supported by N_2O and NO_2, and the modeled flame speed was compared to the experimental results obtained by Parker and Wolfhard using the bunsen burner technique (Table 1). Also shown are the burning velocities obtained with the Miller and Bowman mechanism without the modifications discussed in the present investigation. The results indicate that generally good agreement is obtained between the modeling and the experimental data and that the 272 step mechanism gives better results than earlier mechanisms. The burning velocity of the flames with N_2O are significantly higher than those with NO_2 as oxidizer. Two of the calculations are discussed below in more detail in order to indicate the importance of fuel and oxidizer decomposition reactions in flame propagation.

Table 1 gives the calculated and measured results for the burning rate of a CH_4/N_2O flame. The calculated flame velocity is 90 cm/sec, very close to the measured velocity of 105 cm/sec. In addition, for this flame we were able to perform analysis on what reactions contribute most strongly to a given specie's production/consumption. It was found that the major reactions leading to the decomposition of CH_4 are in decreasing order of their rate of CH_4 consumption, reaction with H, OH and O. The major reactions leading to the breaking down of N_2O were found to be, in decreasing order of the amount of N_2O they consume, reaction with H and thermal decomposition of N_2O. The importance of the radicals H, OH and O are clearly evident in the propagation of this flame.

A free-standing C_2H_4/NO_2 flame at a pressure of 0.1 atm was modeled and the calculated flame speed was compared to that measured by Parker and Wolfhard. The results are included in Table 1, and as can be seen, the agreement is excellent for this flame. It is possible that the larger mechanism used to model this flame aided in obtaining better agreement with experimental data than was obtained in several of the cases of N_2O-supported flames. More cases would need to be run, however, to draw conclusions on the relative ability of the two mechanisms to model free-standing flames supported by NO_2 and N_2O. Modeling results for the C_2H_4/NO_2 flame showed that the most important reactions contributing to the decomposition of C_2H_4 in the flame were the hydrogen abstraction by OH and H and thermal decomposition. The most important reactions leading to the decomposition of NO_2 were found to be reaction with H and with CO to form NO which is slowly reduced further by H-C-N reaction processes. Initiation of the chemistry in these flames can be seen to be closely tied to reactions producing radical species.

PUBLICATIONS:

1.	M.C. Branch, A. Alfarayedhi, M. Sadeqi and P.J. Van Tiggelen, "Measurements of the Structure of Laminar Premixed Flames of $CH_4/NO_2/O_2$ and $CH_2O/NO_2/O_2$ Mixtures," *Combustion and Flame, 83,* pp. 228-239, 1991.
2.	M.B. Habeebullah, F.N. Alasfour and M.C. Branch, "Structure and Kinetics of CH_4/N_2O Flames," *23rd Symposium (International) on Combustion,* The Combustion Institute, Pittsburgh, pp. 371-378, 1991.
3.	H. Dindi, H.M. Tsai and M.C. Branch, "Combustion Mechanisms of Carbon Monoxide-Nitrous Oxide Flames," *Combustion and Flame, 87,* pp. 13-20, 1991.
4.	J. Vandooren, M.C. Branch and P.J. Van Tiggelen, "Comparisons of the Structure of Stoichiometric CH_4-N_2O-Ar and CH_4-O_2-Ar Flames by Molecular Beam Sampling and Mass Spectrometric Analysis," *Combustion and Flame, 90,* pp. 247-258, 1992.
5.	M.C. Branch and J.J. Cor, "Structure and Chemical Kinetics of Flames Supported by

Nitrogen Oxides," *Pure and Applied Chemistry*, 65, pp. 277-283, 1993.

6. J.V. Volponi and M.C. Branch, "Flame Structure of C₂H₂-O₂-Ar and C₂H₂-NO₂-Ar Laminar Premixed Flames," *24th Symposium (International) on Combustion*, Combustion Institute, Pittsburgh, pp. 823-831, 1993.
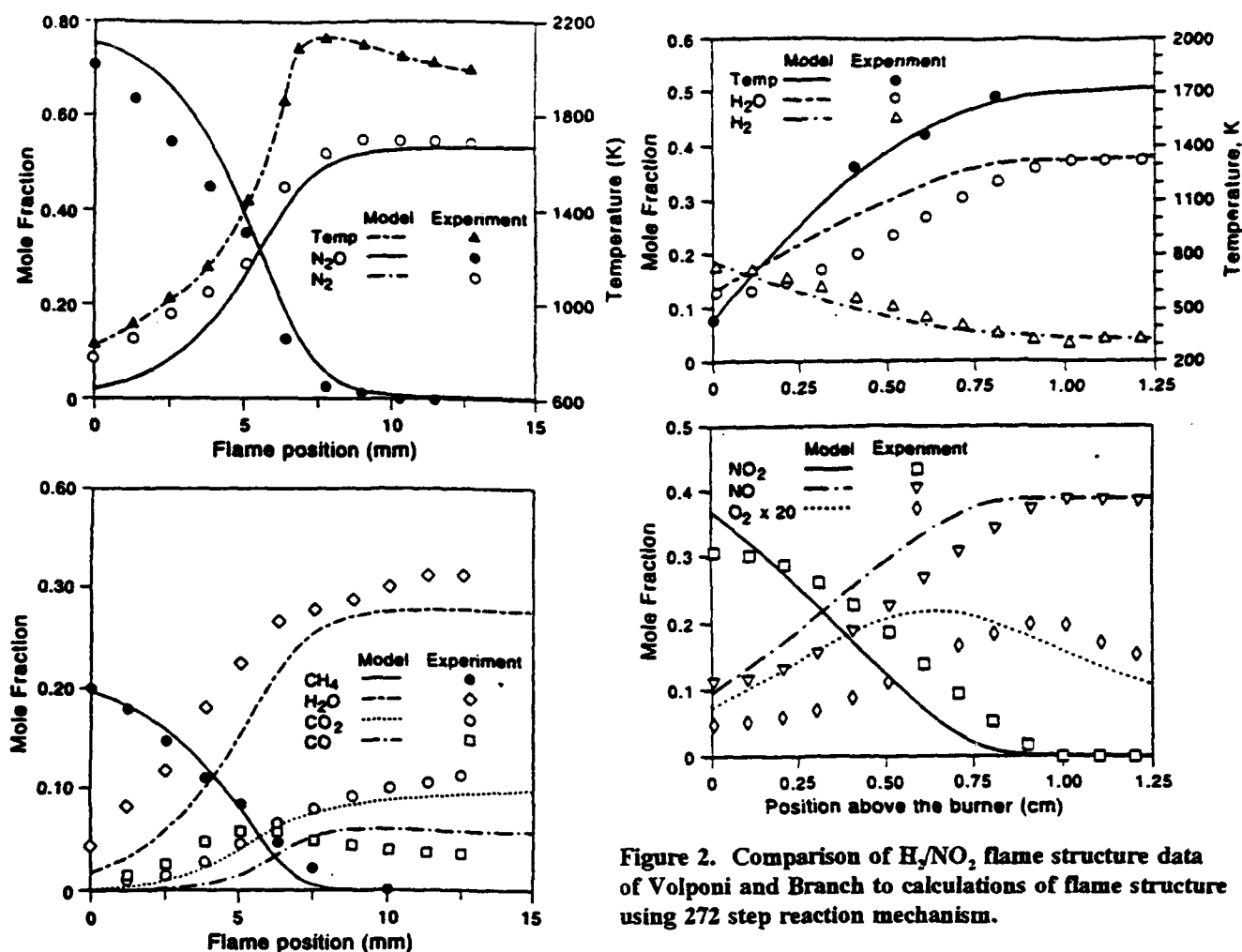
Figure 1. Comparison of CH₄/N₂O flame structure data of Habeebullah et al. to calculations of flame structure using 272 step reaction mechanism.
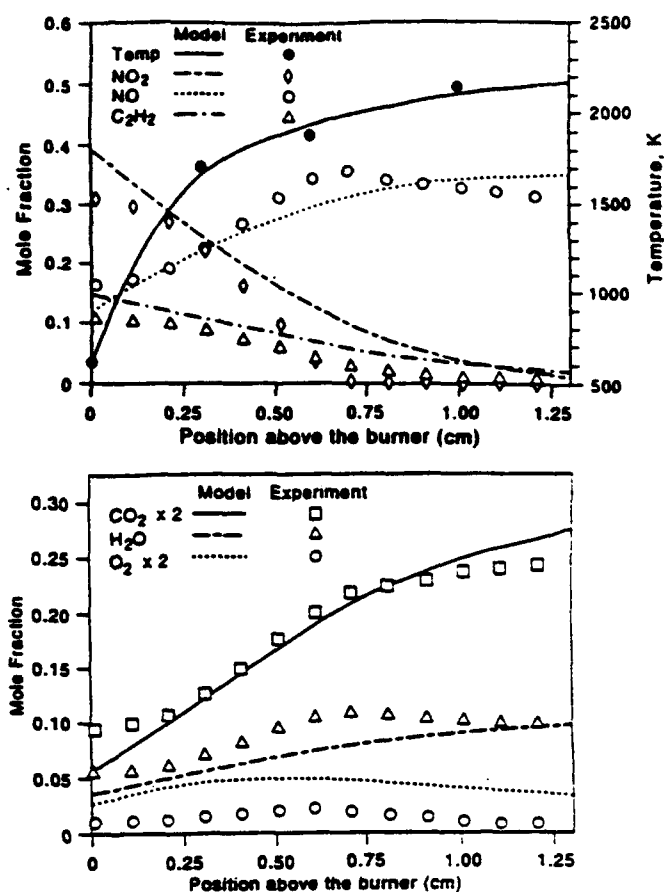
Figure 2. Comparison of H₂/NO₂ flame structure data of Volponi and Branch to calculations of flame structure using 272 step reaction mechanism.

TABLE 1. Comparison of measured and calculated flame speed of fuel/NO$_x$ mixtures[a].

REACTANTS	MEASURED[b]	CALCULATED	
		M/B[c]	This Work[d]
H_2/N_2O	300	227	240
CH_4/N_2O	105	76.2	90
C_2H_2/N_2O	160	128	150
C_2H_4/N_2O	110	94	102
C_2H_4/NO_2	62.5	61	61

(a) All flame speeds given in cm/sec at 0.10 atm and for a stoichiometric mixture.
(b) Parker & Wolfhard
(c) Calculation using mechanism of Miller & Bowman
(d) Calculation using the present 272 step mechanism.

Figure 3. Comparison of C_2H_2/NO_2 flame structure data of Volponi and Branch to calculations of flame structure using 272 step reaction mechanism.

DISTRIBUTED COMBUSTION IN SOLID PROPELLANTS

(AFOSR Grant No: AFOSR-91-0152)

Pricipal Investigator: M.W. Beckstead

Chemical Engineering Department
Brigham Young University
Provo, Utah

Objective: Identify and develop a quantitative understanding of the mechanism of distributed combustion.

Overview: The current work aims at developing an experimental and analytical basis for determining the mechanisms of distributed combustion. A Rijke burner, constructed at BYU, has been initially characterized. In the burner, particles entrained in the flammable gases are ignited by the flame. Law's model for the combustion of aluminum has been modified and incorporated into the Rijke acoustic model to describe distributed combustion. Comparisons of the preliminary results from the experimental and analytical efforts are promising. This burner will continue to be used to study particle combustion in both oscillatory and steady flow. Work is beginning on a high pressure system to allow measuring the burning rate of aluminum at pressures up to 30 atm.

CURRENT PROGRESS

The mathematical model of the Rijke burner was previously developed at BYU by Raun which predicts the frequencies and acoustic growth rates in the Rijke burner both with and without particle combustion. However, quantitative agreement between the model and experimental work has been difficult to attain. This difficulty is believed to be due to the over-simplified descriptions of the interaction of the flame and aluminum combustion with the acoustics. Therefore, an effort to improve these aspects of the mathematical model is currently underway.

The Rijke model has been modified to include metal particle ignition delay and combustion. The vapor phase metal combustion model of Law has been selected as an appropriate, state of the art model, with an analytical instead of numerical solution. The aluminum combustion model has been modified to include radiation and convection heat transfer effects, to allow for multiple oxidizers, and to provide for the effects of oxide migration to the metal particle surface. Preliminary comparison between the model and aluminum combustion experimental data has shown reasonably good agreement.
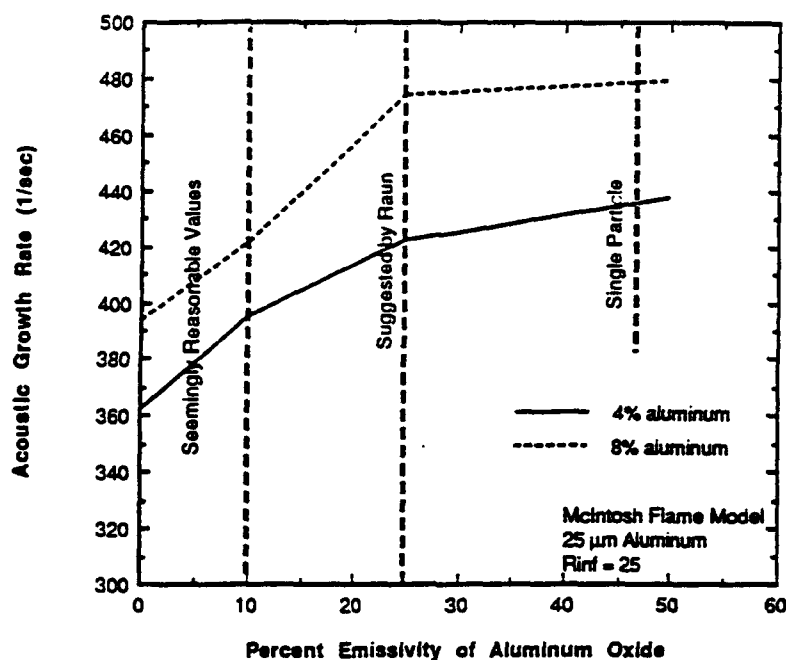
Figure Rijke acoustic model calculated acoustic growth rate as a function of aluminum oxide emissivity. Increased emissivity causes a drop in hot section temperature profile.
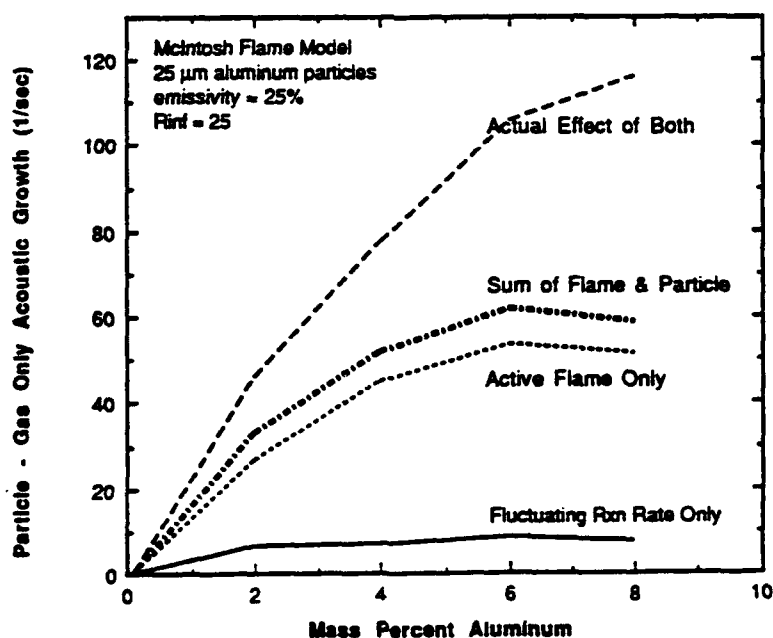
Figure Increase in acoustic growth due to addition of aluminum with and without fluctuating reaction rate and acoustically active flame. Note sharp increase with combined effects as compared to sum of individual effects.
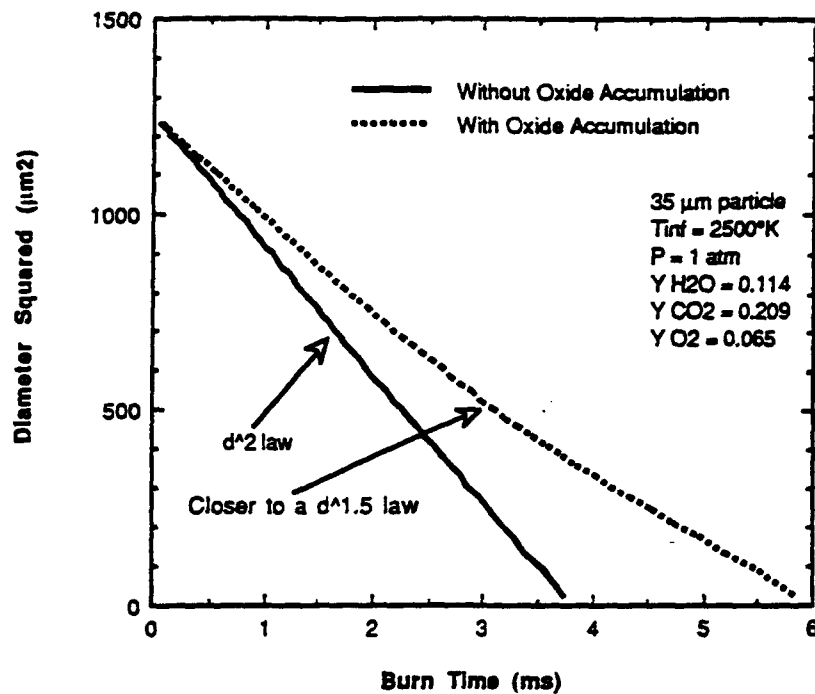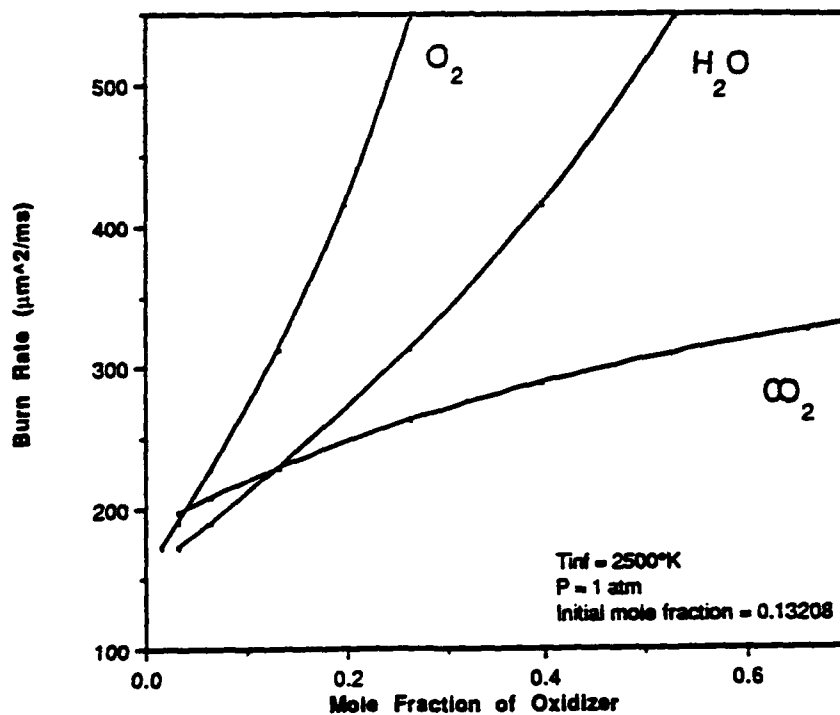
Figure ‑   Effect of Oxide Accumulation the Particle Surface.

The aluminum combustion model showing the effect of adjusting the mole fraction of a single oxidizer, holding the other two constant.

Comparison of Original Law Model and Improved Model

Assumptions of the Original Law Model	Assumptions of the Improved Model
1. Properties Constant everywhere	Calculation of properties based on weighted average of properties at particle surface, flame and infinity.
2. Oxygen only reactant	Multiple species allowed with variable transport and thermodynamic properties.
3. Burning in Stagnant Gas	Accounts for convective effects based on the Nusselt number.
4. Radiation neglected	Accounts for radiation between particle, flame, and surroundings.
4. Lewis Number $= 1$	Allows Lewis numbers different than 1.
6. Oxide on particle surface has no effect.	Reduced burn rate due to oxide surface coverage.
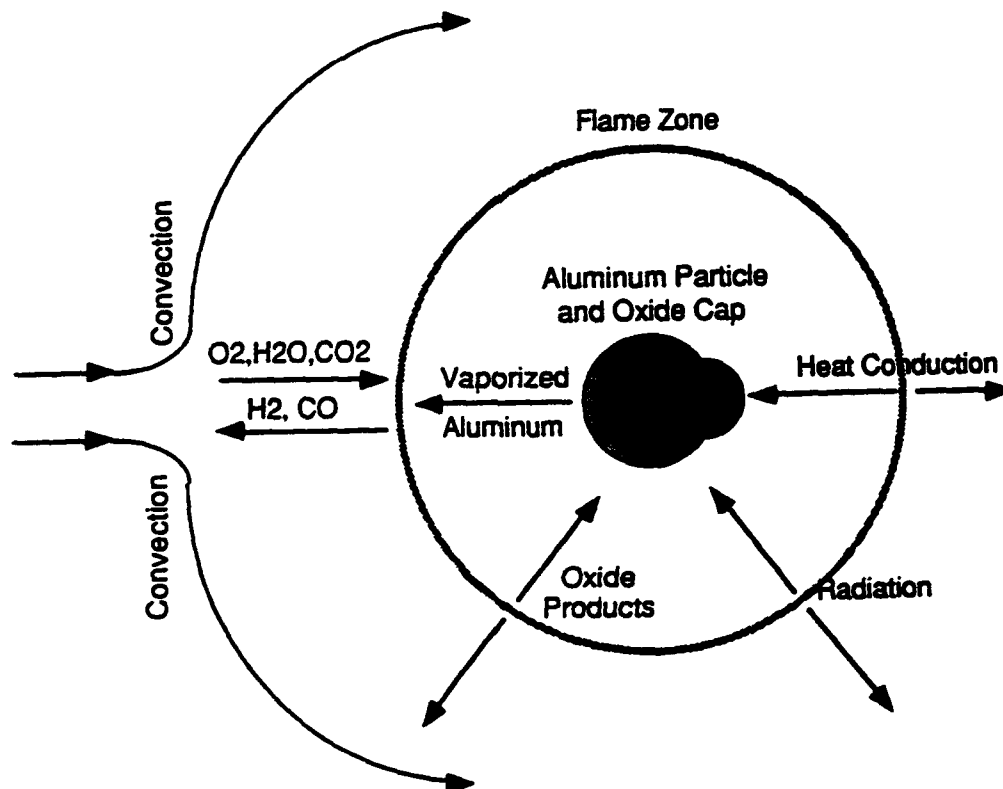
Figure   Schematic of aluminum combustion model used in this study.

DETERMINATION OF CHEMICAL PROCESSES AT A
BURNING PROPELLANT SURFACE

AFOSR-89-0521

Principal Investigator: Thomas B. Brill

Department of Chemistry
University of Delaware
Newark, DE 19716

SUMMARY/OVERVIEW:

Chemical description of the burning surface is vital to any advanced model of solid propellant combustion and combustion instability. A spectroscopically-instrumented, high-rate thermolysis technique developed in our laboratory is being applied to determine the chemical mechanisms at the temperature of the burning surface. The initiating endothermic steps are revealed. The products of these initial steps become the reactants for the first large exothermic reaction near the surface. This latter reaction plays a disproportionally large role in determining the burn rate and how the chamber instability couples to the surface reaction zone.

TECHNICAL DISCUSSION

Elucidation of the chemical mechanisms by which the ingredients of solid propellants rapidly pyrolyze and form the heterogeneous surface reaction zone and the primary flame is vital for detailed models of combustion[1-4]. Species formed in the surface reaction zone chemically link the formulation of the material to the combustion characteristics, such as the structure and temperature distribution of the flame and the stability of combustion.

Information about chemical reactions in the heterogeneous surface region of an energetic material is gained by the use of a technique developed in our laboratory, T-jump/FTIR spectroscopy[5]. A small, thinly spread sample is a snapshot simulation of the burning surface and ensures efficient heat transfer representative of the film-like heterogeneous reaction layer on the burning surface. The sequence of formation and the relative concentrations of the gaseous products from pyrolysis at chosen temperatures following heating at 2000°C/s is determined in the temperature range of the burning surface. Simultaneously with these data, the heat generated or consumed by the sample is determined so that the dominant exothermic chemistry can be separated from the initial decomposition steps. In this way, the semi-global decomposition and reaction mechanisms have been determined at or near the temperatures present on the burning surface of 1,3,5,7-tetranitro-1,3,5,7-tetrazacine (HMX)[6], 1,3,5-trinitro-s-triazine (RDX)[7], ammonium nitrate (AN)[8], ammonium dinitramide (ADN)[8], 1,3,5,5-tetranitrohexahydropyrimidine (DNNC)[9], glycidylazide polymer (GAP)[7], bis(azidomethyl)oxetane

(BAMO)[6], and ammonium perchlorate (AP)[10]. Table 1 gives a summary of key products formed in the initial endothermic decomposition

Table 1		
A Summary of the Initial Decomposition Products and the Reactants for the First Large Heat Generation Reaction		
Compound	Initial Products	Heat Generation Reaction
HMX	$CH_2O + N_2O + NO_2 + HCN$	$CH_2O + NO_2$
RDX		
AN	$NH_3 + NO_2 + HNO_3$ $N_2O + NO$	$NH_3 + NO_2$
ADN		
DNNC	Complicated but similar to HMX and RDX	$CH_2O + NO_2$
AP	$NH_3, HClO_4$	$HNO + HClO_4$
BAMO	$RN + N_2$	RN decomposition
GAP		

steps. These products are the reactants for the first large heat generation reaction. For example, the branching ratio of the initial decomposition steps of HMX and RDX ($CH_2O + N_2O$ branch and $NO_2 + HCN$ branch) is temperature dependent[6]. The $CH_2O + N_2O$ branch is favored at lower temperature, but the $NO_2 + HCN$ branch is favored at the temperature of the burning surface[6].

Attempts are being made to define the mechanism by which materials interact with one another during combustion of a composite propellant. A firm starting point is isomorphously doped crystals of AP, upon which burn rate data have been obtained at NWC[13]. Figure 1 reveals that the time-to-exotherm of AP is strongly affected by isomorphous doping of the lattice with small amounts of K^+ and $Cr_2O_7^{2-}$ ions. In all cases the samples were heated at 2000°C/s to 480°C under 13 atm Ar by our T-jump/FTIR technique. An unmistakable conclusion from Figure 1 is that the dopant ions strongly influence the rate at which reactions occur leading to the large heat release step. The catalysis occurs in the heterogeneous condensed phase because the Pt filament only senses the heat consumed or released by material with which it is in very close thermal contact. Figure 2 reveals that the burn rate values at 50 atm correlate reasonable well with the time-to-exotherm data at 13 atm in Figure 1. The overall positive correlation suggests that the catalytic effect of the dopant is the accelerate or decelerate the decomposition reactions that lead to heat release in the heterogeneous condensed phase. In turn, this effect on the time of heat release increases or decreases the burn rate[7]. This connection is in line with notions that the first strongly exothermic reaction in the mechanism plays a disproportionally large role in controlling the burn rate of the bulk material[7,14]. For AP, the specific reaction that is implicated both experimentally[10,15] and

by kinetic modelling[15,16] is equation 1. The T-jump/FTIR data for AP[10] reveals a large pulse of NO and H_2O at the exotherm of AP.

$$HClO_4 + HNO \longrightarrow NO + H_2O + ClO_3 \tag{1}$$

The same is true of all of the isomorphously doped samples of AP.

1. De Luca, L., <u>Pure Appl. Chem.</u>, 62:825-838 (1990).
2. Lengellé, G.; Duterque, J., Godon, J. C., and Trubert, J. <u>J. Propuls. Power</u>, in press.
3. Kuo, K. K., Litzinger, T. A., and Hsieh, W. H. in "Structure and Properties of Energetic Materials," Materials Research Society, Pittsburgh, PA, 1992, in press.
4. Melius, C. F. in "Chemistry and Physics of Energetic Materials," S. Bulusu, Ed. Kluwer Academic Publishers, Dordrecht, The Netherlands, 1990, p. 51-78.
5. Brill, T. B., Brush, P. J., James, K. J., Shepherd, J. E., and Pfeiffer, K. J., <u>Appl. Spectrosc.</u>, 46:900-911 (1992).
6. Brill, T. B., and Brush, P. J., <u>Phil. Trans. Roy. Soc. Lond. A</u>, 339:377-385 (1992).
7. Brill, T. B., Brush, P. J., Patil, D. G., and Chen, J. K., <u>Twenty-Fourth Symp. (Int.) Combustion.</u>, The Combustion Institute, Pittsburgh, PA, 1992, p. 1907-1914.
8. Brill, T. B.; Brush, P. J., and Patil, D. G., <u>Combust. Flame</u>, 92:178-186 (1993).
9. Brill, T. B., Patil, D. G., Duterque, J., and Lengellé, G., <u>Combust. Flame</u>, submitted.
10. Brill, T. B., Brush, P. J., and Patil, D. G., <u>Combust. Flame</u>, in press.
11. Brill, T. B., and James, K. J., <u>J. Phys. Chem.</u>, submitted.
12. Brill, T. B. and James, K. J., <u>J. Phys. Chem.</u>, submitted.
13. Boggs, T. L., Price, E. W., and Zurn, D. E., <u>Thirteenth Symp. (Int.) Combustion</u>, The Combustion Institute, Pittsburgh, PA, 1971, p. 995-1008.
14. Brill, T. B. in "Structure and Properties of Energetic Materials", Materials Research Society, R. A. Armstrong and J. G. Gilman, Eds., Pittsburgh, PA, 1992, in press.
15. Korobeinichev, O. P., <u>Combust. Explos. Shock Waves</u>, 23:565-576 (1987).
16. Guirao, C., and Williams, F. A., <u>AIAA J.</u>, 9:1345-1356 (1971).
17. Beckstead, M. W., <u>Twenty-Sixth JANNAF Combustion Mtg.</u>, CPIA Publ. 529, 4:255-268 (1989).
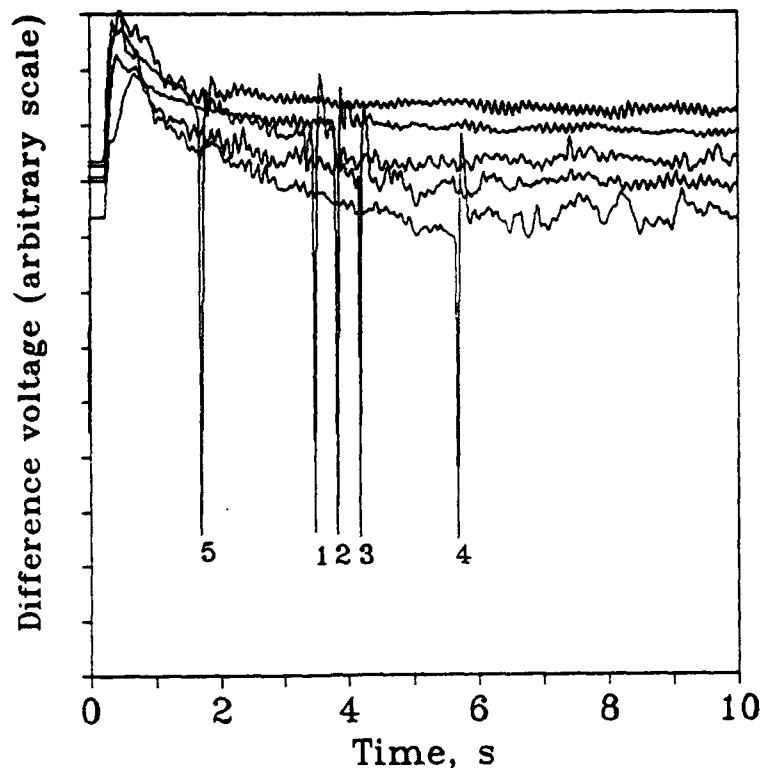
Figure 1. The time-to-exotherm of isomorphously doped AP heated
at 2000°C/s to 480°C under 13 atm Ar. (1) is an AP
single crystal, (2) is K^+ (0.013%), (3) is K^+ (0.13%),
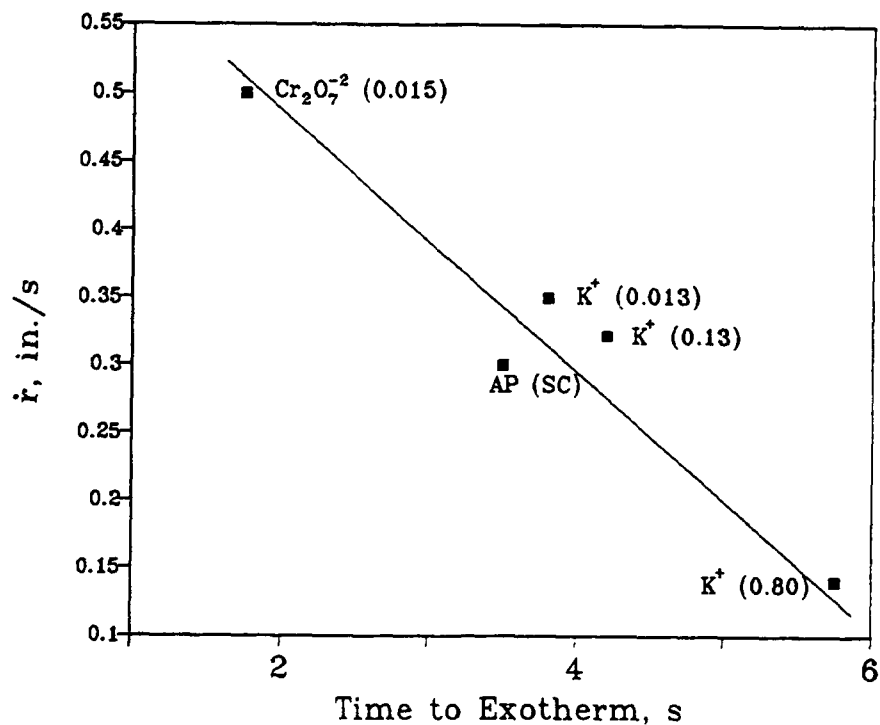(4) is K^+ (0.80%), (5) is $Cr_2O_7^{2-}$ (0.015%).

Figure 2. Comparison of the burn rate at 50 atm of isomorphously
doped AP and the time-to-exotherm at 13 atm.

COMBUSTION KINETICS OF HEDMs AND METALLIC FUELS

AFOSR Grants No. F49620-92-J-0172 and -0346

Principal Investigator: Arthur Fontijn
Research Collaborators: Peter M. Futerko, David P. Belyung

High-Temperature Reaction Kinetics Laboratory
The Isermann Department of Chemical Engineering
Rensselaer Polytechnic Institute
Troy, NY 12180-3590

SUMMARY

The use of new advanced solid rocket propellant constituents, such as, e.g., boron as a HEDM and ammonium nitrate as replacement for halogen-containing oxidants, requires knowledge of their combustion characteristics. The present program provides critical kinetic data to allow modeling of such combustion. Our HTFFR (High-Temperature Fast-Flow Reactor) and Metals-HTP (High-Temperature Photochemistry) facilities are uniquely suited to provide such data over very wide temperature ranges, within the limits 300-1900 K. In this work we investigate reactions of B, BO and BO_2 with O_2, CO, CO_2, H_2O and NO_x, and such AlO reactions with some of these oxidants as may be helpful to elucidate the kinetics of the boron species reactions. Major goals are to establish correlations between the pre-exponentials as well as the activation barriers of B, Al and other metallic species reaction rate coefficients and to investigate the fundamental reasons for any trends thus established to allow predictions for further reactions. Dual military-civilian use aspects of the work are also investigated.

TECHNICAL DISCUSSION

Aluminum Oxidation

The AlO/O_2 reaction system had previously been studied at 300 and 1400 K.[1,2] Comparison of the results led to the conclusion that the reaction had a slight negative activation energy; no pressure dependence was observed. The consequence of the negative activation energy was that the (AlO)-O bond energy had to exceed that of O_2, i.e. be larger than 493 kJ mol^{-1}. This result was in disagreement with a subsequent Knudsen cell evaporation study,[3] which yielded a bond energy of 419 $\pm$ 36 kJ mol^{-1}. This bond energy and the kinetics of the AlO + O_2 system are important to know for calculations on aluminized propellant burning and to allow a better understanding of BO + O_2 and other boron oxidation reactions. Our findings on chromium oxidation[4] had shown how not recognizing pressure effects had led other investigators[5] to erroneous conclusions on the Cr-O bond energy and the kinetics of Cr oxidation. As the wide scatter in our original work on AlO + O_2 could have masked pressure effects and the many apparatus changes since then have sharply reduced scatter,[6] a re-investigation of this AlO reaction appeared in order.

We have found that there is indeed a pressure-dependent and a pressure-independent process. The preliminary rate coefficient values are:

(1) $AlO + O_2 + Ar \rightarrow AlO_3 + Ar$ T = 300 to 1010 K

$\log[k(T)/(cm^6 molecule^{-2}s^{-1})] = -17 - 4.36 \log (T/K)$

(2) $AlO + O_2 \rightarrow AlO_2 + O$ T = 1010 to 1570 K

$k(T) = 1 \times 10^{-9} exp(-10547\ K/T)\ cm^3 molecule^{-1}s^{-1}$

Measurements at a few additional temperatures are in progress. The net effect of these two reactions with opposite temperature dependences is that, in the 5-80 Torr pressure range studied, the apparent rate coefficients pass through a minimum near 1000 K, cf. Fig. 1a. However, when comparing the lowest and highest temperatures there misleadingly appears to be just a slight negative temperature dependence, as the original studies suggested. Reaction (2) dominates at the temperatures of interest to rocket combustion calculations; its rate coefficients are independent of pressure and increase strongly with increasing temperature, cf. Fig. 1b. There is now no remaining contradiction between the kinetic results and the (AlO)-O bond energy value from the evaporation study.

Aluminium Oxide Reduction: Hydrocarbon Conversion

The direct conversion of methane, i.e. natural gas, to liquid fuels and chemicals of commercial interest is an intensely sought goal. A major approach being followed is to pass methane over solid-state catalysts consisting of mixtures of metal oxides with dopants. The first step in this process is to abstract a hydrogen atom from methane CH_4 to produce a highly reactive methyl radical CH_3 to form C-C bonds. To understand these surface reactions better, gas-phase studies of the reactions between methane and metal oxides are desired. *Ab initio* studies had suggested that abstraction should occur at elevated temperatures. Because of our experience with AlO from studies for rocket propellants, we decided to use that oxide to experimentally investigate this potential civilian application. Reaction was indeed observed and we determined $k(590-1380\ K) = 9.6 \times 10^{-39} (T/K)^{7.96} exp(2468\ K/T)$ $cm^3 molecule^{-1}s^{-1}$.[7] This is the first observation of this new group of chemical reactions. Quite likely, reactions between metal oxides and hydrocarbons will be found to be common. However, comparison of the present result to further *ab initio* and conventional transition state theory TST calculations suggests that, while direct abstraction can occur at the higher temperatures, one or more other channels, possibly involving AlO insertion into a C–H bond, dominate in the initial attack step.[7]

Rate Coefficient Predictions and Correlations

Rate coefficient expressions over wide temperature ranges can commonly be described by $k(T) = AT^n exp(-E/RT)$, where A, E and n are constants for a given reaction. We recently showed that, if n is fixed for a series of similar reactions, E can be semi-empirically calculated for each member of the series.[8,9] Work on these correlations is being continued. We have now also begun to address the determination of the AT^n term. This involves the development of new methods for using semi-empirical TST. Such theory is well established for making predictions on hydrocarbon combustion reactions. However, for metal species the necessary input data is lacking, hence a new approach is necessary. This MTST approach[10] uses a valence-force molecular model to estimate rotational constants and vibrational frequencies of the transition state. It is applicable to reactions with early barriers, typical of many exothermic metallic species oxidation reactions.

MTST calculations also allow conclusions regarding reaction mechanisms, as illustrated by Fig. 2 for the AlCl and BCl reactions with O_2. These reactions were

originally thought to proceed by abstraction of an O atom leading to OAlCl and OBCl, respectively. Newer thermochemical calculations[11] suggested this to be unlikely to be correct for the AlCl reaction,[8] which this figure confirms. The data points shown are our measurements and the solid lines represent MTST calculation values based on the assumption of abstraction. The assumption appears valid for BCl, but even at the highest temperatures investigated another process, e.g., adduct formation, appears to dominate for AlCl.

Together these semi-empirical procedures[8-10] make it possible to make reliable estimates of more rate coefficients, needed at high temperatures, than can be measured experimentally within reasonable periods of time.

References

1. A. Fontijn and W. Felder, "High-Temperature Fast-Flow Reactor Kinetic Studies. The AlO/O_2 Reaction near 1400 K," J. Chem. Phys. 64, 1977 (1976).

2. A. Fontijn, W. Felder, and J.J. Houghton, "HTFFR Kinetic Studies. Temperature Dependence of Al/O_2 and AlO/O_2 Kinetics from 300 to 1700/1400 K," 16th Symposium (International) on Combustion, 871 (1977).

3. P.Ho and R.P. Burns, "A Mass Spectrometric Study of the AlO_2 Molecule," High Temp. Sci. 12, 31 (1980).

4. A.S. Narayan, A.G. Slavejkov, and A. Fontijn, "The Metals-HTP Technique: Kinetics of the Cr/O_2/Ar Reaction System from 290 to 1510 K," 24th Symposium (International) on Combustion, 727 (1992).

5. U.S. Akhmadov, I.S. Zaslonko, and V.N. Smirnov, "Mechanism and Kinetics of Interaction of Fe, Cr, Mo and Mn Atoms with Molecular Oxygen," Kin. and Catal. (Eng. Transl.) 29, 251 (1988).

6. A.G. Slavejkov, P.M. Futerko, and A. Fontijn, "High-Temperature Fast-Flow Reactor Kinetics Study of the Reaction Between BCl and CO_2 from 770 to 1830 K," 23rd Symposium (International) on Combustion, 155 (1990).

7. D.P. Belyung, A. Fontijn, and P. Marshall, "Gas-Phase Reactions Between Hydrocarbons and Metal Oxides. The AlO + CH_4 reaction from 590 to 1380 K", J Phys. Chem., 97, xxxx (8 April 1993).

8. A. Fontijn and P.M. Futerko, "Homogeneous Kinetics of Metal Species over Wide Temperature Ranges: Techniques, Measurements and Correlations," in Gas-Phase Metal Reactions, A. Fontijn, Ed., North-Holland, Amsterdam, 1992, Chap. 6.

9. P.M. Futerko and A. Fontijn, "Activation Barriers for Series of Exothermic Homologous Reactions. I. Metal Atom Reactions with N_2O," J. Chem. Phys. 95, 8065 (1991).

10. P.M. Futerko and A. Fontijn, "Experimental and Transition-State Theory Studies of the Gas-Phase Reactions of AlCl with N_2O, CO_2, and SO_2," J. Phys. Chem., in press.

11. W. Chen, W.L. Hase, and H.B. Schlegel, "Ab initio MO Calculations of the Thermochemistry of BX, AlX, OBX and OAlX (X = O, F, Cl) in Gas-Phase Metal Reactions, A. Fontijn, Ed., North-Holland, Amsterdam, 1992, Chap. 9.
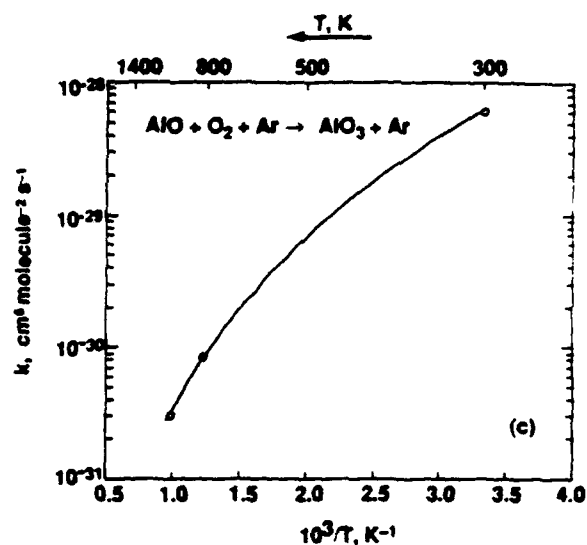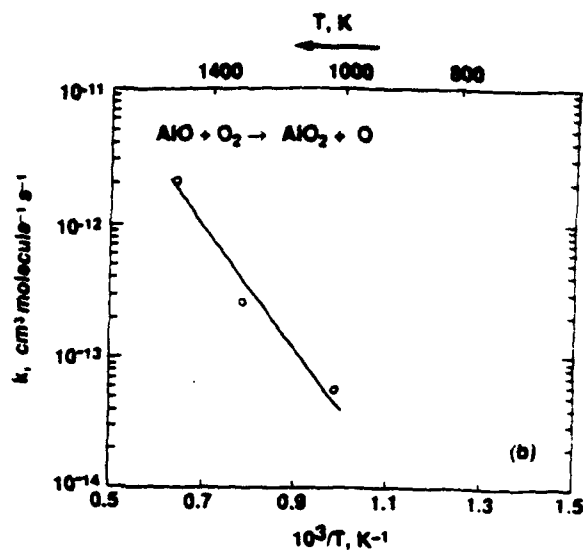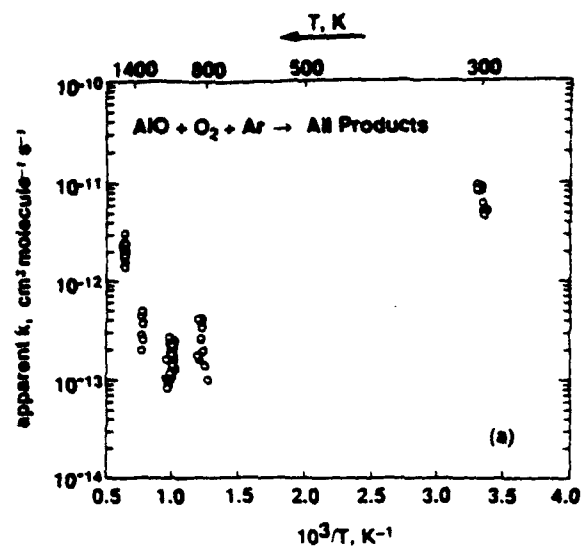
Figures 1a,b,c. Apparent and actual rate coefficients for AlO oxidation reactions.

Figure 2. Comparision of MTST calculations (lines) to experiments (points) are consistent with an abstraction reaction for BCl + O₂, but not for AlCl + O₂.
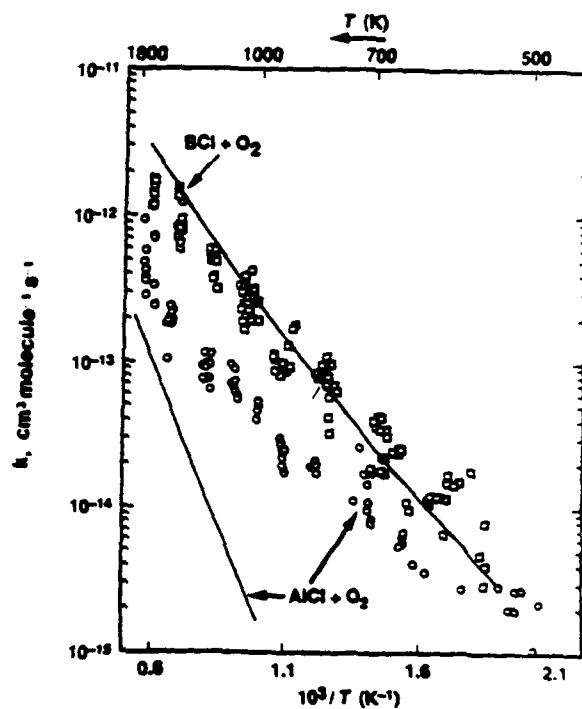
NONLINEAR ACOUSTIC PROCESSES IN SOLID ROCKET ENGINES

Principal Investigator: David R. Kassoy

Mechanical Engineering Department/Center for Combustion Research
University of Colorado, Boulder, CO 80309-0427

SUMMARY:

The present work describes acoustic and rotational disturbances in an injection induced low Mach number flow in a cylindrical engine chamber. An initial-boundary value calculation is done for the disturbances generated by a prescribed end wall velocity characterized by a Mach number similar in size to the mean axial flow value. The disturbances, superimposed on the steady injected,inviscid rotational mean flow, are composed of an irrotational, planar acoustic wave and a vortical, nonplanar component. A multiple scale study shows that the vorticity generated on the side wall is convected out toward the axis by the steady radial flow speed and diffused on a shorter scale by viscosity. This multidimensional study gives a complete solution for the flow field inside a model, stable solid rocket engine chamber subject to end wall forcing.

AUTHORS: Qing Zhao and David R. Kassoy

TECHNICAL DISCUSSION

1. Background

Solid propellant combustion in a cylindrical rocket engine chamber generates gaseous products that cause a spatially distributed velocity field. In a typical engine, the Mach number associated with the radial velocity of the gaseous products adjacent to the propellant is in the range $10^{-3} \leq M \leq 10^{-2}$, and the induced axial Mach number is at most $O(10^{-1})$ for long , thin chambers except near the nozzle.

In this work, a systematic method is developed for determining how an unsteady rotational flow field develops as a result of **boundary forcing** and how it is transported inside the cylindrical chamber. Initially a steady, low Mach number, inviscid, rotational flow exists in a long narrow cylinder, induced by spatially distributed injection from the cylinder wall. An analytical solution describes the solution (Culick 1966). One end of the cylinder is open and it is assumed that the pressure is constant at the exit. The mathematical formulation of the transient problem is in terms of an initial-boundary value problem.

Disturbances are created at the head end wall by imposing a small amplitude oscillatory axial velocity with frequency ω. Travelling acoustic waves arise from the mechanical endwall disturbance, and propagate through the steady inviscid, rotational induced flow. An axial acoustic velocity disturbance of $O(M)$ is linearly superimposed on the steady, inviscid, rotational mean flow also of $O(M)$. Interestingly, the acoustic pressure field always has the form of an axial planar wave in the long narrow cylinder.

The acoustic wave solution does not satisfy the no-slip boundary condition. A transitional region is required to assure that the complete transient solution satisfies that condition. Depending

on parameter values, the transition can be described in terms of a core/boundary layer model or a fully distributed rotational model.

In the core/boundary layer model, a viscous boundary layer adjacent to the walls accomodates the no-slip side wall condition. The structure of the boundary layer is closely related to that for the classical Stokes problem with relatively large wall injection. Small length scale spatial oscillations in the axial velocity are damped out on the global length scale of boundary layer. A multiple scale perturbation method is used to solve the mathematical problem.

The solutions to this model are valid only when the boundary layer is thin relative to the cylinder diameter so that the flow in the core is essentially inviscid and irrotational. There are specific restrictions on the side wall injection rate and end wall driving frequency. If these constraints are not satisfied, a new multiple scale peturbation technique is needed to find solutions where rotational effects fill the entire cylinder.

Two spatial length scales are important in the more general formulation; the chamber radius of $O(1)$ and a much shorter oscillatory scale of $O(M)$. It is demonstrated that the side wall is the source of unsteady vorticity generation. Once generated, it is convected toward the axis by the steady radial velocity and diffused by the weak viscous effects on the shorter length scale.

This work is a generalization and extension of formulations by Price & Flandro(1993) and Flandro & Roach(1992).

2. Core/Boundary Layer Solution

This more traditional approach divides the rocket chamber into two regions. The inviscid, planar acoustic core solution is valid in most of the chamber but does not satisfy the no-slip wall condition. The transition to no-slip occurs in a thin vortical layer adjacent to the side wall. The acoustic core solution is found by a Fourier analysis. We observe a solution with beats if ω is very close to one of the Fourier frequencies, or one that grows with time linearly if ω is equal to one of the Fourier frequencies.

The transition layer accomodates the planar wave solution on its outer boundary and the no-slip condition on its inner boundary. The overall radial thickness of the layer is characterized by one scale, and within the layer there is an $O(M)$ smaller length scale associated with the radial distance traveled by an injected fluid particle on the axial acoustic time scale. Due to the "hard" injection condition, the boundary layer flow is inviscid and rotational in the first approximation. Viscous stresses appear in the second order description, but are essential to finding the complete solution, as might be expected in a multiple scale analysis.

The effective thickness of the boundary layer depends strongly on each of the modal frequencies Ω in the core and the side wall injection velocity V_w. A large value of Ω promotes relatively rapid exponential decay, implying that high frequency disturbances are associated with thinner transition boundary layers. Thus higher order modes tend to be associated with effectively thinner boundary layers. The same type of argument demonstrates that increasing the value of V_w enhances the overall boundary layer thickness. The spatial distribution of the axial velocity in the transition layer is given in Figure(1) to show that the overall thickness of the layer is determined by the lowest mode in the core solution. The core solution is recovered in an oscillatory manner at a transition layer variable value of $\xi = 10$ for $\Omega = 2.5$ which correspondes to $r = 0.4$(the wall is at $r = 0.5$).

The core/boundary layer structure is valid only when exponential decay of rotational effects occurs close to the cylinder wall (say $r \geq 0.4$). If this condition is not satisfied, then a new multiple scale perturbation technique is needed to find solutions where rotational effects fill the entire chamber.

3. Rotational Flow Across the Chamber

A mathematical model is developed for the disturbance evolution when rotational effects are significant across the entire cylinder. In this case one can expect that vorticity will be convected along with the injected fluid and diffused as well by weak but pervasive viscous effects.

The disturbance is split into an irrotational planar wave and a vortical, nonplanar component. The planar part of the contribution is identical to the core solution in section 2. Once again it is recognized that two disparate length scales are important; the tube radius and an $O(M)$ shorter length associated with the radial distance traveled by a fluid particle on the acoustic timescale.

To leading order, the flow is described by a set of first order hyperbolic equations that are **inviscid and rotational**. Since the axial velocity is zero on the side wall, the sum of the vortical axial velocity and the planar axial velocity must be zero there. It is demonstrated that the vorticity on the wall is equal to the time derivative of the axial acoustic velocity. This means that the side wall is the source of the unsteady vorticity. Since the viscous effects are weak, the vorticity generated is convected by the local steady radial velocity toward the axis. The flow properties are invariant on a characteristic of the hyperbolic equations but change from one characteristic line to another.

A nonlinear diffusion equation is found from higher order analysis to describe the explicit form of the vortical axial velocity. The presence of a viscous term suggests that the vorticity transport process on the $O(1)$ radial length scale is accompanied by diffusion on the $O(M)$ scale.

The diffusion equation is solved using a Galerkin-like method in which Fisher's (1936) analysis is of importance. The results provide a complete description of the vortical component of the $O(M)$ flow field. Figure(2) depicts the spatial distribution of the vortical axial velocity with respect to the radial variable $r_1 = 0.5 - r$ at $t = 40$ and $z = 0.5$ for $M = 0.01$ and $\omega = 1.5$. The front is really a narrow diffusive region. Sixty percent of the chamber is filled with rotational flow. Figure (3a-c) shows the time response of the unsteady axial velocity at $r_1 = 0.15, z = 0.5$ for $M = 0.01$ and $\omega = 1.5$. Figure (3a) depicts the planar acoustic axial velocity response, Figure(3b) is for vortical axial velocity and Figure (3c) is for the total unsteady axial velocity.

REFERENCES

Culick, F.E.C. 1966 Rotational Axisymmetric Mean Flow and Damping of Acoustic Waves in a Solid Propellant Rocket. *AIAA J.* 4(8):1462-1463.

Price, E.W. & Flandro, G.A. 1993 *Combustion Instability in Solid Propellant Rockets.* Book manuscript in preparation.

Flandro, G.A. & Roach, R.L. 1992 *Effects of Vorticity Production on Acoustic Waves in a Combustion Chamber.* Final Technical Report AFOSR-90-0159

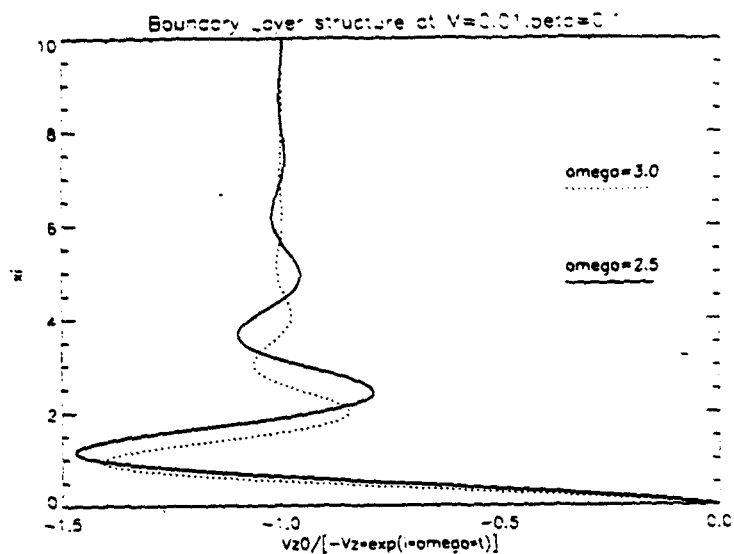Fisher, R.A. 1936 The Wave of Advance of an Advantageous Gene. *Ann. Eugen.* 7,355-369.

Figure 1: The axial velocity in the boundary
layer as a function of the variable ξ for $\beta = 0.1$,
$M = 0.01$ when $\Omega = 2.5$ and 3.0 .The boundary
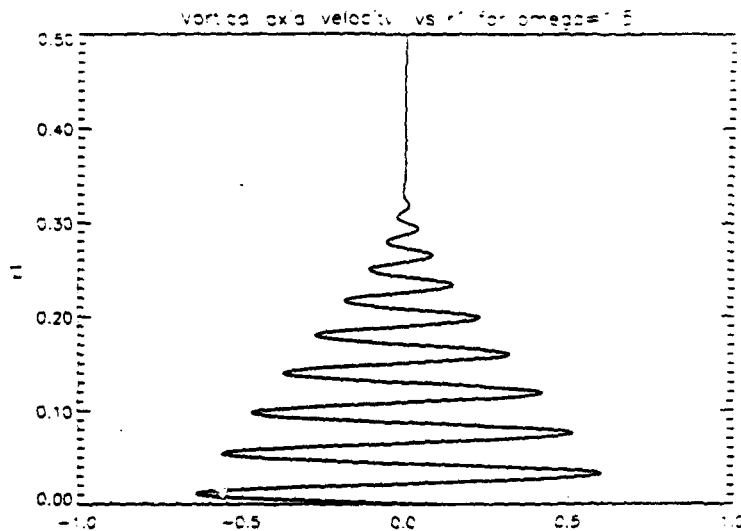layer is thicker for the former frequency value

Figure 2: Vortical Axial Velocity vs r_1
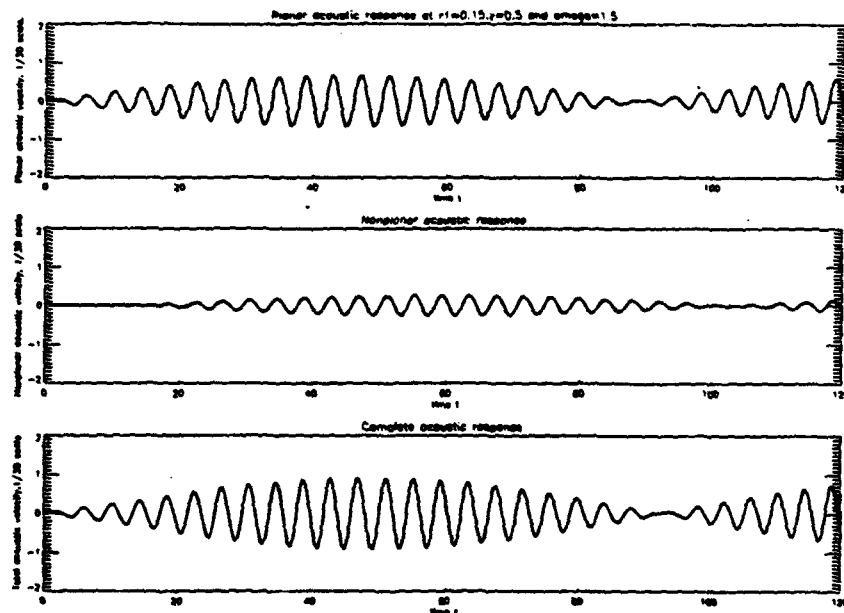at $t = 40, z = 0.5$ for $\omega = 1.5$

Figure 3a,b,c(from top to buttom):The time response of the
axial acoustic , axial rotational and the total unsteady axial
velocity at $r_1 = 0.15, z = 0.5, M = 0.01$ and $\omega = 1.5$

DIRECT NUMERICAL SIMULATION OF ACOUSTIC-MEAN FLOW INTERACTIONS IN SOLID ROCKET MOTORS

(AFOSR Grant/Contract No. F49620-92-J-0451)

Principal Investigator: SHANKAR MAHALINGAM

Center for Combustion Research, Department of Mechanical Engineering
University of Colorado, Boulder, CO 80309-0427

SUMMARY/OVERVIEW:

The present research is directed towards obtaining a fundamental physical understanding of the nature of interaction between the acoustic and mean flow in solid rocket engines. The approach adopted is a direct numerical simulation of the unsteady flowfield in model configurations using a higher-order compact finite difference scheme. It is expected that the results will provide valuable insight into the nonlinear coupling of pressure and velocity fields, flow turning and acoustic streaming phenomena. In addition, a methodology that will enable one to extract acoustic information from numerically simulated data is being addressed in this research. This research will enable development of models that will accurately reflect the important fluid-dynamic phenomena that exists during a combustion instability in solid rocket motors.

AUTHORS   Shankar Mahalingam, and Siming Mu

TECHNICAL DISCUSSION

An imbalance in energy amplification and damping mechanisms dictates whether a combustion-driven acoustic instability is sustained or weakened in solid propellant rocket motors. The relative importance of these mechanisms are strongly dependent on the oscillation mode and type of propellant. Furthermore, due to the the wave-structure of the acoustic field, its phase relative to processes contributing to amplification/damping is extremely critical to the outcome of the interaction. The focus of this research is on the mechanisms of energy exchange between the mean and acoustic flow and amongst various modes of the acoustic flow. A fundamental understanding of these processes is essential in

ultimately obtaining a global understanding of the overall problem of combustion-driven acoustic instability.

Our approach is to perform direct numerical simulations of several model configurations. These have been carefully chosen to complement Wang and Kassoy's (1991 a,b) analytical results and Baum and Levine's (1987) and Vuillot and Avalon's (1991) numerical simulations. Simulation results from these model configurations will enable us to isolate different physical phenomena and thus evaluate cause and effect relationships. These problems are briefly described below:

1. **Acoustic traveling wave-shear flow interaction in a 2D duct**. Initially an acoustic disturbance with constant amplitude across the cross-section is imposed over a steady parallel flow in a duct. Simulation results will be compared to Wang and Kassoy's (1991a), Baum and Levine (1987) and Vuillot and Avalon's (1991) results. An interesting feature of this problem is that a non-uniform amplitude function in the transverse direction can lead to the development of oblique waves even in the absence of a mean shear flow.

2. **Acoustic standing wave-shear flow interaction in a 2D duct**. This is the long-time counterpart of the first problem. The new physics that is introduced is wave reflections from the downstream boundary. Refraction and longitudinal waveform deformations predicted by Wang and Kassoy (1991b) will be studied.

Each of the above problems will also include prescribed mass injection through the side walls in order to simulate the intoduction of a large mass flow rate due to propellant burning in real rocket motors. A schematic representation of this process is shown in Figure 1.

An important objective of this research is the identification of acoustic mode forms from the results of direct numerical simulation. This task requires a synthesis of analytical and numerical approaches and will be accomplished through close collaboration with Kassoy's group.

A unique feature of the present research is the use of higher-order accurate finite differencing schemes coupled with an accurate treatment of boundary conditions. These are essential requirements for the study of acoustic phenomena in which both the amplitude and phase of acoustic signals have to captured accurately. The spatial differencing scheme is based on Pade approximations summarized by Lele (1989). The resulting matrices are tridiagonal for the schemes implemented These yield spectral-like accuracy which means they can accurately capture a greater range of length scales as compared to conventional second- or fourth-order accurate central differencing schemes. This is apparent from a plot of modified wavenumber versus actual wavenumber as depicted in Figure 2. It is clear that for the same grid size, the sixth-order (in the interior) accurate scheme implemented in this research is superior in resolving smaller scales. The boundary conditions

are treated precisely using the characteristic-based conditions developed for the Navier Stokes equations by Poinsot and Lele (1989). These have been used extensively for direct simulation of compressible and reacting flows at the NASA Ames/Stanford Center for Turbulence Research and have proven to be accurate and robust.

To date, we have tested the numerical scheme and boundary conditions on two test problems: steady one-dimensional shock wave (using 60 evenly-spaced grid points), and ignition of a premixed fuel-oxidizer mixture (using 121×121 uniformly spaced grid), using a code developed by Markus Baum and Thierry Poinsot. The primary objective was to ensure that the boundary conditions were treated correctly. Currently the code has been modified to model steady flow in a duct. We plan on imposing acoustic perturbation of constant amplitude across the transverse section and study the traveling wave problem, initially in the absence of injected mass flow through the wall.

REFERENCES

1. BAUM, J. D., AND J. N. LEVINE, "Numerical Investigation of Acoustic Refraction," AIAA Journal, 25(12), 1577-1586, (1987).

2. LELE, S. K., "Direct Numerical Simulation of Compressible Free Shear Flows," AIAA Paper AIAA-89-0374, (1989).

3. POINSOT, T., AND S. K. LELE, "Boundary Conditions for Direct Simulations of Compressible Reacting Flows," Center for Turbulence Research Manuscript No. CTR-102, (1989), also submitted to Journal of Computational Physics.

4. VUILLOT, F., AND G. AVALON, "Acoustic Boundary Layers in Solid Propellant Rocket Motors Using Navier-Stokes equations," Journal of Propulsion, 7(2), 231-239, (1991).

5. WANG, M, AND D. R. KASSOY, "A Perturbation Study of Acoustic Wave Propagation Through a Low Mach Number Shear Flow," Manuscript submitted to Journal of Fluid Mechanics, 1991a.

6. WANG, M, AND D. R. KASSOY, "Standing Acoustic Waves in a Low Mach Number Shear Flow," Manuscript submitted to AIAA Journal, 1991b.
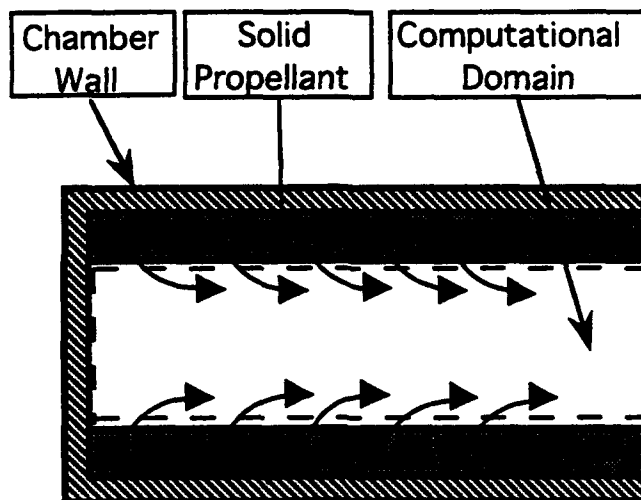
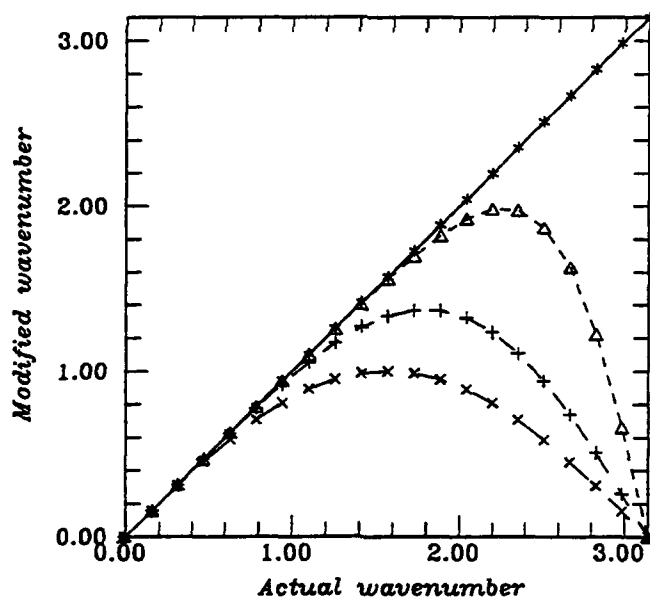Figure 1. Schematic representation of computational domain used in the simulation.

Figure 2. Comparison of various differencing schemes for first derivative. ——✱—— : Fourier;—×— —: 2nd order central difference;— + — —: 4th order central difference;---△---: 6th order presently used compact scheme.

FLAME DRIVING AND FLOW TURNING LOSSES IN SOLID ROCKETS

Principle Investigators: B. T. Zinn and B. R. Daniel

School of Aerospace Engineering
Georgia Institute of Technology
Atlanta, GA 30332

Summary/Overview:

The goal of this research program is to investigate the driving and damping of axial instabilities in solid propellant rocket motors due to gas phase solid propellant combustion and flow turning. This program began with an investigation of the responses of premixed and diffusion flames, stabilized on the side wall of a duct, to an imposed axial acoustic field. The current phase of this study is concerned with developing a greater understanding of the processes that control the flow turning loss and the role that this loss plays in damping combustion instabilities in solid rocket motors. In the first phase of the flow turning investigation, cold flow studies were conducted to determine the behavior of the flow turning loss in a constant temperature flow field. The current phase consists of theoretical and experimental studies of the effects of non-uniform temperature and density distributions in the combustion zone upon the flow turning loss. First, an acoustic stability equation that is applicable to flows with mean temperature gradients was developed to guide the experimental study. Next, the effect of mass injection through a wall mounted burner upon an imposed axial acoustic field was studied experimentally. The latter included measurements of the mean and acoustic velocities, acoustic pressures and the mean density distribution throughout a control volume in the region above the burner where flow turning occurred using LDV, piezoelectric transducers and Rayleigh scattering, respectively. The measured data were then used to evaluate the terms of the developed acoustic stability equation. These results indicate that while the stability equation for flows with temperature gradients differs significantly from the corresponding equation for cold flows, the behavior of the flow turning loss term is essentially unchanged by the presence of temperature gradients in the flow turning region.

Technical Discussion:

The occurrence of combustion instabilities is determined by the relative magnitudes of the driving and damping mechanisms within the combustor that add and remove energy from the oscillations, respectively. In order to eliminate or reduce the severity of acoustic oscillations resulting from combustion instabilities in solid rocket motors, the mechanisms by which energy is added to and removed from these oscillations must be identified and understood. It is generally accepted that the response of the combustion process of the solid propellant to the presence of acoustic oscillations provides the energy necessary to initiate and maintain instabilities in rocket

motors. Other factors, such as nozzle damping, viscous dissipation and flow turning, tend to remove energy from the oscillations and, thus, stabilize the system. In previous phases of this program, the mechanisms by which premixed and diffusion flames, which are present in the gas phase of the propellant flame, contribute to the driving of axial acoustic instabilities were investigated. The current program is concerned with the development of an understanding of the flow turning loss mechanism that is included in state of the art solid rocket stability prediction programs.

A theoretical investigation of the flow turning loss, based upon an acoustic energy conservation approach, was initiated during the previous reporting period in an effort to develop a practical method for its experimental investigation. This study confirmed that the classical flow turning loss term is indeed a part of the one dimensional acoustic stability equation, as originally predicted by Culick[1]. The analysis also confirmed Van Moorhem's[2] conclusion that the flow turning loss term is a result of the cross-sectional averaging that is involved in deriving the one dimensional conservation equations and, therefore, need not be included to a multidimensional rocket stability analysis. An experimental investigation of the behavior of the flow turning loss under cold flow conditions was then performed. For each set of test conditions, the mean and acoustic velocities as well as the acoustic pressures were measured throughout a control volume in the region where the flow turning loss was expected to occur. The measured data were used to evaluate the terms of the developed acoustic stability equation. Experiments were performed to determine the effects of the frequency and amplitude of the oscillation, the magnitudes of the injection and core flow Mach numbers, and the location of the flow turning relative to the standing axial acoustic wave upon the magnitude of the flow turning loss in the investigated control volume. The measured flow turning losses were found to be in agreement with the developed model and Culick's predictions.

The following efforts investigated the effects of temperature and density gradients in the flow turning region upon the flow turning loss and the overall acoustic stability of an "acoustic" cavity. The acoustic stability equation that describes this case is given by:

$$-2\alpha E^2 = \left[\left\langle p'u' + \overline{\rho}\,\overline{u}\,u'^2 \right\rangle \right]_0^L + \int_0^L \left\langle \frac{p'\overline{u}}{\overline{\rho}\overline{c}^2}\left(\frac{\partial p'}{\partial x}\right) + \frac{\rho'\overline{u}}{\overline{\rho}}\left(\frac{\partial p'}{\partial x}\right) + \frac{p'^2}{\overline{p}}\left(\frac{\partial \overline{u}}{\partial x}\right) \right\rangle_{y,t} dx$$

$$+ \left\langle \frac{1}{H}\int_0^L \left\{ \left\langle p' \right\rangle_y [v']_0^H + \left\langle \frac{p'^2}{\overline{p}} \right\rangle_y [\overline{v}]_0^H + \left\langle \overline{\rho}u' \right\rangle_y [v'\overline{u}]_0^H + \left\langle \overline{\rho}u' \right\rangle_y [u'\overline{v}]_0^H \right.\right.$$

$$\left.\left. - \left\langle \overline{\rho}u'^2 \right\rangle_y [\overline{v}]_0^H + \left\langle \overline{u}\,u'\,v' \right\rangle_y [\overline{\rho}]_0^H \right\} dx \right\rangle_t$$

where α is the growth rate constant. The contribution of the flow turning loss term to the growth rate constant of the oscillations is given by:

---

[1]Culick, F. E. C., "The Stability of One Dimensional Motions in a Rocket Motor," *Combustion Science and Technology*, Vol. 7, 1973.

[2]Van Moorhem, W. K., "Theoretical Basis of the Flow Turning Effect in Combustion Stability," Final Report, AFOSR Grant No. 78-3654, March 1980.

$$\alpha_{FTL} = \frac{-\left\langle \frac{1}{H} \int_0^L \left\langle \widetilde{\rho} u'^2 \right\rangle_y [\overline{v}]_0^H dx \right\rangle_t}{2E^2}$$

These theoretical results were used to correlate data measured in hot flow experiments where large temperature gradients were present in the flow turning region.

The experimental study was conducted in the setup shown schematically in Fig. 1. It was designed to simulate flow phenomena near the burning surface of a solid propellant in a rocket motor experiencing an axial acoustic instability. It consists of a 2.5 meter long, 3.75 x 7.5 cm^2 duct with a burner mounted on the bottom wall. The utilized multi-diffusion flame burner (MDFB) produced a flame consisting of an array of small diffusion flamelets that simulated gas phase solid propellant flames. The MDFB consists of a matrix of hypodermic tubes that supply oxidizer flow, simulating the flow of combustion products from burning ammonium perchlorate particles, while the fuel is supplied through the spaces between the tubes, which simulates the flow of pyrolysis products from the fuel binder. Two acoustic drivers mounted on opposing duct walls just upstream of the exit plane are used to excite a standing acoustic wave in the duct that simulates an axial instability in a rocket motor. An axial core flow is injected at the upstream end of the duct through a movable porous plate injector. The location of the MDFB relative to the standing acoustic wave can be varied by translation of the axial flow injector. Quartz windows in the side walls adjacent to the burner allow for laser Doppler velocimetry and Rayleigh scattering temperature and density measurements.

The behavior of the flow turning loss under cold flow condition and with a flame at the burner surface was investigated. For each set of test conditions, the mean and acoustic velocities, the acoustic pressures and the mean density distribution were mapped in a control volume that enclosed the flow turning region. The measured data was then used to evaluate the terms of the developed acoustic stability equation. The dependence of the flow turning loss in the investigated region upon the injection and core velocities and the location of the flow turning region (i.e., burner) relative to the standing axial acoustic wave were investigated. The dependence of α_{FTL} upon the burner flow rate and the location of the burner relative to the standing pressure wave in hot and cold flow is described in Figs. 2 and 3. While the behavior of α_{FTL} in the hot and cold flow experiments is qualitatively similar, the magnitude of the loss is generally higher in the cold experiments. This is believed to be due to the fact that for a given burner flow rate the steady flow velocity at the burner surface is higher. Consequently, a higher degree of turning is attained within the investigated control volume in the cold flow studies than in the hot flow investigations, resulting in a higher flow turning loss in the cold flow experiments. The similarity in the trends exhibited by flow turning losses measured in the cold and hot flow experiments also indicate that while the stability equations that describe these experiments differ significantly, the behavior of the flow turning loss term does not seem to be affected by the presence of temperature gradients in the flow turning region.

In summary, this study shows that the flow turning loss needs to be included only in analyses of axial instabilities in solid propellant rocket motors. Furthermore, an evaluation of the magnitudes of the various terms that appear in the rocket stability equation suggests that the terms that are independent of the mean flow Mach numbers are generally an order of magnitude larger than terms that are proportional to the mean flow Mach number.
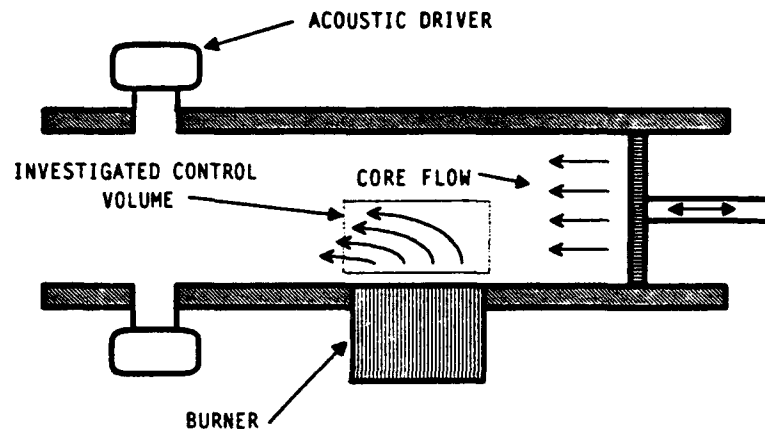
Figure 1. A schematic of the experimental setup used in the flow turning studies.
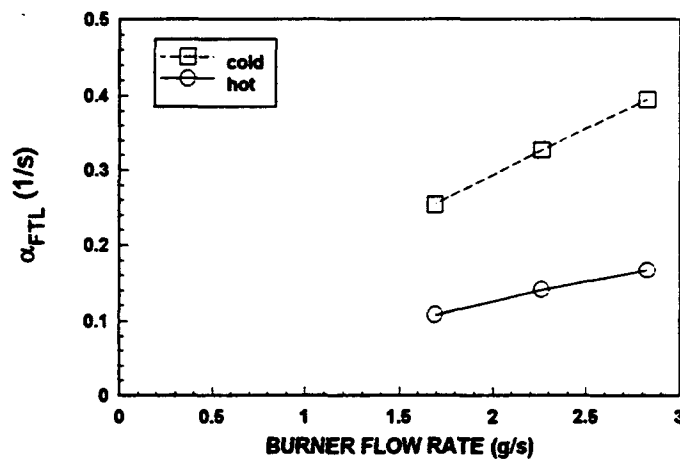

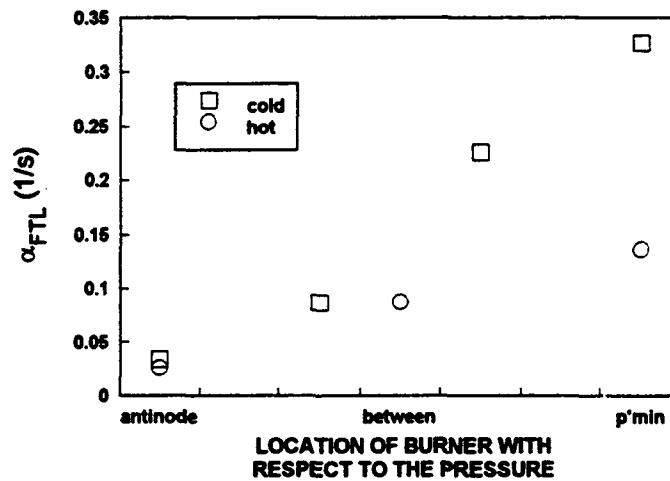Figure 2. The variation of α_{FTL} with the burner injection flow rate.

Figure 3. The effect of the burner location upon α_{FTL}.

Combustion and Plume Studies

D. H. Campbell, I. Wysong, G. L. Vaghjiani, Angelo Alfano, and D. P. Weaver
Phillips Laboratory, OLAC PL/RKFA
Rocket Propulsion Directorate
9 Antares Road
Edwards AFB, Ca. 93524-7660

SUMMARY/OVERVIEW:

In this program, research is performed in the areas of rocket exhaust plume physics and rocket propellant combustion. Both experimental measurements and theoretical computational investigations are carried out. Laser diagnostic techniques are used in both areas to map the properties, such as temperature and density, of gases in various combusting and non-combusting environments. Chemical kinetic measurements are also carried out to determine the specific reaction pathways and kinetic rates for specific reactions of interest. Results of these investigations are used to help in the design of future rocket propellants and to further our understanding of the chemical and collisional processes in rocket exhaust plumes that give rise to emissions in the infrared, visible and ultraviolet spectral regions so that better predictions of these emissions can be used in designing SDI detector systems. Typical results obtained in several of the research areas are detailed below.

TECHNICAL DISCUSSION:

Both theoretical and experimental studies have been carried out, during the last year, to investigate the characteristics of the flowfield structure in rapidly expanding high altitude plumes. The Direct Simulation Monte Carlo (DSMC) computational method has been used to investigate the interaction of the plume expansion with a hypersonic atmospheric freestream at altitudes in the 90-150 km range. Traditional scaling laws based on the plume Knudsen number or other distance scales in plume-freestream interactions in the transitional flow regime (densities at which the flow is between the continuum regime and the free molecular regime) have been shown to have limited ability to predict the spatial distribution of density and temperature in these flows. Significant non-equilibrium between the plume and freestream gas components of these flows has also been found. These results indicate that detailed modeling of the type used in these studies will be necessary for accurate prediction of the structure of these flows.

Experimental studies were continued during the last year in order to test and verify DSMC flow field predictions. Laser-induced fluorescence (LIF) of nitric oxide has been developed as a diagnostic technique. LIF measurements, after being properly corrected for quenching effects and rotational partition function, yield number density and rotational temperature at a given point in the flow field and have excellent sensitivity (10^{12} cm^{-3}) and spatial resolution. Results for the temperature and number density along the symmetry axis of a vacuum plume expansion show good agreement with predicted values. Attempts to measure the

rarefied, high-angle region of the flow field were frustrated by background gas interference due to limited pumping capacity for the LIF-NO measurements. Therefore, a pulsed jet orifice was installed and used as a nozzle source. Results from the high-angle region of the pulsed jet flow field show good agreement with calculations. Experimental studies on argon and nitrogen expansions using the electron beam fluorescence technique have also been continued. Comparisons of this experimental data with our direct simulation model have been performed and, again, results have been extremely good. As a result of these encouraging comparisons, work has proceeded on modification of the energy exchange models used in the DSMC collisional analysis. Experimental/analytical comparisons of rotational relaxation in low temperature expansions will be presented and key modeling issues discussed (Figure 1). Initial work on changes in vibrational relaxation modeling and approaches for effective chemical modeling have been started and initial results will be presented.

A key element in the understanding of the influence of nonequilibrium processes on flow phenomena is an experimentally verified analytical tool of sufficient capability to allow assessment of the interrelated influences of translational, rotational, vibrational, and electronic nonequilibriums as well as the influence of chemistry on the fluid flow properties of concern. Current monoprocessor code development is well below the computational capability required for such analysis, and as a result, an effort has been started to develop a multiprocessor based approach to direct simulation modeling that will significantly increase our computational power. Initial results from a parallel processing DSMC effort will be presented and implications regarding nonequilibrium flow prediction will be discussed.

Construction of a second-generation, higher flux atomic oxygen source flow was completed. This new continuous source is housed in a cryogenically-pumped cell that can provide a flow field simulation of the plume/freestream interaction. Initial work with the new source has demonstrated at least an order of magnitude increase in oxygen flux and a much reduced energy spread. A new resonance charge exchange approach for neutralizing atomic oxygen was evaluated and much higher flux levels were obtained from the new source than originally anticipated. Several new ceramic ring jet sources were tried and the resulting best design determined. Summary results will be presented.

Construction of a discharge-flow/flash-photolysis apparatus to study elementary gas phase reactions important in the oxidation of hydrazine was completed. The apparatus has a high detection sensitivity for OH, H and O radicals whose chemistry with hydrazine propellants will be investigated in this work. Specific work completed this year includes the measurement of the relative ultraviolet absorption cross sections at 298 K in the wavelength range from 200 to 285 nm . The absolute UV cross section of hydrazine vapor at 253.65 nm was determined. Further, the quantum yield of $H(^2S)$ production during 248 and 222 nm photodissociation has been measured. This was found for 248 nm photolysis of N_2H_4 to be 0.82, +/- 0.10. Kinetics studies also have been performed for the

rate coefficient, $k_1 = 1.48 \times 10^{-13}$ cm^3 molec^{-1}s^{-1} for the reaction H + N2H4 $\leftrightarrow$ products (Figure 2).

The necessity to understand the critical energy release mechanisms of high energy density propellants has created a need for an experimental capability to accomplish the simultaneous objectives: detection of molecular/ radical intermediates and stable products during combustion/pyrolysis; conservation of sample size due to limited availability of candidate propellant molecules; and inclusion of a general diagnostic to complement optical techniques. This need has resulted in the construction of a new facility to heat these reactive species to over 1000 K in a few microseconds and to determine the pyrolysis and combustion products. A CO_2 laser has been obtained along with gas chromatographic and mass spectrometric diagnostic equipment to obtain this information. A conventional flow reactor with controlled temperatures in excess of 1000 C has also been constructed. The calibration of this apparatus using the well known pyrolysis mechanism and kinetics of propane as a standard is nearly complete. Strained ring hydrocarbon molecules, quadricyclane and triangulanes, will be studied initially to determine their mechanisms of thermal decomposition and combustion. These molecules are currently being evaluated as performance boosting additives for RP-1 fuel. Early results of decomposition studies on quadricyclanes will be presented.
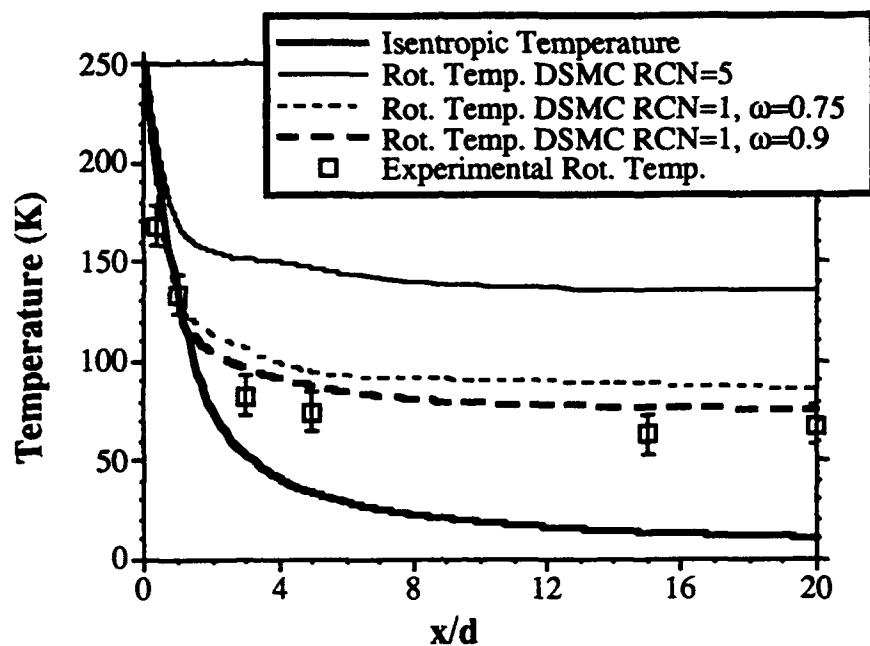
Figure 1. Comparison of centerline rotational temperatures for NO pulsed valve vacuum expansion.
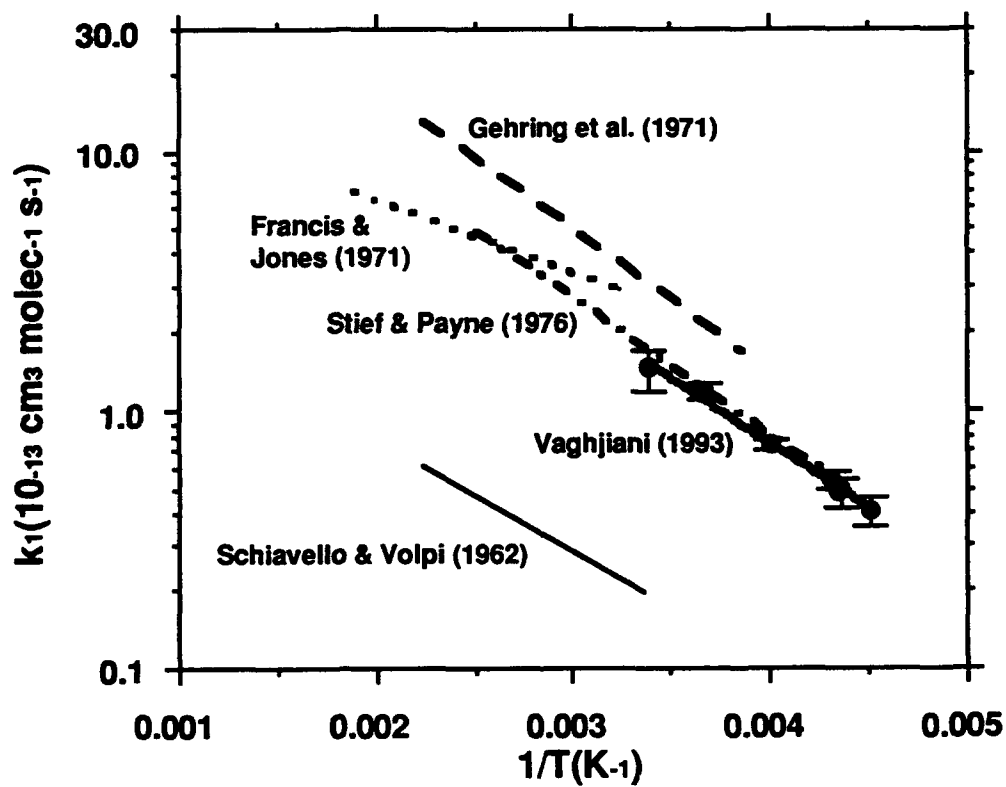

Figure 2. H + N_2H_4 rate constants.

LASER FLUORESCENCE DIAGNOSTICS FOR ARCJET THRUSTERS

Principal Investigator: Dennis Keefer

The University of Tennessee Space Institute
B. H. Goethert Parkway
Tullahoma, Tennessee 37388-8897

SUMMARY/OVERVIEW:

A multiplexed laser induced fluorescence (LIF) method is being used to provide accurate measurements of velocity and temperature in the exhaust flow of small arcjets. The narrow linewidth of a single frequency stabilized ring dye laser is used to measure the velocity distribution function of an excited state in the flow which then determines the velocity and temperature. The laser beam is divided, then each beam is modulated at a different chopper frequency and recombined at an angle to provide a point measurement of two vector components of the flow velocity. The flowfield measurements will be compared with the UTSI arcjet code predictions to determine the validity of the physical models used to describe the nonequilibrium processes in the arcjet constrictor and nozzle. Detailed flowfield measurements were obtained in a water-cooled argon arcjet. Similar measurements are now being made using the 1 kW NASA arcjet operating with a simulated ammonia propellant.

TECHNICAL DISCUSSION

A multiplexed LIF diagnostic method was developed to provide accurate measurements of the velocity distribution function of an excited atomic state in an arcjet exhaust plume. Point measurements of two velocity components are obtained simultaneously using a multiplex method. The beam from a frequency stabilized (Coherent 699-21) dye laser is split into two parallel beams, each of which is modulated at a different chopper frequency. The modulated beams are crossed using a lens to provide a measurement volume which samples two vector components of the velocity distribution function simultaneously. An absolute frequency reference is determined at the same time using the optogalvanic effect from the same atomic transition in a hollow cathode lamp. The narrow linewidth of the laser (approx. 500 kHz) provides an ultimate precision of approximately 1 m/s.

Extensive flowfield measurements were made in the exhaust flow of a small water-cooled arcjet operated with argon propellant to demonstrate the measurement technique [1]. However, the argon arcjet would not operate in a consistent steady state,

and the measurement technique is now being applied to the 1 kW NASA arcjet operating with a simulated ammonia propellant. High resolution emission spectra have also been recorded for the ammonia arcjet to determine the chemical species present in the exhaust flow and provide an independent estimate of the temperature. The estimated temperatures obtained from the emission spectra are shown as a function of axial position in Figure 1. Temperature estimates were obtained from the rotational spectrum of NH, the Doppler broadened line profile of H_α and the excitation temperature of the hydrogen Balmer series obtained from line-of-sight integrated spectra.

We have just begun the LIF measurements on the ammonia arcjet. The LIF signal obtained from the H_α transition is considerably weaker than the transition used in the argon measurements, and we are currently using a single beam, single component measurement on the ammonia arcjet to improve the signal level. A measurement of the intensity distribution and the radial velocity as a function of radial position is shown in Figure 2. At our present laser power the H_α transition is saturated, and the optical system is being modified to decrease the intensity in the measurement volume and increase the f/number of the detector optics. This should provide a sufficient increase in signal level to use the two beam multiplexing needed for vector measurements.
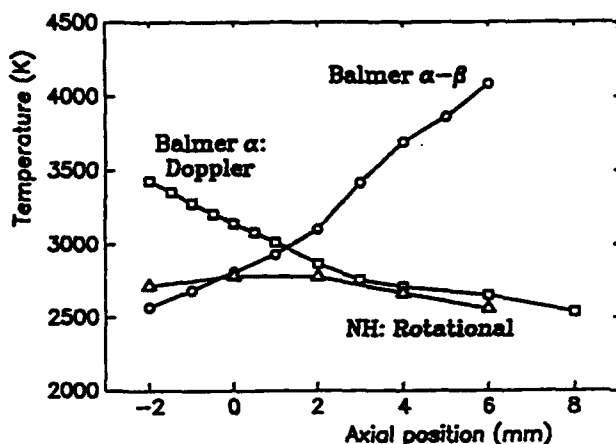
Fig. 1. Temperature estimates obtained from line-of-sight intergrated emission spectra.
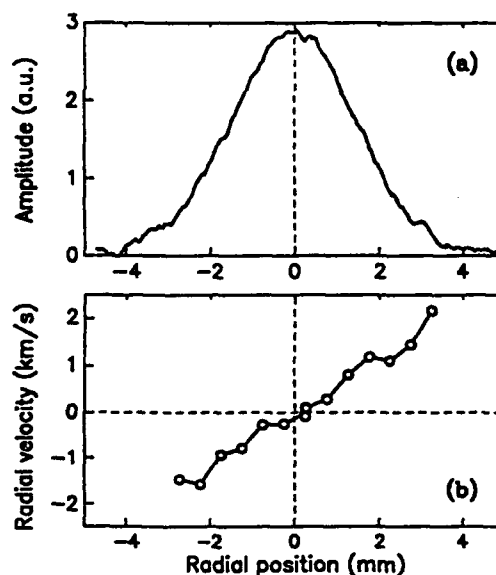
Fig. 2. LIF signed amptitude and radial velocity obtained from the H_α tramsition 2 mm downstream of ammonia arcjet exit plane.

The UTSI code [2], developed under the sponsorship of NASA/LeRC, has now been modified to include finite rate chemistry, species diffusion and separate energy equations for the electrons and heavy particles. Currently, the code uses only hydrogen for the propellant and has four species: molecular hydrogen, atomic hydrogen, positive hydrogen ions and electrons. There are several possible choices for the two energy equations used to determine the electron and heavy particle temperatures. We chose to use the electron energy equation and a separate equation for the static energy of the mixture of electrons and heavy species since, at least formally, the energy balance for the mixture is the same for equilibrium and nonequilibrium flows.

Chemical rate coefficients with one exception were taken from the work of McCay [3]. This exception is the rate of ionization of H atom by electrons which was calculated from ionization cross-section data. Ionization may occur by a two-step process where an electron first excites an H atom and this excited atom is then ionized by a collision with a second electron. This second process will be fast compared to the first because of the relatively small energy required to ionize an excited atom. To implement this effect without introducing a new species (excited H), the threshold energy for the ionization cross section was taken to be the excitation potential (10.2 eV) rather than the ionization potential (13.5 eV).

This new code has been applied only to the 10 kW NASA arcjet for one experimental condition. Significant differences are found between the old (equilibrium) version of the code and the new (nonequilibrium) code. An example is shown in Figure 3 where the electron and heavy particle temperatures are plotted as a function of radius at the exit plane. The equilibrium solution is also plotted for comparison. The center-line temperature predicted by the equilibrium code is a factor of two larger than the temperatures predicted by the nonequilibrium code. These large differences illustrate the need for detailed measurements to validate the physical models used in the codes.
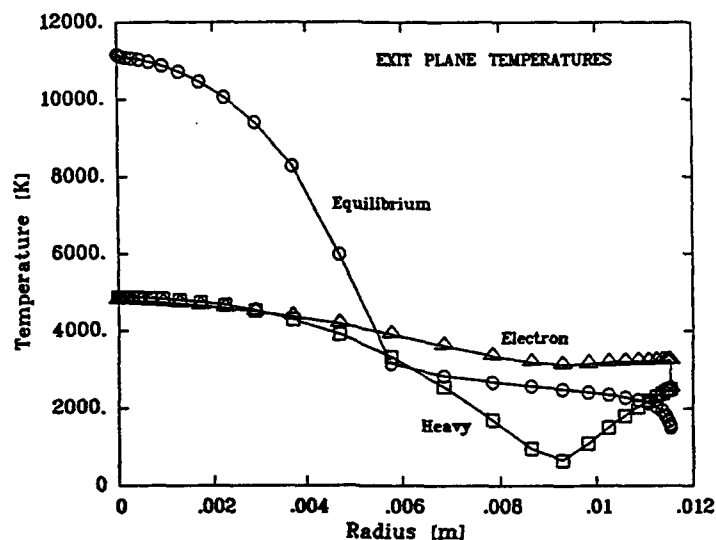
Fig. 3. Equilibrium and nonequilibrium code predictions of temperatures at the exit plane.

The UTSI equilibrium code has also been used in an attempt to understand the large difference in thrust, specific impulse and efficiency observed in experiments with 10 kW hydrogen arcjets having water cooled and radiation cooled anodes. The experimental data and temperature boundary conditions used for these comparisons were supplied to us by Bernd Glocker of The Institut fur Rahmfahrtsysteme (IRS) at the University of Stuttgart. Convergence of the code was readily obtained for the arcjet that used a radiation cooled anode, but simulation of the watercooled anode did not attain the same level of convergence. Performance predictions for both cases are shown in Table 1 together with the experimentally measured values. The code overpredicts the performance parameters for the hot anode by 7 to 9 percent, but the difference is much larger (29 to 73 percent) for the cold anode. Some overprediction of performance is expected with the equilibrium code since frozen flow losses are neglected. However, the large discrepancy in the cold anode case may be due to the use of incorrect electrical and thermal conductivities based on LTE assumptions, especially in the colder flow near the anode surface, and the difficulty in obtaining convergence levels comparable to the hot anode simulation. Detailed flowfield measurements will help to determine which models for the transport properties must be modified to improve the predictions in the cold anode simulations.

TABLE 1

	Radiation Cooled Thruster (MARC thruster)		Water Cooled Thruster (TT1 thruster)	
	Numerical	Experimental	Numerical	Experimental
Thrust (N)	0.924	0.866	0.8095	0.626
Isp (sec)	943.3	882.8	826.0	638.2
Efficiency (%)	45.12	41.42	32.02	18.52

REFERENCES

1. D. Keefer and W. Ruyten, "Laser Fluorescence Velocimetry of an Arcjet Exhaust Plume," AIDAA/AIAA/DGLR/JSASS 22nd International Electric Propulsion Conference, Viareggio, Italy, October 14-17, 1991, IEPC-91-093.

2. R. P. Rhodes and D. Keefer, "Comparison of Model Calculations with Experimental Data from Hydrogen Arcjets," AIDAA/AIAA/DGLR/JSASS 22nd International Electric Propulsion Conference, Viareggio, Italy, October 14-17, 1991, IEPC-91-111.

3. T. D. McCay and C. E. Dexter, "Chemical Kinetic Performance Loss for a Hydrogen Laser Thermal Thruster," J. Spacecraft, Vol 24, No. 4, 1987, pp. 372-376.

FUNDAMENTAL STUDIES OF THE ELECTRODE REGIONS
IN ARCJET THRUSTERS

Principal Investigator: M.A. Cappelli

High Temperature Gasdynamics Laboratory
Stanford University
Stanford, CA 94305-3032

SUMMARY/OVERVIEW

The primary objective of this research program is to provide a more fundamental interpretation of the processes that occur in the vicinity of hydrogen arcjet thruster electrodes. Our present research program is an extension of our past efforts in the development of optical-based arcjet thruster diagnostics. We employ laser-induced fluorescence, optical emission spectroscopy, and absorption spectroscopy, to measure flowfield properties such as temperature and velocity, and to characterize nonequilibrium behavior in arcjet flows. Together with physical models of arc attachment, these measurements help us to understand the fundamental behavior of the near-electrode regions in these devices, and assist in identifying the necessary physics to be included in more elaborate models of overall arcjet thruster performance.

TECHNICAL DISCUSSION

There is an increasing need to better understand the internal plasmadynamic flowfield characteristics of arcjet thrusters. As demands are made for higher arcjet operating powers (3-30 kW) or higher thrust efficiencies at low powers (1-3 kW), it is recognized that there is a need for a more fundamental understanding of the physics which limits arcjet performance and the scaling of these devices to higher thrust levels. Such an understanding must come from a combination of experiments and theory, and will lead to the development of arcjet performance models that will assist in overall arcjet thruster designs.

The predictive capabilities of many existing arcjet models are limited by the simplified treatment of the regions in the vicinity of cathodes and anodes[1-3]. These near-electrode regions control the mode of arc attachment ("diffuse" or "constricted"), and, in the case of arc attachment at the anode, may be the performance-limiting factor in high power operation. Little attention has been paid, in the past, to the physics associated with arc attachment at the electrodes. Recently, in various models, we have addressed issues relating to: (i) the sustaining of the plasma in the electrical boundary layer in the vicinity of anodes and cathodes, in particular, the role of ionization non-equilibrium and how it is influenced by the flowfield[4], (ii) the non-thermal equilibrium nature of this boundary layer and the properties that distinguish between a "diffuse" mode of arc attachment (resulting from a positive electrical boundary layer impedance) and a "constricted" mode of arc attachment (negative impedance)[5], and (iii) the role that is played by the electrical sheath in establishing a current balance at the electrode surface[6]. In this last study, we have found that the structure of this near-electrode region is strongly influenced by the emissive behavior of the cathode or adsorptive behavior of the anode. The emissive behavior of the cathode is strongly related to its temperature, which is determined by a heat balance and the heat flux from the plasma, which in turn is controlled to a great extent by the structure of the electrical boundary layer. It is obvious that the electrical "boundary condition" at the cathode is coupled to the nearby plasma in a complex non-linear fashion.

In previous related programs[7], we have developed and applied laser-induced fluorescence[8], emission[9], and vacuum ultraviolet absorption diagnostics[9] to the characterization of low power hydrogen arcjet plumes. The measured flowfield properties (temperature, velocity, atomic hydrogen number densities) compare favorably to the predictions made on the basis of a resistive MHD code[1] developed by Olin-Rocket Research Company. We

have presented a detailed comparison of code predictions to experimental results in Reference 2. Despite the good agreement between predicted and measured center-line axial velocity over a range of specific powers (see Figure 1), there is considerable disagreement between the predicted and measured temperature above a power level of about 1 kW. This disagreement implies that the model is likely to overpredict thrust efficiency at the higher power levels.

Our aim in the present program, is to extend these diagnostics to study the internal features of these devices. Our emphasis is on the measurement of plasma properties in the vicinity of the cathode and anode, and the development of an understanding of the structure of these near-electrode regions by a combination of experiment and model development. Our efforts in the first phase of this work has been focused on three activities: (i) the use of optical emission spectroscopy to measure plasma properties in the vicinity of the cathode/constrictor, as well as the cathode temperature (ii), the extension of our LIF diagnostics to higher pressure ($1 < p \leq 50$ Torr) so as to interrogate further upstream into the expansion nozzle, and (iii) the development of a self-consistent model of the near-electrode region and arc attachment. A brief description of the results of these activities is described in the sections below.

(i) Measurements of Near-Cathode Plasma Properties and Cathode Temperature

During the past seven months, we have used the numerical simulations of hydrogen arcjet thruster flows presented in Reference 1 and 2 to numerically calculate the spectral radiance that would be observed along the axial direction. We anticipate that the region near the cathode will be the most luminous, in which case, the measured spectral radiance will be biased to reflect the local spectral emission of the plasma at this location. Along the arcjet centerline, in the vicinity of the cathode and constrictor, the plasma is highly dissociated, and we consider emission attributed to atomic hydrogen only.

The numerical calculations of spectral radiance consist of an integration of the radiative transfer equation along the centerline of the arcjet from the cathode tip to the exit plane and beyond into the plume of the plasma. For the calculations presented here, we consider bound-bound transitions only. The spectral emission and absorption coefficients are expressed in terms of the excited state number densities and spectral lineshape for each transition. The lineshape accounts for both Stark and Doppler broadening as well as Doppler shifts. The number densities are calculated from a ten-level collisional-radiative model including the ion, the ground state atom and eight excited states. The plasma is taken to be optically thin for all transitions other than those of the Lyman series (which terminate on the ground state) which are assumed to be fully trapped. In calculating collisional excitation and de-excitation rates, the free electrons are assumed to have a Maxwellian velocity distribution. We include departures from LTE driven by convective transport of electrons, ions, and ground state neutral atomic hydrogen. In order to solve the system of equations representing the time rate of change in excited state number densities, plasma properties such as pressure, electron and atom kinetic temperatures, dissociation fraction, and axial velocity, were entered into the calculations from the MHD model predictions[2].

A sample of the results of these calculations is shown in Figure 2. Here the spectral intensity of the H_a transition has been integrated from the cathode ($x = 0$) to the arcjet exit plane, x_e, and to three intermediate positions for comparison. The figure shows that the largest contribution to the emission comes from the inner ten percent of the arcjet, that is, from within the cathode and constrictor region. The extent of reabsorption by the cooler expansion flow is seen to be about 20 percent at line center. The effect of the Doppler shift is seen as an asymmetry that is most pronounced at $x = 0.5 \, x_e$. It is apparent that there is little change in the spectrum as the radiation passes through the arcjet plume. Thus, axial line-of-sight emission measurements are expected to yield lineshapes similar to those at the arcjet exit plane. It is also apparent that the axial emission spectrum reflects structure that originates primarily near the region of the cathode.

The spectrum calculations extend over a region that includes the most intense of Balmer series transitions. An example of the calculated spectral radiance between 300 and 700 nm is shown in Figure 3. Recombination radiation is not included in the spectrum shown. The broad background radiation in the figure is the contribution from the gray body emission of the cathode, which is made of tungsten (emissivity = 0.34), and taken to be at its melting point of 3400 K. Evidently, the simulations indicate the in the 500 - 650 nm range, the cathode emission is comparable in strength to that of the H_β transitions, suggesting that this would be a possible window in which

in-situ cathode temperature measurements can be made. Axial emission measurements from a 1 kW class radiatively-cooled laboratory-type arcjet thruster are in progress.

(ii) LIF Diagnostics

In past research[7-9], we have demonstrated the usefulness of LIF spectroscopy (H_α resonance fluorescence) to the characterization of hydrogen arcjet thruster plumes. The pressures downstream of the exit plane where previous measurements have been made are estimated to be about 1 Torr and less. In future studies, we plan to extend these measurements to higher pressure regions within the expansion nozzle. At higher pressures, the plasma becomes more luminous, and the intense background may signal may lead to detector saturation. As a preliminary study, we extended these measurements to exit plane pressures of about 30 Torr, and still find that we can maintain reasonable signal to background intensity ratios. We shall describe the outcome of these preliminary exit-plane high pressure studies, and the prospects of moving upstream into the nozzle, where fluorescence is collected through holes machined in a specially fabricated anode nozzle.

(ii) Modeling the Near-Electrode Region

In previous work[4,5], we have investigated the effects of fluid flow and thermal boundary layers on the structure of a plasma adjacent an anode or cathode. In these studies, we have paid particular attention to understanding conditions necessary to maintain a diffuse anode arc attachment. Since maintaining a diffuse arc attachment is critical to the operation of low power arcjet thrusters, increasing our understanding of this phenomenon will directly impact the optimization of arcjet thruster behavior. We have extended this model to include the formation of a sheath. Figure 4 illustrates the plasma sheath structure for an atmospheric pressure, LTE argon plasma at 6000 K flowing against an electrically floating surface (J = 0). The free stream velocity for this case shown is 500 cm/s. Also included in the figure is the quasi-neutral solution. We see that there is a significant departure from the quasi-neutral approximation very near the electrode. We also note however, that the dependence of our solution on the plasma sheath is largely governed by our choice of electron recombination rates at the electrode surface. A full analysis of this dependence is in progress, and the variation in sheath structure as current is drawn to or from the electrode will be presented.

REFERENCES

1. G.W. Butler, B.A. Kashiwa, and D.Q. King, "Numerical Modeling of Arcjet Performance", AIAA 90-1474, 21st Fluid Dynamics, Plasma Dynamics and Lasers Conference, Seattle, WA, June 1990.

2. M.A. Cappelli, J.G. Liebeskind, R.K. Hanson, G.W. Butler, and D.Q. King; "A Comparison of Arcjet Plume Properties to Model Predictions"; AIAA-93-0820; 31st Aerospace Sciences Meeting, Reno, NV, January 1993.

3. R. Rhodes and D. Keefer, "Comparison of Model Calculations with Experimental Data from Hydrogen Arcjets, IEPC-92-111, 22nd International Electric Propulsion Conference, Viareggio, Italy, October 1991.

4. M.A. Cappelli, "The Non-equilibrium Region of an Electrode in Contact with a Flowing Thermal Plasma", IEEE Transactions on Plasma Sciences 21, 1, 1993.

5. E. Meeks and M.A. Cappelli, "Two-temperature Fluid Model for High Pressure Plasmas in Contact with Cooled Electrodes", to appear in Journal of Applied Physics, April, 1993.

6. E. Meeks and M.A. Cappelli, "Modeling the Near-Electrode region of Arcjets II:, Inclusion of the Plasma Sheath with Full Coupling to the Thermal and Velocity Boundary Layers", 29th Joint Propulsion Conference, Monterey, CA, July, 1993.

7. Our previous program has been supported by NASA (SDIO), AFOSR, and Rocket Research Company.

8. J.G. Liebeskind, R.K. Hanson, and M.A. Cappelli; "Flow Diagnostics of an Arcjet Using Laser-Induced Fluorescence"; AIAA-92-3243; 28th AIAA/SAE/ASME/ASEE Joint Propulsion Conference, July 1992

9.   M.A. Cappelli, R.K. Hanson, J.G. Liebeskind, and D.H. Manzella; "Optical Diagnostics of a Low Power Hydrogen Arcjet"; IEPC-91-091; 22nd AIDAA/AIAA/DGLR/JSASS International Electric Propulsion Conference, October 1991.
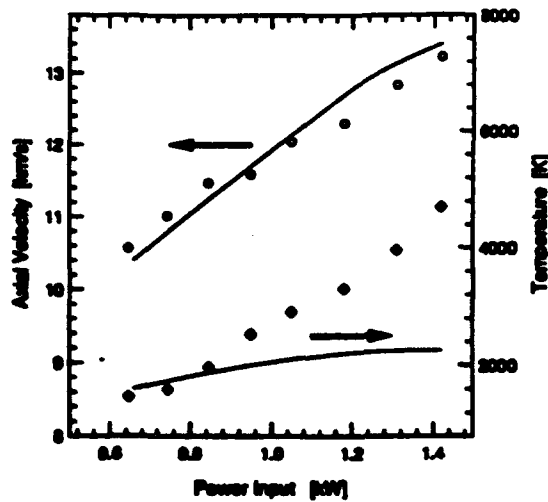
Figure 1

Comparison between computed (solid line) and measured (open symbols) variation in centerline axial velocity and temperature with arcjet power. The mass flow rate for this study was 13.1 mg/s (taken from Reference 2).
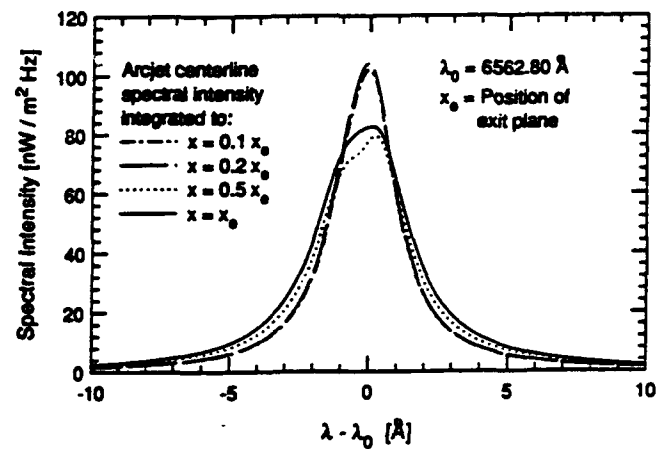

Figure 2

Predicted H_α emission lineshape from axial integration.
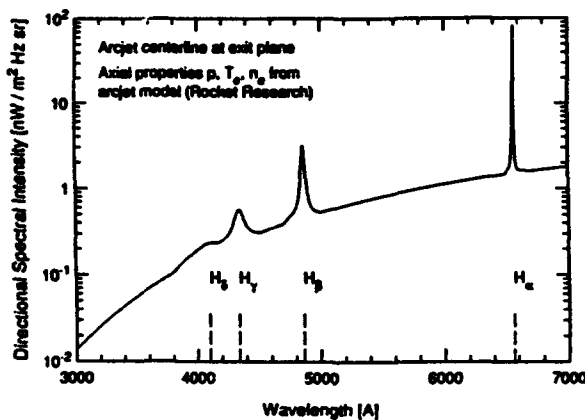
Figure 3

Predicted spectral radiance over the entire visible region of the spectrum, as viewed along the axial direction of the flow.
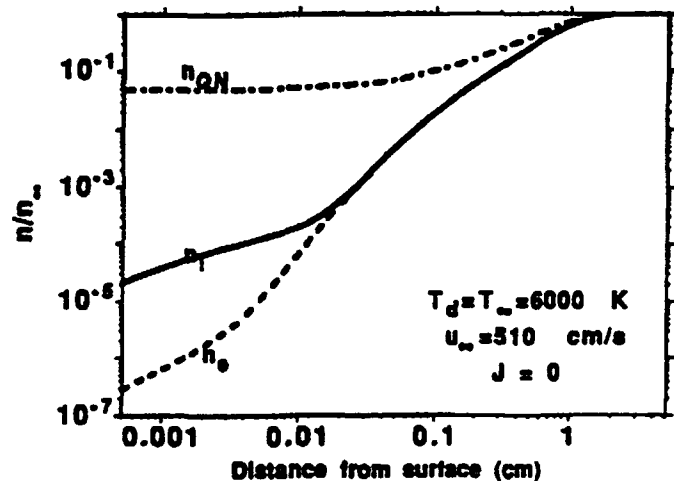
Figure 4

Predicted electron and ion number densities in the sheath region of a flowing plasma in contact with an electrically floating surface. The sheath structure calculation is compared to the results of a quasi-neutral (QN) formulation.

Performance Effects of Interaction Between a Low-Power Arcjet and its Power Processing Unit

Principal Investigator: Ronald Spores
Collaborator: Daniel A. Erwin

Phillips Laboratory
Rocket Propulsion Directorate
Edwards AFB, |CA 93524

SUMMARY

The effects of a high-frequency switching power processing unit (PPU) on the operating characteristics of a 1 kW class arcjet are being investigated. The combination of a low-power thruster and switching PPU is expected to play a significant role in near-Earth missions in coming years; a detailed understanding of the how these two components interact is of considerable interest to satellite system designers. Results indicate that energy deposited in atomic excited states (frozen flow losses) is modulated by the current ripple induced by the power processing unit. However, the exhaust propellant momentum flux is found to remain essentially constant throughout the PPU switching cycle.

TECHNICAL DISCUSSION

High frequency switching power supplies have several characteristics that make them highly desirable for space applications including light weight and demonstrated efficiency of greater than 90%. The effect of PPU switching operation is apparent in the arcjet current profile, which exhibits a sawtooth-shaped current profile at the PPU switching frequency. A typical plot of arcjet voltage, current and power is shown in figure 1. Current ripple is observed to be about 17% while overall power fluctuates at about 14%. This current ripple results in a fluctuation in the energy dissipation inside of the arcjet. The arcjet used in this study is operating on hydrogen propellant and the PPU switching frequency is 16.6 kHz.

This work looks into how the continuously varying energy dissipation inside the arcjet thruster affects overall performance. The first task was to investigate if the current ripple resulted in any optical emission variation from the plume. To investigate the optical fluctuations a 1-m scanning spectrometer is used to collect light in the axial direction while a photomultiplier tube in conjunction with narrowband interference filters were used to look at particular transition lines in the radial direction, see figure 2. Figure 3 shows a typical plot of Balmer α emission, measured radially just downstream of the nozzle exit plane. The emission ripple is roughly in phase with the current, and shows a peak-to-peak fluctuation of 33%. The presence of this emission ripple indicates a modulation of excited state density (one type of frozen flow loss) by the PPU switching. Note that in these experiments, the recording of emission waveforms are phase-locked with the power supply switching cycle. Unfortunately, it is still unclear how the current ripple affects other more important types of frozen flow losses, i.e.- dissociation and ionization.

Next, the emission ripple as a function of axial distance downstream was analyzed. Figure 4 shows a sequence of Balmer α emission plots taken in the radial direction at a series of axial locations. The curves have been normalized and shifted up in ascending order to emphasize the phase relationship; note that the phase is retarded from one station to the next. This retardation indicates that a disturbance or modulation of the excited-state density (for the hydrogen Balmer α line, the density of the n=3 atomic level) convects at a finite rate. By measuring the rate of propagation for the modulation over a given distance, the plume convection velocity can be determined. Measurements out to a distance of 5 cm downstream of the nozzle exit indicated a very linear relationship between modulation distance downstream and time for convection; an overall velocity of 4.0 km/sec was measured. This speed seems low compared to LIF measured centerline values of 14.0 km/sec; note, however that this represents an integrated radially averaged value that includes a large boundary layer contribution.

By measuring the axial velocity at a series of radial locations across the nozzle exit plane and then employing the Abel inversion technique more commonly associated with spectroscopy, one can obtain complete radial velocity profiles of an arcjet. Figure 5 illustrates a typical profile using this technique. Although not as accurate as a laser induced fluorescence system, the equipment needed to implement this technique is substantially cheaper.

This effort also looked into the possibility of whether the plume momentum flux (velocity) modulated due to the time-dependent propellant heating inside the thruster. If this effect is significant, it should be observable as a time-varying Doppler shift in emission, where the emission is collected up the centerline axis of the thruster nozzle. Horizontal cuts through figure 6 give the fluctuating emission at a particular wavelength, while vertical cuts give the spectral profile at an instant in time. The large central peak in the spectrum at all times is due to nonshifted Balmer α light from the arcjet core. Below this is a time varying horizontal 'ridge' which corresponds to the Doppler shifted emission of the plume. Although plume emission varies in amplitude throughout the switching cycle, there is no observable variation in Doppler shift and thus no observable fluctuation in velocity is caused by the PPU current ripple.

The measurement of plume radiation modulation due to the PPU ripple can lend insight into the mechanism of plume emission. One current hypothesis states that arcjet plume emission is primarily due to resonant scattering of photons emitted by the highly luminous arc plasma within the constrictor. If this were true the whole plume would absorb the core emission and reemit at essentially the same time. However, this work shows that there is clearly a downstream convection taking place of the PPU induced plume modulation. A competing explanation of plume radiation that explains this modulation is that plume emission is the result of fluctuations in electron density emitted from the arcjet core and the emission is primarily due to electron recombination.

To verify the hypothesis that the arcjet plume emission mechanism is primarily due to electron recombination, the electron density and electron temperature fluctuations in the plume is presently being measured . A triple Langmuir probe setup is being used to obtain instantaneous measurements in the plume. It is anticipated that the results of this task with reveal a phase relationship between electron density fluctuations and PPU ripple.
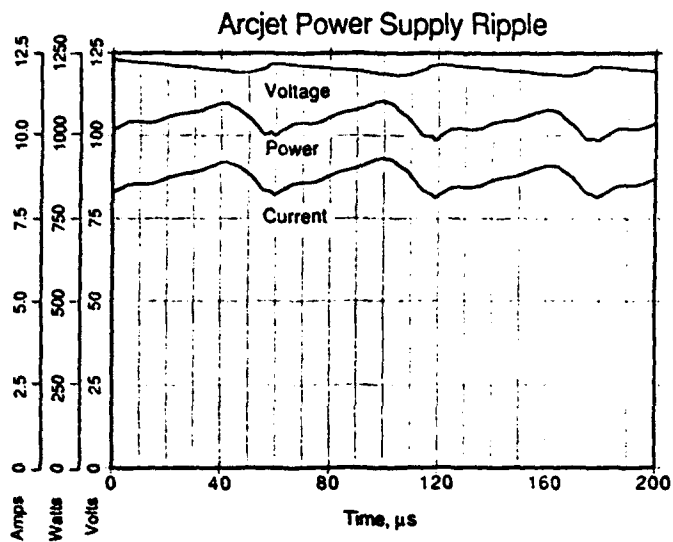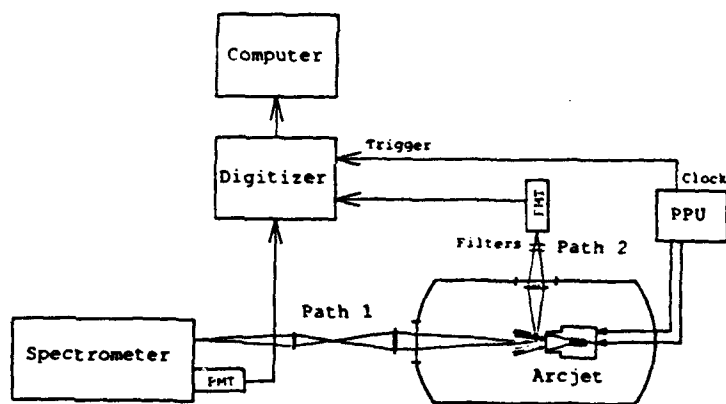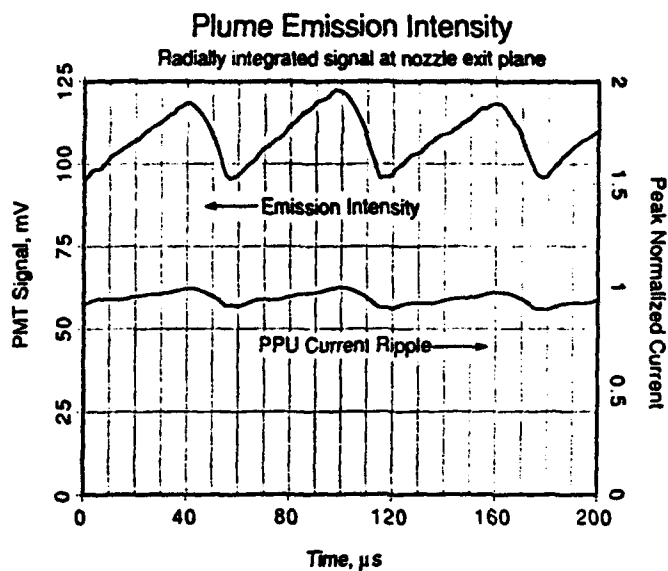
Figure 1

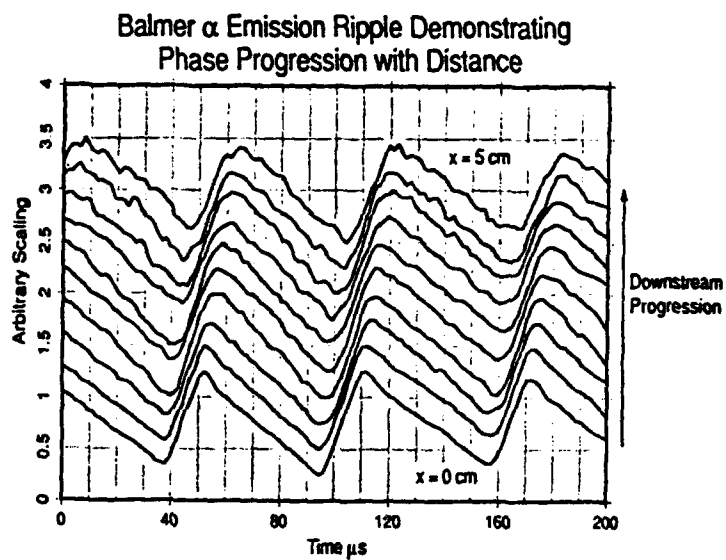## Experimental Setup

Figure 2
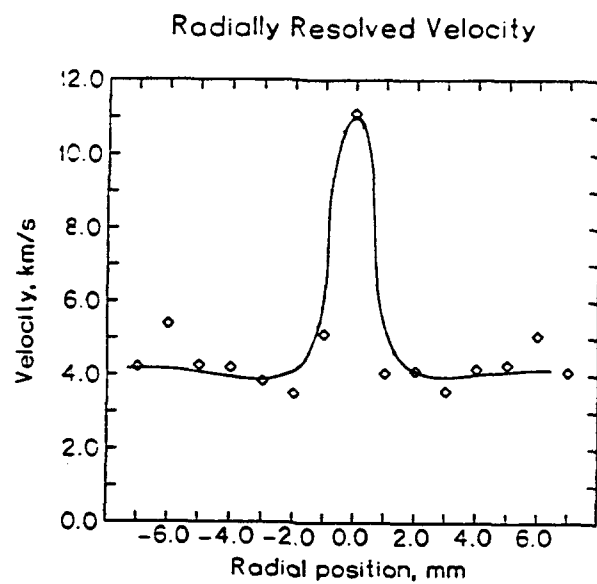

Figure 3

Figure 4

Radially Resolved Velocity

Figure 5
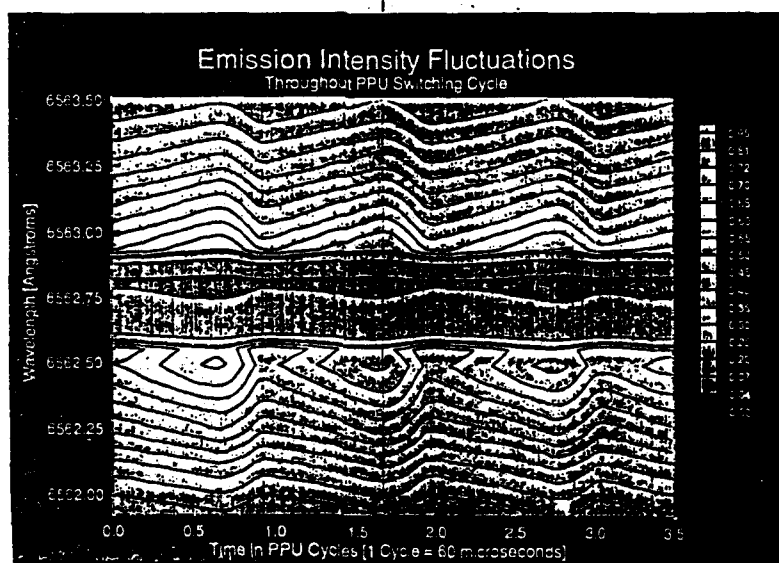

Figure 6

PERFORMANCE POTENTIAL OF PLASMA THRUSTERS
AFOSR Grant No. 91-0256

Principal Investigator: Manuel Martinez-Sanchez

Massachusetts Institute of Technology
77 Massachusetts Avenue
Bldg. 37-401
Cambridge, MA 02139

OVERVIEW

The object of this investigation has been the development of reliable performance prediction methods for arcjets and Hall thrusters. For arcjets, two very different models were developed: (a) A simplified two-stream quasi-one D model, and (b) A very detailed 2-D model with allowance for most physical effects of interest. Model (a) is capable of predicting Isp and η to within $\pm 10\%$ in most cases over a very broad parameter range and with a minimum of computational effort. Model (b) shows similar or better overall results, plus a wealth of information on flow and thermal details, including predictions of detailed heat flux distributions. For Hall (SPT) thrusters, we have developed a 1-D model which includes detailed ion production, loss and extraction physics, electron diffusion and ion-neutral interactions. The model yields accurate ($\pm 10\%$) prediction of Isp and efficiency, including the breakdown of losses through several measured mechanisms.

TECHNICAL DISCUSSION

The formulation of the simplified arcjet model was presented at last year's meeting. We have now completed this work with a series of computations in which the results were compared to data from four different arcjets running on a variety of fuels (H_2, N_2, N_2H_4), cooling modes and other operating conditions. The model cannot predict the anode voltage loss ΔV_A, the initial external gas temperature or the arc attachment point. These parameters need to be provided as inputs from previous experience or independent data, and they do affect the calculated results in significant ways. Other secondary inputs, such a cathode-side arc temperature and radius, and friction coefficients, have only minor influences. The calculation then proceeds from given geometry, type of gas, flow rate and current, and yields thruster voltage, thrust, etc. Physical trends, such as a slight decrease of voltage with current, an increased specific impulse with higher wall temperature, etc., are well reproduced. The predicted arc width matches well with visually determined widths, and the performance (particularly Isp) is usually better than $\pm 10\%$ accurate. Because of the uncertainty in ΔV_A and attachment point, voltage is somewhat less accurate, but comparisons of results to data yield guidelines for selecting these parameters, depending on cooling and flow rate. Full results will be presented at the Meeting, and also at the Joint Propulsion Conference (Monterrey, June 29th).

The detailed 2-D model formulation was also discussed last year, although refinements have been added since. The essential improvements over other models are in the allowance for thermal non equilibrium ($T_e \neq T_{gas}$) and ambipolar diffusion of charge pairs. These effects are found to be necessary for allowing prediction of the arc attachment point to the anode, something that was not possible so far. Essentially, the elevated T_e forms a conductive bridge from the arc core to the early part of the nozzle, and, together with non-equilibrium ionization sustained by charge pairs diffusing towards the cold wall, allows current to cross a region where Tgas is not high enough for sustaining conduction. This is illustrated in Figs. 1 and 2 (from a paper to be presented at the Joint Propulsion Conference:
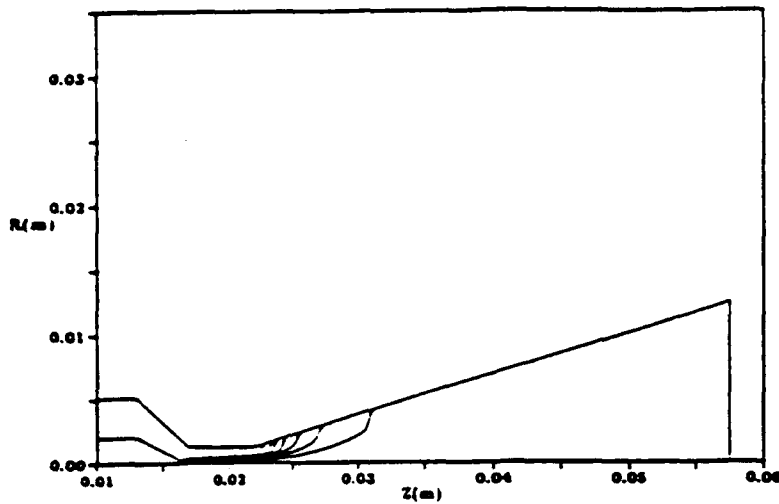
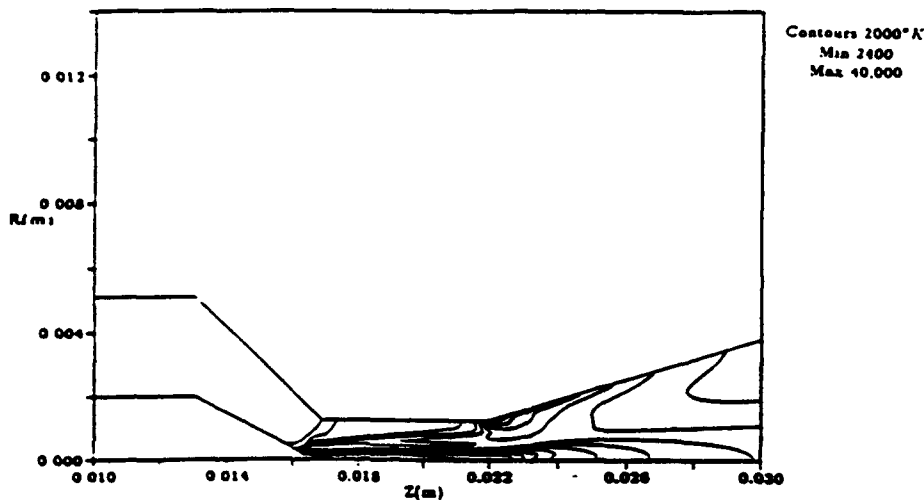Figure 1: Enclosed Current Contours for Baseline Case of $I = 100A$, $\dot{m} = 0.1g/s$

Figure 2: Electron Temperature Contours for Baseline Case of $I = 100A$, $\dot{m} = 0.1g/s$

The code can also calculate self consistently the block anode temperatures and the feed gas temperature in the cathode chamber. Results for thrust and voltage are very close to experimental data over a range of currents and flows. Only H_2 fuel is currently implemented, with N_2 and Argon being easy to add. Mixed N_2-H_2 fuels present additional challenge.

The Hall thruster model extends and refines a similar model by Komurasaki et al (1991). Ions are created through electron-neutral collisions and can be lost to walls through ambipolar diffusion. They are electrostatically accelerated from their site of birth, but can lose momentum through ion-neutral collisions along their path. Electrons Bohm diffuse across the radial magnetic field, and their energy balance is used to calculate T_e, which then controls ionization rate. Neutrals accelerate (but only moderately) by collision with ions. A secondary emission coefficient factor from the walls is included. The physically enclosed channel is extended into a neutralizing region, where electrons are injected and the potential settles to the outside level. Comparison of results to data of Komurasaki et al. indicate good agreement in terms of both, Isp and efficiency, η. Further, the separation of η into a utilization factor, a backstreaming efficiency and an ion velocity nonuniformity factor is correctly predicted. Figs. 3 and 4 show some results of one such comparison.

Figure 3: Heavy Particle Axial Velocities
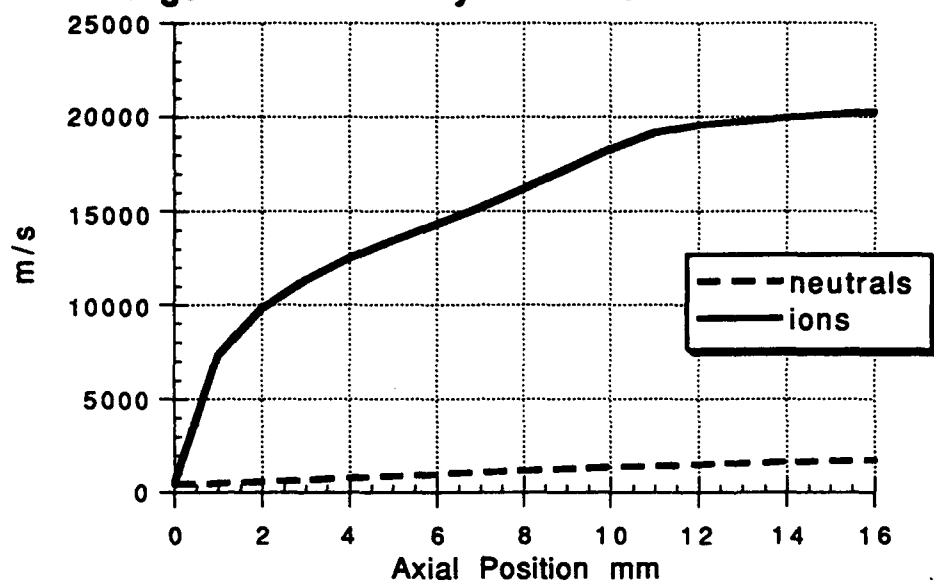
Figure 4: Ion Density
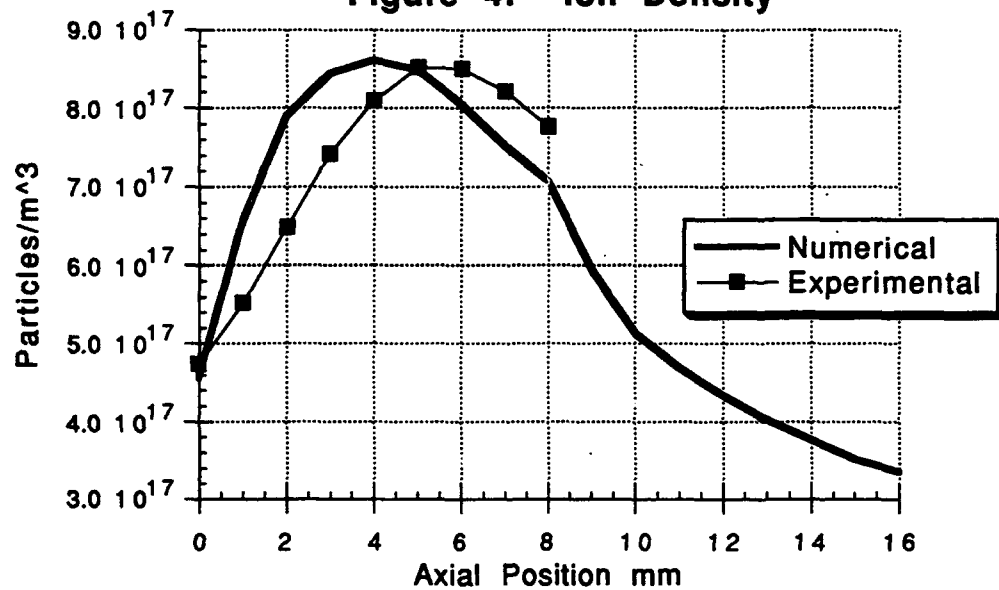
TWO TEMPERATURE MODELING
OF MULTICOMPONENT ARCJETS
WITH EXPERIMENTAL VALIDATION

Principle Investigators: Herman Krier and Rodney Burton

Department of Mech. & Ind. Engineering; Department of Aero. & Astro. Engineering
University of Illinois at Urbana-Champaign (UIUC)

SUMMARY/OVERVIEW:

Although the basic concepts for an arcjet plasma thruster are well known, i.e., the transfer of electrical energy to propellant thermal energy through the use of an electric discharge in a constrictor region with further conversion to kinetic energy in a supersonic nozzle, what is not known is the precise state of all species (electrons, ions, and neutrals). The conditions within the flowing gas(es) of the electric discharge vary from the arc core to the wall and to the anode surface in the divergent section, and it is highly unlikely that the usual assumption of local thermodynamic equilibrium (LTE) is proper at all operating conditions.

Therefore we are developing a generalized model for the arc plasma which will treat at least two temperatures (energies), for multicomponent gases with accurate sub-models for species diffusion, thermal and electric conduction, species production (and destruction) rates, and both local and non-local radiation. Information on distinct electron and heavy particle kinetic temperatures and non-equilibrium species densities will help explain the limits of arcjet performance. Clearly verification of key predicted flow states by meaningful experiments with instrumented arcjet thrusters will provide data to explain further the physics of the arcjet plasma in a thruster mode. Our group is actively pursuing both experimental and theoretical research on this propulsion topic.

TECHNICAL DISCUSSION:

Experiments

Several diagnostic techniques are employed to validate the non-equilibrium plasma model of a NASA Lewis 1 kW arcjet at the UIUC Electric Propulsion Laboratory. The arcjet is mounted in a 1.5 m³ chamber equipped with a 2500 CFM capacity vacuum system. Consistent with modeling capabilities, variable mixtures of nitrogen, hydrogen and trace gases are supplied to the thruster with three independent mass flow controllers. With this system, gas flow rates range from several $\mu gm/s$ to tens of mg/s. Chamber back pressures are maintained between 20 and 60 mTorr for the propellant flow rates supplied. A schematic of the arcjet may be seen in Figure 1.

The following techniques are selected to validate model assumptions and predictions. Emission spectroscopy is utilized to measure exit plane electron density n_e via Stark broadening of hydrogen emission lines and electron temperature T_e. In addition, this diagnostic technique will aid in determining which chemical species are present in the thruster, which will help define the species included in the model. Quadruple probe techniques are used to validate the spectroscopy measurements and, in some cases, add to the data that are available from the spectroscopic technique. Quadruple probes (see Figure 2) combine the use of the triple probe method for determination of n_e and species temperatures and the crossed probe technique for the determination of ion velocity (Burton, DelMedico and Andrews, 1993). The probe can be swept through any portion of the arcjet plume. However, initial measurements focus on the exit plane in order to compare experimental results with predictions at the boundary of the plasma model computational domain. Thus far, these techniques are being utilized on the NASA Lewis 1kW arcjet with simulated hydrazine as the propellant. Future efforts may include measurements of the plasma

properties in the nozzle and constrictor. Anode temperature measurements made with infra-red pyrometry and thermocouples will provide thermal boundary conditions for the model. In addition, a magnetic field of approximately 1 Tesla will be applied to the thruster to guide anode arc attachment and study the effects of axial and radial magnetic field components on thruster performance.

Modeling

The status of previous work done in the area of arcjet modeling is summarized in Table 1 and indicates the need for a more complete model. The UIUC arcjet model is a steady state two temperature single fluid model which includes flow swirl in a converging-diverging constrictor-nozzle geometry matching that of the experimental thruster. The model assumes plasma radiation to be optically thin and therefore lost to the surroundings. The model gas is a combination of nitrogen and hydrogen written generically as N_xH, with x varying from 0 to 1. All three components of the magnetic field are included to allow for use of an applied magnetic field for direct comparison with experiments. Input parameters to the model are the thruster geometry, mass flow rate, total applied current and the inlet swirl angle.

The solution algorithm for the arcjet model is based upon the two temperature laser sustained plasma model algorithm of Mertogul and Krier (1993). That work assumed the possibility of kinetic nonequilibrium between the electrons and heavy species in an axisymmetric domain. Therefore an energy equation for electron temperature T_e as well as an energy equation for gas temperature T_g are required. Since flow swirl is included, three momentum equations are necessary. The computation of species densities is based on an algorithm including the appropriate laws of mass action along with the multi-temperature plasma equation of state and the assumption of quasineutrality. A magnetic induction equation based on the generalized Ohm's law including the Hall term is used to compute the azimuthal component of the magnetic field. The axial and radial components of the magnetic field are dominated by the geometry of the applied external field.

The model equations are transformed from a body fitted grid in the physical plane to a computational plane for solution allowing flexibility of thruster geometry. The equations are solved iteratively using a finite volume method. The mass continuity and momentum equations are solved through the application of the PISO algorithm. A flowchart of the complete solution algorithm may be seen in Figure 3.

Future Issues

Issues that are yet to be resolved include heat conduction through the anode and modeling of the electrode sheath regions. Presently the anode surface temperature is modeled through a prescribed temperature distribution or as an adiabatic surface.
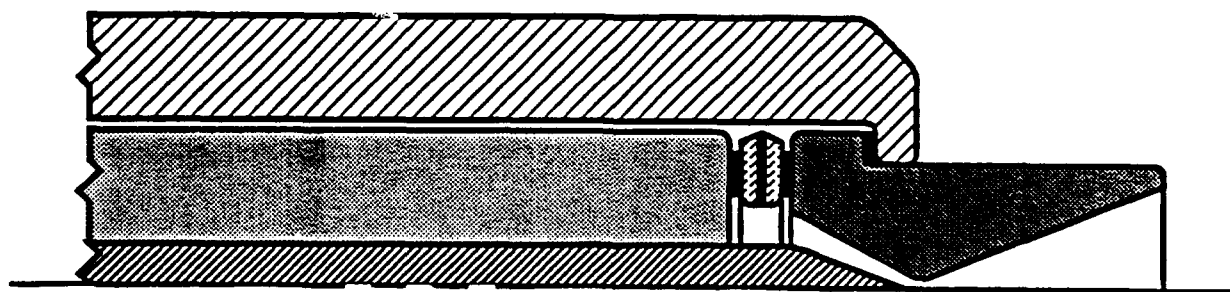

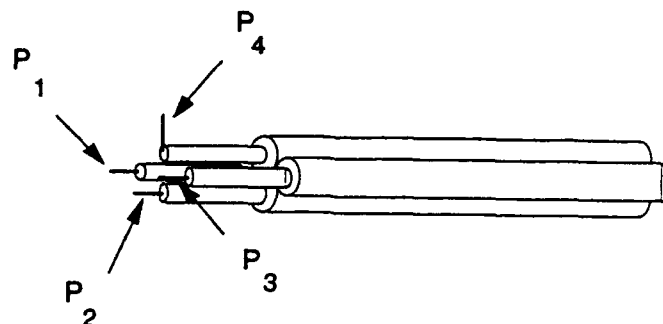Figure 1   Diagram of 1 kW NASA Lewis arcjet thruster

Figure 2 Diagram of quadruple probe used for velocity, temperature, and electron number density measurements in the arcjet plume.

Table 1 Summary of Arcjet Models

Arcjet Models

Author(s), year	Title, source	# Temperatures	# Fluids	Solutions?	Radiation?	Gas	Magnetic Field	Geometry	Quasineutrality	Chem. Kinetics	Algorithm, Comments
Le Toulouzan, et al. (1987)	Experimental and Theoretical Study of a Low-Pressure Arcjet AIAA Journal v25, n1, 1987.	1	1	Y	neglected	Helium	N/A	Free jet	N/A	N	Semi Implicit Method for Pressure Linked Equations
Tanaka and Kimura (1988)	Current Distribution and Plasma Acceleration in MPD Arcjets with Applied Magnetic Fields J.P.P., v4, n5, 1988.	1	1	Y	neglected	?	$B_{\theta,r,x}$	C/N	N/A	N	1 dimensional Galerkin Weighted Residuals Method σ constant
Butler, Kashiwa and King (1990)	Numerical Modeling of Arcjet Performance AIAA Paper 90-1474	1	1	Y	thin	N_2	$B_{\theta,r,x}$	C/N	Y	Y	Modified Los Alamos Magnetohydrodynamic Code
Rhodes and Keefer (1990)	Numerical Modeling of an Arcjet Thruster AIAA Paper 90-2614	1	1	Y	thick/thin	NH_3	B_θ only	C/N	Y	N	Pressure Implicit Split Operator Method
King and Butler (1990)	Modeling and Measurement of N2 Arcjet Performance AIAA Paper 90-2616	1	1	Y	thin	N_2	$B_{\theta,r,x}$	C/N	Y	Y	Modified Los Alamos Magnetohydrodynamic Code
Rhodes and Keefer (1991)	Modeling Arcjet Space Thrusters AIAA Paper 91-1994	1	1	Y	thick/thin	NH_3, H_2	B_θ only	C/N	Y	N	Pressure Implicit Split Operator Method
Butler and King (1992)	Single and Two Fluid Simulations of Arcjet Performance AIAA Paper 92-3104	2	2	N	?	H_2	?	C/N	Y	Y	Modified Los Alamos Magnetohydrodynamic Code
Moeller, et al. (1992)	Comparison of Experimental and Numerical Results for an Argon Arcjet AIAA Paper 92-3105	1	1	Y	thick/thin	Argon	B_θ only	C/N	Y	N	Pressure Implicit Split Operator Method
Flowe, et al. (1992)	Numerical Modeling of Fluid and Electromagnetic Phenomena in an Arcjet AIAA Paper 92-3106	1	1	Y	thin	?	B_θ only	C/N	Y	N	MacCormack's Flux Split Implicit
Cappelli (1992)	Modeling of the Near Electrode Regions of Arcjets 1 AIAA Paper 92-3109	1	2	Y	neglected	Argon	neglected	Stag. Pt.	Y	Y	Numerical Integration No details presented
Cappelli, et al. (1993)	A Comparison of Arcjet Plume Properties to Model Predictions AIAA Paper 93-0820	1	1	Y	thin	N_2	$B_{\theta,r,x}$	C/N	Y	Y	Modified Los Alamos Magnetohydrodynamic Code

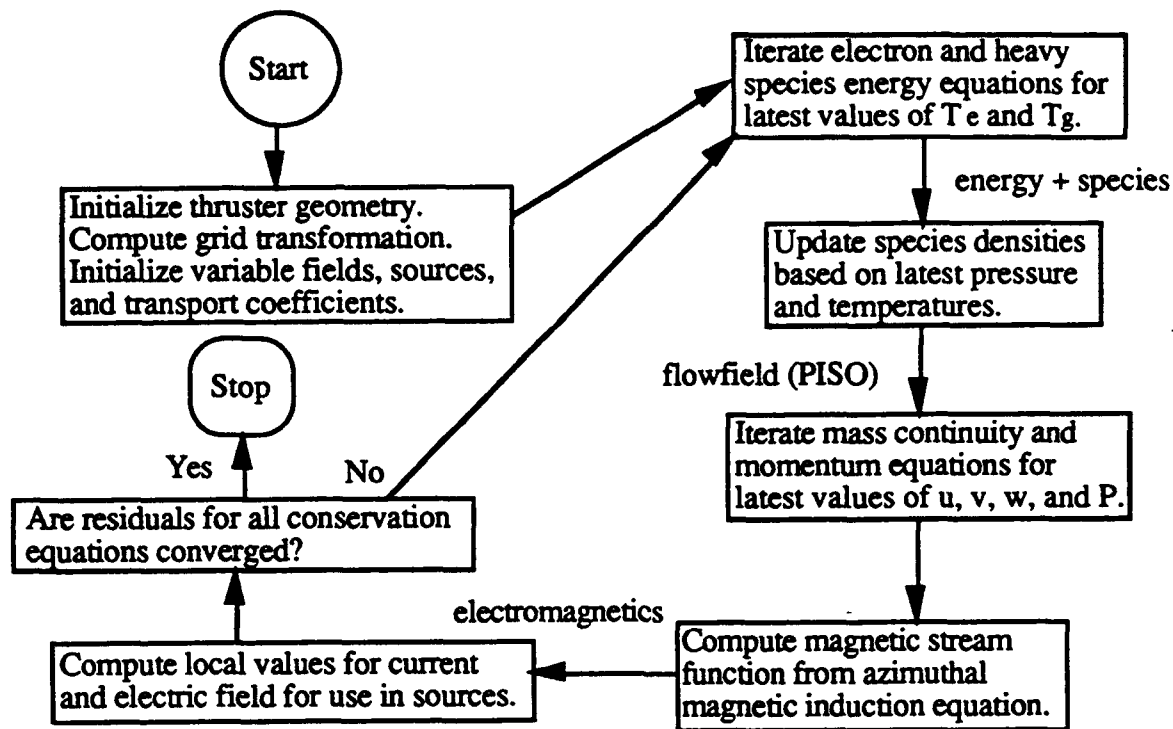Figure 3　　*Flowchart of UIUC arcjet model solution algorithm*

REFERENCES:

Burton, R.L., DelMedico, S.G. and Andrews, J.C. (1993). "Quadruple Probe Measurements of an MPD Thruster Plume," accepted for publication, *Journal of Propulsion and Power*, 1993.

Mertogul, A., and Krier, H. (1993). "Nonequilibrium modeling of Laser Sustained Hydrogen Plasmas," AIAA Paper No. 93-3224, to be presented at the 24th AIAA Plasmadynamics and Lasers Conference, Orlando Florida, July 6-9, 1993.

A HIGH THRUST DENSITY, C_{60} CLUSTER, ION THRUSTER*

V.J. Hruby**

BUSEK CO. INC.
19 Kearney Road
Needham, MA 02194

INTRODUCTION

Electrostatic thrusters require propellants with high atomic or molecular mass and low ionization potential. A Fullerene (C_{60}) has these and other important attributes which make it ideally suited to replace Xenon (Xe) as the preferred ion thruster propellant. Fullerenes are recently discovered carbon molecules that in their atomic arrangement resemble the geodesic dome designed by Buckminster Fuller. A C_{60} fullerene ion thruster has the potential to achieve unprecedented performance. It could deliver up 30 times larger thrust density than Xe fueled thruster while simultaneously reducing the relative losses by a factor up to 5.5. This makes it suitable for current ion thruster missions as well as future multimegawatt interplanetary missions where it would function as the main thruster.

PROGRAM OBJECTIVES

The overall program objective was to experimentally demonstrate the feasibility of the fullerene fueled ion thruster. To do so, several issues were addressed. Those that were deemed critical are listed below and the results of the their investigation are discussed in subsequent sections:

1. Vapor generation and control

2. Electrode poisoning (function of insulating layer on electrodes by C_{60} deposition) and discharge voltage

3. Fragmentation of C_{60} upon ionization

BUSEK

EXPERIMENTAL APPARATUS

The fullerene fueled ion thruster experiment is housed in our 4 ft. diameter space chamber as depicted in Fig. 1. The experimental apparatus is contained with the block labeled "oven" where the entire fullerene exposed flow train could be heated up to 800°C. This flow train consisting of fullerene vaporization chamber, flow orifice, discharge/ionization chamber plus the accelerating grids is shown in Fig. 2. The vaporization and the discharge chamber are made of quartz. Quartz was selected because of our initial material compatibility experiments performed in separate apparatus. The oven and its content are mounted on a water cooled balanced scale platform to measure the apparatus weight change rate as the fullerenes evaporate giving a real time fullerene mass flow.

The fullerenes, in the form of a loose powder composed of about 80% C_{60} and 20% C_{70} were loaded into the vaporization chamber prior to the experiment, typically up to 10 grams at a time. When heated the vapor flows through a choked orifice (initially made of stainless steel and subsequently of quartz) into the ionization/discharge chamber. Fullerene ionization is achieved by electron bombardment from a heated 2% thoriated tungsten filament cathode with 0.015 to 0.020" diameter. Slightly diverging axial magnetic field with a 30 Gauss peak value is provided by the heating coils of the oven. During the initial experiments gold plated quartz screen and accelerating grids were used. These proved inadequate and were later replaced by stainless steel and molybdenum grids. The ions or neutrals exiting the grid are condensed on either a collector/target plate or in a condenser tube as shown in Fig. 1. This prevents condensation of the fullerenes on the balanced beam scale and corresponding errors in the weight change measurements. A heated collector plate was used during some discharge and acceleration experiments to prevent fullerene condensation and formation of highly resistive fullerite layer that is likely to block ion beam current.

The typical electrical connections of the experiment are shown in Fig. 3. They were slightly modified in the course of the experiments as required. Selected data were recorded on a strip chart recorder. The balanced beam scale was locked in position and the load cell was disabled during ionization and acceleration experiments because the number of power connections restricted movement of the beam and made weight change determination impossible. The oven was controlled by a programmable controller that could maintain any temperature ramp or hold within a few degrees. All other power supplies were controlled manually.

RESULTS

The major results and accomplishments of this study are:

1) Fullerene compatibility with various metallic and dielectric materials was studied. Milligram quantities of fullerenes were evaporated from stainless steel (SST), molybdenum, alumina, boron nitride, aluminum nitride, and quartz substrates. Substrates and residue of fullerenes were analyzed. No reaction has been found with any materials although some substrates were visually stained. Quartz was selected for the experiments although
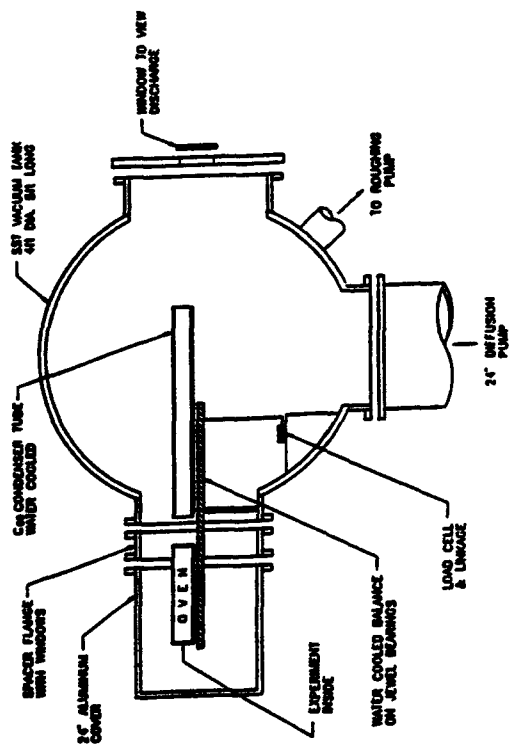
BUSEK

containment of fullerene solids and vapor in SST vessels should be no problem.

2) FTIR spectroscopy was not able to detect diffused molecular stream of fullerene vapor but it did detect fullerene condensation coating on IR windows and the presence of solvents coming off the fullerenes during heating.

3) Fullerene vapor generation and control was demonstrated. Samples of up to 9 grams were evaporated from a quartz vessel. Mass flow was measured real time by measuring weight loss rate of the sample and verified by pre and post test sample weight measurements. As much as 7% of the initial sample weight remained as process residue not vaporizable at 700°C.

4) A discharge in fullerene vapor was established using 2% thoriated tungsten filament in a quartz chamber. The lowest discharge voltage measured during the herein reported program was approximately 60 volts which increased to 190 volts in steps of 30 to 40 volts each time the discharge was re-initiated. Experiments performed after the completion of the present program demonstrated approximately 40 volt discharge with a maximum current of 3.4 Amps. However, upon restart the discharge again required 190 volts.

5) Graphite coating was found on the cathode as well as possible layer of thorium carbide. Possible explanation for the high 190 volts discharge voltage may be the continuously forming, insulating fullerite layer that must be converted to graphite to maintain discharge.

6) No anode coating was observed

7) No fullerene fragmentation occurred due to vaporization, ionization, and acceleration as determined from samples collected in various parts of the system with the exception of an area in the back of the cathode where the deposit was found to be graphitic.

8) An ion beam of approximately 20 mA was recorded. The beam ion energy cost was estimated to be 900 to 1000 eV/beam ion. Propellant utilization assuming single ionization was estimated to be 70%.
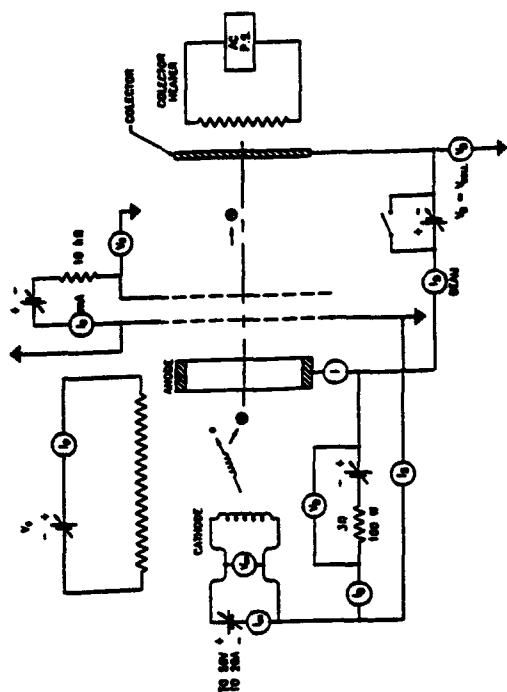
CONCLUSIONS

A high performance fullerene ion thruster appears feasible. Future work should focus on the development of suitable cathode.
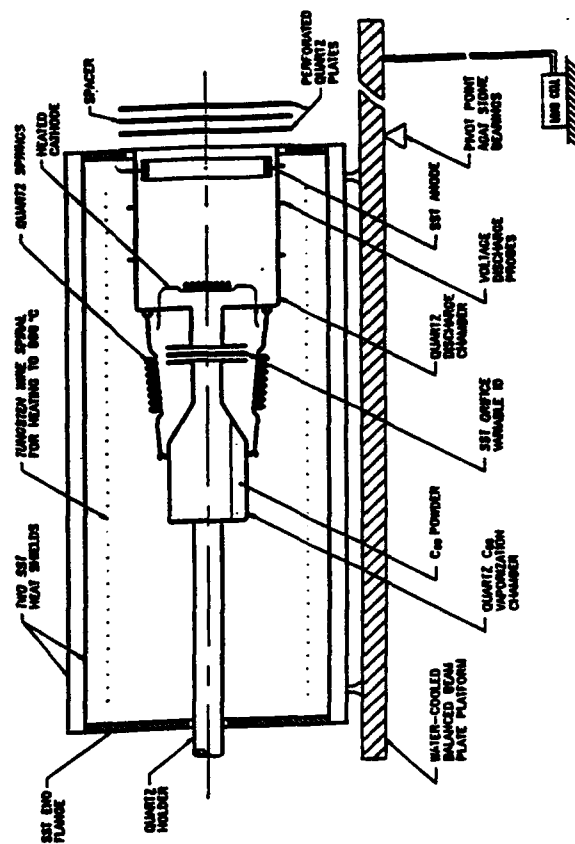
BUSEK

Fig. 3   Fullerene Ion Thruster Electrical Schematic

Fig. 1   Overall Vacuum System Schematic - C60 Fullerene Ion Th

Fig. 2   Fullerene Oven, Vaporization and Discharge Chamber Schematic

Electrostatic Ion Propulsion Using C_{60} Molecules

Research Program Overview

D. Goodwin, S. Leifer, S. Srivastava, S. Trajmar,

G. Jong, W. Saunders

California Institute of Technology

Pasadena, California

I. INTRODUCTION

Since the discovery of a method for producing macroscopic quantities of C_{60}, a flurry of activity has ensued in the scientific community. Efforts to characterize this new allotrope of carbon and to identify applications has resulted in exciting insights into its unusual properties.

Many potential applications for C_{60}, also known as buckminsterfullerene, have been suggested. Large research programs have emerged for the study of superconducting fullerene films doped with alkali metals. Crtical temperatures as high as 42 K have been observed for Rubidium and Thallium doped C_{60}. Recently, researchers at AT&T Bell Labs announced that intercalation of Ammonia in Sodium doped C_{60} raised the critical temperature for that superconductor 3-fold. While other potential application for C_{60} have been investigated including use as a precursor for diamond film growth and as a lubricant, one of the most promising potential applications is as a propellant for ion propulsion.

Ion propulsion for space flight has long sought a high mass propellant molecule or cluster that will not fragment when ionized. Use of a heavy propellant in an electric

thruster results in higher efficiency at moderate specific impulse and allows higher power handling capabilty and higher achievable thrusts. C_{60} posesses a remarkable resilience, high mass, and low ionization potential, indicating that it could make an excellent ion engine propellant.

Ion thrusters operating with C60 would be important for satellite station keeping, orbit transfer, or long duration robotic exploration missions. The higher efficiency at moderate specific impulse can result in either longer mission life or increased available payload.

II. PROGRAM OBJECTIVES AND ACCOMPLISHMENTS

The development of an efficient, reliable ion thruster which utilizes a fullerne propellant requires a knowledge of many of the properties of these new molecules. Our research program is focussed on determining some of these properties and their effect on the behavior of C_{60} in a plasma environment. The experiments we have undertaken fall into three distinct categories: time-of-flight mass spectrometry, electron energy loss spectroscopy, and discharge chamber experiments.

A. Time-Of-Flight Mass Spectrometry

We use a crossed electron beam - molecular beam geometry to create ions which are analyzed in a time-of-flight mass spectrometer. We are able to observe both the charge-to-mass spectrum, which displays relative intensities of all ions created in the collision region, and the variation in ion intensity as a function of electron energy. The latter yields the relative cross sections for ionization by electron impact. These curves can be normalized to obtain absolute cross sections. We have obtained ionization efficiency curves for the production of both C_{60}^{+} and C_{60}^{++} ions, in addition to an exhaustive study of the cracking patterns as a function of electron energy. These

data have enabled us to identify an appearance potential of $8.0 \pm .2$ eV for C_{60}^+. The appearance potential has been determined by photoionization to be 7.6 eV. Ionization by electron impact is typically a much less efficient process than by photoionization. Hence the ionization cross section curves will rise much less rapidly than the photoionization curves. This explains the slightly higher value for appearance potential obtained in our studies. Appearance potential for other fullerene ions are also being obtained. The cracking patterns indicate no appreciable fragmentation of C_{60} below 80 eV electron energy. This is certainly above the energy range of interest for ion engine operation.

Presently, we are attempting to obtain absolute cross sections for ionization by electron impact. We will then study negative fullerene ion formation.

B. Electron Energy Loss Studies

Another focus of this project has been to conduct studies of the electron energy loss spectra (EELS) of gas phase C_{60} and C_{70} in the energy range of interest for electric propulsion. These data can be used to determine total excitation cross section when integrated over all scattering angles. Preliminary results in this research have led to the identification of two large features at approximately 6 eV and 28 eV, which correspond well with the plasmon excitations observed for fullerenes in the solid state.

In addition, studies of the fluorescence spectrum of pure C_{60} were performed, showing two luminescence features induced by electron impact in the ultraviolet. The region explored spanned from 180 to 500 nm. Electron energies of 20, 30, and 103 eV were used.

C. Discharge Chamber Experiments

Because of cooperative support from NASA, we have been able to construct a

discharge chamber for initial demonstration of a C_{60} plasma discharge. This apparatus will later be modified for determination of energy cost for production of beam ions.

The discharge chamber has been operated for a maximum duration of 15 minutes with C_{60} at a discharge voltage of 50 V. Initial difficulties were encountered with severe erosion of the tungsten filament cathode. In addition, rapid heating of the mixed fullerene sample in the effusive cell with impurities present (toluene and water) resulted in decomposition of the fullerene at temperatures above 1073 K. Vacuum levels were in the 10^{-5} Torr range during this heating.

III. FULLERENE PRODUCTION, EXTRACTION, AND PURIFICATION

We have established a facility for the production of fullerene samples. However, prices for fullerene-containing soot have dropped substantially in the past year. For this reason, most of the mixed fullerene samples we use in our studies are presently obtained by Soxhlet extraction of purchased soot. Our facility will be used for the production of endohedral complexes of C_{60}.

IV. PUBLICATIONS

Dr. Sandor Trajmar has submitted a paper to Physics Review Letters on the fluorescence spectrum of C_{60} and C_{70} ions. He also is preparing two more papers on the EELS studies for publication. A paper on the electron impact ionization studies is being prepared by Dr. Santosh Srivastava for Rapid Communications in Mass Spectroscopy. An abstract submitted by Stephanie Leifer to the Fullerenes '93 conference has also been accepted.

FUNDAMENTALS OF ACOUSTIC INSTABILITIES IN LIQUID-PROPELLANT ROCKETS
(AFOSR Grant No. 91-0130)

Principal Investigator : F. A. Williams

Department of Applied Mechanics and Engineering Sciences
University of California at San Diego
La Jolla, CA 92093-0310

Summary/Overview

The objective of this research is to improve understanding of the mechanisms by which flow, mixing and combustion process are coupled to acoustic fields in liquid-propellant rocket motors. Particular attention has been focused on effects of spatial and temporal inhomogeneities of the acoustic media which are associated with turbulence and with two-phase flow. Appropriate statistical approaches are provided for different types of inhomogeneities. In addition, amplification mechanisms coupled with finite-rate chemical reactions are being analyzed by use of activation-energy asymptotics and other asymptotic methods.

Technical Discussion

The previous year's summary described the research on rotational inviscid flow in laterally burning solid-propellant rocket motors. This work has now been completed, and the final citation for the publication is available [1]. The present summary concerns ongoing studies of effects of spatial and temporal inhomogeneities on acoustic instabilities in liquid-propellant rocket motors and analyses of acoustic amplification mechanisms with finite-rate chemistry by asymptotic methods. These latter topics are discussed below.

Effects of Spatial and Temporal Inhomogeneities Produced by Turbulence and by Two-Phase Flow

Two distinct approaches to the theory of stochastic effects in the combustion instability of liquid-propellant rockets were developed. In one approach [2], dealing with effects of spatial inhomogeneities in the acoustic medium associated with two-phase flow and with turbulence, attention is restricted to the particular class of interaction in which the characteristic time scale of turbulence is asymptotically large compared with that of acoustic waves, so that the acoustic medium is considered to be a quasistationary random medium. In addition, it is assumed that the acoustic wavelength is long compared with any scale of inhomogeneity within the chamber, motivating a homogenized description, in which averages of state variable becomes appropriate. On the basis of these assumptions, the Navier-Stokes equations for two-phase flows were reduced to a nonhomogeneous stochastic Helmholtz equation [2]. Source terms of the equation were identified as arising mainly from phase change, from homogeneous chemical reaction, and from spatial variations of wave properties such as sound speed.

To handle the stochastic wave equation, the method of smooth perturbation was used and resulted in a Helmholtz equation for an equivalent deterministic acoustic medium. With use made of Green's integral theorem, the dispersion relation for transverse acoustic modes in cylindrical

chambers was obtained in the form $k^2 = k_0^2 + i k_0^2 a + k_0 \mathbf{b} \cdot \mathbf{k} + k_0^4 c$, where a, $\mathbf{b}$ and c are calculated from appropriate averages of source terms. In particular, the $k_0^4 c$ term corresponds to the stochastic contributions arising mainly from the spatial correlations of the sound speed with the pressure response function, and of the local Mach number with the velocity response function. Compared with the deterministic contributions to the linear growth (or damping) rate, the stochastic contributions are found to be of the order of $(\ell_t / R)^{3/2}$ where ℓ_t is the characteristic length scale for turbulence and R is the chamber diameter, thus implying that most of the stochastic contributions comes from the larger turbulent eddies. The stochastic effects are expected to be significant in the transition regime in which the deterministic growth rate is close enough to zero for transition between stable and unstable domains to occur reasonably frequently by stochastic variations of the growth rate.

In another approach [3], emphasizing influences of turbulent-induced noise, the behavior of high-frequency combustion instabilities influenced by random temporal variation of the linear growth rate in this same transition regime are addressed. The Rayleigh criterion was generalized to account for turbulence-related spatial variations of the combustion response. Special attention was given to the distinguished limit in which the acoustic oscillations are rapid compared with the turbulent fluctuations, which in turn are rapid compared with the linear growth rate of the instability. It was shown that nonlinear acoustics of the instabilities need to be considered to describe the influences of turbulence. When this nonlinearity involves supercritical bifurcation, the turbulence tends to decrease the most probable intensity of the instability. When it involves subcritical bifurcation, the turbulence can produce a bimodal probability density function for the intensity of the instability, with appreciable probabilities of high-amplitude and low-amplitude acoustic oscillations but small probabilities of oscillations of intermediate amplitudes. These phenomena can have a bearing on erratic pressure-amplitude bursts sometimes observed in liquid-propellant engines.

A key observation of this last study is that the turbulence influences on the acoustics appear as multiplicative rather than additive noise. Comparison of the turbulence coherence time with the characteristic time of the combustion instabilities identifies two distinct interaction classes, depending on whether the coherence time is or is not much smaller than the characteristic instability growth time. Larger instabilities are associated with the second of these classes while the transition behavior in the first class involves random walks of the stochastic linear growth rate, requiring a statistical description. In a white-noise approximation, the Stratonovich rather Ito interpretation of the stochastic integral must be employed, and the Markov property of the white-noise process then enables the evolution of the probability density of the pressure amplitude to be described by a Fokker-Planck equation, whose stationary solutions lead to the results shown in Figure 1, which demonstrates that the transition behavior depends on the character of the bifurcation. The bimodal behavior is seen in Figure 1 for subcritical bifurcation in the hysteresis region. The size of the bimodal transition region is proportional to the time integral of the autocorrelation function of the turbulence-induced fluctuations of the linear growth rate. This result provides a possible mechanism for resurging patterns of the pressure amplitude.

Amplification Mechanisms Coupled with Finite-Rate Chemistry

Many different processes can contribute to linear amplification of acoustic oscillations in liquid-propellant rockets, and asymptotic analyses of these processes can help in assessing combustion instabilities. It is the intent of the present investigation to analyze a number of these processes. One such process is the strained planar diffusion flame considered here [4]. Previous studies of diffusion-flame response postulated infinite chemical reaction rates (the Burke-Schumann approximation), while the present work is taking into account the influences of finite-rate chemistry, which can become important in environments having high turbulence intensities. The results demonstrate

that the high sensitivity of the chemical reaction rates to temperature fluctuations can underlie important amplification mechanisms. As an initial simplification, a one-step, irreversible Arrhenius-type chemical reaction rate is employed, and a gaseous counterflow diffusion flame is adopted to represent flamelets subjected to nonuniform flow fields caused by turbulent fluctuations. It is intended later to introduce rate-ratio asymptotics for hydrogen-oxygen systems.

The analysis was performed by activation-energy asymptotics. The resulting flame structure for a given value of the reaction-sheet location is described by two sets of equations, one for the transport of momentum, thermal energy and reactant, and the other for the corresponding overall reaction rate of the flame. The acoustic response of the flame, obtained from the linear analysis, is found to be determined by two mechanisms, namely, oscillations of the reaction sheet induced by acoustic-produced fluctuations of the reaction rate, and oscillations of the field variables produced by the transport-zone response. Results for the rate of amplification associated with the finite reaction time are shown in Figures 2 and 3 in terms of the nondimensional amplitudes for fluctuations of the heat release rates, $\tilde{h} = \tilde{h}_a + \tilde{h}_r$, where the subscripts a and r denote the contributions from the acoustic field and from the oscillations of the reaction sheet, respectively. Amplification occurs if the real part of $\tilde{h}$ is positive. It is shown in Figure 2 that, throughout most of the range of Damköhler number, amplification associated with the oscillations of the reaction sheet is dominant compared with that associated directly with the acoustic field. Figure 3 shows that the total amplification for various values of the nondimensional frequency steadily increases as the extinction Damköhler number is approached, at which point the sensitivity of the reaction rate to the finite reaction time is greatest. An implication of these results is that analyses for the acoustic response of flames that do not consider finite reaction rates could significantly underestimate the amplification rate. Future works will apply similar methods to different types of flamelets which may be more realistic for rocket-engine combustion, such as single-droplet combustion, with and without forced convection and supercriticality.

References

[1] G. Balakrishnan, A. Liñán and F. A. Williams, Rotational Inviscid Flow in Laterally Burning Solid-Propellant Rocket Motors, *Journal of Propulsion and Power*, 8, pp. 1167-1176 (1992).

[2] J. S. Kim, A Formulation for Transverse Acoustic Instability in Liquid-Propellant Rocket Motors, CECR Report No. 92-01, University of California at San Diego, La Jolla, CA, 1992, also to appear in *Proceedings of the First International Symposium on Liquid Rocket Engine Combustion Instability*.

[3] P. Clavin, J. S. Kim and F. A. Williams, Turbulence-Induced Noise Effects on High-Frequency Combustion Instabilities, CECR Report No. 93-01, University of California at San Diego, La Jolla, CA, 1993, also submitted to *Combustion Science and Technology*, 1993.

[4] J. S. Kim and F. A. Williams, Contribution of Strained Diffusion Flames to Acoustic Pressure Response, CECR Report No. 93-02, University of California at San Diego, La Jolla, CA, 1993, also to be submitted to *Combustion and Flame*.
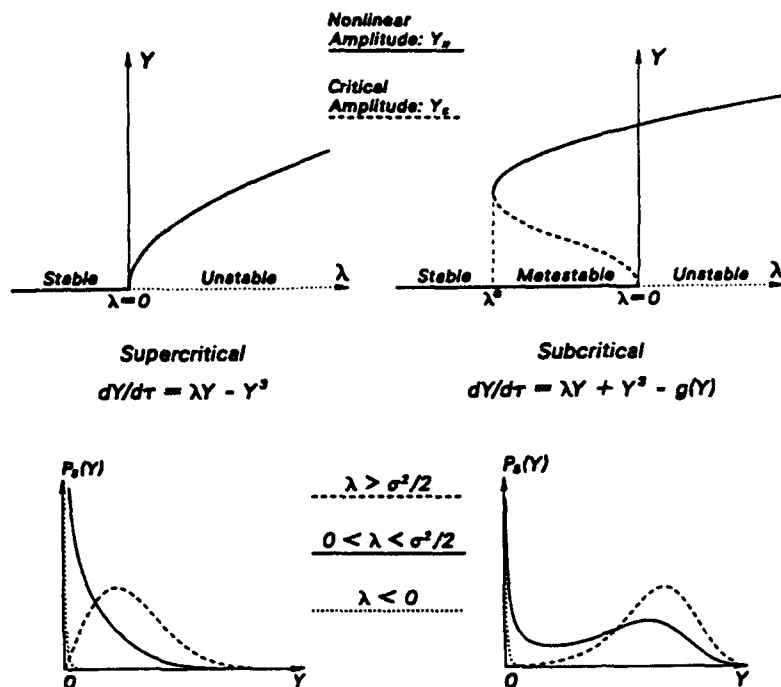
Figure 1. Supercritical and subcritical bifurcations, illustrating the resulting unimodal and bimodal probability-density functions for the pressure amplitude
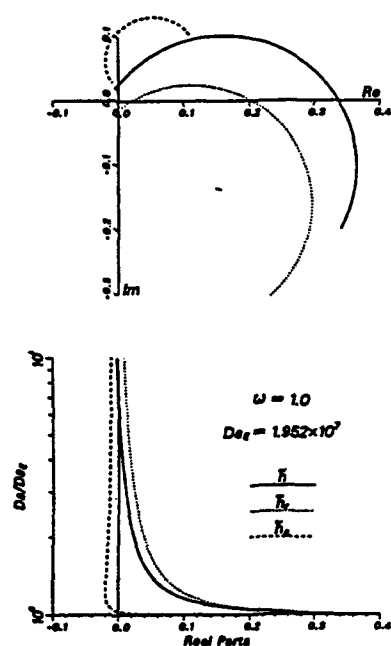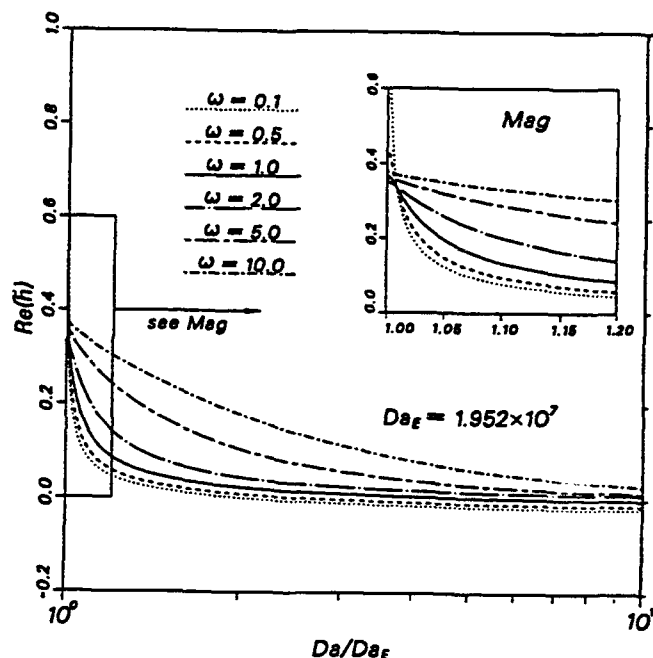

Figure 2. Variations of the nondimensional amplitudes for fluctuations of the total heat-release rate, $\tilde{h}$, of the heat-release rate induced by the reaction-sheet oscillations, $\tilde{h}_r$, and of the heat-release rate induced by the acoustic fluctuations, $\tilde{h}_a$, with the Damköhler number for the nondimensional acoustic frequency $\omega = 1$

Figure 3. Variations of the nondimensional amplitude for fluctuations of the total heat-release rate, $\tilde{h}$, with the Damköhler number for the nondimensional acoustic frequencies $\omega = 0.1, 0.5, 1, 2, 5, 10$

MODELING LIQUID JET ATOMIZATION PROCESSES

AFOSR Contract No. F49620-92-J-03990

Stephen D. Heister

School of Aeronautics and Astronautics
Purdue University
W. Lafayette, IN 47907

Summary/Overview

The atomization of liquid jets is a fundamental problem of particular interest in determining the performance and combustion stability of liquid rocket engines. This research effort is focused on a new analytic treatment of this free surface flow utilizing Boundary Element Methods (BEMs). This analytic approach is attractive for problems of this nature due to its inherent efficiency (as compared to more traditional CFD methods) and its high accuracy in determining the time-dependent evolution of the free surface for a reasonable computational expense.

While initial efforts have been focused on development of an inviscid liquid model, future efforts will include the effects of liquid and/or gas viscosity to incorporate the necessary physics to investigate the atomization regime. Current inviscid models are capable of addressing jet behavior in the presence of arbitrary time-dependent supply pressure oscillations and reveal significant nonlinear corrections to the linear theory of Rayleigh[1]. Ultimately, we hope to include the effects of injector geometry on the atomization process and characterize the initial droplet size distribution created by the atomizing jet.

Technical Discussion

Background and Model Description

Our understanding of the complex combustion phenomena present in liquid rocket engines begins with the fundamental process of fuel and oxidizer jet atomization. Since the atomization process can be greatly effected by acoustic disturbances[2], it appears as a primary focus[3] in studies involving combustion stability. For this reason, both analytic and experimental research are necessary to increase our understanding of the complex interactions between the droplet field formed by the jet and the combustion process.

Our approach centers on the use of Boundary Element Methods (BEMs) which can be used to accurately describe the time-dependent evolution of waves forming on the surfaces of the jet. We believe that BEMs are superior to more traditional Computational Fluid Dynamic (CFD) methods since the BEM formulation requires a discretization of only the external surface of the jet rather than the entire liquid domain. This distinction is important

since a typical BEM can model a surface much more accurately than a CFD approach for a fixed amount of computational power.

Boundary element methods (a.k.a. boundary integral methods), are developed using Green's function solutions to the free space problem. For a potential flow, the velocity potential ϕ is governed by Laplace's equation which has the following integral representation:

$$2 \alpha \phi(\vec{r_i}) + \int_\Gamma [\phi \frac{\partial G}{\partial n} - qG] d\Gamma = 0 \tag{1}$$

where $\phi(\vec{r_i})$ is the value of the potential at a point $\vec{r_i}$, Γ denotes the boundary of the domain, and G is the Green's function corresponding to the governing equation as shown in Fig. 1. Since Eq. 1 involves an integration only around the boundary, we need not discretize the entire domain. It is presumed that either ϕ or $q = \partial\phi/\partial n$ is specified at each node on the boundary and a linear variation in both ϕ and q is assumed along a given segment. Four point Gaussian integration is employed to evaluate the complex integrals associated with the axisymmetric Green's functions utilized in Eq. 1.

Finally, the quantity α in Eq. 1 results from singularities introduced as the integration passes over the boundary point, $\vec{r_i}$. For an axisymmetric formulation, α is related to the angle between successive nodes on the boundary. For example, nodes lying along a straight line will have $\alpha = \pi$, while a node on a corner would have $\alpha = \pi/2$.

Points on the free surface are moved vertically using a Lagrangian treatment by implementing the kinematic condition:

$$\frac{\partial r}{dt} = \frac{\partial \phi}{\partial r} - \frac{\partial \phi}{\partial z} tan \ \beta \tag{2}$$

where β represents the slope of the wave with respect to the horizontal (z) direction. Finally, the values of the potential on the free surface are updated using the unsteady Bernoulli equation:

$$\frac{\partial \phi}{\partial t} = \frac{1}{2}[(\frac{\partial \phi}{\partial r})^2 - (\frac{\partial \phi}{\partial z})^2 + 2\frac{\partial \phi}{\partial r}\frac{\partial \phi}{\partial z} tan \ \beta - \kappa] \tag{3}$$

where κ represents the local surface curvature. Surface slope and curvature are obtained using Lagrangian interpolation polynomials, while the time-dependent relations in Eqs. 2 and 3 are integrated using the Adams-Bashforth-Moulton procedure as described in Longuet-Higgins and Cokelet[4]. Finally, we have assumed that linear distances are normalized by the jet radius, a, and that velocities are normalized by the quantity $\sqrt{2\sigma/(\rho a)}$ where σ and ρ are fluid surface tension and density, respectively.

Results

Initial validation efforts were aimed at generating solutions to the nonlinear Rayleigh problem first solved by Mansour and Lundgren[5]. In this problem, the jet is assumed to be infinite in extent and subject to an initial small periodic disturbance as highlighted in Fig. 2. We presume that inclusion of three waves is adequate for the simulation of an infinite jet and implement periodic conditions on the outer two waves.

Results from the model indicate a very accurate predictions of Rayleigh's stability curve as indicated in Fig. 3. In this figure, k represents the dimensionless wave number, while the

growth rate (w) is essentially a reflection of the vertical velocity of the jet. Nonlinear aspects of the model were checked against results of Mansour and Lundgren for the case $k = 0.3$ as shown in Fig. 4 at two distinct times in the process. Good agreement is obtained with our model even though we used about 1/3 as many points due to the linear boundary elements employed in the formulation.

Having validated the model, we next turned our attention to the semi-infinite jet. In this case, the presence of the orifice (and its influence on the nonlinear evolution of unstable surface waves) is included. Much effort was expended in creating a non-reflecting outflow boundary condition for the finite length of the computational domain. The resulting formulation is similar to that employed by Fasel[6] in his numerical analysis of boundary layer instabilities. The domain for initial calculations presumed an initially unperturbed jet which was disturbed by introducing a fluctuating velocity at the orifice of the form $v = 1 + \epsilon \sin(kt)$ where ϵ determines the size of the perturbation. Figure 5 indicates the evolution of the surface with time in the case where $k = 0.7$ and $\epsilon = 0.01$.

₁uture Efforts

The calculation in Fig. 5 indicates the initial response of the jet to an imposed oscillation. In order to handle the "quasi-steady" response, we must be able to continue the calculation beyond the initial break of the jet. Another approach to be investigated begins with computational nodes at the orifice exit and allows the size of the domain to increase with time by permitting the points to move with the local fluid velocity. Finally, upon completion of the inviscid formulation, a viscous model will be developed. We anticipate that the free surface treatment developed for the inviscid model will be applicable to the viscous model as well; therefore we are justified in working out these problems on the simpler inviscid case.

References

1. Rayleigh, Lord, "On the Instability of Jets," Proc. of London Mathematical Society, Vol. 10, pp. 4-13, 1878.

2. Reba, I., and Brosilow, C., "Combustion Instability Liquid Stream and Droplet Behavior. Part III: The Response of Liquid Jets to Large Amplitude Sonic Oscillations," Polytechnic Institute of Brooklyn, WADC Technical Report No. 59-720, Part III, 1960.

3. Jensen, R., (Ed.), "JANNAF Subcommittee on Combustion Stability - Annual Report," 27th JANNAF Combustion Meeting, Cheyenne, Wyoming, 1990.

4. Longuet-Higgins, M. S., and Cokelet, E. D., "The deformation of steep surface waves on water. I. A numerical method of computation," *Proc. R. Soc. Lond. A*, **350**, pp. 1-26, 1976.

5. Mansour, N. N., and Lundgren, T. S., "Satellite Formation in Capillary Jet Breakup", *Physics of Fluids*, V2, pp 1141-1144, 1990.

6. Fasel, H., "Investigation of the Stability of Boundary Layers by a Finite-Difference Model of the Navier-Stokes Equations", *J. Fluid Mechanics*, V78, No. 2, pp 355-383, 1976.
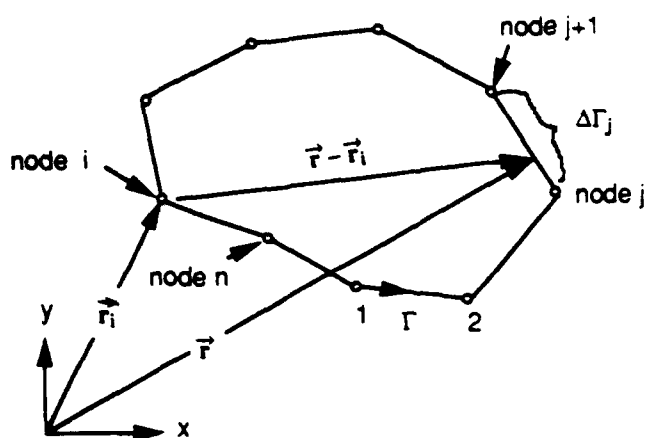
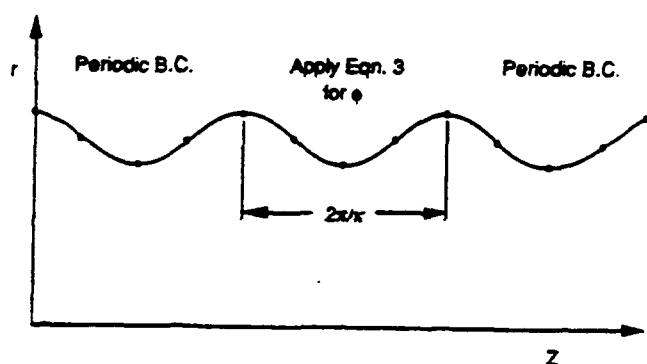Figure 1: Geometry and Nomenclature for BEM Formulation

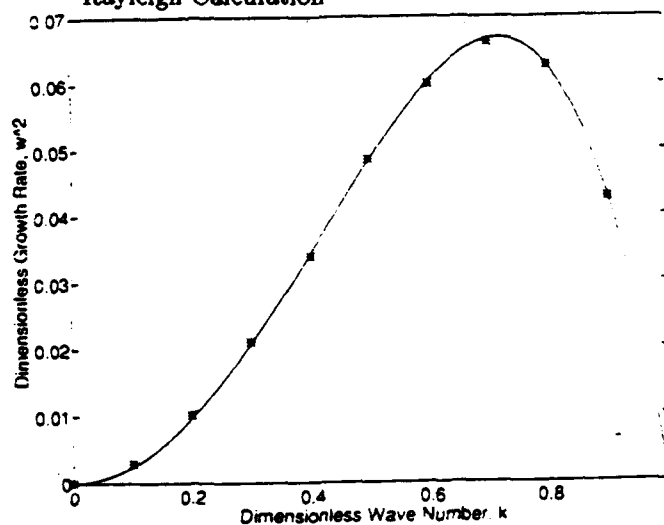Figure 2: Geometry and Formulation of Nonlinear Rayleigh Calculation

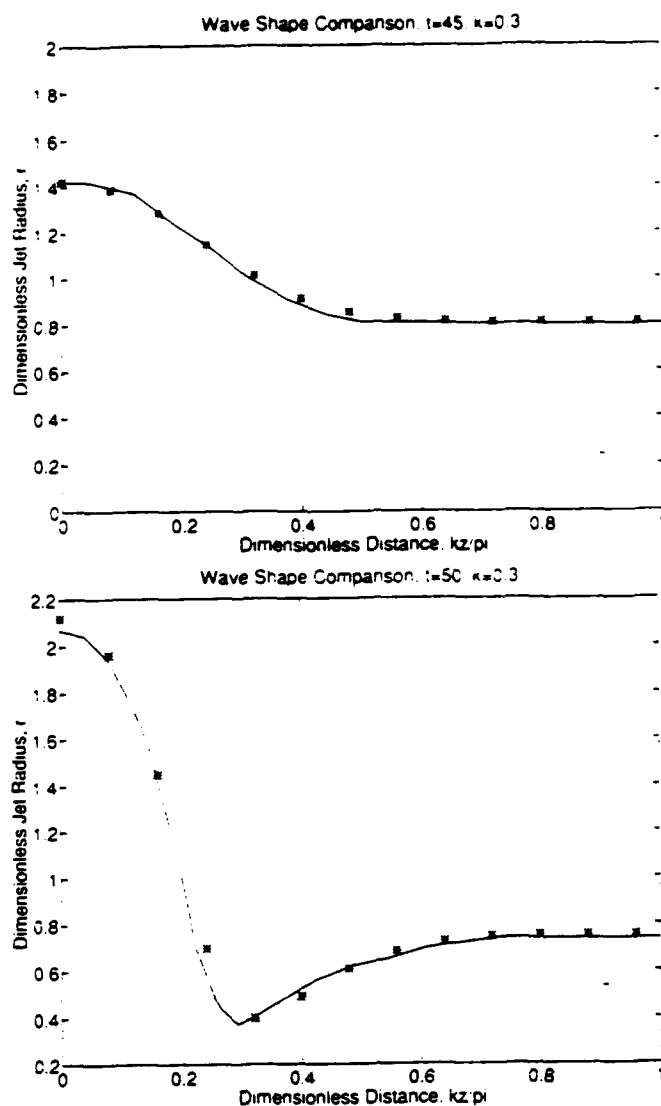Figure 3: Jet Stability Curve Comparison. — Rayleigh, * - BEM Calculation

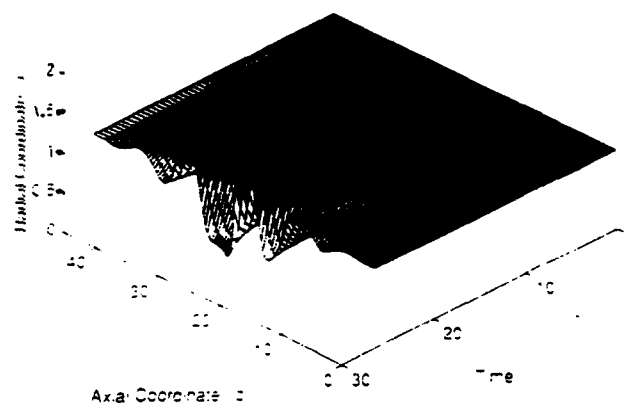Figure 4: Jet Profile Comparison, k=0.3. —- Mansour and Lundgren, * - BEM Calculation

Figure 5: Evolution of a Jet Exposed to Sinusoidal Inflow Velocity Perturbation. k=0.7. $\epsilon = 0.01$

- 142 -

ACOUSTIC WAVES IN COMPLICATED GEOMETRIES AND THEIR INTERACTIONS WITH LIQUID-PROPELLANT DROPLET COMBUSTION

(AFOSR Contract No. 91-0171)

Vigor Yang
Department of Mechanical Engineering and
Propulsion Research Engineering Center
The Pennsylvania State University
University Park, PA 16802

SUMMARY/OVERVIEW

A focused theoretical program is being conducted to investigate acoustic wave characteristics in liquid-propellant rocket engines with injector-face baffles. The work primarily addresses the combustion stability behavior of a complicated geometry and the damping mechanism of baffles -- how does the baffle work in various environments; and what are the physical processes responsible for suppressing unsteady motions in a baffled combustor? In addition, the dynamic responses of liquid-propellant droplet combustion to ambient flow oscillations in the baffle region are examined in detail.

TECHNICAL DISCUSSION

1. Relevance

Injector-face baffles provide significant stabilizing effects on pressure oscillations liquid-propellant rocket engines, and have been widely used since 1954. Three mechanisms have been suggested with regard to the suppression of transverse modes of instabilities. These are (1) modification of acoustic properties in combustion chambers, (2) restriction of unsteady motions between baffle blades, thus protecting the sensitive mechanisms for instabilities, and (3) damping of oscillations by vortex shedding, flow separation, and viscous dissipation near baffle tips. Because of the complex nature of the flowfield in the baffle region, the effects of baffles on wave motions have never been understood quantitatively. The most important and least understood aspect of baffle design is how to ensure that baffles will eliminate instability. At present, no well-defined criteria exist for selection of baffle configurations that will lead to stable operation of an engine. Most designs in use today are based on experience with similar combustor configurations, propellant combinations, and operating conditions, thereby making development of a new system a costly trial-and-error process. For example, the development of F-1 engines for the Saturn-V launch vehicles required 15 baffle design iterations and 3,200 tests before a stable configuration was obtained.

2. Research Objectives

The primary purpose of this research is to develop a comprehensive theoretical analysis within which multi-dimensional acoustic waves in a baffled combustor and their mutual coupling with liquid-propellant combustion can be treated properly. The work involves the following two tasks:

1. investigation of linear and nonlinear acoustic wave characteristics in baffled

combustion chambers.

2. study of acoustic wave-induced vorticity and its interaction with mean flow.

3. Acoustic Waves in Baffled Combustors

Because of the geometrical discontinuities associated with baffle blades, the unsteady motions in the baffle compartments and the main chamber are best treated separately and then linked together at the interface, as shown in Fig. 1. The acoustic field in each region can be formulated using the general analysis constructed by the principal investigator. Briefly stated, a wave equation governing the flow oscillations is derived from the conservation equations for a two-phase mixture, with expansion of the dependent variables in two small parameters measuring the Mach number of the mean flow and the amplitude of the unsteady motion. This equation can be written in the form

$$\frac{1}{\overline{a}^2}\frac{\partial^2 p'}{\partial t^2} - \nabla^2 p' = -h$$

The function h contains all influences of droplet vaporization and combustion, mean flow/acoustics coupling, and two-phase interaction. It can be correctly modeled as a distribution of time-varying mass, momentum, and energy perturbations to the acoustic field. The next step lies in expressing the unsteady motions as a synthesis of modes described by the eigenfunctions of the wave equation. Finally, with appropriate matching of the acoustic pressure and velocity fields at the interface between the baffle compartments and the main chamber, a transcendental equation is obtained for the complex wave number characterizing the oscillatory flow in the entire chamber. The major advantage of this approach is the provision of an analytical framework for studying mechanisms proposed as the stabilizing effects of baffles.

Calculations have been conducted to study the oscillatory flowfield in both two-dimensional and three-dimensional baffled combustion chambers. Figure 2 shows the acoustic pressure contours (top) and velocity vectors (bottom) together for the first transverse mode in a two-baffle chamber, illustrating two main effects of baffles. One is longitudinalization of the transverse wave and subsequent concentration of fluctuation amplitude near the injector face, as shown in the upper section. The other is severe restriction of fluctuating velocities within the baffle compartments, as depicted in the lower part. Since both of these effects are felt near the injector, where pressure- and/or velocity- sensitive processes are concentrated, they can have a substantial impact on overall stability. If pressure-sensitive processes dominate, the longitudinalization may have a destabilizing influence; however, if the instability is sensitive to velocity fluctuations, the baffles can act to stabilize the system. It should be noted that another effect of baffles is the depression of acoustic frequency with increasing baffle length.

Two types of nonlinear combustion instability commonly observed in liquid rocket engines were also studied. First, limit cycle oscillations were considered, in which a small initial disturbance grows and finally reaches a steady-state oscillation. Second, pulse-triggered instabilities were investigated, as shown in Fig. 3. If an initial disturbance is less than a certain threshold value, it decays and damps out. However, if the initial disturbance exceeds the threshold value, it grows and exercises steady-state fluctuations, similar to the case of the standard dynamic stability rating ("bomb") test. The overall physical nonlinear process

can be explained by an energy cascade among acoustic modes. In this nonlinear analysis, an approach is developed to predict these two types of combustion instabilities. It is the first of its kind in analyzing nonlinear unsteady motions in baffled rocket engines.

4. Acoustic Wave-Induced Vorticity

The second part of the present research is to examine the vortical motion induced by the interaction of the acoustic wave with the mean flow near the baffle blade. Although the acoustic mode shapes in baffled chambers are accurately described by inviscid equations, viscosity does have an important effect. The acoustic motions along the baffle blades can interact with the viscous boundary layer by enforcing the no-slip condition. The ensuing vortex shedding from the baffle tips may appreciably modify the mean flowfield and combustion distribution in the main chamber. Furthermore, mechanical energy can be transferred from the acoustic waves to vortical motions, and eventually be either convected out of the chamber with the mean flow or to a much lesser extent dissipated by viscous friction. This cascade of mechanical energy transfer from the acoustic to vortical field, together with modification of combustion distribution, represents a major mechanism for stabilizing unsteady motions in baffled chambers.

The basis of the analysis is the Lagrangian vortex dynamics method. This approach treats the vorticity field as an assembly of n vortex elements, and solves for the entire flowfield under mutual interaction of all the elements. The domain of computation ranges from the trailing edge of the baffle blade to the exit of the combustion chamber. At each time step, a vortex element is released from the baffle tip and rolls up into a large structure. The associated vorticity due to the acoustic motion can be found by integrating the instantaneous acoustic velocity surrounding the element at the baffle tip, where the contour integral is performed over a path length set by the mean flow and the time step duration. The subsequent motion of the element is tracked with a simple first order accurate integration in accordance with the Kelvin-Helmholtz theory. Figure 4 shows the vortical flow velocity component for a chamber with a baffle blade length of 0.1 times the chamber height. The chamber size and parameters are similar to the F-1 engine.
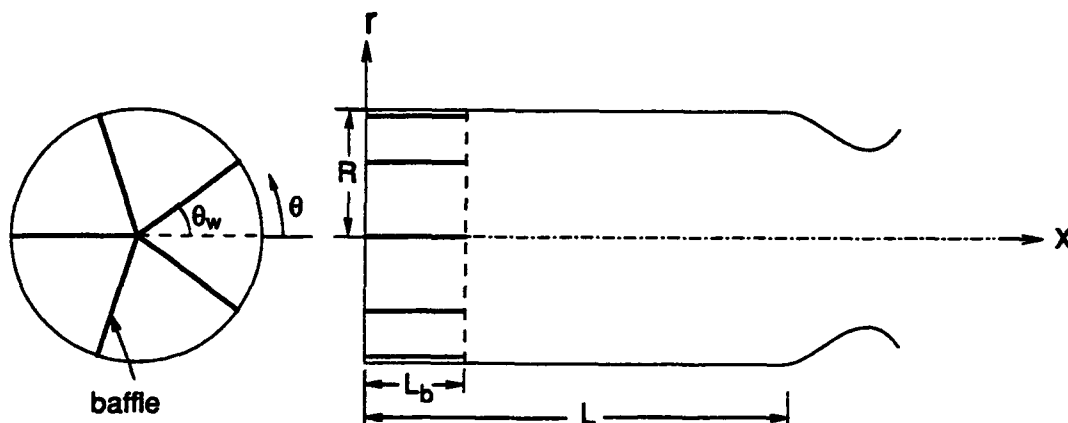

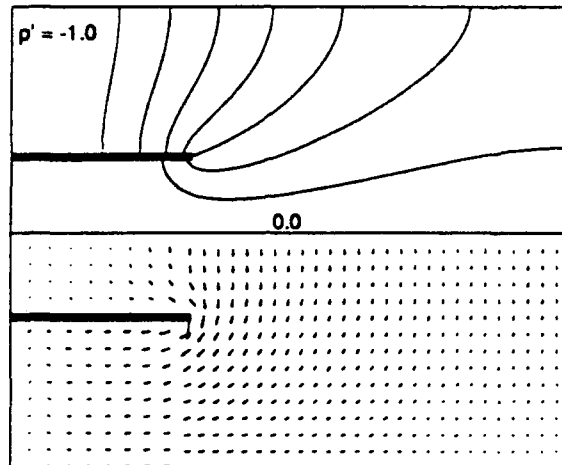Figure 1. Schematic of a Baffled Combustor.

Figure 2. Acoustic Pressure and Velocity Fields in a
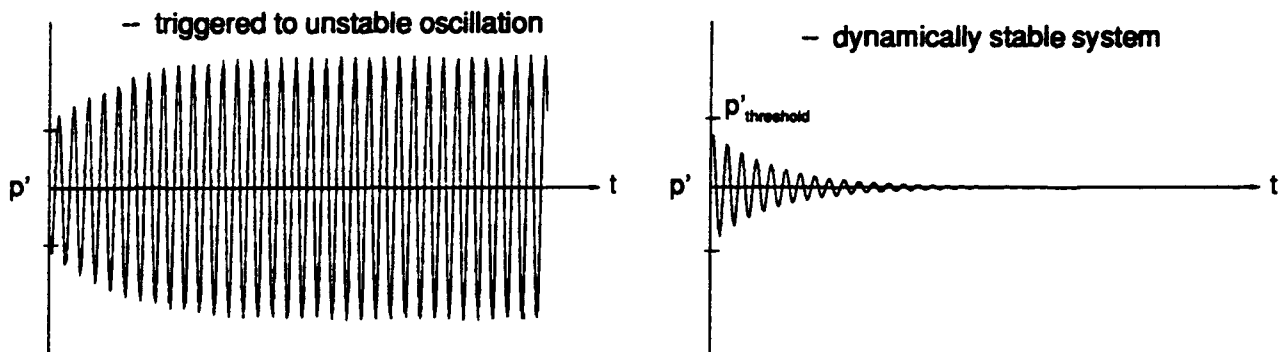Two-Baffle Combustion Chamber.

Figure 3. Time Histories of Pressure Oscillations Showing
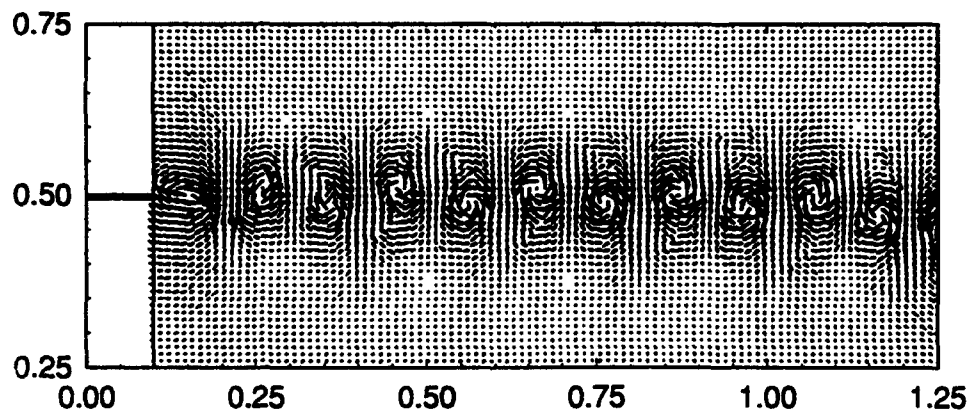Pulse-Triggered Combustion Instability.

Figure 4. Acoustic-Wave Induced Vortical Velocity Field
in a Baffled Combustion Chamber.

SUPERCRITICAL DROPLET BEHAVIOR

AFOSR Task 2308AP

Principle Investigator: D.G. Talley

Aerophysics Branch, Fundamental Technologies Division
Propulsion Directorate
OLAC Phillips Laboratory
Edwards AFB, CA 93524-7660

Summary/Overview:

This research addresses the transcritical behavior of vaporizing and burning droplets, by ·ch is meant the behavior of droplets injected at supercritical pressures but initially at a subcritical temperature, which then undergo a transition to a supercritical state as they are heated in a hot environment. An experimental approach is taken using a free droplet technique, whereby monodisperse droplets are studied as they fall freely in a pressure chamber. In addition to steady state environments, transcritical behavior will also be studied under the influence of acoustic waves.

Authors: D.G. Talley and J.C. Pan

Technical Discussion:

Supercritical combustion processes are expected to play an increasingly greater role in future Air Force air breathing and rocket propulsion systems. In high pressure liquid rockets, the liquid oxygen is subjected to supercritical pressures but reaches a supercritical temperature only after injection and subsequent heating in the combustion chamber—the so-called transcritical process.

Transcritical droplet vaporization/combustion is much less well understood than the equivalent subcritical processes. Gas/liquid density ratios are near unity, so the quasi steady gas phase assumption commonly employed in subcritical studies is no longer valid. The equilibrium "wet bulb" condition may also not exist. Thus transcritical droplet vaporization/combustion is a fully unsteady phenomenon. The computation of properties becomes significantly more complicated in that properties such as diffusion coefficients become functions of pressure as well as temperature, and the solubility of the gas phase in the liquid phase increases significantly. The latter effect can mean that the effective critical pressure of the soluble mixture can be several times the critical pressure of the pure phase. Other property anomalies can lead to singular behavior near the critical condition. For instance, the burning rate has been observed to reach a maximum near the critical pressure due to the competing influences of decreasing enthalpy of vaporization (which vanishes at the critical point) and increasing resistance to mass diffusion [1,2]. The surface tension also vanishes, resulting in the possibility of droplet deformation to an unknown extent. Finally, the degree to which transcritical droplet processes might couple with combustion instabilities is almost entirely unknown.

A number of models have recently been developed that begin to address these issues [3,4], but these remain experimentally unverified. The present investigation is therefore an experimental study. With only a few exceptions [5,6], most previous experimental studies of transcritical droplet processes were performed using some variant of a captured droplet technique, whereby droplets are suspended on a thermocouple or other supporting fiber. The disadvantage of this technique is that the suspension mechanism can have a significant effect on the droplet behavior, especially in the liquid phase. Therefore a free droplet technique will be used here. Monodisperse droplets formed at a supercritical pressure but at a subcritical temperature will be observed as they fall freely and heat in a hot, high pressure environment. The experiment is being designed to handle a wide variety of fluids including cryogenics. Droplets will be subjected to both vaporization and burning conditions, in environments containing combustion products as well as other gases. Furthermore, in order to investigate possible coupling mechanisms with combustion instabilities, provision will be made to subject the droplets to high pressure acoustic fields. Imaging techniques will initially be used to visualize droplet behavior, but other diagnostic techniques such as droplet slicing [7] will be explored later.

Efforts during this initial reporting period have concentrated on the development of a suitable droplet generator and a suitable acoustic driver. An initial droplet generator design, illustrated in Fig. 1, has been constructed and evaluated. The generator uses a disk-shaped piezoelectric crystal in a reservoir just upstream of an orifice to acoustically excite a stream in Rayleigh breakup to produce monodisperse droplets, and is designed with materials and sufficient cooling to handle liquid nitrogen. The generator was found to operate satisfactorily at atmospheric pressure, but was unable to produce droplets at elevated pressures, breaking up instead into a small spray. The Weber number was subsequently determined to be too high. Efforts to reduce the Weber number by reducing the stream velocity were found to produce clogging downstream of the orifice using this design. An alternative droplet generator has therefore been designed as illustrated in Fig. 2. The new generator is a hybrid design capable of operating in a combination of modes. The generator uses a cylindrically shaped piezo and is more pencil-shaped, which should allow it to operate either in a Rayleigh mode or in a drop-on-demand mode. In addition, an aerodynamic shroud has been added to provide the option of operating in an aerodynamic breakup mode. Construction will begin as soon as parts are received.

The other major effort during this reporting period was to develop an acoustic driver capable of operating at high pressures. Most conventional drivers are designed for operation at atmospheric pressure, and do not operate well at elevated pressures. The main alternative for high pressures has in the past been the use of a rotating toothed wheel at the exit of a choked orifice. This approach requires a mean flow through the pressure vessel. Use will be made here of an alternative piezoelectric approach that has been developed in a separate program at this laboratory through the SBIR program. The approach does not require a mean flow. A prototype driver has been demonstrated to operate in an impedance tube at sound pressure levels exceeding 150 dB at pressures up to 1000 psi. Improvements in this performance appear to be possible with further development.

Over the next year, droplet generator development will be completed and a suitable pressure vessel will be designed and fabricated. "Steady state" (*i.e.* non-acoustically perturbed) measurements will be initiated. Improved versions of the acoustic driver will be developed under the SBIR program, and adapted under this AFOSR program to drive the transcritical droplet experiments. Attempts will be made to obtain some initial acoustically driven data.

References

1. Faeth, G.M. Dominicis, D.P. Tulpinsky, J.F., and Olson, D.R., "Supercritical Bipropellant Droplet Combustion," *Twelfth Symposium (International) on Combustion,* The Combustion Institute, pp. 9–18 (1969).
2. Sato, J., Tsue, M., and Kono, M., "Effects of Natural Convection on High Pressure Droplet Combustion," *Comb. Fl.* 82: 142–150 (1990).
3. Shuen, J.S., Yang, V., and Hsiao, C.C., "Combustion of Liquid Fuel Droplets in Supercritical Conditions," *Comb. Fl.* 89: 299–319 (1992).
4. Delplanque, J.-P., and Sirignano, W.A., "Numerical Study of the Transient Vaporization of an Oxygen Droplet at Sub- and Supercritical Conditions," *Int. J. Heat Mass Transfer* 36: 303–314 (1993).
5. Natarajan, R., and Brzustowski, T.A., "Some New Observations on the Combustion of Hydrocarbon Droplets at Elevated Pressures," *Comb. Sci. and Tech.* 2: 259–269 (1970).
6. Sowles, R.E., "An Experimental Study of Carbon Dioxide Droplets Falling Through Inert High Pressure High Temperature Environments," Ph.D. Thesis, Dept. of Mech. Eng., University of Wisconsin (1973).
7. Winter, M., "Droplet Slicing Measurements of Internal Circulation," 31st AIAA Aerospace Sciences Meeting & Exhibit, Reno, NV, paper 93–0900 (1993).
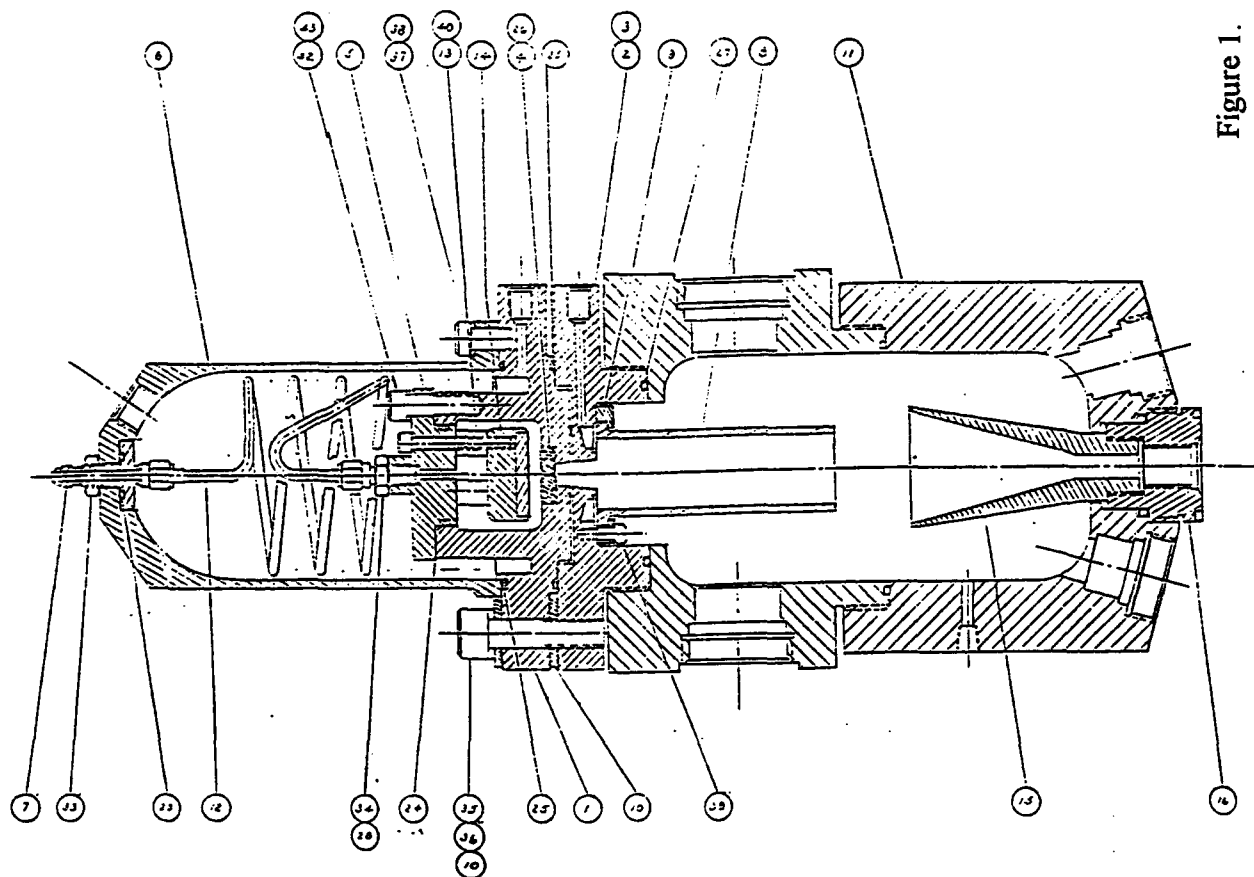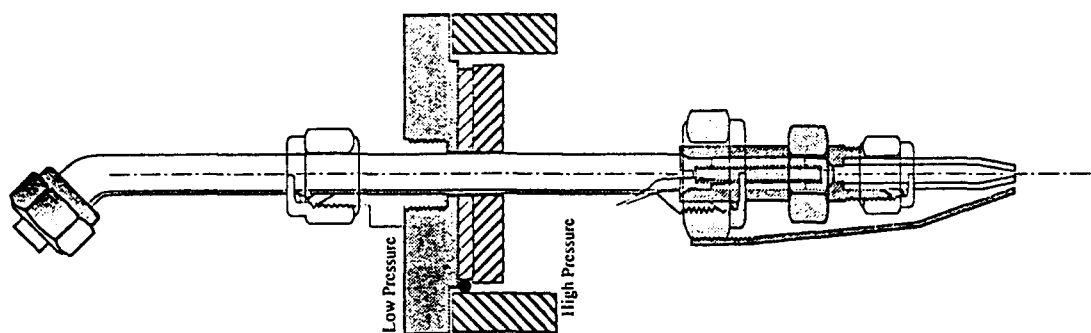
Figure 2.

Figure 1.

Low Pressure

High Pressure

- 150 -

COMBUSTION INSTABILITY PHENOMENA OF IMPORTANCE
TO LIQUID PROPELLANT ROCKET ENGINES

Principal Investigators: R.J. Santoro and W.E. Anderson

Propulsion Engineering Research Center
and
Department of Mechanical Engineering
The Pennsylvania State University
University Park, PA 16802

SUMMARY/OVERVIEW:

Injection systems that use jet impingement to atomize and mix propellant streams are the standard type of injector for rocket engines where both oxidizer and fuel enter the thrust chamber as liquids (e.g., LOX/hydrocarbon and storable propellant combinations), and also represent an attractive alternative to coaxial injectors typically used in LOX/H$_2$ engines. A significant problem exists in the use of impinging jet injectors, however, in that current empirical design practices dictate a compromise in performance to achieve a dynamically stable combustor. The goal of this research is to help clarify operative combustion instability mechanisms and provide a basis for the development of performance and stability design analysis models that can accurately predict the effects of injector geometry and operating conditions. A systematic investigation of the effects of jet condition (laminar versus turbulent), orifice diameter, impingement angle and jet velocity on primary atomization of impinging water jets has been completed. Measurements of atomization length, drop diameter, sheet shape, and breakup frequency have been compared to predictions based on current theories of impinging-jet sheet breakup and liquid sheet breakup. Experiments contrasting laminar and turbulent jet conditions clearly indicate that the jet conditions prior to impingement have a dramatic effect on the atomization process.

TECHNICAL DISCUSSION:

Impinging liquid jets form a fan in a plane perpendicular to the plane containing both jets. Instantaneous images of sheets formed by turbulent and laminar impinging jets are shown in Fig. 1. In each case, the atomization of the liquid sheet can be regarded as a two-step process: first, the liquid fan breaks up into ligaments in an apparently periodic fashion; and second, the detached ligaments subsequently disintegrate into spherical drops due to surface tension forces. Previous studies have shown that the fan structure, ligament/drop formation frequency and drop size are sensitive to injector design and operating parameters, and that a clear link between combustion instability and these processes can be established.[1] The objectives of the present study are to extend and confirm previous experimental work on impinging jet atomization, and to provide a firm basis from which to address combustion instability phenomena associated with impinging injectors.

Measurements of fan breakup length, x_b, drop size, d_D, and surface wave (λ_w) and periodic ligament formation phenomena are presented, and the degree to which current modeling approaches represent the observed breakup and drop formation processes is evaluated. The two models considered include a stationary antisymmetric wave-based model developed by Ibrahim and Przekwas[2] which predicts the sheet shape formed by two impinging jets applicable for low liquid Weber number regimes (We$=\rho_l U_j^2 d_o/\sigma < 2000$), and a linear stability-based model in which the sheet disintegration process is controlled by the growth of aerodynamic-induced waves on the sheet surface.[3] The details of the experimental set-up as well as a brief review of the foundations of the two aforementioned models are described elsewhere.[4,5]

The spray field resulting from the impingement of two liquid jets was examined as a function of orifice diameter, d_o, jet velocity, U_j, half-impingement angle, θ, and jet flow condition (laminar or turbulent). Instantaneous images of these spray fields were acquired using a CID solid state camera (512 x 512 pixels) with diffuse backlighting provided by a strobe light (flash duration $\sim 5\mu s$). From these images the breakup length, x_b, the maximum spray width, W, and the distance between adjacent periodic structures, λ, were measured. Drop

size and velocity measurements were made for the turbulent jet case for a set of parametric conditions at 16 mm and 41 mm downstream of the impingement point using an argon-ion laser-based FFT Phase Doppler Particle Analyzer.[4]

Distinct differences in the sheet structure between the turbulent and laminar impinging jet cases are observed, as shown in Fig. 1. The sheets formed by laminar impinging jets tend to be larger and less chaotic than for the turbulent impinging jet case under similar flow conditions.

In Fig. 2, the non-dimensional breakup length, x_b/d_o, for different diameter glass tubes for a fixed impingement angle, $2\theta = 60°$, is plotted versus a non-dimensional correlating factor, $We(1-\cos\theta)^2/\sin^3\theta$, that contains liquid Weber number ($We = \rho_l U_j^2 d_o/\sigma$) and impingement geometry effects. For turbulent impinging jets, the measured non-dimensional breakup lengths for various orifice diameters essentially collapse to a single curve for a fixed impingement angle; a family of curves can be obtained for different impingement angles. Also shown in Fig. 2 are non-dimensional breakup lengths predicted by the stationary antisymmetric wave-based model[2,5] and by the linear stability-based model.[3,4,5] Values of non-dimensional breakup length predicted for different impingement angles by the linear stability-based model collapse to a single curve when plotted versus the correlating parameter. For the laminar impinging jet case, the peak in the non-dimensional breakup length and the general trends as a function of Weber number are explained well by both models. The measured non-dimensional breakup length of sheets formed by turbulent impinging jets, however, does not compare well with predictions from either model.

The drop size, d_D, non-dimensionalized with respect to the orifice diameter, d_o, is plotted versus the non-dimensionalized parameter $We(1-\cos\theta)^2/\sin^3\theta$ in Fig. 3. The drop size measurements were made along the spray centerline, 16 mm from the impingement point, for the turbulent impinging jet case. The measured drop sizes are polydispersed, and the arithmetic mean diameter, D_{10}, is taken for comparison purposes. Values for the non-dimensional drop diameter predicted by the linear stability-based model for different impingement angles collapsed to a single curve. In a similar fashion, the measured values of the non-dimensional drop size also collapsed to a single curve when plotted versus the correlating parameter. The predicted drop size is about a factor of two higher than the measured drop size, however, better agreement would be obtained if a higher order moment diameter for the measurements was used. The arithmetic mean diameter was selected for comparison because the model predicts a monodispersed drop size.

The instantaneous images for the turbulent impinging jet case were also examined for apparent dominant wave structures. Three different periodic structures were identified: surface waves apparent on the sheet surface; edge ligaments defined as strands of liquid attached to the intact sheet periphery; and detached ligaments defined as strands of fluid either completely or nearly completely separated from the downstream edge of the intact sheet. The separation distance between adjacent identical wave types was measured from the instantaneous spray images. The separation distance between adjacent detached ligaments was consistently about twice as long as both edge and surface wave separation distances. In Fig. 4, the wavelength of surface waves on the sheet, λ_{sw}, non-dimensionalized with orifice diameter, d_o, is plotted versus Weber number. As shown in Fig. 4, the measured non-dimensional surface wavelength is generally independent of Weber number, and collapses to a value between 2 and 2.5 for different orifice diameters. In terms of primitive variables, the surface wavelength, λ_{sw}, was insensitive to changes in jet velocity, U_j, and increased with increasing orifice diameter, d_o. These trends are inconsistent with the linear stability-based model, which predicts a strong wavelength dependence on jet velocity and no dependence on orifice diameter.

An estimate of the forces involved in the impinging jet system reveals that the liquid inertial force at impact is an order of magnitude greater than any of the other surface or body forces, implying that the jet dynamics at impact have a major effect on the behavior of the sheet. At impingement, oscillations in jet inertia can cause large deflections of the sheet surface. Further downstream, the sheet can rip and form ligaments at these deflections as the sheet thins. Potential sources of oscillations in the impingement region consistent with these observations include large eddies in the jet and long-wavelength jet instabilities,[6] both of which show the same dependence on jet diameter as the measured surface wavelength does.

The measurements discussed above were all performed with large length-to-orifice diameter ratio (L/d_o) precision-bore glass tubes at atmospheric pressure. Recent work has focused on experiments more representative of practical injector systems. A rectangular transparent pressure chamber equipped with acoustic drivers has been fabricated. Instead of long glass tubes, short L/d_o orifices that are twist-drilled into a brass injector are used. In Fig. 5, the measured non-dimensional breakup length obtained at atmospheric pressure with the glass tubes is compared to the measured non-dimensional breakup length obtained with a twist-drilled brass injector ($L/d_o = 10$) at operating pressures of one and nine atmospheres. Note that the non-dimensional breakup length, x_b/d_o, is plotted as a function of the gas Weber number, We_g ($= \rho_g U_j^2 d_o/\sigma$), in Fig. 5. The data in Fig. 5 indicates that geometric differences between the glass tubes and the drilled brass injector are not

important at one atmosphere. At higher operating pressures, breakup length noticeably decreases. Recent experimental results from Wu et al.[7] have indicated that single turbulent jet breakup processes can be affected by operating pressure at liquid-gas density ratios less than 500, which corresponds to ambient pressures of about two atmospheres for our study. In the case of impinging jets, it is likely that these aerodynamic stresses affect the jets prior to impingement and the liquid fan.

From the above described results, the basic structure of the atomization process involved in impinging injectors has been elucidated. The importance of the initial jet conditions (laminar or turbulent) have clearly been demonstrated in agreement with previous studies.[5] Specific tasks in progress include development of a primary atomization model that can account for pre-impingement jet conditions; studies of the atomization process in the presence of externally applied acoustic fields; design and execution of a hot-fire test program to determine combustion effects; and development and application of a combustion response model to relate the experimental results of this study to the proven empirical stability correlations.

REFERENCES:

1.   Anderson, W. E., Ryan, H. M. and Santoro, R. J., "Combustion Instability Phenomena of Importance to Liquid Bi-Propellant Rocket Engines,"28th JANNAF Combustion Meeting, San Antonio, TX, Oct. 28 - Nov. 1, 1991.

2.   Ibrahim, E. A. and Przekwas, A. J., "Impinging Jets Atomization," Phys. Fluids A, Vol. 3, No. 12, Dec. 1991.

3.   Dombrowski, N. and Johns, W. R., "The Aerodynamic Instability and Disintegration of Viscous Liquid Sheets," Chem. Eng. Science, Vol. 18, 1963, pp. 203-214.

4.   Anderson, W. E., Ryan, H. M., Pal, S. and Santoro, R. J., "Fundamental Studies of Impinging Liquid Jets," AIAA paper 92-0458, 30th Aerospace Sciences Meeting, Reno, NV., Jan. 6-9, 1992.

5.   Ryan, H. M., Anderson, W. E., Pal, S. and Santoro, R. J., "Atomization Characteristics of Impinging Liquid Jets," AIAA paper 93-0230, 31st Aerospace Sciences Meeting, Reno, NV., Jan. 11-14, 1993.

6.   Levich, V., G., Physicochemical Hydrodynamics, Prentice-Hall, Englewood Cliffs, NJ, 1962, Chapter 11.

7.   Wu, P. -K., Hsiang, L. -P. and Faeth, G. M., "Aerodynamic Effects on Primary and Secondary Spray Breakup", First International Symposium on Liquid Rocket Engine Instability, University Park, PA, January 18-20, 1993.
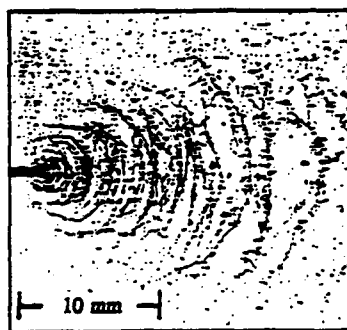
1a) $U_j = 18.5$ m/s
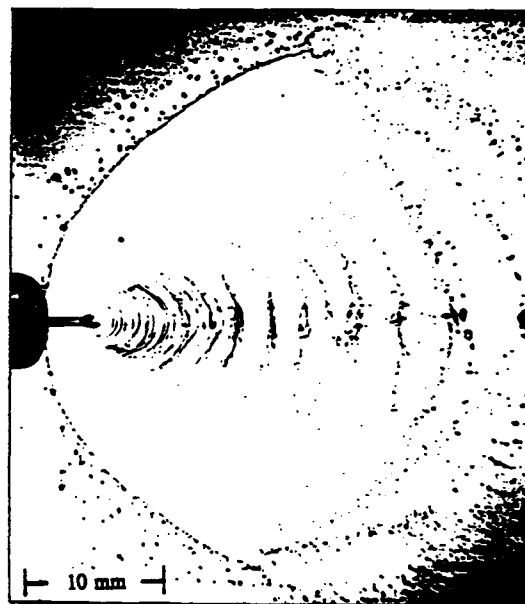
1b) $U_j = 17.9$ m/s

Fig. 1.   Instantaneous image of a spray formed by turbulent impinging water jets (Fig. 1a) and laminar impinging water jets (Fig. 1b) for similar flow conditions.
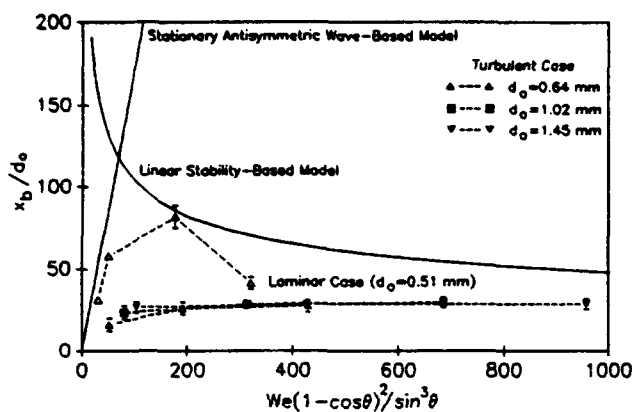
Fig. 2. The measured and predicted non-dimensional breakup length, x_b/d_o, plotted as a function of the correlating parameter $We(1-\cos\theta)^2/\sin^3\theta$, where We $(=\rho_l U_j^2 d_o/\sigma)$ is the Weber number and θ is the impingement half-angle.
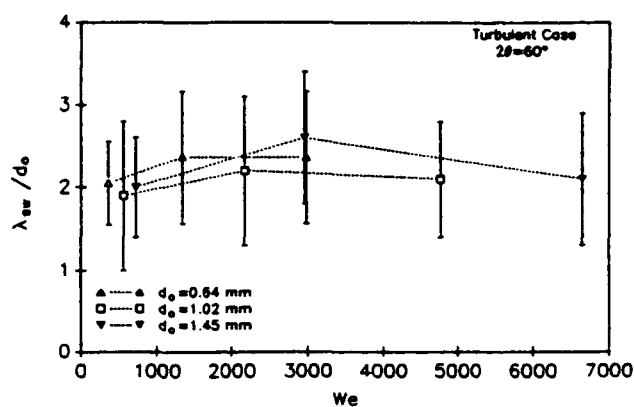

Fig. 4. The measured non-dimensional separation distance between adjacent surface waves, λ_{sw}/d_o, plotted as a function of the Weber number, We $(=\rho_l U_j^2 d_o/\sigma)$, and orifice diameter, d_o.
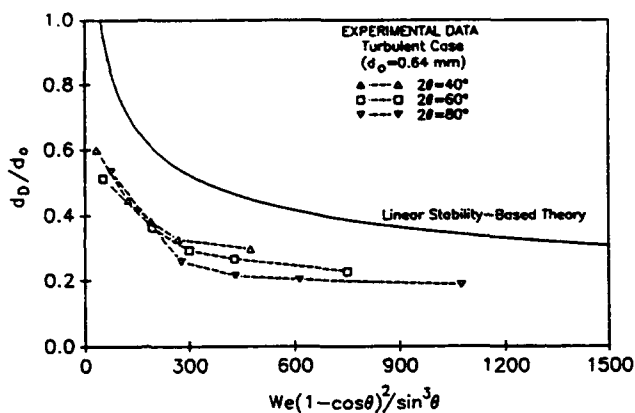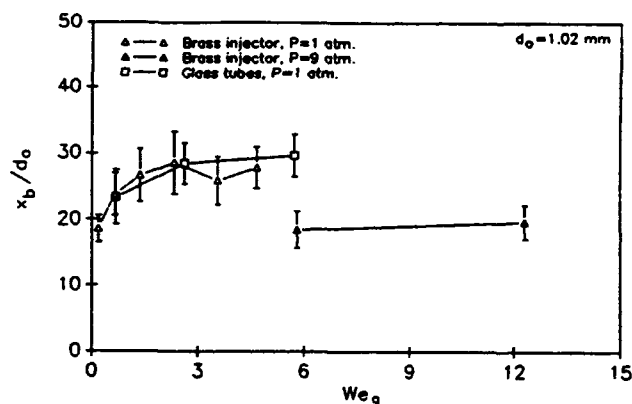

Fig. 3. The measured and predicted non-dimensional drop size, d_D/d_o, plotted as a function of the correlating parameter, $We(1-\cos\theta)^2/\sin^3\theta$, and impingement angle, 2θ.

Fig. 5. The measured non-dimensional breakup length, x_b/d_o, plotted as a function of the gas Weber number, We_g $(=\rho_g U_j^2 d_o/\sigma)$, ambient pressure and injector type.

- 154 -

LIQUID ROCKET MOTOR COMBUSTION STABILITY
USING COAXIAL INJECTORS

Michael M. Micci

Aerospace Engineering Department &
Propulsion Engineering Research Center
The Pennsylvania State University
University Park, PA 16802

SUMMARY/OVERVIEW:

Although the hydrogen temperature ramping technique is used to determine the stability characteristics of hydrogen/oxygen coaxial liquid rocket motor injectors, there is no definitive knowledge of the effect of the hydrogen temperature on the stability characteristics of the injectors. Possible explanations are a detrimental change in the atomization characteristics due to a decrease in the velocity ratio, the disappearance of a stabilizing recirculation region at the base of the LOX post or a change in the gas side injector pressure drop allowing acoustic coupling to the propellant feed system. This program will provide the first quantitative measurements of droplet size and velocity distributions as a function of the injector velocity ratio and of injector pressure drop as a function of gas temperature. It will also be the first experimental examination of the recirculation region at the base of the injector LOX post. Due to the ability to use liquid oxygen at pressures occurring in actual liquid rocket motors, a high level of similitude can be achieved.

TECHNICAL DISCUSSION:

Although stable operating regimes for cryogenic coaxial injectors have been empirically determined, there is no knowledge of the spray characteristics corresponding to stable operation or the physical processes which produce the atomization patterns that result in stable or unstable operation. The current engineering method for determining the stable operating regime of a cryogenic coaxial injector is the "hydrogen temperature ramping" method, however there is still no definitive knowledge of the effect of the hydrogen temperature on the stability characteristics of coaxial injectors. The physical significance of the hydrogen temperature ramping technique may come from the atomization process occurring in coaxial injectors where the high velocity outer gaseous hydrogen flow strips droplets from the lower velocity inner liquid oxygen flow. Experiments at ONERA using water as the liquid oxygen simulant have shown that a higher relative velocity between the two flows results in smaller droplets and complete atomization closer to the injector exit[1].

---

[1]Vingert, L., "Coaxial Injector Spray Characterization for the Ariane 5 Vulcain Engine," 6th Annual Conference "Liquid Atomization and Spray Systems - Europe," July 4-6, 1990.

Lowering the gaseous hydrogen temperature increases its density, thus lowering its injection velocity relative to the liquid in order to maintain the same mass flow. Wanhainen et al have shown that it is not the hydrogen temperature itself causing the transition to instability but the ratio of the gas to liquid injection velocities[2]. From this one might infer that the instability arises because of an increase in the liquid oxygen drop sizes along with an extension in the length of the atomization zone. A primary purpose of the experiments is to identify what effect the velocity ratio has on atomization.

Another proposed explanation for the emergence of unstable operation in the hydrogen temperature ramping test is that a recirculation region acting as a flameholder exists downstream of the LOX post tip. Below a minimum relative velocity between the liquid oxygen and gaseous hydrogen, the recirculation region becomes too weak to act as a flameholder and the combustion zone moves away from the injector face to a location where it can interact more strongly with the chamber acoustic modes. Liang and Schumann have examined this idea with an experimental and computational investigation of gaseous oxygen and hydrogen coaxial injectors[3]. They examined several injectors designed to produce recirculation regions of different sizes but found that all injectors tested showed the combustion region anchored to the base of the injector.

The first nine months of the grant period were spent designing a liquid nitrogen cooled heat exchanger to lower the temperature of the injected gas, either hydrogen or helium, from ambient down to 80K. The design has been completed and construction has begun. The heat exchanger will be used for the final series of experiments to simulate the hydrogen temperature ramping test and examine the effect of temperature induced gas velocity changes on the resultant atomization and its subsequent effect on motor instability.

An injector with the same dimensions as the SSME preburner injector has been constructed and tested with water and air at atmospheric conditions (Fig. 1). The SSME preburner injector was selected because the test facility is capable of providing the required gas and liquid mass flow rates for a full size injector and as large an injector as possible was desired to provide the possibility of optical access. The initial tests of the injector used air and water injecting into atmospheric ambient pressure.

PDPA measurements were made of the droplet size and velocity as a function of axial and radial position. Figures 2a and b show the measured droplet Sauter mean diameters and velocities as a function of axial and radial position. The results show no change in the droplet Sauter mean diameter as a function of position while the droplet velocities peak along the axis and decrease (but only at locations near the axis) as one moves downstream from the injector. Both the magnitudes and the trends of the measured Sauter mean diameters and velocities agree well with results obtained by Zaller and Klem[4]

[2]Wanhainen, J.P., Parish, H.C. and Conrad, E.W., Effect of Propellant Injection Temperature on Screech in 20,000-Pound Hydrogen-Oxygen Rocket Engine, NASA TN D-3373, April 1966.

[3]Liang, P.-Y. and Schumann, M.D., "A Numerical Investigation of the Flame-Holding Mechanism Downstream of a Coaxial Injector Element," Proceedings of the 24th JANNAF Combustion Meeting, CPIA Publication 476, Vol. 3, Oct. 5-9, 1987, pp. 599-610.

[4]Zaller, M., and Klem, M., "Shear Coaxial Injector Spray Characterization," Proceedings of the First International Symposium on Liquid Rocket Engine Combustion Instability, Jan. 18-20, 1993, University Park, PA.

using a similar injector and air and water flow rates. The main purpose for this limited series of tests was to confirm the operation of the PDPA system as well as the injector. The effects of varying the PDPA PMT voltage and of taking measurements through plexiglass windows of varying thickness were quantified. A windowed cold flow high pressure chamber has been designed, constructed and pressure tested to 9 MPa. The next series of PDPA measurements will use liquid and gaseous nitrogen at pressures of a few MPa.

In order to determine if a recirculation region exists at the base of the LOX post, a miniature diode laser LDV system has been assembled. It will be used to probe the region at the base of the LOX post to determine if and under what circumstances a recirculation region exists. The LDV will use liquid droplets produced by the atomization process as the seeding particles. If a recirculation region is found to exist, an attempt will be made with the LDV to measure its strength.

In the course of an extensive literature review conducted during the course of this year, some previous experimental evidence was found that indicated that the spontaneous stability condition for a hydrogen/oxygen rocket was determined by the hydrogen pressure drop through the injector[5,6]. Below a critical minimum value for the pressure drop, chamber oscillations evidently can couple to the propellant feed system, causing a combustion instability in the chamber. However, the value of this critical pressure drop was a function of the injector and chamber design. Measurements of the injector pressure drop as a function of the relative gas/liquid flow velocity and injector geometry are planned. The results of these measurements will be used as input to a stability model of the propellant feed system to determine the magnitude of the influence of the injector pressure drop on the combustion stability of the entire motor.
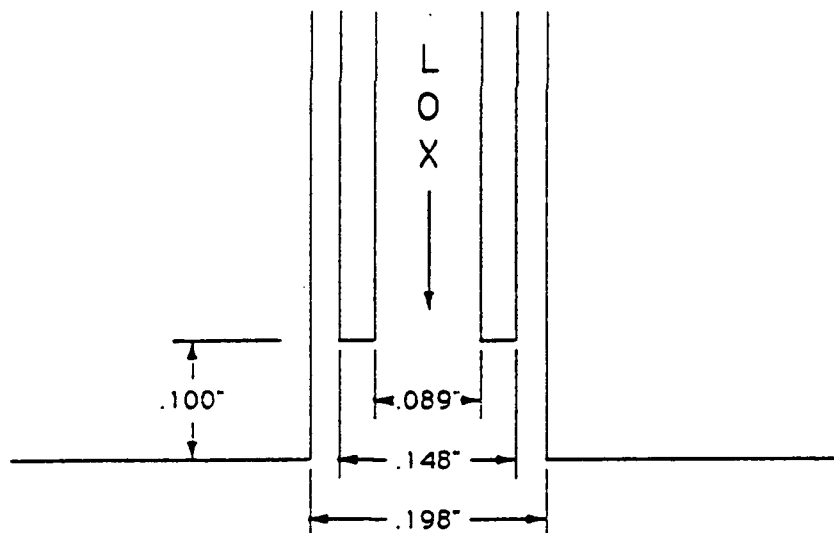

Fig. 1 Dimensions of SSME preburner injector.

[5]Conrad, E.W, Bloomer, H.E., Wanhainen, J.P. and Vincent, D.W., Interim Summary of Liquid Rocket Acoustic-Mode-Instability Studies at a Nominal Thrust of 20,000 Pounds, NASA TN D-4968, Dec. 1968.

[6]Hannum, N.P., Russell, L.M., Vincent, D.W. and Conrad, E.W., Some Injector Element Detail Effects on Screech in Hydrogen-Oxygen Rockets, NASA TM X-2982, Feb. 1974.
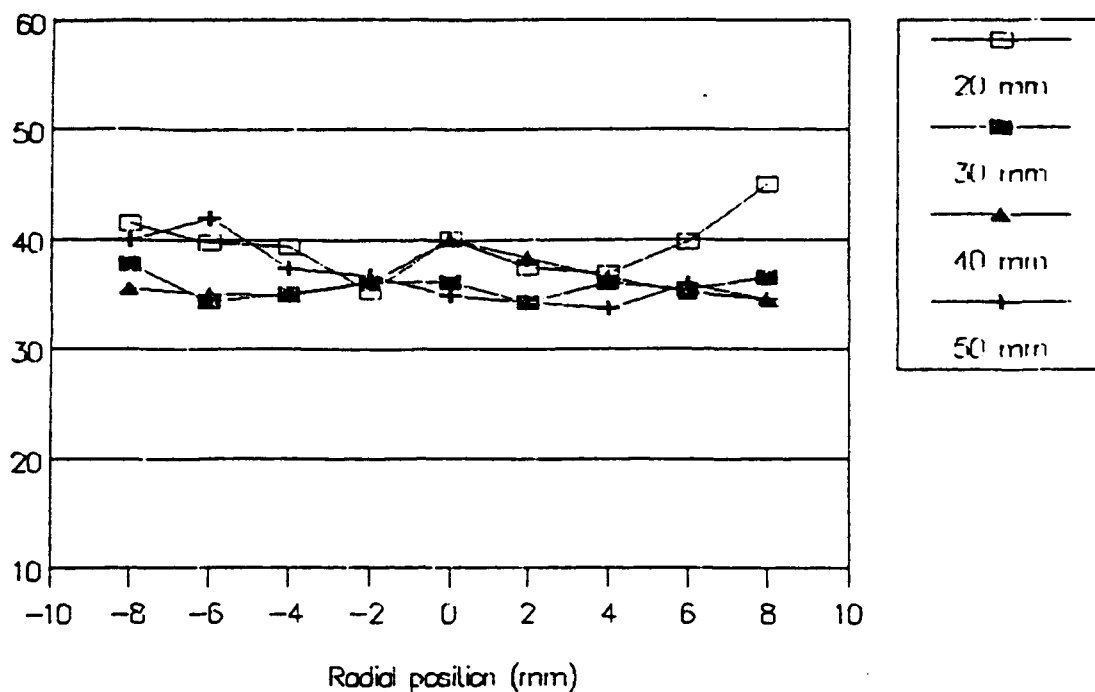
Fig. 2a   Droplet Sauter mean diameter for an atmospheric water/air shear coaxial injector spray as a function of radial and axial position.

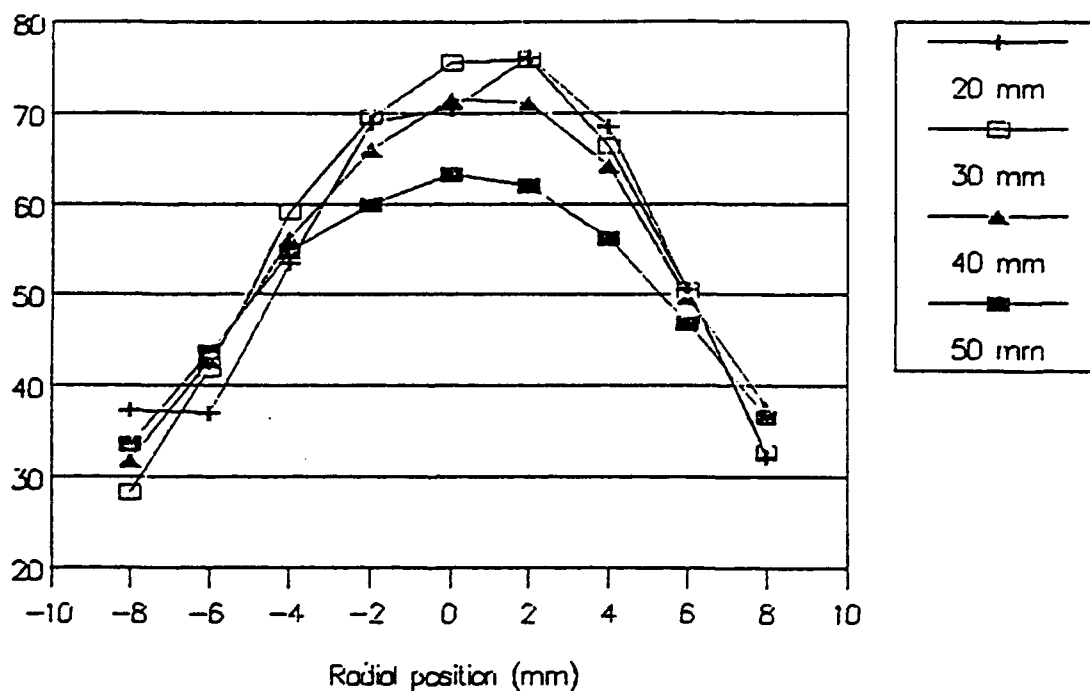Fig. 2b   Droplet velocities for a water/air shear coaxial injector spray as a function of radial and axial position.

ADDITIONAL

ABSTRACTS

which are not

PRESENTED

AFOSR SPONSORED RESEARCH IN AIRBREATHING COMBUSTION

PROGRAM MANAGER: JULIAN M. TISHKOFF

AFOSR/NA
110 Duncan Avenue, Suite B115
BOLLING AFB DC 20332-0001

SUMMARY/OVERVIEW: The Air Force Office of Scientific Research (AFOSR) program in airbreathing combustion currently is focused on seven areas of study: supersonic combustion, reacting flow, soot, sprays, kinetics, ram accelerators, and supercritical fuel behavior. An assessment of major research needs in each of these areas is presented.

TECHNICAL DISCUSSION

AFOSR is the single manager for Air Force basic research, including efforts based on external proposals and in-house work at Air Force laboratories. Airbreathing combustion is assigned to the AFOSR Directorate of Aerospace Sciences along with programs in rocket propulsion, propulsion diagnostics, and fluid and solid mechanics.

Interests of the AFOSR airbreathing combustion task are given in the SUMMARY section above. Many achievements can be cited for these interests, yet imposing fundamental research challenges remain. The objective of the program is publications in the refereed scientific literature describing significant new understanding of multiphase turbulent reacting flow. Incremental improvements to existing scientific approaches, hardware development and computer codes fall outside the scope of this objective.

Decisions on support for research proposals are based on scientific opportunities and technology needs. Current AFOSR perceptions of scientific opportunities appear in Figure 1, and areas of emphasis are indicated by arrows with positive slopes.

Two major emphases define the main thrusts of current and near term future research activity: supersonic combustion to support hypersonic airbreathing propulsion technology and issues affecting the future utilization of hydrocarbon fuels. Starting in 1987 new research efforts were directed at novel means for achieving ignition, combustion enhancement, low-loss flameholding, and complete chemical energy release in supersonic combustion. 1989 saw new research in interactive control of fluid transport processes. These opportunities reflect a generic interest in interdisciplinary efforts between researchers in control theory and fluid transport behavior. For hypersonic propulsion a particular focus of interactive flow control is the investigation of means to

overcome the suppression of mixing which high Mach number flows experience in relation to subsonic flows.

A new area of interest is the changing requirements for the utilization of hydrocarbon fuels in propulsion systems. Future systems will require fuels to absorb substantial thermal energy, raising fuel temperatures to supercritical thermodynamic conditions. Understanding and controlling fuel properties at these conditions will be crucial for avoiding thermal degradation and for subsequent processes within the combustor. Environmental concerns and the availability of petroleum supplies also will contribute to future propulsion system design and operational needs.

In the rapidly changing international environment we also are examining how we conduct our research activities in relation to both Air Force and civilian needs. We now recognize a new set of research objectives, including achieving rapid technology transitioning and dual military and civilian technological use for Air Force basic research. We welcome your ideas on fostering better working relationships among universities, industry, and Government scientists and technologists.

The purpose of this abstract has been to communicate AFOSR perceptions of research trends to the university and industrial research communities. However, communication from those communities back to AFOSR also is desirable and essential for creating new research opportunities. Therefore, all proposals and inquiries for fundamental research are encouraged even if the content does not fall within the areas of emphasis described herein. Comments and criticisms of current AFOSR programs also are welcome.

Air Force Basic Research

Aerospace Sciences

Airbreathing Combustion

Research Area	Trend	Decrease	Increase
Supersonic Combustion	↑		
Reacting Flow	↑		
Soot	↑		Comprehensive Growth Modeling
Sprays	↖		Supercritical Behavior - FY94 Init
Kinetics	↑		Lumping And Reduction Methods
Ram Accelerators	↑		New Air Force Laboratory Task
Supercritical Fuel Behavior	↖		FY93 And FY94 Initiatives

NUMERICAL ANALYSIS OF A TIME DEPENDENT
TWO-PHASE NON-REACTING FLOW

Principal Investigator: Suresh K. Aggarwal
Address: Department of Mechanical Engineering (M/C 251)
                              University of Illinois at Chicago
                              Chicago, Illinois 60680

SUMMARY

The objective of this research is to study the dispersion and vaporization behavior of droplets in turbulent shear flows dominated by large vortical structures. The two-phase flow algorithm is based on a large eddy simulation for the gas phase and a Lagrangian approach for the liquid phase. The work completed during the past year includes: (i) the development of correlation between the Stokes number and the intrinsic frequencies in particle-laden shear flows and (ii) the study of droplet dispersion in a transitional axisymmetric jet . The research currently in progress is focussing on the effect of external forcing on droplet dispersion in a jet flow and the dispersion behavior of evaporating droplets in heated shear flows.

INTRODUCTION

Particle-laden turbulent flows occur in numerous technological applications. The traditional approach for modelling these flows is based on the assumption that the turbulence is isotropic and statistical in nature. Numerous recent studies, however, indicate that the turbulent flows are dominated by large-scale coherent vortical structures. This has raised a number of important questions regarding the role of large-scale structures in determining the entrainment, mixing, and spray processes. Further interest in the study of large scale structures stems from the fact that by manipulating these structures, one may be able to control and enhance the performance of systems whose dynamics is strongly influenced by these structures.

The objective of this research is to study the dispersion and vaporization behavior of droplets in transitional shear layers dominated by large vortical structures. The earlier efforts, focussing on the droplet dispersion behavior in both naturally developing and forced planar shear layers, are described in Publications 1-2. The results obtained during the past year and the work currently in progress are summarized in the following sections.

Correlation Between the Stokes Number and Intrinsic Frequencies

Numerical results are obtained to characterize the dependence of particle dispersion on the Stokes number, and to identify the appropriate particle response time and flow time scales used for defining the Stokes number. Two particle-laden shear flows considered for illustrating these scales are a planar shear layer and an axisymmetric jet. Large-scale features of these flows are computed by using the flux corrected transport (FCT), time step-splitting algorithm. Particles of

different sizes are injected into the shear layer and their dispersion behavior is quantified by using a global dispersion function. Results indicate that the particle dispersion maximizes at a certain value of the Stokes number, defined as a ratio of the particle aerodynamic response time to the characteristic flow time. It is suggested, however, that a correct flow time should be based on the local scales rather than on the global length and velocity scales of the flow. It is further speculated that an appropriate local flow time scale for the Stokes number can be calculated from the dominant frequencies associated with the large-scale structures. Results from our simulations and several experimental studies on particle dispersion are used to support our speculation. In addition, the validity of the Stokes drag law in defining the particle response time in realistic two-phase flow is examined. Further details are given in Publication 3.

Droplet Dispersion in a Transitional Axisymmetric Jet

In this study, the dynamics and dispersion of droplets in the near field of a transitional, axisymmetric jet is considered. A large eddy simulation model based on a fourth-order phase-accurate Flux Corrected Transport (FCT) algorithm is employed for the numerical simulation of the Kelvin-Helmholtz instability and the dynamics of vortical structures in the jet shear layer. A second-order Runge-Kutta procedure is employed for the trajectories of droplets injected into the shear layer. Both the nature and dynamics of dispersion, and the mechanism responsible for it are established through detailed flow visualization, analyses of droplet motion and quantified dispersion behavior. The flow visualization, based on the streaklines for the tracer particles and the trajectories of individual droplets in a reference frame stationary with respect to the vortex ring structures, indicates three droplet dispersion mechanisms. The very small droplets (Stokes number St < 0.02) are subjected to the "vortex" mechanism, whereby the droplets follow the behavior of tracer particles in the vortex structures. In the second mechanism, termed as the "centrifugal" mechanism, the droplets are trapped in the structures and flung out of them, and, subsequently gather around their periphery. This mechanism is responsible for the enhanced dispersion of intermediate size droplets, and the second merging has the most influence on droplet dispersion during this droplet-vortex interaction. The third mechanism, "inertial" mechanism, is operative on large droplets injected in the shear layer or on small droplets injected in the core region. Quantified dispersion results are presented to identify the range of Stokes number for the three mechanisms, and to establish the effects of important parameters on dispersion. One such result is given in Fig. 1, showing the variation of non-dimensional dispersion with the Stokes number for three different droplet injection velocities. The enhanced droplet dispersion for the intermediate Stokes number ($0.02<St<4.0$ for Vinj=200 m/s), where the centrifugal mechanism is operative, is clearly seen in the figure. In addition, it is shown that the Stokes number range for enhanced dispersion can be significantly increased by changing the injection parameters. The details are discussed in Publications 4-5.

Research in Progress

Two efforts are currently in progress. The first deals with the effects of external forcing on droplet-vortex interactions in high-speed axisymmetric jets. Preliminary results indicate that with low amplitude forcing, both random and periodic, the droplet dispersion can be enhanced. A parametric study is underway to study the effects of forcing parameters on the dispersion

behavior. The second effort concerns with the dispersion of evaporating droplets in axisymmetric low-speed heated jets. A heated jet at a velocity of 1.0 m/s issuing from a nozzle of 2.54 cm diameter into a coflowing jet at 0.2 m/s is being considered. The selection of these parameters is based on the anticipated experimental study at the WPAFB. For this case, the gas-phase simulation is based an implicit, time-dependent, third-order accurate, finite-difference algorithm. A preliminary result showing the iso-temperature contours for a heated jet issuing into a cold flow is given in Fig. 2. The results, shown for zero gravity and normal gravity, clearly indicate the buoyancy-driven structures, but no shear-driven structures, a result that is qualitatively different from that observed in a diffusion flame. The dispersion behavior of non-evaporating and evaporating droplets in these structures is currently being investigated. These two efforts will continue during the next year.

List of Publications

1. S.K. Aggarwal, G. Chen, J.B. Yapo, F.F.Grinstein, and K. Kailasnath," Numerical Simulations of Particle Dynamics in Planar Shear Layer", Paper AIAA-92-0109, 30th Aerospace Sciences Meeting, Reno, Nevada, Jan. 6-9, 1992. Also submitted to Computers and Fluids.

2. S.K. Aggarwal and Y. Xiao, " Droplet Dispersion in a Perturbed Transitional Shear Layer", Central States Section Meeting, The Combustion Institute, Columbus, April 1992. Also submitted to Journal of Propulsion and Power.

3. S.K. Aggarwal, Y. Xiao, J.P. Uthuppan," Effect of Stokes Number on Droplet Dispersion," Submitted to Atomization and Spray.

4. J. Uthuppan," Droplet Dispersion in a Transitional Axisymmetric Jet: A Numerical Study", M.S. Thesis, Department of Mechanical Engineering, University of Illinois at Chicago, 1992.

5. J.P. Uthuppan, S.K. Aggarwal, F.F.Grinstein, and K. Kailasnath," Particle Dispersion in a Transitional Free Jet", Paper 93-0105, 31th Aerospace Sciences Meeting, Reno, Nevada, 1993. Also submitted to AIAA Journal.
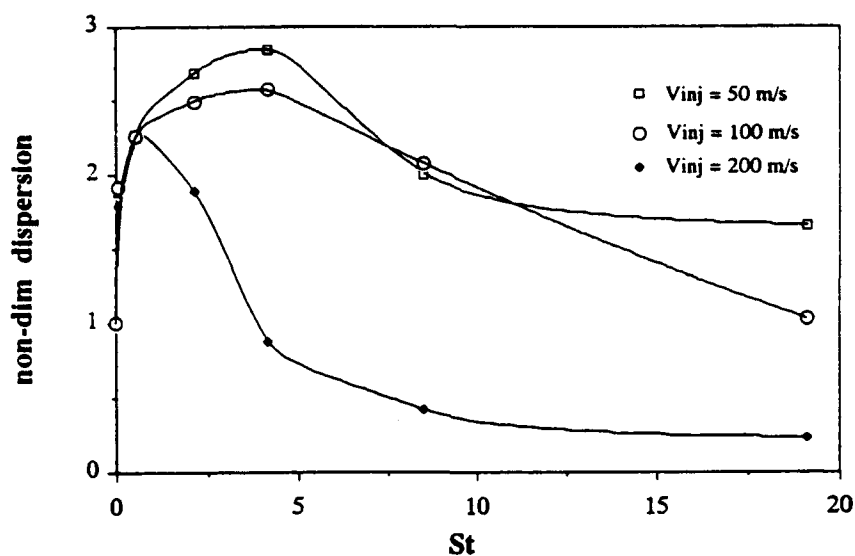
Figure 1   Non-dimension dispersion function vs. Stokes number for three droplet injection velocities. The jet velocity is 200 m/s.
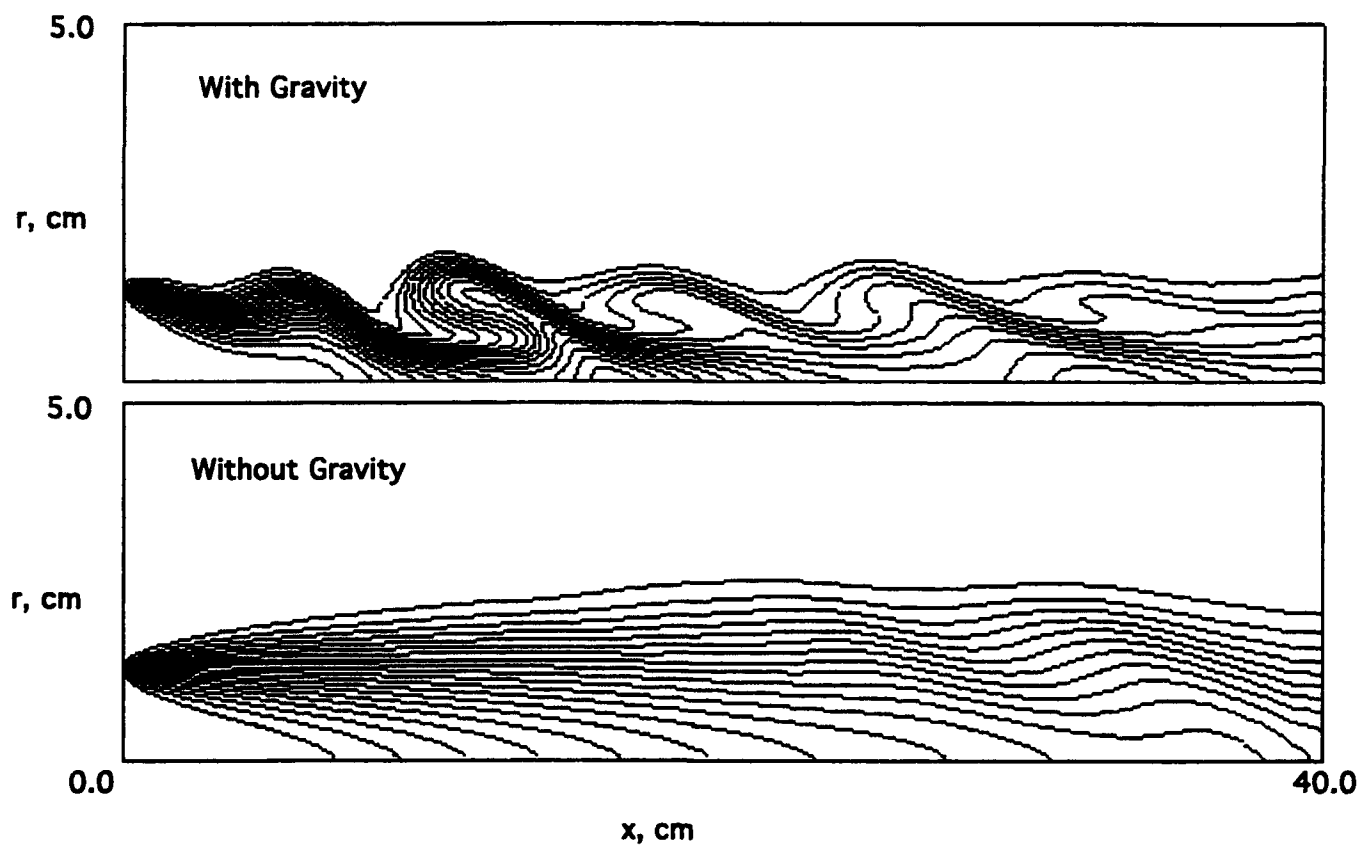

Figure 2   Iso-temperature contours in a heated jet with normal gravity and zero gravity. The jet velocity is 1.0 m/s and temperature is 1200 K. The coflowing jet velocity is 0.2 m/s and temperature 298 K.

MODELING STUDY TO EVALUATE THE IONIC MECHANISM OF SOOT FORMATION

Principal Investigator: H.F. Calcote

AeroChem Research Laboratories, Inc.
P.O. Box 12, Princeton, New Jersey 08542

SUMMARY/OVERVIEW

An understanding of the mechanism of soot nucleation remains the major deficiency in our understanding of soot formation in flames. The ionic mechanism of soot nucleation is being evaluated by computer modeling to determine whether or not an ionic model can account for the experimental results. During this year we have also initiated a comparison between measured and equilibrium calculated acetylene concentrations, soot concentrations, and temperature for a series of fuel/air/oxygen flames.

TECHNICAL DISCUSSION

We recently presented a comparison between neutral mechanisms and the ionic mechanism of soot formation in flames which indicates that ionic growth of a soot precursor is more rapid than neutral growth [1]. We continue to pursue a detailed computer model of ion growth in flames and compare the results with the well-documented acetylene/oxygen flame burning on a flat flame burner at a pressure of 2.67 kPa and a linear unburned flow velocity of 50 cm/s.

During this last year we improved the thermodynamic data base for ions important in the mechanism by updating some of the small ions based upon new literature data. This helped improve the agreement between calculated and experimental ion profiles for the small ions. We also extended the data base to large ions, some neutral species, and estimated the thermodynamics of a realistic soot particle, i.e., with $C/H = 10$. Incorporation of the extended Langevin theory of ion-molecule reactions [2] into the mechanism has made very little difference in the calculated ion profiles, but does eliminate the concern that the ion-molecule rate coefficients are unrealistic.

A set of 51 reactions is employed to go from the propargyl ion, $C_3H_3^+$ to $C_{13}H_9^+$. Only ions observed experimentally are included in the mechanism, and all observed ions are included. The reactions are written toward increasing molecular size; thus the free energy of reaction becomes more positive as the temperature is increased due to entropy effects. Thermodynamic equilibrium has a much greater effect on the ion-molecule reactions than expected (the reverse reactions are calculated from the forward rate and the equilibrium constant); this shows up as a strong temperature dependence. This same effect, of course, controls neutral mechanisms and may explain why the rate of soot formation peaks in the temperature range of about 1400 to 1900 K. The usual explanation involves a competition between the rates of soot formation and soot oxidation. To avoid excessively fast reverse reactions, the forward reaction rate coefficients are limited so that the reverse reaction rates determined by equilibrium never exceed the reverse Langevin rates.

The ions disappear by either ion-electron or positive ion-negative ion recombin̈̈̈̈̈̈̈̈. Negative ion recombination rate coefficients are about one to two orders of magnitude than electron recombination rate coefficients, but have not been included because there are no g ̈easurements of

negative ion concentrations in fuel-rich flames. There is, however, evidence for the presence of large negative ions in soot forming flames. Their inclusion would increase the cation concentrations.

The SANDIA flame code, modified to accommodate ions, is being used to calculate ion profiles [3]. The ability to input experimental ion and neutral profiles makes it possible to test the ionic mechanism independent of complications in the neutral mechanism and without concern for calculating the chemiionization rate which depends on reaction coefficients and concentrations of neutral species which are not well known. Inclusion of the mechanism of forming ions from neutral species (especially radicals) previously gave ion concentrations exceeding experimental values [4]. For this set of runs, the experimental concentration profile of the propargyl and phenyl ion and all of the neutral species involved in the ionic mechanism, e.g., acetylene, diacetylene, allene, and hydrogen, were used as input profiles, as was the corrected experimental temperature profile.

Figure 1 shows a comparison between the calculated and experimental maximum ion concentrations. The arrangement of C and H in the formula indicates the isomer that gave the closest agreement with experiment. Calculated and experimental ion profiles are compared in Fig. 2. To obtain satisfactory agreement between calculated and experimental values we modified the experimental temperature profile by linearly reducing it from 0% at the burner to 10% at the maximum. Mass 39 for $C_3H_3^+$ was interpreted as that of the propargyl cation, $C_3H_3(l)^+$, rather than cyclopropenium, $C_3H_3(c)^+$, although cyclopropenium is the more stable. The equilibrium ratio of $C_3H_3(l)^+/C_3H_3(c)^+$ increases from 5×10^{-18} at 300 K to 0.03 at 2000 K. Future fine tuning will address this problem in more detail.

For most of the ions, the calculated and experimental profiles were in agreement within the accuracy of the data. The cation $C_{11}H_9^+$ measured value exceeded the calculated value by three orders of magnitude. This led to large discrepancies for $C_{12}H_9^+$ and $C_{13}H_9^+$. Large cations have many isomers, but the estimated thermodynamics for those we chose had little effect on the agreement. Arbitrarily increasing the stability of $C_{11}H_9^+$ by 100 kJ, about 10%, achieved the agreement reported in Figs. 1 and 2. The ion growth paths through even and odd carbon atoms are only loosely coupled.

Our next efforts will be to extend the comparison between calculated and experimental ion concentrations to 560 u, the maximum for which experimental data are available. We will then return to the problem of starting the model with neutral reactions; presumably the neutral mechanism will be in better shape by then so that this can be done. It would be advantageous to remeasure the smaller ion profiles in this flame and to measure the negative ion profiles.

To better understand the driving force for soot format... we have begun to evaluate the thermodynamics of the soot formation process including estimating the thermodynamics of a typical soot molecule and including it in the equilibrium calculation where we previously neglected large polycyclic aromatic hydrocarbons. Motivation for our interest is twofold. In some earlier work at AeroChem [5], it was observed that the threshold soot index, TSI, for a number of fuels occurred at a fixed experimental temperature which was much lower than the adiabatic flame temperature. This implied that the energy which should have gone into raising the gas temperature was expended in producing soot. It would be unrealistic to assume that radiation was the major factor at the soot threshold. Another motive was to better understand a problem associated with the ionic mechanism of soot formation. In a fuel-rich system the total ion concentration decreases with increasing equivalence ratio until some critical equivalence ratio beyond the TSI where the cation concentration increases and anions are observed [6]. At this critical equivalence ratio, the nature of the ions changes and large ions begin to increase with increasing equivalence ratio. The question is, why does soot appear when the ion concentration is still falling if ions are important to the mechanism of soot formation?

Data from the literature on soot yield, acetylene concentration (the assumed soot growth species), and measured flame temperatures as a function of equivalence ratio were compared with these values

calculated using an equilibrium program which included either graphite or the soot species calculated above and a selection of large ions and large PCAH species. The choice of graphite or the calculated soot particle made little difference in the result. This comparison was made for the following systems: methane/oxygen; propane/oxygen; ethylene/air; benzene/oxygen; toluene/air; and acetylene/oxygen. Except for acetylene fuel, the experimental and calculated concentrations of acetylene and soot and where they appear with respect to equivalence ratio, differ dramatically. They both clearly appear at much lower equivalence ratios than predicted. The ratio of measured to calculated concentrations of acetylene is especially dramatic, varying from 10 for fuel acetylene to 10^8 for methane. Results for methane are presented in Fig. 3. Measured flame temperatures are consistently lower than adiabatic. $CO+H_2$ on the abscissa indicates where writing the stoichiometry for combustion leads to CO and H_2. This point is very important in determining when thermodynamics predicts the appearance of soot formation.

Since soot is a nonequilibrium product it requires a driving force from a nonequilibrium precursor; something must be present in excess of equilibrium to initiate the process. For the free radical mechanism, it is assumed that the hydrogen atom concentration exceeds equilibrium and is the driving force. The ionic mechanism assumes that chemiions formed in excess of equilibrium are the driving force. The importance of nonequilibrium acetylene, and presumably diacetylene, concentrations is apparent from this study. Hydrogen atoms or ions might still play a role, because it has been demonstrated that the mechanism does not involve the polymerization of acetylene. Since more acetylene is involved in the growth phase of the ionic mechanism than ions, only one ion per soot particle is involved, the soot formation process may be written:

$$\frac{d\ (SOOT)}{dt} = k \times I \times A^n$$

where k is a rate constant, I is the concentration of ions, A is the concentration of acetylene and n is an integer much greater than 1. Thus both ions and acetylene must be present, and this occurs at an equivalence ratio where the ion concentration is falling and the acetylene concentration is rising with increasing equivalence ratio.

The following people have made a major contribution to this program: Drs. R.J. Gill and D.G. Keil

REFERENCES

1. Calcote, H.F., "The Role of Ions in Soot Formation," AeroChem TP-501, presented at International Workshop, Mechanisms and Models of Soot Formation, Ruprecht-Karls-Universitat, Heidelberg, Germany, 29 September-2 October 1991.

2. Berman, C.H. and Calcote, H.F., "Extension of Langevin Theory for Ion-Molecules to Large Ions," in preparation.

3. Calcote, H.F., Gill, R.J., and Egolfopoulos, F.N., "A Detailed Model of an Ionic Mechanism of Cation Growth in Flames," in preparation.

4. Calcote, H.F., Gill, R.J., and Berman, C.H., "Modeling Study to Evaluate the Ionic Mechanism of Soot Formation," Annual Report, AeroChem TP-508, April 1992.

5. Olson, D.B., "Soot Formation in Synfuels," Final Report, AeroChem TP-433, DOE/PC 30304-5, June 198; see also, Olson, D.B. and Madronich, S., Combust. Flame 60, 203-213 (1985).

6. Keil, D.G., Gill, R.J., Olson, D.B., and Calcote, H.F., Twentieth Symposium (International) on Combustion (The Combustion Institute, Pittsburgh, 1985) pp. 1129-1137.
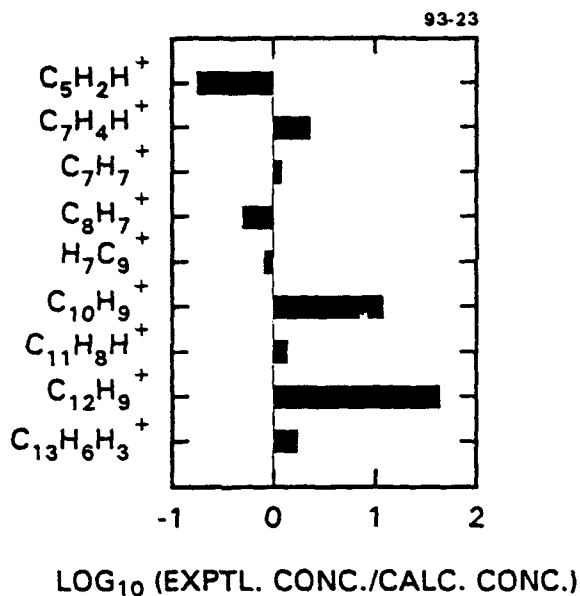
93-23

$C_5H_2H^+$
$C_7H_4H^+$
$C_7H_7^+$
$C_8H_7^+$
$H_7C_9^+$
$C_{10}H_9^+$
$C_{11}H_8H^+$
$C_{12}H_9^+$
$C_{13}H_6H_3^+$

-1 0 1 2

LOG_{10} (EXPTL. CONC./CALC. CONC.)

Fig. 1 Comparison of Maximum
Calculated and Experimental
Cation Concentrations.
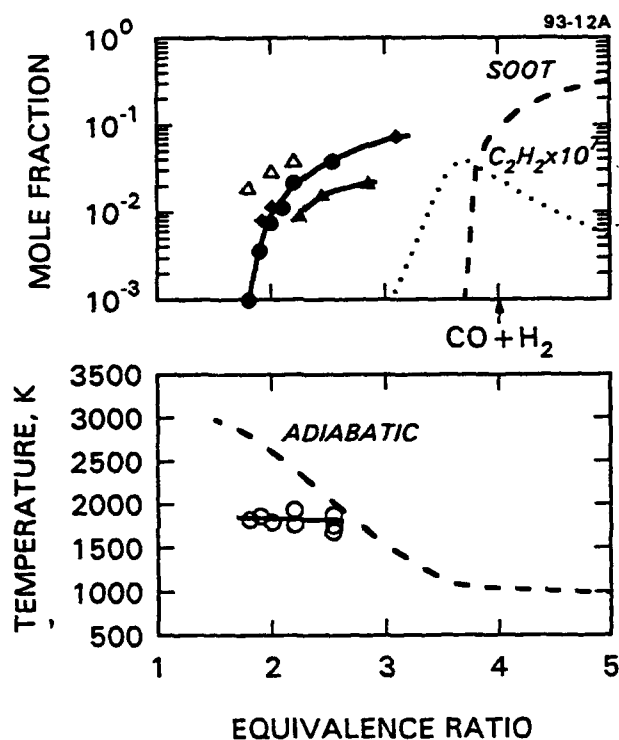Acetylene/Oxygen Flames at 2.67 kPa,
Equivalence Ratio = 3.0

93-12A

MOLE FRACTION

10^0
10^{-1}
10^{-2}
10^{-3}

SOOT
$C_2H_2 \times 10$
CO + H_2

TEMPERATURE, K

3500
3000
2500
2000
1500
1000
500

ADIABATIC

1 2 3 4 5

EQUIVALENCE RATIO

Fig. 3 Comparison of
Equilibrium and Experimental
Acetylene, Soot, and Flame
Temperatures for Methane/Oxygen
Flames at 1 atm

93-25

MOLE FRACTION

10^{-8}
10^{-9}
10^{-10}
10^{-11}
10^{-12}
10^{-13}

$H_7C_9^+$

$C_{10}H_9^+$

$C_{11}H_8H^+$

$C_{12}H_9^+$

$C_{13}H_6H_3^+$

0.0 0.5 1.0 1.5 2.0 2.5

DISTANCE, cm
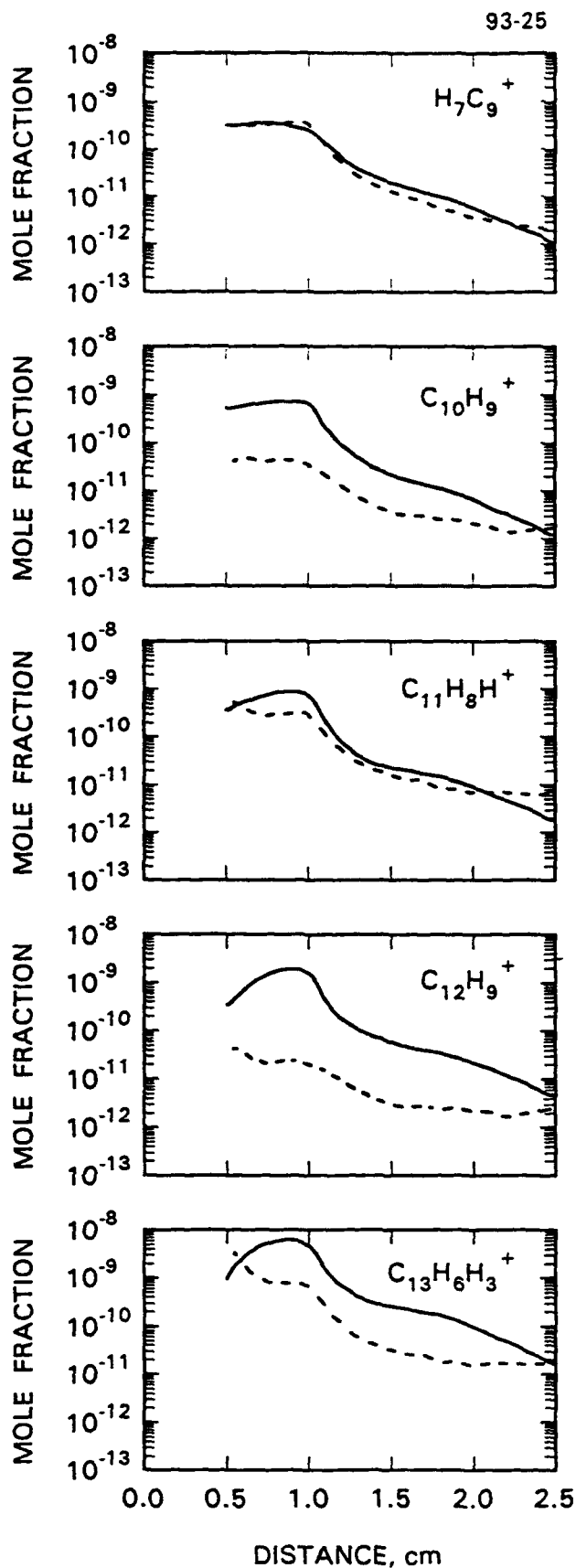
Fig. 2 Comparison of
Calculated (− −) and Experimental (—)
Cation Profiles

TITLE: HEAT TRANSFER, FOULING, AND COMBUSTION OF SUPERCRITICAL FUELS

Contract No. F49620-92-J-0462

Principal Investigator:

L.-D. Chen
The University of Iowa
Department of Mechanical Engineering
Iowa City, Iowa 52242

SUMMARY/OVERVIEW:

A simulant fluid is used to study the spray of supercritical fuel injection into high pressure combustor-like environments. A combined theoretical and experimental approach is employed. The experiments will identify the regimes of supercritical sprays into combustor-like environments. The analysis will provide information on the spray regimes from thermodynamic considerations, and simulation for spray structures.

TECHNICAL DISCUSSION

A simulant fluid is used to study the spray of supercritical fuel injection into to combustor-like environments. The simulant fluid is sulfur hexafluoride (SF_6); its critical temperature is 318.7 K and critical pressure is 37.1 atm. SF_6 was injected into a pressure chamber, filled with N_2. The nitrogen was maintained at near- or super-critical pressures of SF_6, but at room temperature or subcritical temperature of SF_6. The pressure chamber is fitted with four viewing windows of 15 mm by 300 mm in size. The apparatus is shown in Fig. 1. During the experiments, liquid SF_6 was delivered to a feed cylinder (2.5 liters in volume) and pressurized by helium to desired pressures. Heating of the pressurized SF_6 is accomplished by passing the fluid through a hot water bath. A straight-through nozzle with the injector diameter of 135 μm is used. The spray chamber and the nozzle assembly were designed by G.L. Switzer (SRL, a Division of Arvin/Calspan).

The planar light scattering technique was used for visualization of the spray. The light source is a He-Ne laser (2 mW); in conjunction with a cylindrical lens, a thin laser sheet is formed. The laser sheet is position through the center of the spray. The light scattering from the spray is recorded by a CCD video camera which is positioned at a right angle from the laser sheet.

During the injection of subcritical SF_6 (Pr = 0.91 and Tr = 0.91, where Pr is the reduced pressure and Tr the reduced temperature) into a subcritical environment, a "usual" spray image is seen, cf. Fig. 2(a). "Reduced" pressure (Pr') and "reduced" temperature (Tr'), based on SF_6 critical properties, will be used to denote the nitrogen condition. The chamber temperature is kept constant throughout the experiments reported here. The nitrogen of Fig. 2(a) is maintained at Pr' = 0.85 and Tr' = 0.92. When the SF_6 pressure is increased to Pr = 1.15, but not its temperature, a similar spray pattern is observed, cf. Fig. 2(b). The chamber pressure of Fig. 2(b) is increased to Pr' = 1.06; a similar pressure drop across the spray nozzle is maintained, however. When SF_6 is heated to Tr = 1.00 and Pr kept at 1.12, a slightly longer spray penetration length and a wider spray angle can be seen from Fig. 2(c), compared to Fig. 2(b), although the pressure drop in Fig. 2(c) is about 25% lower than Fig. 2(b). The chamber nitrogen is maintained at Pr' = 1.06.

When SF_6 temperature is increased to Tr = 1.03, and keeping Pr = 1.13, a substantial decrease in spray penetration length is seen, cf. Fig. 2(d). The chamber pressure is at Pr' = 1.07. Under the condition of Fig. 2(d), the injection process seems to show characteristics of dense fluid mixing.
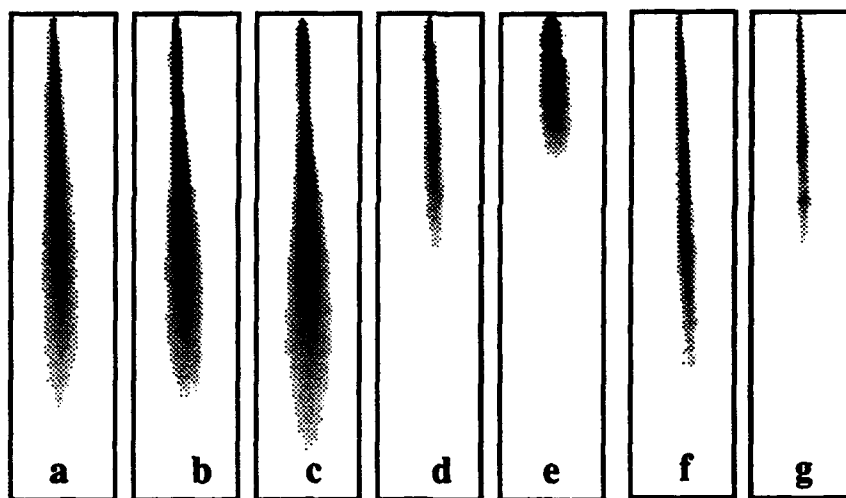
Figure 1. Experimental Set-Up

Figure 2. Light Scattering of Spray Patterns. Injector Conditions (Tr, Pr) and Chamber Pressure (Pr') are (Tr, Pr; Pr') = (a) (.91, .91; .85), (b) (.91, 1.15; 1.06), (c) (1.00, 1.12; 1.06), (d) (1.03, 1.13; 1.07), (e) (1.07, 1.10; 1.04), (f) (1.05, .96; 1.03), (g) (1.07, 1.15; 1.13).

The discrete liquid drops typical of spray process is not obvious at the conditions examined. The "dense fluid" mixing is reproducible, and it is even more evident when the injected SF_6 temperature is further increased, e.g., to Tr = 1.07, shown in Fig. 2(e). The chamber pressure of Fig. 2(e) is maintained at Pr = 1.04; thus, a similar pressure drop as the condition of Fig. 2 (d) is maintained.

When the injector (SF_6) pressure is reduced to subcritical pressure, although a supercritical temperature is maintained, a narrow spray pattern is seen in Fig. 2(f). The spray penetration length is much longer than Fig. 3(d) which has a higher SF_6 pressure and a lower SF_6 temperature. The injector pressure drop is also higher in Fig. 3(d). When the injector pressure is increased to Pr = 1.15, the spray penetration length is reduced, Fig. 2(g). At this condition, the spray pattern is similar to Fig. 2(d).

The light scattering visualization of supercritical fluid injection into high pressure environments suggest that the thermodynamic state of the injector fluid is an important physical property. When both the temperature and pressure are maintained above the critical values of the injected fluid, the light scattering region is confined to a relatively narrow region in the flow. This observation suggests that the flow field, except the core region of the jet, seems to be characteristic of dense fluid mixing.

To assist our understanding of the mixing process in the injection of supercritical fluid, the state relationship is obtained based on the adiabatic mixing and isobaric injection assumptions. The enthalpy departure functions due to compressibility effects are obtained following the Lee-Kesler formulation, and the mixing rule of Chueh and Prausnitz is used to estimate the binary interaction coefficients for mixture critical properties. The results based on the injected fluid at $Pr = 1$ and $Tr = 1$, and chamber nitrogen at $Pr' = 1$ and $Tr' = 0.94$ are shown in Fig. 3. The prediction shows that when mixture fraction (f) is greater than 0.8, the mixture temperature and pressure are below its critical values. Conversely, liquid phase may be present in the region of f > 0.8. This narrow region in mixture fraction space is consistent with the short and narrow core of the spray image illustrated in Fig. 2 during the injection of supercritical fluids.

It must be cautioned that several essential questions need to be answered before a definitive assessment can be given to the spray regimes resulting from the injection of supercritical fluids. The first question is the detectability of the light scattering and the effects due to aerodynamic atomization versus the effects due to the injector thermodynamic states. The question on the detectability of light scattering will be addressed by employing, simultaneously, the techniques of laser induced fluorescence (to mark the vapor phase) and light scattering (to mark the droplets). A better flow control system for the injector fluid will be acquired. This flow system will deliver the injector fluid at prescribed flow rates, and at desired pressures and temperatures. Also will be investigated are simulant fluid pairs for better simulation of the fuel injection process for advanced jet engine considerations.
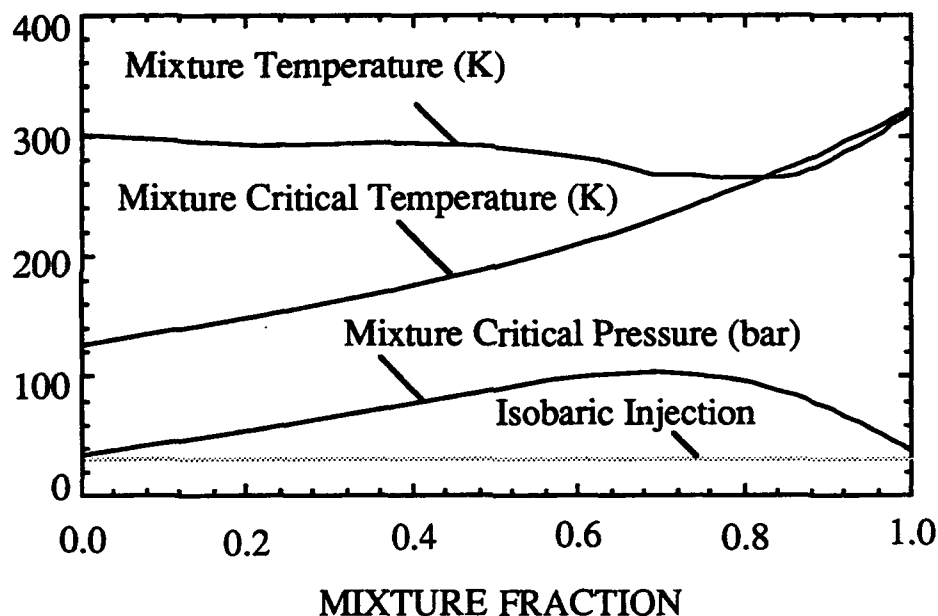

Figure 3. State Relation of SF_6 Injection Into N_2; SF_6 at $Pr = 1$ and $Tr = 1$, and N_2 at $Pr' = 1$ and $Tr' = 0.94$.

During the report period, numerical investigation of heat transfer to supercritical fuels is also conducted. A subcooled fuel inlet state for hexadecane (at 298 K and 14 atm) is considered under a constant wall temperature condition. The wall temperature is maintained at the critical temperature of hexadecane (722 K) and the system pressure is maintained at its critical pressure (14 atm). The purpose of the calculation is to examine the effects on the heat transfer due to property variations near thermodynamic critical point. The initial results suggest that the heat transfer effectiveness decreases when it is compared to the calculation using the liquid properties without corrections for near-critical point behavior. More calculations are needed before we can reach a conclusive assessment regarding the property effects to laminar forced convective heat transfer. Calculations to predict the turbulent heat transfer behavior to fluids at a near critical state will be performed with smooth, as well as rough, heated surfaces, following the conclusion of the laminar heat transfer study. The rough surface is intended to simulate the fouling in fuel passages of the jet engines. Unsteady flow calculation will also be performed to evaluate the effects or enhancements of heat transfer due to flow unsteadiness.

DEVELOPMENT OF A TECHNIQUE TO DETERMINE THE MORPHOLOGY AND DYNAMICS OF AGGLOMERATES IN CHEMICALLY REACTING FLOWS

AFOSR   GRANT   F49620-92-J-0447

Principal   Investigator: Tryfon   Charalampopoulos

Mechanical   Engineering   Department
Louisiana   State   University
Baton   Rouge,   LA   70803

SUMMARY/OVERVIEW

Knowledge of the size and shape of particulates formed in chemically reacting flows such as hydrocarbon flames or liquid fuel jet systems is significant in various areas of research and practical applications.   Information about the size and shape of particulates can be used in predicting their growth and oxidation in flame systems. Production of ceramic and superconducting materials through the aerosol route requires monitoring of the particle size and shape under flame conditions.   On the other hand, fine particle control in the electronics industry requires reliable methods for determining the physical properties of particulates.   The objective of this study is to determine the morphology and dynamics of flame particulates under in-situ conditions utilizing their absorption/scattering and optical anisotropic properties.   In the next section it is shown that the approximate relations for scattering/absorption cross-section of agglomerated soot particles are accurate to within 20% and that the depolarization ratios may be used as a diagnostic tool for soot agglomerate characterization under flame conditions.

TECHNICAL DISCUSSION

The existence of aggomerated soot structures in flame systems has been noted by several investigators [1-4].   The absorption and scattering cross sections of agglomerates can be predicted using the integral equation formulation [2-3] and by approximate, less computationally intensive, relations [5-6].   Recently it was noted that depolarized light scattering measurements in sooting flames possess the potential to yield agglomerate morphology information when combined with scattering/absorption agglomerate and dissymmetry measurements.   Limited calculations of the depolarized components of the scattering field were presented by Jones [6] and it was concluded that the reciprocity relation is valid, namely it was inferred that $H_V = V_H$ (see Figure 1).   Here the subscripts represent the state of polarization of the incident light beam and the symbols V and H represent the state of polarization of the scattered beam.   More specifically V or v and H or h represent the vertical and horizontal polarization orientation respectively.   The approximate expression for the extinction cross section of the agglomerate is given as

$$C_{e,a} = N_p \, C_{e,s}$$

where N_p is the number of primary particles in an agglomerate and $C_{e,s}$ is the extinction cross section of a single spherical particle having same diameter and refractive index as the primary particles.

The percentage difference in extinction cross section using the exact [6] and approximate expression was calculated for different types of agglomerates and different ranges of agglomerate parameters. Results for straight chain agglomerate are shown in Figure 2 and 3. With reference to Figure 3 it may be seen that the percentage error is an increasing function of both real and imaginary part of refractive index, and is within 14.75%. In Figure 2 it is shown that the percentage error between the exact and approximate expression of extinction cross section is within 18%. It is also noted that the difference increases with increasing number of primary particles whereas it is a weak function of the size parameter. Similar trends of percentage error are observed for clusters. Specifically, the percentage difference is below 5% for the range of refractive indices ($1.4 \leq n \leq 20$ and $0.4 \leq k \leq 1.0$), the number of primary particles ($3 \leq N_p \leq 30$) and the size parameter ($0.01 \leq x_p \leq 0.1$). For a random chain agglomerate the percentage difference is within 10% and varies randomly with the size parameter, the number of primary particles and the refractive index.

The depolarized scattered intensities H_v and V_h were calculated for straight chains, cluster and random structures using Jones' model as function of the diameter of primary particles, number of primary particles and refractive index. The refractive indices of the flame soot used in the calculations were those obtained in a propane oxygen flame [7]. In Figure 3 the H_v to V_h ratio for straight chain is shown as a function of the scattering angle for conditions corresponding to different residence times in premixed propane/oxygen flame. The maximum deviation from the reciprocity theorem ($H_v/V_h = 1.0$) varies between -15% and 35%. For clusters the maximum deviation was between -15% to 335%. Calculations of H_v to V_h ratio for random chain as function of the scattering angle and of the primary particle number ($3 \leq N_p \leq 18$) (with $m = 1.6 + 0.53 i$, and $d_p = 0.0156 \mu m$) resulted in a 20% deviation. This result indicates that H_v and V_h when measured independently will yield independent pieces of data that can be used in the data analysis for morphology characterization of the agglomerate.

The results of the numerical calculations pointed to the need of experimental measurements to further study the validity of the reciprocity relations for agglomerates. It should be noted that in the agglomerate model multiple scattering between the primary particles was accounted for. Extinction and multiangle light scattering measurements of polystyrene particles (0.22 micron diameter) dispersed in purified deionized water were used in the present study. The differential scattering coefficient of the vertical-vertical polarization at 90°, the transmission and the depolarized scattering coefficient at different angles were measured. The differential scattering coefficient was determined by an internal calibration procedure using propane gas [7]. In order to test the light scattering set-up the ratio of the measured propane and methane differential scattering cross-sections at 90° were compared to previous results [8] before each experimental run.

The measured scattered intensity from the polystyrene suspension normalized with the scattered intensity at 90°, was compared with the Mie theory prediction at different scattering angles for dilute suspensions. It was observed that reflections from the scattering cell contributed to the scattered intensities in the forward and backward scattering directions. The best agreement with the Mie theory predictions was in the angular range of 60° to 130°.

In order to simulate the effects of multiple scattering, high particle number densities were used to measure the H_v and V_h components of the scattered intensities at different scattering angles. Figure 4 shows the measured depolarized scattering coefficients for H_v and V_h orientation and their ratio as a function of scattering

angle at transmission level of 19.8%. It was observed that the H_v and V_h intensities increase with decrease in transmission or increase in number density. Their ratio is also seen to be function of transmission. Work is underway with smaller polysterene size particles to further investigate this anomaly.

In summary:

1. The approximate expression for extinction cross section of an agglomerate was found to be accurate to within 20% irrespective of the type of agglomerate, size range and number of primary particles.
2. The ratio of the depolarized scattering components (H_v/V_h) was found to depend strongly on agglomerate parameters and the type of agglomerate.
3. The preliminary experimental results indicate that there is a need for further investigation of the validity of the reciprocity relations in dense particle dispersions, and
4. The depolarization ratios may be used as diagnostic tools for agglomerate characterization.

References

1. Jones, A.R. and Wong, W. Combust. Flame 24:139 (1975).
2. Jones, A.R. J. Phys. D.: Appl. Phys. 12:166 (1979).
3. Jones, A.R. Proc. R. Soc. London A361:111 (1979).
4. Charalampopoulos, T.T. Prog. Energy and Comb. Sci. 18:13 (1992).
5. Charalampopoulos, T.T. and Chang, H. Comb. Flame 87:89 (1991).
6. Kumar, S. and Tien, C.L., Comb. Sc. Technol. 66:199 (1989).
7. Chang, H. and Charalampopoulos, T.T. Proc. R. Soc. London 430:577 (1991).
8. Rudder, R.R. and Bach, D.R. J. Opt. Soc. Amer. 58:1260 (1968).
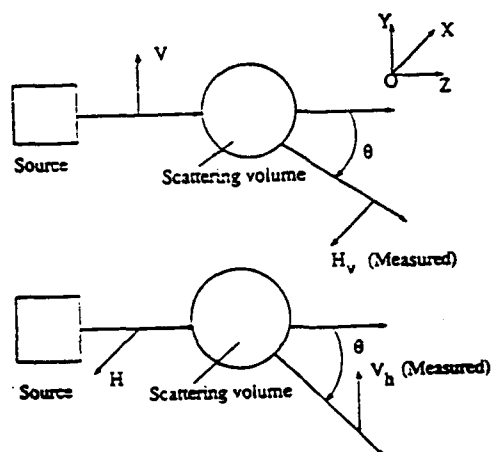
RECIPROCITY THEOREM

$$H_v = V_h$$

Figure 1. Depolarized scattering coordinate system.
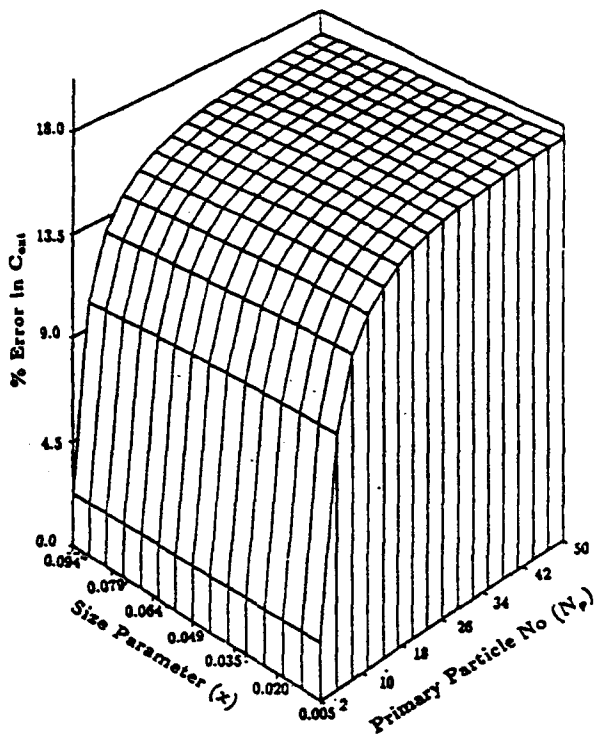
Figure 2. Percentage error in extinction cross section of straight chain with $\bar{m} = 2.0 + 1.0\,i$ with correction.
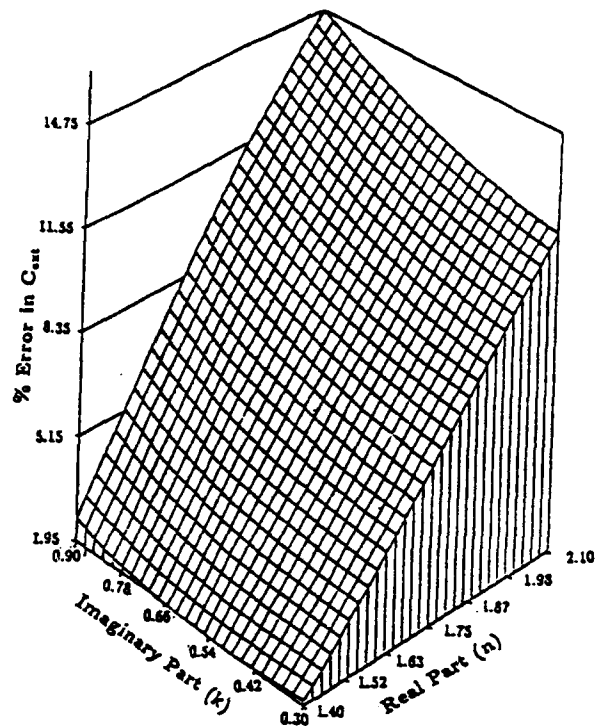
Figure 3. Percentage error in extinction cross-section of straight chain with $N_p = 10$ and size parameter of 0.01 with correction
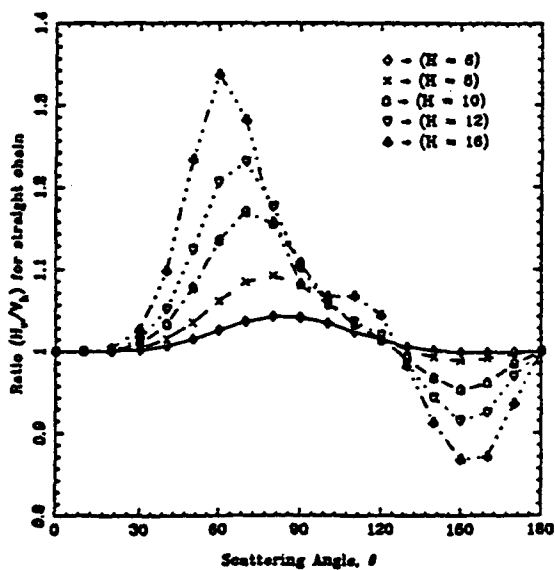
Figure 4. H_v to V_h ratio with respect to scattering angle for straight chain at different positions in the flame.
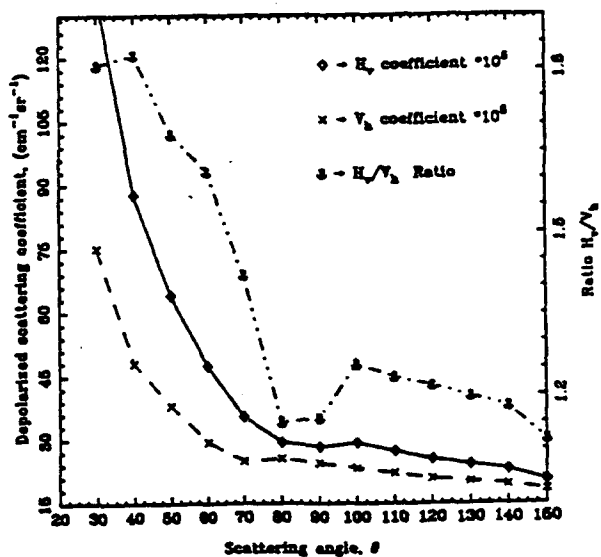
Figure 5. Depolarised scattering coefficients and their ratio versus scattering angle for polystyrene sphere 0.22 μm in diameter at 19.9% transmission.

MECHANISTIC MODELS FOR SOOT FORMATION

AFOSR Contract No. F49620-91-C-0056

Principal Investigators: M. B. Colket, III and R. J. Hall

United Technologies Research Center
East Hartford, CT 06108

SUMMARY/OVERVIEW

The overall objectives of this work are to (1) refine and update an existing soot formation model and (2) with the assistance of M. Smooke, incorporate this soot model into a code describing a laminar, opposed jet diffusion flame. To help advance the understanding of chemical limitations of PAH formation in the soot model, hydrocarbons have been pyrolyzed in a single-pulse shock tube. Benzene production and radiation phenomena have been modeled in an opposed jet diffusion flame and where possible these calculations have been compared to experimental results. A sectional aerosol model has been added to the diffusion flame code as well as related subroutines on soot formation, growth, and oxidation and the debugging of the code is nearly complete.

TECHNICAL DISCUSSION

A. Pyrolysis of Phenylacetylene

Phenylacetylene (0.25% in a bath of argon) has been pyrolyzed in a single-pulse shock tube as part of an effort to understand growth reactions, i.e., PAH formation, during the pyrolysis of hydrocarbons. Products have been analyzed using a gas chromatograph coupled to a mass selective detector. Light hydrocarbons are principally acetylene, diacetylene, and benzene.

Several principal product species have a mass 178 amu and the most dominant of these is believed to be phenanthrene. The less dominant species with this mass are believed to be isomers of ethynylbiphenyl. Small concentrations of napthalene, diethenylbenzene, naphthylacetylene, and acenaphthylene are also observed. The lack of anthracene production supports arguments that phenanthrene formation is kinetically limited and (at least for the phenylacetylene system) the growth mechanism involves interactions between aromatic rings and acetylenic species. The dominance of phenanthrene in the mass 178 amu species supports arguments for rapid isomerizations and acetylene elimination steps to form resonantly stabilized aromatic structures. The lack of substantial concentrations of pyrene and larger species suggests very rapid reactions between these species and phenylacetylene causing additional growth.

B. Benzene Predictions in Methane/Air Diffusion Flames

Last year it was shown that benzene products during the oxidative pyrolysis of methane was due to reactions between C_3H_x species. Using this result a simplified benzene production model was constructed[1] together with several steps describing benzene pyrolysis and oxidation., This mechanism was added to a methane kinetics set (including

C_2-hydrocarbon chemistry) which has been used previously for modeling methane opposed jet flames. Benzene profiles were then predicted in an opposed jet diffusion flame. Peak benzene profiles are shown in Fig. 1 for flames with very low stretch through extinction. As shown in Fig. 1, as flame stretch increases, benzene production initially drops rapidly and then decreases more slowly with increasing stretch. Du, Axelbaum and Law[2] found that the sooting limit occurs in the region of rapid benzene decrease with flame stretch, and these results are therefore qualitatively consistent with linkage between benzene production and soot limits.

Temperatures at the location of peak benzene concentrations are plotted along with peak flame temperatures in Fig. 2 for flames of varying stretch. This figure indicates that benzene production in diffusion flames occurs at temperatures near 1400K, much lower than 1800K at which benzene was formed in the shock tube experiments on rich methane oxidation. Since dominant kinetic pathways can be altered by a substantial shift in temperature, the full kinetics set (all known mechanisms of benzene formation included) were used to recalculate selected diffusion flames. Under all conditions only trivial changes were observed in the benzene profile, confirming the earlier result of the importance of propargyl species to benzene production in methane systems.

In addition, an attempt was made to model a nitrogen diluted methane studied by Zhang, Atreya and Lee[3]. All major species were predicted well. Shapes of C_2-species were described well but typically peak concentrations were modeled only within a factor of two to three, perhaps due to the use of only a skeleton C_2-hydrocarbon mechanism. Benzene profiles were predicted very well (shape and peak concentration) although this result may be somewhat fortuitous due to the inadequacy in the comparison of the C_2-species.

In general, these kinetic results are very encouraging for the soot modeling effort in that opposed jet diffusion flames can be modeled fairly inexpensively with chemistry describing species as large as benzene. For example, in order to determine benzene concentrations, etc., as a function of strain rate, 567 flames were calculated in 12 hours using an IBM RS6000 workstation.

C. Radiative Transfer in Sooting Opposed Jet Flames

Our previous investigations of radiative transfer in non-sooting opposed jet flames showed that, for realistic values of strain rate, up to 5% of the flame enthalpy release could be converted to thermal radiation. The accompanying reduction in peak flame temperatures gave rise to substantial reductions of about 33% in the peak NO concentrations[4]. At very low strain rates and high pressures, where the pressure-flame width product can be one atm-cm or more, it was shown that optical thickness effects can become important and an expression was derived for self-absorption[5]. Radiative loss effects can be particularly large in sooting flames. To assess the effect in sooting opposed jet flames, the gas band expressions for the net cooling rate have been extended to include soot. The problem has traditionally been a difficult one because of the overlaps between the broadband soot absorption profile and the molecular resonances. Net gas cooling results from radiative emission minus self-absoprtion. The self-absorption term has been derived from a solution for the radiative intensity by taking hemispherical and wavelength averages. The result is a semi-analytical expression for the net cooling rate in which the emission is offset by soot and gas self-absorption, and by soot-gas radiative interchange[6]. Figure 3 shows the calculated radiative loss in a model sooting diffusion flame in which a band of soot has been synthetically inserted between the flame and the stagnation plane, and the peak soot volume fraction varied parametrically. The flame is at 10.5 atmospheres and the strain rate

is 20 sec^{-1}; the fuel and oxidizer temperatures have been chosen to give a peak flame temperature approximating that of jet fuel[4]. The assumed location of the sooting region is such as to produce an effective radiation temperature for the soot of about 1500K, about 900K cooler than the peak flame temperature. Gas band self-absorption is important at this combination of pressure and strain rate. For peak soot volume fractions in excess of roughly 10^{-5}, soot radiative transfer begins to dominate, and predicted radiative loss fractions rise to the level of 20%. At the highest volume fractions, the reduction in temperature in the sooting region is large enough to raise the possibility of strong interactions between soot growth and soot radiation. These effects are, however, strongly sensitive to the presumed location and radiative temperature of the soot. A self-consistent analysis will be provided by the coupled soot growth-opposed jet flow code whose development is described below.

D. Coupling of Soot Growth Model and Opposed Jet Flow Code

The soot growth equations have been programmed into an opposed jet flow solver, and debugging is proceeding. The dynamical equations for the particulate concentrations include nucleation coupled to the benzene production rate, particle coalescence, surface growth, and oxidation. This work marks the first time that particle sectional growth equations have been coupled to the conservation equations for a diffusion flame. Particle diffusion and thermophoresis velocities in the free molecule regime have been included. The first set of calculations have been based on a perturbation approximation in which particle thermochemistry and depletion of gas phase species like acetylene by surface growth are assumed to be small. The next stage will include these effects, as well as radiative loss.

References

1. M. B. Colket and M. D. Smooke, "The Formation of Benzene from Methane", Presented to the Joint Technical Meeting of The Central and Eastern States Sections of the Combustion Institute, New Orleans, March 15-17, 1993.

2. D. X. Du, R. L. Axelbaum, and C. K. Law, Twenty-Second Symposium (International) on Combustion, The Combustion Institute, p. 387, 1988.

3. C. Zhang, A. Atreya, and K. Lee, Twenty-Fourth Symposium (International) on Combustion, The Combustion Institute, p. 1049, 1992.

4. A. Vranos and R.J. Hall, "Influence of Radiative Loss on Nitric Oxide Formation in Counterflow Diffusion Flames at High Pressure", to appear in Combustion and Flame, 1993. Also see R. J. Hall, "Radiative Transfer in Sooting Counterflow Flames", Presented to the Joint Technical Meeting of the Central and Eastern States Sections of the Combustion Institute, New Orleans, March 15-17, 1993.

5. R.J. Hall, "The Radiative Source Term for Plane-Parallel Layers of Reacting Combustion Gases", to appear in JQSRT, 1993.

6. R. J. Hall, "Radiative Dissipation in Planar Gas-Soot Mixtures", to be submitted to JQSRT, 1993.

Fig. 1
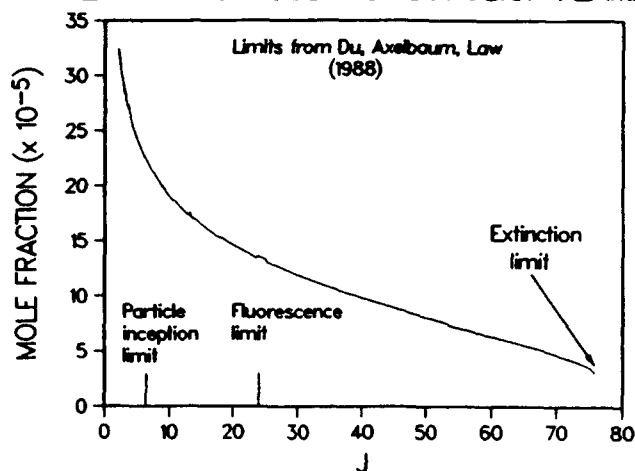## PEAK BENZENE AS FUNCTION OF STRAIN
LAMINAR OPPOSED JET DIFFUSION FLAME

Fig. 2
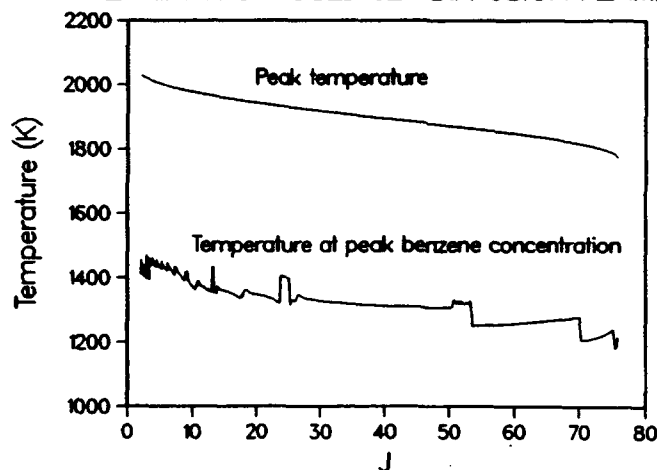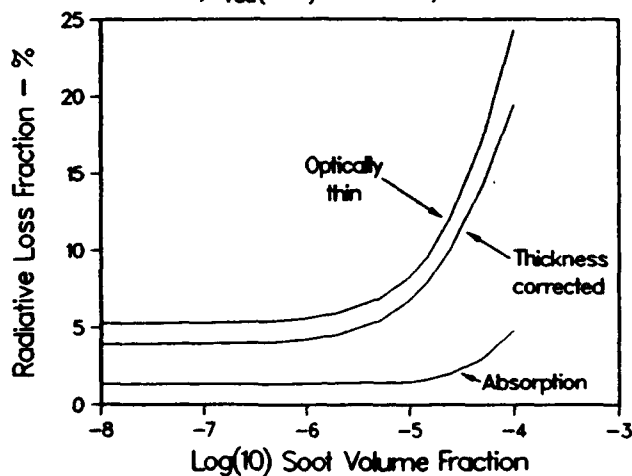## TEMPERATURES vs. STRAIN RATE
LAMINAR OPPOSED JET DIFFUSION FLAME

Fig. 3
RADIATIVE LOSS vs SOOT LOADING
10.5 atm; T_{rad}(soot) = 1500 K; a = 20.5 sec^{-1}

COMPUTER SIMULATION OF MOLECULAR INTERACTIONS IN SUPERCRITICAL SOLVENTS

(AFOSR GRANT NO. F49620-93-1-0040)

Principal Investigator: Pablo G. Debenedetti

Department of Chemical Engineering
Princeton University
Princeton, NJ 08544-5263

SUMMARY/OVERVIEW

The cooling requirements of future aircraft are expected to be sufficiently demanding as to require the fuel to operate at supercritical conditions. Currently, there is a lack of fundamental understanding of key aspects of the behavior of fluids and their mixtures at supercritical conditions (e.g., molecular interactions, solvation mechanisms, transport properties, reaction kinetics, and mechanisms of nucleation and particle growth). A large body of experimental [1-7], theoretical [8-10] and computational [11-12] evidence suggests that in so-called attractive [13] supercritical mi, tures, the local environment surrounding solute molecules (microstructure) differs appreciably from the bulk. The goal of this project is to investigate solute-solute, solute-solvent, and solute-cosolvent molecular interactions at supercritical conditions using computer simulations and theoretical calculations, and to compare the calculations with spectroscopic probe experiments of solvation dynamics at supercritical conditions. The work reported here is a theoretical investigation, via integral equations, of the microstructure around solute molecules in dilute supercritical mixtures, and its relationship to solubility.

TECHNICAL DISCUSSION

Two binary Lennard-Jones mixtures were studied: one, attractive (in which a large solute molecule having a relatively large characteristic interaction energy is dissolved in a smaller, more weakly interacting solvent); the other, repulsive (in which a small solute molecule is dissolved in a larger, more strongly interacting solvent) [13]. Both systems were studied at high dilution, at supercritical temperature, and over a broad range of reduced densities ($0.33 < \rho/\rho_c < 1.6$ for the attractive system; $0.33 < \rho/\rho_c < 2.3$ for the repulsive one). The attractive system exhibited significant short-ranged solvent enrichment around the solute. In contrast, the repulsive system exhibited solvent depletion. The solute's fugacity coefficient (whose reciprocal is proportional to the solubility enhancement with respect to ideal gas behavior) was calculated as a function of a variable distance cutoff, beyond which the mixture was assumed to be uniform. The value of the cutoff beyond which no further change in the fugacity coefficient results is thus an unambiguous measure of the size of the local region around solute molecules that is important for solubility. Over the range of conditions studied here, this quantity ranged from 3 to 5 solvent diameters for the attractive mixture, with the maximum occurring close to the solvent's critical density.

The intermolecular potential parameters for the two model mixtures used in this study are given in Table 1.

Table 1: Lennard-Jones Potential Parameters for Model Mixtures[a,b]

Mixture	Interaction	σ (Å)	ε/k (K)
Attractive	Solute-solute	6.199	554.4
	Solvent-solvent	3.794	225.5
	Solute-solvent	4.996	353.4
Repulsive	Solute-solute	2.820	32.8
	Solvent-solvent	4.047	231.0
	Solute-solvent	3.433	87.0

[a] The asymmetry of the attractive mixture corresponds to naphthalene (solute) in carbon dioxide (supercritical solvent). The asymmetry of the repulsive mixture corresponds to Neon (solute) in Xenon (supercritical solvent).

[b] The Lennard-Jones potential is given by $\phi(r) = 4\varepsilon [(\sigma/r)^{12} - (\sigma/r)^{6}]$.

For each of these mixtures, calculations were performed using the Percus-Yevick closure [14] of the Ornstein-Zernicke equations, and the Gillan-Labik numerical technique [15-16] to solve the resulting system of equations. To simulate infinite dilution, the solute's mole fraction was fixed at 10^{-9}. All calculations were done at a reduced temperature of 1.07 with respect to the solvent's critical point. The critical density and temperature of the Lennard-Jones fluid in the Percus-Yevick approximation are $\rho\sigma^3 = 0.28$ and $kT/\varepsilon = 1.31$, respectively.

Figure 1 shows the solute-solute pair correlation function for the attractive mixture (hence naphthalene-naphthalene). Particularly noteworthy is the very high first peak, which attains its maximum value at a reduced density of 0.58 (with respect to the solvent's critical density). Figure 2 shows the relationship between local and bulk densities around solute molecules within three solvation shells, also for the attractive mixture. Note the broad range of bulk densities within which the local density is substantially higher than in the bulk.

In sharp contrast with the solvent enrichment around the solute for attractive mixtures, Figure 3 shows the relationship between local and bulk Xe densities around Ne. Here, a local density at a particular radial location denotes the average density within the given sphere. Note the remarkable correlation hole at near-critical density. This is a highly unusual feature, insofar as correlation holes normally occur only in structured, complex molecules at very high density, due to packing constraints.

The most significant result of this study is shown in Figure 4. It depicts the size of the region needed to recover a given percentage of the true fugacity coefficient. Note the

peak around the critical density. This is an unambiguous determination of the size of the local region that contribute to solvation.

In the attractive mixture, the microstructure is solvent-rich with respect to the bulk. This enrichment persists even when the solvent's density is averaged over three solvation shells, and is more pronounced in the reduced density range $0.5 < \rho/\rho < 0.8$. While the magnitude of the density enhancement in the first solvation shell is unrelated to proximity to the solvent's critical point, the persistence length of this density perturbation is directly affected by the growth of the correlation length. In the repulsive mixture, the microstructure is solvent-lean. Deviations between local and bulk conditions are particularly pronounced at the solvent's critical density.

REFERENCES

[1] Kim, S., and K.P. Johnston, **AIChEJ.**, **33**, 1603 (1987a)

[2] Kim, S., and K.P. Johnston, **Ind. Eng. Chem. Res.**, **26**, 1207 (1987b)

[3] Johnston, K.P., S. Kim, and J. Combes, **ACS Symp. Ser. 406**, 52 (1989)

[4] Brennecke, J.F., and C.A. Eckert, **Int. Symp. Supercrit. Fluids (I)**, Nice, Fr., 263 (1988)

[5] Brennecke, J.F., and C.A. Eckert, **ACS Symp. Ser. 406**, 14 (1989)

[6] Brennecke, J.F., D.L. Tomasko, J. Peshkin, and C.A. Eckert, **Ind. Eng. Chem. Res.**, **29**, 263 (1990)

[7] Brennecke, J.F., D.L. Tomasko, and C.A. Eckert, **J. Phys. Chem.**, **94**, 7692 (1990)

[8] Wu, R.S., L.L. Lee, and H.D. Cochran, **Ind. Eng. Chem. Res.**, **29**, 977 (1990)

[9] Munoz, F., and E.H. Chimowitz, **Fluid Phase Equil.**, **71**, 327 (1992)

[10] Petsche, I.B., and P.G. Debenedetti, **J.Phys.Chem.**, **95**, 386 (1991)

[11] Petsche, I.B., and P.G. Debenedetti, **J. Chem. Phys.**, **91**, 7075 (1989)

[12] Knutson, B.L., D.L. Tomasko, C.A. Eckert, P.G. Debenedetti, and A.A. Chialvo, **ACS Symp. Ser. 488**, 60 (1992)

[13] Debenedetti, P.G., and R.S. Mohamed, **J. Chem.Phys.**, **90**, 4528 (1989)

[14] Percus, J.K., and G.J. Yevick, Phys. Rev., 110, 1 (1958)

[15] Gillan, M.J., **Mol. Phys.**, **38**, 1781 (1979)

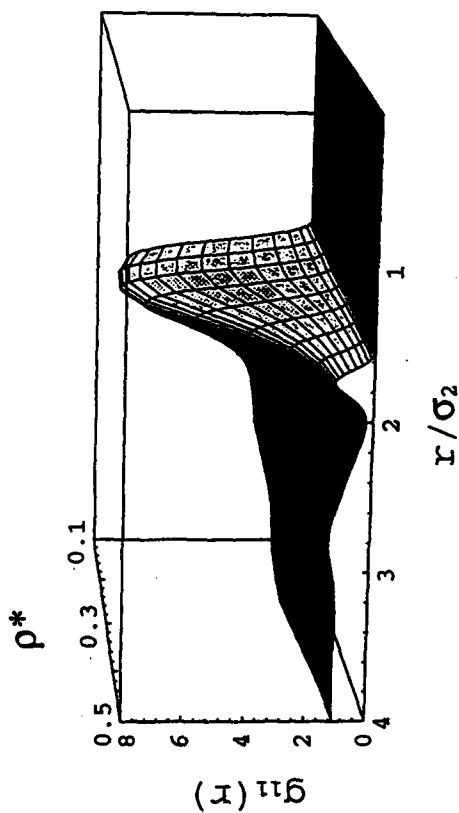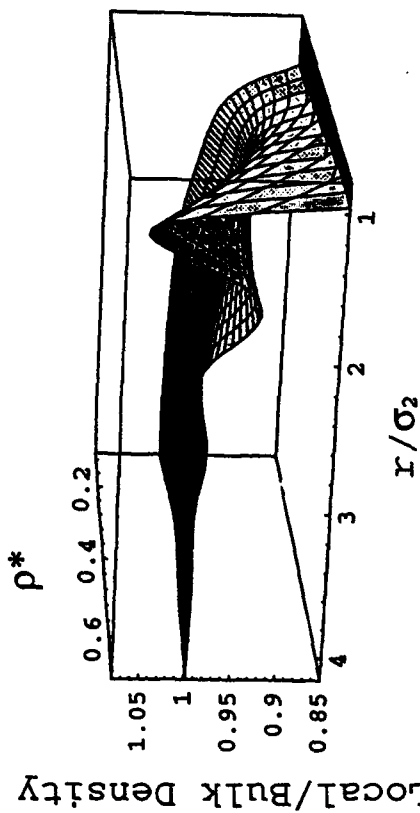[16] Labik, S., A. Malijevsky, and P.A. Vonka, **Mol. Phys.**, **56**, 709 (1985)

Figure 3: Relationship between local and bulk densities around solute molecules in the repulsive mixture (neon in xenon). Note the correlation hole at near-critical densities.
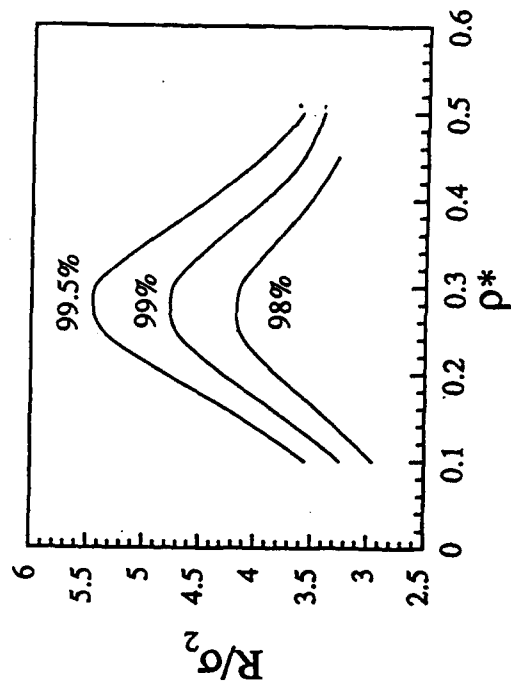

Figure 4: Radius of the spherical region around solute molecules that contributes 98%, 99%, and 99.5% of the asymptotic value of the solute's fugacity coefficient. Attractive mixture (naphthalene in carbon dioxide).

Figure 1: Density dependence of the solute-solute pair correlation function for the attractive mixture (naphthalene in carbon dioxide). The dimensionless temperature is $kT/\varepsilon_2 = 1.4$; the dimensionless number density is defined as $\rho^* = \rho(\sigma_2)^3$; the solute mole fraction is 10^{-9}. 1 and 2 denote solute and solvent, respectively.
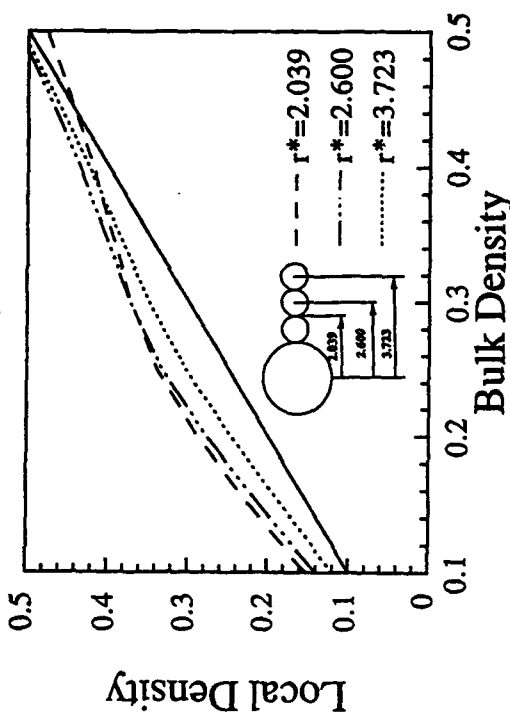
Figure 2: Relationship between local and bulk densities around solute molecules in the attractive mixture (naphthalene in carbon dioxide) at a reduced temperature of 1.07 with respect to the solvent's critical point. Each curve corresponds to a different solvation shell, whose radius is given in units of the solvent σ (see insert). Dimensionless density defined as in Figure 1.

BREAKUP AND TURBULENCE GENERATION IN DENSE SPRAYS

Principal Investigator: G.M. Faeth

218 Aerospace Engineering Building
The University of Michigan
Ann Arbor, Michigan 48109-2140

SUMMARY/OVERVIEW

Secondary drop breakup and turbulence generation by drops are being studied. Work on secondary drop breakup has yielded the regimes, dynamics and outcomes of drop deformation and breakup, using pulsed holography and photography. It was found that deformation and breakup are inhibited by liquid viscous forces at the high Ohnesorge numbers (which are reached as drops approach their thermodynamic critical points). Current work is emphasizing the dynamics of deformation/drag interactions and phenomena responsible for the initiation and termination of drop breakup. Work on turbulence generation has shown that drop-generated turbulence differs from conventional turbulence and suggests that the properties of this flow involve a stochastic combination of randomly-arriving drop (particle) wakes. Thus, current work is concentrating on the properties of low Reynolds number wakes (typical of conditions in dense sprays) in both nonturbulent and turbulent environments.

TECHNICAL DISCUSSION

Introduction. Past work on the structure of dense sprays has highlighted the importance of secondary drop breakup and turbulence generation by drops (Faeth, 1990; Ruff et al., 1989, 1991, 1992; Tseng et al., 1992a,b,; P.-K. Wu et al., 1991, 1992, 1993). Work under the present investigation is studying these processes as discussed in the following.

Secondary Drop Breakup. Studies of liquid atomization have shown that drops produced by primary breakup generally are unstable to secondary breakup (Ruff et al., 1989, 1991, 1992; P.-K. Wu et al., 1991, 1992, 1993). Thus, secondary breakup is being studied during this phase of the investigation, see Hsiang and Faeth (1992, 1993) for initial findings.

The breakup of individual drops is being observed within a windowed shock tube. Flash cinematography and pulsed holography are used to observe the dynamics and outcomes of breakup, while phenomenological theories are used to interpret the measurements. Various drop generating techniques are used to create drops having a range of viscous/surface tension forces (or Ohnesorge numbers): vibrating capillary tube with electrostatic selection for low Ohnesorge numbers and acoustic levitation of diluted viscous drops for high Ohnesorge numbers.

The levitation system has allowed us to extend our earlier deformation and breakup regime map up to Ohnesorge numbers of roughly 1000. The new map, showing the regimes as a function of Weber and Ohnesorge numbers for liquid/gas density ratios of 580-12000, appears in Fig. 1. It is evident that both deformation and breakup are inhibited at high Ohnesorge numbers, implying reduced tendencies for drops to shatter as they approach their thermodynamic critical points.

Earlier problems with drop size distributions after shear breakup (Hsiang and Faeth, 1992) were resolved by treating the core (drop-forming) drop separately from the drop population; then, drop sizes after breakup always satisfy the root-normal distribution with $MMD/SMD = 1.2$. The velocity and size of the core drop after shear breakup were correlated successfully by considering drop motion during breakup and observing that the Eötvös number at the end of drop stripping was a constant, $Eo = 16$ (notably, this value is nearly the same as at the onset of breakup for gradual

disturbances). The relative velocities of drops are reduced significantly during secondary breakup (30-70%, depending on drop size) due to the large drag coefficients of the deformation stage and the reduced relaxation times of smaller drops. These effects were correlated successfully for all three breakup regimes, as illustrated in Fig. 2, based on simplified analysis of drop motion. These considerations also provide a crude estimate of core drop velocities as illustrated in the figure, however, specific results for core drops provide more accurate estimates (Hsiang and Faeth, 1993). The results show that drop Weber numbers after secondary breakup can exceed values associated with the onset of breakup for abrupt disturbances, however, Eötvös numbers are smaller than values associated with the onset of breakup for gradual disturbances.

Current work is considering effects of density ratio on deformation and breakup, emphasizing low liquid/gas density ratios characteristic of high-pressure spray combustion. This involves measurements and analysis of deformation and drag prior to breakup, as well as breakup outcomes.

Turbulence Generation. Turbulence generation by drops controls turbulence properties in dense sprays (Faeth, 1990; Ruff et al., 1989, 1991, 1992). Drop generated turbulence differs from conventional turbulence; however, stochastic analysis based on the random arrival of drop wakes appears to be promising for describing the flow (Parthasarathy and Faeth, 1990; Mizukami et al., 1992). This approach requires information about drop wakes in turbulent environments which is not available in the literature; thus, current work is studying these wake properties. Initial results for nonturbulent and turbulent environments appear in J.-S. Wu and Faeth (1993a,b).

Wakes in nonturbulent environments (turbulence intensity $\leq 0.5\%$) exhibit classical turbulent and laminar wake regions (J.-S. Wu and Faeth, 1993a). In contrast, wakes in turbulent environments (turbulence intensities $\geq 4\%$) exhibit only a laminar-like turbulent wake region that has not been observed before (J.-S. Wu and Faeth, 1993b). Distributions of mean streamwise velocities, $\bar{u}$, are plotted in Fig. 3 as a function of radial distance, r, at various streamwise distances, x, from the virtual origin, x_0 — see J.-S. Wu and Faeth (1993b) for other notation. Although these wakes are turbulent, it is seen that they scale like self-preserving laminar wakes.

The main difference between laminar and laminar-like turbulent wakes is that the latter have enhanced effective viscosities, v_t, due to the presence of turbulence. This behavior is illustrated in Fig. 4 where v_t, normalized by the molecular viscosity, v, is plotted as a function of the sphere Reynolds number, Re. Values of v_t/v are independent of position in the wake but increase with increasing Re. Additionally, v_t/v exhibits low and high Re regimes, with transition between those regimes for Re in the range 300-600. This transition appears to be related to the onset of vortex shedding from the spheres, which begins at Re ca. 300.

Results in Figs. 3 and 4 are limited to an ambient turbulence intensity of 4%. Thus, current work is considering effects of ambient turbulence intensity on v_t/v, the appearance of the laminar-like turbulent wake region, and the properties of the final decay of laminar-like turbulent wakes. The first application of these results will be to gain a better understanding of turbulence generation and to evaluate the stochastic theory for this flow.

REFERENCES

Faeth, G.M. (1990) Twenty-Third Symposium (International) on Combustion, The Combustion Institute, Pittsburgh, 1315-1352.

Hsiang, L.-P. and Faeth, G.M. (1992) Int. J. Multiphase Flow, 18, 635-652.

Hsiang, L.-P. and Faeth, G.M. (1993) Int. J. Multiphase Flow, submitted.

Mizukami, M., Parthasarathy, R.N. and Faeth, G.M. (1992) Int. J. Multiphase Flow, 18, 397-412.

Parthasarathy, R.N. and Faeth, G.M. (1990) J. Fluid Mech., 220, 485-537.

Ruff, G.A., Sagar, A.D. and Faeth, G.M. (1989) AIAA J., 27, 901-908.

Ruff, G.A., Bernal, L.P. and Faeth, G.M. (1991) J. Prop. Power, 7, 221-230.

Ruff, G.A., Wu, P.-K., Bernal, L. P. and Faeth, G.M. (1992) J. Prop. Power, 8, 280-289.

Tseng, L.-K., Ruff, G.A. and Faeth, G.M. (1992a) AIAA J., 30, 1537-1544.

Tseng, L.-K., Wu, P.-K., and Faeth, G.M. (1992b) J. Prop. Power, 8, 1157-1166.

Wu, J.-S. and Faeth, G.M. (1993a) AIAA J., in press.

Wu, J.-S. and Faeth, G.M. (1993b) AIAA J., submitted.

Wu, P.-K., Ruff, G.A. and Faeth, G.M. (1991) Atom. Sprays, 1, 421-440.

Wu, P.-K., Tseng, L.-K. and Faeth, G.M. (1992) Atom. Sprays, 2, 295-317.

Wu, P.-K. and Faeth, G.M. (1993) Atom. Sprays, in press.
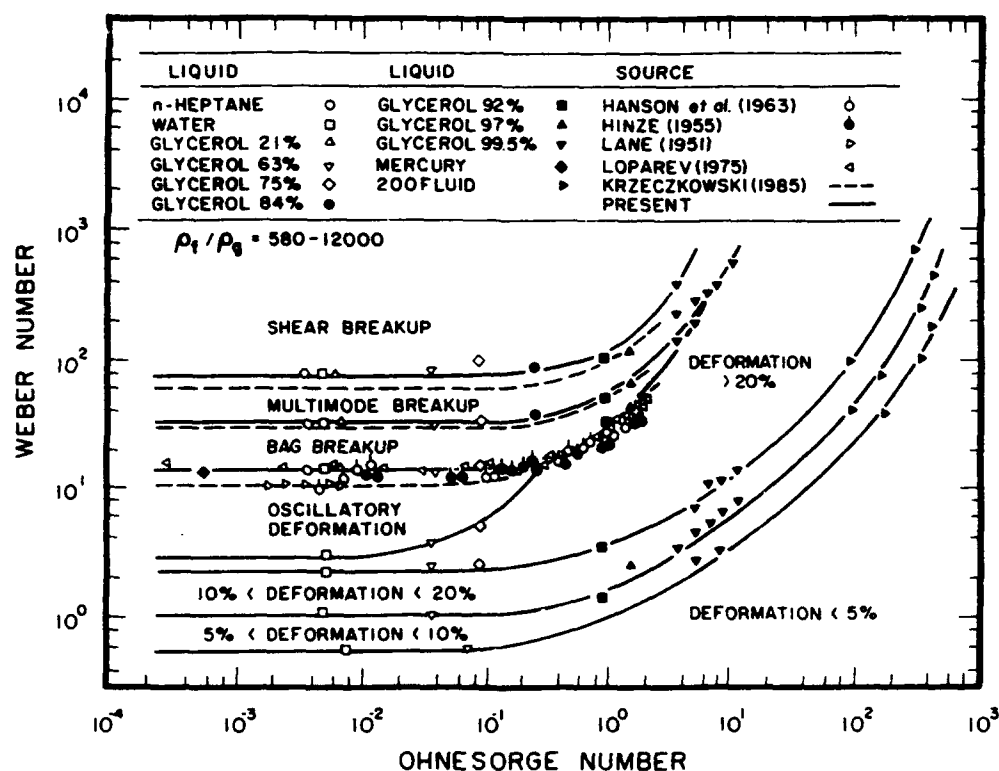
Fig. 1   Drop deformation and breakup regime map.
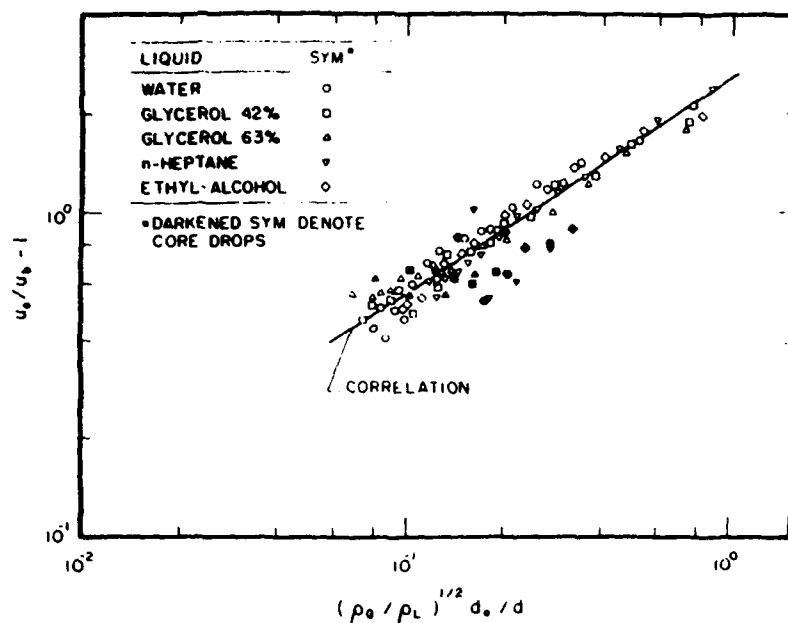
Fig. 2   Correlation of drop velocities after secondary breakup as a function of drop size.
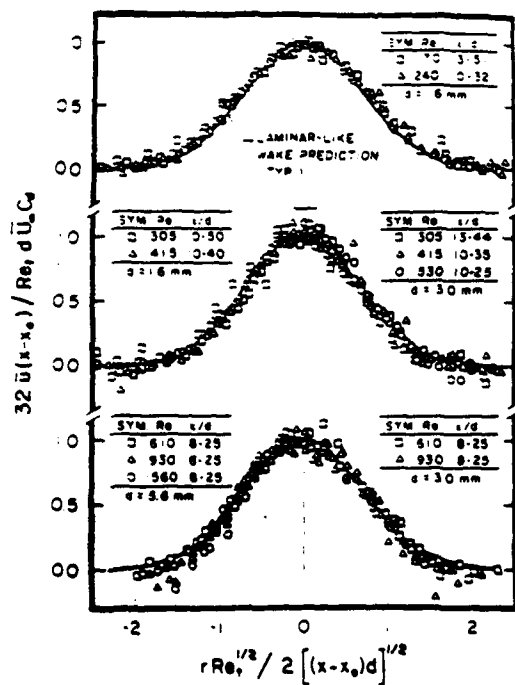
Fig. 3   Mean streamwise velocities in the laminar-like turbulent wake region.
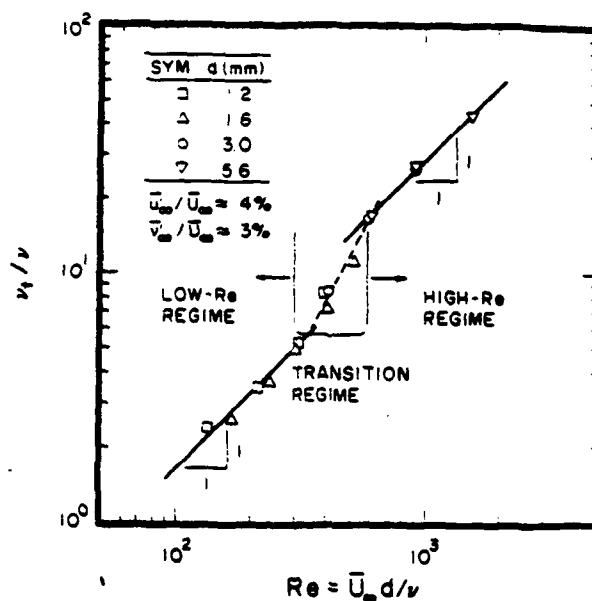
Fig. 4   Variation of turbulent viscosity with sphere Reynolds number.

DEVELOPMENT OF PREDICTIVE REACTION MODELS OF SOOT FORMATION

(AFOSR Grant No. 91-0129)

Principal Investigator: M. Frenklach

Fuel Science Program
Department of Materials Science and Engineering
The Pennsylvania State University
University Park, PA 16802

SUMMARY/OVERVIEW:

The ultimate goal of this program is to develop a predictive reaction model for soot formation in hydrocarbon flames. The specific objectives of the current 3-year study are to extend the modeling efforts to computer simulation and analysis of more complex sooting phenomena and to further refine the underlying reaction mechanism of soot formation. During the past year, progress has been made in the following areas: (1) The computational study of sooting limits in laminar premixed flames was completed. It was found that the critical equivalence ratios for soot appearance, both the absolute values and temperature dependencies, can be predicted fairly close to the experimental observations. Sensitivity and reaction-path analyses were performed to examine the factors responsible for the predicted behavior. (2) New estimation techniques were developed and applied for calculations of standard-state enthalpies of formation and binary gaseous diffusion coefficients of polycyclic aromatic hydrocarbons (PAHs) and their radicals, thus providing critical information for accurate modeling of soot formation in flames. (3) Theoretical studies of a bench-mark ion-molecule reaction were completed. (4) Computer simulations of the effect of pressure on soot formation were initiated.

TECHNICAL DISCUSSION

Detailed Simulation of Sooting Limits in Laminar Premixed Flames

The critical equivalence ratios were determined for several atmospheric laminar premixed flames of C_2-fuels: ethane, ethylene and acetylene. The value of the critical equivalence ratio, ϕ_c, for a given fuel and a given maximum flame temperature, T_m, was determined by computing flames with different equivalence ratios. The maximum flame temperature in these runs was maintained approximately the same by adjusting, similarly to the experiment, the amount of N_2 in the mixture. For each of the fuels, at least two series of flames were simulated, each at a different maximum flame temperature, in order to test the temperature dependence predicted for ϕ_c.

The numerical simulation of soot particle formation was performed in two stages: first, the production of the initial PAH species; and second, PAH further growth and nucleation and growth of soot particles. In the first stage, PAH formation up to coronene was simulated in a burner-stabilized flame configuration with a specified temperature profile and flow rate. The

maximum temperature reached in the free-flame simulation, with a given ϕ, was matched to the corresponding experimental value measured by Harris et al.[1]. The adjustment of the maximum flame temperature was accomplished, similarly to the experiment, by varying the amount of N_2 present in the mixture, but not necessarily equal to the experimental level of dilution, and being typically 5% higher in N_2 mole fraction. In the second stage, the profiles of H, H_2, C_2H_2, O_2, OH, H_2O and acepyrene (A_4R5) obtained in the flame simulation were used as input for the simulation of the growth of PAHs beyond acepyrene by the technique of chemical lumping and the soot particle nucleation and growth by a method of moments.

The critical equivalence ratios determined in this manner for the three fuels are displayed in Fig. 1, where they are compared with the experimental data of Harris et al.[1] As can be seen in this figure, the computed critical equivalence ratios follow the correct temperature dependence for each fuel, i.e., the critical equivalence ratio increases as the flame temperature increases, and the correct dependence on fuel type, for a constant flame temperature T_m, i.e., acetylene soots earlier than ethylene which soots earlier than ethane. The quantitative agreement between the computed and experimental values of ϕ_c is also reasonable, considering the lack of the precise experimental data for model input and boundary conditions, uncertainties in the model parameters, and the fact that the reaction mechanism was adopted from the previous study[2] without any adjustments.
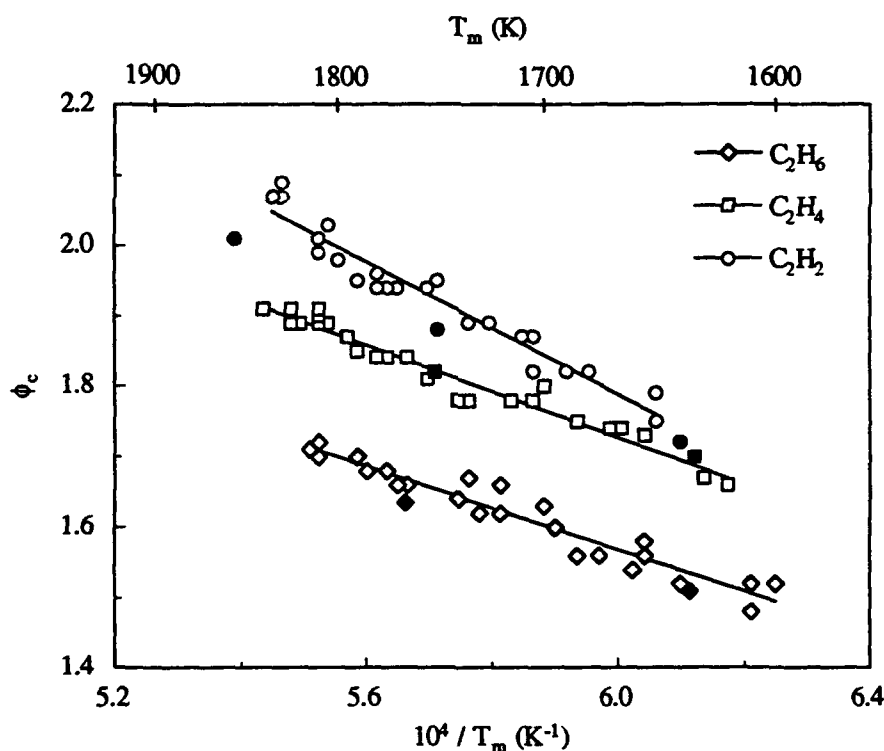

Figure 1. Comparison of the computed and experimentally determined critical equivalence ratios ϕ_c for ethane, ethylene and acetylene flames, as a function of the maximum flame temperature T_m. The open symbols represent the experimental data of Harris et al.,[1] solid lines—linear fits to the experimental points, and solid symbols—the present computational predictions.

The analysis of the computational results strongly suggested that the appearance of soot and hence the sooting limits in these flames is controlled by two factors: concentration of acetylene and the growth of PAHs. The second factor—the PAH build-up—is limited by the rise in flame temperature towards the end of the main reaction zone. The oxidation of PAHs, the molecular precursors to soot particles, was not found to be a controlling factor. This does not mean, however, that hydrocarbon oxidation does not play a role in soot formation. On the contrary, oxidation of pre-aromatic-ring species, like C_2H_3 by O_2, determines to a great degree the concentration level of phenyl, the first aromatic ring. Also, the oxidation of PAHs by OH begins to be more pronounced in locations away from the main flame zone, where OH becomes the dominant oxidant.

Evaluation of the Enthalpies of Formation of PAH Molecules and Radicals

As part of the ongoing efforts on soot formation model development and refinement, the enthalpies of formation of polycyclic aromatic hydrocarbon (PAH) molecules, radicals and substituted aromatics were investigated. The enthalpy data used in previous and current modeling efforts have been mainly derived from Benson's group additivity method. Recent results from ab initio quantum mechanical calculations have shown that for large peri-condensed PAHs, the enthalpies of formation predicted by the group additivity method could be off by as much as 10 kcal/mol.[3] The objective of our work was to determine accurately the enthalpies of formation for the major aromatic species involved in the growth of PAHs and soot in high-temperature environments. These species include PAH molecules up to 3-circumcoronene, PAH radicals up to coronyl, and some substituted aromatics.

A method for accurate and economical estimation of the enthalpies of formation for benzenoid aromatic species was developed which combines semiempirical quantum-mechanical calculations with group corrections. In this method, the deviation between experimental and calculated enthalpies of formation is partitioned into structural groups. The general idea is to use a calculation method which is computationally less demanding than quantum ab initio but physically more realistic than group-additivity calculations, and then to correct the results using a group-additivity scheme for the numerical inaccuracy of the semiempirical quantum-chemical method. The advantage of this approach is that it can be applied consistently to both molecules and radicals. The obtained with this method standard-state enthalpies of formation compare well with the experimental data and with the results of ab initio quantum-mechanical calculations available in the literature. The calculated enthalpies of formation for large peri-condensed aromatic molecules are extended smoothly to the limit of a graphite monolayer.

The developed method was also applied to examine the stability of aryl radicals as functions of molecular size and radical position, which indicates that the strength of aryl–H bond is essentially independent of molecular size, but dependent on the neighboring geometry of the C–H bonds. Smaller aryl–H bond strengths are predicted for the C–H bonds situated in the bay region of the aromatic molecules and are the results of larger steric repulsion between the neighboring H atoms.

Transport Properties of Polycyclic Aromatic Hydrocarbons

Diffusion of gaseous PAHs is an important process that significantly affects the results of numerical simulations of soot formation in hydrocarbon flames. Although several empirical correlations are available for estimation of diffusion coefficients of aromatic compounds, they

are not easy to implement in the computer codes now in use by the combustion community. The common practice is to compute transport properties, including diffusion coefficients, through the parameters of Lennard-Jones 12-6 (LJ) potential, and hence the LJ collision diameters σ and potential energy well depths ε, specified for individual chemical compounds, serve as input to flame codes. Such approach assures not only consistency among various transport properties, such as gaseous viscosities and thermal conductivities, but also consistency in evaluation of transport properties with calculations of reaction rates, such as those encountered in coagulation of PAH species.

A method was developed for systematic evaluation of the Lennard-Jones parameters for PAH compounds, in which correlations for these parameters are derived using a group contribution technique for critical temperatures and pressures and the Tee-Gotoh-Stewart correlations of corresponding states. The Lennard-Jones self-collision diameters and well depths of 29 polycyclic aromatic hydrocarbons were estimated using this approach and are shown to correlate with the molecular weights of aromatics. The correlation obtained for the self-collision diameters exhibits the one-third power in the molecular weight, indicating that, due to rotation, planar gaseous PAH molecules behave like spherical particles. The gaseous binary diffusion coefficients of aromatics in common gases were calculated with Chapman-Enskog equation using the estimated Lennard-Jones parameters and were found to compare well with the available experimental data and the predictions of one of the most reliable empirical approximations.

Semiempirical Quantum-Mechanical and RRKM Studies of Reaction $C_8H_7^+ + C_2H_2 \rightarrow C_{10}H_9^+$

The title reaction is one of the key steps in the mechanism proposed by Calcote and coworkers.[4] Seven major isomers for the $C_{10}H_9^+$ adduct and 11 possible product channels were identified in our study, indicating the complexity of the reaction. The energetics and molecular parameters of the reactants, intermediate species, products, and transition states were evaluated using the semiempirical quantum-mechanical AM1 method. The rate coefficients and their pressure and temperature dependence were then calculated using the RRKM theory with a full consideration of angular momentum conservation. The microscopic rate coefficients for the reaction channels involving the dissociation of the energized complexes were determined with the microcanonical variational transition state theory. The RRKM calculations were performed at a pressure of 20 torr for temperatures from 300 to 2000 K. These conditions are the same as those assumed in our previous kinetic modeling study of ion formation in flames. The major results of this study can be summarized as follows. At temperatures below 1000 K, the overall rate coefficient is equal to that of the Langevin limit, 6×10^{14} cm^{3}mol^{-1}s^{-1}. However, at flame temperatures (1500K < T < 2000K), the overall rate coefficients are more than an order of magnitude lower than the Langevin limit. The latter result suggests that the rate coefficients used in the reaction model of ion formation proposed by Calcote and coworkers[4] may be an order of magnitude too high.

REFERENCES

1. Harris, M. M., King, G. B. and Laurendeau, N. M., *Combust. Flame* **64**, 99 (1986); **67**, 269 (1987).
2. Frenklach, M. and Wang. H., *Twenty-Third Symposium (International) on Combustion*, The Combustion Institute, Pittsburgh, 1991, p. 1559.
3. Disch, R. L., Schulman, J. M., and Peck, R. C., *J. Phys. Chem.* **96**, 3998 (1992).
4. Calcote, H. F. and Gill, R. J., "Computer modeling of soot formation comparing free radical and ionic mechanisms," Final Report to AFOSR, TP-495, 1991.

RAPID CONCENTRATION MEASUREMENTS BY
PICOSECOND TIME-RESOLVED LASER-INDUCED FLUORESCENCE

AFOSR Grant No. AFOSR-91-0365

Principal Investigators: Galen B. King and Normand M. Laurendeau

Flame Diagnostics Laboratory
School of Mechanical Engineering
Purdue University
West Lafayette, IN 47907

SUMMARY/OVERVIEW

This research is concerned with the development of a laser-based diagnostic technique for the measurement of minor species concentrations in turbulent flames called picosecond time-resolved laser-induced fluorescence (PITLIF). Current diagnostic techniques have the capability to measure probability distribution functions (PDFs), but in many cases they lack the temporal resolution needed to measure power spectral densities (PSDs). The PITLIF instrument employs a high repetition rate mode-locked laser which gives it the temporal resolution and power necessary to rapidly obtain PSDs in addition to PDFs. The specific objective of this project is to develop the PITLIF instrument and to demonstrate its viability for obtaining PDFs and PSDs of concentration in turbulent flames.

TECHNICAL DISCUSSION

Turbulent flames are characterized by random fluctuations in flow variables such as velocity or concentration.[1] These fluctuations must be described statistically using PDFs and PSDs. Laser-induced fluorescence (LIF) is commonly employed for measurement of minor species concentrations.[2] Typically, CW or Q-switched laser systems are employed for LIF measurements of PDFs, but these systems lack the power and temporal resolution necessary to measure PSDs of concentration in turbulent flames. We report here on current investigations with picosecond time-resolved laser-induced fluorescence (PITLIF), a new diagnostic technique which has the potential to rapidly and simultaneously measure both PDFs and PSDs of concentration in a turbulent flame.

A block diagram of the PITLIF instrument is shown in Figure 1. The laser system consists of a broadband dye laser synchronously pumped by a mode-locked frequency-doubled Nd:YAG laser. The laser system delivers a series of mode-locked laser pulses of approximately 50 ps FWHM at a repetition rate of 82 MHz. The laser system irradiates a region of the flame, and through interaction with atoms or molecules in the flame, light is absorbed and spontaneously emitted. The detector, a photomultiplier tube, measures some of this emitted light. The output of the detector is fed into two parallel data acquisition channels. The low-bandwidth acquisition system uses a low-pass filter to filter out individual laser pulses and records the integrated fluorescence signal which provides a measure of the low frequency (<10 kHz) fluctuations in the LIF signal. The high-bandwidth acquisition system (0-2 GHz) has the temporal resolution necessary to record each laser pulse, and thus can be used to measure the lifetime of the decay for the excited state. Thus, when the high-bandwidth system is used in conjunction with the

[1] J. O. Hinze, *Turbulence*, McGraw Hill, New York (1975).

[2] M. C. Drake and R. W. Pitz, "Comparison of turbulent diffusion flame measurements of OH by planar fluorescence and saturated fluorescence", *Experiments in Fluids*. 3, 283 (1985).

low-bandwidth system, the PITLIF instrument can be used to measure concentration fluctuations in systems where the variation in quenching is large.

The output of the low-bandwidth acquisition channel (S_F) is

$$S_F = \eta W_{12} \Delta t A_{21} V_c \tau N_0$$

where η is the instrument efficiency, W_{12} is the rate coefficient for stimulated absorption, Δt is the temporal width of the laser pulse, A_{21} is the rate coefficient for spontaneous emission, V_c is the collection volume, N_0 is the initial number density, and τ is the excited state lifetime.[3] All of the terms can be determined through calibration except τ and N_0. Thus, evaluation of N_0 requires that τ be determined using the high-bandwidth acquisition channel.

Current investigations with the PITLIF instrument have been concerned with non-concurrent low- and high-bandwidth data acquisition. We have elected to study atomic sodium seeded into a laminar diffusion flame. The burner employs a concentric tube diffusion design in which hydrogen flows through a circular tube, and an oxygen/argon mixture flows through a surrounding annulus. Sodium is seeded into the oxygen/argon mixture using an atomizer. The fluctuations in sodium are caused primarily by the atomization process. However, using this simple flame, we are able to demonstrate the utility of the technique for systems where concentration fluctuations are caused by turbulent mixing in the flame.

The low-bandwidth system has previously demonstrated its utility for obtaining the PDFs and PSDs of sodium concentration. Five records of 5000 points collected at 2 kHz have proved sufficient to characterize the turbulent statistics of the signal. The high-bandwidth portion of the PITLIF instrument enables measurement of the local quenching environment. Each laser pulse induces a fluorescent decay which is depicted in Fig. 2. The instrument response to Rayleigh scattering from the laser pulse is also included in Fig. 2. Data was acquired using random equivalent time sampling at an effective 20 Gsamples/s. The waveforms in Fig. 2 were smoothed using a digital n-pole filter with a time constant of 700 ps after averaging over 500 waveforms. The FWHM of the laser pulse is approximately 2 ns while that of the fluorescence decay is approximately 6 ns. Since the instrument response time is on the same order of magnitude as the lifetime of the decay, a convolute-and-compare technique must be utilized to obtain the lifetime.

The lifetimes measured using the convolute-and-compare technique ranged from 2 to 4 ns. The lifetime of sodium in a premixed $H_2/O_2/Ar$ flame depends strongly on equivalence ratio with maximum lifetimes occurring near stoichiometric conditions.[4] Lifetimes measured across the radius of the flame at a height of 10 mm above the burner are displayed in Fig. 3. The lifetime is found to vary with radial location, with the maximum located approximately 2 mm from the center of the burner, where near stoichiometric conditions exist.

The excited state lifetimes are necessary to obtain the number density of the atom or molecule under study. This is seen in Fig. 4, which compares uncorrected sodium number densities with those corrected for quenching on a relative basis. The values are based on the mean fluorescence signals for the various locations in the flame. To demonstrate the effect of collisional quenching, the uncorrected value obtained at x = 10 mm and r = 0 mm was normalized to unity and all subsequent positions were normalized with respect to this point. Similarly, all relative number densities corrected for quenching were normalized relative to the value found at x = 10 mm and r = 0 mm. As seen in Figure 4, the effect of collisional quenching is non-uniform across the flame, and thus local measurements of this quantity are vital for accurate number density measurements.

We have demonstrated that the variations in the quenching environment can be measured utilizing the high-bandwidth system in a random equivalent time sampling mode. These measurements make it possible to correct the concentration measurements for collisional quenching. Future work will focus on the development of real-time acquisition for the high-bandwidth system, as well as adapting the measurement system to enable OH concentration measurements.

[3] B. D. Thompson, "Flame measurements using picosecond time-resolved laser-induced fluorescence", M.S. Thesis, Purdue University, W. Lafayette, IN (1992).

[4] N. S. Ham and P. Hannaford, "Direct observation of lifetimes of excited atoms in a flame at atmospheric pressure", *J. Phys. B: Atom. Molec. Phys.* **12**, L199 (1979).
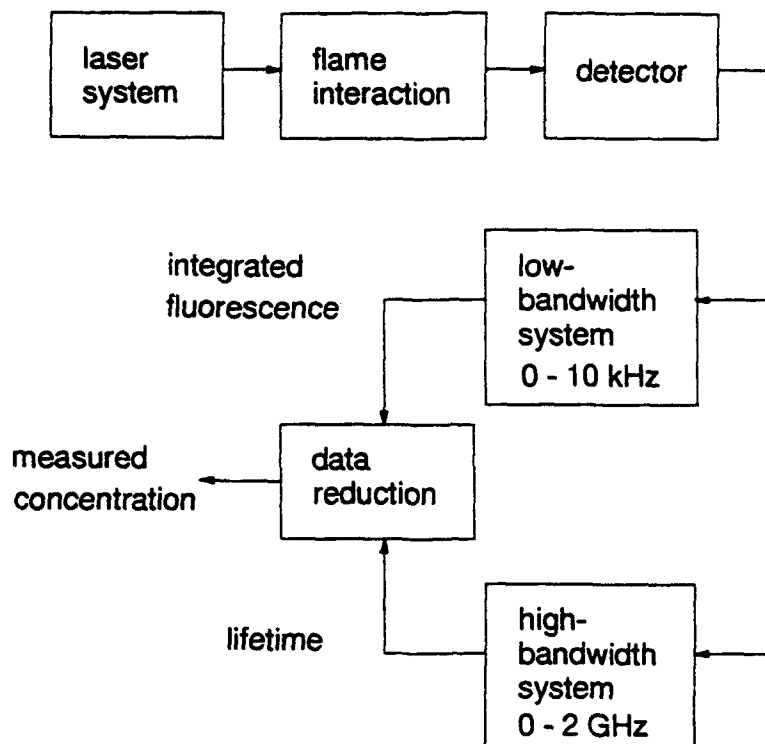
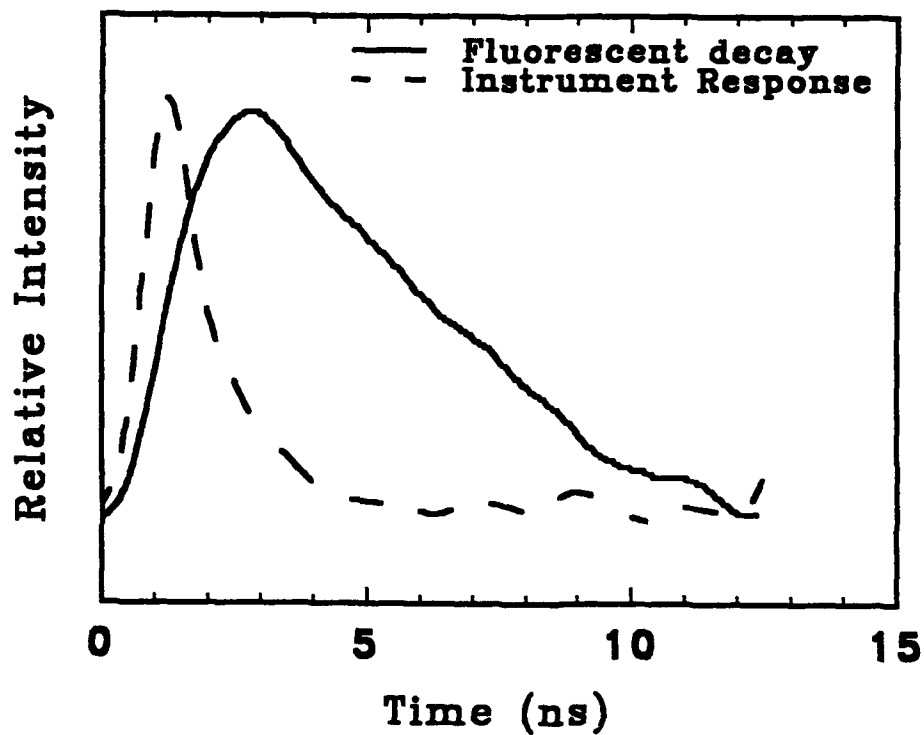Fig. 1 Block diagram of the PITLIF instrument.

Fig. 2 Typical fluorescent decay induced by the picosecond laser. The instrument response to a scattered laser pulse is also shown. Each waveform was obtained using random equivalent time sampling averaged over 500 waveforms and smoothed using a n-pole Bessel filter.
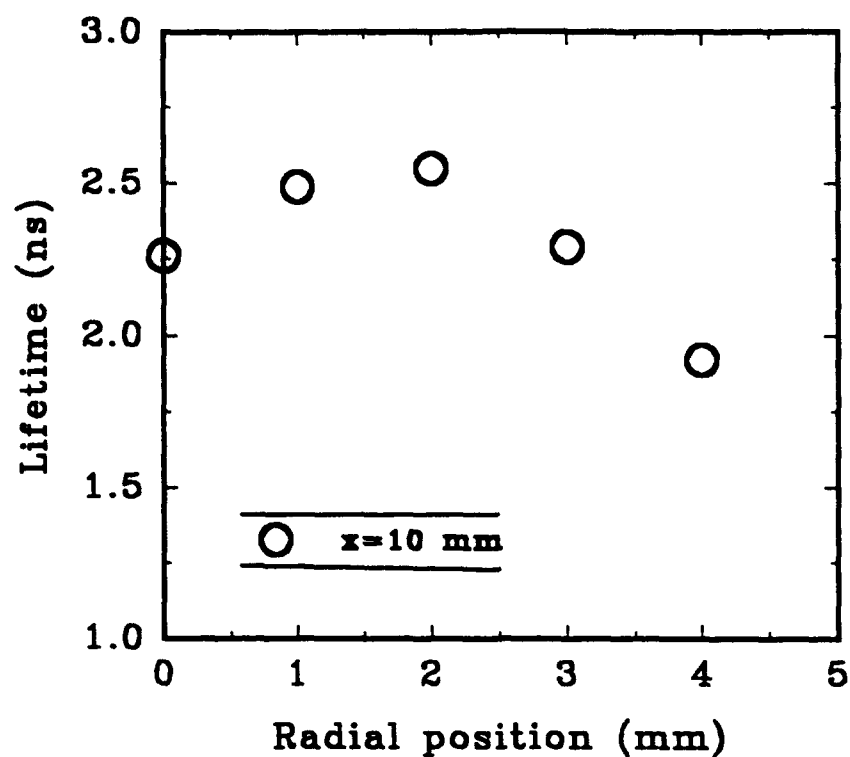
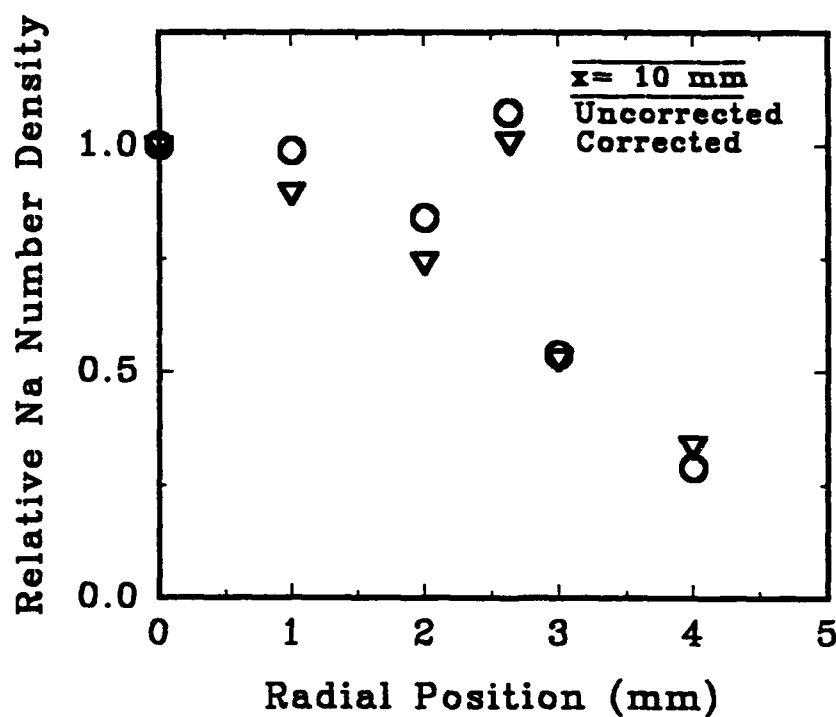Fig. 3 Measured excited state lifetimes of sodium for various radial positions at x = 10 mm.

Fig. 4 Normalized ground state number densities with and without corrections for collisional quenching. The values for both the corrected and uncorrected number densities are normalized with respect to the corresponding value found at x = 10 mm and r = 0 mm.

LIQUID-PHASE CIRCULATION AND MIXING IN MULTICOMPONENT DROPLETS

Principal Investigator: Constantine M. Megaridis
Research Collaborator: Joseph T. Hodges*

Department of Mechanical Engineering
University of Illinois at Chicago
Chicago IL 60607-7022

SUMMARY/OVERVIEW

The objective of this work is to provide high-resolution information on the fundamental transport processes in convective multicomponent droplet vaporization, by combining the predictions of detailed numerical models and an experimental program conducted at the National Institute of Standards and Technology. Laser light slicing and fluorescence measurements are employed to analyze flow patterns developed within liquid droplets exposed to steady gaseous streams. During the first phase of the work large needle-suspended droplets were examined in order to fine-tune the experimental techniques. Our measurements consistently revealed complex, shear-induced, droplet internal circulation patterns. These observations suggest that droplet rotation might be an important parameter in droplet dynamics. Electrodynamically levitated droplets of 100 μm diameter are currently being examined in order to produce flow patterns within droplets of sizes characteristic of spray combustion systems.

TECHNICAL DISCUSSION

Shear-induced circulation within vaporizing liquid droplets exposed to gaseous streams is a long-debated issue. Numerical models have demonstrated the occurrence of droplet internal circulation, and have provided substantial insight. However, the comparatively slow development of relevant experimental diagnostic techniques has produced limited evidence of these phenomena. The first configuration examined in this study involved the visualization of droplet internal convective motion by planar laser induced fluorescence. Nearly spherical (typical aspect ratios around 0.8) water droplets with diameters of the order of 2 mm were suspended on a flat-tipped hypodermic needle of diameter 0.7 mm (Fig. 1). The axis of the suspending needle was vertical. Fluorescence signals were generated from small amounts of dilute aqueous laser dye solutions (Rhodamine B/H_2O) that were gently injected into the suspended droplets through the syringe. Observations in the absence of external gas flow indicated that molecular diffusion of the injected dye within the quiescent liquid was negligible. The droplets were subsequently exposed to a steady air stream emanating from a flow straightening device. The flow straightener produced a uniform velocity of the order of 1 m/s in a direction perpendicular to the syringe needle (Fig. 1). The Reynolds numbers associated with the flows considered were characteristic of practical situations of interest (from 10 to 100).

Each droplet was illuminated by a thin laser sheet passing through its midplane at two orthogonal orientations (planes A, B in Fig. 1). Internal motion was visualized from two perpendicular directions (views A and B, in Fig. 1) by imaging the fluorescent emission from the dye as it was transported within the laser sheet. The fluorescent emission used to follow the liquid-phase circula-

---

* National Institute of Standards and Technology, Gaithersburg, MD 20899

tion was recorded with a microscope/CCD camera/video recording system. This diagnostic system offers a very high spatial resolution for visualization of the laser induced fluorescence.

Real-time observations performed on a series of water droplets showed distinct patterns of internal circulation throughout the range of Reynolds numbers examined. Since the water droplets vaporized with time, the Reynolds number gradually decreased as a result of droplet size reduction. Our observations focused primarily on the early stages of droplet lifetime during which the effect of the suspender is expected to be lower. Figure 2 displays two typical sequences of images obtained when droplets 2 mm in diameter were exposed to a uniform air stream of velocity 1 m/s (Re = 100). The two sequences correspond to the different perspectives (A and B) shown in Fig. 1. It should be noted that each set displayed in Fig. 2 corresponds to a unique injection event. Each sequence covers a time span of 4-5 seconds. The fluorescence images reveal a complex internal motion that in plane A conforms to a helical pattern. This motion had a characteristic frequency of 4-5 Hz. The helical flow was clockwise as viewed with the air flow propagating from right to left (Fig. 2A). The gradual weakening of the fluorescence signal, as displayed in Fig. 2A, was found to be related to the secondary motion displayed in sequence B. Despite the presence of the 0.7mm-diameter needle, the planar images of Fig. 2B displayed a remarkable symmetry with respect to both vertical and horizontal axes through the droplet center. The secondary motion depicted in Fig. 2B displayed a quad-cell pattern (see last image), and was characterized by a frequency at least by an order of magnitude lower than that on plane A.

A numerical model predicting the three-dimensional droplet internal motion for specific droplet surface conditions has been developed. It is currently being used to reproduce the experimentally observed flow patterns. Preliminary results show that the presence of the suspending needle may significantly influence the development of the complex motion observed. The flow patterns depicted in Figs. 2A and 2B were reproduced using the numerical model by imposing appropriate droplet boundary conditions. Figure 3 shows the velocity vector fields corresponding to perspectives A and B of Fig. 1 as predicted by the model. In addition, portions of two particle paths have been drawn on perspective A. The qualitative agreement with the experimentally determined convective patterns is worth noting. In conclusion, our observations showed that given sufficient levels of shear, flow rotational modes of motion within suspended droplets do indeed occur. This suggests that droplet rotation may be significant in practical situations involving droplet convective transport.

The current phase of the study is focused on the use of small ($< 150 \mu m$) levitated droplets that are suspended within a hyperboloidal electrodynamic balance. Nonvolatile droplets have been routinely levitated in the balance under quiescent ambient conditions. The design of the balance enclosure has been modified to accommodate convective flows. In addition, a position sensor/electronic feedback control system is currently being developed. This system will allow us to maintain the levitation of evaporating droplets exposed to sufficiently strong convective gas streams. Time-varying spatially-resolved qualitative data on liquid-phase mixing and circulation within levitated droplets are expected to be produced in the near future.

The following publications have resulted from the development of the numerical models that are used in conjunction with the optical measurements to elucidate the transport mechanisms affecting droplet internal circulation and mixing.

1) C. M. Megaridis, "Comparison Between Experimental Measurements and Numerical Predictions of Internal Temperature Distributions of a Droplet Vaporizing under High-Temperature Convective Conditions," *Combustion and Flame*, in press, 1993.

2) C. M. Megaridis, "Liquid-Phase Variable Property Effects in Multicomponent Droplet Convective Evaporation," *Combustion Science and Technology*, accepted, 1993.

3) T. M. Shih and C. M. Megaridis, "Finite-Difference Discretization Effects on Multidimensional Droplet Evaporation Modeling," *Numerical Heat Transfer*, accepted, 1993.
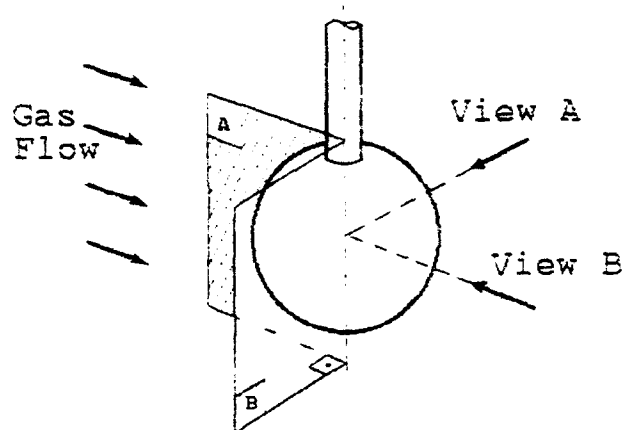
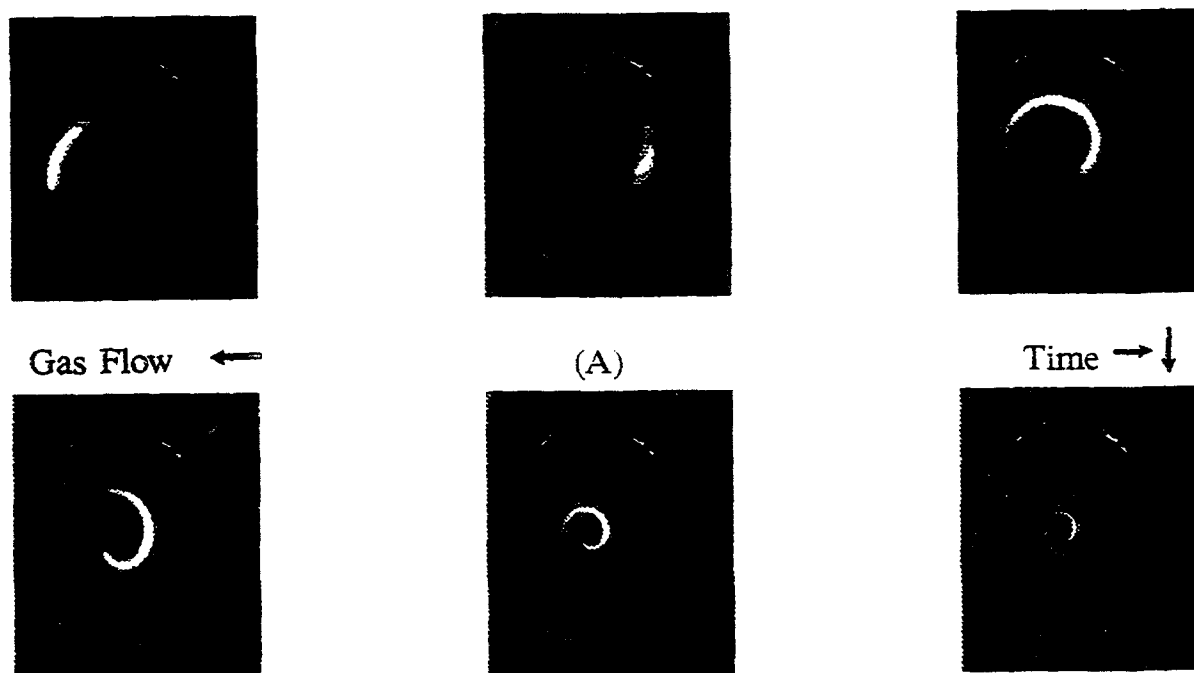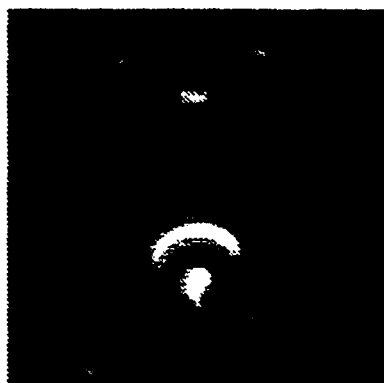Fig. 1 Suspended-droplet experimental configuration.

Gas Flow ←   (A)   Time →↓

Fig. 2A Fluorescence images for perspective A displayed in Fig. 1.

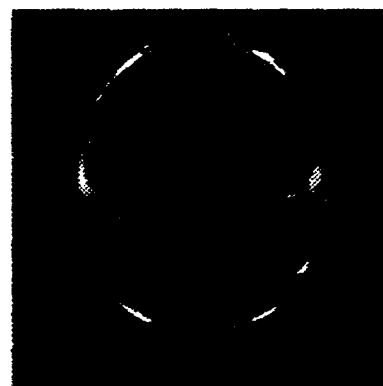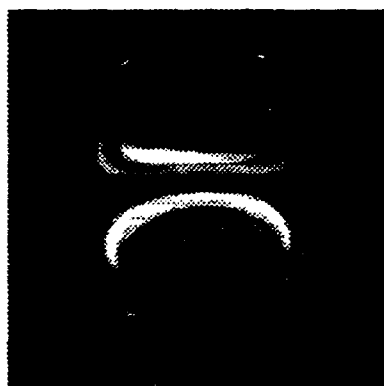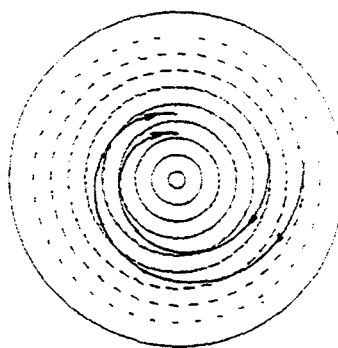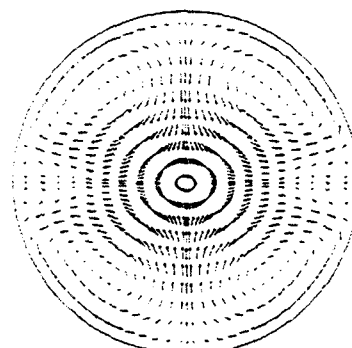Gas Flow ⊙   (B)   Time ➡ ↓

Fig. 2B Fluorescence images for perspective B displayed in Fig. 1.

Case A   Case B

Fig. 3 Numerically-predicted velocity vector fields corresponding to perspectives A and B of Fig. 1.

INVESTIGATION OF THE APPLICATIONS OF LASER-INDUCED FLUORESCENCE TO FUEL SPRAY AND SINGLE DROPLET VAPORIZATION

ARO Contract No. DAAL03-91-G-0033

Principal Investigator: Lynn A. Melton
Research Collaborator: Michael Winter*

Department of Chemistry
University of Texas at Dallas
Richardson, TX 75083-0688

SUMMARY/OVERVIEW:

A series of laser diagnostic techniques has been developed to measure heat and mass transfer associated with individual droplets characteristic of a spray. Techniques under development and/or available now include exciplex-fluorescence thermometry, "droplet slicing" and flow-pattern imaging, correction for refraction effects by droplet surfaces, measurement of the temperature field within droplets, and production of monodisperse droplets at high pressures. Also under development and recently demonstrated are an apparatus and techniques for lifetime imaging, which holds the potential for imaging of the equivalence ratio. New results include refinements to droplet slicing for unambiguously determining the presence of internal circulation, and further interpretation of droplet slicing results using inverse ray tracing (IRT).

TECHNICAL DISCUSSION:

At UTRC, measurement of internal circulation using laser-induced, oxygen-quenched, fluorescence are being pursued under known initial conditions. Decane doped with naphthalene is used to form droplets from either a droplet-on-demand generator or an aerodynamic droplet generator; they fall a short distance in a chamber filled with a carefully-controlled shear flow of nitrogen and a variable amount of oxygen. A thin sheet of ultra-violet light from the fourth harmonic of a Nd:YAG laser illuminates single droplets. Sheet thickness has been significantly reduced by careful selection of a uniform portion of the initial laser beam waist. A Questar QM100, long-working-distance microscope with uv quartz optics is used to provide high quality images despite the presence of thick windows in a high pressure test vessel. The microscope produces a highly-magnified image of the naphthalene fluorescence which is recorded digitally using an intensified, two-dimensional, CCD detector interfaced to a laboratory computer. An off-the-shelf, low $f^{\#}$, microscope is particularly useful in careful quantification of the imaging modulation transfer function that is used for ray tracing corrections on droplet slicing image data. Since oxygen is a strong fluorescence quencher, any liquid volume element which has been

---

*United Technologies Research Center, East Hartford, CT 06108

exposed to it by surface contact or diffusion will suffer a reduction in fluorescence intensity. Convection from the surface due to internal circulation as well as diffusion cause image regions to appear darker. Oxygen−free experiments provide a baseline case for comparison.

An approach to determine unambiguously the source of the internal circulation is being explored which is based on aerodynamic droplet generators[1] that supply droplets within the core of an axisymmetric jet and introduce internal circulation of the opposite sense to that induced by the shear flow surrounding a falling droplet. A hypodermic needle is situated within the plenum with its end at the throat of a converging diverging nozzle. The gas flow around the end of the needle strips off droplets at a frequency characteristic of the jet and monodisperse droplets are produced at a regular interval. Since the gas flow velocity is greater than the initial droplet velocity, the shear environment accelerates the droplet surface inside the nozzle and potential core of the jet. Once the droplet leaves the generator flowfield, the shear forces are reversed and the droplet surface is decelerated. Although these generators produce droplets in a repeatable manner, care must be taken to maintain laminar flow around the droplets. Generators of this design have produced extremely regular droplets at fixed time intervals.

Using the droplet−on−demand generators described above, droplets were released with virtually zero initial velocity into a chamber containing quiescent nitrogen or oxygen. Previous results show a comparison between an image of the fluorescence from a single droplet falling in a pure nitrogen environment, to that of one falling in an oxygen environment. A sequence of images showing the evolution of the vortex is shown in Fig. 1.

At UTD, projects involving the optics of droplets have been pursued in the last year. Inverse ray tracing (IRT) methods for computing the true spatial distributions when necessarily−distorted images are obtained in "droplet slicing" experiments.

In "droplet slicing" experiments, the image is significantly distorted, with the central portion being expanded linearly and the outer portions being compressed near the droplet edge. Algorithms for the removal of these distortions have been developed. Recovery of the central portions of the image is straightforward, but accurate recovery of the outer portions is difficult. Initial attempts at data analysis using noisy data proved unstable. Least−squares−fitting of functional forms, such as polynomials, appears to have controlled the instability problem, and actual recovery of "droplet slicing" images is now underway.

The work presented here is an effort to restore the distorted droplet slicing images and obtain quantitative information. A numerical technique has been developed, which simulates the image formation processes in a laser droplet slicing imaging experiments. Transformations from droplet central plane (object plane) to the image plane have been derived and computer codes have been developed. A distorted image from droplet slicing imaging can be numerically simu-

lated by a forward transformation, whereas an inverse mapping process yields the restoration of the distorted images. Quantitative information is obtained from the restored images.

Since the inverse process is ill−posed, the distorted droplet slicing images can only be restored partially. A reasonable rule of thumb is that an object well seen on the image can be restored, whereas an object difficult to see on the image can not be recovered. The droplet functions as a magnifying glass at its central part, but compresses its outer region, both in size and intensity, into a narrow rim on the image, which can be hardly seen. At 90° observation, this outer region is not recoverable. However, the outer region is the most important for heat and mass transfer studies. An off−90° observation arrangement is proposed in this work. With an observation angle less than 90°, the outer region on the acute angle side can be seen clearly on the image and hence can be restored.

An example gives comparisons between 90°, Fig. 2 (a−c), and off−90°(60°), Fig. 2 (d−f), observations. The object was a Chinese character for "image". Figure 2(a) and (d) were taken directly by a CCD camera (Photometrics STAR I) with a Nikkor (35 mm, 1:1.4) lens set at the smallest aperture. Figures 2(b) and (e) were the "droplet−slicing images", which were taken by the same camera−lens system with the character being covered by a solid hemisphere (a hemispherical, thin plastic shell filled with water). Figure 2(c) and (f) show the restorations. At 90° observation a central region symmetric about the origin is restored well. However, outside that region numerical oscillations preclude restoration. In contrast, at 60° observation the restoration extended to the lower edge of the character, with sacrifices of information about its upper edge.

Figure 3 shows a real droplet−slicing image (a) and the restoration (b). The data are those of Fig. 1. This image is typical of good experimental data on droplet slicing; the RMS fluctuation from pixel to pixel is about 10%, and the contrast between oxygen free and oxygen−containing zones is modest. The least−squares estimation recovers a central region about 77% of the radius, well. Beyond that region the object was not recoverable.

REFERENCES

1.   G. J. Green, F. Takahshi, D. E. Walsh, and F. L. Dryer: *Aerodynamic Device for Generating Mono−disperse Fuel Droplets*, Rev. Sci. Instrum. 60 (4), April 1989.

2.   H. C. Andrews and B. R. Hunt: *Digital Image Restorations*, Prentice−Hall, Inc., New Jersey, (1977).
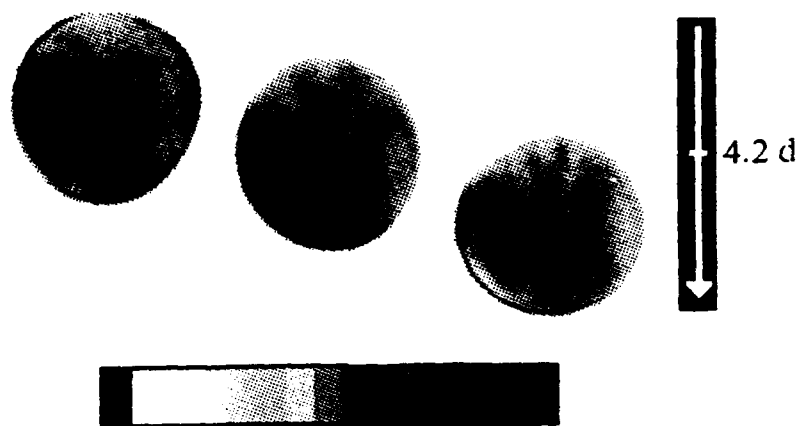
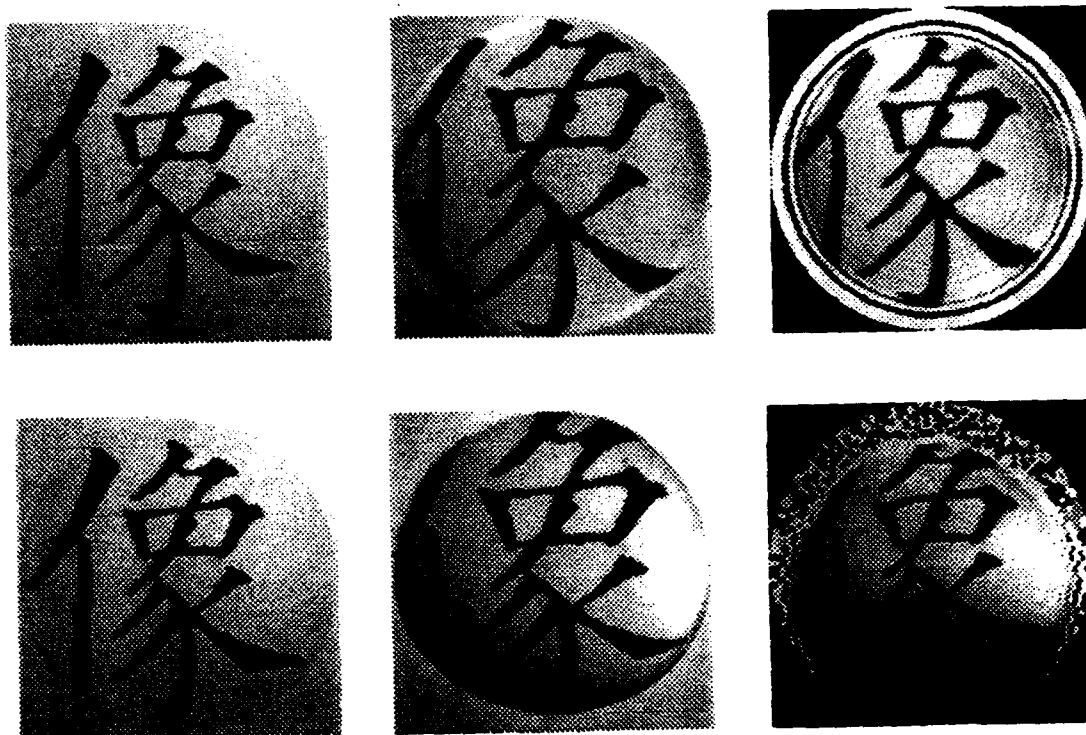Figure 1. A sequence of images showing the evolution of the vortex.

Figure 2. Comparison of 90° and off–90° observations. (a – c) 90° observation,
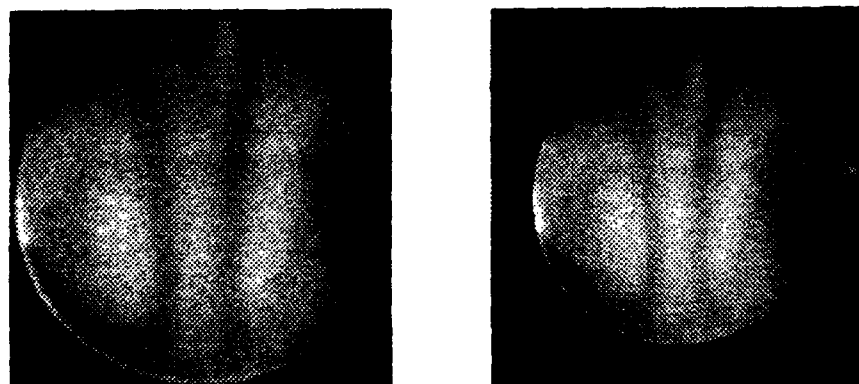(d – f) off–90° observation (60°).

Figure 3. Droplet slicing image and restoration. (a) image and (b) restoration.

TRANSPORT PHENOMENA AND INTERFACIAL KINETICS IN MULTIPHASE COMBUSTION SYSTEMS[†]

AFOSR Grant No. 91-0170

Principal Investigator: Daniel E. Rosner[‡]
High Temperature Chemical Reaction Engineering Laboratory
Department of Chemical Engineering, Yale University
New Haven, CT 06520-2159,USA

SUMMARY/OVERVIEW

The performance of ramjets burning slurry fuels (leading to oxide aerosols and deposits), and gas turbine engines in dusty atmospheres depends upon the formation and transport of small particles, often in non-isothermal combustion gas boundary layers (BLs). Even airbreathing engines burning "clean" hydrocarbon fuels can experience *soot* formation/deposition problems (*e.g.*, combustor liner burnout, turbine blade erosion,....). Moreover, particle formation and transport are important in chemical reactors used to synthesize or process aerospace materials (turbine coatings, optical waveguides, ceramic precursor powders,....). Accordingly, our research is directed toward providing chemical propulsion system and materials engineers with new techniques and quantitative information on important particle- and vapor-mass transport mechanisms and rates. An interactive experimental/theoretical approach is being used to gain understanding of performance-limiting chemical-, and mass/energy transfer-phenomena at or near interfaces. This includes the development and exploitation of seeded laboratory burners (Section 2), flow-reactors (Section 4), and new diagnostic techniques. Resulting experimental rate data, together with the predictions of asymptotic theories (Sections 1,3,4), are then used to propose and verify simple viewpoints and rational engineering correlations for future design/optimization.

TECHNICAL DISCUSSION

1. TRANSPORT AND STABILITY OF AGGREGATED PARTICLES: THEORY

The ability to reliably predict the transport properties and stability of *aggregated* flame-generated *particles* (carbonaceous soot, Al_2O_3, SiO_2,...) is important to many technologies, including chemical propulsion and refractory materials fabrication.

The *Brownian diffusion*-, inertial-, and optical-properties of *aggregated* particles, as formed in sooting diffusion flames, are quite *sensitive* to size (*e.g.* number N of "primary" particles; see Fig. 1) and morphology (geometrical arrangement of the primary particles). Needed are methods to anticipate coagulation and deposition rates of suspended populations of such particles, especially in combustion systems. Toward this end we have recently devloped improved and efficient methods for predicting the Stokes drag of large 'fractal' aggregates *via* a spatially variable porous sphere model (Figs. 1, 2). Using the Stokes-Einstein equation, the results of Fig. 2 are being used to predict the Brownian diffusivity of such aggregates in the high pressure (near continuum-) limit (proportional to the product of the reciprocal of the ordinate of Fig. 2 and N^{-1/D_f}). This approach is currently being extended to predict the *thermophoretic diffusivity* of such aggregates, an important quantity we have recently found to be much less sensitive to size and morphology than the translational Brownian diffusivity (Rosner *et.al.* 1992). Indeed, this provides the theoretical basis for the *thermophoretic sampling* technique being employed in our current experimental studies (Section 2). These new methods/results, together with recent results on the *spread* of aggregate sizes in coagulating populations, are now being used to predict wall *capture rates* by the mechanisms of convective-diffusion, turbulent eddy-impaction, and thermophoresis (Rosner, Tassopoulos and Tandon,1993). Also needed are methods to predict

---

interactions between aggregates and their surrounding *vapor* environment---interactions which can lead to primary particle growth, or burn-out. Toward this end we have also developed new and efficient methods to predict the "accessible surface area" of aggregates (expressed as a fraction , η, of the true surface area in Fig. 3), including its dependence on size (N), structure (fractal dimension, D_f), probing molecule reaction probability α, and pressure level (*via* Knudsen number based on primary particle diameter). Figure 4 shows the test of our "effective Damkohler number" correlation approach when compared with exact results of many numerical integrations (Rosner and Tandon,1993).

Also in progress are studies of the *restructuring kinetics* of aggregates — *ie.* those factors which determine the observed size of the apparent "primary particles" comprising soot particles, and the "collapse" of surface area observed in some high temperature systems.

2. FORMATION, TRANSPORT AND STABILITY OF COMBUSTION-GENERATED PARTICLES:
LAMINAR COUNTERFLOW DIFFUSION FLAME EXPERIMENTS

A manuscript describing our measurements of the *thermophoretic diffusivity* of flame-generated submicron "soot" particles using a $(TiCl_4(g)-)$seeded low strain-rate counterflow laminar diffusion flame (CDF-) technique has just appeared (Gomez and Rosner, 1993). A knowledge of the relative positions of the gas and particle stagnation planes and the associated chemical environments, can be used to control the composition and morphology of flame-synthesized particles. These factors should also influence particle production and *radiation* from *turbulent* non-premixed "sooting" flames, as discussed further in Gomez and Rosner, 1993.

To extend this work to obtain fundamental information on nucleation, growth and aggregate restructuring, during this past year we have developed an improved "slot-type" burner (Fig. 5) and introduced instruments to carry out *in situ* measurements of particle Brownian motion ("dynamic light scattering"). We have also developed a thermophoretic sampler (Fig. 6) to extract aggregates from various positions in the seeded-CDF for morphological analysis using electron microscope images. Aggregate data obtained from CH_4 flames seeded with titanium tetra-isopropoxide (TTIP-) vapor are now being obtained and analyzed using the theoretical methods briefly outlined in Sections 1,3.

3. MULTIPHASE BOUNDARY LAYER THEORY: NUCLEATION, GROWTH, THERMOPHORESIS AND INERTIA

Our *IJHMT J* paper giving comprehensive results of Seeded micro-combustor experiments, and ancillary theoretical calculations on the interesting competition between particle *inertia* and particle *thermophoresis* for the case of laminar gaseous boundary layers on surfaces with streamwise curvature (*e.g.*, turbine blades) should appear this Fall (Konstandopoulos and Rosner, 1993).

We are now carrying out theoretical studies on the structure of thin reaction-nucleation-coagulation 'sublayers' within laminar boundary layers, including stagnation flows similar to those achieved in our counterflow burner (Fig. 5) and CVD-impingement reactor (see Fig. 7 below).

An account of our recent studies of the *unusual population dynamics* of coagulating absorbing-emitting particles in strong *radiation fields* is about to appear in *Aerosol Sci. Tech.* (Mackowski *et.al.*, 1993). For a useful overview of our recent work on these and other effects of energy transfer on suspended particle dynamics, see Rosner, *et. al.*, 1992.

4. KINETICS AND MORPHOLOGY OF CVD-MATERIALS IN MULTI-PHASE ENVIRONMENTS

A small impinging jet (stagnation flow) reactor (Fig. 7) is being used to study the chemical vapor deposition (CVD-)-rates of refractory layers on inductively (over-)heated substrates. These measurements are being used to understand deposition rates and associated deposit microstructures observed in highly non-isothermal, often particle-containing local CVD environments. Figure 8 shows (logarithmic ordinate) our apparent first order deposition rate constants *vs.* reciprocal surface temperature for $TiO_2(s)$ obtained from $TTIP(g)$. The dark points show our predicted surface temperatures for the onset of vapor phase reactions ("vapor phase ignition"(VPI)) within the boundary layer and the onset of vapor phase diffusion control of the heterogeneous reaction.

CONCLUSIONS, FUTURE RESEARCH

In our 1992-1993 OSR-sponsored Yale HTCRE Lab research (briefly described above, and in greater detail in the archival references cited and updated below) we have shown that new methods for rapidly measuring vapor- and particle-mass transfer rates , combined with advances in multiphase transport theory, provide useful means to identify and incorporate important, often previously neglected, transport phenomena in propulsion/materials engineering design/ optimization calculations. We are now extending our work on the effects of these new "phoretic" phenomena involving aggregated particles to include their stability (with respect to high temperature restructuring leading to a loss of surface area). For this purpose an improved CDF burner has been brought on line (Fig. 5), along with supplementary optical and thermophoretic sampling diagnostics (Fig. 6). These techniques, together with closely coupled theoretical calculations of particle birth/dynamics in such mixing layers, promise to lead to a valuable understanding of the origin and fate of combustion-generated ultra-fine particles.

REFERENCES

Albagli, D. and Rosner, D.E., "Factors Governing the Accessible Surface Area of Combustion-Generated Ultrafine Particles", (in preparation, 1993).

Castillo, J.L. and Rosner, D.E., "Role of High Activation Energy Homogeneous Reactions in Affecting CVD-rates and Deposit Quality for Heated Surfaces", submitted to *J. Electrochem. Soc.* (1993).

Gomez, A., and Rosner, D.E., "Thermophoretic Effects on Particles in Counterflow Laminar Diffusion Flames", *Combust. Sci. and Tech.* **89**, 335-362 (1993).

Konstandopoulos, A.G., **Effects of Particle Inertia on Aerosol Transport and Deposit Growth Dynamics**, PhD Dissertation, Yale University (December 1991).

Konstandopoulos, A.G. and Rosner, D.E.,"Inertial Effects on Thermophoretic Transport of Small Particles to Walls With Streamwise Curvature---I. Experiment, II. Theory", *Int. J. Heat Mass Transfer* (in press 1993).

Mackowski, D.W., "Phoretic Behavior of Asymmetric Particles in Thermal Non-equilibrium with the Gas : Two-Sphere Aggregates", *J. Colloid and Interface Science* **140** (1), 138-1576 (1990).

Mackowski, D.W., Tassopoulos, M. and Rosner, D.E.,"Effect of Radiative Heat Transfer on the Coagulation Dynamics of Combustion-Generated Particles", *Aerosol Sci. Technol (AAAR)* (in press 1993).

Rosner, D.E., **Transport Processes in Chemically Reacting Flow Systems**, Butterworth-Heinemann (Stoneham MA), 3d Printing 1990.

Rosner, D.E., Cohen, R.D. and Tandon, P., "Development of Pseudo-Continuum Theories of the Restructuring Kinetics of Large (Multi-Particle) Aggregates in Combustion Systems", prepared for presentation at the AAAR **1993 Annual Mtg.**, Oak Brook, IL (Oct. 11-15, 1993).

Rosner, D.E., Collins, J. and Castillo, J.L., "Onset Conditions for Gas Phase Reactions and Particle Nucleation/Growth in CVD Boundary Layers", 12th **International Conference on CVD**, Electrochem. Soc., Hawaii (May 15-21, 1993); see, also, "Effects of Homogeneous Reactions on Deposition Rates and Microstructure in Organometallic CVD of TiO$_2$", prepared for presentation at the AIChE **1993 Annual Mtg.**, St. Louis, MO (Nov. 8-12, 1993).

Rosner, D.E., Konstandopoulos, A.G., Tassopoulos, M., and Mackowski, D.W, "Deposition Dynamics of Combustion-Generated Particles: Summary of Recent Studies of Particle Transport Mechanisms, Capture Rates, and Resulting Deposit Microstructure/Properties", *Proc. Engineering Foundation/ASME Conference*: **Inorganic Transformations and Ash Deposition During Combustion**, 585-606 (1992).

Rosner, D.E., Mackowski, D.W and Garcia-Ybarra, P., "Size and Structure-Insensitivity of the Thermophoretic Transport of Aggregated 'Soot' Particles in Gases", *Comb. Sci & Technology* **80** (1-3), 87-101 (1991).

Rosner, D.E., Mackowski, D.W, Tassopoulos,M., Castillo, J.L., and Garcia-Ybarra, P., "Effects of Heat Transfer on the Dynamics and Transport of Small Particles in Gases", *I&EC-Research (ACS)* **31** (3), 760-769 (1992).

Rosner, D.E. and Tandon, P., "Pseudo-Continuum Theories of the Transport Properties of Large (Multi-Particle) Suspended Aggregates", prepared for presentation at the AIChE **1993 Annual Mtg.**, St. Louis, MO (Nov. 8-12, 1993).

Rosner, D.E.and Tassopoulos, M.,"Deposition Rates from 'Polydispersed' Particle Populations of Arbitrary Spread", *AIChE J.* **35** (9) 1497-1508 (1989)

Rosner, D.E.and Tassopoulos, M.," Direct Solutions to the Canonical 'Inverse' Problem of Aerosol Sampling Theory: Coagulation and Size-dependent Wall Loss Corrections for Log-Normally Distributed Aerosols in Upstream Sampling Tubes", *J. Aerosol Sci.* **22** (7) 843-867 (1991).

Rosner, D.E., Tassopoulos, M. and Tandon, P., "Sensitivity of Total Mass Deposition Rate and Resulting Deposit Microstructure to Morphology of Coagulation-Aged Aerosol Populations of Aggregated Primary Particles", prepared for presentation at the **Eurotherm Seminar No. 33**, Paris (Oct. 13-14, 1993).
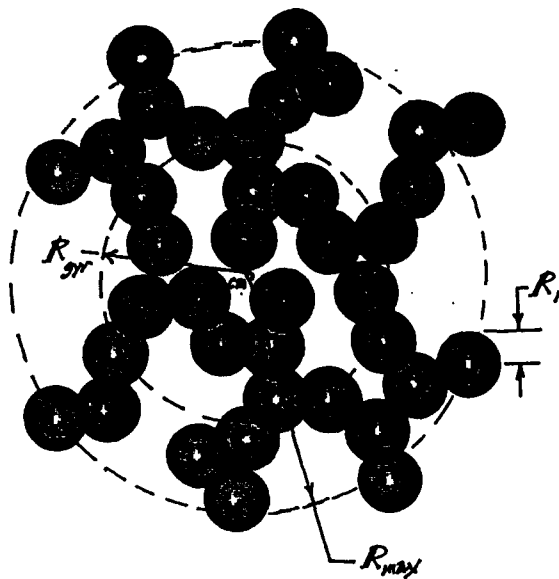
Fig.1 "Porous sphere" model of large fractal aggregate suspended in a background gas; basis for the calculation of translational and rotational Brownian diffusion coefficients, thermophoretic diffusivity, "stopping time", accessible area, and restructuring kinetics (after Rosner and Tandon, 1993, Rosner, Cohen and Tandon, 1993)
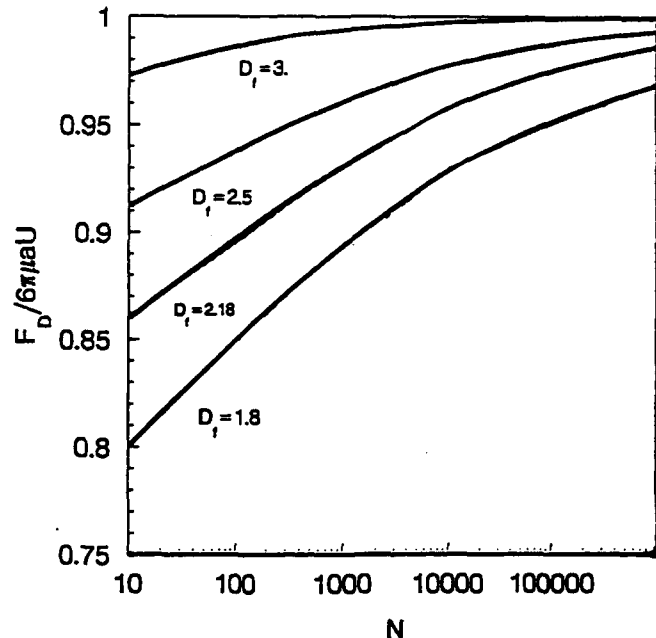
Fig. 2 Drag reduction associated with effective permeability for quasi-spherical "fractal" aggregates comprised of N primary spheres in the continuum regime (a = R_{max}= $\{(3/2) \cdot [D_f+2)/D_f]\}^{1/2} R_{gyration}$) (after Rosner and Tandon, 1993)
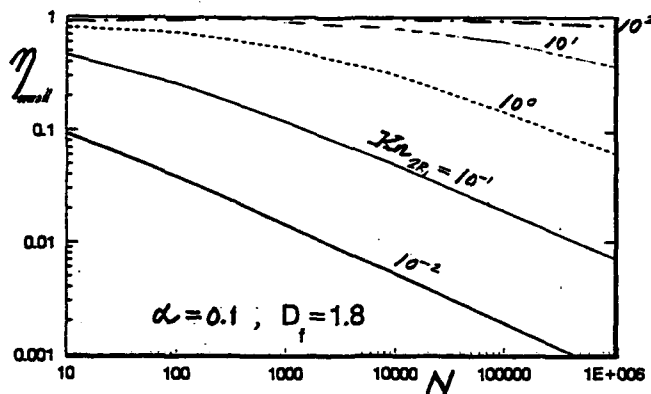
Fig. 3 Pressure dependence (*via* the Knudsen number based on primary sphere diameter) of the *accessible surface area* of large "open" (D_f=1.8) aggregates; reaction probability, α, of probing molecule 0.1; (after Rosner and Tandon, 1993)
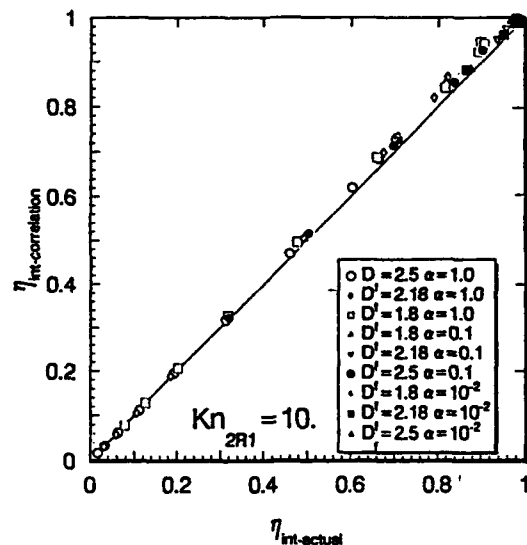
Fig. 4 Test of an "effective Damköhler number" correlation for the *accessible surface area* of a large fractal aggregate (after Rosner and Tandon,1993); success makes possible the efficient calculation of the accessible area evolution of polydispersed *populations* of aggregated particles in combustion gases.
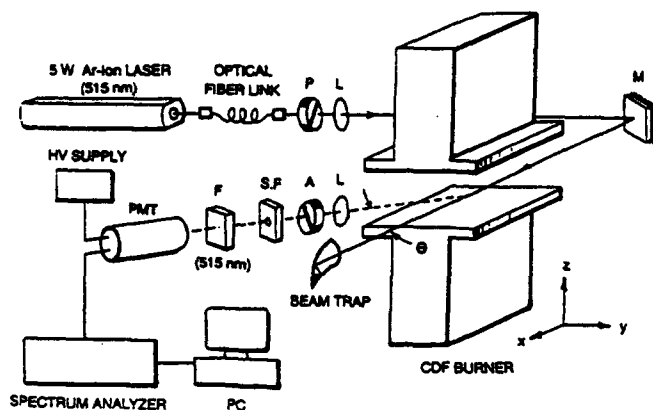
Fig.5 "Slot"-type counterflow diffusion flame (CDF-) burner set-up for *in situ* and extractive experimental studies of the nucleation, growth, transport and restructuring of aggregates in flames (after Albagli and Rosner, 1993; see, also, Gomez and Rosner, 1993)
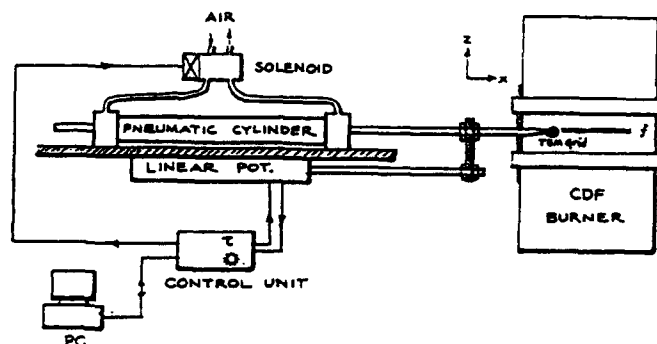
Fig.6 Probe for rapid local extraction (exploiting thermophoretic transport) of aggregates formed in a laminar counterflow diffusion flame (after Albagli and Rosner,1993; see, also: Rosner *et.al.* 1991)
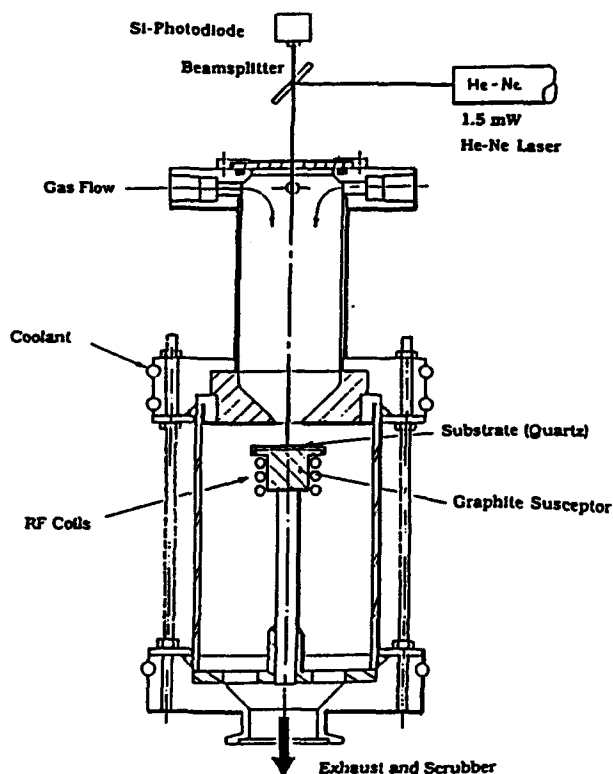

Fig. 7 Axisymmetric impinging jet CVD-reactor with inductively heated "pedestal" (after Rosner, Collins and Castillo, 1993)
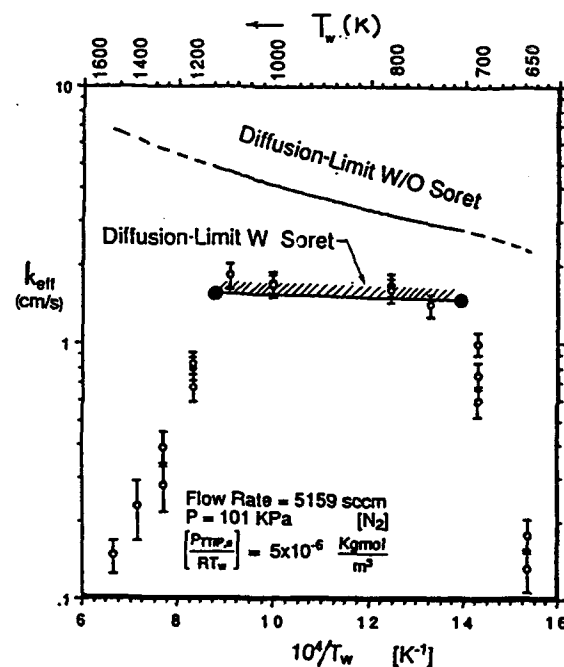
Fig.8 TiO$_2$(s) deposition rate data (reported as an apparent first order heterogeneous rate constant) from TTIP/O$_2$/N$_2$ mainstream showing calculated limiting surface temperatures and associated deposition rates (after Rosner, Collins and Castillo, 1993)

TURBULENCE-FLAME INTERACTIONS

Principal Investigator: D. A. Santavicca

Department of Mechanical Engineering
Propulsion Engineering Research Center
Penn State University
University Park, PA 16802

SUMMARY/OVERVIEW:

Turbulence-flame interactions in the reaction sheet regime can be viewed as the interaction between the flame front and vortices in the turbulent flow. With this phenomenological description in mind, the objective of this study is to investigate the interaction between individual vortices and laminar flame fronts. Experiments are conducted where PIV is used to characterize the velocity field and planar laser induced fluorescence is used to characterize the flame structure. In addition, a model based on a kinematical relationship between flame propagation and vortex motion is employed. This study is intended to address a number of important fundamental issues regarding flame-turbulence interactions including the effect of vortex size and strength on flame area production, flame curvature, and the minimum scale of flame wrinkling, as well as the relationship between the local flame curvature and strain and the local flame structure and speed. Also of interest is the temporal evolution of the flame structure, particularly as it relates to the vortex spacing.

TECHNICAL DISCUSSION:

Premixed flames interacting with Kármán vortex streets have been experimentally investigated. Local flame responses consistent with the results of stretched laminar flame theories are observed in that the OH LIF intensity increases when the local flame curvature becomes positive (negative) for thermodiffusively unstable (stable) flames. Departure of the peak OH LIF intensity for hydrogen flames ranges from 20 to 150% of the value at zero flame curvature for flame curvature ranging from -1.5 to 0.7 mm^{-1}, while for propane/air flames, the variation is within $\pm$ 20% of the value at zero curvature (Figure 1). Variation in the average peak OH LIF intensity is nearly linear with respect to the variation in flame curvature from -1.2 to 0.8 mm^{-1} (Figure 2). The flame area during interactions with Kármán vortex streets increases as a relatively weak function of the vortex velocity, while the vortex size affects the flame area increase in that smaller vortices are found to be less effective in generating flame area (Figure 3). The effect of Lewis number on the flame front is to enhance (suppress) the amplitude of the wrinkles generated by vortices for thermodiffusively unstable (stable) flames, thus resulting in larger (smaller) flame area (Figure 4). The flame curvature pdf's for flames interacting with Kármán vortex streets exhibit a bias toward positive flame curvature due to the large area of positively-curved flame elements that develop downstream along the V-flame. A decrease in vortex size tends to increase the flame curvature and thus broaden the pdf's, while the vortex velocity and Lewis number have relatively small effects on the flame curvature pdf's (Figure 5). The flame orientation distribution is peaked near the normal direction of flame propagation for small vortex velocity, while an increase in vortex velocity results in broadening of the flame orientation distribution and a shift toward larger flame angle due to the increased distortions in the flame front and increase in the effective flame propagation speed, respectively (Figure 6).
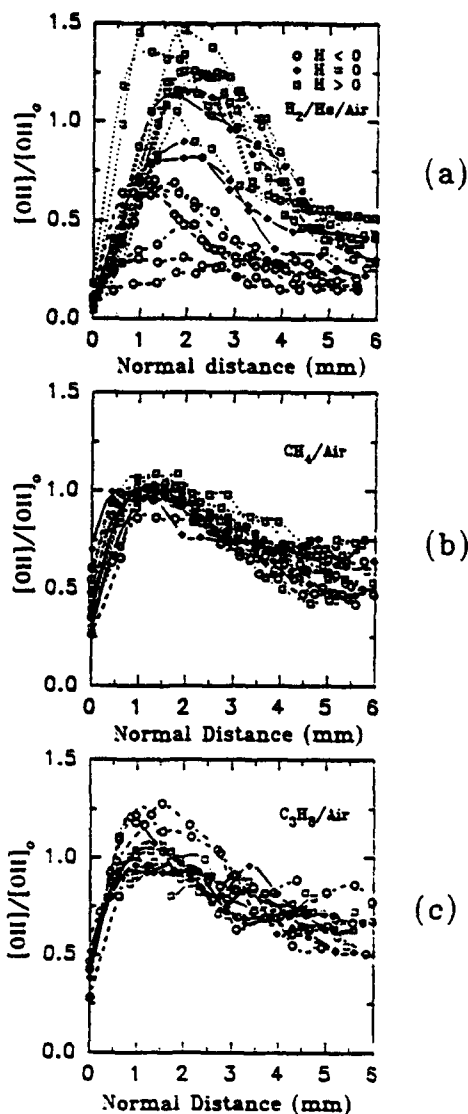
Figure 1. OH LIF intensity profiles normal to the flame front at (a) Le = 0.21, (b) 0.94 and (c) 1.79.
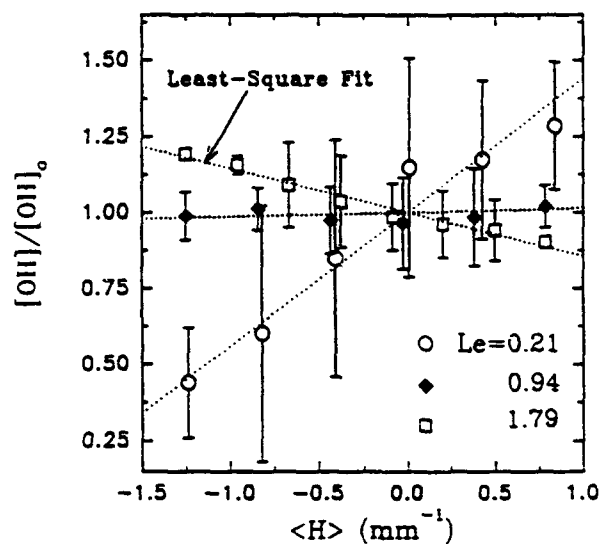
Figure 2. Averaged peak OH LIF intensity as a function of local flame curvature at various Lewis numbers.
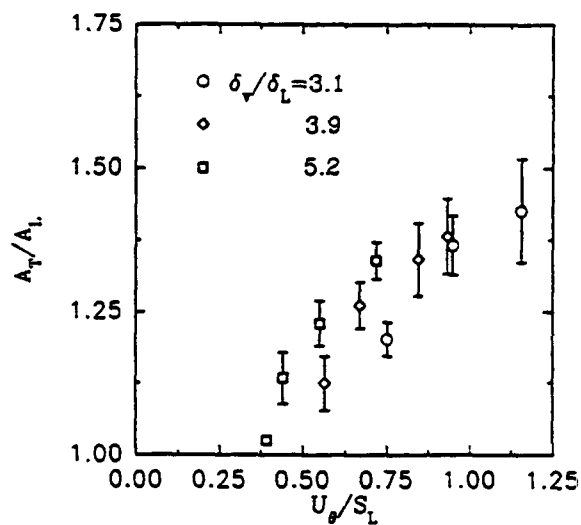
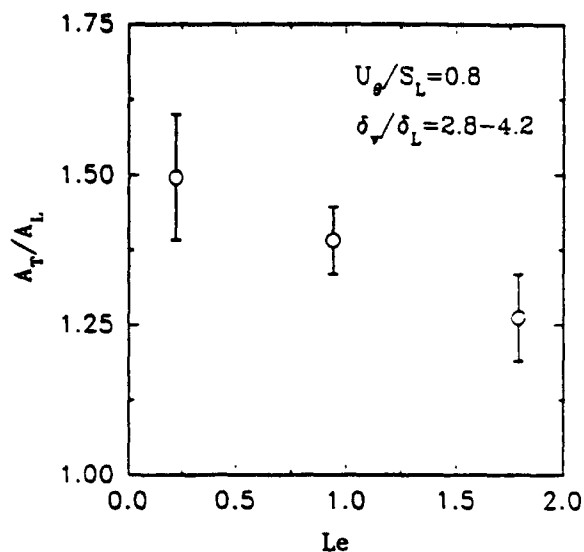Figure 3. Flame area increase as a function of U_θ/S_L.
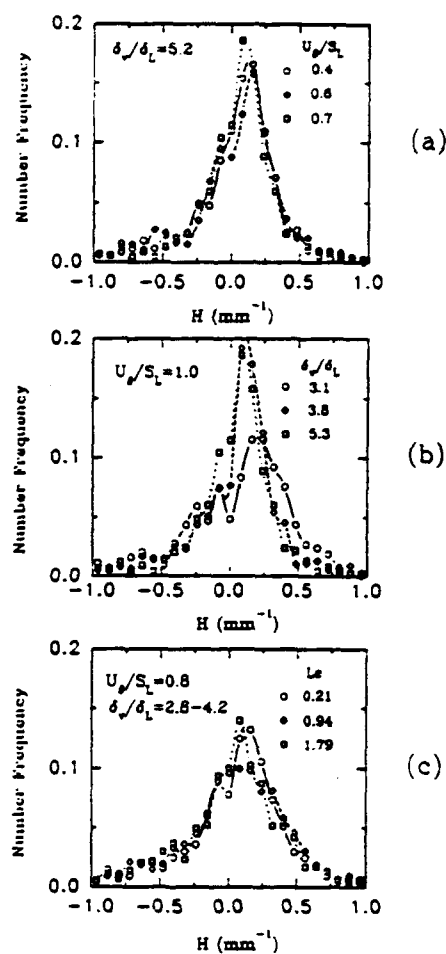
Figure 4. Effect of Lewis number on flame area.

Figure 5. Flame curvature pdf's at various (a) U_θ/S_L, (b) $\delta_v/_L$ and (c) Le.

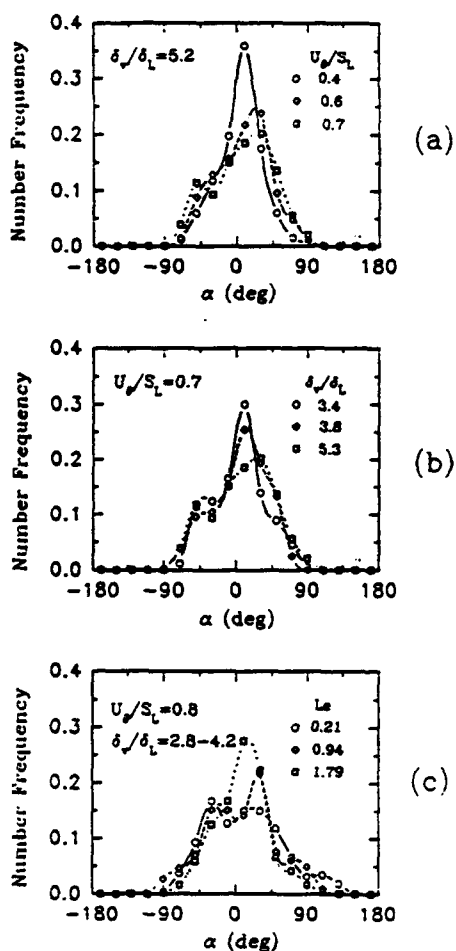**Figure 6.** Flame orientation distributions at various (a) U_θ/S_L, (b) $\delta_v/_L$ and (c) Le.

DETAILED STUDIES OF SOOT FORMATION IN LAMINAR DIFFUSION
FLAMES FOR APPLICATION TO MODELING STUDIES

Principal Investigator: Robert J. Santoro

Department of Mechanical Engineering
Propulsion Engineering Research Center
The Pennsylvania State University
University Park, PA 16802-2320

SUMMARY/OVERVIEW:

The primary objective of the present research program is to provide a fundamental understanding of the processes which control soot particle formation under conditions applicable to gas turbine engine operation. Current efforts emphasize laminar diffusion flame studies to elucidate fuel structure effects on particle precursor, inception and surface growth processes. Through extensive measurements of the gas and particle fields, direct comparison with detailed soot formation models can be undertaken to determine the controlling processes. Recently developed soot formation models based on premixed and diffusion flame studies have shown reasonable predictive capability. However, data for model validation remains limited and is a major deficiency in extending current understanding to practical problems. In the present study, emphasis has been given to species concentrations measurements made using mass spectrometric techniques. In particular, measurements have been obtained of acetylene, diacetylene, benzene and stable combustion products throughout methane/air and ethene/air laminar diffusion flames. Combining these measurements with previous soot particle and velocity field measurements it has been possible to follow the soot growth process along individual particle paths. These results establish that soot particle growth ceases due to the depletion of growth species not through the loss of soot particle reactivity as observed in premixed flame studies. Similarly, laser-induced fluorescence measurements of polynuclear aromatic hydrocarbons have been undertaken to follow the evolution of the soot precursor field. These measurements have established that laser-induced fluorescence can be used to reveal the qualitative structure of the molecular growth process leading to soot particle formation.

TECHNICAL DISCUSSION

The objective of this research effort is to investigate the fundamental phenomena controlling soot particle formation and destruction in combustion systems. The emphasis and approach chosen for the present studies is based on previous results which have proven the soundness of the methodology being utilized [1-5]. The present studies are conducted in well-characterized laminar diffusion flames in which fuel constituents, temperature, concentration and transport processes are systematically varied and/or measured. During the first year of this study efforts have emphasized measurements of species concentration, especially acetylene and benzene concentrations, throughout the flame using a mass spectrometric approach. Additionally, laser-induced fluorescence measurements have been obtained to characterize the evolution of large polynuclear aromatic species (PAH) formed in the flame. These measurements are being combined with previous determinations of the soot particle, velocity and temperature fields to yield more detailed information on the soot growth process.

Species Concentration Measurements

Detailed species concentration measurements have been obtained in laminar diffusion flames burning methane and ethene fuels in air. Both these flames have been previously studied in our laboratory and, thus, the present species concentration measurements significantly enhance that available data base. In particular for the ethene diffusion flame, a large data base exists on soot volume fraction, number density and particle diameter as well as on temperature, velocity, OH concentrations and PAH fluorescence [1-5]. The species concentration measurements complement this existing data and allow more sophisticated analysis of the soot formation process for this flame. Consequently, the ethene flame results will receive emphasis in the remainder of this abstract.

Species concentration measurements were obtained in an ethene/air laminar diffusion flame having a fuel flow rate of 3.85 cm^3/s. Although this flame does not emit soot particles from its tip, the peak soot

volume fraction observed in this flame exceeds 10^{-5}. Consequently, use of a novel electromagnetic sonic microprobe, previously developed at Penn State [5], is essential to achieving measurements in this flame. The major species considered in the flame were N_2, O_2, C_2H_4, CH_4, H_2O, CO_2, H_2, C_2H_2 and Ar. Preliminary measurements were also obtained for diacetylene (C_4H_2) and benzene (C_6H_6).

Figure 1 shows the measured mole fraction profiles of C_2H_4, C_2H_2 and H_2 at three axial locations in the ethene/air diffusion flame. As Figure 1a indicates, the fuel is rapidly consumed as it diffuses to the flame front and by 70 mm above the fuel tube exit has completely disappeared. Of marked interest to soot formation phenomena are the profiles of C_2H_2 which is generally viewed as the major species involved in soot particle surface growth. Acetylene (C_2H_2) shows slightly different features as compared to the C_2H_4 results (see Figure 1b). Although it is also totally consumed by the 70 mm axial location, C_2H_2 initially appears to be formed away from the center line region as indicated by the local maximums near 9 and 19 mm along the horizontal coordinate for the 7 mm axial location. Additionally, the mole fraction of C_2H_2 increases with height until the 20 mm axial location after which it rapidly decreases to zero at the 70 mm axial location. Hydrogen follows a similar trend (see Figure 1c), showing initially an increase in concentration as a function of axial location followed by a rapid decrease at the higher heights. The magnitude of the C_2H_2 mole fractions are nearly a factor of 8 larger in the ethene flame as compared to similar measurements made in a methane flame, which is consistent with the much more heavily sooting characteristics of the ethene flame. It is interesting to note that the hydrogen mole fractions were quite similar in the two flames, in contrast to the acetylene results.

Looking with more detail at the ethene flame results, one observes the profile of C_2H_2 is broad at the 7 mm axial location, suggesting that production occurs throughout much of the fuel rich part of the flame below this height (see Figure 1b). The doubling of the peak mole fraction from 0.03 at 7 mm to 0.06 at 20 mm attests to the continued net production of C_2H_2 throughout this region. During this time, the source of acetylene, the ethene fuel, has decreased from a peak of 0.7 at 7 mm to 0.14 at 20 mm. Therefore, with the source decreasing, the C_2H_2 peak at 40 mm decreases to 1/6 of its value at 20 mm. This 40 mm height coincides with almost total consumption of the fuel and the location of the greatest local soot volume fraction [1,2]. The total amount of carbon contained as soot at this height represents 14% of the total carbon flow rate, while the major species remaining to be oxidized are H_2 and C_2H_2 with 0.02 and 0.01 mole fractions respectively.

Soot Growth Mechanism

As was mentioned earlier an advantage in obtaining species concentration measurements for the ethene/air diffusion flame is the availability of other related measurements [1-5]. In particular, an extensive set of measurements on the evolution of the soot particle field is available along with related temperature and velocity field determinations. From the velocity measurements, soot particle paths can be determined and, thus, the detailed evolution of soot particle growth and oxidation can be obtained. In the present case, the soot growth process will be examined in relationship to the acetylene concentration field. In examining this process, three particle paths will be considered. One path includes the region of the flame where the maximum soot volume fraction is observed. A second considers the center line region of the flame while the third involves an intermediate particle path located between these other two paths.

Figure 2 shows soot volume fraction f_v, and the acetylene mole fraction as a function of time along each of these particle paths. These measurements represent the first time that such detailed species concentration information has been available in diffusion flames with accompanying detail soot particle information. Each of the particle paths shows the same trend. The soot volume fraction achieves a maximum at the same location where the acetylene concentration has approached zero. Thus, the depletion of growth species is the reason for soot growth ceasing. In the premixed flames, similar measurements indicate that significant acetylene concentrations exist well after soot growth stops. This observation has been used to argue that decreases in soot particle reactivity are responsible for the termination of soot mass addition. The present measurements show that, in the case of ethene diffusion flames, a different mechanism is operative. This result is quite significant since it rules out one of three possible mechanisms responsible for soot growth ceasing, that is loss of surface reactivity. The other two mechanisms remain to be investigated.

Of the two remaining mechanisms, one involves a decrease in the acetylene concentration because the source of acetylene decreases while the sink for acetylene, surface reactions with soot particles, continues to deplete the acetylene in the flame. The second mechanism involves the competition between formation and oxidation, that is as higher locations in the flame are achieved, oxidation of intermediates and soot particles reduces the net rates of production. It is likely that both mechanisms are important in different parts of the flame.

To fully examine these mechanisms, measurements of only the acetylene concentration are not sufficient. Information on the concentration of oxidizing species is also required. The mass spectrometer measurements do provide a measure of the oxygen (O_2) present in the flame. Another species of interest is hydroxyl radical (OH) which is known to be important in the oxidation of soot particles and possibly early soot precursors. Recently in our laboratory, laser-induced fluorescence has been utilized to obtain measurements of OH in this ethene/air diffusion flame [5].

Figure 3 shows the radial profiles of OH mole fraction at two axial locations in the flame, 7 and 70 mm. The arrows located on the figure indicate the location of the particle path containing the maximum f_v and the intermediate particle path, while the particle path along the center line lies at r equal to 0. The particle path containing the maximum f_v lies at the larger radial position indicated by the arrows. At the lower axial position (see Figure 3a), the particle paths lie inside the region of peak OH concentration and generally experience low concentrations of OH radicals. As the soot particles traverse the flame and reach higher locations, larger OH concentrations are observed in regions where soot particles occur. At these higher axial locations, these OH concentrations contribute to reactions resulting in particle oxidation. These results clearly indicate that OH concentrations can also be particle path resolved in these flames. This analysis is currently on-going and will be combined with the previously described species concentration measurements to investigate the oxidative competition which occurs involving both gas phase species such as C_2H_2 as well as the soot particles.

CONCLUSIONS

In summary, the present investigations have added critical new data needed to establish the mechanism controlling soot growth and oxidation. In particular, the measurements of C_2H_2 have revealed that soot surface growth ceases due to the depletion of growth species not due to the loss of soot particle reactivity. This observation is in agreement with recent work by Honnery and Kent [6], who have shown that in long laminar diffusion flames, soot growth can be extended to very long residence times. The species measurements now need to be combined with complementary soot particle, temperature and OH field measurements to examine other mechanistic questions. Additionally, other fuels should be studied as well in order to take advantage of the previous work done in our laboratory on fuel structure effects.

Measurements of polynuclear aromatic species using a laser-induced fluorescence technique have also been obtained and demonstrated a strong sensitivity of the fluorescence signals to the excitation and detection wavelength conditions utilized. These results have been interpreted as a means to qualitatively follow the growth of large molecular species in the flame.

Future work on this program will extend the current measurements to a wider range of fuel structures and will examine the role of oxidation on the depletion of key surface growth species. Efforts will also continue on furthering the quantitative interpretation of the PAH fluorescence results.

REFERENCES

1.   Santoro, R. J., Semerjian, H. G. and Dobbins, R. A., "Soot Particle Measurements in Diffusion Flames," *Combustion and Flame*, 52, pp. 204-218 (1983).
2.   Santoro, R. J., Yeh, T. T., Horvath, J. J. and Semerjian, H. G., "The Transport and Growth of Soot Particles in Laminar Diffusion Flames," *Combustion Science and Technology*, 53, p. 89 (1987).
3.   Puri, R., Richardson, T. F., Santoro, R. J. and Dobbins, R. A., "Aerosol Dynamic Processes of Soot Aggregates in a Laminar Ethene Diffusion Flame," *Combustion and Flame*, 92, pp. 320-333 (1993).
4.   Puri, R., Moser, M., Santoro, R. J. and Smyth, K. C., "Laser-Induced Fluorescence Measurements of OH Concentration in the Oxidation Region of Laminar, Hydrocarbon Diffusion Flames," *Twenty-Fourth Symposium (International) on Combustion*, The Combustion Institute, Pittsburgh, PA, pp. 1015-1022 (1992).
5.   Puri, R., "The Interaction of Soot Particles and Carbon Monoxide in Laminar Diffusion Flames," Ph.D. Thesis, The Pennsylvania State University (1992).
6.   Honnery, D. R and Kent, J. H. , "Soot Formation in Long Ethylene Diffusion Flames," *Combustion and Flame*, 82, p. 426 (1990).
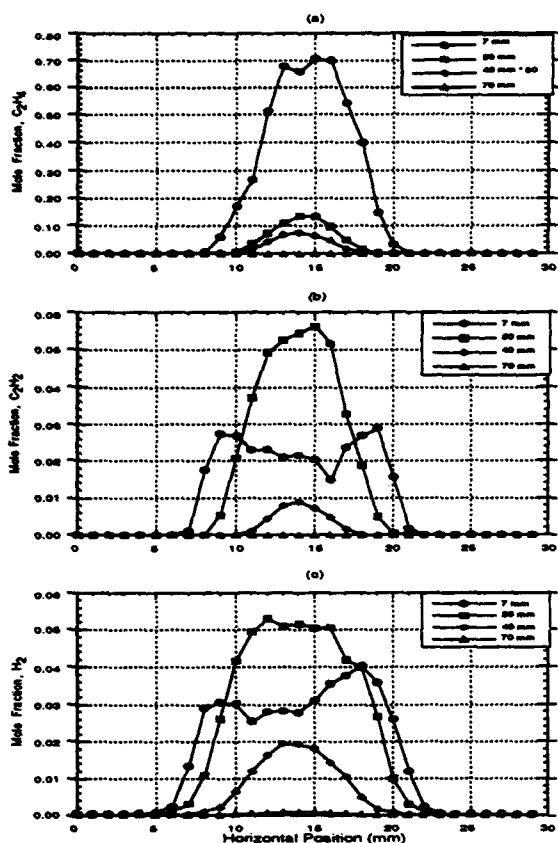
Figure 1: Plots of the measured species mole fractions as a function of horizontal position for several axial locations (7, 20, 40 and 70 mm) in a C_2H_4/Air diffusion flame with a fuel flow rate of 3.85 cm³/s: a) C_2H_4 mole fractions, b) C_2H_2 mole fractions, c) H_2 mole fractions.
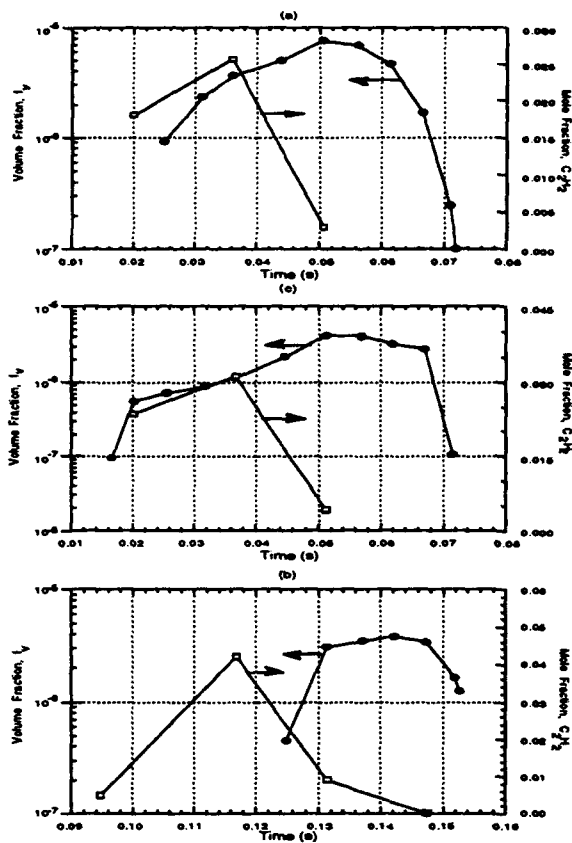
Figure 2: Plots of the soot volume fraction, f_v, and the mole fraction of C_2H_2 as a function of time for a) the particle path containing the maximum soot volume fraction, b) the particle path intermediate to the particle path containing the maximum soot volume fraction and the center line, c) the particle path along the center line.
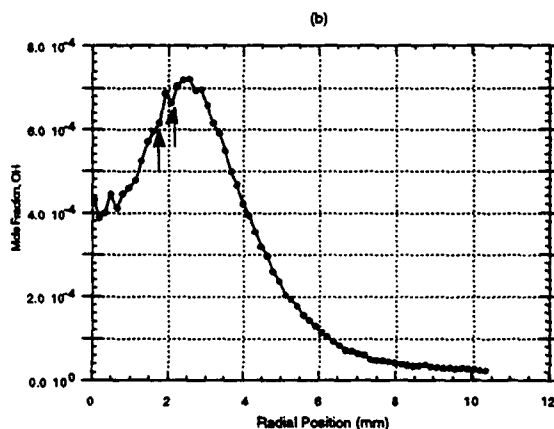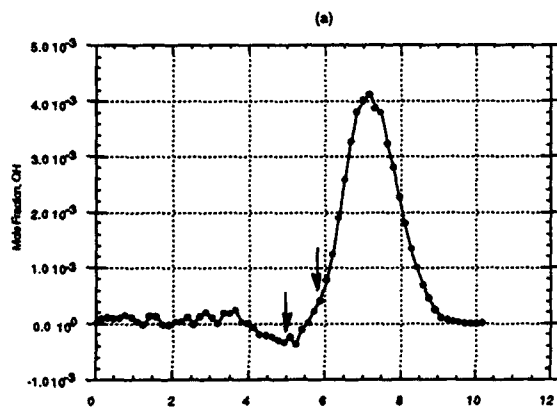

Figure 3: Plots of the OH profile for two axial locations in the ethene/air diffusion flame: a) 7 mm axial location, b) 70 mm axial location. Note arrows indicate where the particle paths discussed in Figure 2 intersect the profiles. Negative values for the OH mole fraction are a result of subtraction errors in analyzing the data.

FUELS COMBUSTION RESEARCH

(AFOSR GRANT 89-0034)

Principal Investigators: I. Glassman and K. Brezinsky

Department of Mechanical and Aerospace Engineering
Princeton University
Princeton, NJ 08544

SUMMARY

In order to provide fundamental insight into the effects that changes in Air Force fuels may have on engine performance, three sets of chemically oriented investigations have been undertaken: 1. The pyrolysis and oxidation of prototypical endothermic fuels 2. The thermal degradation of high temperature hydrocarbon liquids and supercritical fluids 3. The oxidation chemistry of polynuclear aromatics.

Technical Discussion
1) Endothermic Fuels

The current means of aircraft cooling, especially engine cooling, employ ram air, fuel, and fuel recirculation as heat sinks for dissipating the intense heat developed during high speed flight. Fuel recirculation on military aircraft is the primary means of engine cooling. Most fuels can provide this cooling only through their sensible enthalpy. However, some fuels can provide additional cooling through catalytic, endothermic reactions and are thus referred to as endothermic fuels. One example of this fuel type is methylcyclohexane (mch) which, in the liquid phase, is catalytically dehydrogenated to toluene and hydrogen. The toluene and hydrogen produced are then consumed as fuels in the combustor.

Studies have been conducted on the chemistry of this liquid phase dehydrogenation reaction of mch. These studies indicate that the complete dehydrogenation of the fuel is not always achieved. As a result, mch may be a substantial portion of the fuel-oxygen mixture in the combustor. Unfortunately, these liquid phase studies do not offer sufficient insight into the vapor phase reactions that the mch will undergo within the combustor. Knowledge of the vapor phase oxidation of mch will be required to understand its ignition characteristics, reaction time, and pollutant formation. Knowledge of the vapor phase pyrolysis of mch is also necessary to understand the dominant intermediate compounds formed during fuel decay, as well as any soot formation processes that may occur. If mch is to endure as an endothermic fuel, then answers to fundamental questions regarding its oxidation and pyrolysis characteristics in combustor environments need to be investigated. This research attempts to address some of these questions.

The pyrolysis and oxidation studies of mch were performed in the Princeton Atmospheric Turbulent Flow Reactor, which has been extensively described elsewhere. From the experimental results of these studies the normalized fuel concentration (fuel concentration at a given time divided by fuel concentration at the first sampling point) as a function of time for each pyrolysis experiment can be used to generate the rate constant for the unimolecular decomposition of the fuel at each temperature when first order rate analysis is applied. The reaction rate constants obtained and the experimentally obtained reaction temperatures can then be used to determine the overall activation energy and pre-exponential factor for mch pyrolysis. An Arrhenius plot of the data is shown in Figure 1. From linear regression analysis, the activation energy and pre-exponential factor were determined to be 62.55 kcal/mol (262 kJ/mol) and 2.55×10^{13} s^{-1}, respectively. Also shown in Figure 1 is an Arrhenius plot of the sum of the high pressure rate constants of the C-C bond cleavages in the molecule, i.e. cleavage rate of the methyl group of the ring plus the scission rates of the six C-C bonds that form the cyclohexane ring. These expressions were taken from Brown and King, (Int. J. of Chem. Kin., 1989, v. 21. p.251), and were deduced from experiments performed at very low pressure in Knudsen cells. As can be seen from Figure 1, the two Arrhenius plots differ and the overall rate constant of mch decay in the flow reactor is greater than the overall rate constant of mch decay at very low pressure. In fact, the difference between the two plots is actually greater than the sum of the C-C bond cleavage rate constants at each of the four experimental temperatures. Physically, this implies that the majority of mch decay in the flow reactor is occurring by means other than C-C bond cleavage.

The major species profiles as functions of reaction time of a typical mch pyrolysis are shown in Figure 2. These results are typical because in all the pyrolysis experiments conducted, ethene was the highest concentration intermediate produced, followed by butadiene, methane, and propene. Furthermore, a cyclohexane/benzene peak was observed in each pyrolysis experiment. Since both compounds have nearly the same retention time on the DB5 column, additional injections were performed using another Hewlett Packard gas chromatograph (model 5890) equipped with a DB1 column. The benzene and cyclohexane were successfully separated by this column and it was found that the majority of the combined peak was benzene; virtually no cyclohexane was present. Toluene concentrations, also observed at each pyrolysis, remained fairly constant as functions of time and never exceeded 20 ppm. (Thus, while liquid phase catalytic dehydrogenation of mch leads selectively to toluene and hydrogen, the homogeneous vapor phase decomposition of mch produces a minimal amount of toluene.) Isoprene (methyl butadiene) concentration, also shown in Figure 3, never exceeded 100 ppm for any of the pyrolysis studies. Furthermore, isoprene had the highest concentration of any methyl substituted intermediate (e.g. methyl propane, methyl pentene, etc.) produced.

For comparison, mch oxidation experiments were also performed and typical major species profiles versus reaction time are shown in Figures 3. The oxidation and pyrolysis reactions, carried out at nearly identical temperatures, resulted in the formation of similar intermediate species and species profiles. The only compound detected in significant quantities during oxidation experiments that was not detected during the pyrolysis experiments was formaldehyde. However, as can be seen by comparing Figures 2 and 3, reaction rates increased during oxidation. Thus, while the oxygen did not introduce many new stable intermediate species into the reaction pool, it did increase the radical pool which led to faster fuel and intermediate species consumption.

Mechanistic analysis and interpretation of these results are continuing.

2) High Temperature Liquids and Supercritical Hydrocarbon Fluids

In order to study the chemical behavior of aircraft fuel components in an environment beyond their supercritical state, a small scale 'first generation' test rig has been built. Once this apparatus has been fully characterized and calibrated, modifications and redesign can and will be performed to improve the rate and accuracy of the experimental data it generates.

The aromatic hydrocarbon toluene (aromatics are a major component of aircraft fuels), has been chosen as the first chemical to be studied. Since toluene's critical temperature, T_C, and critical pressure, P_C, are 592°K (319°C) and 4.104MPa (40.5Atm), respectively, the apparatus must be able to withstand fairly high temperatures and pressures to operate in toluene's supercritical region.

As a first experiment, toluene will be subjected to a variety of pressures and temperatures, both above and below P_C and T_C, for various residence times in the heated, high pressure reaction zone. The reacted product will then be analyzed to determine if and how the reactant has changed.

To sustain flow in the reaction zone, a pumping system is required which will not only achieve the desired pressures on the order of 600psia, but will also maintain them without fluctuations. Several pumps were tested; these were high pressure liquid chromatography pumps which used one or two reciprocating pistons to drive the fluid. This type of pump was found to have large pressure fluctuations corresponding to their cyclic operation, even with various flow dampeners installed. Because of this drawback, a syringe pump has been chosen to drive the system; this type of pump can hold a constant pressure at any chosen flow rate below its maximum of 200ml/hour (0.056ml/sec).

A diagram of the apparatus is shown in Figure 4. Pressurized by the pump, fluid is heated in the heated reaction coil, cooled by the cooling coil, brought to atmospheric pressure, and collected in sample vials. The fluid flows through nickel capillary tubing whose inside diameter is 0.43mm (0.017in). This size tubing enables the fluid to be rapidly heated and cooled, while still maintaining adequate residence times in the heated zone by choosing the heated coil's length and pump flow rate. Analysis has shown that the various parameters chosen have created the desired idealized 'plug flow' reactor in which each parcel of fluid experiences identical flow histories.

The heated reaction zone is kept at constant temperature with a Techne™ fluidized sandbath. The bath's electric heaters can subject the heated coil to temperatures of up to 600°C (873°K), well beyond the T_C of toluene, current JP fuels, and the proposed "JP-900" fuel's highest operating

temperature of 900°F (482°C). Calibrations of the bath have shown that once it has stabilized, a uniform coil temperature can be maintained to within ±1°C over the entire volume the coil occupies. A water/ice bath envelopes the cooling coil at 0°C.

Pressure is monitored upstream of the heated coil with a standard gauge, and downstream of the heated coil with a mV output pressure transducer. The pressure drop across the heated coil can thus be measured, and has been found to agree almost exactly with theoretical laminar pipe flow pressure loss. Unfortunately, due to the high temperature at the entrance and exit of the heated coil, most transducer electronics will not survive. For this reason the gauge and transducer are currently positioned far from the fluidized bed. The use of special, miniature water-cooled transducers and remote-electronics transducers are being investigated as a potential solution to this problem.

Pressure is currently regulated with a needle valve in combination with a spring-loaded back pressure device which drops 500psi across it. More advanced automatic pressure regulation systems are being considered to increase the accuracy and constant control of the reactant pressure.

Temperature is controlled in the fluidized bed by a Eurotherm™ temperature controller which maintains the heating elements at the desired temperature. Type K thermocouples monitor the heating elements, center of the fluidized bed, and the fluid temperature at the entrances and exits of the heated and cooling coils. Small (0.02in diameter) thermocouples were inserted directly into the tubing unions in order to eliminate the effects of a recirculating "dead volume" which would destroy the plug-flow aspect of the reactor. The samples are collected in vials and directly injected into the gas chromatograph for analysis. This system will be upgraded to an in-line sample valve. Currently, a new Hewlett-Packard™ Gas Chromatograph combined with a Nicolet™ Fourier Transform InfraRed spectrometer (GC-FTIR) is being installed in the laboratory. This state-of-the-art equipment will allow detailed composition studies of the reacted products.

Two samples have been collected during preliminary runs to test the apparatus. Both toluene reactants were subjected to pressures of 680psia ($1.15P_c$) at temperatures of 200°C ($0.8T_c$) and 300°C ($0.97T_c$) respectively. Their residence time in the heated reaction zone was 20.8 minutes. Comparison with an unreacted toluene sample will be performed when the new GC-FTIR is operational.

In sum, the preliminary liquid flow reactor system has been built. Several runs have been performed with toluene as a reactant to evaluate the design, and samples have been taken which are ready for analysis. A new GC-FTIR system will soon be available for sample analysis. Future modifications to the apparatus will include heat resistant pressure transducers, a more accurate pressure control system, an in-line sampling valve, and later a mixing chamber in order to react two different reactants with each other in the heated reaction zone.

3) Polynuclear Aromatics

The study of the oxidation of 1-methyl naphthalene has culminated this year. The results of the study have been presented at the 24th Symposium on Combustion in Sydney, Australia. A Ph.D. degree has been awarded to the student, Chris Shaddix, who has worked on this part of the program. Details of the research are available in his Ph.D. thesis and the article published in the Symposium volume, and therefore will not be reported here.
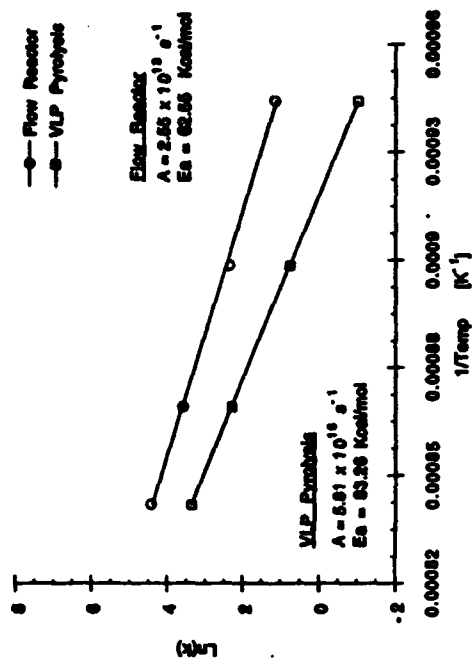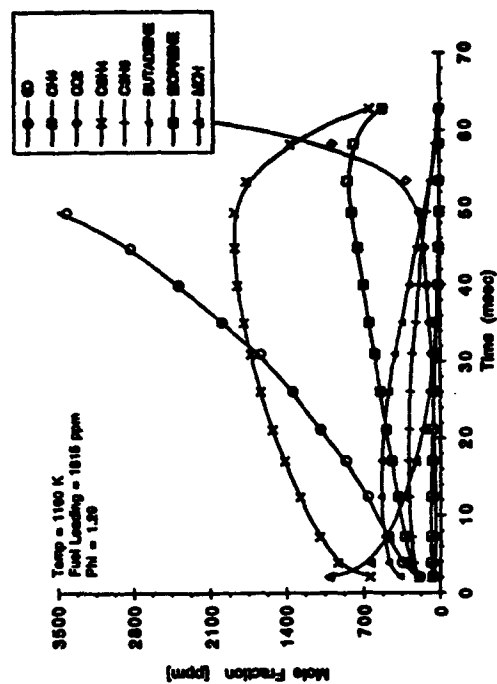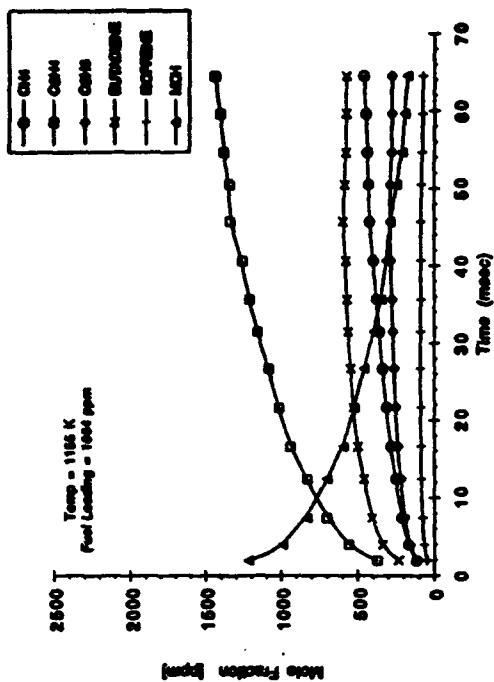
Figure 2: Major Species Profiles of a Typical MCH Pyrolysis

Figure 4: High Temperature Liquid - Supercritical Fluid Reactor Apparatus

Figure 1: Arrhenius Plots of Overall MCH Decay

Figure 3: Major Species Profiles of a Typical MCH Oxidation

ATOMIZATION OF VISCOUS LIQUID SHEETS

Principal Investigator: E. A. Ibrahim

Mechanical Engineering Department
Tuskegee University
Tuskegee, Alabama 36088

SUMMARY

The research has been focused on the atomization of an attenuating viscous liquid sheet due to antisymmetrical waves. It is found that the instability of the sheet is enhanced by a decrease in surface tension or an increase in the gas to liquid density ratio. The liquid viscosity has a greater damping effect on shorter waves than longer waves. Predictions of the size of drops produced by the sheet disintegration agree well with experimental values.

TECHNICAL DISCUSSION

The governing equations for a viscous sheet of thickness 2H which is thinning in time and moving in the x-direction with velocity U through a stationary inviscid gas are derived considering antisymmetrical perturbations. Assuming only movements in the y-direction (Dombrowski and Johns, 1963), the equation of motion of the neutral axis mid-way between the two gas/liquid interfaces is obtained by inter-relating the forces caused by gas pressure, surface tension, liquid inertia and viscosity. The gas pressure is found from the potential of the gas motion. The resulting equation of motion in dimensionless form is given by;

$$h \frac{\partial^2 \eta}{\partial t^2} + \frac{\partial h}{\partial t} \frac{\partial \eta}{\partial t} = \frac{1}{Re}\left(\frac{\partial^3 \eta}{\partial t \partial x^2} - \frac{\partial h}{\partial t} \frac{\partial^2 \eta}{\partial t \partial x}\right) + \frac{1}{We}\frac{\partial^2 \eta}{\partial x^2} + D\,k\,\eta = 0 \tag{1}$$

where h is the instantaneous sheet thickness, η is the sheet centerline perturbation, t is time, Re is the liquid Reynolds number, We is the liquid Weber number, D is the gas to liquid density ratio and k is the wave number. The characteristic length and velocity are half the sheet initial thickness H and the sheet basic velocity U, respectively. The boundary and initial conditions correspond to those of an initially sinusoidal perturbation at the nozzle of amplitude η_0 and frequency $f = U/\lambda$, where λ is the wave length. The governing equations are solved by the finite difference technique for the case when the sheet attenuation follows h = c/t, where c is a constant (Dombrowski and Hooper, 1962). The value of c is reported to be $c = 315 \times 10^{-9}/H^2$ for a wide range of operating conditions (Dombrowski, Hasson and Ward, 1960). However, a theoretical approach to the calculation of c is being developed in

the present effort. The evolution of the sheet perturbation η with time and distance x along the sheet is followed up to the breakup instant. The sheet breakup is assumed to take place when the perturbation grows to exp(12) times its initial amplitude. At breakup, tears occur in the crests and troughs and fragments of sheet, corresponding to one-half wavelength are broken off (Dombrowski and Hooper, 1962, Rangel and Sirignano, 1991, and Mansour and Chigier, 1990). The fragments contract by surface tension into unstable cylindrical ligaments which subsequently break down into drops.

We begin by investigating the effects of the dimensionless quantities, We, Re and D, which contain the liquid and gas properties, sheet initial thickness and velocity, on the stability of the sheet. The results of these computations are shown in Figures 1 through 3. In these Figures the growth rate is computed from $d(\ln(\eta/\eta_0)]/dt$, i. e., that corresponding to an exponentially growing wave.

Figure 1 shows that the sheet becomes more unstable as the Weber number is increased. In other words, surface tension has a stabilizing effect on the sheet perturbations. This is in contrast to the effect of surface tension on the stability of Rayleigh jet where it acts as a destabilizing factor. However, for liquid jets at high Weber numbers, surface tension contributes to a lower growth rate of the instability waves (Lin and Ibrahim, 1990, Ibrahim and Lin, 1992).

In Figure 2 the effect of Reynolds number on the growth rate of instability waves is depicted. It is seen that the growth rate increases with an increase in Reynolds number. The trend in Figure 2 is that as the Reynolds number is decreased the peak growth rate is shifted towards a smaller wave number. Therefore, the higher the liquid viscosity the more the waves of shorter wavelength are damped. This implies that, for a highly viscous liquid sheet, only large ligaments and drops may result during the breakup process.

Figure 3 illustrates the relation between the growth rate of the instability waves and the gas to liquid density ratio. The growth rates are increased and the maximum growth rate shifts to a higher wave number as the density ratio is increased. Accordingly, the liquid sheet will be more unstable and its atomization will result in finer drops if the density ratio is higher. This effect is due to the fact that the principal instability mechanism is the aerodynamic forces in the gas (Squire, 1953). The liquid sheet atomization will be inhibited in the absence of gas inertia.

Some preliminary computations of the size of the drops produced by the liquid sheet atomization due to the growth of antisymmetrical waves are shown in Figure 4. These computations are obtained as follows. If h_b is the sheet thickness at breakup and K is the wave number of the fastest growing wave, then the diameter of the resulting cylindrical ligaments, as obtained by a mass balance is

given by $D^2_L = 8h_b/K$. It has been previously observed (Dombrowski and Fraser, 1954) that ligaments produced from a liquid sheet breakup through symmetrical (or dilational) waves. Weber (1931) has analyzed the properties of these waves where surface tension forces predominate, and for co-current air flow where air reaction assists disintegration. In the present case the ligaments move transversely through the atmosphere. Under these conditions the surrounding atmosphere will have no effect on the wavelength and Weber's (1931) results for surface tension breakup can be assumed to apply. It is assumed that the waves grow until they have an amplitude equal to the radius of the ligament, i. e., one drop will be produced per wavelength. Thus, by mass balance the relation between drop size and wave number is given by, $D^3_D = \pi D^2_L/4K$, which on combination with Weber's (1931) theory yields;

$$D_D = \frac{1}{2K} \left[1 + \frac{3\mu}{(\rho \sigma D_L)^{1/2}} \right]^{1/3} \tag{2}$$

where μ, ρ and σ are the liquid dynamic viscosity, density and surface tension, respectively. Equation 2 is used with D_L from above to calculate the drop sizes. Values of h_b are obtained from the numerical solution of Eq. 1 as $h_b = c/t_b$, where t_b is the total time it takes the perturbation of the sheet surface to grow to the breakup amplitude $\eta_0 \exp(12)$.

In Figure 4 some representative results of the variations of the drop sizes with the sheet basic velocity are shown for the atomization of a sheet of water in atmospheric air. As expected the drop sizes decrease with increasing the sheet velocity. The sizes of the drops fall within the experimental values reported in Mansour and Chigier (1990). However, more validations and refinements of the computational procedure are still needed.

REFERENCES

Dombrowski, N., and Fraser, R. P., 1954, Phil. Trans.,A247,pp. 101.
Dombrowski, N., and Johns, W. R., 1963, Chem. Engng. Sci., 18, pp. 203-214.
Dombrowski, N., Hasson, D., and Ward, D. E., 1960, Chem. Engng. Sci., 12, pp. 35-50.
Dombrowski, N., and Hooper, P., 1962, Chem. Engng. Sci., 17, pp. 291-305.
Ibrahim, E. A., and Lin, S. P., 1992, J. Appl. Mech., 59, pp. S291-296.
Lin, S. P., and Ibrahim, E. A., 1990, J. Fluid Mech., 218, pp. 641-658.
Mansour, A., and Chigier, N., 1990, Phys. Fluids A, 2, pp. 706-719.
Rangel, R. H., and Sirignano, W. A., 1991, Phys. Fluids A, pp. 2392-2400.
Weber, C., 1931, Z. Angew. Math. Mech., 11, pp. 136.
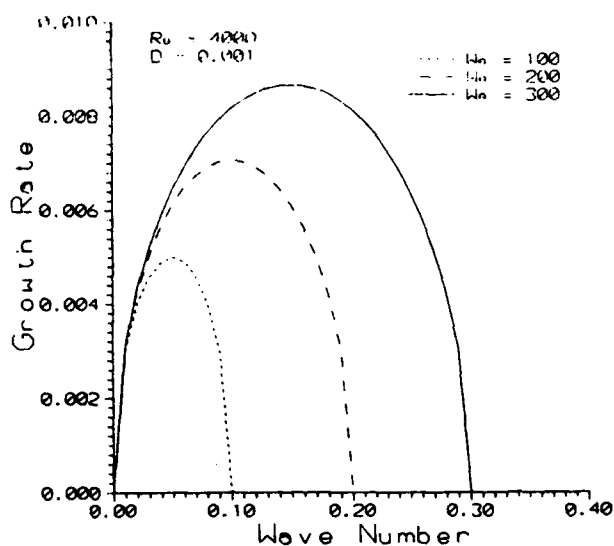Squire, H. B., 1953, Brit. J. Appl. Phys., 4, pp. 167-169.

Figure 1. Effect of Weber
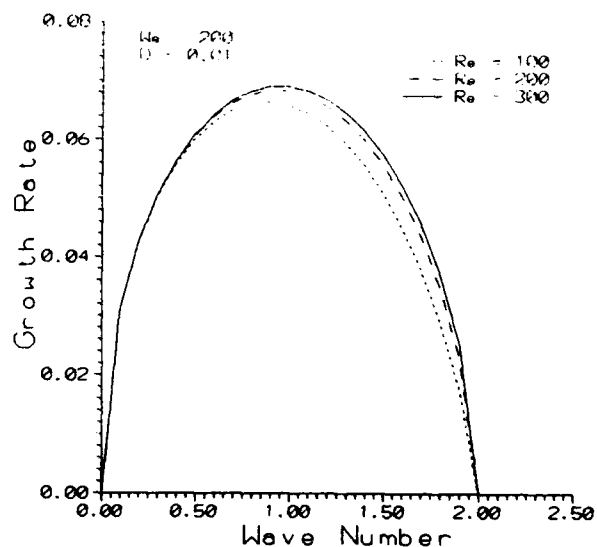number on growth rate

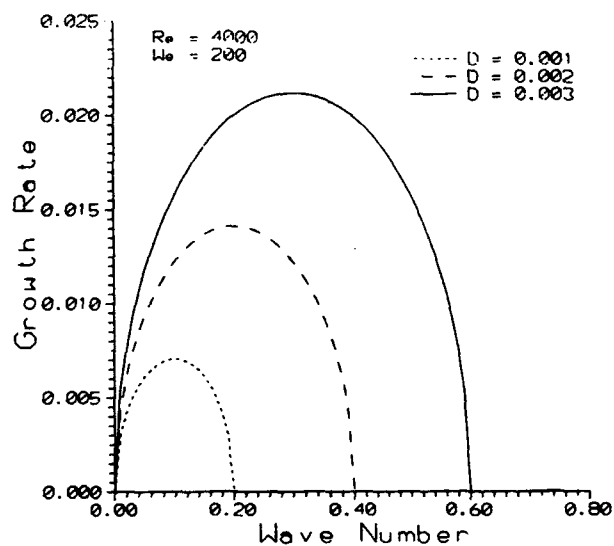Figure 2. Effect of Reynolds
number on growth rate
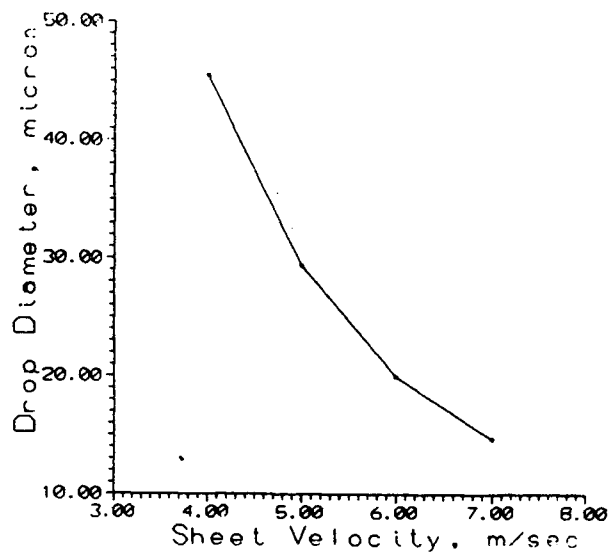

Figure 3. Effect of density
ratio on growth rate

Figure 4. Variation of drop
size with sheet velocity

PARTICLE DISPERSION IN A TURBULENT SHEAR FLOW

Principal investigators: I.M. Kennedy and W. Kollmann

MAME Department, University of California at Davis, CA 95616

SUMMARY

A joint experimental/numerical project is underway to improve the understanding of turbulent spray behavior. In particular, attention has been given to the impact of turbulence on droplet scale processes such as drag, mass transfer and heat transfer. A laser based technique has been used to track particles in a turbulent jet. The computational phase of the project is aimed at the development of a Large Eddy Simulation method for the turbulent jet that has been the object of the experimental study. The goal is to obtain a simulation of the jet under conditions that match the experimental conditions so that droplet dispersion and vaporization rates can be compared and correlations of drag and mass transfer evaluated. Our specific goal in this year of the project was to implement a LES-model for the unresolved scales of the flow into the Navier-Stokes solver and to compare the filtered and unfiltered results to evaluate the effect on particle dispersion and vaporization rates.

TECHNICAL DISCUSSION:

Experimental.

One of the major unknowns in modeling particle dispersion in turbulent flows is the form of the Lagrangian velocity autocorrelation function for fluid and discrete particles. If this function is known, then it is possible to obtain the dispersion i.e., the mean square displacement from a known initial point. Snyder and Lumley (1971) obtained the autocorrelation function in a grid-generated turbulence but there are no data for particles in a turbulent shear flow such as a jet. One phase of the project over the last year has been devoted to obtaining this fundamental information.

The basic experimental methodology has been reported elsewhere (Call and Kennedy, 1991, 1992). A laser sheet is formed with cylindrical lenses. As a droplet passes through the laser sheet, the scattered radiation is collected and imaged onto a position-sensing photomultiplier tube. This scheme has been modified to obtain velocity and correlation information. Two sheets of parallel light are produced with a beam splitter and right angle prism. The parallel sheets are reflected back across the jet with a retro-reflector with an adjustable spacing between the pairs of laser sheets. The time between scattering spikes from each sheet yields droplet velocity data, whatever the droplet location across the jet cross-section. Autocorrelations of the axial particle velocity can be obtained from the two velocity measurements from the two pairs of sheets. The autocorrelations can be reported

in either an Eulerian form as a function of spatial separation or in a quasi-Lagrangian form as a function of time from the first transit through the first set of laser sheets.

We have studied hexadecane droplets ranging in diameter from 50 μm to 35 μm. In addition, hollow glass spheres of 40 μm diameter have been used to approximate fluid particles. Figure 1 shows the quasi-Lagrangian autocorrelation function for axial particle velocity at a number of axial locations along the jet. The correlations approximate exponential functions quite well. Insufficient data are available at longer times to comment on the applicability of other functions, such as the Frenkiel function. The Stokes number of the particles has a clear impact on the correlation function. The turbulence Stokes number (based on a fluid integral length scale) is 0.16 and 0.33 for the 35 and 50 micron droplets respectively.

Comparisons with a stochastic simulation have emphasized the difficulty inherent in the prescription of length and time scales in turbulent flows with a one-point closure model. The stochastic simulation under predicts the integral length scale for droplet motion by a factor of two. Of course, the model constant that prescribes the eddy life time could be adjusted but there is little a priori guidance for the choice of this value.

The experimental facility is being modified to accommodate a true spray. An ultrasonic atomizer has been installed in a chamber to provide a fine spray with droplet diameters from 20 to 80 μm. The ultrasonic atomizer offers the advantage of very low air flow rates so that the flow of air in the experiment is not greatly disturbed. Single droplets that contain a fluorescent dye will be injected by the piezoelectric generator onto the centerline of the spray. A holographic edge filter will remove the Mie scattering from the spray. The fluorescence from the dye-containing droplet will be detected by the position-sensing photomultiplier tube as before. We plan to study the impact of dispersed phase loading in the spray on droplet dispersion with this system.

Theory and Computation.

Direct simulation of turbulent round jets is still not within the capabilities of present computers. Hence, Large Eddy Simulation of the turbulence in round jets is the most realistic approach for the prediction of the flow field and truly Lagrangian particle dynamics. The simulation of turbulent flow fields in round jets is based on highly accurate finite-difference methods, which offer the flexibility necessary for the treatment of non-periodic jet flows emitting from nozzles and the consideration of a variety of exit conditions. This aspect of the project was reported in detail in the final report for grant AFOSR 89-0392. Two new contributions were accomplished during the period 1992-3. The numerical treatment of the coordinate axis $r = 0$ for unsteady flows without symmetries was analyzed and a satisfactory method was found to avoid the loss of accuracy near the axis. The second and main contribution was the implementation of a LES-model for the non-resolved scales of the turbulence. The Navier-Stokes equations are written for filtered variables

$$\bar{f}(\underline{x}, t) \equiv \int d\underline{x}' G(\underline{x} - \underline{x}', t) f(\underline{x}', t) \tag{1}$$

where $G(\underline{x} - \underline{x}', t)$ denotes the filter function and $f(\underline{x}, t)$ a dependent variable. The Navier-Stokes equations (in Cartesian coordinates for convenience) are filtered and emerge as

$$\frac{\partial \bar{v}_\alpha}{\partial x_\alpha} = 0 \tag{2}$$

and

$$\frac{\partial \bar{v}_\alpha}{\partial t} + \frac{\partial}{\partial x_\beta}(\bar{v}_\alpha \bar{v}_\beta) = -\frac{1}{\rho}\frac{\partial \bar{P}}{\partial x_\alpha} + \nu \frac{\partial^2 \bar{v}_\alpha}{\partial x_\beta \partial x_\beta} - \frac{\partial}{\partial x_\beta}(L_{\alpha\beta} + C_{\alpha\beta} + R_{\alpha\beta}) \tag{3}$$

The modified filtered pressure is defined by

$$\bar{P} \equiv \bar{p} + \frac{1}{3}\rho \delta_{\alpha\beta}\overline{v'_\alpha v'_\beta} \tag{4}$$

and the correlations of filtered and sub-grid-scale motion ($v'_\alpha = v_\alpha - \bar{v}_\alpha$) are given by

$$L_{\alpha\beta} \equiv \overline{\bar{v}_\alpha \bar{v}_\beta} - \bar{v}_\alpha \bar{v}_\beta, \quad C_{\alpha\beta} \equiv \overline{v'_\alpha \bar{v}_\beta} + \overline{\bar{v}_\alpha v'_\beta}, \quad R_{\alpha\beta} \equiv \overline{v'_\alpha v'_\beta} - \frac{1}{3}\delta_{\alpha\beta}\overline{v'_\gamma v'_\gamma} \tag{5}$$

The present filter is the top hat filter and the closure for the correlations is given by

$$L_{\alpha\beta} + C_{\alpha\beta} \dot{=} 0 \tag{6}$$

and the Smagorinsky model for $R_{\alpha\beta}$

$$R_{\alpha\beta} \dot{=} -2\nu_T S_{\alpha\beta} \tag{7}$$

where the eddy-viscosity is defined by

$$\nu_T \equiv (c\Delta)^2 (2S_{\alpha\beta}S_{\alpha\beta})^{\frac{1}{2}}, \quad \Delta \equiv (\Delta x \Delta y \Delta z)^{\frac{1}{3}} \tag{8}$$

and

$$S_{\alpha\beta} \equiv \frac{1}{2}\left(\frac{\partial \bar{v}_\alpha}{\partial x_\beta} + \frac{\partial \bar{v}_\beta}{\partial x_\alpha}\right) \tag{9}$$

is the rate of strain produced by the filtered velocity field.

The result of modelling the sub-grid-scale motion is shown in fig.2. The turbulent flow in the round jet of the experiments by Call and Kennedy (1991) at the nominal Reynolds number of $Re = 15,000$ is calculated for $0 \leq \frac{z}{D} \leq 60$ without the LES-model, where the discretiztion error plays the role of the filter (Boris,1990), and with the Smagorinsky model discribed above. The vorticity magnitude for the latter case is reduced but the scale range is still significant. It turns out that the spreading rate in the latter case is in very good agreement with the experimental evidence. More importantly, the effect of the LES-model on the particle statistics is also beneficial as fig.2 proves where the dispersion for heavy vaporizing pentane particle is plotted as function of the time of flight. The LES-model produces results that are closer to the measurements than the predictions without it.

References

Boris, J.P. (1990), "Comments on subgrid turbulence models and large eddy simulations", in *Whither Turbulence? or Turbulence at the Crossroads* (J.L. Lumley ed.), Lecture Notes in Physics vol. 357, Springer V., 344

Call, C.J. and Kennedy, I.M. (1991), "A technique for measuring Lagrangian and Eulerian particle statistics in a turbulent flow", Exper. in Fluids 12, 125.

Call, C.J. and Kennedy, I.M. (1992), "Measurements and predictions of particle dispersion in a turbulent jet",Int. J. Multiphase Flow 18, 891.

Snyder, W.K. and Lumley, J.L. (1971), "Some measurements of particle velocity autocorrelation functions in a turbulent flow", J. Fluid Mech. 48, 41
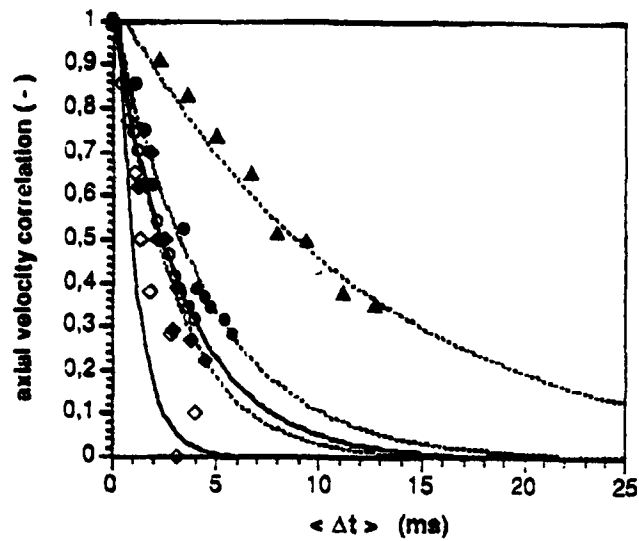
Fig.1

Quasi-Lagrangian axial auto correlations obtained from the mean time of flight data. Solid lines are exponential curve fits. ▲ = 50μm hexadecane droplets, x_i/D = 30; ⊙ = 35 μm hexadecane droplets, x_i/D = 20; ● = 35 μm hexadecane droplets, x_i/D = 30; ◇ = 40 μm hollow glass spheres, x_i/D = 20; ◆ = 40 μm hollow glass spheres, x_i/D = 30.
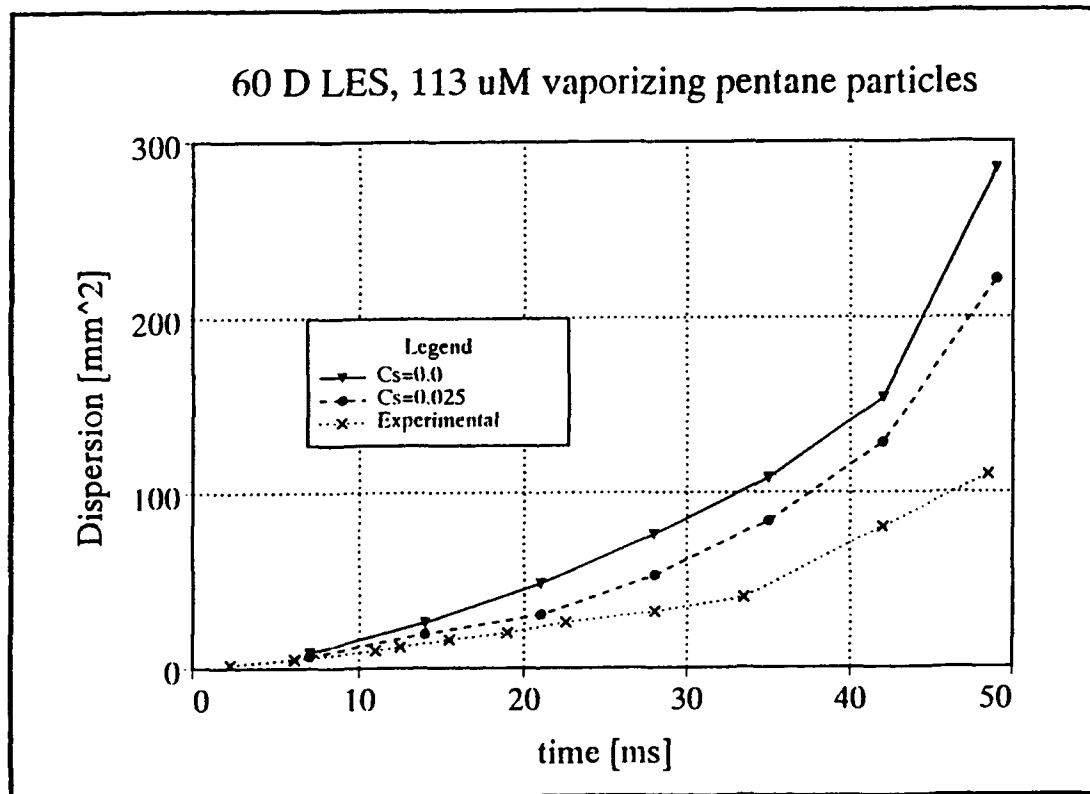

Fig.2 Dispersion of 113 μm vaporizing particles as function of the time of flight in a turbulent round jet at $Re = 15000$.

DROPLET-TURBULENCE INTERACTIONS
OVER A WIDE SPECTRAL RANGE

PRINCIPAL INVESTIGATOR:

W.A. Sirignano

Department of Mechanical and Aerospace Engineering
University of California
Irvine, CA 92717

SUMMARY/OVERVIEW:

The past research program addresses three-dimensional interactions amongst droplets in a dense spray via a fluid dynamical computational approach. Flow fields, trajectories, and vaporization rates are determined. In another task, vaporizing liquid oxygen droplets are studied. A new program concerns the detailed three-dimensional interactions of simulated turbulent flow structures with individual droplets.

AUTHORS

C.H. Chiang	I. Kim
S.E. Elghobashi	W.A. Sirignano

TECHNICAL DISCUSSION

1. Three-Dimensional Interactions of Droplets

Last year, we reported on our study of the interactions between two nonvaporizing droplets which are injected and then move side-by-side into initially quiescent incompressible fluid medium. In the remainder of that program, we have extended our study to the interactions between vaporizing droplets in a high-temperature and high-pressure environment. Figure 1 shows the Nusselt number decreasing as a function of time for a single vaporizing droplet as a test-run. The decrease of the Nusselt number (a dimensionless heat transfer rate) is mainly attributed to the reduction of the Reynolds number due to the droplet deceleration under the action of the drag.

2. Vaporization of LOX Droplets

This study advanced our axisymmetric droplet vaporization model at near critical conditions to deal with the vaporization at supercritical conditions. The previous high-pressure LOX model has included variations of thermophysical properties with respect to temperature for each species component, a compressibility factor in the gas-phase equation of state and the solubility of the fuel vapor in the liquid phase.

The major innovations beyond our previous works in this study are : 1) the formulation of boundary conditions, especially to trace the location of the "droplet interface", 2) the property calculation of the "gas/liquid puff" at the interface. A model has been developed to handle the interface conditions. Here, we briefly describe our strategies step-by-step to make calculations at supercritical conditions. (1) Determine the critical mixing temperature with respect to various pressure levels. The Redlich-Kwong equation of state with the mixing rules of Chueh and Prausnitz is employed for the vapor-liquid equilibria calculation for H_2/O_2 system. The critical mixing temperature is determined when the compressibilities (or mass fractions of a component) at both phases reach the same value. Figure 2 demonstrates that the critical mixing temperature and oxygen mass fraction at the interface reduce, while compressibility increases as pressure increases. (2) The droplet "pseudo-interface location" is determined by the critical mixing temperature. In calculating the vaporization rate, we neglect that the pseudo-interface will slightly deviate from its original spherical shape due to the convective effects. (3) Since there is limited availability of the critical point thermo-physical properties data in the literature, we assume that all thermo-physical properties are also continuous from the liquid to the gas phase. The consideration of singular behavior of some thermo-physical properties is excluded presently. However, the fluxes still remain finite at the interface. The density is obtained from compressibility relations and some existing experimental data. The variation of mass with respect to time is shown in Figure 3. After an early condensing period, the droplet reaches the critical mixing state and the evaporation rate increases dramatically beyond the critical point. The gas and liquid phase equations are solved separately, and the solutions are matched at the interface. In this approach, constant-temperature (at its critical mixing state) and constant-mass-fraction interface conditions are employed. The shear (or normal) stress conditions are applied even though the surface tension vanishes at the interface. Efforts are continuing to overcome some numerical difficulties in this approach.

3. Droplet – Turbulent Interaction Over a Wide Spectral Range

A theoretical/computational study analysis of the interactions of droplets with a turbulent field is being conducted. We are particularly interested in the important and challenging high-frequency domain where turbulent length scales are comparable to droplet size. To simulate the three-dimensional, unsteady interactions, a Navier-Stokes solver was developed. The alternating-Direction-Predictor-Corrector scheme and a pressure correction equation are employed.

We first investigate three-dimensional flow interactions between a vortical (initially cylindrical) structure flowing with the free stream and a spherical particle fixed in space. A schematic of this problem is shown in Figure 4 where the vortex tube, whose diameter is of the order of the sphere diameter, is initially located ten radii upstream from the center of the sphere. The effects of the vortex tube on the sphere are negligible initially because the initial induced velocity field is less than 2 percent of the free stream velocity. The vortex tube has a small core region with a radius σ. The velocity induced by a vortex tube approaches zero as the distance from the center of the vortex tube goes to zero, and at distances greater than σ, the induced velocity is similar to the point vortex. The vortex tube stream function construction as defined by Spalart is used:

$$\psi_v(x,z) = -\frac{\Gamma_t}{4\pi} ln[(x - x_o)^2 + (z - z_o)^2 + \sigma^2] \qquad (1)$$

The tangential velocity distribution of the vortex tube compared with a point vortex is shown in Figure 5 for $\Gamma_t = 5.0$ and $\sigma = 1.0$. Γ_t is the nondimensional circulation around a circular path far away from the center of the vortex tube and is positive when the vortex tube rotates

counterclockwise. The circulation around the vortex tube at a nondimensional radius of unity is given by $\Gamma_v = \Gamma_t/2$.

Figure 6 shows the lift coefficient of the sphere as a function of time for Re (Reynolds number) = 100, d_{off} (offset distance) = 0, and σ (vortex core radius to sphere radius) = 1. The lift coefficient was obtained with four different maximum fluctuation velocities ($v_{max} = \Gamma_v/2\pi$) due to the vortex tube, 0.1, 0.2, 0.3, and 0.4 (normalized by free stream velocity). When the vortex tube approaches the sphere ($0 \le t \le 9.4$), it produces upwash on the sphere, and thus the sphere experiences positive lift force. Maximum positive lift coefficient C_{Lmax1} occurs at $t = 7.2$. Later, the vortex tube produces downwash on the sphere and higher fluid velocity near the bottom of the sphere when it passes the sphere. Thus, the sphere experiences negative lift force, and its magnitude is greater than the positive lift force magnitude. Maximum negative lift coefficient C_{Lmax2} occurs at $t = 11.9$ when the vortex tube passes the plane $z = 1$. The lift coefficient is linearly proportional to the maximum fluctuation velocity (or the circulation of the vortex tube for constant vortex core radius) at each time until the vortex tube contacts the sphere boundary layer ($t \le 9.4$). The maximum positive lift force is simply expressed in dimensionless form by $C_{Lmax1} = 0.8v_{max}$. When $t > 9.4$, the linearity of the lift coefficient to the maximum fluctuation velocity deviates a little, but the maximum negative lift force is linearly proportional to the maximum fluctuation velocity. The maximum negative lift force is simply expressed in dimensionless form by $C_{Lmax2} = -1.65v_{max}$.

After the lift coefficient reaches its maximum negative value, it decays rapidly towards zero because the tube vorticity is diffused in the wake. The average lift coefficients (averaged by time span 24) at each maximum fluctuation velocity are near zero.

The similar calculations as above were performed for four different Reynolds numbers between $20 \le Re \le 80$. The magnitudes of C_{Lmax1} and C_{Lmax2} are not sensitive to the change of the Reynolds numbers and slightly increase linearly as Reynolds number becomes smaller. We also examined the effect of initial vortex core size σ. The magnitudes of C_{Lmax1} and C_{Lmax2} are linearly proportional to the maximum fluctuation velocity v_{max}, but with different proportionality constants for different σ, and approximately expressed by $C_{Lmax} \sim v_{max}\sigma^{1/2}$.
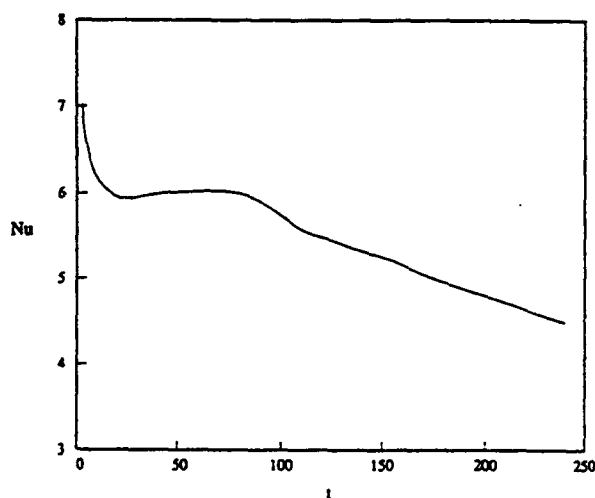

Figure 1. Nusselt number as a function of time for a single vaporizing droplet (initial Reynolds number 100).
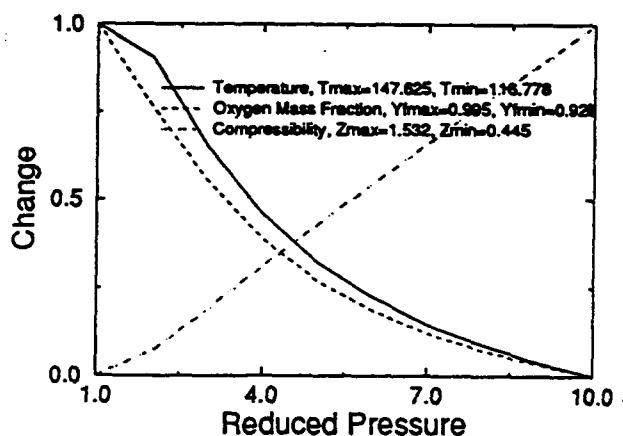

Figure 2. Variations of critical mixing temperature, oxygen mass fraction, and compressibility with respect to pressure.
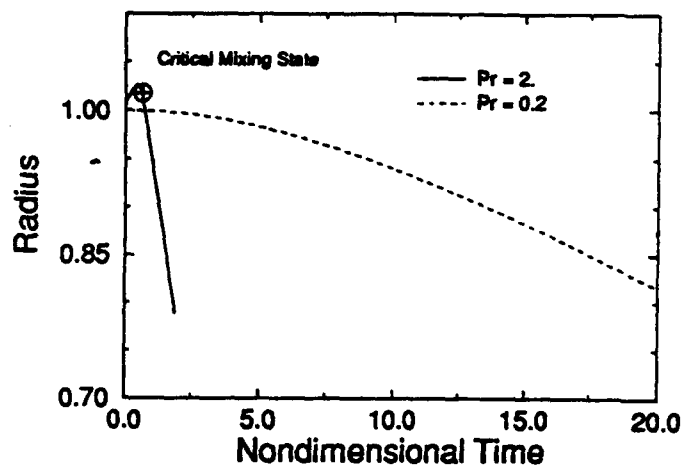
Figure 3. Variations of droplet radius with respect to time for the cases of two different pressure levels.
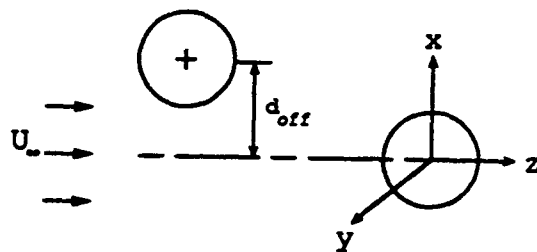

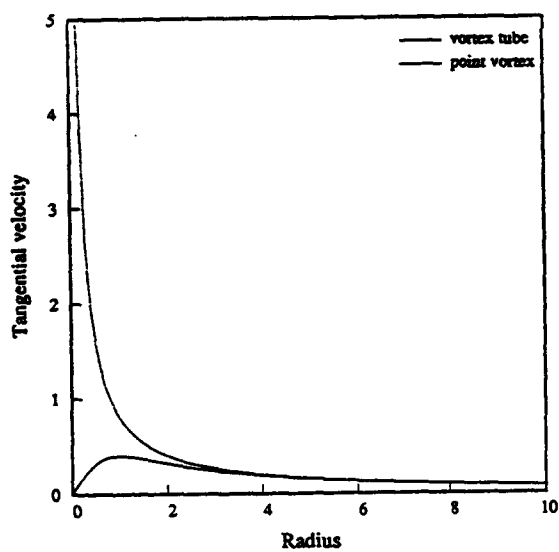Figure 4. Flow geometry and coordinates.

Figure 5. Comparison of radial velocities induced by a vortex tube and a point vortex for $\Gamma_t = 5$ and $\sigma = 1$.
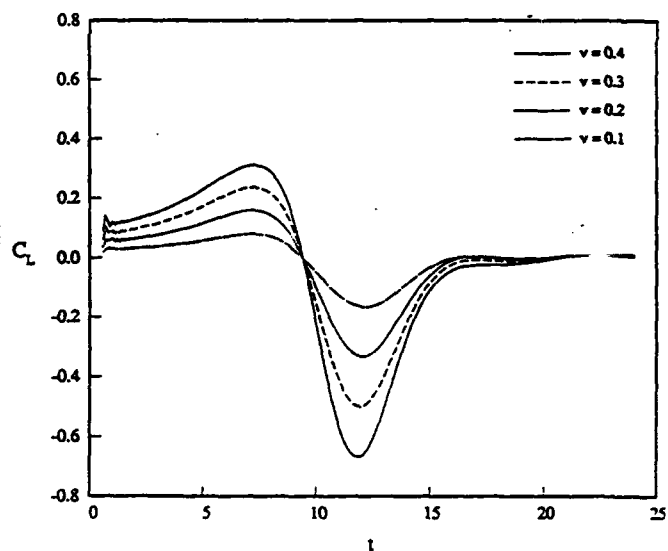

Figure 6. Lift coefficient as a function of time for $Re = 100$, $d_{off} = 1$, and $\sigma = 1$.

USE OF MAXIMUM ENTROPY PRINCIPLE AS A GUIDE
IN DESIGN OF SPRAY NOZZLES

(AFOSR Contract No. F49620-92-J-0389)

Principle Investigator: Richard S. Tankin

Mechanical Engineering Department
McCormick School of Engineering
Northwestern University
Evanston, Illinois 60208

SUMMARY:

A theoretical formulation based on maximum entropy principle (MaxEnt) is used to predict the droplet size, velocity and temperature distributions of sprays. The effect of combustion on the droplet distributions is due to heat transfer between the continuous liquid phase before atomization and the surrounding combusting mixtures. The droplet temperature distribution is "Exponential." The droplet size distribution may be positively skewed mono-modal, uniform size (approaching a delta function), and bi-modal depending on the Weber number of the spray. To test the MaxEnt model experiments are being performed.

AUTHORS:

Long P. Chin and Richard S. Tankin, Northwestern University; T. Jackson and J. Stutrud, Wright-Patterson Air Force Base; G. Switzer, Systems Research Laboratories, Inc.

TECHNICAL DISCUSSION:

To extend MaxEnt method to more complicated spray systems, our previous models [1,2] were modified. First, the effects of heat transfer on the droplet distributions in a combusting environment was added by balancing the thermal energy flux. As a result of heat transfer, the droplets of sprays will have a temperature distribution. Second, all three droplet velocity components for any coordinate system will be included in the momentum flux and kinetic energy flux constraints. As a result, the previous models with fewer velocity components are special cases of this new and more general model. This more general model considers all three velocity components and is applicable to problems such as a spray nozzle where swirl is present. To test this general model, a comparison was made between a set of experimental data obtained using a phase/Doppler particle analyzer (PDPA) and the calculated results.

The nozzle used in these experiments was an Allison hollow cone, non-swirl spray nozzle having a 90° spray angle. A spray of water issues into a quiescent, saturated air environment at 295°K at a flow rate of $2.75 \times 10^{-6} m^3/s$ (2.5 gallons/hr). The water exiting the nozzle forms a liquid sheet, hollow cone in shape, which breaks up into ligaments and droplets. The ligaments breakup into droplets further downstream. It is desirable to measure the spray as close as possible to the sheet break up region — but downstream of the ligament region. Measurements beyond this point will be influenced by local gas aerodynamics and complicate the comparison with calculations. Droplets are sized with an Aerometrics, Inc. two-color, four-beam PDPA.

A droplet size distribution is constructed from the individual point measurements, weighting each measurement by their time of collection and the ratio of their optical probe area to the ring area represented at that location. Droplet size is normalized by the mass mean diameter, D_{30}, which was determined from measurements to be 81.43 microns. The resulting experimentally determined probability size distribution is shown in Fig. 1 - a bi-modal size distribution appears. One peak occurs at $\overline{D} \approx 0.2$ and the second peak at $\overline{D} \approx 1.3$. A physical explanation for the origin of these peaks is as follows: There are two main sources for the droplets in this spray — the droplets that form from the ligaments and those that form from the thin sheet of liquid that lies between the ligaments at breakup. The ligaments breakup via Rayleigh's capillary instability and form the larger droplets associated with those centered around $\overline{D} \approx 1.3$ (in Fig. 1). The droplets from the thin sheet are associated with those centered around $\overline{D} \approx 0.2$. It should be mentioned that such a bimodal size distribution is not typical for this nozzle. However when the nozzle in this study was operated at low flow rates - 2.75×10^{-6} m^3/s - a bimodal size distribution appeared. That was the motivation for operating this nozzle at such low flow rates, since one of the goals was to verify the validity of the MaxEnt model which predicts a bimodal size distribution at particular operating conditions. Also shown in Fig. 1 are the computed results for a one component velocity model, two-component velocity model and a three component velocity model. The three component velocity model exhibits a bimodal shape that is in reasonable agreement with the experiments.

Two important parameters (*We* and β) appear in the joint droplet distribution function . *We*, the Weber number, is defined in this study as the ratio between droplet surface energy and droplet kinetic energy; β is the ratio between droplet thermal energy and droplet kinetic energy. Figures 2 and 3 show the calculated droplet size, and temperature distributions for different values of *We*. Figure 4 shows the calculated droplet temperature distributions for different values of β. The effects of β on droplet size distribution are not shown because its effect is too small to be distinguishable.

In Fig. 2, when *We* is large (e.g., $We \geq 95$), the droplets approach a fairly uniform and symmetrical size distribution. The peak occurs at $\overline{D} \approx 1$. On the other

hand, when *We* is small (e.g., *We* = 71), the peak of the distribution occurs at smaller droplet size ($\overline{D} \approx 0.2$). This type of droplet size distribution is normally described as a positively skewed mono-modal distribution. The above two types of droplet size distributions are frequently observed experimentally in various spray systems [e.g., 3,4]. However, when *We* is in the intermediate range, a distribution with double peaks (bi-modal) appears. When *We* is 87 in Fig. 2, two peaks are observed — one at $\overline{D} \approx 0.2$ and the other at $\overline{D} \approx 1.1$. When *We* (in the intermediate range) is increased, the peak centered at $\overline{D} \approx 1.1$ becomes more dominant; When We is decreased, the peak centered at $\overline{D} \approx 0.2$ becomes more dominant. Although, in this study, the bi-modal droplet size distribution exists over a fairly wide range of *We*, there are only few experimental measurements where this has been reported
 ·., 5,6].

The parameter β only affects the droplet temperature distribution — not the size or velocity distributions. Physically, larger β values indicate more thermal energy is required to raise a droplet to a certain temperature. That also indicates, for the spray as a whole, larger β values yield a lower temperature increase of droplets. Therefore, the number fraction of droplets at lower temperature is much higher when β is large.

REFERENCES:

1. Li, X., Chin, L. P., Tankin, R. S., Jackson, T., Stutrud, J., and Switzer, G., "Comparison Between Experiments and Predictions Based on Maximum Entropy for Sprays from a Pressure Atomizer," *Combustion and Flame*, Vol. 86, pp. 73-89. (1991)
2. Chin, L. P., LaRose, P. G., Tankin, R. S., Jackson, T., Stutrud, J., and Switzer, G., "Droplet Distributions from the Breakup of a Cylindrical Liquid Jet," *Physics of Fluids* A, Vol. 3(8), pp. 1897-1906. (1991)
3. Bachalo, W. D. and Houser, M. J., "Phase/Doppler Spray Analyzer for Simultaneous Measurement of Drop Size and Velocity Distributions," *Optical Engineering*, Vol. 23, pp. 583-590. (1984)
4. Dressler, J. L. and Kraemer, G. O., "A Multiple Drop-Size Drop Generator for Calibration of a Phase-Doppler Particle Analyzer," *Liquid Particle Size Measurement Technique - Vol. II*, pp. 30-44. (1990)
5. Presser, C., Gupta, A. K., Dobbins, A., and Semerjian, H. G., "Influence of Size Distribution on Droplet Mean Diameter Obtained by Ensemble Light Scattering," *Liquid Particle Size Measurement Technique - Vol. II*, pp. 93-111. (1990)
6. Gulder, O. L., "Multiple Scattering Effects in Dense Spray Sizing by Laser Diffraction," *Aerosol Science and Technology*, Vol. 12, pp. 570-577. (1990)
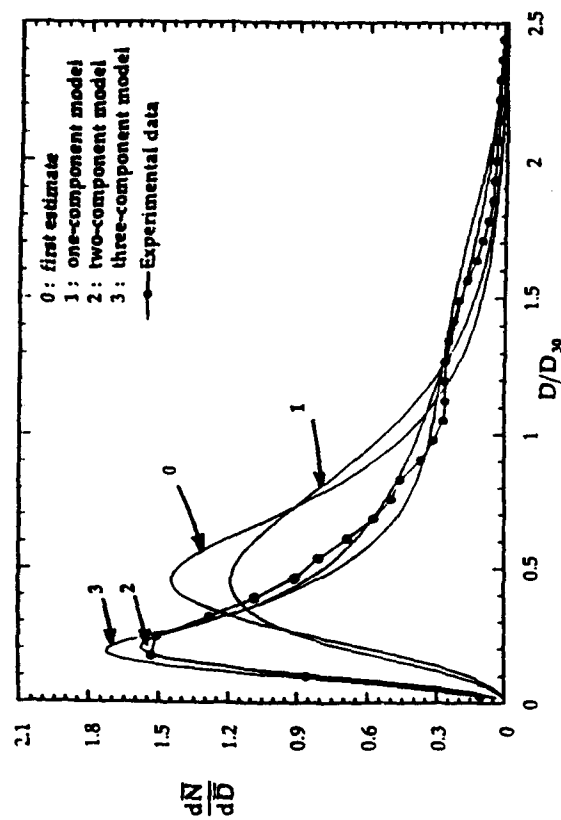
Figure 3. Droplet temperature distributions for different values of droplet Weber number

1: We = 71	
2: We = 75	
3: We = 79	
4: We = 83	
5: We = 87	
6: We = 91	
7: We = 95	
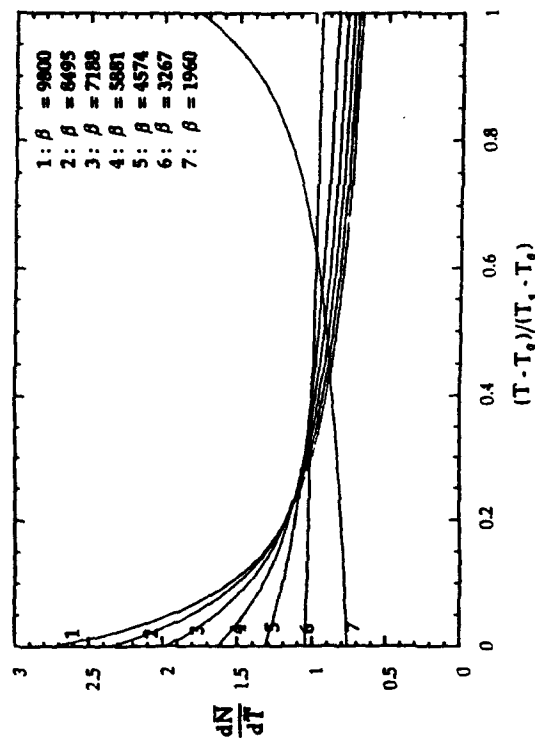
Figure 4. Droplet temperature distributions for different values of β

1: β = 9800	
2: β = 8495	
3: β = 7188	
4: β = 5881	
5: β = 4574	
6: β = 3267	
7: β = 1960	

Figure 1. Comparison of droplet size distributions between experimental measurement and calculated results

0: first estimate
1: one-component model
2: two-component model
3: three-component model
— Experimental data

Figure 2. Calculated droplet size distributions for different values of droplet Weber number

1: We = 71	
2: We = 75	
3: We = 79	
4: We = 83	
5: We = 87	
6: We = 91	
7: We = 95	

HIGH TEMPERATURE REACTION KINETICS OF NON-METAL OXIDES

(AFOSR Contract No. F49620-91-C-0057)
Principal Investigator: Allen Twarowski

Rockwell International Science Center
1049 Camino dos Rios
Thousand Oaks, CA 91360

SUMMARY/OVERVIEW:

Catalysis of heat-releasing H+OH recombination in the nozzle section of a SCRAM-jet could potentially increase the fuel efficiency and therefore the thrust of a hydrogen-fueled air-breathing hypersonic aircraft. The oxides of phosphorus have shown potential as recombination catalysts, but the reaction chemistry of phosphorus combustion products (oxides and acids) is poorly understood at present. The objective of this research program is to construct a reaction mechanism for phosphorus combustion products in a high temperature gas, determine the rate constants for the key reactions and assess the potential of this reaction system for improved fuel efficiency in hypersonic aircraft.

TECHNICAL DISCUSSION:

Hydrogen reacts with oxygen at high temperature to produce water vapor and a considerable amount of heat. In our combustion reactor, gas temperatures of 1500-2500 K are achieved at pressures of 300-750 Torr. At these temperatures the equilibrated combustion products consist of small but significant amounts of radicals such as OH and H. To probe the reaction chemistry of the combustion products, the equilibrated system is perturbed by laser photolysis of H_2O which substantially increases the pool of OH and H radicals. The return of the system to equilibrium is experimentally investigated by recording, as a function of time, the OH absorption at 312 nm.

In the past, we reported[1] a dramatic increase in the rate of OH disappearance following photolysis of water vapor at 1970 K when PH_3 combustion products are present. Analysis of the OH signal using a reaction model employing 13 species and 33 reaction steps supported the interpretation of a catalytic increase in the rate of relaxation of the system back to its initial state following water photolysis. The more rapid disappearance of excess OH when PH_3 combustion products are present in the photolyzed test gas is not proof of an increased rate of H+OH recombination. One may argue that a fast bimolecular reaction step consumes OH but does not generate H_2O until much later. If this were the case, then interest in PH_3 as a possible fuel additive for hydrogen burning hypersonic aircraft would be less compelling even though the high temperature, gas phase reaction chemistry of phosphorus

---

1. Allen Twarowski, "The Influence of Phosphorus Oxides and Acids on the Rate of H+OH Recombination", Combustion and Flame, accepted for publication.

$\sqrt{}/\llcorner$

oxides and acids remains unexplored and of interest. To more completely test the hypothesis that PH_3 combustion products catalyze the overall rate of H+OH recombination, the product side of this reaction was measured. We find an H_2O absorbance signal at 192 nm which results from a rise in temperature caused by heat released when the photolysis products, H and OH, recombine.

A transient signal was observed[2] at 192 nm for both fuel rich and fuel lean test gas mixtures when H_2 is burned with O_2. Figure 1 shows a typical signal for the 10% fuel rich test gas mixture. The absorbance change shown in the figure was calculated by taking the decadic logarithm of the average signal recorded prior to the photolysis pulse divided by the signal itself. The absorbance signals shown in Fig. 1 were recorded with the excimer laser set to the usual operating value of output energy (filled squares) and set to five percent of the that value (empty squares). Comparison of the two figures shows that the absorbance signal depends on the presence of excimer photons and that the noise level of the signal is about 0.0005.

Figure 1.
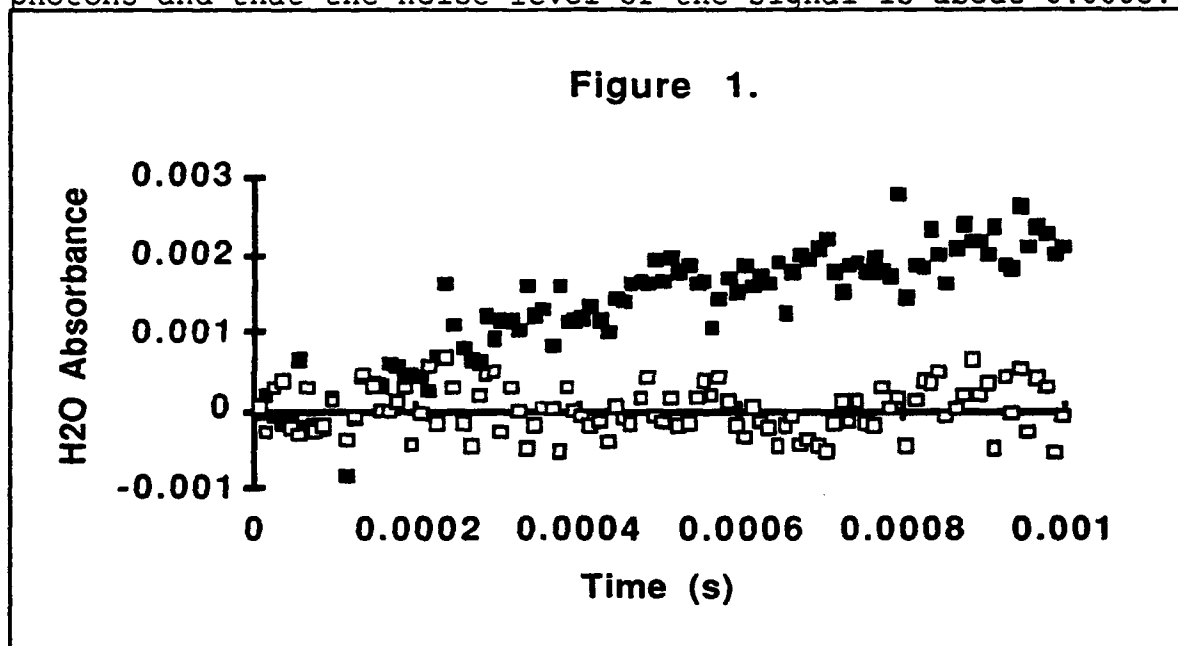
An unexpected feature of Fig. 1 is the sign of the signal. A reasonable expectation would be an initial sharp decrease in absorbance followed by a return to baseline as H_2O is instantaneously photolyzed and later reappears when the system relaxes back to chemical equilibrium. Instead, the signal slowly increases to a positive limiting value of about 0.002 after photolysis. The shape of the signal suggests the appearance of a product developing over the 0.9 ms experimental time period. Photolysis of H_2O by the excimer laser creates excess OH and H radical. When the radicals eventually recombine the laser energy used in photolyzing H_2O appears as thermal energy which raises the temperature of the gas. The signal at 192 nm is in a spectral region where the absorbance of H_2O

2. Allen Twarowski, "Photometric Determination of the Rate of H_2O Formation from H and OH in the Presence of Phosphine Combustion Products", *Combustion and Flame*, accepted for publication.

increases with temperature. Therefore, the transient absorbance
signal at 192 nm has two components that are superposed, an
initial decrease in the absorbance signal due to a decrease in
H_2O density and a gradual increase in the absorbance signal due
to a change in the absorption coefficient caused by an increase
in temperature. The latter component of the signal dominates.

Figure 2.
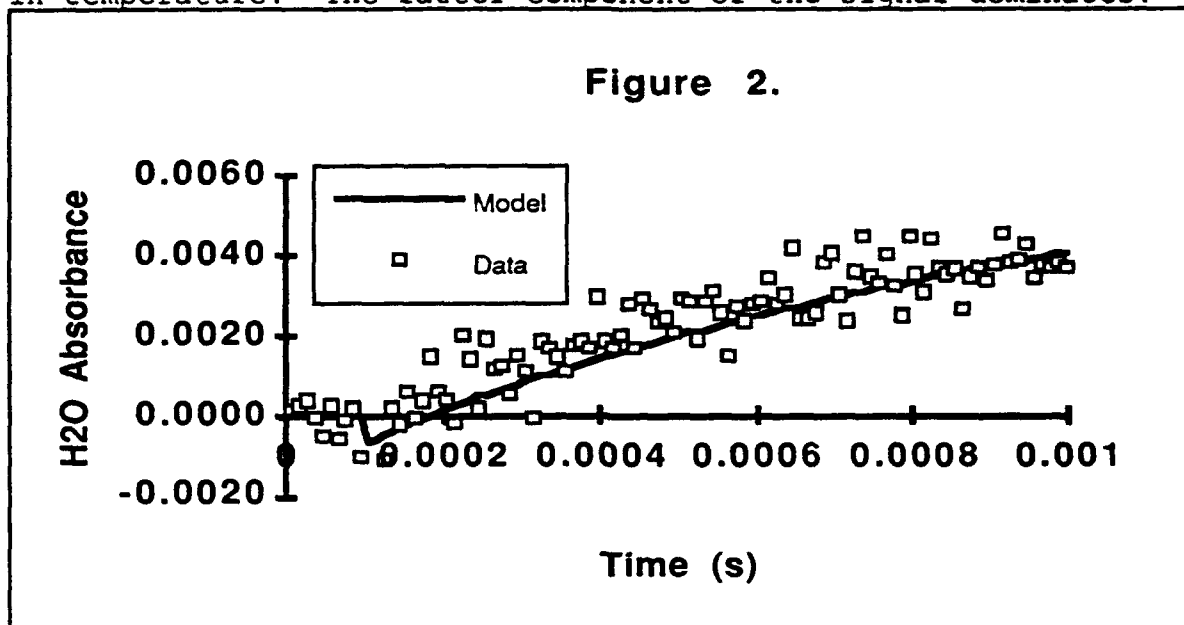
The time dependence of the 192 nm signal was examined in
more detail by modifying the previously developed[1] reaction
model to calculate the change in H_2O absorbance as a function of
time subsequent to photolysis. The reaction model contains a
set of 33 reactions describing the chemistry of 13 species (H_2,
O_2, H, O, OH, H_2O, HO_2, PO, PO_2, PO_3, HOPO, $HOPO_2$, HPO). It was
used to simultaneously fit the OH and H_2O absorbance signals for
fuel rich and lean conditions (four data sets in all) when pure
hydrogen was combusted. The sum of the absolute value of the
deviations between the calculated signal and the data was
minimized as three fitting parameters were varied, the rate
constant for the ternary reaction H+OH+M $\rightarrow$ H_2O+M (where M is a
third body), a scaling factor for the calculated H_2O absorbance
signal, and the density of photons absorbed by the gas. Figure
2 compares the results of this analysis with the experimentally
determined change in H_2O absorbance as a function of time for
the case of the lean fuel mixture. The fits between the
experimental data and the model calculations are reasonably good
for both rich (not shown) and lean fuel mixtures and the fitting
parameters give reasonable values. The good agreement of
calculated and experimental H_2O absorbance changes observed for
the pure hydrogen combustion data set suggests that the source
of the absorbance signal is the heating of the test gas caused
by relaxation of the system back to its equilibrium state.

In a previous study[1], the OH signal of a photolyzed gas
mixture was found to relax to its initial value at a much faster
rate when PH_3 was added to the H_2 fuel and burned with O_2. If
the more rapid relaxation rate for the OH density is the result
of an increased net H+OH recombination rate, then the H_2O signal

should rise more quickly to its limiting value when PH_3 combustion products are present in the test gas mixture. Figure 3 compares the H_2O absorbance signals recorded with and without 0.1% PH_3 present in the H_2 fuel stream for the fuel lean case. A faster rise in the H_2O signal at earlier times is clearly observed when PH_3 is added to the fuel. Comparison of experimental data for pure hydrogen combustion and phosphine combustion demonstrates that heat release is more rapid when phosphine combustion products are present in the test gas mixture. These observations provide further support for the hypothesis that phosphine combustion products open new channels for H+OH recombination.

Figure 3.
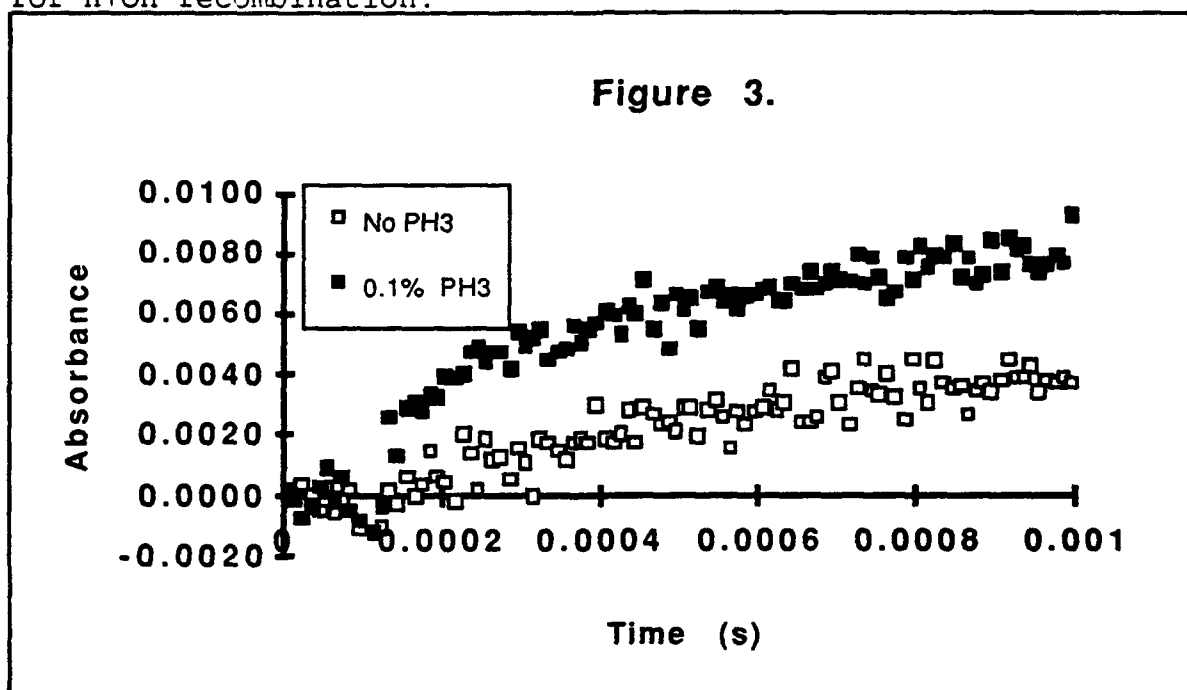
The reaction model which provided a good fit to the pure H_2/O_2 combustion data was used to calculate the OH density change and H_2O absorbance change as a function of time for the reaction mixtures containing 0.1 per cent phosphine in the H_2 fuel stream. The three fitting parameters of the model were fixed at the best fit values found for analysis of the pure H_2/O_2 data. Agreement of the model calculations with experimental data is not as good as for the pure H_2/O_2 results. The model calculations for the rich fuel mixture overestimate the H_2O signal while those for the lean fuel mixture underestimate the H_2O signal by about 40 percent. These variances are also reflected in the OH absorbance signal consistent with the H_2O signal variances. The model calculations show a faster return to equilibrium of the OH density for the rich fuel mixture than is observed and a slower return for the lean fuel mixture. The phosphorus reaction chemistry is far less well understood than the H_2/O_2 reaction chemistry and a disagreement of 40 percent in fitting the H_2O temporal profiles is not altogether surprising.

AFOSR SPONSORED RESEARCH IN PROPULSION DIAGNOSTICS

PROGRAM MANAGER: JULIAN M. TISHKOFF

AFOSR/NA
110 Duncan Avenue, Suite B115
BOLLING AFB DC 20332-0001

SUMMARY/OVERVIEW: The Air Force Office of Scientific Research (AFOSR) program in diagnostics in reacting media currently is focused on three areas of study: gas-phase measurements, plasmas, and particle/droplet measurements. An assessment of major research needs in each of these areas is presented.

TECHNICAL DISCUSSION

AFOSR is the single manager for Air Force basic research, including efforts based on external proposals and in-house work at Air Force laboratories. The diagnostics of reacting flows task is assigned to the AFOSR Directorate of Aerospace Sciences along with programs in rocket propulsion, airbreathing combustion, and fluid and solid mechanics.

Interests of the AFOSR diagnostics in reacting media subarea are given in the SUMMARY section above. This program, now in its tenth year, has produced many "first-ever" laser-based measurements. The instrumentation with which these measurements were made is becoming commonly available for laboratory and bench test utilization. Measurements range from microscopic to macroscopic scales with relevance to: plasma acceleration; combustion aerothermochemistry; the behavior and synthesis of advanced energetic materials; characterization of exhaust plume formation and radiation; and dynamic control of propulsion, weapon and power generation systems.

Decisions on support for research proposals are based on scientific opportunities and technology needs. Current AFOSR perceptions of scientific opportunities appear in Figure 1. As indicated by the orientation of the arrows in Figure 1, the task areas with the greatest growth potential are plasmas and measurements in supercritical fluids.

In the rapidly changing international environment we also are examining how we conduct our research activities in relation to both Air Force and civilian needs. We now recognize a new set of research objectives, including achieving rapid technology transitioning and dual military and civilian technological use for Air Force basic research. We welcome your ideas on fostering better working relationships among universities, industry, and Government scientists and technologists.

The purpose of this abstract has been to communicate AFOSR perceptions of research trends to the university and industrial research communities. However, communication from those communities back to AFOSR also is desirable and essential for creating new research opportunities. Therefore, all proposals and inquiries for fundamental research are encouraged even if the content does not fall within the areas of emphasis described herein. Comments and criticisms of current AFOSR programs also are welcome.

Air Force Basic Research

Aerospace Sciences

Propulsion Diagnostics

Research Area	Trend	Decrease	Increase
Gas-Phase Measurements	↑		Degenerate Four-Wave Mixing
Plasmas	↑		Degenerate Four-Wave Mixing
Particle/Droplet Measurements	↗		Supercritical Behavior - FY94 Init

TWO DIMENSIONAL COHERENT ANTI-STOKES RAMAN SCATTERING WITH APPLICATION TO THE HYDROGEN ARCJET

Project Order No. AFOSR-PO-89-0029

Principal Investigator:

EDWARD J. BEITING

The Aerospace Corporation
P. O. Box 92957
Los Angeles , CA 90009

SUMMARY/OVERVIEW

This is an experimental program to extend the utility of coherent anti-Stokes Raman spectroscopy (CARS) as a diagnostic of flows and plasmas. This diagnostic technique is especially useful for probing the internal states of molecules that have no easily accessible absorptions and is applicable to highly luminous and turbulent environments. An initial application will be to the exit plane of a hydrogen arcjet thruster. Pump and Stokes radiation focused into a sheet produces a line of anti-Stokes radiation in the cross section of a flow. The anti-Stokes radiation detected with a multichannel array provides one angle of projection data. A cross section of an asymmetrical region is calculated from projection data taken at several angles using tomographic algorithms. Only one projection is required to reconstruct the cross section of a cylindrically symmetric flow. This technique allows the measurement of field maps of internal state distributions (temperatures) and number densities. Currently, CARS is restricted to collecting data sequentially at single points in space.

TECHNICAL DISCUSSION
METHOD

In the CARS process, three fields $E_1(\omega_1)$, $E_2(\omega_2)$, and $E_3(\omega_3)$ impinge on a medium and mix through the third order nonlinear susceptibility χ_{ijkl} to generate a fourth wave $E_4(\omega_4)$ at a frequency ω_4. If we assume the input fields are plane monochromatic waves propagating in the z direction with aligned polarizations, and the medium has no spatial symmetry, then χ_{ijkl} can be written as a scalar and the solution of Maxwell's equations with a nonlinear polarization source term yields

$$\frac{\partial^2 E_4}{\partial z^2} + 2ik_3\frac{\partial E_4}{\partial z} = -4\pi \left(\frac{\omega_4}{c}\right)^2 \chi(\omega_1,\omega_2,\omega_3)E_1 E_2^* E_3 \exp(i\Delta k z) \qquad (1)$$

where $\Delta k = 2k_1 - k_2 - k_3$ and $k \equiv n\omega/c$. Assuming a solution of the form $E_4(z) = E_4^0(z)\exp(ik_4 z)$ and noting $\Delta k << 2k_3$ for phasematched geometries, the spatial variation of E_4^0 is small and the second derivative can be ignored. Accordingly, the spatial variation of the amplitude of the CARS field can be written

- 246 -

$$\frac{dE_4^0}{dz} = K(\omega_4)\chi(\omega_1,\omega_2,\omega_3)E_1 E_2^* E_3 \exp(i\Delta kz) \qquad (2)$$

where $K(\omega_4)$ is a known function of ω_4. This expression can be simplified further using the following assumptions which are valid for most experimental implementations of CARS: $\Delta k = 0$ (phasematched waves); the amplitudes of E_1, E_2, and E_3 are independent of z over the region they coherently interact; $E_1(\omega_1) = E_3(\omega_3)$; and $\omega_1 = \omega_3$. Then Eq. (2) becomes

$$E_4^0(\omega_4) = K(\omega_4)E_1^2 E_2^* \int \chi(\omega_1,\omega_2)dz. \qquad (3)$$

The susceptibility can be expressed as a sum of the nonresonant part, χ_{nr}, and a resonant part with real and imaginary components, i.e. $\chi_j = \chi_{nr} + \chi_j^r + \chi_j^i$. If the lasers are focused into a thin sheet with a transverse coordinate x and ω_2 is tuned away from all resonances then the signal that results is due primarily to the interaction of the waves with the nonresonant susceptibility. Noting $I_4(\omega_4) = \frac{n_4 c}{8\pi}|E_4^0(\omega_4)|^2$, a projection in terms of the molecular density can be written:

$$P(x) \equiv [\tilde{I}_4(\omega_4)]^{\frac{1}{2}} = \int \chi_{nr}(x,z)dz = \bar{\chi}_{nr}\int n(x,z)dz \qquad (4)$$

where $\bar{\chi}_{nr}$ is a known constant and $n(z)$ is the number density of the gas. A reconstruction from this projection yields a map of the density directly. If ω_2 is tuned to a strong isolated resonance then

$$P(x) \equiv [\tilde{I}_4(\omega_4)]^{\frac{1}{2}} = \int \chi_j^i(x,z)dz. \qquad (5)$$

Since $\chi_j^i \propto n(x,z)\Delta_j(x,z)$ one can obtain a spatial map of Δ_j, the population difference between the two states in the Raman resonance j. In thermal equilibrium this defines a temperature. Under nonequilibrium conditions, measuring $\Delta v = 1$ transitions for a line from each vibrational level starting with $v = 0$ allows spatial maps of the population of the vibrational energy levels to be constructed.

PROGRESS

During the past year, work continued on development of a technique to obtain CARS single pulse projections in an atmospheric pressure noncylindrically symmetric flow and to acquire time-averaged projection data point-by-point across the plume of a hydrogen arcjet thruster.

Work on the single-pulse projection technique centered on the ability to recover predictable projections when large shot-to-shot variations of the lasers' mode structures, frequencies, and phases take place. The method used to accomplish this is to carefully split the pump and Stokes laser beams into nearly identical overlapped, collinearly phased matched signal and reference beams that are focused into flat sheets. The ratio of the signals produced by these two beams must be constant in space and time when created in constant flows. Experimentally it was found that point-to-point, shot-to-shot variations in the signal-to-reference ratios consistently varied between 10% and 50%. These large variations occurred even when the CARS images in both reference and signal legs appeared to be identical in both spatial dimensions. Considerable effort was expended to overcome this deficiency.

Theoretically the ratio of the signal and reference channels should be constant regardless of the composition of the individual pump and Stokes beams, however, in practice it has been

difficult to accurately reference CARS signals if both lasers are not single mode [1]. Because space and monetary considerations preclude using a pulse-amplified ring dye laser, a single mode grazing incidence oscillator was built (see Fig. 1). Tests continued during the past year using this single longitudinal mode system. These tests did not produce better results. Consequently, given the large number of experimental variations tested without success (see previous annual reports), the single pulse implementation was deemed impractical and attention was turned to the testing of a time-averaged technique.

To this end, effort was begun to verify the CATCARS technique by translating convention-ally focused collinearly phase-matched beams across a well-known, asymmetric, atmospheric pressure flow. Software and hardware were developed to automatically translated the flow through the focused beams allowing a number of signal pulses to be collected at each posi-tion in the projection before rotating the flow to collect data for the next projection. Initial data showed pulse-to-pulse amplitude variations of greater that 400%. These large variations were traced to mode hops in the single mode dye laser. That is, although the output of the laser on any given shot was a single longitudinal mode, the mode number would randomly change from shot to shot. The intermode stability of the oscillator varied from day to day. Unfortunately, the resultant large variations in signal intensity could not be selectively rejected because mode hops often occurred on too high a fraction of the pulses in an averaged data set. Additional investigation showed that the long term drift of the laser frequency was too great for the time duration required to complete a complete set of translations and rotations. Furthermore, smaller variations of the signal strength ($< 100\%$) were also observed. These are probably due to shot-to-shot variations in the center frequency of a given longitudinal mode. This frequency jitter of 300 to 400 MHz caused by variations in the index of the flowing dye are not measurable with instruments currently available in this laboratory. Since the hydrogen Q(3) Raman linewidth is 380 MHz at this temperature and pressure, this jitter contributes substantially to the signal instability. (The single shot bandwidth of the laser is reputed to be 150 MHz.) Clearly, the simple oscillator constructed with components available on hand would have to be substantially upgraded for quantitative measurements on this system.

This upgrade is being undertaken. A mechanical drive with a custom designed flexture rotation stage was designed and built by an outside contractor. High tolerance optical compo-nents and mounts were purchased and specialized mounts were built in Aerospace's shops. The system is being assembled on a temperature controlled, enclosed platform. The system will use refrigerated dye flowing through a system equipped with pressure wave dampening components. The oscillator will have two active stabilization circuits. The first was devised by Sandia Na-tional Labs [2] to prevent mode hopping during scanning. The second is an etalon based system that will limit long term frequency drift to less than 50 MHz. It is projected that this system will have a single shot bandwidth of 150 MHz and an average bandwidth of less than 300 MHz. With its single mode scanning ability, it will also allow Doppler based velocity measurements to be made. This system requires the construction of a number of electronic circuits and the development of additional driving software. At this writing, the system is approximately 75% complete.

As noted in last year's report, considerable work was undertaken in developing an arcjet facility and shakedown CARS measurements were made in a cold and operating arcjet. These initial tests indicated a number of modifications were required before quantitative measure-ments could be made in the new facility. Furthermore, it was decided that CARS velocity measurements were also feasible for both arcjets and resistojets (an electric propulsion system also of great interest to the Air Force) using the high resolution laser system under develop-ment. Consequently, as shown in Fig. 1, the modifications are to include the ability to rotate and translate the jets and diffuser system (described in last years report) under computer con-

trol in the vacuum tank. At this writing, all the charges to the arcjet system and the laser system indicated by the initial series of measurements have been completed. The design work for modifications to the arcjet facility are completed and fabrication and assembly is projected to be complete in 8 weeks (depending on component delivery and shop turn around). All the components for a resistojet test system have been assembled.

References: [1] Personal communications with D. A. Greenhaugh, R. Farrow, and G. Rosasco. [2] T. D. Raymond, P. Esherick, A. V. Smith, Opt. Lett. **14**, 1116-1118 (1989).
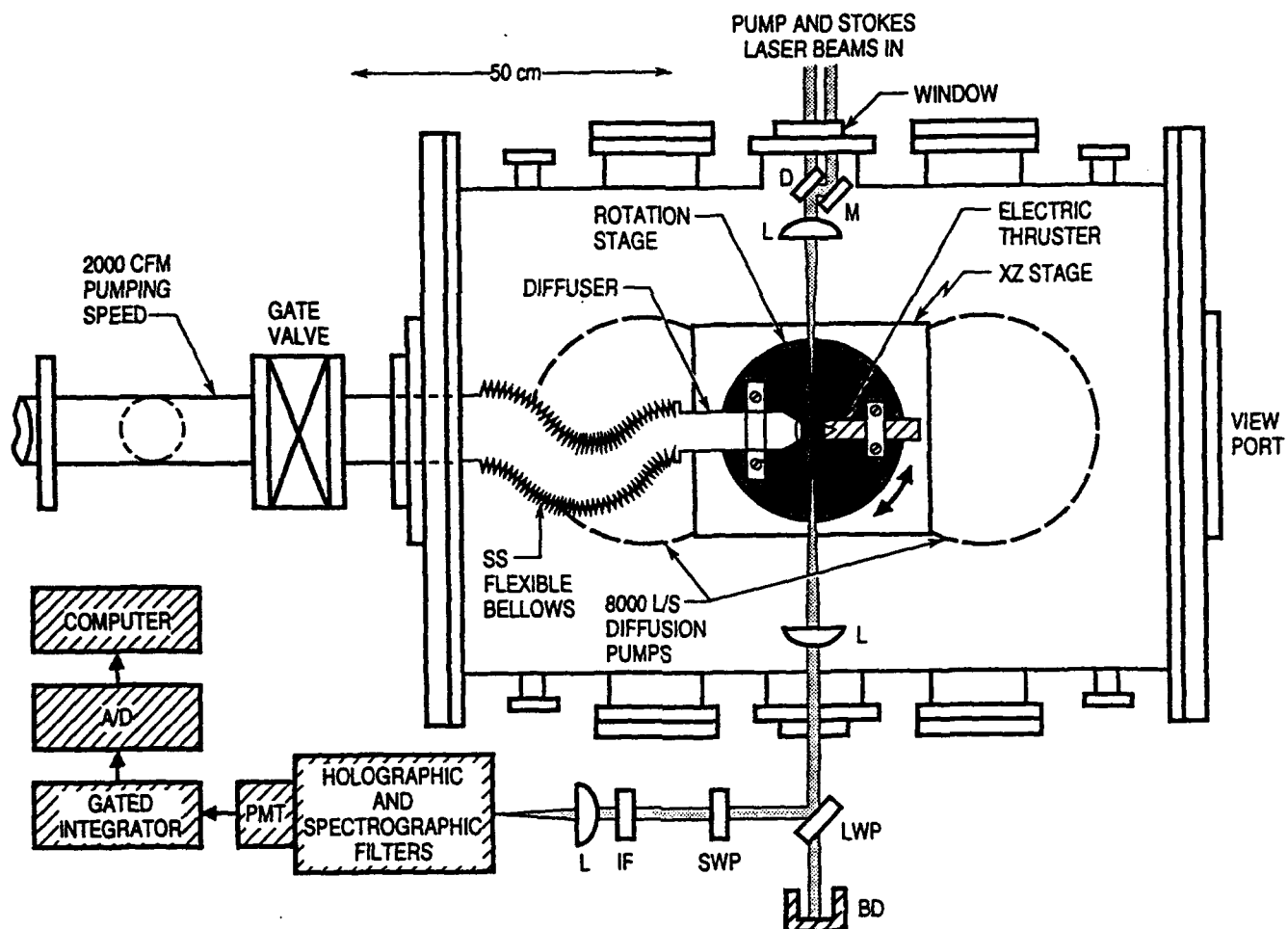
Figure 1. Diagram of arcjet thruster diagnostic facility. A flexible bellows has been added to a redesigned diffuser and both the diffuser and the electric thruster are mounted on a rotation stage to allow CARS velocity measurements.

ADVANCED DIAGNOSTICS FOR REACTING FLOWS

AFOSR90-89-0067

Principal Investigator: Ronald K. Hanson

High Temperature Gasdynamics Laboratory
Mechanical Engineering Department
Stanford University, Stanford, CA

SUMMARY/OVERVIEW

This research is directed toward innovation of advanced diagnostic techniques applicable to combustion gases and plasmas, with some emphasis on high speed flows. The primary flowfield parameters of interest are species concentrations, temperature, pressure, mass density, electron density, velocity, and quantities derivable from these parameters such as mass flux and thrust (calculable from mass density and velocity). Principal techniques under study include spectrally-resolved absorption and fluorescence, using wavelength-modulated cw ring dye laser and cw semiconductor diode laser sources; planar laser-induced fluorescence (PLIF), using tunable pulsed laser sources (excimer-pumped dye and narrow-linewidth excimer); and diagnostic techniques based on degenerate four-wave mixing.

TECHNICAL DISCUSSION

In the following paragraphs we highlight primary activities of the past year.

Plasma Diagnostics

Recent effort has focussed on the use of tunable semiconductor diode lasers for the measurement of plasma properties. Techniques under study include line-of-sight absorption, laser-induced fluorescence (LIF) and degenerate four-wave mixing (DFWM). The work on absorption and LIF has been carried out in a custom-built RF-powered plasma torch (1.4 kW) which provides a convenient bench-top plasma source with good optical access. The torch normally operates at atmospheric pressure on argon, producing temperatures up to 9000K and electron densities up to $10^{16}/cm^3$, but in the past year we have extended the torch operation to mixed gases, e.g., argon with 10-15% O_2. The objective of the research has been to develop plasma diagnostics based on spectrally resolved lineshapes of atomic transitions. For example, we have recorded lineshapes of excited-state atomic oxygen (at 777.2 nm) and argon (at 842.5 nm), and used these data to infer: kinetic temperatures (from the Doppler-broadening contribution to the linewidths), population temperatures (from the integrated absorption), electron density (two ways, from both the Stark shift of the lines and from the Stark-broadening component of linewidth), and the electron temperature (from the ratio of Stark broadening and shift). These data utilized only line-of-sight absorption for atomic oxygen, but both absorption and LIF measurements were feasible with argon, thereby providing a basis for verifying the radial distribution of plasma properties inferred from Abel inversion of absorption data. Although most measurements were made with linear excitation energies, LIF measurements at partial saturation intensities were also carried out. This latter study led to a new approach for inferring critical collisional transfer rates needed in modelling the Stern-Volmer (fluorescence yield) factor in LIF. Details of the above work may be found in Refs. 1-3.

PLIF Imaging in Shock Tube Flows

Shock tubes and tunnels provide a convenient environment for the development of advanced diagnostic methods relevant to advanced air-breathing propulsion systems. A wide variety of high-enthalpy and high-velocity flows can be easily generated, and at modest expense relative to continuous-flow facilities. During the past year we have continued to use a simple pressure-driven

shock tube and tunnel for two projects aimed at developing PLIF diagnostics for scramjet and nonequilibrium hypersonic flow studies. A particular accomplishment has been the successful demonstration of quantitative, single-shot imaging of temperature in a model scramjet flow. Our measurement scheme utilizes two pulsed dye lasers and two gated intensified CCD cameras to acquire two separate but essentially simultaneous single-shot PLIF images, in a common flowfield plane, for excitation of two different rotational states of NO. The ratio of these image intensities can be used to infer the translational/rotational temperature at each point in the image. The flow of interest is the interaction between a supersonic stream of high temperature air and a transverse jet of hydrogen fuel. By seeding only the fuel jet with NO, information on mixing is also obtained. To summarize our findings, we were able to achieve good accuracy in the single-shot temperature images, but only when suitable on-line diagnostics were employed for the laser pulse energy, laser sheet distribution, and the laser spectral lineshape. A schematic of the overall experimental set-up is shown in Fig. 1. Detailed results are available in Ref. 4.

CW Ring Dye Laser Techniques

Tunable monochromatic laser sources provide opportunities for new measurement concepts based on spectrally resolved absorption lineshapes. For example, cw ring dye lasers can be rapidly modulated in wavelength (using schemes developed previously in this program) to record a pair of absorption lines, using either line-of-sight absorption or single-point LIF, allowing inference of gas temperature through the ratio of the signals for the two lines. The static pressure can be inferred from the width of the lines or the absolute absorption (if the species mol fraction is known), and the velocity can be inferred from the shift in line position caused by the Doppler effect. The density can be calculated once the pressure and temperature are known, as can propulsion quantities such as the mass flux (product of density and velocity) and the momentum flux (thrust). Thus the absorption lineshape is seen to be critically dependent on gasdynamic properties, and an analysis of fully resolved lineshapes can simultaneously yield information on multiple flowfield parameters. As our laser can be modulated at 4 kHz for wavelengths relevant to OH, NO and O_2, these multiple-parameter measurements can be executed at a high repetition rate. Relevant details may be found in Refs. 5-7.

Semiconductor Diode Laser Techniques

Tunable diode lasers offer the possibility of an economical, rugged and compact alternative to cw ring dye lasers for spectrally resolved absorption and fluorescence spectroscopy. Such lasers are presently available in several wavelength intervals at wavelengths generally in excess of 650 nm, although operation at shorter wavelengths is expected in the future. These lasers have significant potential advantages, including the possibility of high frequency modulation of laser wavelength through current modulation. In the past three years, we have pursued application of these laser sources to monitor O_2 at 760 nm (Refs. 8,9), H_2O near 1.4 microns (Ref. 10), and most recently, O-atoms near 777 nm (Ref. 11). Our objective with the molecular oxygen and water vapor work was to develop quantitative line-of-sight diagnostics for nonintrusive probing of inlet and exhaust streams of supersonic combustors. For example, the O_2 diagnostic is able, in principle, to yield the information required to characterize the inlet air mass flux in ground- or flight-test environments, while the H_2O diagnostic should yield similar information on propulsion performance (e.g., combustion efficiency, temperature, water mol fraction, momentum flux, etc.) at the combustor exhaust. Thus far we have tested these ideas using a simple shock tube to produce a controlled supersonic flow of these gases. Future work will include extension of these ideas to remote, fiberoptically coupled measurements in larger scale test facilities, at NASA Ames Research Center.

Current work has been concerned with extending these ideas to very high enthalpy conditions, as might be found in hypersonic flowfields (e.g., the NASP vehicle). The species of interest is atomic oxygen since molecular oxygen will be dissociated at temperatures above about 6000K. Our approach is to use reflected shock wave heating to prepare samples of atomic oxygen at high temperatures. A tunable GaAlAs diode laser is scanned over the O-atom transition near 777 nm to infer the kinetic and population (electronic) temperatures from the Doppler-broadened

linewidth and the integrated absorption, respectively. An experimental schematic and a typical reduced lineshape profile are shown in Figs. 2 and 3. Note the good agreement between the two temperatures (near 9500 K), which confirms that the electronic distribution is properly equilibrated at the conditions of these experiments. See Ref. 11 for details.

Digital Camera for High-Speed Imaging

Work is nearing completion on the development and characterization of a high-speed digital camera for recording instantaneous 3-d images and fast 2-d image "movies." The basic concept utilizes a modified commercial image converter camera to incorporate CCD detection. This system is capable of recording up to 20 images at 10 million frames per second, and with higher light throughput than obtainable with standard lens-coupled image-converter cameras. Results have been obtained in simple laboratory flows using Mie scattering and laser-induced fluorescence. An important aspect of the work has been the development of computer-based schemes for correcting image distortions introduced by the image converter camera. See Ref. 12 for further details.

REFERENCES

1. D. S. Baer and R. K. Hanson, "Tunable Diode Laser Absorption Diagnostics for Atmospheric Pressure Plasmas," Jour. of Quant. Spectrosc. and Radiative Transfer 47, 455-475 (1992).

2. D. S. Baer and R. K. Hanson, "Semiconductor Laser-Based Measurements of Quench Rates in an Atmospheric Pressure Plasma Using Saturated-Fluorescence Spectroscopy," Applied Optics 32, 948-955 (1993).

3. D. S. Baer and R. K. Hanson, "Semiconductor Laser Absorption Diagnostics of Atomic Oxygen in an Atmospheric-Pressure Plasma," J. Quant. Spectrosc. and Radiat. Transfer, submitted March 1993.

4. B. K. McMillin, J. L. Palmer and R. K. Hanson, "Instantaneous Temperature Imaging of a H_2/NO Jet in Supersonic Crossflow Using Two-Line PLIF," Applied Optics, submitted July 1992.

5. A. Y. Chang, M. D. DiRosa, D. F. Davidson and R. K. Hanson, "Rapid-Tuning CW Laser Technique for Measurements of Gas Velocity, Temperature, Pressure, Density and Mass Flux Using NO," Applied Optics 30, 3011-3011 (1991).

6. D. F. Davidson, A. Y. Chang, M. D. DiRosa and R. K. Hanson, "Continuous Wave Laser Absorption Techniques for Gasdynamic Measurements in Supersonic Flows," Applied Optics 30, 2598-2608 (1991).

7. M. D. DiRosa, L. C. Philippe, P. Arroyo and R. K. Hanson, "CW Laser Strategies for Simultaneous Multi-Parameter Measurements in High-Speed Flows," paper AIAA-92-3955 at 17th Aerospace Ground Testing Conference, Nashville, July 6-8, 1992.

8. L. C. Philippe and R. K. Hanson, "Laser-Absorption Mass Flux Sensor for High-Speed Air Flows," Opt. Letters 16, 2002-2004 (1992).

9. L. C. Philippe and R. K. Hanson, "Sensitive Diode Laser Absorption Technique for Aerodynamic Measurements," paper AIAA 92-0139, AIAA 30th Aerospace Sciences Meeting, Reno, Jan. 1992, also Applied Optics, in press.

10. M. P. Arroyo, S. Langlois, and R. K. Hanson, "Diode Laser Absorption Technique for Simultaneous Measurements of Multiple Gasdynamic Parameters in High-Speed Flows Containing Water Vapor," Applied Optics, submitted 2/93.

11. H. A. Chang, D. S. Baer and R. K. Hanson, "Semiconductor Laser Diagnostics of Atomic Oxygen for Hypersonic Flowfield Measurements," paper AIAA-93-0628, AIAA 31st Aerospace Sciences Meeting, Reno, Jan. 1993.

12. B. J. Patrie, J. M. Seitzman and R. K. Hanson, "Planar Imaging at High Framing Rates: System Characterization and Measurements, Part II," paper AIAA-93-0364, AIAA 31st Aerospace Sciences Meeting, Reno, Jan. 1993.
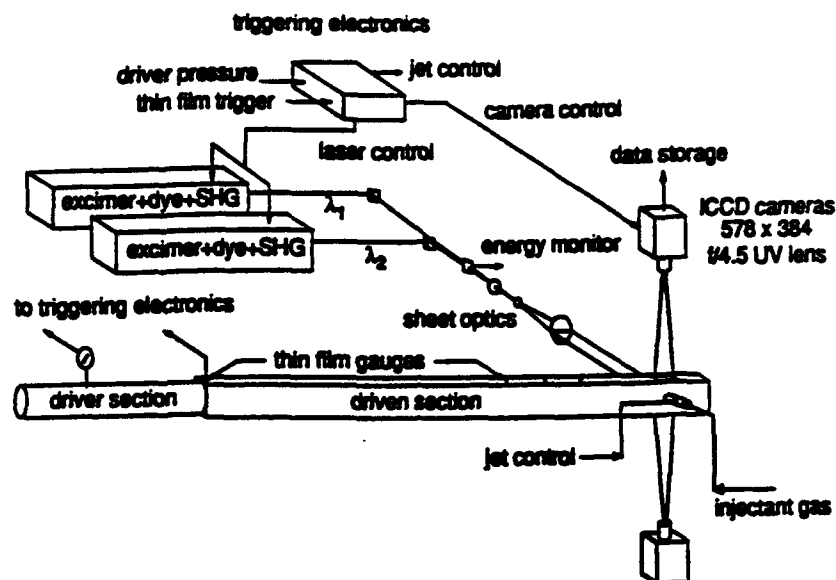
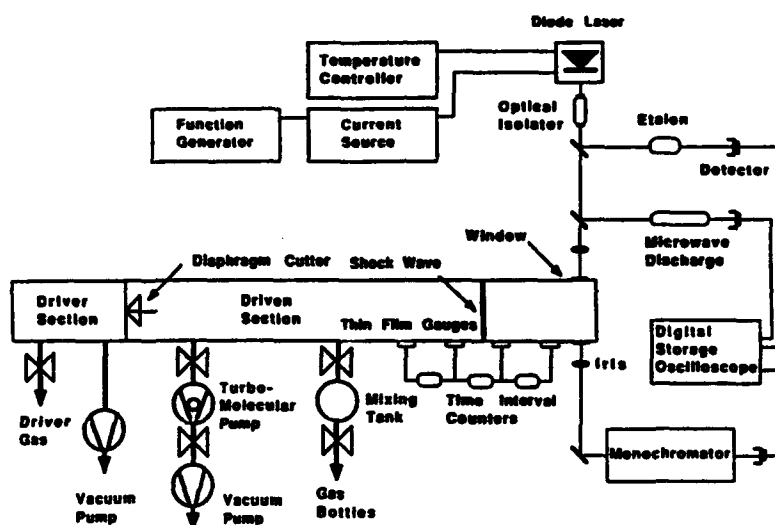Fig. 1. Schematic of the shock tube and PLIF imaging facility.

Fig. 2. Schematic diagram of the experimental setup for O-atom measurements.
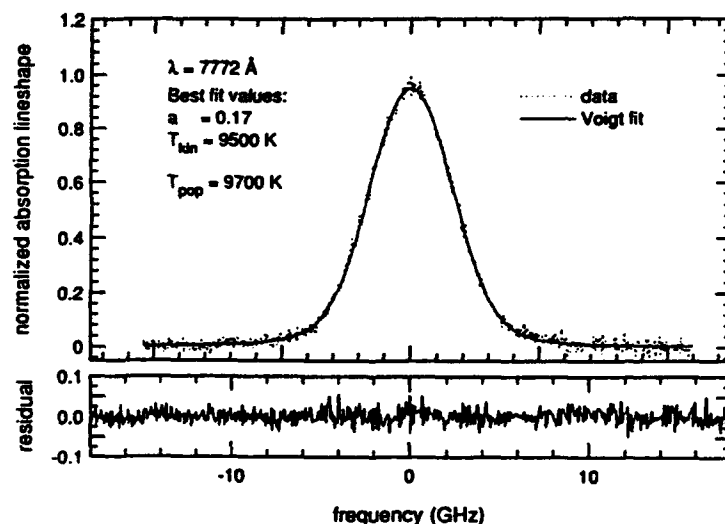

Fig. 3. Example of reduced absorption lineshapes for a single scan of the oxygen $3s^5S_2{}^o \rightarrow 3p^5P_3$ transition. The residual is the difference between the data and the best-fit Voigt profile.

NOVEL NONLINEAR LASER DIAGNOSTIC TECHNIQUES

Principal Investigators: David L. Huestis, Gregory W. Faris, and Jay B. Jeffries

SRI International
Molecular Physics Laboratory
Menlo Park, CA 94025

SUMMARY/OVERVIEW:

Task 1: UV and VUV Generation and Detection Techniques

We are developing techniques for the extension of laser-based diagnostics into the vuv for detection of atomic ions, planar imaging of light atoms, and other applications. In the past year, we have confirmed that we can perform two-photon excitation at wavelengths as short as 133 nm, increased our energies by more than a factor of three, and produced tunable radiation now as short as 122 nm.

Task 2: Laser-Excited Amplified Spontaneous Emission (ASE)

During the past year, we have explored the use of amplified spontaneous emission (ASE) to measure gas temperature and concentration of atomic oxygen. Our ASE demonstration measurements have shown that the ASE bandwidth of oxygen can be measured in low-pressure flames, and we have developed a model of the ASE signal intensity and bandwidth to extract gas temperature and velocity from such measurements. We have demonstrated that direct gain measurements on a diode probe laser are possible from laser excited atoms; such direct gain measurements can determine atom concentration. Because the ASE signal is collimated along the excitation laser beam, ASE measurements require minimal optical access, and thus appear to be an attractive method to measure atom concentration, directed velocity, and gas temperature in high speed reacting flows.

TECHNICAL DISCUSSION

Task 1: UV and VUV Generation and Detection Techniques

A number of diagnostic problems can only be solved using high power vuv radiation. Detection of atomic ions is important for applications including plasma propulsion, the study of highly-ionized flows, plasma lithography, and magnetically confined fusion. The very high photon energies for excitation of light atomic ions require that two-photon excitation using vuv radiation must be used for detection of these species. High power single-photon excitation with vuv radiation is an attractive approach for the planar imaging of light atoms. Other significant applications for high power vuv radiation include high sensitivity single- or multiple-photon laser ionization detection techniques and single-photon calibration of multiple-photon diagnostic techniques.

As a source for widely tunable vuv radiation, we are using a two-photon-resonant difference-frequency generation technique that we have developed which can potentially tune from 110 to 180 nm.[1] Tunable ArF radiation is mixed with radiation from a Nd:YAG-pumped dye laser in a process enhanced by two-photon resonances for the ArF laser in krypton and hydrogen. Last year we reported preliminary measurements of two-photon-excited fluorescence detection of neon using 133 nm radiation from this source. This was a significant result as it demonstrated the ability to perform the two-photon-excited fluorescence process well in the vacuum ultraviolet such as would be required for detection of atomic ions. Experimental improvements have allowed the performance of a power dependence of the fluorescence signal, confirming that we are indeed performing a two-photon-resonant excitation.[2] For these measurements, we had the luxury of being able to operate at fairly high atom densities (pressure of ~100 Torr). For detection of atomic ions, we must be able to detect significantly lower densities. To successfully perform such measurements, we will require significantly higher powers.

Based on measurements of the transmission of our optics in the vuv using a hydrogen arc light source and a vuv spectrometer, we have found that much of the energy that we generate is absorbed by the MgF_2 optics we use, apparently through color center formation.[2] To take better advantage of the energies that we produce, we have changed our optical setup to greatly reduce the optical path through MgF_2 for the vuv. Instead of using a separate collimating lens and dispersing prism, amounting to perhaps 5 cm of optical path, we use a single lens placed off axis to both focus the vuv and separate the vuv from the pump beams, resulting in an optical path of only a few mm. The apparatus for this arrangement is shown in Figure 1. With this arrangement, we have been able to increase our generated energies by over a factor of 3, from 20 μJ to over 65 μJ. These energies were measured directly using a pyroelectric energy meter in vacuum.
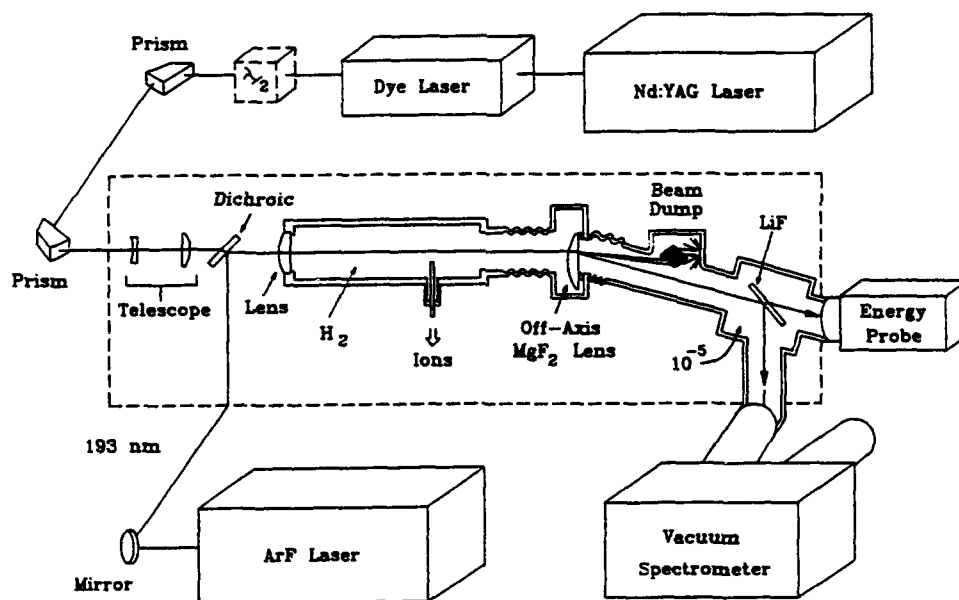

Figure 1. Off axis lens apparatus for high power vuv generation.

We are now pursuing generation of shorter wavelengths, in the region of 120 nm. There are a number of motivations for exploring this region. By using mixtures of krypton and hydrogen, we can use the negative dispersion of krypton to phase match the mixing process. Phase matching offers the potential for significantly increased vuv powers, which will be essential for the demonstration of the detection of atomic ions. In addition, a number of significant transitions occur in this region. Lyman alpha radiation at 121.6 nm is a very important wavelength for many reasons, including the potential for performing planar imaging of hydrogen atoms. Planar imaging of N atoms can be performed using 120 nm, and two-photon-excited fluorescence of N^+ can be performed using 117 nm. We have obtained vuv radiation at about 122 nm and are in the process

of improving the system to allow production of calibrated energies. We should know soon the practicality of some of these diagnostic possibilities.

Task 2: Laser-Excited Amplified Spontaneous Emission (ASE)

Laser-excited amplified spontaneous emission (ASE) is an attractive method to detect atomic species in reacting gas flows and plasmas because the signal shares the same beam path with the excitation laser light. Multiphoton laser excitation of atoms is traditionally detected by fluorescence or ionization which either requires large solid angle fluorescence collection or a probe for ion/electron collection. ASE provides an alternative detection method which requires minimal optical access and no intrusive probes; however, performing quantitative ASE measurements requires understanding the nonlinear optical gain in the laser-excited sample. For example, two-photon selection rules produce atoms in excited states which do not have allowed one-photon transitions back to the ground state but radiate instead to an intermediate excited state. For atomic species found in propulsion like hydrogen and oxygen, these intermediate states are more than 10 eV above the ground state, and at combustion temperatures there is nearly no thermal population in states with such a large excitation energy. Thus, a population inversion can readily be produced by the laser two-photon excitation; any spontaneous emission along the excitation laser beam can experience gain. This gain produces ASE propagating forward and backward along the laser beam.

During the past year, we have studied two-photon excited ASE of atomic oxygen in a variety of low-pressure flames. We have explored the feasibility of ASE measurements of concentration, gas velocity, and gas temperature. We have observed simultaneous LIF and ASE from oxygen atoms in all the flames studied. We discovered that ASE intensity is more sensitive to the collisional environment than LIF which makes the interpretation of ASE intensity quite difficult. However, a direct gain measurements can avoid this difficulty and provide stimulated emission determinations of atom concentration. A cw laser is tuned to the ASE transition and directed through the pulsed laser excited atoms. If the cw probe laser is at a slight angle to the pump laser, gain can be observed on the cw seed and loss on the spontaneous ASE. Figure 2 shows the stimulated loss in spontaneous ASE as a function of diode probe laser power. Although the measurements are preliminary, they are quite encouraging: we observed gains from the laser excited oxygen atoms that produced increases of 0.3 - 25 % of the diode probe laser intensity. This gain
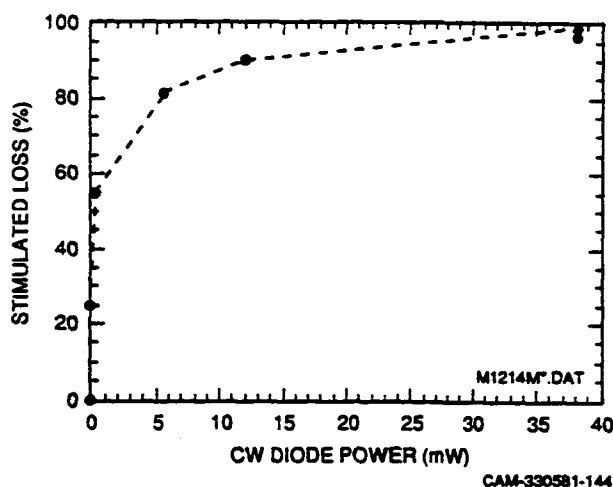

Figure 2. Depletion of spontaneous ASE from two-photon laser excited oxygen atoms in a 7 Torr H_2/O_2 flame.
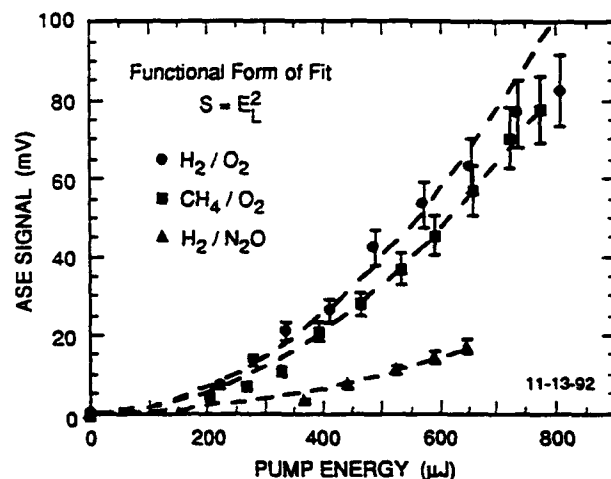
Figure 3. O atom ASE versus excitation pulse energy.

is proportional to the number of laser excited atoms, and from the excitation parameters, we can determine the number density of ground state atoms. Thus, accurate single shot atom concentration measurements are feasible using the stimulated emission gain of a probe laser beam.

We have developed a model of ASE that relates ASE intensity to atom number density and ASE bandwidth to gas temperature. To extract gas temperature from ASE bandwidth, we must know some details about the two-photon pumping and subsequent ASE emission. The ASE process is intrinsically nonlinear and attention must be paid to excitation saturation, gain narrowing, and any ac Stark shifting or broadening. Measurement of the relative O atom ASE signal after exciting J=1 and J=2 components of the 3p ^3P from the 2p ^3P as a function of laser power allows measuring the saturation intensity, $I_{sat} = 430$ MW/cm^2 for the J=2 $\leftarrow$ 2 transition. Thus, if we use a focusing lens of 50 cm focal length, pulse energies below 600 µJ are well below the saturation limit. Figure 3 demonstrates that the O atom ASE signal in all three flames is proportional to the pulse energy squared for pulse energies below 600 µJ.

The model of the ASE bandwidth must also include the finite bandwidth of the excitation laser. Figure 4 shows the predicted ASE bandwidth versus excitation laser bandwidth for gas temperatures of 1200 K and 1800 K, which correspond to measurement temperatures in the H$_2$/O$_2$ and CH$_4$/O$_2$ flames. Notice that at the dye laser bandwidth must be greater than the two-photon Doppler width for the ASE bandwidth to become independent of the excitation laser bandwidth. Narrow bandwidth excitation preferentially excites on a selected velocity group of the thermal distribution of atoms; if ASE occurs before the excited distribution collides and thermalizes the velocity distribution, the ASE will be excitation narrowed.
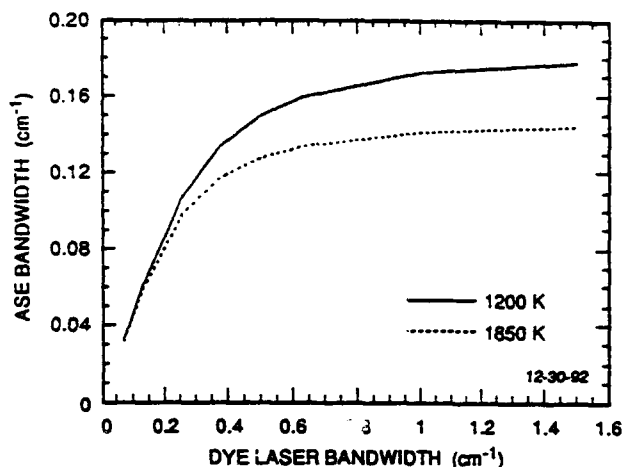

Figure 4. ASE bandwidth versus excitation laser bandwidth in the small gain limit.

We have made the first measurement of the spectral bandwidth of ASE, and demonstrated that single laser shot measurements are possible. Measurements at 1200 K in a low-pressure hydrogen/oxygen flame agree well with the model predictions. Thus, we have also found ASE gas temperatures and gas velocity measurements are feasible.

REFERENCES

1. G. W. Faris and M. J. Dyer, "Multiphoton Spectroscopy Using Tunable VUV Radiation from a Raman-Shifted Excimer Laser," in *Short Wavelength Coherent Radiation: Generation and Applications,* Philip H. Bucksbaum and Natale M. Ceglio, Eds. (Optical Society of America, Washington, DC, 1991).

2. G. W. Faris and M. J. Dyer, "Two-Photon-Excitation of Ne at 133 nm," Opt. Lett. **18**, 382-384 (1993).

TUNABLE PLASMA ROCKETS WITH RF-HEATING
AND MAGNETIC THRUST CHAMBERS

Franklin R. Chang Diaz and T. F. Yang*
Astronaut Office, NASA Johnson Space Center
Houston, Texas 77058; April 1993

Abstract

Theoretical and experimental research in tunable plasma propulsion (variable I_{sp}/thrust at constant power) has been carried out over the last decade. Important developments include: 1) the demonstration of an increased RF-to-plasma coupling efficiency (68%) as a result of antenna design and relocation, as well as wave launching techniques; 2) Theoretical demonstration of plasma-field detachment at the rocket exhaust, and 3) experimental validation of predicted performance parameters. including direct thrust measurements using a ballistic double-pendulum capacitance sensor. Other results include the estimation of attractive power specific mass or "alpha" values of 8 Kg/kW, including the power system, and using off-the-shelf components. Substantial improvements to these values are expected with emerging technologies in high temperature superconductivity and RF-confinement.

Summary

Important developments include the demonstration of an increased RF-to-plasma coupling efficiency and experimental validation of predicted performance parameters, including direct thrust measurements using a ballistic double-pendulum sensor. New system developments point out that specific weight can be reduced to 6Kg/kW.

*Dr. Yang is presently at the M.I.T. Plasma Fusion Center
Cambridge, Massachusetts.

ANOMALOUS IONIZATION AND THE MPD THRUSTER:
Investigations of the Critical Ionization Velocity (CIV) Phenomenon in Space

PI's: Edgar Y. Choueiri, Robert G. Jahn and Arnold J. Kelly
Electric Propulsion and Plasma Dynamics Lab. (EEPDyL)
Princeton University
Princeton, NJ. 08544

Scientific Collaborators:
Hideo Okuda *Princeton Plasma Physics Lab.*,
Torsten Neubert *Space Physics Lab., Univ of Michigan*
Viktor Oraevsky, Vladimir Dokukin and
Alexander Volokitin *IZMIRAN, Russia*

1 Summary

An understanding of the physics of ionization in the MPD thruster is of utmost importance since ionization losses are highly irrecoverable and are a major cause of inefficiency in high-power self-field MPD thrusters. There are many theoretical and experimental indications that ionization in the MPD thruster is anomalous *i.e.* enhanced by turbulence. The fundamental mechanism underlying anomalous ionization is still poorly understood. Active space experiments are ideal to stage plasma interactions involving anomalous ionization, such as the critical ionization velocity (CIV) interaction, which can be monitored and studied using onboard plasma diagnostics. The goals of our present study are to conduct active space experiments onboard the Russian APEX satellite to investigate the fundamentals of anomalous ionization, to develop experimentally verified models and to include the resulting models in state of the art MPD

thruster fluid codes much like we did for anomalous resistivity and heating in our previous AFOSR-sponsored work.

2 Technical Discussion

2.1 Background and Relevance of Anomalous Ionization

A spectroscopic investigation of the ionization process in the MPD thruster conducted recently in our laboratory[1] has yielded the first hard evidence implicating anomalous ionization. The study found that classical ionization rates are exceeded by two to four orders of magnitude. Such findings effectively imply that the role of plasma microinstabilities in enhancing ionization must be invoked. This has reinforced our earlier theoretical speculations[2] on the role of the critical ionization velocity (CIV) phenomenon in MPD thruster physics.

The critical ionization velocity (CIV) phenomenon is an instability-driven ionization process that is central to many problems in plasma dynamics. It has been first hypothesized by Alfvén in 1942 and then invoked in the context of cometary physics, the formation of the solar system, planetary tori and more practically interaction of spacecraft exhaust with plasma environment, ionization processes in plasma guns and self-field MPD thrusters (see the recent review in ref. [3]).

In all situations where CIV is invoked, a plasma microinstability (of the streaming type) is believed to heat (through the resulting turbulence) the high energy population of the electrons thus significantly enhancing electron-impact ionization. Since the relative motion becomes strongly coupled to the ionization process through the instability, an equipartition of energy leads to the breaking of the relative motion of the plasma down to a characteristic velocity u_{ci}, ($u_{ci} \equiv \sqrt{2\epsilon_i/M}$) that is dependent on the ionization potential (ϵ_i) and mass (M) of the neutral atom and is called *critical ionization velocity*. The characteristic velocity u_{ci} thus plays a threshold role for the initiation of enhanced ionization.

In the self-field MPD thruster the ionization and acceleration processes can become coupled through a current-driven instability. A CIV-type interaction can thus result without a relative motion between ions and neutrals since the relative motion between ions and electrons (i.e. the current) can provide the source of energy channeled by the instability to the ionizing electrons.

The presence and importance of current-driven microinstabilities in the MPD thruster have been unambiguously proven by theoretical, numerical and experimental work in the past 5 years[4, 5]. The unstable modes have characteristic frequencies near the lower hybrid frequency much like the unstable modes excited by the ion-streaming instabilities behind the space manifestations of CIV. Moreover, the importance of u_{ci} as a characteristic velocity and scaling parameter in the performance of MPD thrusters has been demonstrated in 1985 through experimental testing of an MPD thruster with various propellants[2]

(argon, krypton and xenon).

2.2 Using Active Space Experiments to study CIV

One obstacle in studying the CIV phenomenon experimentally within the MPD thruster is the smallness of the ionization front (about 1 mm thick[1]) and its location (near the gas inlet) which render the ionization region very difficult for access by standard probing techniques.

The importance of the Earth ionosphere and magnetosphere as an ideal laboratory to test the CIV phenomenon has been widely recognized in the past ten years[6]. The relative velocity between a neutral gas injected from a spacecraft and the background plasma is effectively the orbital velocity which is larger than u_{ci} for many gases. Moreover, he use of plasma diagnostics onboard satellites and subsatellites could allow for a thorough and parametric test of CIV.

The overall objectives of our current work are to conduct such tests in space and use the observations from these tests and other similar tests[7] along with computer particle simulations and theoretical techniques to synthesize anomalous ionization models. These models will be formulated in terms of macroscopic parameters to facilitate their inclusion in fluid flow codes of the MPD thruster such as the one developed and currently being used at our laboratory[8].

APEX (Active Plasma Experiment in Space) is a project of the Institute of Terrestrial Magnetism Ionosphere and Radio Wave Propagation (IZMIRAN) in Russia. The APEX satellite was launched on December 18 1992 and consists an extensive battery of plasma diagnostics and a sub-satellite.

We have recently finished a series of planned neutral gas releases from APEX. During these experiments we staged releases of neutral xenon at different altitudes (between 400 and 3000 km) setting up a supracritical relative motion between the injected cloud and the ambient plasma. Under the proper conditions the relative streaming between seed ions in the injected neutral cloud and ions in the ambient plasma can excite microinstability and sustain a CIV interaction.

A charged particle analyzer was used to measure the energy and pitch angle distribution of electrons and ions with energies between 30 eV and 30 keV. The instrument has 12 directions of view. A complete spectrum is measured in one second. An electron flux analyzer, intended for satellite potential measurements was used to measure the flux of precipitating electrons with energies ranging between 5 and 1000 eV. Langmuir probes and retarding potential analyzers were used to measure ambient plasma parameters with T_e between .1 and 10 eV. A radio-frequency ion composition analyzer was also available (1-60 a.u.m.). The LF wave diagnostics permitted the measurement of three components of the electric field up to 700 mV/m with a frequency range of $.01 - 22$ kHz and a sensitivity of 2×10^{-7}-2×10^{-8} V/m/$\sqrt{\text{Hz}}$. The LF wave unit was supposed to measure three components of the magnetic field in the frequency range of $.1 - 22$ kHz with a sensitivity of 4×10^{-6} nT/$\sqrt{\text{Hz}}$ but unfortunately

failed prior to the CIV tests. The HF wave unit allowed the measurement of one component of the electric field and magnetic fields between .1 and 10 MHz. Data from the onboard scanning spectrometer and the photometer were recorded and might be useful for the portion of the tests conducted in darkness. The dc magnetic field is measured with a 3-axis fluxgate magnetometer with a dynamic range of ±6400 nT.

A specialized computer code for the deconvolution, reduction and display of the instrument data from the raw digitized telemetry tapes is currently being developed at Princeton. Some preliminary results showing evidence of plasma density enhancement that could possibly be attributed to a CIV process will be shown at the contractors meeting.

References

[1] T.M. Randolph, W.F. Von Jaskowsky, A. J. Kelly, and R. G. Jahn. Measurement of ionization levels in the interelectrode region of an MPD thruster. In 28th *Joint Propulsion Conference*, Nashville, TN, 1992. AIAA-92-3460.

[2] E.Y. Choueiri, A.J. Kelly, and R.G. Jahn. The manifestation of Alfvén's hypothesis of critical ionization velocity in the performance of MPD thrusters. In 18th *International Electric Propulsion Conference*, Alexandria, Virginia, USA, 1985. AIAA-85-2037.

[3] N. Brenning. Review of the CIV phenomenon. *Space Science Reviews*, 59:209–314, 1992.

[4] E.Y. Choueiri, A. J. Kelly, and R. G. Jahn. Current-driven plasma acceleration versus current-driven energy dissipation part II : Electromagnetic wave stability theory and experiments. In 22nd *International Electric Propulsion Conference*, Viareggio, Italy, 1991. IEPC-91-100.

[5] D.L. Tilley, E.Y. Choueiri, A.J. Kelly, and R.G. Jahn. An investigation of microinstabilities in a kW level self-field MPD thruster. In 22nd *International Electric Propulsion Conference*, Viareggio, Italy, 1991. IEPC-91-122.

[6] E. Möbius, R.W. Boswell, A. Piel, and D. Henry. A Spacelab experiment on the critical ionization velocity. *Geophysical Research Letters*, 6:29–31, 1979.

[7] J.A. Marshall, J.L. Burch, E.Y. Choueiri, and N. Kawashima. CIV experiments on ATLAS-1. *Geophysical Research Letters*, 20(6):499–502, 1993.

[8] G. Caldo, E.Y. Choueiri, A. J. Kelly, and R. G. Jahn. Numerical simulation of MPD thruster flows with anomalous transport. In 28th *Joint Propulsion Conference*, Nashville, TN, 1992. AIAA-92-3738.

LIQUID ROCKET ENGINE CHAMBER PRESSURE RESPONSE TO ACOUSTIC PERTURBATION

AFOSR Grant Contract No. AFOSR-90-0121

Principal Investigators: J. W. Daily and S. Mahalingam

Center for Combustion Research
Mechanical Engineering Department
University of Colorado
Boulder, CO 80309-0427

SUMMARY/OVERVIEW

The effect of acoustic perturbation upon the time variation of the chamber pressure in an experimental liquid rocket engine with a coaxial injector is being investigated. A pair of compression drivers are used to excite a transverse acoustic field at strengths of up to 155.6 dB in the combustion chamber. Ethanol and oxygen enriched air are used as the fuel and oxidizer. Increasing the equivalence ratio from 3.8 to 7.4 decreases the chamber pressure response to acoustic excitation. Increasing the excitation amplitude from 147 dB to 156 dB increases the chamber pressure response. This study will elucidate the effect of different physical mechanisms on the dynamic behavior of liquid propellant rocket engines.

AUTHORS: A. Ghafourian, S. Mahalingam and J. W. Daily

TECHNICAL DISCUSSION

Rocket engine manufacturers rely heavily on empirical and actual test data during the design stage of rocket engines in order to prevent the occurrence of instabilities during flight operation. This is clearly an expensive approach. Thus, the long term objective of our research is to develop predictive models that will help rocket designers build high performance, stable liquid rocket engines. Injectors in liquid rocket engines are exposed to relatively high amplitude pressure and velocity field oscillations (acoustic waves). These oscillations have a pronounced effect on the atomization of liquid propellant. Sufficient evidence from past work[1,2,3] and our present research reveals that the structure and characteristics of atomization under unsteady conditions (as would occur during a combustion instability) deviate considerably from atomization behavior under steady conditions. Thus, the dynamic behavior of liquid propellant atomization is of major importance, especially when atomization pro   very small droplets.

In this work, external excitation is used to induce pressure and velocity fluctuations. The advantage is a complete control over frequency, and amplitude, so that linear and nonlinear forcing regimes can be investigated. Although, the dynamic response of atomizers has been

shown to be important in theoretical studies on the possible coupling between atomization and acoustic waves leading to combustion instability, it has never been measured. Its knowledge can lead to the use of linear stability theory to clarify the role of atomization in high frequency combustion instability.

The uni-element coaxial combustor used in this study has transverse dimensions of 5 cm x 5 cm. Its length can be varied from 28 to 43 cm by moving the exit nozzle location. The coaxial injector has a center post with an inside diameter of 1 mm and with a 4 mm width surrounding annulus. A complete description of the experimental facility used in this study is given in Huynh et al. (1992). A Kistler Piezotron transducer is used to measure the chamber pressure 1.5 cm downstream of the injection plane.

Results

Recent experimentation has been conducted to determine the effect of equivalence ratio and excitation amplitude upon the time variation of chamber pressure under forced and unforced conditions. The gas phase and liquid phase velocities were held constant at 92 m/s and 15 m/s, respectively. The equivalence ratio was varied by the addition of pure oxygen to the gas phase resulting in a range from 3.8 to 7.4 . This procedures was adopted in order to keep the atomization characteristics of the system constant. The thermophysical properties of oxygen are essentially similar to air. Thus, atomization parameters including Weber number and density ratio were held relatively constant. However, the static chamber pressure varied with equivalence ratio. This was caused by the use of the same size chamber exit nozzle for all the experiments. A variety of exit nozzles are under construction in order to decouple the chamber pressure from equivalence ratio.

Unexcited chamber pressure recording for an equivalence ratio of 3.8 is shown in Figure 1. The power spectra of these signals indic   presence of three frequency ranges. The first range is centered at 200 Hz and the othe   ranges are centered at 1250 Hz and 2500 Hz. There is a slight increasing shift of these ranges as the equivalence ratio is reduced. This is probably caused by the fact that at lower equivalence ratios the chamber experiences higher temperatures and thus higher sound speeds, and hence increased oscillation frequency.

The acoustic compression drivers were tuned to excite the chamber at 2950 Hz. Chamber pressure record under forced condition, for an equivalence ratio of 3.8 is shown in Figure 2. The power spectra of these signals indicate a peak at the excitation frequency. This is expected because the combustion chamber, excitation system, and pressure transducer are in a closed system. The interesting result is that the observed peak at the excitation frequency increases as the equivalence ratio is decreased. The peak power at the excitation frequency versus equivalence ratio is displayed in Figure 3. The effect of excitation amplitude for a fixed equivalence ratio of 3.8, holding all other parameters constant, was examined. As shown in Figure 4, the peak power at the excitation frequency increases as the excitation amplitude is increased.

FUTURE WORK

Currently, work is under way to determine the effect of gas phase velocity, equivalence

ratio, excitation frequency, chamber length, and injector post recess upon the time variation of chamber pressure and localized heat release (C2 emission) between forced and unforced conditions. Schlierien images are being acquired to analyze the fluid mechanical response to excitation. The analysis includes an examination of the frequency content (power spectra) of the measured signals to determine if the acoustic forcing frequency can drive the physical process under investigation. The phase and amplitude response of the signals relative to the perturbation will also be obtained. This information is a direct measure of the (n, τ) parameters applied to (n, τ) correlations commonly used in industry to predict instability behavior. In addition, auto- and cross-correlations of these signals will be acquired to determine the periodicity and similarity of the measured signals and perturbation.

REFERENCES

1. Buffum, F.G., and Willams, F.A., "The response of a Turbulent Jet to Transverse Acoustic Fields," *Proceedings of the 1967 Heat Transfer and Fluid Mechanics Institute*, P.A. Libby, D.B. Olfe and C.W. Van Atta, Eds., Stanford University Press, 1967, pp. 247-276.

2. Heidmann, M.F., "Oxygen-Jet Behavior During Combustion Instability in a Two-Dimensional Combustor," *NASA TN D-2725*, 1965.

3. Ingebo, R.D., "Atomization of Ethanol Jets in a Combustor With Oscillatory Combustion-Gas Flow," *NASA TN D-3513*, 1966.

4. Huynh, C., Ghafourian, A., Mahalingam, S., and Daily, J.W.,"Combustor Design for Atomization Study in Liquid Rocket Engines," *30th Aerospace Sciences Meeting*, Reno, NV, AIAA 92-0465, January 6-9, 1992.
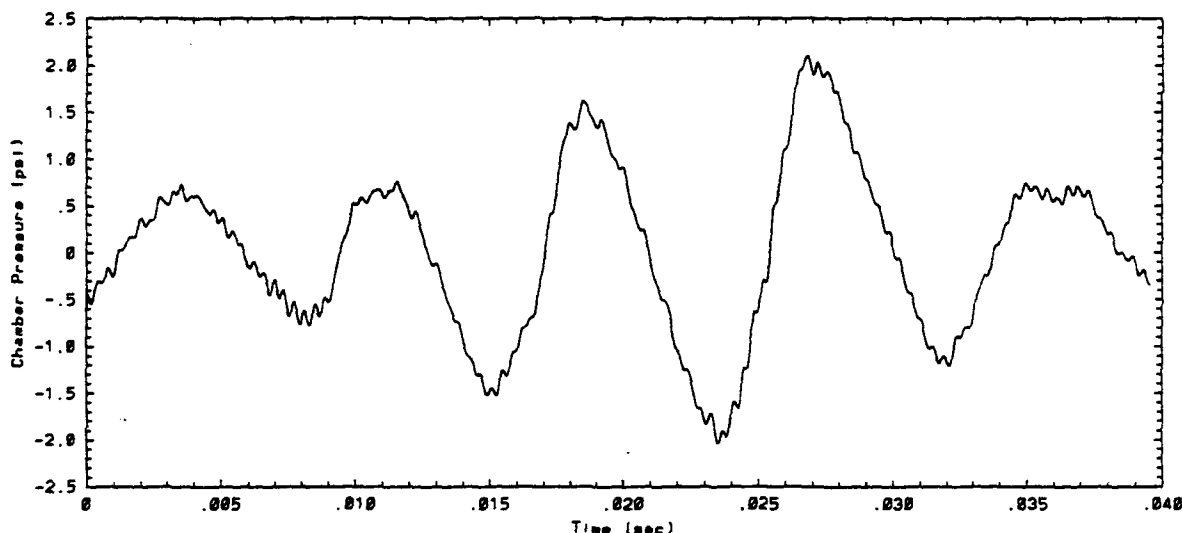
Figure 1: Unexcited chamber pressure, gas phase velocity=93 m/sec, liquid velocity=15 m/sec, equivalence ratio=3.8
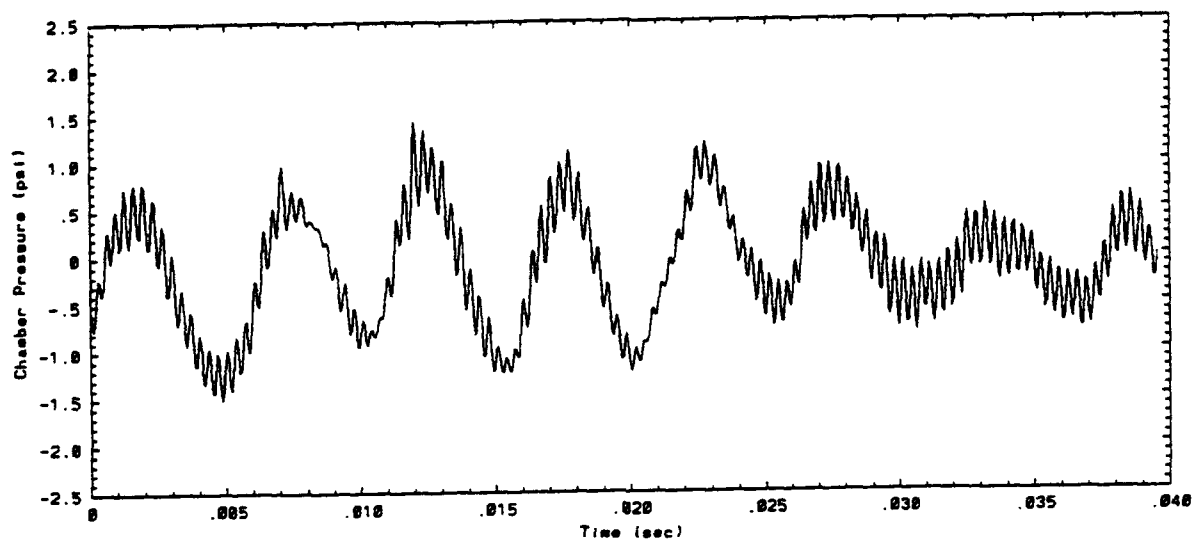
Figure 2: Excited chamber pressure, gas phase velocity=93 m/sec,
liquid velocity=15 m/sec, equivalence ratio=3.8, excitation frequency=2950 Hz
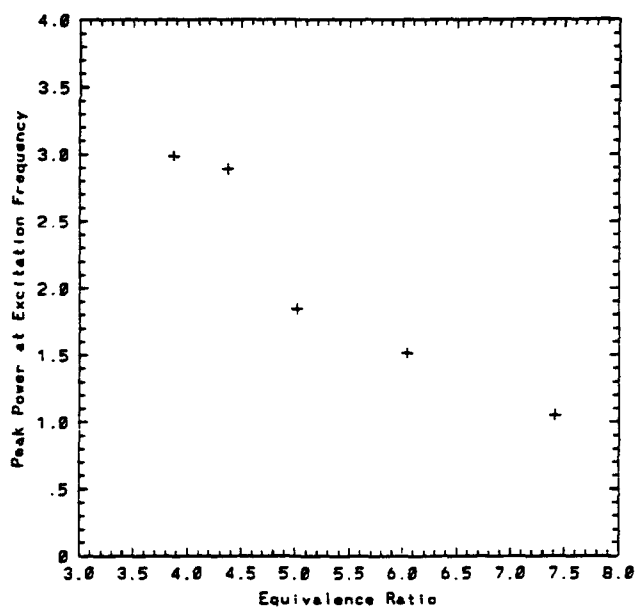

Figure 3: Peak power spectrum
amplitude at excitation frequency
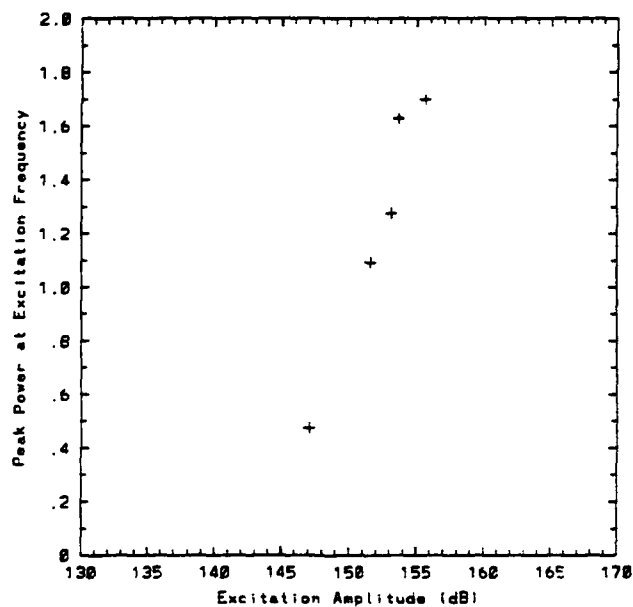vs. equivalence ratio

Figure 4: Peak power spectrum
amplitude at excitation frequency
vs. excitation amplitude

THE USE OF VORTEX SEPARATION TO CLEAN NUCLEAR ROCKET PLUMES

Massachusetts Institute of Technology
Cambridge, MA 02139

SUMMARY

This purpose of this work is to develop a system which will remove radioactive material from the plumes of nuclear rockets. The work to date includes a detailed computational analysis of a vortex separation system, which has identified the system's critical parameters. Ongoing work is intended to: 1) determine whether vortex separation will work and 2) identify the critical parameters which are of interest to the designer. This research addresses the need for a plume cleaning system if nuclear rockets are to be tested on the ground or used in the near-Earth environment. In addition, this research addresses an area in which, to the best of our knowledge, there has been no previous work of any type.

AUTHORS: David Oh, Research Assistant.
            Daniel Hastings, Professor of Aeronautics and Astronautics

TECHNICAL DISCUSSION

Nuclear thermal rockets have existed as a concept since the 1950's, and offer a combination of high thrust and high specific impulse that make them ideal systems for the transportation of large payloads in a timely manner. Over the past two decades, a great deal of experimental and theoretical work has been done on these systems and, given the need, solid core rockets could be built and flown within the decade. However, the presence of radioactive material creates very serious safety and contamination issues if these devices are to be ground tested or used in the near earth environment. In particular, during the NERVA tests of the 1960's, it was observed that even solid core rockets can emit highly radioactive hydrogen plumes. These plumes not only make it difficult and expensive to test these systems, but may actually contaminate the exterior surfaces of the spacecraft with radioactive material. Unfortunately, there is very little experimental data available on the composition of these plumes, but judging from what is available, it seems reasonable to assume that both gaseous and solid radioactive material will be present in the exhaust. This research will investigate a system which uses artificially induced swirl to remove solid material from the exhaust plume before it leaves the rocket nozzle.

The basic principle behind vortex particle separation is a simple one: since the radioactive material in the plume has a much higher density than hydrogen gas, centrifugal forces can be used to force it to the outside of the flow where it can be "skimmed" off before it passes through the nozzle. Such forces can be created by passing the flow through a fixed vane swirler and creating a vortex in a separation chamber. A diagram of this system in shown in figure 1, below.
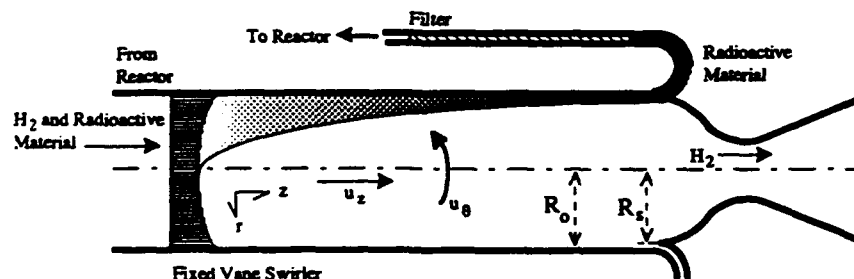

Figure 1: Proposed Vortex Separation System

Centrifugal separation systems have has been used for decades in chemical processing and uranium enrichment systems. This particular system, however, is unique because the flow velocity places severe constraints on the separation time. Under typical conditions, the hydrogen might leave the combustion chamber at velocities near 1100 m/s ($M_z = 0.3$). Therefore, if the separation chamber is to be a meter in length, the separation time must be on the order of a millisecond or less.

Once the flow has passed through the separation chamber, its outer portion can skimmed off and filtered to remove radioactive material. The non-radioactive portion of the flow can then be returned to the reactor and reused as a propellant. The result is a regenerative cleaning scenario which greatly lowers the engine's I_{sp} losses (though the lost mass flow still lowers the overall thrust of the system). There are additional performance penalties associated with the mass of the separation chamber, the filtering system, and their associated cooling systems, but the present work does not examine these issues. Instead, it deals with the vortex separation process and the ability of this system to keep radioactive material from escaping out the rocket nozzle.

In order to study this process, a two part computational simulation has been developed to model the flow of particles in a swirling flow. The first part consists of an invicid flow solver to model to flow in the channel using a MacCormick finite difference scheme. The second part consists of a particle tracking code to model the motion of particles in the flow produced by part one. The simulation was run on the 115x30 computational domain which simulates a constant radius channel with a choked exit. For the work shown here, it is assumed that the system is coupled to a NERVA class nuclear rocket with a nominal thrust of 300,000 N, a chamber temperature of 2500K, and a chamber pressure of 29 atm.

The type of swirl profile produced by the fixed vane swirler is entirely controlled by the designer. Initial studies focused on swirlers which produce solid body rotation profiles, i.e.

$$u_\theta = \Omega r$$

In general, there are five parameters which control the system's efficiency: the chamber length, the particle density, the particle radius, the skimming ratio*, and the flow rotation rate. However, in the effort to identify the system's most critical parameters, several of these parameters have been combined or eliminated. First of all, it has been noted that there is a linear relationship between the skimming ratio and a modified version of the system efficiency. In particular, if one defines a linear efficiency, η', with the following (implicit) relationship:

$$\eta = 1 - \sqrt{1 - \eta'}$$

The following equation is found to be accurate to within 10% under all conditions simulated:

$$\eta' = \eta_o' + \left(1 - \eta_o'\right)s_r$$

Where η'_o is the linear efficiency for a skimming ratio of zero. The result of this relationship is that this equation and a table of values replaces what would otherwise be pages of graphs based on simulated computational data.

The other major parameter which has been identified is a dimensionless frequency, v, which is defined as the product of the rotation rate and the transit time of particles through the chamber. This parameter is of great interest to the designer, as it determine the relationship between the rotation rate and the length of the separation chamber. Figure 2 shows a plot of data

---

* Skimming ratio is a dimensionless measure of the portion of the flow "skimmed off" at the end of the separation chamber. Using the variables shown in figure 1, it is defined by the following equation:
$$s_r = \frac{R_o - R_s}{R_o}$$
The higher the skimming ratio, the more material is skimmed off and filtered.

from five different simulations plotted vs. ν. The interesting result is that data from a variety of runs collapses to a single curve so long as the size and density of the particles remain constant.
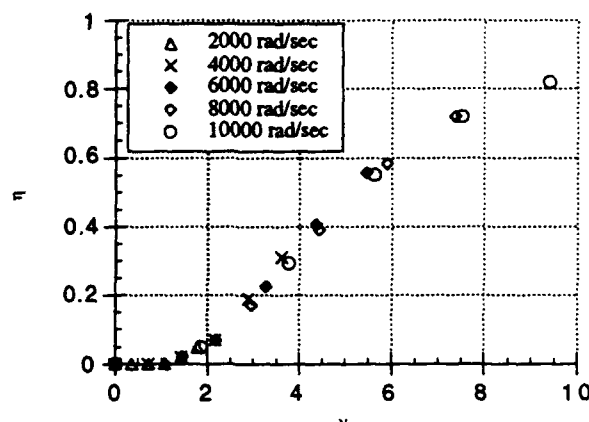

Figure 2: System Efficiency vs. ν for 40 μm graphite particles.

A series of plots like those in figure 2, but for particles of different sizes and densities, shows that there is a strong relationship between the system efficiency and the size and density of the particles in the flow. Based on this observation, it is possible to define another critical parameter, the centrifugal to drag force ratio, which is (approximately) given by the following expression:

$$\frac{F_c}{F_d} = \frac{2}{3} \frac{1}{C_d} \frac{a}{r} \frac{\rho_p}{\rho_f} \frac{u_\theta^2}{(r\Omega - u_\theta)^2}$$

Based on this expression, is it possible to define the critical velocity, v_c, as the value of u_θ which produces a force ratio of unity under a given set of conditions. The computational results show that this system operates most effectively when this critical velocities is equal to 1/3 to 2/3 of the flow's maximum tangential velocity. The reason for this correlation can be seen in the particle tracking plot below:
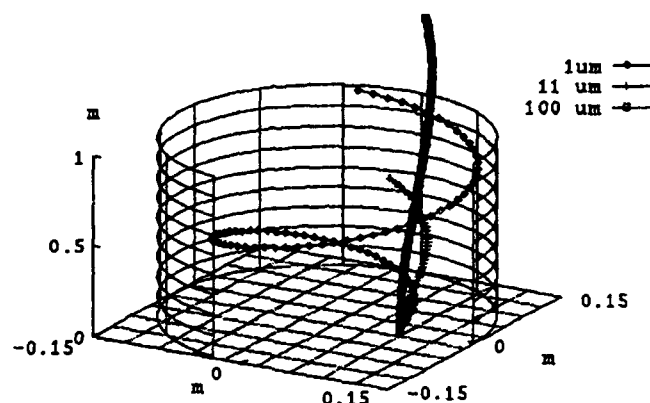

Figure 3: Particle Tracking Data for Particles with Different Critical Velocities

Figure 3 shows that particles with different critical velocities follow radically different paths in the separation chamber. The 1 μm graphite particle, which has a high critical velocity, remains coupled to the flow down most of the length of the channel and follows a long, spiral path towards the outside wall. The 100 μm particle, on the other hand, has a low critical velocity and uncouples from the flow very quickly. As a result, it travels directly down the channel, ignoring

the influence of the fluid all together. Neither particle moves to the outside of the flow in a particularly efficient manner. In the first case, although the particle is quickly accelerated to a high tangential velocity, drag forces dominate its motion and prevent it from gaining too high a radial velocity. In the second case, the particle uncouples too quickly and practically never accelerates at all. As a result, the particles which are separated most efficiently are those with intermediate critical velocities, such that the particles remain coupled to the fluid long enough to reach a high tangential velocity, and then uncouple as they travel towards the outside of the channel.

To date, the work done on solid body rotation systems has identified three parameters which are of importance to the vortex separation process: the skimming ratio, the dimensionless frequency, v, and the critical velocity, v_c. The critical velocity is the most important of these parameters, as it determine the distribution (size and density) of the particles which are removed from the flow. The dimensionless frequency, v, is also of great interest to the designer, as it sets a lower limit on the channel length and rotation rate and can be used to carry out basic design trades on the system. Finally, the skimming ratio has a linear, and relatively weak, influence on the efficiency, but is important because it determines how much of the flow is "lost" to the filtering system.

In an actual system, constant angle swirlers would probably be of more interest than solid body rotation systems because they can achieve higher efficiencies at a given rate of swirl. Figure 4 shows an efficiency graph taken under conditions similar to those used for figure 2, but for 1 µm Uranium particles in a constant angle swirling flow.
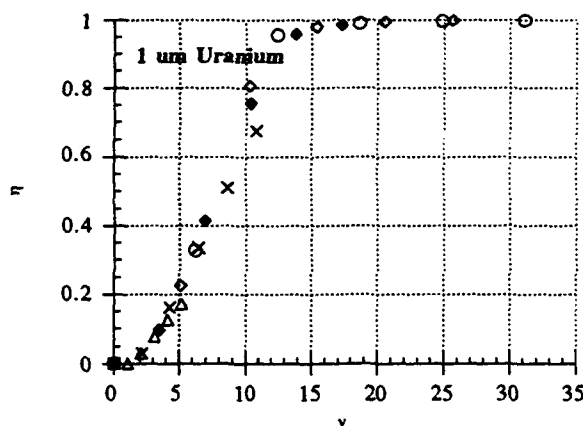

Figure 4: Constant Angle Swirl Results, 1 µm Uranium particles.

Note that the simulated data shows that constant angle systems can easily reach efficiencies greater than 95% under these simulated conditions.

In conclusion, vortex separation system shows some promise. While the lack of experimental data makes it impossible to draw final conclusions, it is clear that, at least for particles with the correct distribution of sizes and densities, this system can easily achieve efficiencies greater than 95%. The research done to date has characterized the governing parameters of this system to the extent that, once experimental particle distribution data is available, one can easily determine the practical value of vortex separation as a cleaning system for nuclear rocket plumes.

DROPLET COLLISION IN LIQUID PROPELLANT COMBUSTION

(AFOSR GRANT No. F49620-92-J-0355)

Principal Investigator: Chung K. Law

Princeton University
Princeton, NJ 08544

SUMMARY/OVERVIEW

Droplet collision is an essential process in spray combustion, intimately influencing the spray characteristics in the dense spray region. The present study aims to gain fundamental understanding on the mechanisms governing the observed phenomena of permanent coalescence, bouncing, and separation upon collision. Specific issues of interest include the extent of droplet deformation, the dynamics of the inter-droplet flow, the relative importance of the gas resistance force as compared to the collisional inertia, and the relevant rheological properties of the gases and liquids. Extensive experiments have been performed for various liquids, environment gases, and system pressures. Valuable insights have been gained regarding the specific mechanisms and factors controlling the various droplet collision outcomes.

TECHNICAL DISCUSSIONS

Our previous experimental results indicate that the collisional dynamics of hydrocarbon droplets can be significantly different from those of water droplets. Specifically, earlier literature results on water droplet collision at one atmosphere pressure showed that coalescence and separation are respectively favored for small and large Weber numbers (We), as shown in Fig.1a, in which B is the collision impact parameter. Our experimental observation, however, showed that the transition between coalescence and separation for hydrocarbon droplets at one atmosphere is far from being monotonic. Indeed, as shown in Fig. 1e, there are five collision outcome regimes, representing (I) coalescence with small droplet deformation, (II) bouncing, (III) coalescence with large droplet deformation, (IV) separation after near head-on coalescence, and (V) separation after off-center coalescence. Regimes (I) to (IV) occur for near head-on collisions with increasing We, while Regime (V) is characteristic of large values of We and B. Regime II is absent for water droplets such that Regimes I and III merge.

During the reporting period we continued our investigation, aiming to understand the fundamental mechanisms governing the different collision outcomes. We are especially interested in the transition between the five regimes identified above and the factors governing the qualitative difference in the collision behavior between water and hydrocarbon droplets. The above phenomena are expected to be inter-related such that they should be describable within a unified viewpoint.

The crucial factor responsible for the different behavior of water and hydrocarbon droplets is clearly the transition between Regimes I, II and III. Here, as the droplets collide, they become deformed due to the pressure buildup in the gas film between the droplets. This deformation absorbs the kinetic energy of collision, therefore reduces the ability for the inter-droplet gas film to be squeezed out in order to effect coalescence. Since the extent of deformation depends on the surface tension of the liquid, it is reasonable to expect a different behavior for water and hydrocarbons. Further, since displacement of the gas film depends on the density and viscosity of the gas, one may also expect that the collision outcome depend on the gas properties.

In the present investigation we have manipulated the effects of the gas and liquid properties by conducting experiments with both water and hydrocarbon droplets in environments of different gases (e.g. air, nitrogen, helium) and pressures (ranging from 0.6 to 12 atmospheres). The experimental results show that the collision behavior of water and hydrocarbon droplets are actually similar when the influence of the environment gas density is taken into account. A preliminary theoretical study relating the droplet collisional dynamics with the inter-droplet gas motion has also been performed. These results are presented in the following.

Figures 1a to 1c show the collision outcomes of water droplets with increasing pressure. It is seen that while Regime II does not exist at 1 atmosphere, as mentioned earlier, it is observed for off-center collisions when the pressure is increased to 1.68 atmosphere. When the pressure is further increased to 2.77 atmospheres, a fully-developed Regime II is observed in that droplet bouncing occurs for both off-center and head-on collisions. Thus with increasing gas pressure, and hence increasing gas density, bouncing is facilitated because of the increased amount of mass of the gas film that needs to be squeezed out. This result therefore demonstrates that there is no fundamental difference in the collision behavior of water and hydrocarbon droplets.

Figures 1d to 1f show the collision transition boundaries for tetradecane droplets with increasing pressure. Figures 1d and 1e basically correspond to Figs. 1b and 1c for the water droplets in that, with increasing pressure, a fully-developed Regime II is obtained. Figure 1f, however, shows an additional phenomenon, namely with further increase in pressure, Regime I occurs for such small values of We that it is basically unobservable. This further substantiates the importance of gas density in promoting droplet bouncing in Regime II.

By using helium as the environment gas, the same pressure dependence was observed. The effect, however, is weaker than that of air or nitrogen such that higher ranges of pressures are needed for the same phenomena. This is consistent with our understanding because helium has a lower density than nitrogen at the same pressure

We next consider the transition from Regime III to Regimes IV and V. Since the transition now occurs at higher We, and since coalescence is always possible, we expect that the dominance of the collision inertia should make the collision outcome less sensitive to the gas properties. Thus the important factors here should be the kinetic energy of collision and the surface tension of the liquid. The former promotes separation, through the extent of deformation, while the latter controls the resistance to separation. Since these two factors are collectively represented by We, the transition boundary should primarily depend on We. Figure 2 shows that this is indeed the case for the liquids tested.

A theory is also being formulated to describe the transition behavior related to Regimes I, II, and III. It is based on the observation that the droplets are already sufficiently deformed at the transition boundaries, and on the importance of the interaction time during collision. Preliminary results indeed indicate a non-monotonic behavior in the minimum distance of approach with increasing We. This theory will be further developed during the coming year.
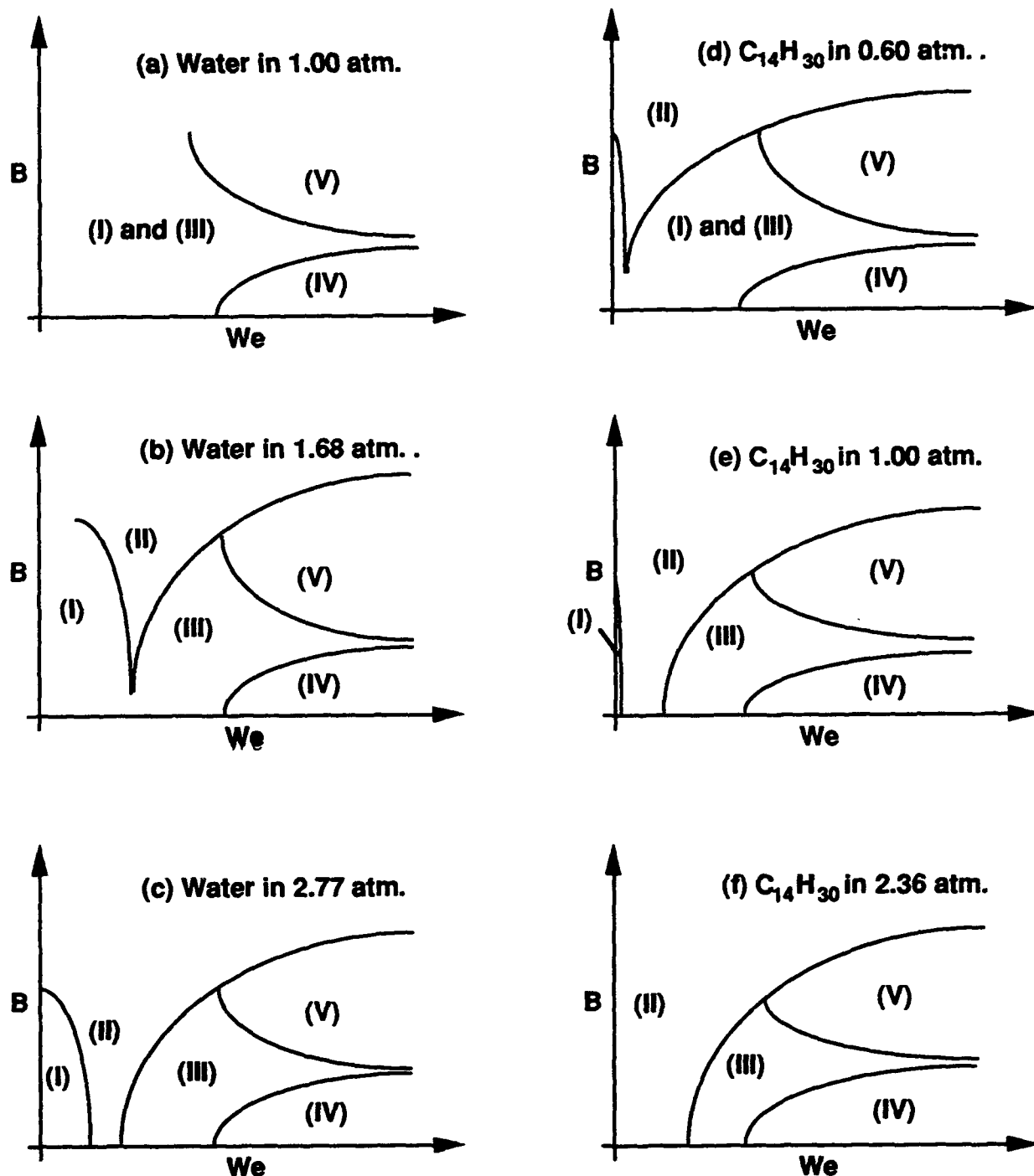
Figure 1 Water and Tetradecanec ($C_{14}H_{30}$) droplet collision outcomes at different pressures in nitrogen.

(I) Coalescence   (II) Bouncing   (III) Coalescence

(IV) Near head-on separation   (V) Off-center separation
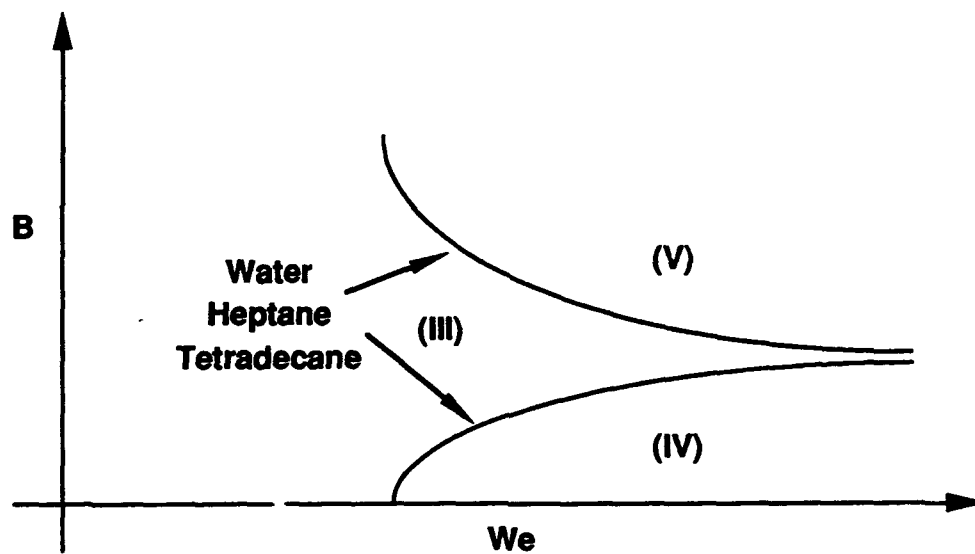
Figure 2. A schematic of the boundaries between regions (III) and (IV), (III) and (IV) for water and hydrocarbon droplet collisions at different pressures in different gases.

TITLE : DETERMINATION OF STRUCTURE, TEMPERATURE AND CONCENTRATION IN THE NEAR INJECTOR REGION OF IMPINGING JETS USING HOLOGRAPHIC TECHNIQUES

Principal Investigator : Prof. Dimos Poulikakos

Department of Mechanical Engineering
University of Illinois at Chicago
842 W. Taylor St.
Chicago, IL 60607-7022

SUMMARY/OVERVIEW

The purpose of this research is to study the fluid dynamics of high speed impinging jets using state-of-the-art single and double pulse holographic techniques that can provide information and evidence which more conventional techniques (such as LDV and PDPA) cannot provide. The effect of several factors on the atomization process will be examined including, to a certain extent, the presence of a high pressure and temperature ambient.

TECHNICAL DISCUSSION

During the first year of the research a major effort was expended toward : a) The design and fabrication of the experimental apparatus. b) The development and instrumentation of the optical setup for the holographic technique. With reference to the former, the experimental apparatus was designed, fabricated and tested. It can produce very reliably pairs of impinging jets of velocities up to 30 m/sec in the turbulent regime, jet diameters in the range 0.5 - 1.5 mm and impingement angles in the range 10° - 90°. The experimental apparatus was successfully tested in-situ. With reference to the latter, the intricate holographic technique was finalized after a tedious process through which various alternatives were considered for optimization purposes. Single pulse holograms showing three dimensional images of the structure of the impingement region both at the microscopic level and at the macroscopic level were recently fabricated successfully. Fabrication of additional holograms and image processing of the relevent data is currently in progress. Due to space limitations the details of the experimental apparatus and the intricate holographic techniques will not be discussed herein. Preliminary results will be discussed next.

Figure 1 shows photographs of holograms of the impingement region corresponding to an impingement angle $\theta = 50°$, jet velocity $V_j = 4.8$ m/s and jet diameter $d_j = 1.0$ mm. The working fluid is water. The abovementioned velocity is in the moderate velocity regime. Figure 1(a) shows an overview of the liquid sheet produced by the impingement. The liquid sheet is basically of the

closed rim type although near its bottom tip some disintegration of the edge is observed. Atomization is generated at the periphery of the tip. A wave structure is clearly visible on the surface of the sheet. Figure 1(b) shows the details of the flow structure near the sheet edge in the region identified as no. 1 in the earlier Figure 1(a). Liquid ligaments are pulled from the edge of the rim eventually breaking off. The shape of the edge of the sheet is reminiscent of interfaces in the presence of Kelvin-Helmholtz instabilities. Figure 1(c) is interesting, indeed. It focuses on the microscopic details of region no. 2 identified in Figure 1(a). It shows simultaneously the wave structure of the surface of the sheet as it meets the edge of the rim, as well as the ligament-droplet generation in the edge vicinity. Finally, Figure 1(d) shows the microscopic details of the flow structure near the disintegrating tip of the rim identified as region no. 3 in Figure 1(a). Of interest here is the presence of a surface wave pattern in the direction perpendicular to the main wave pattern of the surface leading to the tip disintegration.

The results of Figure 2 are for conditions identical to those of Figure 1 with the exception that the jet velocity is now considerably higher, $V_j = 10.9$ m/s. Figure 2(a) is an overview of the impingement region revealing the presence of an open, partially disintegrated sheet, with atomization occuring even on top of the impingement region. Of great interest is the presence of "holes" creating discontinuities on the partially disintegrated sheet the importance of which will be discussed later (in connection with Figure 2d). Details of the fluid dynamics of the impingement region are shown in Figure 2(b),(c),(d) which correspond to regions 1,2, and 3 on Figure 2(a), respectively. As shown in Figure 2b, liquid ligaments are separated backward, from the edge of the sheet leading to small droplets. The size of the droplets is visibly smaller than that observed in Figure 1. Some wave structure combined with rippling caused by aerodynamic effects is visible near the edge of the sheet. The details of Figure 2(c) (region 2 in Fig 2a) are similar to those of Figure 2(b). Again, the presence of much smaller droplets compared to those of Figure 1 is obvious. Figure 2(d) focuses on one of the holes (discontinuities) of the partially disintegrated sheet (region 3 in Figure 2a). This photograph is evidence of additional atomization occuring around the edge of the hole aiding the creation of the spray and contributing to the disappearance of the sheet at higher velocities.
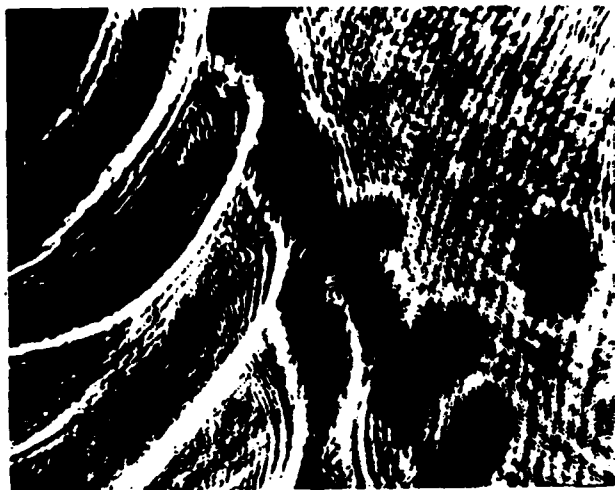
A thorough production of holographic data for single and double pulse cases (which will yield velocity data for the liquid elements) as well as image processing of the data is currently in progress.
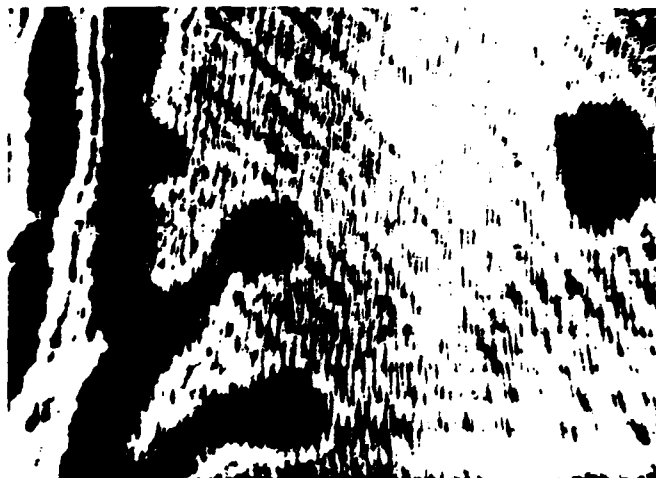
Figure 1 Photographs of hologram revealing the structure of the impingement region of two jets with impingement angle $\theta = 50°$, $V_{jet} = 4.8$ m/s, $d_{jet} = 1.0$ mm
(a) overview of the liquid sheet,   (b) microscopic detail of the region identified by no. 1 in Figure 1 (a),   (c) microscopic detail of the region identified by no.2 in Figure 1 (a),   (d) microscopic detail of the region identified by no. 3 in Figure 1 (a).
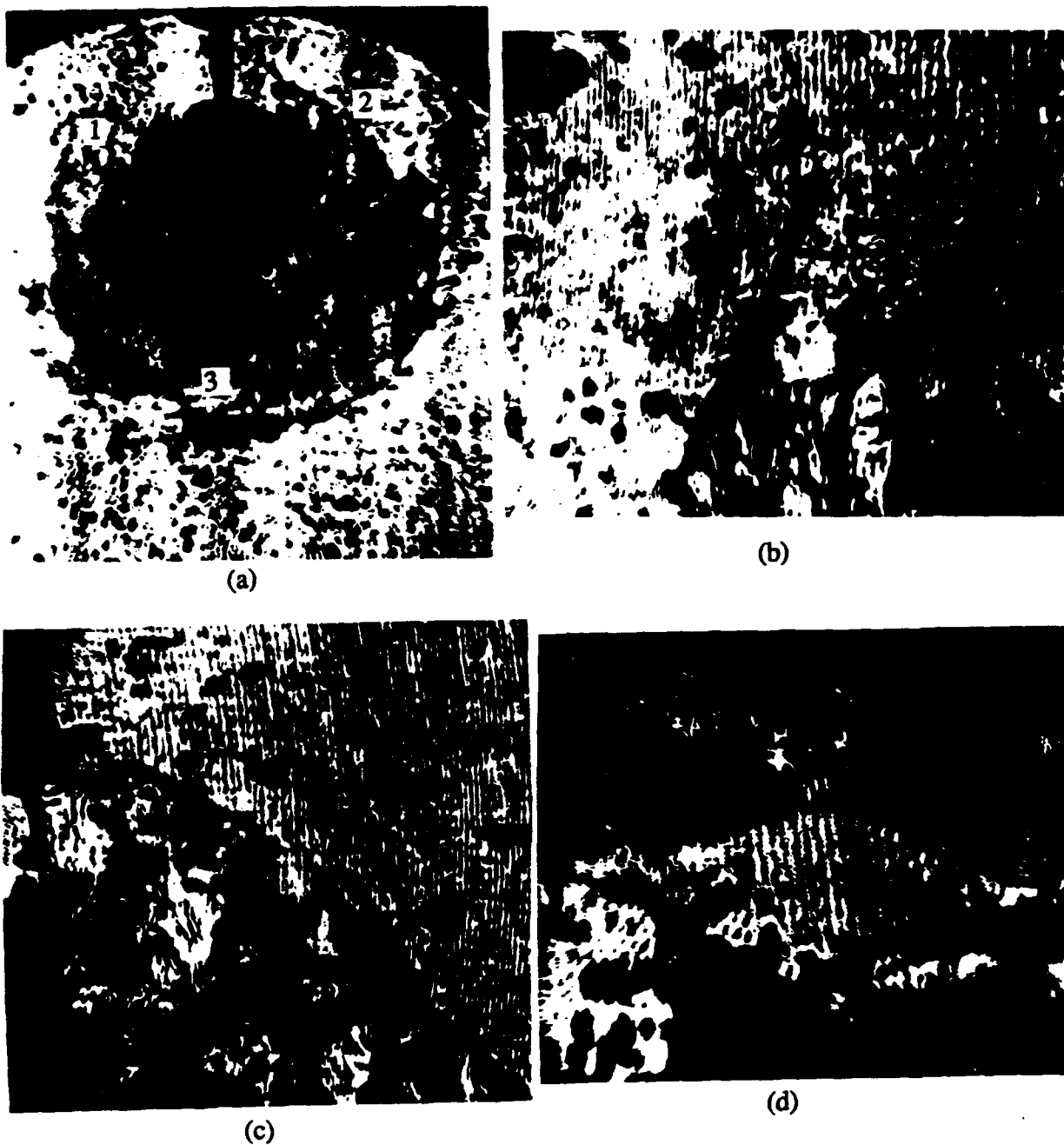
Figure 2 Photographs of hologram revealing the structure of the impingement region of two jets with impingement angle $\theta = 50°$, $V_{jet} = 10.9$ m/s, $d_{jet} = 1.0$ mm
(a) overview of the impingement region, (b) microscopic detail of the region identified by no. 1 in Figure 2 (a), (c) microscopic detail of the region identified by no.2 in Figure 2 (a), (d) microscopic detail of the region identified by no. 3 in Figure 2 (a).

RECOVERY OF FROZEN FLOW LOSSES IN ARCJETS

AFOSR Grant No. 91-0318

Principal Investigator: V. V. Subramaniam

Department of Mechanical Engineering
The Ohio State University
206 West 18th Avenue
Columbus, Ohio 43210

SUMMARY/OVERVIEW:

The performance of arcjet thrusters operating on molecular propellants such as ammonia (NH_3) or hydrazine (H_4N_2) is limited by frozen flow losses. A significant fraction of the input electrical energy into the device can be lost in various internal modes of the propellant molecules (vibration, electronic excitation, dissociation, and ionization). These modes take precious energy away from the directed kinetic energy of translational motion of the molecules which is required to generate useful thrust. Scale-up of existing designs to higher powers requires a fundamental understanding of the various mechanisms of frozen flow losses, and the ability to accurately quantify them. This is our primary objective. Additionally, injection of simple monatomic species into the propellant stream to V-T (vibration-translation) relax the gas is being explored. This has the potential to extend the present limits on specific impulse for the ammonia and hydrazine arcjets.

TECHNICAL DISCUSSION:

The arcjet thruster is one in a class of devices known as electrothermal thrusters. Electrothermal thrusters derive their thrust by conversion of electrical energy (transmitted by a current on the order of a hundred amperes) into directed kinetic energy. This is achieved primarily by ohmic heating of the propellant, followed by expansion through a nozzle. The typical arcjet geometry consists of a plenum (subsonic flow), a constrictor (subsonic or sonic flow), and a diverging nozzle (supersonic flow). The propellant (typically hydrogen, ammonia, or hydrazine) is introduced via injection ports in a boron nitride backplate with a swirling (azimuthal) component of velocity. This swirl is thought to be required to stabilize arcs operating above atmospheric pressure. The arc itself consists of a region of high temperature gas confined to dimensions smaller than the constrictor diameter, but then expands to attach downstream on the nozzle walls. Despite the apparent simplicity of the device and its operation, current understanding of the processes of mass, momentum, energy, and species transport in such flows is poor. It is also not clear whether a rational basis exists for the present geometries of the 1 KW and 30 KW arcjet thrusters.

The nozzle region of the arcjet serves essentially as an energy conversion device to convert the input electrical energy into directed kinetic energy or thrust. The gas in the nozzle region undergoes a rapid expansion wherein the translational temperature decreases rapidly in the flow direction. While the translational temperature decreases in real flows however, internal processes such as vibrational and electronic energy transfer require times much longer than the characteristic flow time in order to equilibrate. Therefore, a substantial portion of the input electrical energy (30%-50% by simple estimates) remains "frozen" in these internal modes. This has dramatic implications for performance characteristics, and will influence the choice of propellant for a given mission. The focus of this proposed research is to (1) utilize existing and our own on-going state-resolved measurements of chemical rates in order to accurately calculate the amount of frozen flow losses in ammonia and nitrogen arcjets, and to (2) explore the possibility of reducing these losses either by pre-mixing a fast VT (vibration-translation) relaxing monatomic gas (such as He, Ne, Ar, etc.) in the propellant stream, or by injecting into the downstream nozzle section. In these respects, the present work differs from other on-going work[1-3].

Frozen flow losses in the nozzle region are due to vibrational, rotational, and electronic non-equilibrium. This type of non-equilibrium is not unique to arcjets. Such high speed non-equilibrium flows are common in the

study of various gas dynamic lasers[4]. Extensive experimental and numerical work has been performed at The Ohio State University[5-9]. A distinct feature of the arcjet however, is the presence of the arc in the plenum, constrictor, and nozzle regions. This arc is confined to only some regions of the flow and therefore, necessitates the inclusion of charged particles in the simulation of these regions. By contrast, the cooler regions of the flow are free of charged particles. This means that the chemical kinetics together with finite rate ionization and recombination will render the numerical solution stiff. Consequently, a 2-D, axisymmetric (but with swirl), viscous, cold-flow (no reactions) model of the arcjet fluid mechanics was developed[9]. This is an important step before including multiple species (electrons, ions, atoms, and molecules), multiple temperatures, and electromagnetics, but without including vibrational and electronic non-equilibrium[8]. This pathological case is useful for model verification, and to ensure that boundary conditions are adequately satisfied. A 2-D axisymmetric model with swirl, including the latter effects is currently being developed and is near completion. Finally, the full chemical kinetics and state-resolved molecular energy transfer kinetics will be incorporated in a fully 3-D model.

The numerical methods for highly non-equilibrium high speed reacting *internal* flows is not by any means trivial. Although the numerical techniques of MacCormack[10-12] and Beam and Warming[13] are well developed for supersonic *external* compressible flows, the incorporation of finite rate kinetics and the problem of *internal* flow complicates the schemes substantially. Stringent demands must therefore be placed on computational speed, stability, and accuracy especially if a 3-D simulation is the ultimate goal. The chosen numerical scheme known as the Linear Block Implicit (LBI) method first developed by Briley and McDonald[14] shows tremendous promise. We have shown that this method scales extremely well from quasi 1-D to 2-D[8,9]. This method also shows tremendous promise for 3-D simulations of supersonic, reacting, internal flows.The LBI scheme also scales extremely well on vector machines, with the size of the blocks in the resulting block matrix equations arising from the discretization. It is therefore ideally suited to complex multi-dimensional flows with many species, and state-resolved kinetics describing the evolution of the respective species populations.

We have identified certain key parameters in the arcjet geometry that can influence its performance. These are the design mass flow rate, the distance from the inlet plenum to the beginning of the converging section, and the ratio of the inlet area to the throat area. These critical quantities have been identified on the basis of cold-flow simulations, and are expected to be even more critical for the real gas flow. Notable are the following differences between the two geometries: (1) The inlet area ratio (defined as the inlet channel cross sectional area at the location of the propellant injectors divided by the throat area) for the 30 KW arcjet is much smaller than that for the 1 KW arcjet (12 versus 86), (2) the cathode tip extends much farther into the constrictor for the 1 KW geometry than for the 30 KW geometry, and (3) the exit area ratio (defined as the cross sectional area at the exit plane divided by the throat area) is significantly larger for the 1 KW case than for the 30 KW case (171 versus 25). The reason for the significance of these parameters is related to the issue of whether or not the injected swirl survives through the constrictor. This can have important ramifications for arc stability as well as presence of swirl at the exit plane.

As an illustration, we consider tangential swirl injectors which introduce a maximum non-dimensional swirl velocity of 0.1 (non-dimensionalized with respect to the frozen speed of sound at the reservoir temperature). Contours of swirl are shown in Fig. 1 (for the 30 KW geometry) and Fig. 2 (for the 30 KW geometry with a **shorter** plenum) for a mass flow rate of 17 mg/s. As can be seen from these figures, the swirl persists and is **enhanced** upon passing through the converging section. The mass flow rate (Reynold's number) at which this occurs is important. If the mass flow rate (Reynold's number) were higher, the injected swirl would decay before reaching the constrictor. When the same velocity profile but with a maximum swirl of 0.2 is injected into the 1 KW geometry, the swirl is seen to decay but persist so that the presence of swirl in the constrictor is negligible (see Figs. 3). Note that in both geometries the swirl decays through the plenum, and increases in the converging section. In the 30 KW case, this increase leads to a swirl above that injected initially, whereas in the 1 KW case this increase leads nowhere near the initial value.

These results may best be understood by considering the principle of conservation of angular momentum. In brief, this principle states that the influx of angular momentum into a control volume (cv) is equal to the efflux of angular momentum exiting the cv plus the torque due to viscous forces. The torque due to viscous forces is in turn composed of two quantities; first, the torque due to shear stresses within the cv (integrated over the cv), and second, the torque due to the shear stresses at the walls. At low mass flow rates, the shear stress at the anode and cathode surfaces are insufficient to overcome the influx of angular momentum due to the injected swirl. Consequently, the swirl survives until the converging section. In the converging section, the swirl gets enhanced due to the decreasing cross sectional area provided the torque from the viscous forces is small here. This is why this

effect is most noticeable at low mass flow rates or low Re. At the higher mass flow rates or Re, the wall shear (and hence torque) becomes large enough to counter the effect of area variation. In the 30 KW geometry, the streamwise component of the inlet velocity is larger than in the case of the 1 KW geometry due to the respective differences in inlet area ratios. Consequently, the influx of angular momentum is small in the 1 KW geometry. It is clear therefore that the design mass flow rate, inlet area ratio, length of the plenum from inlet to the beginning of the converging section, and length of the converging section are critical design parameters.

As part of any good computational effort, there must be a parallel theoretical component. This is to ensure the accuracy and correctness of the numerical model, as well as to provide physical insight into any numerically generated solutions. Although analytical models of the arcjet flow with chemistry are impossible, simple models with *judicious* approximations can simulate and explain *some* of the phenomena in the arcjet[2,3].

REFERENCES:

(1) R. P. Rhodes, and D. Keefer, "Numerical Modeling of an Arcjet Thruster", paper AIAA-90-2614, presented at the 21st International Electric Propulsion Conference, July 18-20, 1990, Orlando, Florida.

(2) B. Glocker, H. O. Schrade, and P. C. Sleziona, "Numerical Prediction of Arcjet Performance", paper AIAA-90-2612, presented at the 21st International Electric Propulsion Conference, July 18-20, 1990, Orlando, Florida.

(3) M. Auweter-Kurtz, H. L. Kurtz, H. O. Schrade, and P. C. Sleziona, **J. Propulsion & Power**, Vol. 5, No. 1, Jan.-Feb. 1989.

(4) J. D. Anderson, Jr., *Gasdynamic Lasers: An introduction*, Academic Press, New York, 1976.

(5) W. Urban, J. X. Lin, V. V. Subramaniam, M. Havenith, and J. W. Rich, **Chem. Phys. 130**, p. 389, 1989.

(6) C. Flament, T. George, K. A. Meister, J. C. Tufts, J. W. Rich, V. V. Subramaniam, J. P. Martin, B. Piar, and M. Y. Perrin, **Chem. Phys. 163**, p. 241, 1992.

(7) A. Chiroux de Gavelle de Roany, C. Flament, J. W. Rich, V. V. Subramaniam, and W. R. Warren, **AIAA J.**, Vol. 31, No. 1, p. 119, 1993.

(8) V. Babu, and V. V. Subramaniam, "Quasi 1-D Nozzle Flow Solutions with Strong Vibrational Non-equilibrium", submitted to **AIAA J.** (under review).

(9) V. Babu, and V. V. Subramaniam, "Numerical Solutions of Viscous, Internal, Supersonic Flows", submitted to **AIAA J.** (under review).

(10) R. W. MacCormack, "The Effect of Viscosity in Hypervelocity Impact Cratering", paper AIAA-69-354, presented at the AIAA Hypervelocity Impact Conference, April 30-May 2, 1969, Cincinnati, Ohio.

(11) R. W. MacCormack, "A Numerical Method for Solving the Equations of Compressible Viscous Flow", paper AIAA-81-0110, presented at the AIAA 19th Aerospace Sciences Meeting, January 12-15, 1981, St. Louis, Missouri.

(12) R. W. MacCormack, Lecture Notes on "Numerical Methods for Compressible Viscous Flow", presented during a short course on Advances in Computational Fluid Dynamics, December 6-10, 1982, The University of Tennessee Space Institute, Tullahoma, Tennessee.

(13) R. M. Beam, and R. F. Warming, "An Implicit Factored Scheme for the Compressible Navier-Stokes Equations II: The Numerical ODE Connection", paper AIAA-79-1446, presented at the AIAA 4th Computational Fluid Dynamics Conference, July 23-24, 1979, Williamsburg, Virginia.

(14) W. R. Briley, and H. McDonald, "Solution of the Multidimensional Compressible Navier-Stokes Equations by a Generalized Implicit Method", **J. Comp. Phys. 24**, pp. 372-397, 1977.
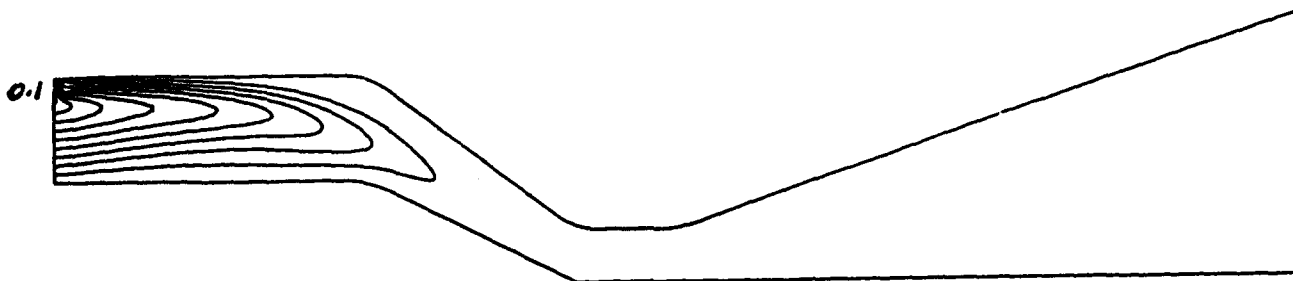
Fig. 1: Non-dimensional swirl contours for the 30 KW geometry. Note that the injected swirl is overcome by viscous effects and fails to survive into the converging section or the constrictor.
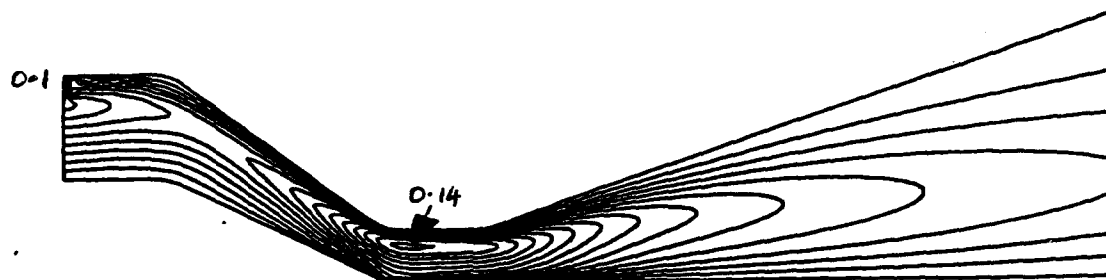

Fig. 2: Non-dimensional swirl contours for the 30 KW geometry with a shorter plenum, showing pockets of high swirl at the injection point, as well as in the constrictor. The maximum swirl at the constrictor is 0.14 versus 0.1 at the inlet, indicating enhancement.
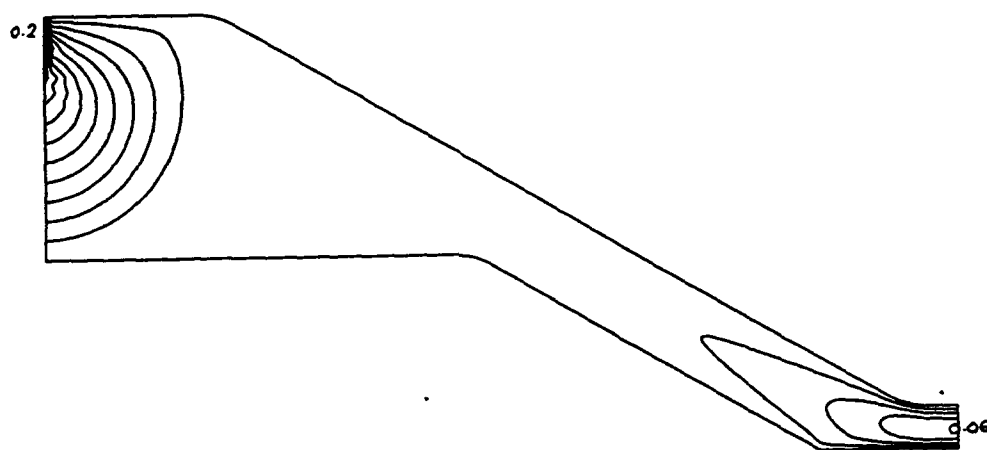

Fig. 3: Non-dimensional swirl contours for the 1 KW geometry, showing pockets of high swirl at the injection point, as well as in the constrictor. Note that the maximum swirl at the constrictor is 0.06 versus 0.2 at the inlet indicating that although the swirl survives until the constrictor, it is not enhanced as in the 30 KW case.

AIRBREATHING COMBUSTION

Invitees

Dr Suresh P Aggarwal
Mechanical Engineering Dept
University of Illinois
   at Chicago
Chicago IL 60680
(312)996-2235

Dr Griffin Anderson
NASA Langley Research Center
M/S 168
Hampton VA 23665
(804)864-3772

Dr Scott Anderson
Department of Chemistry
State University of New York
Stony Brook NY 11794-3400
(516)632-7915

Dr K Annamalai
Mechanical Engineering Dept
Texas A&M University
College Station TX 77843-3123

Dr Kurt Annen
Aerodyne Research, Inc.
45 Manning Road
Manning Park Research Center
Billerica MA 01821-3976
(508)663-9500
FAX:663-4918

Dr Jad Batteh
Science Applications
International Corporation
1519 Johnson Ferry Rd #300
Marietta GA 30062
(404)973-8935
FAX:973-6971

Dr Simon Bauer
Department of Chemistry
Cornell University
Ithaca NY 14853-1301

Dr S L Baughcum
Boeing Company
P O Box 3999, MS 87-08
Seattle WA 98124
(206)965-0426
FAX:234-4543

Dr Howard Baum
National Institute of
Standards and Technology
Center for Fire Research
Gaithersburg MD 20899
(301)975-6668

Dr John Bdzil
Los Alamos National Laboratory
Los Alamos NM 87545

Dr H L Beach
NASA Langley Research Center
MS 168
Hampton VA 23665-5225
(804)864-3772
(804)864-2658

Dr Josette Bellan
Applied Technologies Section
Jet Propulsion Laboratory
4800 Oak Grove Drive
Pasadena CA 91109
(818)354-6959

Dr Michael Berman
AFOSR/NC
110 Duncan Avenue, Suite B115
Bolling AFB DC 20332-0001
(202)767-4963
DSN 297-4963

Dr Paul Bonczyk
United Technologies Research
  Center
Silver Lane
East Hartford CT 06108
(203)727-7162

Dr Gary Borman
University of Wisconsin
Engine Research Lab, ME Dept
1500 Johnson Drive, Rm 119 ERB
Madison WI 53706
(608)263-1616
FAX:262-6707

Dr Kevin Bowcutt
Rockwell International
Mail Code NA40
12214 Lakewood Boulevard
Downey CA 90241
(213)420-0317

Dr C T Bowman
Department of Mechanical
Engineering
Stanford University
Stanford CA 94305-3032
(415)723-1745
FAX:723-1748

Dr K N C Bray
University of Cambridge
Department of Engineering
Trumpington Street
Cambridge CB2 1PZ, England UK
0223 332744
0223 337733
FAX0223 332662

Dr Robert Breidenthal
Department of Aeronautics and
  Astronautics
University of Washington, FS10
Seattle WA 98195
(206)685-1098

Dr Kenneth Brezinsky
Department of Mechanical and
  Aerospace Engineering
Princeton University
Princeton NJ 08544-5263
(609)258-5225

Dr J E Broadwell
Graduate Aeronautical Labs
California Institute of
Technology
Pasadena CA 91125

Dr Garry Brown
Department of Mechanical and
    Aerospace Engineering
Princeton University
Princeton NJ 08544-5263
(609)258-6083

Dr R C Brown
Aerodyne Research, Inc.
45 Manning Road
Manning Park Research Center
Billerica MA 01821-3976
(508)663-9500
FAX:663-4918

Dr John D Buckmaster
Department of Aerospace
    Engineering
University of Illinois
Urbana IL 61801

Lt Col Larry Burggraf
AFOSR/NC
110 Duncan Avenue, Suite B115
Bolling AFB DC 20332-0001
(202)767-4960
DSN 297-4960
burggraf@afosr.af.mil

Dr Dennis Bushnell
NASA Langley Research Center
Mail Stop 168
Hampton VA 23665
(804)864-4546

Dr Ron Butler
WL/POSF
Building 490
1790 Loop Road, N
Wright-Patterson AFB OH 45433-7103

Dr T D Butler
Group T-3
Los Alamos National Laboratory
Los Alamos NM 87545
(505)667-4156

Dr H F Calcote
AeroChem Research Laboratories
    Inc.
P. O. Box 12
Princeton NJ 08542
(609)921-7070

Dr Graham V Candler
Department of Aerospace
    Engineering & Mechanics
University of Minnesota
Minneapolis MN 55455

Dr Brian Cantwell
Department of
     Mechanical Engineering
Stanford University
Stanford CA 94305-3032
(415)723-4825

Dr Tryfon Charalampopoulos
Mechanical Engineering Dept.
Louisiana State University
Baton Rouge LA 70803
(504)388-5792
(504)388-5799

Dr Lea D Chen
Mechanical Engineering Dept
University of Iowa
Iowa City IA 52242
(319)335-5674
FAX:335-5669
ldchen@icaen.uiowa.edu

Dr Norman Chigier
Department of Mechnanical
     Engineering
Carnegie-Mellon University
Pittsburgh PA 15213-3890
(412)578-2498

Dr Robert Childs
Nielsen Engineering and
     Research, Inc.
510 Clyde Avenue
Mountain View CA 94043-2287
(415)968-9457

Dr S Y Cho
Department of Mechanical and
     Aerospace Engineering
Princeton University
Princeton NJ 08544-5263

Dr M-S Chou
Building R1, Room 1044
TRW Space and Technology Group
One Space Park
Redondo Beach CA 90278
(213)535-4321

Mr R.W. Claus
NASA Lewis Research Center
21000 Brookpark Road
Cleveland OH 44135-3127
(216)433-5869

Mr Steven Clouser
Research and Technology Group
Naval Air Propulsion Center
Trenton NJ 08628
(609)896-5752
DSN 442-7752

Dr M B Colket
United Technologies Research
     Center
Silver Lane
East Hartford CT 06108
(203)727-7481

Mr Stephen Corda
Applied Physics Laboratory
Johns Hopkins University
Johns Hopkins Road
Laurel MD 20707-6099
(301)953-5000
Ext 4654

Dr S M Correa
General Electric - Corporate
Research and Development
P. O. Box 8
Schenectady NY 12301
(518)387-5853

Dr C Criner
Mach I, Inc
346 East Church Road
King of Prussia PA 19406
(803)292-3345

Dr Clayton Crowe
Department of Mechanical
    Engineering
Washington State University
Pullman WA 99164-2920
(509)335-3214

Dr E T Curran
WL/PO
Building 18
1921 Sixth Street, Suite 5
Wright-Patterson AFB OH 45433-7650
(513)255-2520
DSN 785-2520
FAX:476-4657

Dr Eli Dabora
Mechanical Engineering Dept
Universit of Connecticut
Box U-139 ME
Storrs CT 06268
(203)486-2415
(203)486-2189

Dr Werner Dahm
Department of Aerospace
    Engineering
The University of Michigan
Ann Arbor MI 48109-2140
(313)764-4318
FAX:763-0578

Dr Sanford M Dash
Science Applications
International Corporation
501 Office Ctr Dr, Suite 420
Fort Washington PA 19034-3211
(215)542-1200
FAX:542-8567

Dr Ron Davis
Chemical Science and Techn Lab
Building 221, Room B312
National Inst of Stds & Tech
Gaithersburg MD 20899

Lt Col Larry Davis
AFOSR/TEO
Andrews AFB DC 20334
(301)981-7882
DSN 858-7882

Dr Pablo G Debenedetti
Department of Chemical
    Engineering
Princeton University
Princeton NJ 08544-5263
(609)258-5480
PDEBENE@pucc.princeton.edu

Dr R W Dibble
Department of Mechanical Eng
6159 Etcheverry Hall
University of California
Berkeley CA 94720
(415)642-4901
FAX:642-6163

Mr Lee Dodge
Southwest Research Institute
P O Drawer 28510
San Antonio TX 78284
(512)684-5111
Ext 3251

Capt Randy Drabczuk
WL/MNSH
Eglin AFB FL 32542-5434
DSN 872-0360
(904)882-0360

Dr Frederick Dryer
Department of Mechanical and
    Aerospace Engineering
Princeton University
Princeton NJ 08544-5263
(609)258-5206

Dr George Deiwert
NASA Ames Research Center
MS 230-2
Moffett Field CA 94035
(415)604-6198

Dr Paul Dimotakis
Graduate Aeronautical Labs
California Institute of
    Technology
Pasadena CA 91125
(818)356-4456
pxd@hydra0.caltech.edu

Dr David Dolling
Department of Aerospace Engrg
    and Engineering Mechanics
University of Texas at Austin
Austin TX 78712
(512)471-4470
(512)471-7593

Dr Michael Drake
Physical Chemistry Department
General Motors Research Labs
Twelve Mile and Mound Roads
Warren MI 48090-9055

Dr C Dutton
Department of Mechanical and
    Industrial Engineering
University of Illinois
Urbana IL 61801

Dr Harry Dwyer
Department of Mechanical
   Engineering
University of California
Davis CA 95616

Dr Raymond Edelman
WC 70
Rocketdyne
6633 Canoga Avenue
Canoga Park CA 91304
(805)371-7196

Dr J T Edwards
WL/POSF
Building 490
1790 Loop Road, N
Wright-Patterson AFB OH 45433-7103
(513)476-7393
DSN 986-7393
FAX:255-1125

Ms Charlotte Eigel
WL/POSF
Building 490
1790 Loop Road, N
Wright-Patterson AFB OH 45433-7103
(513)255-5106
DSN 785-5106

Dr Said Elghobashi
Department of Mechanical
   Engineering
University of California
Irvine CA 92717
(714)856-6002

Dr Phillip Emmerman
Harry Diamond Laboratories
Attn. SLCHD-ST-RD
2800 Powder Mill Road
Adelphi MD 20783-1197
(301)394-3000

Mr Peter Erbland
National Aero-Space Plane JPO
ASC/NAF, Building 52
2475 K Street, Suite 3
Wright-Patterson AFB OH 45433-7644
(513)255-9757
DSN 785-9757

Dr K C Ernst
Pratt and Whitney Aircraft
   Group
Government Products Division
West Palm Beach FL 33402

Mr John Facey
Code RP
NASA
400 Maryland Avenue, SW
Washington DC 20546
(202)453-2854

Dr G M Faeth
Department of Aerospace
   Engineering
University of Michigan
Ann Arbor MI 48109-2140
(313)764-7202
FAX:764-0578

Dr Francis Fendell
TRW Space and Technology Group
Building R1, Room 1022
One Space Park
Redondo Beach CA 90278
(213)812-0327

Dr Michael Frenklach
202 Academic Projects Building
The Pennsylvania State
   University
University Park PA 16802
(814)865-4392

Mr Jack Fultz
WL/POPR
Wright-Patterson AFB OH 45433-6563
(513)255-2175
DSN 785-2175

Dr David Fyfe
Laboratory for Computational
   Physics & Fluid Dynamics
Naval Research Laboratory
Washington DC 20375-5344
(202)767-6583
DSN 297-6583

Dr Alon Gany
Department of Aeronautical Eng
Technion-Israel Institute of
   Technology
32000 Haifa, ISRAEL
04-292308

Dr Ahmed Ghoniem
Department of Mechanical
   Engineering
MIT
Cambridge MA 02139
(617)253-2295
FAX:253-5981

Mr R Giffen
General Electric Company
Aircraft Engine Group
Neumann Way
Cincinnati OH 45215

Dr P Givi
Department of Mechanical and
   Aerospace Engineering
State University of New York
Buffalo NY 14260

Dr Irvin Glassman
Department of Mechanical and
   Aerospace Engineering
Princeton University
Princeton NJ 08544-5263
(609)258-5199
(813)442-1118

Dr A D Gosman
Department of Mechanical Engrg
Imperial College of Science
   and Technology
London WS7 2BX UK

Dr Frederick Gouldin
Department of Mechanical and
   Aerospace Engineering
Cornell University
Ithaca NY 14853-1301
(607)255-5280

Dr F Grinstein
Laboratory for Computational
   Physics & Fluid Dynamics
Naval Research Laboratory
Washington DC 20375-5344

Dr Ephraim Gutmark
Research Department
Code 3892
Naval Air Warfare Center
China Lake CA 93555-6001
(619)939-3745
DSN 437-3745

Dr Howard Hanley
Chem & Sci Tech Lab
National Inst of Stds & Tech
325 Broadway
Boulder CO 80303-3328
(303)497-3320

Dr Robert Hansen
Office of Naval Research
Code 1215
800 North Quincy Street
Arlington VA 22217-5000
(202)696-4715

Dr Stephen Harris
Physical Chemistry Department
General Motors Research Labs
30500 Mound Road
Warren MI 48090-9055
(313)986-1305

Dr S Henbest
Aeronautical Research Labs
506 Lorimer St, Fishermen's Bn
Box 4331, P O
Melbourne, Victoria AUSTRALIA 3207

Dr James Hermanson
Propulsion Technology
United Technologies Research
   Center
East Hartford CT 06108

Mr Norman Hirsch
WL/POPR
Wright-Patterson AFB OH 45433-6563
(513)255-2175
DSN 785-2175

Dr David Hofeldt
125 Mechanical Engineering
111 Church Street, S E
University of Minnesota
Minneapolis MN 55455
(612)625-2045

Mr Robert Holland
United Technologies Chemical
    Systems Division
P O Box 49028
San Jose CA 95161-9028
(408)224-7656

Dr Hans G Hornung
Graduate Aeronautical Labs
California Institute of
    Technology
Pasadena CA 91125
(818)356-4551

Dr Lawrence Hunter
Applied Physics Laboratory
Johns Hopkins University
Johns Hopkins Road
Laurel MD 20707-6099
(301)953-5000
Ext. 7406

Dr M Y Hussain
ICASE, Mail Stop 132C
NASA Langley Research Center
Hampton VA 23665
(804)864-2175

Dr A K M F Hussain
Department of Mechanical
    Engineering
University of Houston
Houston TX 77004
(713)749-4444

Dr Essam A Ibrahim
Department of Mechanical
    Engineering
Tuskegee University
Tuskegee AL 36088
(205)727-8974

Dr T A Jackson
WL/POSF
Building 490
1790 Loop Road, N
Wright-Patterson AFB OH 45433-7103
(513)255-6462
DSN 785-6462
FAX:255-1125

Mr Gordon Jensen
United Technologies Chemical
    Systems Division
P O Box 49028
San Jose CA 95161-9028
(408)365-5552

Dr Sheridan Johnston
Combustion Sciences
Sandia National Laboratories
Livermore CA 94551-0969
(510)294-2138

Dr W-H Jou
M/S 7K-06
P. O. Box 3707
Seattle WA 98124-2207
(206)865-6102

Dr K Kailasanath
Code 6410, LCP&FD
US Naval Research Laboratory
Washington DC 20375-5344
(202)767-2402
FAX:767-4798
KAILASANATH@lcp.nrl.navy.mil

Dr Ann Karagozian
Mechanical, Aerospace and
Nuclear Engineering Department
University of California, LA
Los Angeles CA 90024
(213)825-5653

Dr Laurence R Keefe
Nielsen Engineering and
    Research, Inc.
510 Clyde Avenue
Mountain View CA 94043-2287
(415)968-9457
FAX:968-1410

Dr Arnold Kelly
Department of Mechanical and
    Aerospace Engineering
Princeton University
Princeton NJ 08544-5263
(609)258-5221

Dr John Kelly
Altex Technologies Corporation
650 Nuttman Road
Suite 114
Santa Clara CA 95054
(408)980-8610

Dr Lawrence A Kennedy
Department of Mechanical
    Engineering
The Ohio State University
Columbus OH 43210-1107
(614)292-5782

Dr Ian Kennedy
Mechanical Engineering Dept
University of California,
    Davis
Davis CA 95616
(916)752-2796
IMKENNEDY@poppy.engr.ucdavis.edu

Dr James Kezerle
Gas Research Institute
8600 West Bryn Mawr Avenue
Chicago IL 60631
(312)399-8331

Dr Merrill K King
NASA Headquarters
Code SNB
300 E Street, SW
Washington DC 20546
(202)358-0818

Dr Galen King
Department of Mechanical
    Engineering
Purdue University
West Lafayette IN 47907
(317)494-2713

Mr R Kirby
Garrett Turbine Engine Company
111 South 34th Street
P. O. Box 5217
Phoenix 85010

Dr William H Kirchhoff
Division of Chemical Sciences
Office of Basic Energy Science
Department of Energy
Washington DC 20585

Dr Charles Kolb
Aerodyne Research, Inc.
45 Manning Road
Manning Park Research Center
Billerica MA 01821-3976
(508)663-9500
FAX:663-4918

Dr Wolfgang Kollmann
Mechanical Engineering Dept
University of California,
   Davis
Davis CA 95616
(916)752-1452

Mr William E Koop
HQ AFMC/STTA
4375 Chidlaw Road, Suite 6
Wright-Patterson AFB OH 45433-5006

Dr George Kosaly
Department of Mechanical
   Engineering
University of Washington
Seattle WA 98195
(206)543-6933
FAX:685-8047

Dr C R Krishna
Department of Nuclear Energy
Brookhaven National Laboratory
Upton NY 11973

Mr David Kruczynski
Attn SLCBR-IBA
Interior Ballistics Division
Army Research Laboratory
Aberdeen Proving Gnd MD 21005-5066
(410)278-6202
DSN 298-6202

Dr Kenneth Kuo
Department of Mechanical
   Engineering
Pennsylvania State University
University Park PA 16802
(814)865-6741
FAX:863-3203

Dr Samuel C Lambert
WL/CA-M
101 West Eglin Boulevard
Suite 101
Eglin AFB FL 32542-6810
(904)882-3002
DSN 872-3002
FAX:882-8689

Dr Marshall Lapp
High Temperature Interfaces
    Division
Sandia National Laboratories
Livermore CA 94551-0969
(510)294-2435

Dr John Larue
Department of Mechanical
    Engineering
University of California
Irvine CA 92717

Dr A Laufer
Office of Energy Research
U. S. Department of Energy
1000 Independence Avenue, N.W.
Washington DC 20585
(202)903-5820

Dr N M Laurendeau
Department of Mechanical
    Engineering
Purdue University
West Lafayette IN 47907
(317)494-2713

Dr Moshe Lavid
ML Energia, Inc.
P. O. Box 1468
Princeton NJ 08540
(609)799-7970

Dr C K Law
Department of Mechanical and
    Aerospace Engineering
Princeton University
Princeton NJ 08544-5263
(609)258-5271
FAX:258-6109

Dr Stan Lawton
McDonnell Douglas Research Lab
McDonnell Douglas Corporation
PO Box 516
St Louis MO 63166-0516
(314)233-2547

Dr J Carl Leader
McDonnell Douglas Research Lab
McDonnell Douglas Corporation
PO Box 516
St Louis MO 63166-0516
(314)232-4687

Dr C C Lee
Environmental Protection
    Agency
Cincinnati OH 45268
(513)569-7520

Dr Spiro Lekoudis
Office of Naval Research
Mechanics Division, Code 432
800 North Quincy Street
Arlington VA 22217-5000
(703)696-4406

Dr Anthony Leonard
Graduate Aeronautical Labs
California Institute of
    Technology
Pasadena CA 91125
(818)356-4465

Dr R S Levine
National Institute of
Standards and Technology
Center for Fire Research
Gaithersburg MD 20899
(301)921-3845

Dr Erwin Lezberg
NASA Lewis Research Center
21000 Brookpark Road
Cleveland OH 44135-3127
(216)433-5884

Dr Chiping Li
Laboratory for Computational
    Physics & Fluid Dynamics
Naval Research Laboratory
Washington DC 20375-5344
(202)767-3254
FAX:767-4798
LI@lcp.nrl.navy.mil

Dr Paul Libby
Center for Energy and
    Combustion Research, 0411
University of California
La Jolla CA 92093-0411
(619)534-3168

Dr Wilbert Lick
Department of Mechanical and
    Environmental Engineering
University of California
Santa Barbara CA 93106

Dr Hans Liepmann
Graduat Aeronautical Labs
California Institute of
    Technology
Pasadena CA 91125
(818)356-4535

Dr Marshall Long
Department of Mechanical
    Engineering
Yale University
New Haven CT 06520
(203)432-4229

Dr F E Lytle
Department of Chemistry
Purdue University
West Lafayette IN 47907
(317)494-5261

Dr Andrej Macek
National Institute of
Standards and Technology
Physics Building, B-312
Gaithersburg MD 20899
(301)975-2610

Dr James Madson
McDonnell Douglas Research Lab
McDonnell Douglas Corporation
PO Box 516
St Louis MO 63166-0516

Dr Edward Mahefkey
WL/POOC-5
Wright-Patterson AFB OH 45433-6563
(513)255-6241
DSN 785-6241

Mr Nick Makris
SA-ALC/SFT
Kelly AFB TX 78241-5000
AV945-8212
FAX:945-9964

Dr Oscar Manley
US Department of Energy
Office of Energy Research
1000 Independence Avenue, SW
Washington DC 20585
(202)353-5822

Dr David Mann
U. S. Army Research Office
Engineering Sciences Division
P. O. Box 12211
Research Triangle Pk NC 27709-2211
(919)549-4249
DSN 832-4249
FAX:549-4310
david@aro-emh1.army.mil

Dr Nagi Mansour
Computational Fluid Mechanics
    Branch, RFT 202A-1
NASA Ames Research Center
Moffett Field CA 94035
(415)604-6420

Dr Frank Marble
Engrg. and Appl. Sci. Dept.
California Institute of
    Technology
Pasadena CA 91125
(818)356-4784

Dr John Marek
NASA Lewis Research Center
21000 Brookpark Road
Cleveland OH 44135-3127

Dr Bruce Masson
PL/ARDF
Kirtland AFB NM 87117-6008
(505)844-0208
DSN 244-0208

Dr James McDonald
Code 6110
Naval Research Laboratory
Chemistry Division
Washington DC 20375-5342
(202)767-3340
DSN 297-3340

Dr D K McLaughlin
233 Hammond Building
Pennsylvania State University
University Park PA 16802
(814)865-2569

Dr James McMichael
AFOSR/NA
110 Duncan Avenue, Suite B115
Bolling AFB DC 20332-0001
(202)767-4936
DSN 297-4936
FAX:767-4988
mcmichael@afosr.af.mil

Dr Constantine M Megaridis
University of Illinois-Chicago
Mechanical Engineering Dept
842 West Taylor St, Box 4348
Chicago IL 60680
(312)996-3436
cmm@dino.me.uic.edu

Dr A M Mellor
Mech & Matls Eng Department
Station B, Box 6019
Vanderbilt University
Nashville TN 37235
(615)343-6214

Dr Lynn Melton
Programs in Chemistry
University of Texas, Dallas
P. O. Box 830688
Richardson TX 75083-0688
(214)690-2913
FAX:690-2925

Dr R Metcalfe
Department of Mechanical
    Engineering
University of Houston
Houston TX 77004
(713)749-2439

Maj Howard Meyer
AL/EQC
139 Barnes Drive
Suite 2
Tyndall AFB FL 32403-5319
(904)283-6038
DSN 523-6038
FAX:283-6090
MeyerH@AFCESA1.AF.MIL

Dr D L Mingori
Mechanical, Aerospace and
    Nuclear Engineering Dept
University of California
Los Angeles CA 90024
(213)825-1265

Dr Andrzej Miziolek
Ignition and Combustion Branch
Interior Ballistics Division
Army Research Laboratory
Aberdeen Proving Gnd MD 21005-5066
(410)278-6157
FAX:278-6094

Dr Parviz Moin
Center for Turbulence Research
Stanford University
Stanford CA 94305-3032
(415)725-2081

Dr H Mongia
General Motors Corporation
Allison Gas Turbine Operations
P. O. Box 420
Indianapolis IN 46206-0420
(317)230-5945

Dr Peter Monkewitz
Mechanical, Aerospace and
    Nuclear Engineering Dept
University of California
Los Angeles CA 90024
(213)825-5217

Dr P J Morris
233-L Hammond Building
Pennsylvania State University
University Park PA 16802
(814)863-0157

Dr Edward Mularz
Aviation Res. and Tech. Activ.
NASA Lewis Res. Ctr., MS 5-11
21000 Brookpark Road
Cleveland OH 44135-3127
(216)433-5850

Dr M G Mungal
Department of Mechanical
    Engineering
Stanford University
Stanford CA 94305-3032
(415)725-2019
FAX:723-1748

Dr Phillip E Muntz
Department of Aerospace Engrg
Univ of Southern California
854 West 36th Place, RRB 101
Los Angeles CA 90089-1191
(213)740-5366

Dr Arje Nachman
AFOSR/NM
110 Duncan Avenue, Suite B115
Bolling AFB DC 20332-0001
(202)767-5028
DSN 297-5028
nachman@afosr.af.mil

Dr Abdollah Nejad
WL/POPT
Building 18
1921 Sixth Street, Suite 10
Wright-Patterson AFB OH 45433-7655
(513)255-9991
DSN 785-9991
FAX:255-1759

Dr Herbert Nelson
Code 6110, Chemistry Division
Naval Research Laboratory
Washington DC 20375-5342
(202)767-3686

Dr David Nixon
Department of Aeronautical Eng
The Queen's Univer of Belfast
Stranmillis Road
Belfast BT9 5AG N Ireland UK
(0232)245133
FAX0232 382701

Dr G B Northam
NASA Langley Research Center
MS 168
Hampton VA 23665-5225
(804)864-6248

Dr R C Oldenborg
Chemistry Division
Los Alamos National Laboratory
Los Alamos NM 87545
(505)667-2096
(505)667-3758

Dr A K Oppenheim
Department of Mechanical
    Engineering
University of California
Berkeley CA 94720
(415)642-0211

Dr Elaine Oran
Code 6404, LCP&FD
US Naval Research Laboratory
Washington DC 20375-5344
(202)767-2960
FAX:767-4798
ORAN@lcp.nrl.navy.mil

Dr Simon Ostrach
Case Western Reserve Univ
Department of Mechanical and
    Aerospace Engineering
Cleveland OH 44106

Dr Richard Peterson
Department of Mechanical
    Engineering
Oregon State University
Corvallis OR 97331-6001
(503)754-2567

Dr W M Pitts
National Institute of
Standards and Technology
Center for Fire Research
Gaithersburg MD 20899
(301)975-6486

Dr Robert Pitz
Department of Mechanical and
    Materials Engineering
Vanderbilt University
Nashville TN 37235
(615)322-0209

Dr S B Pope
Department of Mechanical and
    Aerospace Engineering
Cornell University
Ithaca NY 14853-1301
(607)255-4314

Dr C L Proctor II
Department of Mechanical
    Engineering
University of Florida
Gainesville FL 32611
(904)392-7555

Dr Herschel Rabitz
Department of Chemistry
Princeton University
Princeton NJ 08544-1009
(609)258-3917
FAX:258-6746

Dr Saad Ragab
Engrg Sci & Mechanics Dept
Virginia Polytechnic Institute
and State University
Blacksburg VA 24061
(703)231-5950

Dr S R Ray
National Institute of
Standards and Technology
Center for Chemical Engrg
Gaithersburg MD 20899

Dr R G Rehm
National Institute of
Standards and Technology
Center for Fire Research
Gaithersburg MD 20899
(301)975-2704

Dr Rolf D Reitz
Mechanical Engineering Dept
University of Wisconsin
1500 Johnson Drive
Madison WI 53706
(608)262-0145
FAX:262-6717

Dr M Renksizbulut
Department of Mechanical
Engineering
University of Waterloo
Waterloo, Ontario CN N2L 3G1
(519)885-1211
Ext 3977

Dr David Reuss
Fluid Mechanics Department
General Motors Research Labs
30500 Mound Road
Warren MI 48090-9055
(313)986-0029

Dr William Reynolds
Department of Mechanical
Engineering
Stanford University
Stanford CA 94305-3032
(415)723-3840

Dr James Riley
Mechanical Engineering Dept
University of Washington
Seattle WA 98195
(206)543-5347

Dr Michael Roco
National Science Foundation
Chemical and Thermal Syst Div
1800 G Street, N W
Washington DC 20550
(202)357-9606

Dr U S Rohatgi
Department of Nuclear Energy
Brookhaven National Laboratory
Upton NY 11973
(516)282-2475

Dr Glenn Rolader
Science Applications
International Corporation
1247-B N Eglin Parkway
Shalimar FL 32579
DSN 872-0391
(904)882-0391

Dr W M Roquemore
WL/POSF
Building 490
1790 Loop Road, N
Wright-Patterson AFB OH 45433-7103
(513)255-6813
DSN 785-6813
FAX:255-1125

Dr Anatol Roshko
Graduate Aeronautical Labs
California Institute of
   Technology
Pasadena CA 91125
(818)356-4484

Dr Daniel Rosner
Department of Chemical
   Engineering
Yale University
New Haven CT 06520
(203)432-4391

Dr John Ross
Department of Chemistry
Stanford University
Stanford CA 94305-3032
(415)723-9203

Dr Gabriel Roy
Office of Naval Research
Mechanics Division, Code 1132
800 North Quincy Street
Arlington VA 22217-5000
(703)696-4405
FAX:696-0934
roy@ocnr-hq.navy.mil

Mr Kurt Sacksteder
NASA Lewis Research Center
MS 500-217
21000 Brookpark Road
Cleveland OH 44135
(216)433-2857

Dr Leonidas Sakell
AFOSR/NA
110 Duncan Avenue, Suite B115
Bolling AFB DC 20332-0001
(202)767-4935
DSN 297-4935
FAX:767-4988
sakell@afosr.af.mil

Dr Mohammad Samimy
Ohio State University
Mechanical Engineering Dept
206 West 18th Street
Columbus OH 43210-1107
(614)422-6988

Dr G S Samuelsen
Department of Mechanical
  Engineering
University of California
Irvine CA 92717
(714)856-5468

Mr John Sanborn
Garrett Turbine Engine Company
111 South 34th Street
P. O. Box 5217
Phoenix AZ 85010
(602)231-2588

Dr Billy Sanders
University of California
Davis CA 95616

Dr Joseph Sangiovanni
United Technologies Research
  Center
Silver Lane
East Hartford CT 06108
(203)727-7328

Dr Lakshmi Sankar
School of Aerospace Engrg
Georgia Institute of
  Technology
Atlanta GA 30332
(404)894-3014

Dr Domenic Santavicca
Department of Mechanical
  Engineering
Pennsylvania State University
University Park PA 16802
(814)863-1863

Dr R J Santoro
Department of Mechanical
  Engineering
Pennsylvania State University
University Park PA 16801
(814)863-1285

Mr William Scallion
NASA Langley Research Center
Mail Stop 408
Hampton VA 23665
(804)864-5235

Dr Klaus Schadow
Naval Air Warfare Center
Code 3892
China Lake CA 93555-6001
(619)939-6532
DSN 437-6532
FAX:939-6569

Dr John Schaefer
Energy and Environmental Div.
Acurex Corporation
555 Clyde Ave., P. O. Box 7555
Mountain View CA 94039

Dr W H Schofield
Aeronautical Research Labs
506 Lorimer St, Fishermen's Bn
Box 4331, P O
Melbourne, Victoria AUSTRALIA 3001

Dr Thomas A Seder
Rockwell International Sci Ctr
1049 Camino dos Rios
P O Box 1085
Thousand Oaks CA 91360
(805)373-4576

Dr D J Seery
United Technologies Research
    Center
Silver Lane
East Hartford CT 06108

Dr Hratch Semerjian
National Institute of
Standards and Technology
Chem Sci & Tech Laboratory
Gaithersburg MD 20899
(301)975-3145
FAX:975-3845
HRATCH@NBSMICF

Dr K Seshadri
Center for Energy and
    Combustion Research, 0411
University of California
La Jolla CA 92093-0411
(619)534-4876

Dr G S Settles
309 Mechanical Engrg Building
Pennsylvania State University
University Park PA 16802
(814)863-1504

Dr Robert Shaw
Division of Chemical and
    Biological Sciences
U S Army Research Office
Research Triangle Park NC 27709-221
(919)549-0641

Mr Harold Simmons
Parker Hannifin Corporation
Gas Turbine Fuel Systems Div.
17325 Euclid Avenue
Cleveland OH 44143
(216)531-3000
Ext 2309

Dr Neeraj Sinha
Science Applications
International Corporation
501 Office Ctr Dr, Suite 420
Fort Washington PA 19034-3211
(215)542-1200
FAX:542-8567

Dr William Sirignano
School of Engineering
University of California
Irvine CA 92717
(714)856-6002

Dr Bernard Spielvogel
U S Army Research Office
P O Box 12211
Research Triangle Pk NC 27709-2211

Dr F Dee Stevenson
Office of Basic Energy Science
U. S. Department of Energy
1000 Independence Avenue, N W
Washington DC 20585

Dr David Stewart
Department of Theoretical and
   Applied Mechanics
University of Illinois
Urbana IL 61801

Dr Anthony Strawa
NASA Ames Research Center
MS 230-2
Moffett Field CA 94035
(415)604-3437

Dr F D Stull
WL/POPS
Wright-Patterson AFB OH 45433-6563
(513)255-5210
DSN 785-5210

Dr Geoffrey J Sturgess
Pratt & Whtiney Aircraft Group
United Technologies Corpor
400 Main Street
East Hartford CT 06108
(203)565-5437

Dr B Sturtevant
Engrg and Appl Sci Dept
California Institute of
   Technology
Pasadena CA 91125

Dr G Sullins
Applied Physics Laboratory
Johns Hopkins University
Johns Hopkins Road
Laurel MD 20707-6099
(301)953-5000

Dr Dexter Sutterfield
National Institute for
Petroleum and Energy Research
Post Office Box 2128
Bartlesville OK 74005
(918)337-4251

Dr Larry Talbot
Department of Mechanical
   Engineering
University of California
Berkeley CA 94720
(415)642-6780

Dr Richard Tam
Department of Mathematics
Indiana University-Purdue
    University
Indianapolis IN 46205

Dr Christopher Tam
Department of Mathematics
Florida State University
Tallahasee FL 32306-3027
(904)644-2455

S Richard Tankin
Mechanical Engineering Dept
Northwestern University
Evanston IL 60208-3111
(708)491-3532

Dr Julian Tishkoff
AFOSR/NA
110 Duncan Avenue, Suite B115
Bolling AFB DC 20332-0001
(202)767-0465
DSN 297-0465
FAX:767-4988
tishkoff@afosr.af.mil

Dr T Y Toong
Department of Mechanical
    Engineering
MIT
Cambridge MA 02139
(617)253-3358

Dr Michael Trenary
Department of Chemistry
The University of Illinois
Chicago IL 60680

Dr Timothy Troutt
Department of Mechanical
    Engineering
Washington State University
Pullman WA 99164-2920

Dr Allen Twarowski
Rockwell International Sci Ctr
1049 Camino dos Rios
P O Box 1085
Thousand Oaks CA 91360
(805)373-4576

Dr C J Ultee
United Technologies Research
    Center
Silver Lane
East Hartford CT 06108

Dr A D Vakili
University of Tennessee
Space Institute
Tullahoma TN 37388

Dr S P Vanka
Department of Mechanical
    and Industrial Engrg
University of Illinois
Urbana IL 61801

Dr Earl VanLandingham
National Aeronautics & Space
    Administration, Code RB
400 Maryland Avenue, SW
Washington DC 20546
(202)453-2847

Dr P J Waltrup
Applied Physics Laboratory
Johns Hopkins University
Johns Hopkins Road
Laurel MD 20707-6099
(301)953-5000
Ext. 5626

Dr Joe Wanders
AL/EQS
139 Barnes Drive
Tyndall AFB FL 32403-5319
(904)283-6026
DSN 523-6026

Dr Charles Westbrook
Lawrence Livermore National
    Laboratories
P. O. Box 808
Livermore CA 94550

Dr James Whitelaw
Department of Mechanical Engrg
Imperial College of Science
    and Technology
London SW7 2BX UK

Dr Forman Williams
Center for Energy and
    Combustion Research, 0411
University of California
La Jolla CA 92093-0411
(619)534-5492

Dr Michael Winter
Propulsion Science
United Technologies Research
    Center
East Hartford CT 06108
(203)727-7805

Mr Steve Wirick
WL/AAWW-3
Wright-Patterson AFB OH 45433-6543
(513)255-4174
DSN 785-4174
FAX:476-4642

Dr Bernard T Wolfson
Wolfson Associates
    International
4797 Lake Valencia Blvd West
Palm Harbor FL 33563
(813)786-3007

Dr J M Wu
University of Tennessee
Space Institute
Tullahoma TN 37388

Dr Richard Yetter
Department of Mechanical and
    Aerospace Engineering
Princeton University
Princeton NJ 08544-5263

Dr Pui-kuen Yeung
School of Aerospace Engrg
Georgia Institute of
    Technology
Atlanta GA 30332-0150
(404)894-9341
FAX:894-2760
yeung@peach.gatech.edu

Dr Shaye Yungster
Institute for Computational
Mechanics in Propulsion
NASA Lewis Research Ctr
Cleveland OH 44135
(216)433-6680

Dr Michael Zachariah
National Institute of
Standards and Technology
Center for Chemical Engrg
Gaithersburg MD 20899
(301)975-2063

Mr Fred Zarlingo
Code 3246
Naval Air Warfare Center
China Lake CA 93555-6001
(619)939-7395
DSN 437-7395

Dr E E Zukoski
Engrg. and Appl. Sci. Dept.
California Institute of
    Technology
Pasadena CA 91125
(818)356-4785

ROCKET PROPULSION

Invitees

Dr George Adams
USA-BRL
AMXBR-I8D
Aberdeen Proving Gnd MD 21005-5006
(410)278-6168
(410)278-6783

Dr Horst Adolph
Synthesis and Formulations Br
Naval Surface Weapons Center
10901 New Hampshire Avenue
Silver Spring MD 20903-5000

Dr William E Anderson
Department of Mechanical
    Engineering
Pennsylvania State University
University Park PA 16802
(814)863-6289

Lt John Andreshak
OLAC PL/LKLR
Stop 24
Edwards AFB CA 93523-5000
(805)275-5194
AV525-5194

Mr Chris Andrews
OLAC PL/LSVE
Edwards AFB CA 93523-5000
(805)275-5766
AV 525-5766

Dr Ron Atkins
Naval Weapons Center
China Lake CA 93555-6001
(619)939-1630
AV437-1630

Dr William Bailey
AFIT/ENP
Wright-Patterson AFB OH 45433-6583
(513)255-4498
AV785-4498

Dr Joseph Baum
SAIC
1710 Goodridge Drive
P.O. Box 1303,
McLean VA 22102
(703)827-4952

Dr Roger Becker
KL-462
Research Institute
University of Dayton
Dayton OH 45469
(513)229-3938

Mr Charles Beckman
OLAC PL/MKPA
Stop 24
Edwards AFB CA 93523-5000
(805)275-5487
AV525-5487

Dr Merrill Beckstead
Dept of Chemical Engineering
Brigham Young University
Provo UT 84602
(801)378-6239

Dr Robert Beddini
Univ of Illinois
AAE Department
104 South Mathews Avenue
Urbana IL 61801-2997
(217)333-4239

Dr Clifford Bedford
SRI International
Chemistry Laboratory
Menlo Park CA 94025
(415)859-4449

Dr S J Bennett
Adv Technology Projects Div
Morton Thiokol, Inc, Wasatch
Box 524
Brigham City UT 84302
(801)863-2980

Dr Greg Berry
Argonne National Laboratory
9700 South Cass Avenue
Argonne IL 60439
(312)972-6160

Dr Oscar Biblarz
Department of Aeronautics
Naval Post Graduate School
Monterey CA 93943-5100
(408)646-2972
AV878-2972

Dr S Binkley
Combustion Research Facility
Sandia National Laboratories
Livermore CA 94551-0969

Dr Mitat Birkan
AFOSR/NA
110 Duncan Ave, Suite B115
Bolling AFB DC 20332-0001
(202)767-4938
AV297-4938

Dr Fred Blomshield
Code 3892,Propulsion
Research Branch
Naval Weapons Center
China Lake CA 93555
(619)939-3650
AV437-3650

Dr Arthur Bracut
ARDC
LCWSL
Dover NJ 07801
(201)724-3788
AV880-3788

Dr Mel Branch
Mechanical Engineering Dept
University of Colorado
Boulder CO 80309-0427
(303)492-6318
(303)492-7151

Dr John Brandenburg
Mission Research Corporation
8560 Cinderbed Road
Suite 700
Newington VA 22122
(703)339-6500

Dr Thomas Brill
University of Delaware
Department of Chemistry
Newark DE 19716
(302)831-6079

Dr Robert Brown
486 Birch Way
Santa Clara CA 95051
(408)248-8522

Dr Rodney Burton
Dept. of Aero. And Astro. Engg
University Of Illinois-UC
101 Transportation Building
Urbana IL 61801-2997
(217)333-2651

Mr David Byers
NASA Lewis Research Center
MS 500-219
21000 Brookpark Road
Cleveland OH 44135-3127
(216)433-2447

Dr George Caledonia
Physical Sciences Inc
20 New England Business Center
Andover MA 01810
(617)475-9030

Dr David Campbell
OLAC PL/RKFA
9 Antares Road
Edwards AFB CA 93523-5000
(805)275 6177

Dr Mark Cappelli
Stanford University
Mechanical Engineering Dept.
Stanford CA 94305-3032
(415)723-1745
Fax 723-1748

Dr Robert Carrol
Pratt & Whitney
P.O. Box 109600
West Palm Beach FL 33410-9600
(407)796-2889

Dr Robert Cassel
Naval Sea Systems Command
Code 62D
Washington DC 20362
(202)692-8635

Dr Leonard Caveny
OSD/SDIO/IST
Pentagon
Washington DC 20301-7100
(703)693-1687

Dr Yunus Ali Cengel
University of Nevada-Reno
Dept of Mechanical Engg
Reno NV 89557-0030

Dr Baki M. Cetegen
Mechanical Engineering Dept
U-139 ME
University of Connecticut
Storrs CT 06268
(203)486-2966

Dr May Chan
Naval Weapons Center
China Lake CA 93555-6001
(619)939-7519
AV437-7519

Dr C I Chang
AFOSR/NA
110 Duncan Ave, Suite B115
Bolling AFB DC 20332-6448
(202)767-4987
FAX:767-4988

Dr Franklin Chang-Diaz
Lyndon B Johnson Space Center
Code CB
Houston TX 77058
(713)483-2714

Dr Robert Chapman
OLAC PL/LKLR
Stop 24
Edwards AFB CA 93523-5000
(805)275-5416
AV525-5416

Dr Malcolm Chase
Center for Chemical Physics
National Inst of Stds & Tech
Building 222, Room A158
Gaithersburg MD 20899
(301)975-2526

Dr Fan-Bill Cheung
Penn State University
208 Mechanical Engineering
University Park PA 16802
(814)863-4281
FAX 865-3389

Dr Peck Cho
Dept. of Mechanical Engg.
College of Engineering
Michigan Technological Univ.
Houghton MI 49931

Dr Won-Ho Choe
214 Nuclear Engineering Lab
University of Illinois
103 South Goodwin Avenue
Urbana IL 61801
(217)333-2821

Dr Chan K Choi
Purdue University
School of Nuclear Engrg
West Lafayette IN 47907
(317)494-6789

Dr Edgar Choueriri
Department of Mechanical And
Aerospace Engineering
Princeton University
Princeton NJ 08544-5263
(609)258-5221

Dr Karl Christe
Rocketdyne Division
Rockwell International
6633 Canoga Ave
Canoga Park CA 91304
(818)710-3268

Dr T J Chung
University of Alabama
Huntsville AL 35801
(205)895-6394

Dr George Clark
Aerojet Tactical Systems
PO Box 13400
Building 0525
Sacramento CA 95813
(916)988-6919

Dr William Clark
Naval Weapons Center
Code 3895
China Lake CA 93555-6001

Dr Ronald Cohen
The Aerospace Corporation
PO Box 92957
Mail Stop M5-754
Los Angeles CA 90009
(213)336-5946

Dr Norman Cohen
Aerospace Corporation
PO Box 92957
M/S 747
Los Angeles CA 90045
(213)648-7427

Dr Norman Cohen
Professional Services
141 Channing St
Redlands CA 92373
(714)792-8807

Dr Cliff Coon
Lawrence Livermore National
Laboratories
Livermore CA 94550
(415)422-6311

Dr Robert Corley
OLAC PL/DYC
Stop 24
Edwards AFB CA 93523-5000
(805)275-5620
AV525-5353

Dr George Cox
United Technologies
Pratt-Whitney
P.O. Box 109600
West Palm Beach FL 33410-9600
(407)796-2887
FAX 796-5825

Dr F E C Culick
Engrg and Appl Sci Dept
California Institute of
    Technology
Pasadena CA 91125
(818)356-4470

Dr C L Dailey
TRW Space and Technology Group
Applied Technology Division
One Space Park
Redondo Beach CA 90278
(213)536-1874

Dr John Daily
University of Colorado
Engineering Center ME 1-13
Campus Box 427
Boulder CO 80309-0427
(303)492-7110

Dr B R Daniel
School of Aerospace Rngrg
Georgia Institute of
    Technology
Atlanta GA 30332

Mr S T Demetriades
STD Research Corp
P.O. Box C
Arcadia CA 91006
(818)357-2311

Dr Gregory Dobbs
United Technologies Res. Ctr.
MS 129-90 Silver Lane
East Hartford CT 06108
(203)727-7145
FAX 727-7669

Dr Joel Dubow
Materials Science
Univ of Utah
2008B Mechanical Engrg Bldg
Salt Lake City UT 84112
(801)581-8388

Dr John Eisch
Department of Chemistry
State University of New York
Binghamton NY 13901
(607)798-3994

Dr Daniel A Erwin
Dept of Aerospace Engg
University of Southern
California
Los Angeles CA 90089-1191
(213)740-5358

Dr William Escher
NASA Headquarters
Code RP
Washington DC 20546
(202)453-9111

Dr James Fang
Rockwell/Rocketdyne Division
6633 Canoga Park
Canoga Park CA 91303
(818)718-3728
FAX 718-3600

Mrs Karen Farner
OLAC PL/RKLB
Edwards AFB CA 93523-5000
(805)275-5198
AV525-5198

Dr Allan Ferrenberg
Manager, Advanced Comb. Device
Rocketdyne Div, Rockwell Int.
Mail Stop IR06,6633 Canoga Ave
Canoga Park CA 91303
(818)718-3713

Dr John Fischer
Code 3853
Naval Weapons Center
China Lake CA 93555-6001
(619)939-1641
AV437-1641

Dr J E Flanagan
Rocketdyne
6633 Canoga
Canoga Park CA 91304
(818)710-2466

Dr Gary Flandro
Univ. of Tennessee
Space Institute
Tullahoma TN 37388
(615)455-0631
(615)393 7217

Dr Arthur Fontijn
Chemical & Environmental
  Engineering Department
Rensselaer Polytechnic Inst.
Troy NY 12180-3590
(518)276-6508

Dr Milt Frankel
Rocketdyne
6633 Canoga Avenue
Canoga Park CA 91304
(818)710-4803
(818)710-5088

Dr R A Frederick
Sverdrup Technology, Inc
Mail Stop 900
Arnold AFB TN 37389-9998
(615)454-3130

Dr Sheilah Fultz
Naval Weapons Center
China Lake CA 93555-6001
(619)939-7521
AV437-7521

Dr Eugene Gerber
Univ of Dayton Research
  Institute
KL465
Dayton OH 45419
(513)229-3221

Dr Robert Ghirardelli
U.S. Army Research Office
P.O. Box 12211
Research Triangle Pk NC 27709-2211
(919)549-0641
AV935-3331

Dr David Golden
SRI International
333 Ravenswood Avenue
Menlo Park CA 94025-3696
(415)859-0811

Dr D Goodwin
Mech. Engg&Applied Science
California inst. of Tech.
Mail Stop 213-6
Pasadena CA 91125
(818)356-4249

Dr B B Goshgarian
OLAC PL/MKPB
Stop 24
Edwards AFB CA 93523-5000
(805)275-5183
AV525-5183

Dr William Graham
Morton Thiokol, Inc
Huntsville Division
Huntsville AL 35807-7501
(205)882-8397

Dr Alten Grandt
Department of Aeronautics
and Astronautics
Purdue University
West Lafayette IN 47907

Dr Ashwani K Gupta
Director, Combustion Lab.
The University of Maryland
Dept. of Mechanical Engrg.
College Park MD 20742
(301)454-8865

Mr Eugene Haberman
OLAC PL/MK
Stop 24
Edwards AFB CA 93523-5000
(805)275-5420
AV525-5420

Dr Kirk E. Hackett
EOARD
PSC 802 BOX 14
FPO, AE 09499-0200
071-409-4354
F071-402-9618

Dr Marc Hallada
PSC 802 BOX 14
FPO AE 09499-0200
71 409-4437
fx71402-9618

Dr V E Haloulakos
Advanced Propulsion
McDonnell Douglas
5301 Bolsa Avenue
Huntington Beach CA 92647
(714)896-3456

Dr Elmer Hansen
Department of Mechanical
Engineering
University of Florida
Gainesville FL 32611
(904)392-0802

Lt Col George Haritos
AFOSR/NA
Bolling AFB DC 20332-6448
(202)767-4987
FAX:767-0466

Dr Kenneth Harstad
Jet Propulsion Laboratory
4800 Oak Grove Drive
Pasadena CA 91109

Dr David Hastings
Department of Aeronautics
and Astronautics
Massachusetts Inst of Tech
Cambridge MA 02139
(617)253-0906

Ms Sharon Hasty
John Hopkins Univ/APL
CPIA
John Hopkins Road
Laurel MD 20707
(301)992-7306

Dr Donald Hautman
United Technologies Res. Ctr.
Silver Lane
East Hartford CT 06108
(203)727-7424

Dr Clark W. Hawk
Mechanical Engineering Dept
College of Engineering
Propulsion Research Center
Huntsville AL 35899
(205)895-6474
Fax 895-6758

Dr Thomas Hawkins
OLAC/PL/LKLR
Stop 24
Edwards AFB
CA 93523-5000
(805)275-5749
AV 525-5749

Dr Stephen D Heister
School of Aeronautics
and Astronautics
323 Grissom Hall
West Lafayette IN 47907
(317)494-0307
F 494-0307

Dr Helmut Hellwig
AFOSR/CC
110 Duncan Ave,Suite B115
Bolling AFB DC 20332-0001
(202)767-5017
AV297-5017

Dr Alan Hersh
Hersh Acoustical Engineering
9545 Cozycroft Avenue
Chatsworth CA 91311
(818)998-8311
FAX 341-0978

Dr Rich Hollins
Naval Weapons Center
China Lake CA 93555-6001
(619)939-1650
AV437-1650

Dr H R Jacobs
Mechanical Engg Bldg, 208
Penn State University
University Park PA 16802
(814)863-2519
FAX 865-3389

Dr J I Jagoda
Aerospace Engineering Dept
Georgia Institute of
Technology
Atlanta GA 30329
(404)894-3060

Dr Donald Jassowski
Aerojet Technical Systems Co
PO Box 13222
Sacramento CA 95813
(916)355-2849

Dr S M Jeng
Dept. of Aero&Engineering
University of Cincinnati
797 Rhodes Hall#70
Cincinnati OH 45221-0070

Dr Robert Jensen
Rockwell/Rocketdyne Division
6633 Canoga Ave
Canoga Park CA 91303
(818)718-3730
FAX 718-3600

Dr M W Johnson
Head of Neutron Inst. Division
Rutherford Appleton Laboratory
Science Department
Chilton, Didcot, Oxon UK OX11 OQX
0235-21900
0235-44-5720F

Dr Abraham Kadish
Earth and Space Sciences Div.
Atmospheric Sciences Group
Mail Stop D466, LANL
Los Alamos NM 87545

Dr Jordin Kare
Building 197, Room 1020
Lawrence Livermore Nat'l Lab
P O Box 808
Livermore CA 94550
(415)423-8300

Dr David Kassoy
Dept of Mechanical Engineering
University of Colorado at
Boulder, Campus Box 427
Boulder CO 80309
(303)492-2991
(303)492-7694

Dr Myron Kaufman
Department of Chemistry
Emory University
Atlanta GA 30322
(404)727-6619

Dr Dennis Keefer
University of Tennessee
Space Institute
Tullahoma TN 37388
(615)455-0631

Dr Arnold A Kelly
Department of Mechanical and
    Aerospace Engineering
Princeton University
Princeton NJ 08544-5263
(206)452-5221

Dr Philip Kessel
OLAC PL/LSCF
Edwards AFB CA 93523-5000

Dr Sue Kim
California State University
6000 J Street
Sacramento CA 95819
(916)454-6712

Mr Mark Kleim
NASA Lewis Research Center
21000 Brookpark Rd
MS 510-219
Cleveland OH 44135

Dr Kenneth Kolouko
Morton Thiokol
Wasatch Division
P.O. Box 524
Brigham City UT 84302
(801)863-4220

Dr James Komar
Atlantic Research Corp
5390 Cherokee Avenue
Alexandria VA 23312
(703)642-4473

Dr Herman Krier
Dept of Mechanical and
    Industrial Engineering
University of Illinois
Urbana IL 61801
(217)333-0529

Prof M Kristiansen
P.W. Horn Professor
Dept of Electrical Engg,MS3102
Texas Tech University
Lubbock TX 79409-4439
(806)792-3007

Dr Warren Krueger
167 Alvana Street, NW16-160
Massachusetts Institute of
    Technology
Cambridge MA 02139
(617)253-0236

Dr Paul Kuentzmann
Office National D'Etudes et de
rechersches Aerospatiales
29,Ave. de la Division Leclerc
Chatillon-sous-Bagneux France

Dr Kenneth Kuo
Penn State University
208 Mechanical Engineering
University Park PA 16802
(814)863-6741
FAX 863-3203

Dr William Larson
OLAC PL/LSVF
Edwards AFB CA 93523-5000
(805)275-5657
AV525-5657

Dr C K Law
Department of Mechanical and
    Aerospace Engineering
Princeton University
Princeton NJ 08544-5263
(609)258-5271

Dr Joel Lebowitz
Rutgers-The State University
Department of Mathematics
Hill Center-Busch Campus
New Brunswick NJ 08903
(201)932-3117

Mr Edward Lee
Special Projects Leader
P.O. Box 808,L-368
LLNL-University of California
Livermore CA 94550
(415)422-1316

Dr Ja H Lee
NASA Langley Research Center
M/S493
Hampton VA 23665
(804)864-4332

Dr G Lengelle'
Office National D'Etudes et de
Recherches Aerospatiales
29,Ave de la Division Lecherc
France

Mr Jay Levine
OLAC PL/LSCF
Edwards AFB CA 93523-5000
(805)275-5366
AV 525-5366

Dr P Y Liang
Advanced Combustion Devices
Rocketdyne Div, Rockwell Int.
6633 Canoga Avenue
Canoga Park CA 91303

Lt Col R Lisowski
EOARD
Box 14
FPO NY 09510-0200
71-402-4505
AV235-4505

Dr George Lo
Lockheed Palo Alto Research
    Laboratory
3251 Hanover St, 8204-93-50
Palo Alto CA 94304
(415)424-2514

Dr Shankar Mahalingam
Dept of Mechanical Engineering
The University of Colorado
Boulder CO 80309-0019
(303)492-7236

Dr David Mann
Army Research Office
P.O. Box 12211
Research Triangle Pk NC 27709-2211
(919)549-4249
AV832-4249

Dr Stephen Margolis
Combustion Research Facility
Sandia National Laboratories
Livermore CA 94551-0969

Dr Manuel Martinez-Sanchez
Aeronautics and Astronautics
Massachusetts Inst of Tech
Building 37-401
Cambridge MA 02139
(617)253-5613

Dr Jyotirmoy Mazumder
Department of Mechanical and
    Industrial Engineering
University of Illinois
Urbana IL 61801
(217)333-1964

Dr Geoffrey Main
School of Mechanical Engrg
Georgia Institute of
    Technology
Atlanta GA 30332-0420
(404)894-3242
(404)951-8058

Prof Alan Marchand
Dept of Chemistry
North Texas State Univ
NTSU Station, Box 13767
Denton TX 76203-5068
(817)565-3823

Lt Col Charles Martin
Nuclear Weapons Development
The Pentagon
Room 5D543
Washington DC 20330-5040
(202)693-6303
AV244-6303

Dr Peter Mattern
Combustion Sciences
Sandia National Laboratories
Livermore CA 94551-0969

Dr John McKee
McDonnell Douglas Astronautics
5301 Bolsa Avenue
Huntington Beach CA 92647
(714)896-1133

Dr John McVey
Rasor Associates, Inc
253 Humboldt Court
Sunnyvale CA 94086
(408)734-1622

Dr Franklin Mead
OLAC PL/LKVE
Edwards AFB CA 93523-5000
(805)275-5540
AV525-5540

Dr Carl Melius
Sandia National Laboratories
Livermore CA 94551-0969
(415)294-2650

Dr Charles Merkle
205 ME
Pennsylvania State University
University Park PA 16802
(814)863-1501
FAX 865-3389

Dr Claude Merrill
OLAC PL/MKPL
Stop 24
Edwards AFB CA 93523-5000
(805)275-5169
AV525-5169

Prof Dr Ernst Messerschmid
University of Stuttgart
Pfaffenwaldring 31
D-7000, Stuttgart 80
Germany
0711-685-2375
fax 685-2010

Dr Michael Micci
233 Hammond Building
Pennsylvania State University
University Park Pa 16802
(814)863-0043

Dr George Miley
University of Illinois
103 South Goodwin Avenue
214 Nuclear Engineering Lab
Urbana IL 61801
(217)333-3772

Dr Richard Miller
Office of Naval Research
Mechanics Division, Code 432
800 North Quincy Street
Arlington VA 22217-5000
(202)696-4403

Dr Charles Mitchell
Dept. of Mechanical Engineerin
Colorado State University
Fort Collins CO 80523
(303)491-6654

Mr T S Mogstad
McDonnell Douglas Astr.Co-West
Design And Tech. Center
Huntington Beach CA 92647
(714)896-3437

Dr Robert Moriarty
University of Illinois
    (Chicago Circle)
Department of Chemistry
Chicago IL 60680
(312)996-2364

Dr Kenneth Moses
Fusion Physics and Technology
3547 Voyager Street, Suite 104
Torrance CA 90503-1667
(213)542-3800

Dr Philip Muntz
Dept. of Aerospace Engineering
University of Southern
    California
Los Angeles CA 90089

Dr S N B Murthy
Dept of Mechanical Engineering
Purdue University
West Lafayette IN 47907
(317)494-1509
(317)494-5639

Dr Subhash Narang
Chemistry Laboratory
SRI International
333 Ravenswood Avenue
Menlo Park CA 94025-3696

Dr Vittorio Nardi
Stevens Institute of
    Technology
Castile Point Station
Hoboken NJ 07030
(201)420-5938

Dr Thong Nguyen
Aerojet Techsystems
P.O. Box 13222
Sacramento CA 95813
(916)355-3664

Dr Jim Nichols
OLAC PL/RKLB
Edwards AFB CA 93523-5000
(805)275-5249
AV 525-5249

Dr Gary Nickerson
Software&Engineering Assoc.
1000 E. William St., Suite 200
Carson City NV 89701
(702)882-1966

Dr Arnold Nielsen
Naval Weapons Center
China Lake CA 93555-6001
(619)939-1614
AV437-1614

Mr Randy Nishiyama
R/E/WPS
US Dept of Commerce
NOAA, 325 Broadway
Boulder CO 80303-3328

Dr Douglas Olson
AeroChem Research Laboratories
    Inc.
P. O. Box 12
Princeton NJ 08542
(609)921-7070

Dr Tae-Woo Park
OLAC PL/TODP
Stop 24
Edwards AFB CA 93523-5000
(805)275-5196
AV525-5196

Col Arthur Pavel
AFOSR/CD
110 Duncan Ave, Suite B115
Bolling AFB DC 20332-0001
(202)767-5018
AV297-5018

Ms Dorothy Pecker
The John Hopkins Univ/APL
John Hopkins Rd
Laurel MD 20707

Dr Don Penn
OLAC PL/RKLB
Edwards AFB CA 93523-5000
(805)275-5316
AV525-5316

Dr Jerry Pieper
Aerojet Techsystems
P.O. Box 13222
Sacramento CA 95813
(916)355-3087

Dr Robert Poeschel
Plasma Physics Department
Hughes Research Laboratories
3011 Malibu Canyon Road
Malibu CA 90265
(213)317-5443

Dr Dimos Poulikakos
University of Illinois
(Chicago Circle)
Dept. of Mechanical Engg.
Chicago IL 60680
(312)996-5239

Dr Edward Price
School of Aerospace Engrg
Georgia Institute of
    Technology
Atlanta GA 30332-0420
(404)894-3063

Dr Richard Priem
Priem Consultants
13533 Mohawk Trail
Cleveland OH 44130
(216)845-1083

Dr Lawrence Quinn
OLAC PL/DYC
Edwards AFB CA 93523-5000
(805)275-5353
AV 525-5353

Dr Frederick Reardon
Cal State U.-Sacramento
Dept of Mechanical Engineering
6000 J Street
Sacramento CA 95616
(916)278-6727

Dr Russell Reed
Naval Weapons Center
China Lake CA 93555-6001
(619)939-7296
AV437-7296

Dr Robert Rhein
Research Chemist
Code 3244
Naval Weapons Center
China Lake CA 93555-6001
(619)939-7392
AV 437-7310

Dr J W Rich
Department of Mechanical
    Engineering
The Ohio State University
Columbus OH 43212-1194
(614)292-6309

Dr Frank Roberto
OLAC PL/MKP
Stop 24
Edwards AFB CA 93523-5000
(805)275-5430
AV525-5430

Dr Stephen Rodgers
OLAC PL/LKLR
Stop 24
Edwards AFB CA 93523-5000
(805)275-5416
AV525-5416

Mr Wayne Roe
OLAC PL/XRX
Stop 24
Edwards AFB CA 93523-5000
(805)275-5206
AV525-5206

Dr David Rosen
Physical Sciences Inc.
Dascomb Research Park
Andover MA 01810
(617)475-9030

Dr S D Rosenberg
P O Box 13222
Sacramento CA 95813
(916)355-2609

Dr Thomas Rosfjord
United Technologies Res.Ctr.
Silver Lane
East Hartford CT 06108
(203)727-7418

Dr David Ross
Director,Physical Organic Chem
SRI International
333 Ravenswood Avenue
Menlo Park CA 94025-3696
(415)859-2430

Dr J Reece Roth
Dept of Elec and Comp Engrg
316 Ferris Hall
The University of Tennessee
Knoxville TN 37996-2100
(615)974-4446

Dr Gabriel Roy
ONR Code 1132P
800 North Quincy Street
Arlington VA 22217
(202)696-4405

Dr Kevin Rudolph
Martin Marietta Corporation
Mail Stop S8071
PO Box 179
Denver CO 80201
(303)977-3681

Dr Mark Salita
Morton Thiokol/Wasatch Div
MS 280B
PO Box 524
Brigham City UT 84302
(801)863-2163

Dr Michael Salkind
President
Ohio Aerospace Institute
2001 Aerospace Parkway
Brookpark OH 44142
(216)891-2100

Dr Robert Santoro
Penn State University
Mechanical Engineering Dept
208 Mechanical Engineering
University Park PA 16801
(814)863-1285
FAX 865-3389

Dr Robert Schmitt
Chemistry Lab
SRI International
333 Ravenswood Avenue
Menlo Park CA 94025-3696
(415)859-5579

Dr Keith Schofield
Quantum Institute
University of California,
    Santa Barbara
Santa Barbara CA 93106

Dr Herbert Schrade
Institut Fur Raumfahrtantriabe
Universitat Stuttgart
Pfaffenwaldring 31
D-7000 Stuttgart GE
7116-852-383
or 375

Dr Michael Schuller
Phillips Lab/VTPN
Kirtland AFB
Albuquerque NM 87117
(505)846-2878

Dr Gary Sega
Aerospace Corp
P.O. Box 92957
MS/747
Los Angeles CA 90004
(213)648-6501

Dr Ilter Serbetci
Cleveland State University
Mechanical Engineering Dept.
MC-219
Cleveland OH 44115
(216)687-2576

Maj Scott Shackelford
F J Seiler Research Laboratory
United States Air Force Acad
Colorado Springs CO 80840
(719)472-2655

Dr R Shoureshi
School of Mechanical
    Engineering
Purdue University
West Lafayette IN 47907
(317)494-5639

Prof Jean'ne Shreeve
Dept of Chemistry
University of Idaho
Moscow ID 83843
(208)885-6552

Dr Isaac F Silvera
Harvard University
Department of Physics
Cambridge MA 02138
(617)495-9075

Dr William Sirignano
College of Engineering
University of California
Irvine CA 92717
(714)856-6002

Ms Elizabeth Slimak
OLAC PL/LSCF
Edwards AFB CA 93523-5000

Lt Col LaRell Smith
EOARD/LRC
Box 14
FPO NY 09510-0200
AV235-4505

Dr Ronald Spores
OLAC PL/LSVE
Edwards AFB CA 93523-5000
(805)275-5766
AV 525-5766

Dr Warren Strahle
School of Aerospace Engrg
Georgia Institute of
    Technology
Atlanta GA 30332
(404)894-3032

Dr William C Stwalley
The University of Iowa
Iowa Laser Facility
Chemistry and Physics
Iowa City IA 52242-1294
(319)335-1299

Dr V V Subramaniam
Department of Mechanical
    Engineering
The Ohio State University
Columbus OH 43212-1194
(614)292-6096

Dr Douglas Talley
OLAC PL/RKFT
Edwards AFB CA 93523-5000
(805)275-6174
AV525-6174

Mr Robert L Talley
Viritay Technologoies, Inc
4845 Millersport Highway
East Amherst NY 14051
(716)689-0177

Dr Mostafa Talukder
OLAC PL/LKLR
Edwards AFB CA 93523-5000
(805)275-5416
AV525-5416

Dr James Tien
Case Western Reserve
    University
Glennan Building, Room 415
Cleveland OH 44106
(216)368-4581

Prof William Trogler
Department of Chemistry
University of California, San
    Diego
La Jolla CA 92093-0310
(619)452-6175

Dr Wing Tsang
National Institute of Standard
and Technology
Chemical Kinetics Division
Gaithersburg MD 20899
(301)975-3507

Dr Peter Turchi
Aero/Astro Engineering
328 CAE Building
Ohio State University
Columbus OH 43210
(614)292-2691

Mr Gary Vogt
OLAC PL/DYCR
Stop 24
Edwards AFB CA 93523-5000
(805)275-5258
AV525-5258

Dr Robert Vondra
PO Box 596
Wrightwood CA 92397
(619)249-3451

Dr Francois Vuillot
Office National D'Etudes et de
resherches Aerospatiales
29,Ave de la Division Lecherc
Chatillon-sous-Bagneux France

Dr R H Woodrow Waesche
Atlantic Research Corporation
7511 Wellington Road
Gainesville VA 22065

Dr Richard Walker
Aerojet Techsystems
P.O. Box 13222
Sacramento CA 95813
(916)355-2694

Dr Peter Wayner
Dept of Chemical and
    Environmental Engineering
Rensselaer Polytechnic Inst
Troy NY 12180-3590
(518)276-6199

Dr David Weaver
OLAC PL/DYCR
Edwards AFB CA 93523-5000
(805)275-6177
fax 275-5886

Dr Jim Weber
Rocketdyne Division
Rockwell International Corp.
6633 Canoga Ave
Canoga Park CA 91303
(818)710-5558

Dr Richard Weiss
OLAC PL/CA
Edwards AFB CA 93523-5000
(805)275-5622
AV525-5622

Dr Rodney Willer
Morton Thiokol Inc
Elkton Division
P.O. Box 241
Elkton MD 21921
(301)398-3000
(301)398-4440

Dr Forman A Williams
Center for Energy and
    Combustion Research, 0411
University of California
La Jolla CA 92093-0411
(619)534-5492

Dr W S Williamson
Plasma Physics Department
Hughes Research Laboratories
3011 Malibu Canyon Road
Malibu CA 90265
(213)317-5443

Dr D O Woolery
Rocketdyne
6633 Canoga Avenue
Canoga Park CA 91304

Dr Ted Yang
Massachusetts Institute of
    Technology
167 Albany Street
Cambridge MA 02139
(617)253-8453

Dr Vigor Yang
Department of Mechanical
    Engineering
Pennsylvania State University
University Park PA 16802
(814)863-1502
FAX 865-3389

Dr Thomas York
AERO/ASTRO Engineering
328 CAE Building
Ohio State University
Columbus OH 43210
(614)292-2691

Dr Ben Zinn
School of Aerospace Engrg
Georgia Institute of
   Technology
Atlanta GA 30332
(404)894-3033

Mr Robert Zurawski
Program Manager
Propulsion Technology Programs
NASA HQA, OAST-MAIL CODE RP
Washington DC 20546
(202)453-2261

PROPULSION DIAGNOSTICS

Invitees

Mr Leonard Angello
Electric Power Research
    Institute
3412 Hillview Avenue
Palo Alto CA 94303
(415)855-2873

Dr William Bachalo
Aerometrics, Inc.
550 Del Rey Avenue
Unit A
Sunnyvale CA 94086
(408)738-6688

Dr Edward Beiting
Aerophysics Lab, Prop & Env Sc
The Aerospace Corporation
P O Box 92957, M5/754
Los Angeles CA 90009-2957
(310)336-7035

Dr William Bischel
Coherent, Inc.
3210 Porter Drive
Palo Alto CA 94304
(415)858-7639

Dr Richard Chang
Electrical Engineering Dept.
P. O. Box 2157, Yale Station
Yale University
New Haven CT 06520
(203)432-4272

Dr Wai K Cheng
Department of Mechanical
    Engineering
MIT
Cambridge MA 02139
(617)253-4531

Dr David Crosley
Molecular Physics Department
SRI International
333 Ravenswood Avenue
Menlo Park CA 94025-3696
(415)326-6200

Dr Gregory Dobbs
United Technologies Research
    Center - Mail Stop 90
Silver Lane
East Hartford CT 06108
(203)727-7145

Dr A C Eckbreth
United Technologies Research
    Center
Silver Lane
East Hartford CT 06108
(203)727-7269

Dr Thomas Ehlert
Department of Chemistry
Marquette University
Milwaukee WI 53233
(414)288-7066

Dr Gregory Faris
SRI International
333 Ravenswood Avenue
Menlo Park CA 94025-3493
(415)859-4131

Dr Richard Field
U. S. Army Armament R&D Center
DRSMC-LCA-G(D)
Building 382-S
Dover NJ 07801
(201)724-5844
(201)724-5682

Dr Bish Ganguly
WL/POOC-3
Wright-Patterson AFB OH 45433-6563
(513)255-2923
DSN 785-2923
FAX:476-4095

Dr Alan Garscadden
WL/CA-P
Building 18
1921 Sixth Street, Suite 5
Wright-Patterson AFB OH 45433-7650
(513)255-2246
DSN 785-2246
FAX:476-4657

Dr Larry Goss
Research Applications Division
Systems Research Labs, Inc.
2800 Indian Ripple Road
Dayton OH 45440-3696
(513)252-2706

Dr Ronald Hanson
Department of Mechanical
    Engineering
Stanford University
Stanford CA 94305-3032
(415)723-1745
FAX:723-1748

Dr D L Hartley
Combustion Sciences
Sandia National Laboratories
Livermore CA 94551-0969

Dr L Hesselink
Department of Aeronautics and
    Astronautics
Stanford University
Stanford CA 94305-3032
(415)723-3466

Dr E D Hirleman
Department of Mechanical and
    Aerospace Engineering
Arizona State University
Tempe AZ 85287
(602)965-3895
FAX:965-1384

Dr Donald Holve
Insitec
28 Bobbie Court
Danville CA 94526
(415)837-1330

Dr David Huestis
SRI International
333 Ravenswood Avenue
Menlo Park CA 94025-3493
(415)859-3464

Dr Thomas Ishii
Department of Electrical
    Engineering
Marquette University
Milwaukee WI 53233
(414)288-6998
FAX:288-7082

Dr Jay Jeffries
SRI International
333 Ravenswood Avenue
Menlo Park CA 94025-3493
(415)859-6341

Dr Roman Kuc
Department of Electrical
    Engineering
Yale University
New Haven CT 06520
(203)432-4891

Dr Marshall Long
Department of Mechanical
    Engineering
Yale University
New Haven CT 06520
(203)432-4229

Dr Bruce MacDonald
Research Applications Division
Systems Research Labs, Inc.
2800 Indian Ripple Road
Dayton OH 45440-3696
(513)252-2706

Dr T E Parker
Physical Sciences
20 New England Business Center
Andover MA 01810
(508)689-3232

Dr Timothy Parr
Naval Weapons Center
Code 3893
China Lake CA 93555
(619)939-2521

Dr S S Penner
Center for Energy and
    Combustion Research, 0411
University of California
La Jolla CA 92093-0411
(619)534-4284

Dr Emil Pfender
Department of Mechanical Engrg
125 Mechanical Engineering
The University of Minnesota
Minneapolis MN 55455

Dr John Renie
Department of Mechanical and
    Industrial Engineering
University of Illinois
Urbana IL 61801
(217)333-6199

Dr Won B Roh
Department of Engrg Physics
Air Force Institute of
    Teechnology
Wright-Patterson AFB OH 45433-6583

Dr Gregory Smith
Department of Chem Kinetics
SRI International
333 Ravenswood Avenue
Menlo Park CA 94025-3493
(415)859-3496

Dr Alan Stanton
Southwest Sciences, Inc.
1570 Pacheco Street
Suite E-11
Santa Fe NM 87501
(505)984-1322

Dr James Trolinger
MetroLaser
18006 Skypark Circle
Suite 108
Irvine CA 92714-6428
(714)553-0688

Dr John Vanderhoff
Ballistic Research Laboratory
DRSMC-BLI(A)
Aberdeen Proving Ground MD 21005
(410)278-6642

Dr James Verdieck
Rockwell International
Rocketdyne Div, M/S FA26
6633 Canoga Avenue
Canoga Park CA 91303
(818)700-4709

Dr Joda Wormhoudt
Aerodyne Research, Inc.
45 Manning Road
Manning Park Research Center
Billerica MA 01821-3976
(508)663-9500
FAX:663-4918